博士論文

Development for an improved comparison of proton-to-antiproton charge-to-mass ratio

（陽子反陽子間の質量電荷比比較の精度向上に向けた開発）

Takashi Higuchi
樋口　嵩

Development for an improved comparison of proton-to-antiproton charge-to-mass ratio

（陽子反陽子間の質量電荷比比較の精度向上に向けた開発）

Ph.D. thesis presented to

Graduate School of Arts and Sciences

the University of Tokyo

by

Takashi Higuchi

樋口　嵩

Date of submission: October 31, 2018

Date of defense: December 6, 2018

Through the creatures Thou hast made
Show the brightness of Thy glory,
Be eternal Truth displayed
In their substance transitory,
Till green Earth and Ocean hoary,
Massy rock and tender blade
Tell the same unending story —
"We are Truth in Form arrayed."

Teach me so Thy works to read
That my faith, — new strength accruing, —
May from world to world proceed,
Wisdom's fruitful search pursuing;
Till, thy truth my mind imbuing,
I proclaim the Eternal Creed,
Oft the glorious theme renewing
God our Lord is God indeed.

Give me love aright to trace
Thine to everything created,
Preaching to a ransomed race
By Thy mercy renovated,
Till with all thy fulness sated
I behold thee face to face
And with Ardour unabated
Sing the glories of thy grace

James Clerk Maxwell,
A Student's Evening Hymn, 1853

Abstract

Charge, Parity and Time (CPT) symmetry is known to be one of the most fundamental symmetries of the Standard Model of particle physics. As a consequence of CPT symmetry, it is predicted that fundamental properties of matter-antimatter conjugates are identical, apart from signs. Although no CPT violation has ever been observed, the unsolved mystery of matter-antimatter asymmetry in the universe has inspired experimental CPT tests in a variety of fields which compare these properties with high precision. As a part of such physics programs, the BASE collaboration has performed stringent CPT tests in the proton-antiproton system by Penning trap measurements, comparing as their charge-to-mass ratios and the magnetic moments.

This thesis discusses the high-precision proton-to-antiproton comparison of the charge-to-mass ratios conducted by BASE. No CPT violation was observed at a relative precision of 6.9×10^{-11} in a measurement carried out in 2014. Additional developmental works described in this thesis were performed since then to further improve the precision of the comparison.

The principle of charge-to-mass ratio comparison is based on cyclotron frequency measurements of charged particles with a Penning trap. In case of the proton-to-antiproton comparison, cyclotron frequencies are compared between an antiproton and an H^- ion rather than a proton, in order to avoid a systematic effect induced by polarity inversion of the trap.

For improvement of the precision, a two-fold strategy was conceived. The first was to install a new image-current detection system in order to eliminate a source of the most dominant systematic error in the 2014 measurement. The other was to improve the cyclotron frequency stability and therefore to reduce of the statistical uncertainty. For this purpose, an improved magnetic field shielding was developed and environment conditions of the apparatus were optimized. These upgrades and developments have been installed and commissioned in BASE 2017 antiproton run, leading to a significantly improved measurement condition. Under this condition, an improvement of precision at least by a factor of 3 over the last measurement is expected.

Contents

List of Figures

List of Tables

Part I

Introduction

1

Introduction

1.1 Background

Precision measurements have played important roles in the advances of modern physics. As represented by the history of atomic hydrogen spectroscopy in the course of the development of quantum mechanics, experiments with higher precision [1–4] have often showed a way for the theory to follow [5–9]. One notable example among them is the measurement of the energy difference between the $2S_{1/2}$ and $2P_{1/2}$ levels conducted by W. E. Lamb Jr. and R. C. Retherford [4], which discovered a limitation of the Dirac's relativistic quantum mechanics accepted at the time, and eventually led to the development of quantum electrodynamics (QED) [9].

The relevance of such precision studies remains today, which can be seen through the situation of today's particle physics. The Standard Model of particle physics [10] has been established over the last century, which describes the elementary particles as fermions and their interactions with $\mathrm{SU}(3) \otimes \mathrm{SU}(2) \otimes \mathrm{U}(1)$ gauge theory. On one hand, it has achieved significant successes. For example, the value of fine-structure constant α, which defines the electromagnetic coupling, has been measured by various experiments, and the measurements agree with the theoretical calculation based on the Standard Model with relative precisions on a level of 10^{-10} [11, 12]. The Standard Model has also correctly predicted masses of the W and the Z bosons, which are the carriers of the weak interaction [13]. In 2012, the Higgs boson, the last missing piece of the Standard Model, was discovered by experiments at the Large Hadron Collider (LHC) at CERN [14, 15].

On the other hand, the Standard Model is known to be incomplete. For example, the neutrino masses, which are necessary to explain recently discovered neutrino oscillations [16], are not included in the Standard Model. It cannot explain the observed asymmetry between abundance of matter and antimatter in the universe. Nor the gravitational interaction is included. Because of such insufficien-

cies, it is commonly believed that the Standard Model is a low-energy limit of a more fundamental theory. This led various theories beyond the Standard Model (BSM) to be proposed [17–19]. Many efforts have been made to directly detect new particles or new interactions predicted by the BSM theories in high energy experiments as represented by experiments at the LHC [20, 21]. However, none of the experiments have given a proof for the BSM theories to this present day. This is where the precision studies are highly relevant. Ultra-high precision measurements at low energies can search for undiscovered deviations from the Standard Model, which could point to new physics [22, 23]. This complementary approach enables us to indirectly search new particles and/or set limits on coupling constants in an energy region which are not accessible even by future accelerators.

The subject of this thesis is precision studies of the fundamental properties of the antiproton, the antiparticle of the proton.

Antimatter has been an intriguing subject of research since the prediction [24] and the discovery [25] of the positron, the antiparticle of the electron. Currently, an antiparticle has been found for each quark and lepton [10], and antinucleons and anti-nuclei such as antiprotons [26], antineutrons [27] and anti-helium nuclei [28] have been produced by accelerators. In 1995, antihydrogen atoms were synthesized for the first time at CERN's Low Energy Antiproton Ring (LEAR) [29].

The precision studies of antimatter provide unique tests of fundamental laws of physics, as will be discussed in more detail in the next section. Today, among other experiments on antimatter, there are six experimental groups conducting research at CERN's Antiproton Decelerator (AD) [30], a unique facility in the world which provides low-energy antiprotons usable for precision tests. These experiments are named Antihydrogen TRAP (ATRAP), Atomic Spectroscopy and Collisions Using Slow Antiprotons (ASACUSA), Antihydrogen Laser Physics Apparatus (ALPHA), Antihydrogen Experiment: Gravity, Interferometry, Spectroscopy (AEgIS), Gravitational Behavior of Antihydrogen at Rest (GBAR) and Baryon Antibaryon Symmetry Experiment (BASE)[1].

1.2 Tests of fundamental physics with antiprotons

In this section, some theoretical aspects of fundamental physics which can be addressed by precision studies of antimatter are summarized.

1.2.1 CPT symmetry

Discrete symmetries in the Standard Model

A test of CPT symmetry is one of the primary objectives in high-precision comparison of properties between matter and antimatter. CPT symmetry is defined as a symmetry of the laws of physics under a combined transformation of Charge conjugation (C), Parity transform (P) and Time reversal

[1] Listed in the order of the project approvals.

(T). These discrete operations relate the properties of particles and antiparticles. The fundamental properties of a particle such as its mass, charge, magnetic moment, and lifetime are CPT conjugates with that of its antiparticle. Consequently, CPT symmetry predicts these properties to be equal between the corresponding particle and antiparticle, apart from signs. Therefore, CPT symmetry can be tested by comparison of those physical properties between matter and antimatter.

Among the AD experiments mentioned in the last section, the purpose of ATRAP, ASACUSA, ALPHA, and BASE is to test CPT symmetry by comparison of fundamental properties of antiprotons and protons (ATRAP [31], ASACUSA [32] and BASE [33]) or spectroscopic properties of antihydrogen and hydrogen (ATRAP [34], ASACUSA [35] and ALPHA[36]).

For a long time, it was believed on the basis of the fundamental equations of classical dynamics and electromagnetism that the individual C-, P- and T symmetries are conserved in general physical processes. However, investigations on the weak interaction since the 1950s [37–39] have revealed that C- and P symmetries are violated in the weak interaction. Later, also the T- and CP symmetries were found to be violatedin K meson decays [40]. Currently, C- and P- violations have been understood as the V-A form of the weak interaction [41]. The CP violation has been incorporated in the Standard Model by the CKM matrix [42, 43] which mixes three generations of quarks. Even so, it is worth to note that these theoretical treatments are not determined by the fundamental guiding principles, but chosen among other possibilities to explain experimental observations.

Despite these discoveries of the violations of the other discrete symmetries, CPT symmetry has stood all the experimental tests so far. A theorem called CPT theorem has been proven, which states that CPT symmetry holds for any relativistic quantum field theory on the basis of a few fundamental assumptions: Lorentz invariance, unitarity, locality, and flat space-time [44]. Thus a test of CPT symmetry examines the very foundations of the Standard Model.

Baryon asymmetry

One mystery which motivates to test CPT symmetry is a so-called baryon asymmetry. It is an unexplained dominance of matter over antimatter in the baryonic sector observed in the cosmological scale. The baryon asymmetry η is expressed by

$$\eta = \frac{N_{\mathrm{B}} - N_{\bar{\mathrm{B}}}}{N_{\gamma}} \tag{1.1}$$

where N_{B} and $N_{\bar{\mathrm{B}}}$ represent the number of baryons and antibaryons, respectively. N_{γ} represents the number of photons in the present universe. From the latest observations, the asymmetry is estimated to be $\eta_{\mathrm{obs}} \sim 6 \times 10^{-10}$ [45].

The Standard Model cannot explain this matter-antimatter imbalance. In 1967, A. D. Sakharov postulated three conditions to be fulfilled for the baryon asymmetry to occur in the scenario of the Big Bang theory [46]. They are: (i) non-conservation of baryon number, (ii) violation of C- and CP

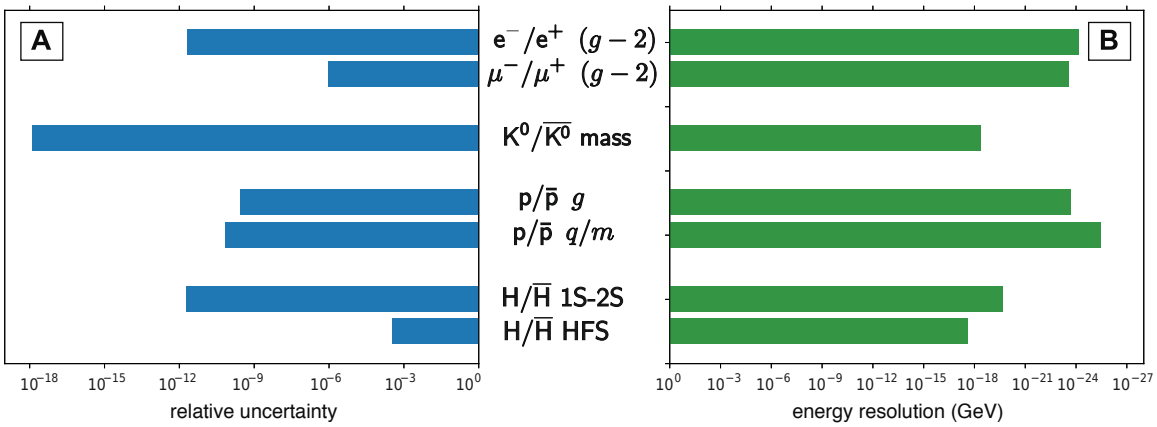

Figure 1.1: Comparison of selected tests of CPT symmetry. (A) is in a unit of relative uncertainty, and (B) in a unit of absolute energy resolution at GeV. From the top row: electron/positron magnetic moment, or $g-2$, comparison [12, 49], muon/antimuon magnetic moment comparison [50, 51], $K_0/\overline{K_0}$ meson mass comparison [10], proton/antiproton magnetic moment comparison [52, 53] and charge-to-mass ratio comparison [54], hydrogen/antihydrogen 1S-2S transition frequency comparison [55, 56], and hyperfine transition frequency comparison [57, 58].

symmetries, and (iii) the interactions occurring out of thermal equilibrium, which are compatible with the Standard Model. However, an estimate based on Sakharov's conditions under the currently known Standard Model CP violations gives only $\eta_{\mathrm{SM}} \sim 10^{-20}$ [47], which is 10 orders of magnitudes too small to explain the observed asymmetry. CPT violation, if ever found, could provide a solution to this mystery [48].

Experimental CPT tests

As we do not know how CPT violation could occur, CPT symmetry should be tested in all systems where the tests are possible.

In Fig. 1.1, some of the most precise CPT tests are listed. They are selected from different sectors: leptons (electron/positron, muon/anti-muon), mesons ($K^0/\overline{K^0}$ mesons), baryons (proton/antiproton) and atoms (hydrogen/antihydrogen). They are shown in a unit of relative uncertainty in Fig. 1.1 (A), and in (B), in a unit of absolute energy resolution, which is often used as a measure to compare sensitivities between different CPT tests. In this perspective, the proton-antiproton comparisons provide stringent CPT tests in the baryonic sector with high energy resolution.

1.2.2 Antimatter gravity

Another interest antimatter experiments is to study how antimatter behaves in a gravitational field. This is of special interest in view of the absence of a successful quantum gravity theory.

A specific subject of the investigation is a test of the weak equivalence principle. The weak equivalence principle, also known as the universality of free fall, is one of the foundations of General Relativity. It states that in a uniform gravitational field, any body experiences the same acceleration.

This universality has been thoroughly tested for ordinary matter at relative precisions on the order of 10^{-13} [59], but has not been well tested on antimatter. In fact, even the sign of the interaction has not been experimentally determined, which has led some to propose theories which suppose antimatter to repel matter in the gravitational interaction [60–62]. These, so-called anti-gravity theories could explain some aspects of the above-discussed baryon asymmetry [63].

The difficulty of gravity tests of antimatter is that electrically neutral objects are not readily available unlike the case of ordinary matter. Some experiments in the AD are currently aiming to test the weak equivalence principle on the antimatter by measuring the gravitational acceleration of antihydrogen atoms. In 2013, ALPHA constrained the gravitational acceleration $\bar{g}$ of antihydrogen atoms to be [64]

$$-65g < \bar{g} < 110g \quad (95\% \text{ C.L.}) \tag{1.2}$$

from annihilation signals of antihydrogen atoms trapped by and then released from a magnetic trap. Although this was the first bound on antihydrogen atoms, it did not constrain the sign of $\bar{g}$. Recently, an extension of the ALPHA experiment named ALPHA-g was proposed to further improve this measurement by a vertical atom trap [65]. Two other AD experiments, AEgIS [66] and GBAR [67], also aim to perform direct measurements of the gravitational acceleration of antihydrogen.

Although the antiproton measurements discussed in this thesis are not involved in the direct gravity test on antimatter, a result of the proton-to-antiproton charge-to-mass ratio comparison provides an indirect constraint on the possible gravitational anomaly of antimatter by regarding it as the comparison of gravitational redshift acting on a particle and an antiparticle [54] as will be discussed in Section 8.1.2.

1.3 BASE collaboration

In the above context of the antiproton experiments, BASE was proposed in 2012 to test CPT symmetry by high-precision comparisons of the fundamental property of the proton and the antiproton [68]. The particular targets are their charge-to-mass ratios and the magnetic moments. To measure and compare these properties with unprecedented precision, we employ methods of single-particle spectroscopy by an advanced Penning trap system [69].

BASE is an international collaboration of institutes in Japan and Germany. The collaboration operates experiments at three locations, the AD at CERN, Mainz University and Hannover University.

The team at CERN is working on measurements of the magnetic moment of the antiproton [52, 70], and the proton-to-antiproton comparison of the charge-to-mass ratios [54]. The main subjects of the Mainz team are measurements of the proton magnetic moment [53, 71, 72] and development of a sympathetic cooling method [73] which will be transferred to CERN in a later stage. In Hannover, works are being made to develop a novel cooling method and to apply quantum-logic spectroscopy

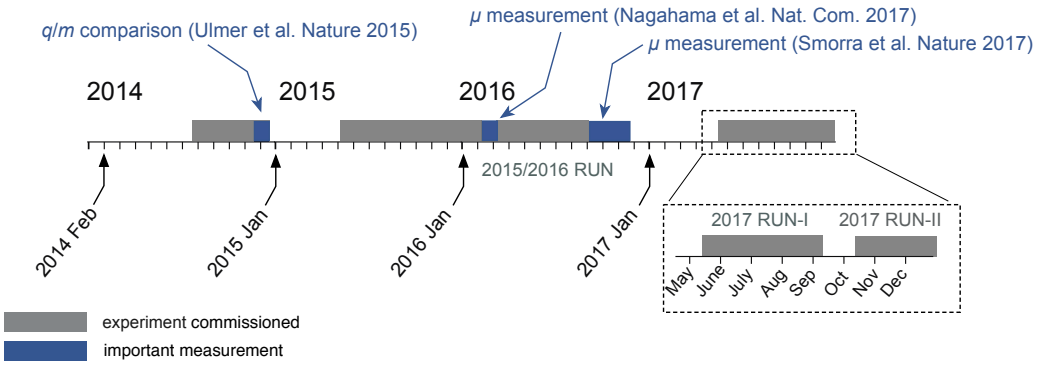

Figure 1.2: Timeline of events described in this thesis. Shown by gray bars are periods when the experiment was assembled and commissioned for the experiments. Blue bars indicate periods when important measurements took place, shown with the respective publications where the results were reported [52, 54, 70].

methods to single protons [74].

1.4 About this thesis

This thesis presents experimental results of the BASE group at CERN to which the author has contributed. In the timeline of Fig. 1.2, experimental activities of the BASE team at CERN are shown for a period during which the author has been a part of.

I joined BASE in February 2014 as a master's student. This was the year when the experiment first became online and received antiproton beams. In this year, BASE performed a high-precision comparison of proton-to-antiproton charge-to-mass ratio at a relative uncertainty of 69 p.p.t.[2] [54]. Aspects of the commissioning of the trap system and the reservoir methods are summarized in my master's thesis [75].

In 2015, I started my Ph.D. course with a focus on an improved comparison of the proton-to-antiproton charge-to-mass ratio. In 2015 and 2016, the works of the BASE at CERN were dedicated to the measurement of the magnetic moment of the antiproton. The experiment from October 2015 to December 2016 was one continuous run, maintained with antiprotons stored in a reservoir trap [33]. This is referred to as 2015/2016 run in this thesis. In this period, BASE achieved two measurements of the magnetic moment of the antiproton by different methods with respective relative uncertainties at 0.8 p.p.m. [70] and 1.5 p.p.b. [52]. In addition, storage of antiprotons in the reservoir allowed us to set an improved lower limit of the directly measured lifetime of the antiproton to be 10.2 a in 68% confidence level (C.L.) [76]. I have contributed to these measurements as a part of the team which maintained the experiment. In parallel, upgrades for improvement of the charge-to-mass ratio comparison (Chapters 10 and 11) were developed and used to help these measurements [77].

In 2017, the experiment was commissioned for a purpose to improve the charge-to-mass ratio

[2] parts per million (p.p.m.) = 10^{-6}, parts per billion (p.p.b.) = 10^{-9}, parts per trillion (p.p.t.) = 10^{-12}

comparison. The 2017 run was divided into two parts by a reinstallation of the apparatus in September/October. They are referred to as 2017 run-I and run-II throughout this thesis. Over the 2017 run, I was involved in all aspects of the experimental operation, and continually checked the frequency stabilities against the conditions of the experiment, which eventually led to a significant improvement of stability compared to the 2014 measurement. The upgrades (Chapters 9 to 11) for this year's run also played important roles. In December 2017, we started data collection of proton-to-antiproton comparison of charge-to-mass ratio with the improved measurement condition.

This thesis summarizes the experimental results above. It contains

1. experimental results obtained from 2014 to 2016 (Part IV)
2. developmental studies and works for an improved charge-to-mass ratio comparison (Part V)
3. experimental works during 2017 run for an improved charge-to-mass ratio comparison (Part VI).

The first is what I contributed as a part of the team, and have been published in recent BASE publications [52, 54, 70, 76]. The second and the third are where I played a major role. A part of their contents has been published as Ref. [78]. However, I note here that the experiment was run by a collaborative effort, and none of the experimental data presented in the thesis would have existed without constructive and collaborative works by the entire team. Most of the operation of the 2017 run was shared by James A. Harrington, and aspects of the run which are not described in this thesis, including final data analysis of the 2017 charge-to-mass ratio comparison, will be discussed in his Ph.D. thesis [79].

What follows is a more detailed outline of the thesis.

Part II gives a review of experimental principles and methods which are referred to in a later part of the thesis. In Chapter 2, the principles of a Penning trap and related experimental methods are discussed. In Chapter 3, experimental methods which allow one to measure physical properties of interest from frequency measurements by a Penning trap are discussed.

Part III is an overview of the experimental setup. After a brief summary about the AD facility in Chapter 4, we shall see the apparatus of BASE in Chapter 5. It has been designed before the author joined BASE, and the purpose of this chapter is to provide a summary of the necessary information for the discussion in a later part. The system is described for its status in 2017 run-II, therefore some details differ from a review article published in Ref. [33]. The characterization of the superconducting magnet in Section 5.1 was made between 2017 run-I and run-II, when we re-energized and shimmed the magnet.

Part IV summarizes the recent experimental results achieved by the BASE team at CERN, to which the author has contributed. Among them, the proton-to-antiproton charge-to-mass ratio comparison performed in 2014 is reviewed in detail in Chapter 7. Based on this, the strategy conceived in the 2017 run for the improvement is discussed.

In Part V, upgrades installed in the 2017 run for an improved charge-to-mass ratio comparison are discussed. The three major upgrades were an axial detection system with a tunable functionality of the resonance frequency (Chapter 9), an advanced magnetic shielding system (Chapter 10), and a monitoring system which constantly record conditions of the apparatus (Chapter 11). Among them, the tunable detection system is founded on work by previous students Hiroki Nagahama [80] and Toya Tanaka [81]. The scope of this thesis is its characterization after installation in the experiment.

What is described in Chapters 10 and 11: design and commissioning of superconducting magnetic shielding system and construction of a data monitoring system to record environmental conditions of the experiment, are primarily the author's work.

Finally in Part VI, experimental results acquired in the 2017 run are discussed. The three principal chapters are Chapters 13, 14 and 16. In Chapter 13 experimental methods to prepare a single antiproton and a single H^- ion needed for the measurement are covered. In Chapter 14, methods to characterize and optimize the trap used for the measurement are explained and their results are discussed. Following that, Chapter 16 presents the development of the cyclotron frequency stability over the course of optimization works performed to the apparatus. In preparation of the discussion of the achieved cyclotron frequency stability, the principal limit of the cyclotron frequency stability under the employed method is discussed in Chapter 15.

Part II

Principles and methods

2

Penning trap

The Penning trap is the central tool of our experiment. First introduced by H. G. Dehmelt in the early 1960s [82, 83], it has proven to be a versatile tool of high-precision measurements of fundamental properties of charged-particles [69, 84–86]. This chapter reviews the principles of a Penning trap and related experimental methods.

2.1 Ideal Penning trap

A Penning trap is a three-dimensional confinement of charged particles by a combination of static magnetic- and electric fields. The principle of the confinement is described in the schematic of Fig. 2.1. The magnetic field applied along the trap axis z provides an effective radial confinement by containing the particles to circular orbits by the Lorentz force. The quadrupole electrostatic potential is superposed to it, which is formed by application of voltages on the trap electrodes, and prevents the particles from escaping in the axial direction.

2.1.1 Eigenmodes of a charged particle in a Penning trap

In the following, we shall discuss behaviors of a single particle with mass m and electric charge q confined in an ideal Penning trap, where we neglect trap imperfections such as magnetic field inhomogeneity, anharmonicity of the electric potential, and ellipticity or tilts of the trap electrodes. The trapping field consists of a homogeneous magnetic field $\boldsymbol{B}$ along the z-axis of a cartesian coordinate system (x, y, z),

$$\boldsymbol{B} = B\hat{\boldsymbol{z}}, \tag{2.1}$$

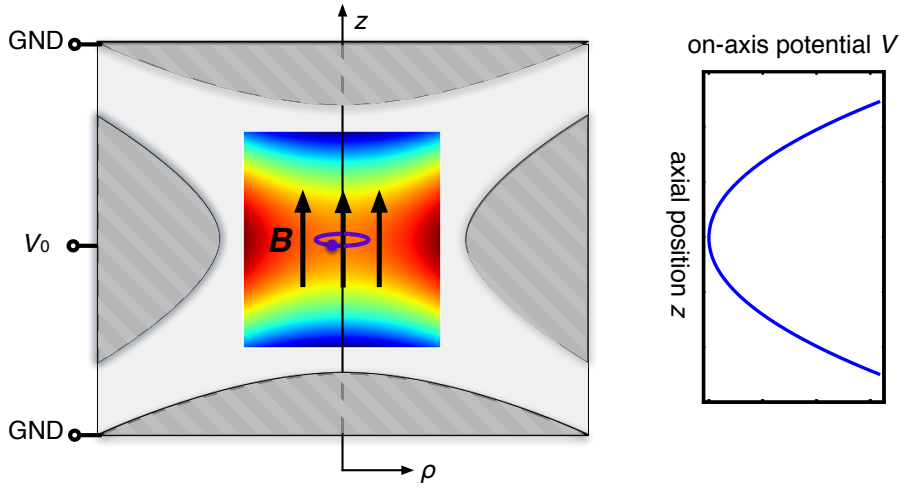

Figure 2.1: Principle of particle confinement with a Penning trap. The magnetic field $\boldsymbol{B}$ in z-direction is applied to provide radial confinement of the particle. The quadrupole electrostatic potential for axial confinement is applied through the hyperbolic electrodes, whose cross sections are represented by the hatched domains in the figure. The on-axis electric potential is a harmonic potential as shown on the right.

and a quadrupole electric potential $\Phi(x, y, z)$

$$\Phi(x, y, z) = V_0 C_2 \left(z^2 - \frac{x^2 + y^2}{2} \right) \tag{2.2}$$

where C_2 is a trap specific parameter with $1/\sqrt{|C_2|}$ having the dimension of length. Two important frequencies[1] are the *cyclotron frequency* ω_c and the *axial frequency* ω_z defined by

$$\omega_c = \frac{qB}{m}, \tag{2.3}$$

$$\omega_z = \sqrt{\frac{2qC_2V_0}{m}}. \tag{2.4}$$

Using these, the Newtonian equation

$$m\ddot{\boldsymbol{x}} = q\dot{\boldsymbol{x}} \times \boldsymbol{B} - q\boldsymbol{\nabla}\Phi(\boldsymbol{x}) \tag{2.5}$$

is expressed as

$$\begin{pmatrix} \ddot{x} - \omega_c\dot{y} - \omega_z^2 x/2 \\ \ddot{y} + \omega_c\dot{x} - \omega_z^2 y/2 \\ \ddot{z} + \omega_z^2 z \end{pmatrix} = \begin{pmatrix} 0 \\ 0 \\ 0 \end{pmatrix}. \tag{2.6}$$

Looking at Eq. (2.6), it can be seen that the z component is the equation of motion of a harmonic oscillation at the axial frequency ω_z. It can also be seen that the x and y motions are coupled to each

[1] Throughout this thesis, a frequency ν and the corresponding angular frequency $\omega = 2\pi\nu$ are both referred to as a frequency interchangeably.

other. By defining a complex variable $u = x + iy$, they can be expressed in a single equation

$$\ddot{u} + i\omega_c\dot{u} - \frac{\omega_z^2}{2}u = 0. \tag{2.7}$$

The general solution of Eq. (2.7) is in a form $u = e^{-i\omega t}$ with ω satisfying

$$\omega^2 - \omega_c\,\omega + \frac{\omega_z^2}{2} = 0. \tag{2.8}$$

This equation has two roots:

$$\omega_\pm = \frac{\omega_c}{2} \pm \frac{\sqrt{\omega_c^2 - 2\omega_z^2}}{2}. \tag{2.9}$$

The eigenfrequencies ω_+ and ω_- are called the *modified cyclotron frequency* and the *magnetron frequency*, respectively. In order that a periodic solution of Eq. (2.8) exists,

$$\omega_c^2 - 2\omega_z^2 > 0 \iff V_0 < \frac{qB^2}{4mC_2} \tag{2.10}$$

is required. This gives a criterion of trap parameters for stable particle storage.

The general solution of Eq. (2.7) is expressed as

$$u(t) = \rho_+ e^{-i(\omega_+ t + \alpha_+)} + \rho_- e^{-i(\omega_- t + \alpha_-)} \tag{2.11}$$

with parameters of real numbers $\rho_\pm > 0$ and $\alpha_\pm$. This represents a superposition of two circular motions with radii ρ_+, ρ_-, frequencies ω_+, ω_-, respectively. Thus the motion of the particle can be decomposed into three eigenmodes with respective eigenfrequencies ω_z, ω_+ and ω_-. An example of the trajectory of the particle is depicted in Fig. 2.2.

Some useful relations between the eigenfrequencies can be derived from Eq. (2.9):

$$\omega_z^2 = 2\omega_+\omega_- \tag{2.12}$$

$$\omega_c = \omega_+ + \omega_- \tag{2.13}$$

$$\omega_c^2 = \omega_+^2 + \omega_z^2 + \omega_-^2. \tag{2.14}$$

Eq. (2.14) is of special importance, which relates the three eigenfrequencies and the cyclotron frequency ω_c, and remains to hold in the presence of dominant trap imperfections, such as elliptical distortion of the potential, or misalignment between the magnetic and electrostatic axes of the trap (Section 2.2). Under usual operating conditions which satisfy Eq. (2.10), a hierarchy between the eigenfrequencies

$$\omega_+ \gg \omega_z \gg \omega_- \tag{2.15}$$

exists. For example, typical eigenfrequencies of a single proton/antiproton in a Precision trap (see

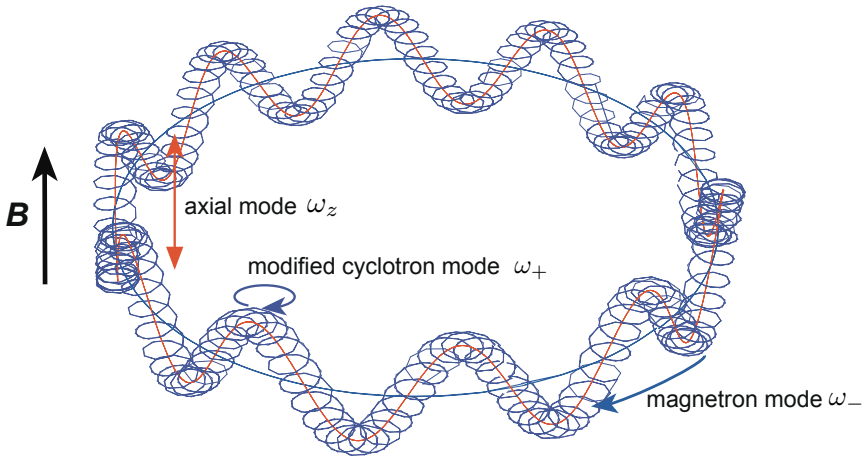

Figure 2.2: Classical trajectory of a charged particle in a Penning trap. The motion of the particle is a superposition of three eigenmodes: the axial mode, the modified cyclotron mode, and the magnetron mode.

Section 5.3) during BASE 2017 run-II, where $B \approx 1.945\,\mathrm{T}$, are

$$\omega_+ \approx 2\pi \times 29.656\,\mathrm{MHz}, \quad \omega_z \approx 2\pi \times 640\,\mathrm{kHz}, \quad \omega_- \approx 2\pi \times 6.9\,\mathrm{kHz}. \tag{2.16}$$

2.1.2 Energy contributions of the eigenmodes

To see the energy contribution of each eigenmode to the total energy, we formulate the Hamiltonian of the system. To introduce the magnetic potential $\boldsymbol{A}$ corresponding to $\boldsymbol{B}$, we choose the Coulomb gauge $\boldsymbol{\nabla} \cdot \boldsymbol{A} = 0$;

$$\boldsymbol{A} = \begin{pmatrix} -yB/2 \\ xB/2 \\ 0 \end{pmatrix}. \tag{2.17}$$

The Hamiltonian of the charged particle in the electric and the magnetic potential is given as [87]

$$H = \frac{1}{2m}\left(\boldsymbol{p} - q\boldsymbol{A}\right)^2 + q\Phi(\boldsymbol{x}) \tag{2.18}$$

with $\boldsymbol{p}$ being the canonical momenta

$$\boldsymbol{p} = m\dot{\boldsymbol{x}} + q\boldsymbol{A}. \tag{2.19}$$

Eq. (2.18) is expanded as

$$\begin{aligned} H &= \frac{1}{2m}\left[\left(p_x + \frac{qBy}{2}\right)^2 + \left(p_y - \frac{qBx}{2}\right)^2 + p_z^2\right] + qV_0C_2\left(z^2 - \frac{x^2+y^2}{2}\right) \\ &= \frac{1}{2m}\left[\left(p_x + \frac{m\omega_c y}{2}\right)^2 + \left(p_y - \frac{m\omega_c x}{2}\right)^2 + p_z^2\right] + \frac{m\omega_z^2}{4}(2z^2 - x^2 - y^2) \\ &= \frac{1}{2m}(p_x^2 + p_y^2 + p_z^2) + \frac{\omega_c}{2}(p_x y - p_y x) + \frac{m\omega_z^2}{2}z^2 + \frac{m\omega_1^2}{8}(x^2+y^2). \end{aligned} \tag{2.20}$$

$\omega_1 \equiv \sqrt{\omega_c^2 - 2\omega_z^2}$ is introduced in the last line to simplify the expression. The canonical transformation $(x, y, z, p_x, p_y, p_z) \mapsto (q_+, q_-, q_3, p_+, p_-, p_3)$ defined below decouples the mixed terms of x and y [88]

$$\begin{aligned} q_+ &= \frac{1}{\sqrt{2}}\left(\sqrt{\frac{m\omega_1}{2}}x - \sqrt{\frac{2}{m\omega_1}}p_y\right) \\ p_+ &= \frac{1}{\sqrt{2}}\left(\sqrt{\frac{m\omega_1}{2}}y + \sqrt{\frac{2}{m\omega_1}}p_x\right) \\ q_- &= \frac{1}{\sqrt{2}}\left(\sqrt{\frac{m\omega_1}{2}}x + \sqrt{\frac{2}{m\omega_1}}p_y\right) \\ p_- &= \frac{1}{\sqrt{2}}\left(-\sqrt{\frac{m\omega_1}{2}}y + \sqrt{\frac{2}{m\omega_1}}p_x\right) \\ q_3 &= \sqrt{m\omega_z}z \\ p_3 &= \frac{1}{\sqrt{m\omega_z}}p_z \end{aligned} \tag{2.21}$$

to obtain

$$H = \frac{\omega_+}{2}(q_+^2 + p_+^2) - \frac{\omega_-}{2}(q_-^2 + p_-^2) + \frac{\omega_z}{2}(q_3^2 + p_3^2). \tag{2.22}$$

Thus the Hamiltonian is expressed by contributions of the three independent harmonic oscillators, corresponding to the three eigenmodes discussed in the last section. It can be seen here that the magnetron mode has a negative energy contribution to the total Hamiltonian unlike the other two modes.

The canonical equations of motions become

$$\begin{aligned} \begin{pmatrix}\dot{q}_+\\ \dot{p}_+\end{pmatrix} &= \begin{pmatrix}\frac{\partial H}{\partial p_+}\\ -\frac{\partial H}{\partial q_+}\end{pmatrix} = \omega_+\begin{pmatrix}p_+\\ -q_+\end{pmatrix} \\ \begin{pmatrix}\dot{q}_-\\ \dot{p}_-\end{pmatrix} &= \begin{pmatrix}\frac{\partial H}{\partial p_-}\\ -\frac{\partial H}{\partial q_-}\end{pmatrix} = -\omega_-\begin{pmatrix}p_-\\ -q_-\end{pmatrix} \\ \begin{pmatrix}\dot{q}_3\\ \dot{p}_3\end{pmatrix} &= \begin{pmatrix}\frac{\partial H}{\partial p_3}\\ -\frac{\partial H}{\partial q_3}\end{pmatrix} = \omega_z\begin{pmatrix}p_3\\ -q_3\end{pmatrix}. \end{aligned} \tag{2.23}$$

General solutions of the radial modes can be expressed with real parameters $Q_+ > 0, Q_- > 0, \eta_+, \eta_-$

as

$$\begin{pmatrix} q_+(t) \\ p_+(t) \end{pmatrix} = Q_+ \begin{pmatrix} \sin(\omega_+ t + \eta_+) \\ \cos(\omega_+ t + \eta_+) \end{pmatrix}, \quad \begin{pmatrix} q_-(t) \\ p_-(t) \end{pmatrix} = Q_- \begin{pmatrix} \cos(\omega_- t + \eta_-) \\ \sin(\omega_- t + \eta_-) \end{pmatrix}. \tag{2.24}$$

From Eq. (2.21), x and y are expressed as

$$\begin{aligned} x &= \frac{q_+ + q_-}{\sqrt{m\omega_1}} = \frac{Q_+}{\sqrt{m\omega_1}} \sin(\omega_+ t + \eta_+) + \frac{Q_-}{\sqrt{m\omega_1}} \cos(\omega_- t + \eta_-) \\ y &= \frac{p_+ - p_-}{\sqrt{m\omega_1}} = \frac{Q_+}{\sqrt{m\omega_1}} \cos(\omega_+ t + \eta_+) - \frac{Q_-}{\sqrt{m\omega_1}} \sin(\omega_- t + \eta_-). \end{aligned} \tag{2.25}$$

With

$$\eta_+ = \alpha_+ + \frac{\pi}{2} + 2\pi N, \quad \eta_- = \alpha_- + 2\pi N \quad (N : \text{integer}), \tag{2.26}$$

we find a correspondence to Eq. (2.11) and hence

$$Q_+ = \sqrt{m\omega_1}\rho_+, \quad Q_- = \sqrt{m\omega_1}\rho_-. \tag{2.27}$$

Denoting the energy contribution of each eigenmode to the Hamiltonian as $H = E_+ + E_- + E_z$, each of them can be expressed by the amplitude of the eigenmode as

$$\begin{aligned} E_+ = \frac{\omega_+}{2}(q_+^2 + p_+^2) &= \frac{1}{2} m\omega_1 \omega_+ \rho_+^2 \\ &= \frac{1}{2} m(\omega_+ - \omega_-)\omega_+ \rho_+^2 \\ &= \frac{1}{2} m\omega_+^2 \rho_+^2 - \frac{1}{4} m\omega_z^2 \rho_+^2, \end{aligned} \tag{2.28}$$

$$\begin{aligned} E_- = -\frac{\omega_-}{2}(q_-^2 + p_-^2) &= -\frac{1}{2} m\omega_1 \omega_- \rho_-^2 \\ &= -\frac{1}{2} m(\omega_+ - \omega_-)\omega_- \rho_-^2 \\ &= \frac{1}{2} m\omega_-^2 \rho_-^2 - \frac{1}{4} m\omega_z^2 \rho_-^2. \end{aligned} \tag{2.29}$$

$$E_z = \frac{\omega_z}{2}(q_3^2 + p_3^2) = \frac{1}{2} m\omega_z^2 z^2. \tag{2.30}$$

Applying the hierarchy of Eq. (2.15),

$$E_+ \approx \frac{1}{2} m\omega_+^2 \rho_+^2, \tag{2.31}$$

$$E_- \approx -\frac{1}{4} m\omega_z^2 \rho_-^2. \tag{2.32}$$

The term $-\frac{1}{4} m\omega_z \rho_\pm^2$ in Eq. (2.28) or Eq. (2.29) represents a repulsive electric potential, whose contribution makes the magnetron energy negative. When the magnetron mode is discussed in the following part of this thesis, the absolute energy $|E_-| = -E_-$ is used for clarification, and the term *cooling* refers to a reduction of the radius ρ_-.

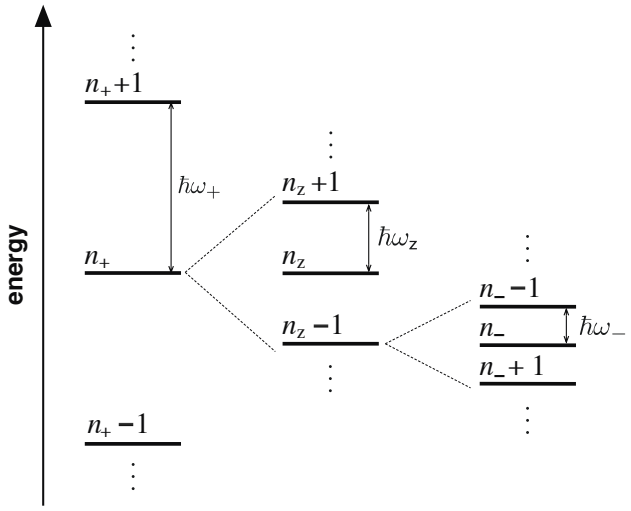

Figure 2.3: Energy diagram of a charged particle in a Penning trap. Note the degeneracy of the levels from the frequency hierarchy $\omega_+ \gg \omega_z \gg \omega_-$. The energy contribution of the magnetron quantum number n_- is negative, opposing to the other modes. See Eq. (2.36) for the values of the energy differences in our setup.

So far we have discussed in the classical framework. The quantum picture is obtained in a straightforward way by the canonical quantization, i.e. to introduce the commutation relations

$$[\hat{q}_j, \hat{p}_k] = i\hbar\delta_{j,k}, \quad [\hat{q}_j, \hat{q}_k] = [\hat{p}_j, \hat{p}_k] = 0 \quad (\text{for } j,k \in \{+,-,3\}). \tag{2.33}$$

By the standard prescription [89], the number operators $\hat{n}_+, \hat{n}_-, \hat{n}_z$ and the eigenstates of the modes $|n_+\rangle, |n_-\rangle, |n_z\rangle$

$$\hat{n}_+ |n_+\rangle = n_+ |n_+\rangle, \quad \hat{n}_- |n_-\rangle = n_- |n_-\rangle, \quad \hat{n}_z |n_z\rangle = n_z |n_z\rangle \tag{2.34}$$

can be defined, with n_+, n_-, n_z being the respective quantum numbers. The Hamiltonian is now written as

$$\hat{H} = \hbar\omega_+ \left(\hat{n}_+ + \frac{1}{2}\right) - \hbar\omega_- \left(\hat{n}_- + \frac{1}{2}\right) + \hbar\omega_z \left(\hat{n}_z + \frac{1}{2}\right). \tag{2.35}$$

The energy diagram is shown in Fig. 2.3. The energy differences between the levels in our typical eigenfrequencies Eq. (2.16) are

$$\hbar\omega_+ \approx 1.23 \times 10^{-7}\,\text{eV}, \quad \hbar\omega_z \approx 2.65 \times 10^{-9}\,\text{eV}, \quad \hbar\omega_- \approx 2.85 \times 10^{-11}\,\text{eV}. \tag{2.36}$$

In practice, the quantum numbers n_+, n_-, n_z are on the order of 10^5 for most of the cases treated in this thesis , therefore the classical treatment suffices.

2.2 Invariance theorem

The relations between the eigenfrequencies Eqs. (2.12) and (2.13) do not hold exactly in the presence of a misalignment of the electrostatic potential in respect of the trap axis, or an asymmetry of the electric potential, which exist in a realistic trap. To take Eq. (2.12) as an example, with two misalignment angles θ, ϕ and a first-order asymmetry parameter ϵ which modify the magnetic field and the electric potential as

$$\boldsymbol{B} = B \begin{pmatrix} \cos\theta \\ \sin\theta\cos\phi \\ \sin\theta\cos\phi \end{pmatrix}, \tag{2.37}$$

$$\Phi(x, y, z) = V_0 C_2 \left(z^2 - \frac{x^2 + y^2}{2} - \epsilon \frac{x^2 - y^2}{2} \right) \tag{2.38}$$

and letting $\overline{\omega}_+, \overline{\omega}_z, \overline{\omega}_-$ be the shifted eigenfrequencies, the error of Eq. (2.12) becomes [90]

$$\overline{\omega}_- - \frac{\overline{\omega}_z^2}{2\overline{\omega}_+} \approx \frac{9}{4}\theta^2 - \frac{1}{2}\epsilon^2. \tag{2.39}$$

However, as for Eq. (2.14), it was proven by L. S. Brown and G. Gabrielse [90] to be insensitive to these trap imperfections, i.e,

$$\omega_c^2 = \overline{\omega}_+^2 + \overline{\omega}_z^2 + \overline{\omega}_-^2. \tag{2.40}$$

This equation, so-called the *invariance theorem*, gives a prescription to determine the cyclotron frequency in the presence of the first order imperfections of a trap, and enables high-precision cyclotron frequency measurements by Penning traps. Eq. (2.39) is useful in approximately determining the magnetron frequency. With a typical order of the trap misalignment and a usually small potential asymmetry, the approximation

$$\overline{\omega}_- \approx \frac{\overline{\omega}_z^2}{2\overline{\omega}_+} \tag{2.41}$$

is valid to a relative precision of $\overline{\omega}_-$ on the order of 10^{-3}.

There are other kinds of imperfections which do not cancel by the invariance theorem. They are e.g. deviations of the electromagnetic field from the homogenous magnetic field and a perfect quadratic electric potential assumed in the ideal Penning trap. Shifts of the eigenfrequencies caused by these imperfections need to be taken into account individually. They are discussed in detail in the following sections.

2.3 Electric and magnetic imperfections

Although the quadruple electric potential and a homogeneous magnetic field defined by Eqs. (2.1) and (2.2) are a good approximation of a Penning trap, a real Penning trap deviates from an ideal Penning trap by having an asymmetry and higher order terms of the electric potential, or inhomogeneities of the magnetic field. In this section, the terms which characterize these imperfections of the field are defined, and their effects on the eigenfrequencies are discussed.

2.3.1 Anharmonicity of the electric potential

Cylindrical Penning trap

For further discussion, a cylindrical Penning trap used by BASE is introduced. We use open-end cylindrical Penning traps [91] such as shown in the schematic of Fig. 2.4, where a quadrupole electrostatic potential is produced by a set of cylindrical electrodes. This type of trap is suited to our experiment as it allows access for particle loading, and transport between adjacent traps. Furthermore, cylindrical electrodes have more precise manufacturing tolerances than hyperbolic electrodes, and possible machining errors can be assessed more simply.

In the following discussion, we shall treat a cylindrical trap with the geometry defined in Fig. 2.4 (A). The trap consists of five electrodes with respective lengths l_i. They are categorized to three types: two *endcap electrodes*, two *correction electrodes*, and one *ring electrode*, having the lengths

$$\begin{cases} l_1 = l_5 = l_{\mathrm{ec}} & : \text{endcap electrodes} \\ l_3 = l_{\mathrm{r}} & : \text{ring electrode} \\ l_2 = l_4 = l_{\mathrm{ce}} & : \text{corerction electrodes.} \end{cases} \tag{2.42}$$

The axial positions of the ends of the electrodes are defined as $z_0, \cdots, z_9$ in the cylindrical coordinate system (ρ, z, θ) defined in Fig. 2.4 (A), having the trap center as its origin $(\rho, z, \theta) = (0, 0, 0)$. The distance between the electrodes is d, the total trap length Λ, and the inner radius of the electrodes a. As shown in Fig. 2.4 (B), voltages $V_1, \cdots, V_5$ are applied to each electrode to form a step-like boundary potential

$$\Phi(a, z) = \begin{cases} V_1 & (z_0 \leq z \leq z_1) \\ V_1 + \dfrac{V_2 - V_1}{z_2 - z_1}(z - z_1) & (z_1 \leq z \leq z_2) \\ V_2 & (z_2 \leq z \leq z_3) \\ \vdots & \vdots \\ V_5 & (z_8 \leq z \leq z_9). \end{cases} \tag{2.43}$$

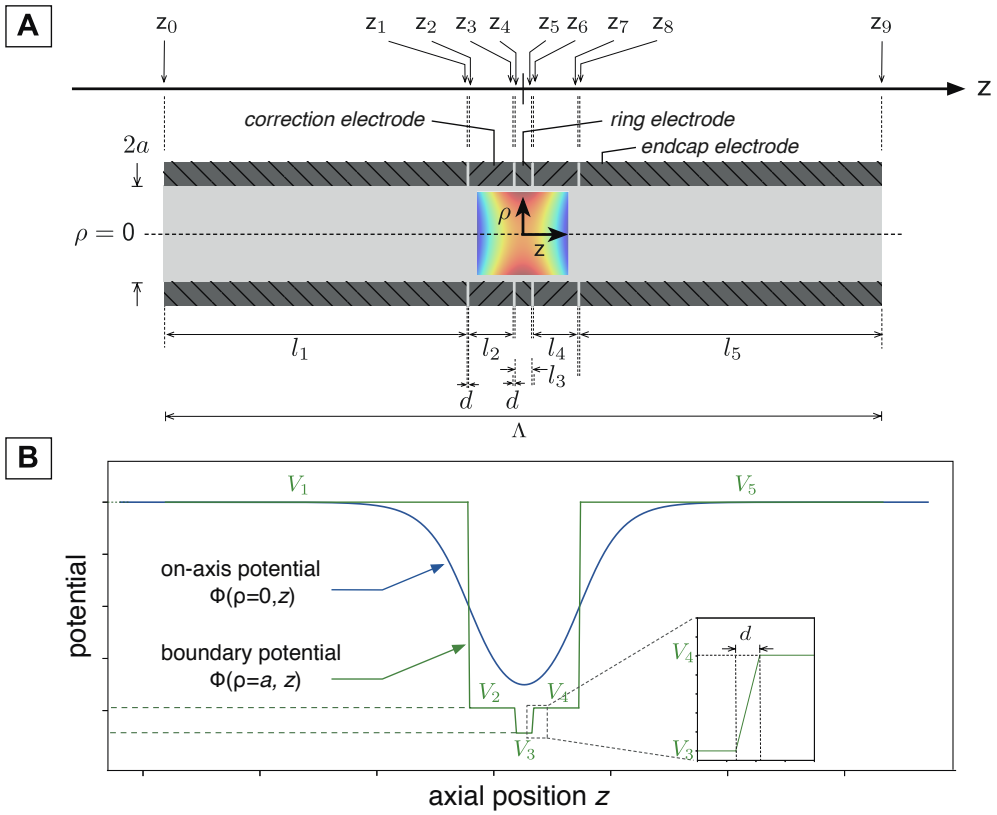

Figure 2.4: Definition of the parameters of a cylindrical Penning trap used in the text. **(A)** A cylindrical coordinate system (ρ, z) is defined with the trap center as the origin, and the trap axis as the z axis. Five electrodes are placed, with the respective lengths defined by $l_i\,(i = 1, \cdots, 5)$ and the inner radius a. and the gap by d. The axial coordinates of the ends of the electrodes are defined by $z_i\,(i = 0, \cdots, 9)$. **(B)** Electric potential formed in the cylindrical trap. The voltage applied to each electrode is defined as $V_i\,(i = 1, \cdots, 5)$, forming the boundary potential at $\rho = a$ shown by the green line. At the center of the trap, quadrupole potential is produced as shown in the color density plot in (A). The blue curve represents the harmonic cross sectional potential at $z = 0$.

Definition and derivation of the potential anharmonicity terms in a cylindrical trap

We define the coefficients which parameterize the anharmonicity of the electric potential. The electric potential in the trap is obtained by solving the Laplace equation $\nabla^2\Phi = 0$ for a Dirichlet boundary condition defined by the boundary potential. In a spherical coordinate system (r, θ, ϕ) originating from the trap center and taking the direction of the trap axis as the zenith direction, the general solution of the Laplace equation can be expressed as [87]

$$\Phi(r,\theta) = \sum_{j=0}^{\infty} V_3 C_j r^j P_j(\cos\theta) \tag{2.44}$$

under the rotational symmetry around the pole. Here P_j are the Legendre polynomials. We define C_j to be parameters which characterize the anharmonicity of the potential, each having the dimension of $[L^{-j}]$. In case of the ideal Penning trap discussed in the last section, $C_j = 0$ for $j \neq 2$ i.e.,

$$\begin{aligned}\Phi(r,\theta) &= V_3 C_2 r^2 \left(\frac{3}{2}\cos^2\theta - 1\right) \\ &= V_3 C_2 \left(z^2 - \frac{x^2+y^2}{2}\right).\end{aligned} \tag{2.45}$$

In what follows, we derive the form of C_j for a cylindrical trap by comparing Eq. (2.44) with a solution of the Laplace equation which can be obtained by applying the boundary condition in the cylindrical coordinates Eq. (2.43).

The Laplace equation in the cylindrical coordinates of Fig. 2.4 reads

$$\frac{1}{\rho}\frac{\partial}{\partial\rho}\left(\rho\frac{\partial\Phi}{\partial\rho}\right) + \frac{\partial^2\Phi}{\partial z^2} = 0, \tag{2.46}$$

under the azimuthal symmetry. The solution is found by a separation-ansatz $\Phi(\rho, z) = R(\rho)Z(z)$, which decouples the Eq. (2.46) into the following two differential equations:

$$\frac{1}{\rho}\frac{\mathrm{d}}{\mathrm{d}\rho}\left(\rho\frac{\mathrm{d}R(\rho)}{\mathrm{d}\rho} - k^2 R(\rho)\right) = 0 \tag{2.47}$$

$$\frac{\mathrm{d}^2 Z(z)}{\mathrm{d}z^2} + k^2 Z(z) = 0 \tag{2.48}$$

with k a real number constant. The solution of Eq. (2.47) is found in a form $R(\rho) \propto I_0(k\rho)$, with I_0 being the modified Bessel function of the first kind of order zero. We impose on Eq. (2.48) a boundary condition $\Phi(\rho, \Lambda/2) = \Phi(\rho, -\Lambda/2) = 0$, that is to set the voltages on the endcap electrodes to ground.

Then the solution is restricted to a form

$$Z(z) \propto \sin\left(k_n z + \frac{n\pi}{2}\right) \quad \left(\text{with } k_n \equiv \frac{n\pi}{\Lambda}\right). \tag{2.49}$$

The solution of Eq. (2.46) is expressed as

$$\Phi(\rho, z) = \sum_{n=1}^{\infty} A_n I_0(k_n \rho) \sin\left(k_n z + \frac{n\pi}{2}\right). \tag{2.50}$$

By comparing Eqs. (2.44) and (2.50) (for a comprehensive derivation, see Section A.1), the relation between A_n and C_j can be found as

$$C_j = \sum_{n=1}^{\infty} \frac{A_n}{V_3} \frac{(-k_n)^{\,j}}{j!} \sin\left(\frac{n-j}{2}\pi\right). \tag{2.51}$$

The explicit forms of A_n and C_j under the boundary condition Eq. (2.43) of the five-electrode Penning trap can be derived as (see Section A.2)

$$\begin{aligned} A_n = \frac{2}{\Lambda I_0(k_n a)} \Bigg[& \frac{1}{k_n}\left(V_5 \sin\left(k_n z_9 + \frac{n\pi}{2}\right) - V_1 \sin\left(k_n z_0 + \frac{n\pi}{2}\right)\right) \\ & + \sum_{i=1}^{4} \frac{V_{i+1} - V_i}{k_n^2 d}\left(\cos\left(k_n z_{2i} + \frac{n\pi}{2}\right) - \cos\left(k_n z_{2i-1} + \frac{n\pi}{2}\right)\right)\Bigg]. \end{aligned} \tag{2.52}$$

$$\begin{aligned} \therefore \Phi(\rho, z) = \sum_{n=1}^{\infty} \Bigg[& \frac{1}{k_n}\left(V_5 \sin\left(k_n z_9 + \frac{n\pi}{2}\right) - V_1 \sin\left(k_n z_0 + \frac{n\pi}{2}\right)\right) \\ & + \sum_{i=1}^{4} \frac{V_{i+1} - V_i}{k_n^2 d}\left(\cos\left(k_n z_{2i} + \frac{n\pi}{2}\right) - \cos\left(k_n z_{2i-1} + \frac{n\pi}{2}\right)\right)\Bigg] \\ & \cdot \frac{2}{\Lambda}\frac{I_0(k_n \rho)}{I_0(k_n a)} \sin\left(k_n z + \frac{n\pi}{2}\right), \end{aligned} \tag{2.53}$$

$$\begin{aligned} C_j = \sum_{n=1}^{\infty} \Bigg[& V_5 \sin\left(k_n z_9 + \frac{n\pi}{2}\right) - V_1 \sin\left(k_n z_0 + \frac{n\pi}{2}\right) \\ & + \sum_{i=1}^{4} \frac{V_{i+1} - V_i}{k_n d}\left(\cos\left(k_n z_{2i} + \frac{n\pi}{2}\right) - \cos\left(k_n z_{2i-1} + \frac{n\pi}{2}\right)\right)\Bigg] \\ & \cdot \frac{2 \cdot (-1)^{\,j}}{j! \Lambda V_3} \cdot \frac{k_n^{\,j-1}}{I_0(k_n a)} \cdot \sin\left(\frac{n-j}{2}\pi\right). \end{aligned} \tag{2.54}$$

The cylindrical trap is operated by setting the voltages to be

$$\begin{cases} V_1 = V_5 = 0 & : \text{endcap electrodes (grounded)} \\ V_3 = V_{\mathrm{R}} & : \text{ring electrode} \\ V_2 = V_4 = \mathrm{TR} \cdot V_{\mathrm{R}} & : \text{correction electrodes.} \end{cases} \tag{2.55}$$

The voltage V_{R} is called the *ring voltage*, and the ratio TR the *tuning ratio*. By choosing an appropriate TR, the potential can be tuned to harmonic. Substituting Eq. (2.55), Eq. (2.54) is reduced to

$$\begin{aligned} C_j = \sum_{n=1}^{\infty} \Bigg[& \mathrm{TR} \cdot (\cos(k_n(l_{\mathrm{ec}} + d)) - \cos(k_n l_{\mathrm{ec}})) \\ & + (\mathrm{TR} - 1) \cdot \left(\cos\left(k_n \left(\frac{\Lambda}{2} - \frac{l_{\mathrm{r}}}{2} - d \right) \right) - \cos\left(k_n \left(\frac{l_{\mathrm{r}}}{2} + \frac{\Lambda}{2} \right) \right) \right) \Bigg] \\ & \cdot (1 + (-1)^n) \cdot \frac{2 \cdot (-1)^j}{j! \Lambda V_3} \cdot \frac{k_n^{j-1}}{I_0(k_n a)} \cdot \sin\left(\frac{n-j}{2} \pi \right). \end{aligned} \tag{2.56}$$

Thus $C_j = 0$ for terms of odd j. These terms are suppressed by the symmetry of the cylindrical trap. However, the C_j with even j are not generally zero. Parameters D_j and E_j associated with the TR are defined by

$$C_j = E_j + D_j \cdot \mathrm{TR}. \tag{2.57}$$

It has been shown by G. Gabrielse, L. Haarsma and S. L. Rolston [91] that by appropriately choosing the lengths $l_{\mathrm{ce}}, l_{\mathrm{r}}$ and the radius a, the trap can be designed to have $D_2 = 0$ (this feature is called *orthogonality*) and that $C_4 = C_6 = 0$ for a specific TR (so-called *compensation*). The compensation of the trap allows suppression of dominant anharmonicity terms, thus realizes a highly harmonic potential. The orthogonality does not improve the precision of the measurements, but an advantageous feature for operation of the trap where the axial frequency $\omega_z \propto \sqrt{C_2 V_{\mathrm{R}}}$ stays constant when the TR needs to be adjusted to optimum. The cylindrical Penning traps in our system employ this orthogonal and compensated design. Further details of the trap design are described in Georg L. Schneider's Master's thesis [92].

2.3.2 Magnetic imperfections

We shall define the higher order terms of the magnetic field such as C_j for the electric potential discussed in the last section. To apply a multipole expansion as in Eq. (2.44), we introduce the magnetic scalar potential Ψ such that

$$\boldsymbol{B} = -\boldsymbol{\nabla}\Psi. \tag{2.58}$$

Since $\boldsymbol{\nabla} \cdot \boldsymbol{B} = 0$, Ψ satisfies the Laplace equation $\nabla^2 \Psi = 0$. We define the principal magnetic field to be $B_0 \hat{\boldsymbol{z}}$. Ψ which gives this term as the magnetic field of order zero is expressed in the spherical coordinates as [87]

$$\Psi(r, \theta) = -\sum_{j=0}^{\infty} \frac{B_j}{j+1} r^{j+1} P_{j+1}(\cos\theta). \tag{2.59}$$

The corresponding magnetic field is

$$\begin{aligned}\boldsymbol{B} &= -\frac{\partial\Psi}{\partial z}\hat{\boldsymbol{z}} - \frac{\partial\Psi}{\partial\rho}\hat{\boldsymbol{\rho}} \\ &= -\left(\cos\theta\frac{\partial\Psi}{\partial r} - \frac{\sin\theta}{r}\frac{\partial\Psi}{\partial\theta}\right)\hat{\boldsymbol{z}} - \left(\sin\theta\frac{\partial\Psi}{\partial r} + \frac{\cos\theta}{r}\frac{\partial\Psi}{\partial\theta}\right)\hat{\boldsymbol{\rho}} \\ &= \sum_{j=0}^{\infty} B_j r^j \left[P_j(\cos\theta)\hat{\boldsymbol{z}} + \frac{1}{j+1}{P_j}^1(\cos\theta)\hat{\boldsymbol{\rho}}\right].\end{aligned} \tag{2.60}$$

Here ${P_j}^1$ are the associated Legendre polynomials defined by

$${P_n}^m(x) = (-1)^m(1-x^2)^{m/2}\left(\frac{\mathrm{d}}{\mathrm{d}x}\right)^m P_n(x). \tag{2.61}$$

Relations between the Legendre polynomials

$$\frac{x^2-1}{n}\frac{\mathrm{d}P_n(x)}{\mathrm{d}x} = xP_n(x) - P_{n-1}(x) \tag{2.62}$$

$$(n+1)P_{n+1}(x) = (2n+1)xP_n(x) - nP_{n-1}(x) \tag{2.63}$$

are used to obtain the last line of Eq. (2.60). To denote the first few terms explicitly,

$$\boldsymbol{B}(\rho,z) = B_0\hat{\boldsymbol{z}} + B_1\left(z\hat{\boldsymbol{z}} - \frac{\rho}{2}\hat{\boldsymbol{\rho}}\right) + B_2\left[\left(z^2 - \frac{\rho^2}{2}\right)\hat{\boldsymbol{z}} - z\rho\hat{\boldsymbol{\rho}}\right] + \cdots. \tag{2.64}$$

2.3.3 Frequency shifts by the electromagnetic imperfections

The electromagnetic imperfections C_j and B_j defined in the last sections cause shifts of the eigenfrequencies depending on the amplitudes of eigenmotions of the particle. These shifts do not cancel by the invariance theorem, and need to be accounted for individual imperfection terms. We shall discuss the effect of each imperfection term in this section. The formulae Eqs. (2.70), (2.76) and (2.80) will be referred to in the later part of this thesis.

Effects of the electric imperfections

The term C_1 results in a constant electric force which shifts the axial equilibrium position of the particle to $z = -C_1/(2C_2)$, but does not influence the frequencies of the particle on the first order. Although Eq. (2.56) requires that the odd terms of C_j vanish from the symmetry of the cylindrical trap, in reality, different offsets voltages on the electrodes can cause the potential to be asymmetric, producing a non-zero C_1. This can be evaluated by Eq. (2.54).

The higher order terms of the potential results in an anharmonic oscillation of each mode. To take

the axial mode as an example, the equation of motion from the electric field at $\rho = 0$ is

$$\begin{aligned}
\ddot{z} &= -\frac{q}{m}\frac{\partial}{\partial z}\Phi(\rho, z)\bigg|_{\rho=0} \\
&= -\frac{q}{m}\frac{\partial}{\partial z}\left(V_{\mathrm{R}}\sum_{j\geq 2} C_j z^j\right) \\
&= -\frac{2qC_2V_{\mathrm{R}}}{m}\left(z + \frac{3C_3}{2C_2}z^2 + \frac{4C_4}{2C_2}z^3 + \cdots\right) \\
\therefore \quad \ddot{z} + \omega_z^2 z &= -\omega_z^2\left(\sum_{j\geq 3}\frac{jC_j}{2C_2}z^{j-1}\right)
\end{aligned} \tag{2.65}$$

In case of $C_1 \neq 0$, the expansion should be done around the equilibrium point $z = -C_1/2C_2$ instead of $z = 0$, leading to the same coefficients in the first order. Eq. (2.65) can be treated in a perturbative way by incorporating the higher term contributions on the right hand side order by order [93]. For the perturbation corresponding to the term C_j, we substitute and ansatz $z^{(j)} = z_0\cos(\widetilde{\omega}t)$ to obtain:

$$\begin{aligned}
\ddot{z}^{(j)} + \omega_z^2 z^{(j)} &= -\omega_z^2\frac{jC_j}{2C_j}(z^{(j)})^{j-1} \\
(-\tilde{\omega}^2 + \omega_z^2)z_0\cos(\tilde{\omega}t) &= -\omega_z^2\frac{jC_j}{2C_j}(z_0\cos(\tilde{\omega}t))^{j-1}.
\end{aligned} \tag{2.66}$$

As the first order perturbation, we only consider the oscillatory term at frequency $\widetilde{\omega}$ by taking

$$\int_0^{2\pi/\tilde{\omega}} \mathrm{d}t\cos(\tilde{\omega}t)\left[\cdots\right]. \tag{2.67}$$

on both sides of Eq. (2.66). By use of

$$\begin{aligned}
\int_0^{2\pi/\tilde{\omega}} \mathrm{d}t\cos(\tilde{\omega}t)^n &= \int_0^{2\pi/\tilde{\omega}} \mathrm{d}t\left(\frac{e^{i\tilde{\omega}t} + e^{-i\tilde{\omega}t}}{2}\right)^n \\
&= \begin{cases} \dfrac{(2k)!}{2^{2k}(k!)^2}\dfrac{2\pi}{\widetilde{\omega}} & (\text{for } n = 2k) \\ 0 & (\text{for } n = 2k+1), \end{cases}
\end{aligned} \tag{2.68}$$

we obtain

$$\frac{\tilde{\omega}^2}{\omega_z^2} = \begin{cases} 1 + \dfrac{jC_j}{2^jC_2}\dfrac{j!}{((j/2)!)^2}z_0^{j-2} & (\text{for } j : \text{even}) \\ 0 & (\text{for } j : \text{odd}) \end{cases} \tag{2.69}$$

thus it can be found that the odd terms of C_j do not contribute on the first order, and that the even terms cause frequency shifts which depend on the amplitude of the mode. Comprehensive calculations

of the frequency shifts can be found in Ref. [94]. The results for C_4 and C_6 are summarized as below:

$$\begin{pmatrix} \frac{\Delta\omega_+}{\omega_+}^{(C_4)} \\ \frac{\Delta\omega_z}{\omega_z}^{(C_4)} \\ \frac{\Delta\omega_-}{\omega_-}^{(C_4)} \end{pmatrix} = \mathcal{M}_{C_4} \begin{pmatrix} E_+ \\ E_z \\ |E_-| \end{pmatrix}, \quad \begin{pmatrix} \frac{\Delta\omega_+}{\omega_+}^{(C_6)} \\ \frac{\Delta\omega_z}{\omega_z}^{(C_6)} \\ \frac{\Delta\omega_-}{\omega_-}^{(C_6)} \end{pmatrix} = \mathcal{M}_{C_6} \begin{pmatrix} E_+^2 \\ E_z^2 \\ |E_-|^2 \\ E_+E_z \\ E_+|E_-| \\ E_z|E_-| \end{pmatrix} \tag{2.70}$$

$$\mathcal{M}_{C_4} \equiv \frac{1}{qV_\mathrm{R}}\frac{C_4}{C_2^2} \begin{pmatrix} \frac{3}{4}\eta^4 & -\frac{3}{2}\eta^2 & -3\eta^2 \\ -\frac{3}{2}\eta^2 & \frac{3}{4} & -3 \\ -3\eta^2 & 3 & -3 \end{pmatrix} \quad \left(\text{with} \quad \eta \equiv \frac{\omega_z}{\omega_+}\right)$$

$$\mathcal{M}_{C_6} \equiv \frac{1}{qV_\mathrm{R}}\frac{C_6}{C_2^3} \begin{pmatrix} -\frac{15}{16}\eta^6 & -\frac{45}{16}\eta^2 & -\frac{45}{4}\eta^2 & \frac{45}{8}\eta^4 & -\frac{45}{4}\eta^4 & \frac{45}{2}\eta^2 \\ \frac{45}{16}\eta^4 & \frac{15}{16} & \frac{45}{4} & -\frac{45}{8}\eta^2 & \frac{45}{2}\eta^2 & -\frac{45}{4} \\ \frac{45}{8}\eta^4 & \frac{45}{8} & \frac{15}{2} & -\frac{45}{2}\eta^2 & \frac{45}{2}\eta^2 & -\frac{45}{2} \end{pmatrix}$$

Here the energies of the eigenmodes Eqs. (2.28) and (2.29) are used instead of the amplitudes, as they are more convenient in application to the experiment.

Effects of the magnetic imperfections

Similarly to C_1, the magnetic gradient B_1 also causes a shift of the equilibrium position, resulting in a shift of the cyclotron frequency. Considering the axial equation of motion including B_1,

$$\begin{aligned} \ddot{z} &= -\frac{2qC_2V_\mathrm{R}}{m}z + \frac{q}{m}\left(\dot{\boldsymbol{x}} \times B_1\left(z\hat{\boldsymbol{z}} - \frac{\rho}{2}\hat{\boldsymbol{\rho}}\right)\right)_z \\ &= -\omega_z^2 z - \frac{q}{m}\frac{B_1}{2}(\dot{x}y - \dot{y}x) \quad \left(\because B_x = \frac{B_\rho}{\rho}x,\, B_y = \frac{B_\rho}{\rho}y\right). \end{aligned} \tag{2.71}$$

Using Eq. (2.11) and $u = x + iy$,

$$\begin{aligned} \dot{x}y - \dot{y}x &= \mathrm{Im}(u\bar{\dot{u}}) \\ &= \omega_+\rho_+^2 + \omega_-\rho_-^2 + \rho_+\rho_-(\omega_+ + \omega_-)\cos((\omega_+ - \omega_-)t + \alpha_+ - \alpha_-) \\ &\approx \frac{L_+ + L_-}{m} \end{aligned} \tag{2.72}$$

with $L_\pm = m\omega_\pm\rho_\pm^2$ being the angular momentum of the modified-cyclotron and the magnetron modes. The oscillatory term in the second line of Eq. (2.72) is averaged to zero when considering the equilibrium state. Such approximation is called the rotating-wave approximation. By denoting the z

component of the angular magnetic moment as μ_l,

$$\mu_l = \frac{q}{2m}(L_+ + L_-). \tag{2.73}$$

Applying Eqs. (2.72) and (2.73) to Eq. (2.71),

$$\ddot{z} = -\omega_z^2 z - \frac{\mu_l B_1}{m}, \tag{2.74}$$

thus the second term on the right hand side represents the force from the corresponding term of the magnetic potential $-\boldsymbol{\mu}_l \cdot \boldsymbol{B}$. The shift of the equilibrium position by B_1 is

$$\delta z^{(B_1)} = -\frac{\mu_l B_1}{m\omega_z^2} \tag{2.75}$$

A consequent shift of magnetic field experienced by the particle leads to a shift of the cyclotron frequency

$$\begin{aligned} \frac{\Delta\omega_{\mathrm{c}}^{(B_1)}}{\omega_{\mathrm{c}}} &\approx -\frac{1}{m\omega_z^2}\left(\frac{B_1}{B_0}\right)^2 (E_+ + |E_-|) \\ &\left(\because L_+ \approx \frac{2E_+}{\omega_+},\ L_- \approx -\frac{2E_-}{\omega_+}\right). \end{aligned} \tag{2.76}$$

This is effectively a difference of the offset of B_0. However, it needs to be accounted when the cyclotron frequencies of two particles at different energies are compared [52].

To consider the effect of the next term B_2, the modified axial equation of motion now reads Eq. (2.71)

$$\ddot{z} = -\left(\omega_z^2 + \frac{2B_2\mu_l}{m}\right) z. \tag{2.77}$$

The shifted axial frequency is

$$\begin{aligned} \sqrt{\omega_z^2 + \frac{2B_2\mu_l}{m}} &= \omega_z\sqrt{1 + \frac{2B_2\mu_l}{m\omega_z^2}} \\ &= \omega_z\left(1 + \frac{B_2\mu_l}{m\omega_z^2} + \cdots\right). \end{aligned} \tag{2.78}$$

Hence the shift $\Delta\omega^{(B_2)}$ is found to be

$$\frac{\Delta\omega_z^{(B_2)}}{\omega_z} \approx \frac{1}{m\omega_z^2}\frac{B_2}{B_0}(E_+ + |E_-|). \tag{2.79}$$

To list the rest of the contributions of B_2 [69],

$$\begin{pmatrix} \frac{\Delta\omega_+}{\omega_+}^{(B_2)} \\ \frac{\Delta\omega_z}{\omega_z}^{(B_2)} \\ \frac{\Delta\omega_-}{\omega_-}^{(B_2)} \end{pmatrix} = \mathcal{M}_{B_2} \begin{pmatrix} E_+ \\ E_z \\ |E_-| \end{pmatrix}, \quad \mathcal{M}_{B_2} \equiv \frac{1}{m\omega_z^2}\frac{B_2}{B_0} \begin{pmatrix} -\eta^2 & 1 & -2 \\ 1 & 0 & 1 \\ 2 & -1 & 2 \end{pmatrix}. \tag{2.80}$$

The higher order terms B_j ($j \geq 4$) can be treated in the same way as C_j by the perturbation method [94].

2.3.4 Other trap effects

The frequency shifts from the imperfections of the electromagnetic fields discussed above are the most relevant trap imperfections in the discussion in this thesis. The other major systematic effects in a real Penning trap, which are orders of magnitude smaller than the above-discussed effects, are briefly summarized below.

Relativistic effect

Variation of the relativistic mass of the particle by the velocity of the motion causes shifts of the eigenfrequencies as [69, 95]

$$\begin{pmatrix} \frac{\Delta\omega_+}{\omega_+}^{(\mathrm{r})} \\ \frac{\Delta\omega_z}{\omega_z}^{(\mathrm{r})} \\ \frac{\Delta\omega_-}{\omega_-}^{(\mathrm{r})} \end{pmatrix} = -\frac{1}{mc^2} \begin{pmatrix} 1 & \frac{1}{2} & \eta^2 \\ \frac{1}{2} & \frac{3}{8} & \frac{\eta^2}{4} \\ -\eta^2 & -\frac{\eta^2}{4} & \frac{\eta^4}{4} \end{pmatrix} \begin{pmatrix} E_+ \\ E_z \\ |E_-| \end{pmatrix}. \tag{2.81}$$

Image-charge effect

This is a frequency shift induced by the electrical interaction with the particle and the trap electrodes. The effect can be treated as an interaction between the particle and the image charges induced in the trap electrode, which results in the following frecency shifts [96]

$$\Delta\omega_z^{(\mathrm{ch})} = -\frac{1}{4\pi\epsilon_0}\frac{q^2}{2m\rho_0^3\omega_z} \tag{2.82}$$

$$\Delta\omega_\pm^{(\mathrm{ch})} = \mp\frac{1}{4\pi\epsilon_0}\frac{2q^2}{m\rho_0^3\omega_\mathrm{c}} \tag{2.83}$$

with ϵ_0 being the permittivity of the free space and ρ_0 a parameter depends on the electrode geometry, which is on the same order as the trap radius.

Image-current shift

For the image-current detection of the particle's frequencies (discussed in Section 2.4), a resonant tank circuit is connected to an electrode, which couples the motion of the particle to the detection circuit via the image-current induced in the trap electrode. This introduces a damping term $\gamma\dot{\rho}_\xi$ in the equation of motion of the coupled mode. The imaginary part of the impedance of the detection system $\mathrm{Im}(Z)$, which can be caused by detuning of the resonant frequency of the detection system, leads to frequency shifts as [97, 98]

$$\frac{\Delta\omega_\xi}{\omega_\xi}^{(\mathrm{cu})} = -\frac{q}{m}\frac{1}{2\omega_\xi D_\xi^2}\,\mathrm{Im}(Z_\xi(\omega_\xi)) \quad (\text{for } \xi \in \{+, z\}). \tag{2.84}$$

Here $Z_\xi(\omega_\xi)$ represents the impedance of the detection system coupled to the corresponding mode, and D_ξ the respective effective electrode distance (see Section 2.4.1), which is on the same order as the size of the trap.

The effects discussed above are on the order of 10^{-11} or below in relative shifts of the cyclotron frequency for an antiproton with our trap parameters [52], each can be corrected with relative uncertainties on the order of 10%. In case of the last charge-to-mass ratio comparison, these shifts influence the frequency ratio on the order of 10^{-14} or below [54].

2.4 Image-current detection

In this section, the principle of frequency measurements of a particle in a Penning trap is discussed. The method we employ was first demonstrated by D. J. Wineland and H. G. Dehmelt [99], which non-destructively measures the eigenfrequencies of a particle by detecting image currents induced by the oscillations. In what follows, the detection principle is discussed for the axial mode, which is the most relevant in the discussion in this thesis.

2.4.1 Interaction of particles with the detection system

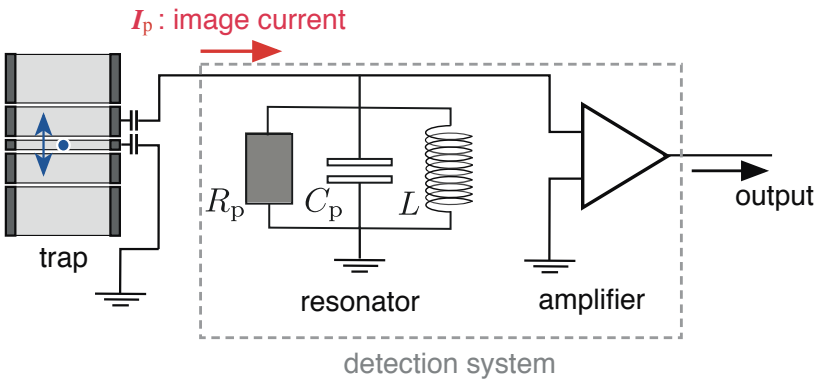

Figure 2.5: Basic setup of the image-current detection. One of the trap electrodes is connected to a detection system which consists of a superconducting resonator and a cryogenic low-noise amplifier. The trap and the detection system is placed at a cryogenic temperature of liquid helium ($\approx 4\,\mathrm{K}$). The image currents induced by the particle's oscillation are detected by the detection system. Note that the DC bias lines which provide the electrostatic potential for trapping are omitted from the figure (so for all the related figures starting from Fig. 2.6). For actual wiring of the trap electrodes, see Fig. 5.12.

A basic setup of the image-current detection is shown in Fig. 2.5. A charged particle is trapped in a Penning trap. One of the trap electrodes is connected to a detection system, which consists of a superconducting resonator and a low-noise amplifier. Image currents induced by the particle motion are detected through the interaction of the particle with the circuit. The oscillation frequency of the particle is measured by analyzing the signal of the detection system.

To discuss the principle of the detection, we shall first see how the image currents induced by the axial mode of a single particle interact with the rest of the circuit. Consider now a situation as depicted in Fig. 2.6 (A), where the trap is connected to a circuit through an impedance Z. The amount of the image current I_p induced by the particle is proportional to its velocity [100]. We introduce a specific length D_z for which

$$\boldsymbol{E}(0,0)\cdot\hat{\boldsymbol{z}} = \frac{U}{D_z}, \tag{2.85}$$

with the left hand side of the equation expressing the z component of the electric field at the center

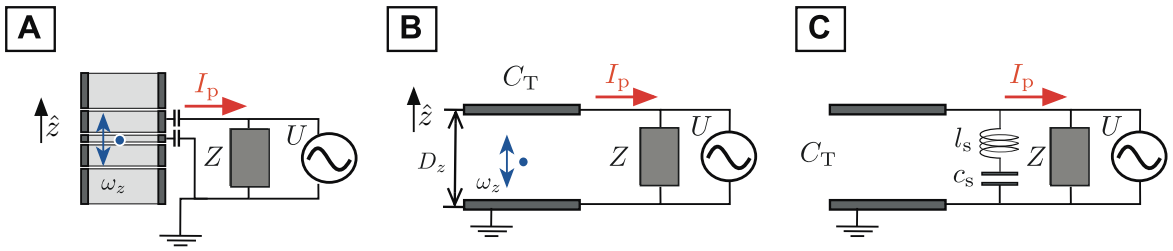

Figure 2.6: Equivalent circuits of an oscillating particle. **(A)** Particle in a Penning trap producing an image current through its axial motion. **(B)** Introduction of the effective electrode distance D_z. The Penning trap electrodes are replaced by an equivalent two-plate capacitor with the electrode distance D_z. **(C)** Particle's axial oscillation replaced by equivalent inductive components introduced in Eq. (2.90).

of the trap, and U the electric potential applied on the pick-up electrode. The length D_z is called the *effective electrode distance*, with which Fig. 2.6 (A) can be considered to be equivalent to (B), where the trap electrodes are simplified to a parallel-plate capacitor whose distance between the plates D_z. D_z can be uniquely evaluated for given geometries and configurations of the trap electrodes [101, 102], and $D_z = 10.3\,\mathrm{mm}$ in case of axial detection with the BASE Precision Trap (see Section 5.3 for naming of the traps). By this D_z, the image current I_p is expressed as

$$I_p = \frac{q\dot{z}}{D_z}. \tag{2.86}$$

The axial equation of motion of the particle is expressed as

$$\ddot{z} + \omega_z^2 z = \frac{F_e}{m} \tag{2.87}$$

with F_e being the external force from the circuit, which is expressed as

$$F_e = \frac{qU}{D_z} + F_{ind}. \tag{2.88}$$

F_{ind} represents a Coulomb force from the image charge induced in the electrode, which is much smaller than the other term, hence can be neglected in this discussion. Then Eq. (2.87) can be rewritten by use of Eq. (2.88) to be

$$l_s \frac{\mathrm{d}I_p}{\mathrm{d}t} + \frac{1}{c_s}\int I_p \mathrm{d}t = U \tag{2.89}$$

with l_s, c_s defined by

$$l_s \equiv \frac{mD_z^2}{q^2}, \quad c_s \equiv \frac{q^2}{m\omega_z^2 D_z^2}, \quad \therefore \omega_z^2 = \frac{1}{l_s c_s} \tag{2.90}$$

Thus the oscillating particle can be regarded as a reactive component of the circuit. In case a resistive component of the impedance Z of the detection system is present $R = \mathrm{Re}(Z) \neq 0$, a damping term

should be added to each of Eqs. (2.87) and (2.89), leading to the following equations of motion

$$\ddot{z} + \gamma_z \dot{z} + \omega_z^2 z = \frac{F_\mathrm{e}}{m} \tag{2.91}$$

$$l_\mathrm{s} \frac{\mathrm{d}I_\mathrm{p}}{\mathrm{d}t} + RI_\mathrm{p} + \frac{1}{c_\mathrm{s}} \int I_\mathrm{p} \mathrm{d}t = U \tag{2.92}$$

with γ_z defined by

$$\gamma_z = \frac{q^2 R}{m D_z^2}. \tag{2.93}$$

Its inverse $\tau_z \equiv 1/\gamma_z$ gives a time constant of the energy dissipation of the particle through R_eff. The above model can be extended to a case of N particles $z_1, z_2, \cdots, z_N$ by considering their center-of-mass (CM) mode

$$z_\mathrm{cm} = \sum_{k=1}^{N} \frac{z_k}{N}. \tag{2.94}$$

The correspondences of Eqs. (2.86), (2.91) and (2.92) are

$$I_{\mathrm{p},N} = \frac{Nq\dot{z}_\mathrm{cm}}{D_z}, \tag{2.95}$$

$$\ddot{z}_\mathrm{cm} + \gamma_{z,N} \dot{z}_\mathrm{cm} + \omega_z^2 z_\mathrm{cm} = \frac{F_\mathrm{e}}{m}, \tag{2.96}$$

$$\frac{l_\mathrm{s}}{N} \frac{\mathrm{d}I_{\mathrm{p},N}}{\mathrm{d}t} + RI_{\mathrm{p},N} + \frac{1}{Nc_\mathrm{s}} \int I_{\mathrm{p},N} \mathrm{d}t = U. \tag{2.97}$$

Therefore, the equivalent LC components $l_{\mathrm{s},N}, c_{\mathrm{s},N}$ and the damping constant $\gamma_{z,N}$ of the CM mode of N particles are

$$l_{\mathrm{s},N} = \frac{l_\mathrm{s}}{N}, \quad c_{\mathrm{s},N} = Nc_\mathrm{s}, \quad \gamma_{z,N} = N\gamma_z. \tag{2.98}$$

2.4.2 Frequency measurement by dip detection

The image current Eq. (2.86) induced by a thermal energy particle is on the order of fA. To provide sufficient impedance to detect such minuscule currents, a high-quality resonator is used in the detection system. The resonator is represented as a parallel tank circuit with its inductance and parallel resistance/capacitance as $L, R_\mathrm{p}, C_\mathrm{p}$ as in Fig. 2.5. The total impedance Z_res is

$$Z_\mathrm{res}(\omega) = \left(\frac{1}{R_\mathrm{p}} + i \left(\omega C_\mathrm{p} - \frac{1}{\omega L} \right) \right)^{-1}, \tag{2.99}$$

whose real component being

$$\mathrm{Re}(Z_\mathrm{res}(\omega)) = \frac{\dfrac{1}{R_\mathrm{p}}}{\dfrac{1}{R_\mathrm{p}^2} + \left(\omega C_\mathrm{p} - \dfrac{1}{\omega L} \right)^2}. \tag{2.100}$$

The resonance frequency $\omega_{0,\mathrm{res}}$ is

$$\omega_{0,\mathrm{res}} = \frac{1}{\sqrt{LC_\mathrm{p}}}. \tag{2.101}$$

The full-width-half maximum (FWHM) of the resonance in the power spectrum is denoted as $\Delta\omega_{0,\mathrm{res}}$ which can be found by solving

$$\mathrm{Re}(Z_\mathrm{res}(\omega_{0,\mathrm{res}} \pm \Delta\omega_{0,\mathrm{res}})) = \frac{1}{2}\,\mathrm{Re}(Z_\mathrm{res}(\omega_{0,\mathrm{res}})) \tag{2.102}$$

to be

$$\Delta\omega_{0,\mathrm{res}} = \frac{1}{\sqrt{C_\mathrm{p}R_\mathrm{p}}}. \tag{2.103}$$

Near the resonance, i.e., $|\omega - \omega_{0,\mathrm{res}}| \ll \omega$, Eq. (2.100) is approximated by

$$\mathrm{Re}(Z_\mathrm{res}(\omega)) \approx \frac{R_\mathrm{p}}{1 + 4\left(\dfrac{\omega - \omega_{0,\mathrm{res}}}{\Delta\omega_{0,\mathrm{res}}}\right)^2}. \tag{2.104}$$

The quality factor Q characterizes the ratio of the energy stored by the oscillation to the energy loss, and defined by

$$Q_\mathrm{res} = \frac{\omega_{0,\mathrm{res}}}{\Delta\omega_{0,\mathrm{res}}} \tag{2.105}$$

$$\therefore Q_\mathrm{res} = \omega_{0,\mathrm{res}} C_\mathrm{p} R_\mathrm{p} = \frac{R_\mathrm{p}}{\omega_{0,\mathrm{res}} L}. \tag{2.106}$$

Eq. (2.106) is an important relation which links the resonator-characteristic R_p to a measurable Q-factor.

In practice, parallel resistances and capacitances of the other components such as the amplifier and the trap electrodes exist. The circuit including these parasitic components is shown in Fig. 2.7 (A). We denote the effective parallel resistance/capacitance of the detection system as a whole, as Fig. 2.7 (B), by $R_\mathrm{eff}, C_\mathrm{eff}$, and redefine $Z_\mathrm{eff}, \omega_{0,\mathrm{eff}}, \Delta\omega_{0,\mathrm{eff}}, Q_\mathrm{eff}$ by the corresponding replacements in Eqs. (2.99) to (2.103), (2.105) and (2.106). The detailed circuit analysis of the actual system will be discussed in Chapter 9.

Now let us discuss a combined system of the detection system and the trapped particle as in Fig. 2.7 (B). Represented by u_th in Fig. 2.7 (B) is the Johnson-Nyquist noise [103, 104] on the resistive component of the system, whose amplitude given by

$$\overline{u_\mathrm{th}^2} = 4k_\mathrm{B}T\,\mathrm{Re}(Z_\mathrm{tot})f_\mathrm{b}, \tag{2.107}$$

with k_B being the Boltzmann constant, T the effective temperature of the detection system, Z_tot the impedance of the combined system of the particle and the detection system, and f_b the measurement bandwidth. The effective temperature T is primarily determined by the physical temperature of

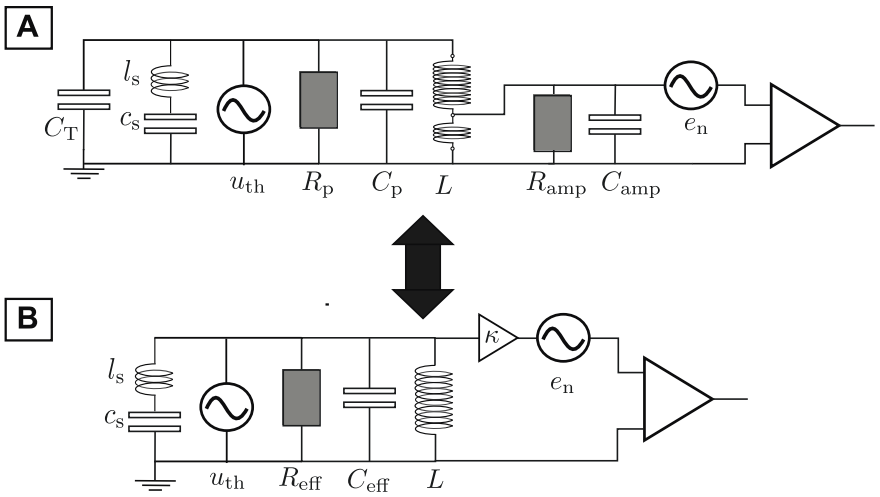

Figure 2.7: **(A)** Example of the circuit of the system which includes the equivalent inductive components of a particle and parasitic capacitances and resistances. u_{th} represents Johnson-Nyquist noise due to the resistive components. **(B)** Equivalent circuit of (A) where effective parallel resistance and capacitance are represented by $C_{\mathrm{eff}}, R_{\mathrm{eff}}$. The coupling κ determines the transmission of the signal from the system to the output.

the components at $\approx 4.2\,\mathrm{K}$ determined by LHe, but can become higher due to electric noise. Axial detection systems of BASE typically have 5–10 K[2].

In the following, we treat a case of $\omega_z \approx \omega_{0,\mathrm{eff}}$ where $\mathrm{Re}(Z_{\mathrm{eff}}) \approx R_{\mathrm{eff}}$.

When the particle has a higher axial energy than $\approx k_{\mathrm{B}}T$, it loses the energy through the dissipation on $\mathrm{Re}(Z_{\mathrm{eff}})$ by the damping constant γ_z

$$\gamma_z = \frac{q^2 R_{\mathrm{eff}}}{m D_z^2} \tag{2.108}$$

until it reaches an equilibrium with the thermal voltage source u_{th}, where

$$\langle E_z \rangle = \frac{1}{2} m \omega_z^2 \langle z^2 \rangle = k_{\mathrm{B}} T. \tag{2.109}$$

This means of cooling of the motional energies of particles is called *resistive cooling*.

The state of the system after the thermalization[3] is what is represent by Fig. 2.7 (B), where the particle behaves as the effective $l_{\mathrm{s}}, c_{\mathrm{s}}$. Then the total impedance Z_{tot} becomes

$$Z_{\mathrm{tot}}(\omega) = \left(\frac{1}{i\left(\omega l_{\mathrm{s}} - \dfrac{1}{\omega c_{\mathrm{s}}}\right)} + \frac{1}{R_{\mathrm{eff}}} + i\left(\omega C_{\mathrm{eff}} - \frac{1}{\omega L}\right) \right)^{-1}, \tag{2.110}$$

[2]The effective temperature of the detection system is important information, therefore is measured regularly (see Section 14.1.1) to assure that it does not vary significantly over the time when the measurements are performed.

[3] In plasma physics, temperature of a cloud of particles is defined from the energy distribution of the ensemble of particles. When we discuss the *temperature* defined for a single particle in this thesis, we always treat a mode of the particle in equilibrium to a certain thermal bath, therefore we stand on the Ergodic hypothesis and define the respective temperature by the energy distribution obtained by repetitive measurements of energy of such a mode of the particle.

$$
\begin{aligned}
\mathrm{Re}(Z_{\mathrm{tot}}(\omega)) &= \frac{R_{\mathrm{eff}}}{1+\left(\frac{1}{\Delta\omega_{0,\mathrm{eff}}}\left(\frac{\omega^2-\omega_{0,\mathrm{eff}}^2}{\omega}\right)-\left(\frac{1}{\gamma_z}\left(\frac{\omega^2-\omega_z^2}{\omega}\right)\right)^{-1}\right)^2} \\
&\approx \frac{R_{\mathrm{eff}}}{1+\left(\frac{2}{\Delta\omega_{0,\mathrm{eff}}}(\omega-\omega_{0,\mathrm{eff}})\right)^2\left(1-\frac{\gamma_z}{2(\omega-\omega_z)}\cdot\frac{\Delta\omega_{0,\mathrm{eff}}}{2(\omega-\omega_{0,\mathrm{eff}})}\right)^2} \\
&= R_{\mathrm{eff}}\left(1+\left(\frac{2(\omega-\omega_0)}{\Delta\omega_0}-\frac{\gamma_z}{2(\omega-\omega_z)}\right)^2\right).^{-1}
\end{aligned}
\tag{2.111}
$$

Approximations by $|\omega-\omega_{0,\mathrm{res}}| \ll \omega$, $|\omega-\omega_z| \ll \omega$ is used in the second last line of Eq. (2.111). The function $\mathrm{Re}(Z_{\mathrm{tot}}(\omega))$ has a peak at $\omega=\omega_{0,\mathrm{eff}}$ with a width $\Delta\omega_{0,\mathrm{eff}}$ and a dip at $\omega=\omega_z$ with a width γ_z. Near the peak of the resonance of the detection system, i.e. $|\omega-\omega_0| \ll \Delta\omega_0$, this is further simplified to

$$
\mathrm{Re}(Z_{\mathrm{tot}}(\omega)) \approx R_{\mathrm{eff}}\left(1+\left(\frac{\gamma_z}{2(\omega-\omega_z)}\right)^2\right)^{-1}. \tag{2.112}
$$

The power spectrum $P_{\mathrm{th}}(\omega)$ of the dissipation by u_{th} is expressed as

$$
\begin{aligned}
P_{\mathrm{th}}(\omega) &= \frac{G^2(\kappa^2\overline{u_{\mathrm{th}}^2}(\omega)+e_{\mathrm{n}}^2)}{R_{\mathrm{in}}} \\
&= \frac{G^2}{R_{\mathrm{in}}}\left(4\kappa^2 k_{\mathrm{B}}T\,\mathrm{Re}(Z_{\mathrm{tot}}(\omega))+e_{\mathrm{n}}^2\right)f_{\mathrm{b}}
\end{aligned}
\tag{2.113}
$$

with G being the gain of the amplifier, e_{n}^2 the equivalent input noise at the amplifier input, and the R_{in} the input impedance of the measurement device. κ $(0<\kappa<1)$ represents a coupling factor defining the coupling strength of the resonator signal to the output, as represented in Fig. 2.7. (see Chapter 9 for details). By sufficient amplification, we can measure the axial frequency by observing this thermally driven resonance Eq. (2.113).

An example of the Fast Fourier Transform (FFT) spectrum of data of an actual detection system is shown in Fig. 2.8. The data points in the blue dots are well fitted by the theoretical line shape based on Eq. (2.111). Thus the axial frequency of the particle is measured by the interaction with the detection system having a close resonance frequency to the oscillation. Merits of this method are that it is non-destructive, and that the particle is measured at low energy, reducing the systematic effects by the trap imperfections discussed earlier. Typical axial amplitudes of a single particle in thermal equilibrium are on the order of 10 µm.

The width of the dip determined by γ_z is called a *dip-width* $\Delta\nu_z$ defined as

$$
\Delta\nu_z \equiv \frac{\gamma_z}{2\pi} = \frac{1}{2\pi}\frac{q^2R_{\mathrm{eff}}}{mD_z^2}, \tag{2.114}
$$

likewise, the width of the resonance $\Delta\nu_0 \equiv \Delta\omega_{0,\mathrm{eff}}/(2\pi)$. The signal height at $\nu=\nu_z\pm\Delta\nu_z/2$ is,

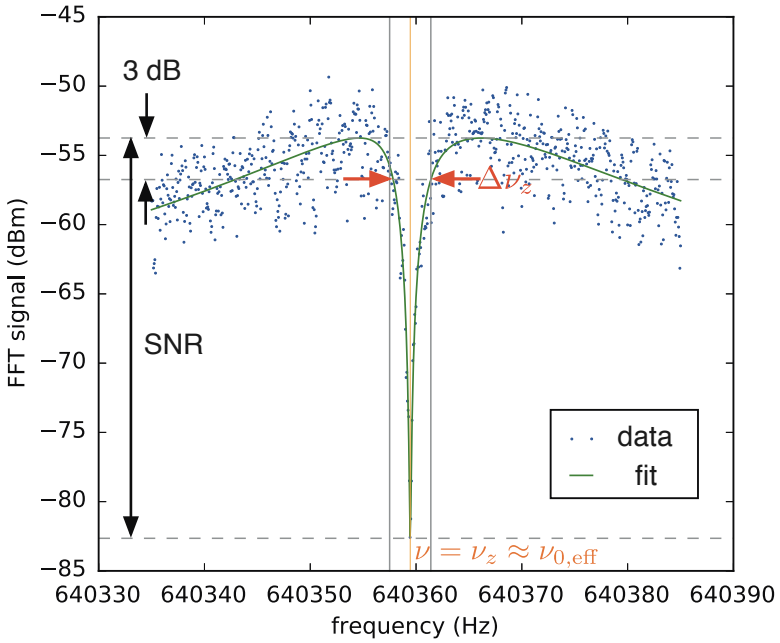

Figure 2.8: FFT spectrum of an axial detection system. A dip produced by a single antiproton is observed at the center of the spectrum.

from Eq. (2.111),

$$\begin{aligned}\frac{P_{\mathrm{th}}(\nu = \nu_z \pm \Delta\nu_z/2)}{P_{\mathrm{th}}(\nu)|_{\max}} &= \left[1 + \left(2\left(\frac{\nu_0 - \nu_z \pm \Delta\nu_z/2}{\Delta\nu_0}\right) \mp 1\right)^2\right]^{-1} \\ &\approx \left[1 + \left(\frac{\Delta\nu_z}{\Delta\nu_0} - 1\right)^2\right]^{-1} \quad (\because \nu_z \approx \nu_z)\end{aligned} \tag{2.115}$$

When $\Delta\nu_z \ll \Delta\nu_0$ (or, equivalently $\gamma_z \ll \Delta\omega_0$), Eq. (2.115) $\approx 1/2$, thus the dip-width appears as the FWHM of the dip as in Fig. 2.8 (the 3 dB width in the log scale of the graph).

The signal-to-noise ratio (SNR) of the dip is determined by the SNR of the resonance of the detection system. We define it in the the ratio of the voltages, as given by

$$\begin{aligned}\mathrm{SNR} = \frac{\sqrt{\overline{u_{\mathrm{th}}^2}(\omega)|_{\omega\approx\omega_{0,\mathrm{eff}}} + e_{\mathrm{n}}^2}}{e_{\mathrm{n}}} &= \frac{\sqrt{4k_{\mathrm{B}}TR_{\mathrm{eff}}\kappa^2 + e_{\mathrm{n}}^2}}{e_{\mathrm{n}}} \\ &\approx \frac{\sqrt{4k_{\mathrm{B}}TR_{\mathrm{eff}}}\kappa}{e_{\mathrm{n}}},\end{aligned} \tag{2.116}$$

where e_{n} represents the equivalent input noise of the amplifier in Fig. 2.7, which defines the baseline of the resonance in Fig. 2.8. It is practical to discuses the SNR in the decibel scale, which we define as

$$\mathrm{SNR}\,[\mathrm{dB}] = 20\log_{10}\left(\frac{\sqrt{4k_{\mathrm{B}}TR_{\mathrm{eff}}}\kappa}{e_{\mathrm{n}}}\right) = 10\log_{10}\left(\frac{4k_{\mathrm{B}}TR_{\mathrm{eff}}\kappa^2}{e_{\mathrm{n}}^2}\right). \tag{2.117}$$

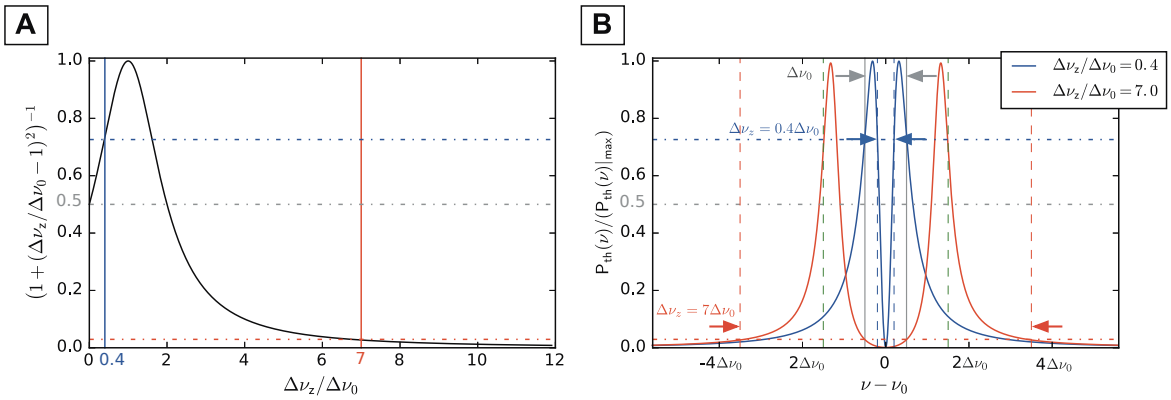

Figure 2.9: **(A)** Signal height of the resonance at $\nu = \nu_z \pm \Delta\nu_z/2$ evaluated from Eq. (2.115), as a function of $\Delta\nu_z/\Delta\nu_0$. **(B)** Example of spectra for $\Delta\nu_z/\Delta\nu_0 = 0.4, 7.0$. The frequencies at $\nu = \nu_z \pm \Delta/2$ are indicated by vertical lines. Note that the vertical axis of (B) is in a linear scale, unlike Fig. 2.8. When the dip-width $\Delta\nu_0$ is sufficiently small compared to $\Delta\nu_0$, $\Delta\nu_z$ corresponds to the FWHM of the dip. As $\Delta\nu_z$ becomes larger, the signal height at $\nu = \nu_z \pm \Delta\nu_z/2$ scales according to (A). For the case $\Delta\nu_z/\Delta\nu_0 = 7.0$, $\Delta\nu_z$ is about twice larger than the FWHM of the dip.

The third expression in Eq. (2.117) is an equivalent definition of the SNR as the ratio of power. In reality, detuning of the dip frequency or instability of the axial frequency can cause the minimum of the dip not to reach the baseline of the resonance. If necessary, we distinguish $\mathrm{SNR}|_{\mathrm{res}}$ and $\mathrm{SNR}|_{\mathrm{dip}}$; $\mathrm{SNR}|_{\mathrm{dip}} \leq \mathrm{SNR}|_{\mathrm{res}}$.

In case of detection of multiple particles, the discussion above can be directly applied to the CM mode of the ensemble. Recalling Eq. (2.98), the dip-width of the signal of N particles is

$$\Delta\nu_{z,N} = \frac{\gamma_{z,N}}{2\pi} = N\Delta\nu_z. \tag{2.118}$$

This relation can be used to count the number of trapped particles from a measured dip-width. When a trap contains many particles; $\Delta\nu_z \gtrsim \Delta\nu_0$, the dip-width no longer corresponds to the 3 dB width of the dip. The general scaling of Eq. (2.115), the signal height at $\nu = \nu_z \pm \Delta\nu_z/2$, is shown in Fig. 2.9, where it can be seen that the "dip-width" in case $\Delta\nu_z > \Delta\nu_0$ is wider than the dip itself. However even in this case, $\Delta\nu_{z,N}$, hence the number of the particles N, can be estimated by fitting a spectrum by the line shape based on Eq. (2.111).

2.4.3 Temperature control by electronic feedback

An important experimental technique associated with the image-current detection is the control of the particle's temperature through electric feedback. It was applied to a Penning trap for the first time by B. D'Urso, B. Odom and G. Gabrielse to cool a trapped electron [105].

To discuss the principle, we consider only the dissipative interaction between the particle and the detection system. In Fig. 2.10 (A), the detection system is simplified as a resistive component R_0. The u_{th} denotes the Johnson-Nyquist noise on R_0, and the temperature T_0 expresses the temperature of

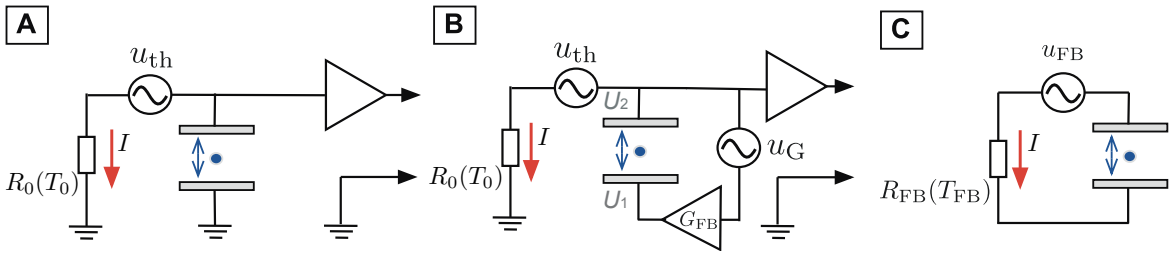

Figure 2.10: Circuit of feedback control of the temperature of the particle. **(A)** Without feedback. The detection system is represented by its effective parallel resistive component R_0. Temperature T_0 represents the temperature of the detection system without feedback, which together with R_0, defines the amplitude of the Johnson-Nyquist noise u_{th} **(B)** Feedback signal is applied to the ground level of the trap with a gain G_{FB}. **(C)** Equivalent circuit of (B) experienced by the particle in the trap.

the system which drives u_{th}. Feedback is applied conceptually as Fig. 2.10 (B). The fluctuating voltage u_{th} is fed back to the lower ground level of the system with a gain G_{FB}. u_{G} expresses noise added by application of the feedback. For the particle in the trap, this system is experienced as Fig. 2.10 (C). The equivalent $R_{\mathrm{FB}}, T_{\mathrm{FB}}, u_{\mathrm{FB}}$ are defined so that the potential induced by the particle damping and the fluctuating potential across the trap electrodes are the same between Fig. 2.10 (B) and (C), i.e.,

$$\begin{cases} \overline{U_2 - U_1} = IR_{\mathrm{FB}} \\ \overline{(U_2 - U_1)^2} - \left(\overline{U_2 - U_1}\right)^2 = \overline{u_{\mathrm{FB}}^2} \end{cases} \tag{2.119}$$

with U_2, U_1 being the potential at the electrodes as indicated in Fig. 2.10 (B). From the property of thermal noise, we assume $\overline{u_{\mathrm{th}}} = \overline{u_{\mathrm{G}}} = \overline{u_{\mathrm{FB}}} = 0$. Then Eq. (2.119) becomes

$$\begin{cases} IR_0(1 - G_{\mathrm{FB}}) = IR_{\mathrm{FB}} \\ (1 - G_{\mathrm{FB}})^2 \overline{u_{\mathrm{th}}^2} + G_{\mathrm{FB}}^2 \overline{u_{\mathrm{G}}^2} = \overline{u_{\mathrm{FB}}^2}, \end{cases} \tag{2.120}$$

$$\therefore R_{\mathrm{FB}} = (1 - G_{\mathrm{FB}})R_0, \quad \overline{u_{\mathrm{FB}}^2} = (1 - G_{\mathrm{FB}})^2 \overline{u_{\mathrm{th}}^2} + G_{\mathrm{FB}}^2 \overline{u_{\mathrm{G}}^2}. \tag{2.121}$$

The effective temperature T_{FB} is defined by

$$\overline{u_{\mathrm{FB}}^2} = 4k_B T_{\mathrm{FB}} R_{\mathrm{FB}}. \tag{2.122}$$

Therefore

$$\begin{aligned} \frac{T_{\mathrm{FB}}}{T_0} &= \left((1 - G_{\mathrm{FB}})^2 + G_{\mathrm{FB}}^2 \cdot \overline{u_{\mathrm{G}}^2} \Big/ \overline{u_{\mathrm{th}}^2}\right) \frac{R_0}{R_{\mathrm{FB}}} \\ &= 1 - G_{\mathrm{FB}} + \frac{G_{\mathrm{FB}}^2}{1 - G_{\mathrm{FB}}} \cdot \overline{u_{\mathrm{G}}^2} \Big/ \overline{u_{\mathrm{th}}^2}\,. \end{aligned} \tag{2.123}$$

Eq. (2.123) states that the temperature achieved by feedback cannot be $T_{\mathrm{FB}} = 0$ because of the

presence of the noise u_{G}. In practical discussion, we can ignore the noise u_{G}. In this case,

$$\frac{T_{\mathrm{FB}}}{T_0} = \frac{R_{\mathrm{FB}}}{R_0} = 1 - G_{\mathrm{FB}}. \tag{2.124}$$

Experimentally, the gain and the phase of the feedback signal can be set by amplifiers and phase-shifting components in the feedback circuit (see Section 9.3). We call $G_{\mathrm{FB}} > 0$ in the setting of Fig. 2.10 *negative feedback* (equivalent to applying a negative-phase feedback signal on the level of U_2), which cools the detection system and hence the particle. *Positive feedback*, corresponding to $G_{\mathrm{FB}} < 0$, can also be applied by an appropriate choice of the phase to heat the particle.

From Eq. (2.106), the effective parallel resistances R_0, R_{FB} are proportional to the Q of the respective resonances of the detection system:

$$\frac{Q_{\mathrm{FB}}}{Q_0} = \frac{T_{\mathrm{FB}}}{T_0}, \tag{2.125}$$

which can be used in practice to estimate the temperature of the system. To discuss the features of the dip signal with the fed-back detection system, we recall Eq. (2.114) to find

$$\frac{\Delta\nu_{z,\mathrm{FB}}}{\Delta\nu_{z,0}} = \frac{\gamma_{z,\mathrm{FB}}}{\gamma_{z,0}} = \frac{T_{\mathrm{FB}}}{T_0}. \tag{2.126}$$

2.5 Sideband coupling method

Among the eigenfrequencies of a particle in a Penning trap, the axial frequency ω_z can be measured by the image-current detection discussed in the last section. The two radial eigenfrequencies ω_+, ω_- can be measured by coupling the radial mode to the axial mode by an external drive. This so-called *sideband coupling method* was first demonstrated by E. A. Cornell et al. [106].

Principle of measurement of the radial eigenfrequencies

We consider an oscillating quadruple electric potential in a form of

$$\Phi_q(t) = \mathcal{E} zx \cos(\omega_{\mathrm{rf}} t + \varphi_{\mathrm{rf}}). \tag{2.127}$$

Here $\mathcal{E}$ corresponds to the gradient of the electric field. Experimentally, such potential can be generated by applying an alternating electric potential on a radially segmented electrode (see Section 5.4.2). Φ_q contributes to the Hamiltonian of the system by an interaction term

$$H_{\mathrm{int}} = q\mathcal{E} zx \cos(\omega_{\mathrm{rf}} t + \varphi_{\mathrm{rf}}). \tag{2.128}$$

By the canonical transform Eq. (2.21) $(x, y, z, p_x, p_y, p_z) \mapsto (q_+, q_-, q_3, p_+, p_-, p_3)$, the term zx can be decomposed to $q_3(q_+ + q_-)$. In the following discussion, it is more convenient to discuss using the mode amplitudes z, r_+, r_- with $r_\pm$ defined as

$$r_+ = \sqrt{m\omega_1}q_+, \quad r_- = \sqrt{m\omega_1}q_- \tag{2.129}$$

with which we rewrite H_{int} as

$$H_{\text{int}} = H_{\text{int},+} + H_{\text{int},-} \tag{2.130}$$

$$\begin{aligned} H_{\text{int},+} &= q\mathcal{E}zr_+ \cos(\omega_{\text{rf}}t + \varphi_{\text{rf}}) \\ H_{\text{int},-} &= q\mathcal{E}zr_- \cos(\omega_{\text{rf}}t + \varphi_{\text{rf}}). \end{aligned} \tag{2.131}$$

Hereafter, we shall treat them individually; first $H_{\text{int},+}$ and then $H_{\text{int},-}$. We will later see that they take effects in different cases. The equations of motion under $H + H_{\text{int},+}$ can be easily found by the canonical equations of motion of q_+, p_+, q_3, p_3 (Eq. (2.23)) with inclusion of $H_{\text{int},+}$. The outcome is

$$\begin{cases} \ddot{r}_+ + \omega_+^2 r_+ &= -\dfrac{q\mathcal{E}}{m} z \cos(\omega_{\text{rf}}t + \varphi_{\text{rf}}) \\ \ddot{z} + \omega_z^2 z &= -\dfrac{q\mathcal{E}}{m} r_+ \cos(\omega_{\text{rf}}t + \varphi_{\text{rf}}) \end{cases} \tag{2.132}$$

From a general knowledge of a forced oscillator, we expect the solution to take forms of modulation of the original oscillations at ω_z and ω_+, hence we bring the ansatzes below:

$$r_+(t) = \text{Re}\left(\frac{C_+(t)}{\sqrt{m\omega_+}} e^{i\omega_+ t}\right), \quad z(t) = \text{Re}\left(\frac{C_z(t)}{\sqrt{m\omega_z}} e^{i\omega_z t}\right). \tag{2.133}$$

The complex notation is introduced to facilitate the calculation. $C_+(t)$ and $C_z(t)$ are defined as complex functions, having dimensions of actions. We also introduce a complex notation for the oscillatory term at ω_{rf}:

$$\frac{q\mathcal{E}}{2\sqrt{m^2\omega_z\omega_+}} \cos(\omega_{\text{rf}}t + \varphi_{\text{rf}}) = \text{Re}\left(\Omega_0^{(z+)} e^{i\omega_{\text{rf}}t}\right), \tag{2.134}$$

with $\Omega_0^{(z+)}$ being a complex number which includes the phase φ_{rf} as $\Omega_0^{(z+)} = |\Omega_0^{(z+)}|e^{i\varphi_{\text{rf}}}$. $\Omega_0^{(z+)}$ is defined to have a dimension of a frequency. Assuming that C_+ and C_z vary much more slowly compared to ω_+ and ω_z, respectively, Eqs. (2.133) and (2.134) rewrite Eq. (2.132) to be

$$\begin{cases} \text{Re}\left(i\omega_+ \dot{C}_+ e^{i\omega_+ t}\right) = -\omega_+ \,\text{Re}(\Omega_0^{(z+)} e^{i\omega_{\text{rf}}t}) \cdot \text{Re}(C_z e^{i\omega_z t}) & (2.135) \\ \text{Re}\left(i\omega_z \dot{C}_z e^{i\omega_z t}\right) = -\omega_z \,\text{Re}(\Omega_0^{(z+)} e^{i\omega_{\text{rf}}t}) \cdot \text{Re}(C_+ e^{i\omega_+ t}). & (2.136) \end{cases}$$

Next, we multiply $e^{-i\omega_+ t}$ to both sides of Eq. (2.135), and $e^{i\omega_z t}$ to Eq. (2.136).

$$\begin{aligned}(\text{Eq. (2.135) L.H.S.}) \cdot e^{-i\omega_+ t} &= \frac{e^{-i\omega_+ t}}{2}\left(i\omega_+ \dot{C}_+ e^{i\omega_+ t} - i\omega_+ \dot{C}_+ e^{-i\omega_+ t}\right) \\ &= \frac{1}{2}\left(i\omega_+ \dot{C}_+ - i\omega_+ \dot{C}_+ e^{-2i\omega_+ t}\right) \qquad (2.137)\end{aligned}$$

$$\begin{aligned}(\text{Eq. (2.135) R.H.S.}) \cdot e^{-i\omega_+ t} &= \frac{(-\omega_+)e^{-i\omega_+ t}}{4}\left(\Omega_0^{(z+)} e^{i\omega_{\text{rf}} t} + \Omega_0^{(z+)*} e^{-i\omega_{\text{rf}} t}\right)\left(C_z e^{i\omega_z t} + C_z e^{-i\omega_z t}\right) \\ &= \frac{-\omega_+ C_z}{4}\Big(\Omega_0^{(z+)} e^{i(\omega_{\text{rf}} - \omega_+ + \omega_z)t} + \Omega_0^{(z+)*} e^{-i(\omega_{\text{rf}} + \omega_+ - \omega_z)t} \\ &\qquad + \Omega_0^{(z+)} e^{i(\omega_{\text{rf}} - \omega_+ - \omega_z)t} + \Omega_0^{(z+)*} e^{-i(\omega_{\text{rf}} + \omega_+ + \omega_z)t}\Big), \qquad (2.138)\end{aligned}$$

with $\Omega_0^{(z+)*}$ expressing the complex conjugate of $\Omega_0^{(z+)}$. In the same way,

$$(\text{Eq. (2.136) L.H.S.}) \cdot e^{-i\omega_z t} = \frac{1}{2}\left(i\omega_z \dot{C}_z - i\omega_z \dot{C}_z e^{-2i\omega_z t}\right) \qquad (2.139)$$

$$\begin{aligned}(\text{Eq. (2.136) R.H.S.}) \cdot e^{-i\omega_z t} = \frac{-\omega_z C_+}{4}\Big(&\Omega_0^{(z+)} e^{i(\omega_{\text{rf}} + \omega_+ - \omega_z)t} + \Omega_0^{(z+)*} e^{-i(\omega_{\text{rf}} - \omega_+ + \omega_z)t} \\ &+ \Omega_0^{(z+)} e^{i(\omega_{\text{rf}} - \omega_+ - \omega_z)t} + \Omega_0^{(z+)*} e^{-i(\omega_{\text{rf}} + \omega_+ + \omega_z)t}\Big). \qquad (2.140)\end{aligned}$$

By the rotating wave approximation, we ignore fast oscillatory terms $\geq \omega_+$ for Eqs. (2.137) and (2.138), and ignore $\geq \omega_z$ for Eqs. (2.139) and (2.140). The secular terms on the right hand sides remain in either of the following two cases:

$$\begin{cases}\text{(i)} & \omega_{\text{rf}} \approx \omega_+ - \omega_z \\ \text{(ii)} & \omega_{\text{rf}} \approx \omega_+ + \omega_z.\end{cases} \qquad (2.141)$$

Otherwise, the equations of motion reduce to the ones without the interaction Hamiltonian, thus the two modes do not couple to each other.

By applying the same procedure as Eqs. (2.135) to (2.141) to the interaction under $H + H_{\text{int},-}$ whose associated equations of motion being

$$\begin{cases}\ddot{r}_- + \omega_-^2 r_- &= \dfrac{q\mathcal{E}}{m} z\cos(\omega_{\text{rf}} t + \varphi_{\text{rf}}) \\ \ddot{z} + \omega_z^2 z &= -\dfrac{q\mathcal{E}}{m} r_- \cos(\omega_{\text{rf}} t + \varphi_{\text{rf}}),\end{cases} \qquad (2.142)$$

with

$$r_-(t) = \text{Re}\left(\frac{C_-(t)}{\sqrt{m\omega_-}} e^{i\omega_- t}\right), \quad \frac{q\mathcal{E}}{2\sqrt{m^2\omega_z\omega_-}}\cos(\omega_{\text{rf}} t + \varphi_{\text{rf}}) = \text{Re}\left(\Omega_0^{(z-)} e^{i\omega_{\text{rf}} t}\right). \qquad (2.143)$$

It is found that the interaction becomes effective only in either of the two cases below:

$$\begin{cases} \text{(iii)} & \omega_{\mathrm{rf}} \approx \omega_z + \omega_- \\ \text{(iv)} & \omega_{\mathrm{rf}} \approx \omega_z - \omega_-. \end{cases} \tag{2.144}$$

Thus the terms $H_{\mathrm{int},+}$ and $H_{\mathrm{int},-}$ become effective separately.

We define the detuning $\delta_{\pm}^{(\pm)}$ as

$$\delta_{+}^{(+)} = \omega_{\mathrm{rf}} - (\omega_+ + \omega_z) \quad (\text{for } \omega_{\mathrm{rf}} \approx \omega_+ + \omega_z) \tag{2.145}$$

$$\delta_{+}^{(-)} = \omega_{\mathrm{rf}} - (\omega_+ - \omega_z) \quad (\text{for } \omega_{\mathrm{rf}} \approx \omega_+ - \omega_z). \tag{2.146}$$

$$\delta_{-}^{(+)} = \omega_{\mathrm{rf}} - (\omega_z + \omega_-) \quad (\text{for } \omega_{\mathrm{rf}} \approx \omega_z + \omega_-) \tag{2.147}$$

$$\delta_{-}^{(-)} = \omega_{\mathrm{rf}} - (\omega_z - \omega_-) \quad (\text{for } \omega_{\mathrm{rf}} \approx \omega_z - \omega_-). \tag{2.148}$$

In case (i) $\omega_{\mathrm{rf}} \approx \omega_+ - \omega_z$, Eqs. (2.135) and (2.136) are simplified to

$$\frac{\mathrm{d}}{\mathrm{d}t}\begin{pmatrix} C_+ \\ C_z \end{pmatrix} = \frac{1}{2}\begin{pmatrix} 0 & i\Omega_0^{(z+)} e^{i\delta_+^{(-)}t} \\ i\Omega_0^{(z+)*} e^{-i\delta_+^{(-)}t} & 0 \end{pmatrix}\begin{pmatrix} C_+ \\ C_z \end{pmatrix}. \tag{2.149}$$

This is analogous to a two-level system driven by an external field [107]. At $\delta_+^{(-)} = 0$, the amplitudes C_+ and C_z, having the dimension of actions, are exchanged at the Rabi frequency $|\Omega_0^{(z+)}|$.

In case $\delta_+^{(-)} \neq 0$, we expect the solution to be expressed by a frequency ω, differing from ω_z by $\epsilon \equiv \omega - \omega_z$ as

$$\begin{pmatrix} C_+(t) \\ C_z(t) \end{pmatrix} = \begin{pmatrix} D_+ e^{i(\epsilon + \delta_+^{(-)})t} \\ D_z e^{i\epsilon t} \end{pmatrix}. \tag{2.150}$$

This is by an analogy of the two-level states [108] where the dressed-states can be expressed in a form $e^{i\varphi/2}|1\rangle \pm e^{-i\varphi/2}|2\rangle$ with $e^{-i\varphi/2}$ being the phase from the external field. (D_+, D_z) is the eigenvector for ϵ.

Substituting Eq. (2.150) to Eq. (2.149) and applying the rotating wave approximation, we obtain

$$\begin{cases} (\epsilon + \delta_+^{(-)}) \cdot D_+ &= \dfrac{\Omega_0^{(z+)}}{2} D_z \\ \epsilon D_z &= \dfrac{\Omega_0^{(z+)*}}{2} D_+ \end{cases} \tag{2.151}$$

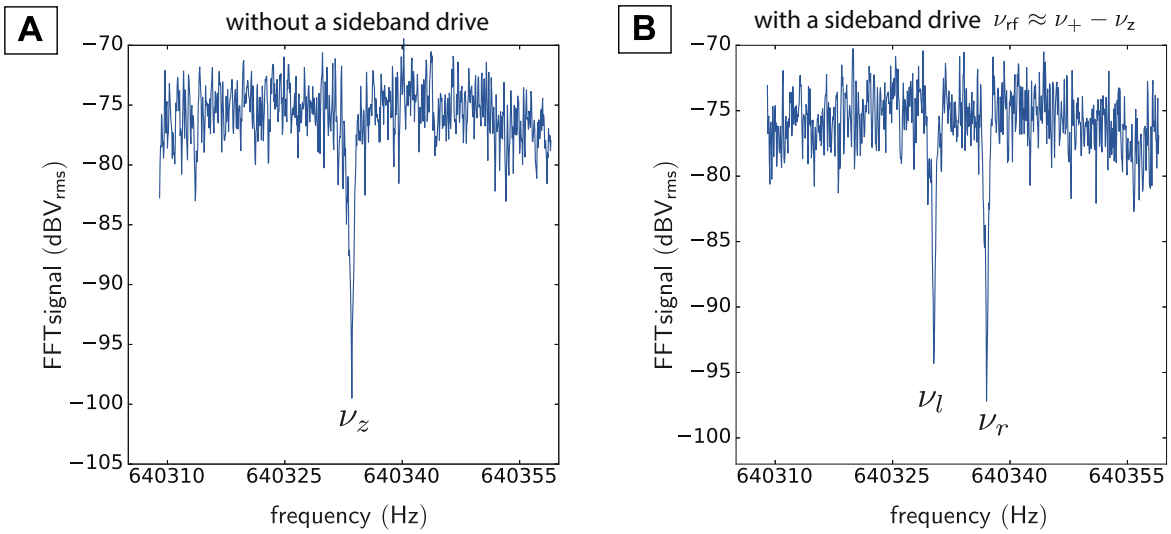

Figure 2.11: Application of the sideband coupling method. **(A)** Axial dip spectrum without application of a drive. **(B)** The spectrum during application of a sideband drive at $\nu_{\mathrm{rf}} \approx \nu_+ - \nu_z$. A double-dip spectrum is observed, where the dip is splint into two frequency component.

from which we obtain the characteristic equation for ϵ below:

$$\begin{aligned} \epsilon^2 + \delta_+^{(-)}\epsilon - \frac{|\Omega_0^{(z+)}|^2}{4} &= 0 \\ \therefore \epsilon = \frac{1}{2}\left(-\delta_+^{(-)} \pm \sqrt{(\delta_+^{(-)})^2 + |\Omega_0^{(z+)}|^2}\right). \end{aligned} \tag{2.152}$$

They represent the frequencies of the new eigenstates in the presence of the drive, between which the action exchange occurs at a Rabi frequency of $\sqrt{(\delta_+^{(-)})^2 + |\Omega_0^{(z+)}|^2}$. In Fig. 2.11, this effect is observed in spectra obtained in an actual measurement. The spectrum in Fig. 2.11 (A) is a spectrum of a dip signal at the axial frequency ν_z without a coupling drive. Fig. 2.11 (B) shows the spectrum while a sideband coupling drive at $\nu_{\mathrm{rf}} \approx \nu_+ - \nu_z$, is applied. The dip is split into two frequency components, labeled by "l" and "r" (meaning "left" and "right"), corresponding to two ϵ of Eq. (2.152). They are called *double-dip*. They can be expressed as

$$\begin{aligned} \nu_{\mathrm{l}} &= \nu_z + \frac{\epsilon_{\mathrm{l}}}{2\pi} \\ \nu_{\mathrm{r}} &= \nu_z + \frac{\epsilon_{\mathrm{r}}}{2\pi} \end{aligned} \tag{2.153}$$

$$\text{with} \quad \epsilon_{\mathrm{l}} \equiv -\frac{\delta_+^{(-)}}{2} - \frac{\sqrt{(\delta_+^{(-)})^2 + |\Omega_0^{(z+)}|^2}}{2}, \; \epsilon_{\mathrm{r}} \equiv -\frac{\delta_+^{(-)}}{2} + \frac{\sqrt{(\delta_+^{(-)})^2 + |\Omega_0^{(z+)}|^2}}{2}$$

Between $\nu_z, \nu_+\nu_{\mathrm{rf}}, \nu_{\mathrm{l}}, \nu_{\mathrm{r}}$, an important relation

$$\nu_+ = \nu_{\mathrm{rf}} - \nu_z + \nu_{\mathrm{l}} + \nu_{\mathrm{r}} \tag{2.154}$$

is found, which cancels the detuning and allows determination of the modified cyclotron frequency ν_+ from $\nu_z, \nu_{\rm rf}, \nu_{\rm l}, \nu_{\rm r}$, which can all be obtained through measurements.

The discussion up to here for case (i) $\omega_{\rm rf} \approx \omega_+ - \omega_z$ can be applied in the same way to the other cases listed in Eqs. (2.141) and (2.144). The relation corresponds to Eq. (2.154) in case (iii) $\omega_{\rm rf} \approx \omega_z + \omega_-$ is

$$\nu_- = \nu_{\rm rf} + \nu_z - (\nu_{\rm l} + \nu_{\rm r}). \tag{2.155}$$

For cases (ii) and (iv), a term in a form of $\sqrt{\delta^2 - \Omega_0^2}$ appears in Eq. (2.152), leading to exponential growths of the modes involved in the coupling. The behavior strongly depends on the initial phases of the modes, and equilibrium states as in cases (i, iii) are not observed.

Mode temperatures during the sideband coupling

During an application of a sideband coupling drive, the action exchange between the involved modes occurs continuously. The temperature can be defined for the mode which is coupled to the axial mode. This can be more easily discussed in the quantum picture. The action exchange discussed on Eq. (2.149) corresponds to an exchange of quanta in the quantum picture. In the following, we take as an example the coupling between the axial- and modified-cyclotron modes by a sideband drive $\omega_{\rm rf} = \omega_+ - \omega_z$.

The possible transitions caused by the drive are either of $(n_+, n_z) \to (n_+ + 1, n_z - 1)$ or $(n_+, n_z) \to (n_+ - 1, n_z + 1)$. The matrix elements of these transitions are calculated to be

$$\begin{aligned} |\langle n_+ + 1, n_z - 1| a_z a_+^\dagger |n_+, n_z\rangle|^2 &= (n_+ + 1) n_z \\ |\langle n_+ - 1, n_z + 1| a_z^\dagger a_+ |n_+, n_z\rangle|^2 &= n_+ (n_z + 1) \end{aligned} \tag{2.156}$$

Therefore if $n_+ > n_z$, $(n_+, n_z) \to (n_+ - 1, n_z + 1)$ occurs with a higher probability, and $(n_+, n_z) \to (n_+ - 1, n_z + 1)$ in case $n_z < n_+$. Thus at thermal equilibrium, $\langle n_+ \rangle = \langle n_z \rangle$. In units of the mode energies, this corresponds to

$$\begin{aligned} \frac{\langle E_+ \rangle}{\hbar \omega_+} = \langle n_+ \rangle + \frac{1}{2} = \langle n_z \rangle + \frac{1}{2} = \frac{\langle E_z \rangle}{\hbar \omega_z} \\ \therefore \langle E_+ \rangle = \frac{\omega_+}{\omega_z} \langle E_z \rangle = \frac{\omega_+}{\omega_z} k_{\rm B} T_z. \end{aligned} \tag{2.157}$$

Likewise, a relation

$$\langle E_- \rangle = \frac{\omega_-}{\omega_z} k_{\rm B} T_z \tag{2.158}$$

is found for the axial-magnetron coupling by $\omega_{\rm rf} = \omega_z + \omega_-$. Thus the ratio of the eigenfrequencies determine the temperature during the coupling. This can be used to cool the radial modes with a detection system interacting on the axial mode. This technique is referred to as *sideband cooling*.

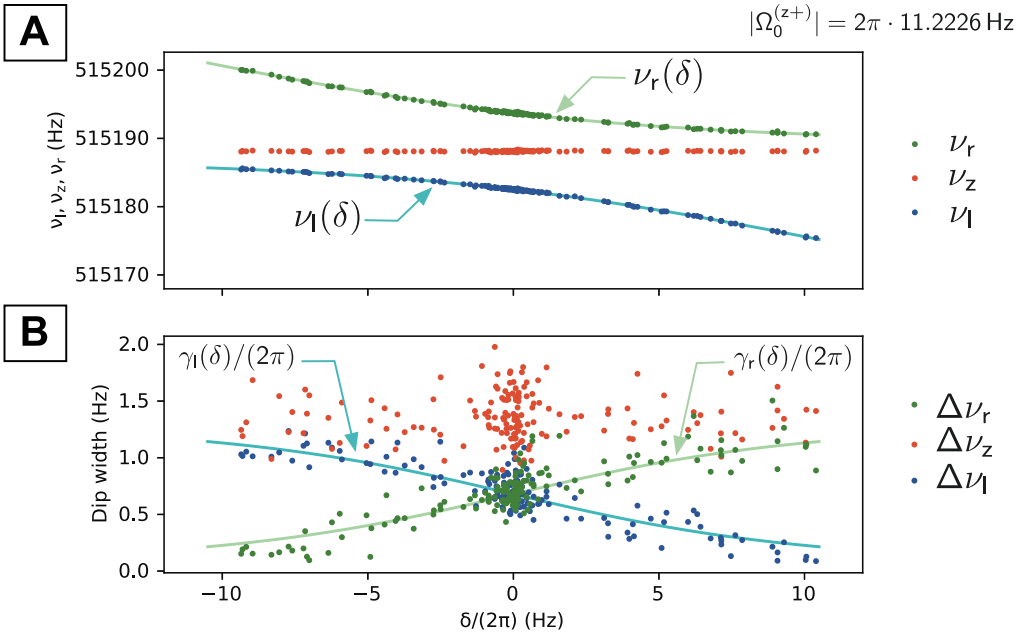

Figure 2.12: Measurement of the classical avoided crossing. The dip frequencies ν_z, ν_-, ν_+ are plotted in (A) and the dip-widths $\Delta\nu_z, \Delta\nu_-, \Delta\nu_+$ in (B) as functions of the detuning $\delta/(2\pi)$. The theoretical curves of Eq. (2.153) is shown in (A) with $|\Omega_0^{(z+)}| = 2\pi \cdot 11.2226\,\mathrm{Hz}$. The curves in (B) are drawn from Eq. (2.165) with $|\Omega_0^{(z+)}| = 2\pi \cdot 11.2226\,\mathrm{Hz}, \nu_z = 515\,188.121\,\mathrm{Hz}, \gamma_z = 2\pi\Delta\nu_z = 2\pi \cdot 1.358\,\mathrm{Hz}$.

Classical Avoided crossing

If the measurement of the double dip is repeated for sideband frequency ν_{rf}, the scaling of the double-dip frequencies ν_-, ν_+ against the detuning δ according to Eq. (2.153) is observed. This property is called the *classical avoided crossing* [106]. The experimentally observed scaling is shown in Fig. 2.12. In Fig. 2.12 (A), the theoretical scaling of Eq. (2.153) with $|\Omega_0^{z+}|/(2\pi) = 11.226\,\mathrm{Hz}$ are shown, which are found to be in good agreement with the measured data points. By looking at Fig. 2.12 (B), we observe that there is also a scaling according to δ for the dip-widths $\Delta\nu_-, \Delta\nu_+$ of the double-dip. This reflects the scaling of the damping experienced by theses dressed eigenmodes, which can be explained as below.

First, we regard the axial mode with the interaction of the detection system as a forced damped oscillation:

$$\ddot{z} + \gamma_z \dot{z} + \omega_z^2 z = f(t). \tag{2.159}$$

The function $f(t)$ on the right hand side represents an external force which drives the oscillation, and can be regarded as the force from the Johnson-Nyquist noise of the detection system. Because $\gamma_z \ll \omega_z$, this is a case of the underdamped oscillation, and γ_z determines the width of the resonance, which is the dip-width in this case [93]. We seek a characteristic frequency by asserting $z = z_0 e^{i\tilde{\omega}t}$

with (L.H.S.) = 0, obtaining the result

$$\tilde{\omega} = \frac{i\gamma_z \pm \sqrt{4\omega_z^2 - \gamma_z^2}}{2} \tag{2.160}$$

Thus a relation between the characteristic frequency $\tilde{\omega}$ and the damping γ_z is found to be

$$\gamma_z = 2\,\mathrm{Im}(\tilde{\omega}). \tag{2.161}$$

Now let us turn back to the example of coupling between the axial and the modified cyclotron mode. Inclusion of the damping term γ_z in the equation of motion of z modifies Eq. (2.149) to

$$\frac{\mathrm{d}}{\mathrm{d}t}\begin{pmatrix} C_+ \\ C_z \end{pmatrix} = \begin{pmatrix} 0 & \frac{i}{2}\Omega_0^{(z+)} e^{i\delta_+^{(-)}t} \\ \frac{i}{2}\frac{\omega_z}{\tilde{\omega}_z}\Omega_0^{(z+)*} e^{-i\delta_+^{(-)}t} & -\frac{\gamma_z}{2}\frac{\omega_z}{\tilde{\omega}_z} \end{pmatrix}\begin{pmatrix} C_+ \\ C_z \end{pmatrix} \tag{2.162}$$

$$\text{with } \tilde{\omega}_z \equiv \omega_z - i\frac{\gamma_z}{2}.$$

We substitute the ansatz Eq. (2.150) again, but allowing ϵ to be complex, then obtain

$$\begin{aligned} \epsilon_\mathrm{l} &= \frac{1}{2}\left(-\delta + i\frac{\gamma_z}{2}\frac{\omega_z}{\tilde{\omega}_z} - \sqrt{\delta^2 + (|\Omega_0^{(z+)}|^2 + i\delta\gamma_z)\frac{\omega_z}{\tilde{\omega}_z} - \frac{\gamma_z^2}{4}\left(\frac{\omega_z}{\tilde{\omega}_z}\right)^2}\right) \\ \epsilon_\mathrm{r} &= \frac{1}{2}\left(-\delta + i\frac{\gamma_z}{2}\frac{\omega_z}{\tilde{\omega}_z} + \sqrt{\delta^2 + (|\Omega_0^{(z+)}|^2 + i\delta\gamma_z)\frac{\omega_z}{\tilde{\omega}_z} - \frac{\gamma_z^2}{4}\left(\frac{\omega_z}{\tilde{\omega}_z}\right)^2}\right). \end{aligned} \tag{2.163}$$

The damping of l- and r modes are obtained from above by

$$\gamma_\mathrm{l} = 2\,\mathrm{Im}(\epsilon_\mathrm{l}), \quad \gamma_\mathrm{r} = 2\,\mathrm{Im}(\epsilon_\mathrm{r}) \tag{2.164}$$

In Fig. 2.12, the scaling of measured dip-widths of the double-dip is shown together with $\gamma_\mathrm{l}/(2\pi)$ and $\gamma_\mathrm{r}/(2\pi)$ calculated from Eq. (2.165), to find a good agreement. At $\delta \approx 0$, Eq. (2.165) is simplified to

$$\begin{aligned} \epsilon_\mathrm{l} &= \frac{1}{2}\left(i\frac{\gamma_z}{2}\frac{\omega_z}{\tilde{\omega}_z} - \sqrt{|\Omega_0^{(z+)}|^2 \cdot \frac{\omega_z}{\tilde{\omega}_z} - \frac{\gamma_z^2}{4}\left(\frac{\omega_z}{\tilde{\omega}_z}\right)^2}\right) \\ &\approx \frac{1}{2}\left(-\frac{\gamma_z^2}{4\omega_z} + i\frac{\gamma_z}{2} - \sqrt{|\Omega_0^{(z+)}|^2\left(1 + i\frac{\gamma_z}{2\omega_z}\right) - \frac{\gamma_z^2}{4}\left(1 - \frac{\gamma_z^2}{4\omega_z^2} + i\frac{\gamma_z}{\omega_z}\right)}\right) \\ &\quad \left(\because \frac{\omega_z}{\tilde{\omega}_z} \approx 1 + i\frac{\gamma_z}{2\omega_z}\right) \end{aligned} \tag{2.165}$$

The imaginary part of the term in the square root of Eq. (2.165) is ≈ 0 under $|\Omega_0^{(z+)}|, \gamma_z \ll \omega_z$.

Therefore at $\delta \approx 0$,

$$\gamma_{\mathrm{l}} \approx \gamma_{\mathrm{r}} \approx \frac{\gamma_z}{2}, \tag{2.166}$$

which can also be observed in the scaling of the measured dip-widths in Fig. 2.12 (B).

3

Measurement of the physical properties

In the last chapter, we have reviewed the principles and methods of measurement of the cyclotron frequency by a Penning trap. On this basis, this chapter discusses how the fundamental properties of interest can be extracted in actual measurements by frequency measurements with a Penning trap. On the course, some more principles and methods are explained.

In Section 3.1, important statistical measures which are used throughout this thesis are introduced. Afterward, we shall discuss the principles and methods of the proton-to-antiproton charge-to-mass comparison and the magnetic moment measurement in Section 3.2 and Section 3.3, respectively.

3.1 Measures of frequency stability and noise characterization

In a later part of this thesis, we will discuss the frequency stability of the system in detail. The purpose of this section is to introduce the essentials of statistics associated with frequency standards, and to formalize important measures of frequency stability for the following discussion.

3.1.1 Definition of the frequency fluctuation

We suppose results of a series of frequency measurements $\{\nu_i\}\,(i = 1, 2, \cdots, N)$, each frequency measurement averaged over a time τ_0, such as seen in Fig. 3.1 (A). The standard deviation of $\{\nu_i\}$ is not generally appropriate as a measure of frequency fluctuations, as it is affected by slow drifts which are present in typical measurements but are not relevant to a short-term stability. Instead, we define

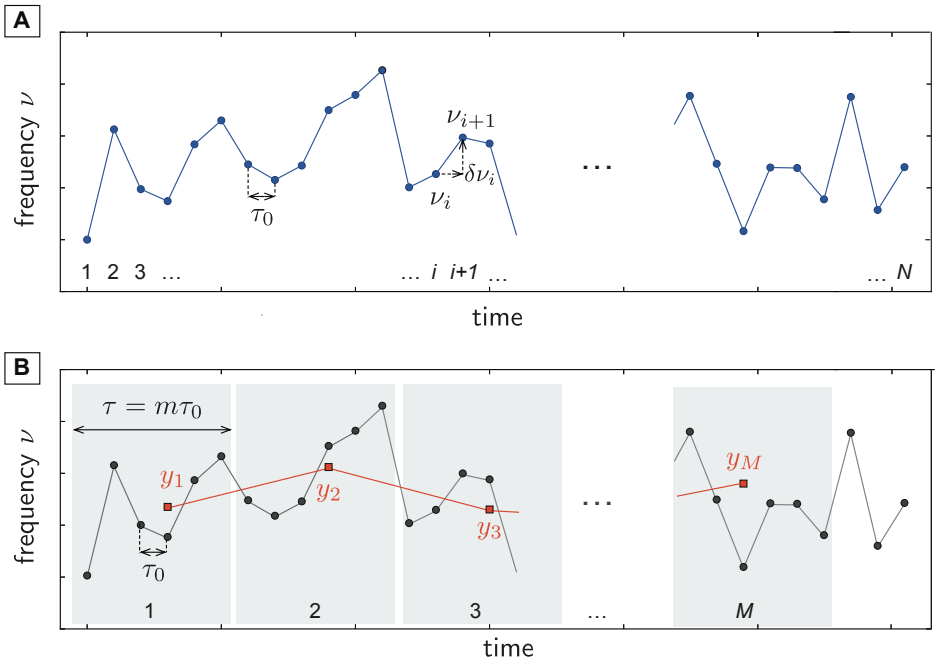

Figure 3.1: Example of a series of frequency measurements $\{\nu_i\}$. The variables used in the text are defined in the figure. **(A)** A series of N frequencies, each sampled in an averaging time τ_0. The fluctuation Ξ is defined by Eq. (3.1) using the differences of the subsequent measurements $\{\delta\nu_i\}$. **(B)** The blocks of m (in this example $m = 6$) measurements are introduced, each defining $\{y_j\}$ by an average of $\{\nu_i\}\,(i = m(j-1)+1, \cdots, mj+1)$.

the *fluctuation* Ξ of the series by

$$\Xi = \sqrt{\frac{1}{N-1}\sum_{i=1}^{N-1}(\delta\nu_i - \overline{\delta\nu})^2} \tag{3.1}$$

with $\{\delta\nu_i\}\,(i = 1, 2, \cdots, N-1)$ being the differences of the subsequent measurements and $\overline{\delta\nu}$ their average:

$$\delta\nu_i = \nu_{i+1} - \nu_i \quad (i = 1, 2, \cdots, N-1) \tag{3.2}$$

$$\begin{aligned}\overline{\delta\nu} &= \frac{1}{N-1}\sum_{i=1}^{N-1}\delta\nu_i \\ &= \frac{\nu_N - \nu_1}{N-1}.\end{aligned} \tag{3.3}$$

The Allan deviation [109] is commonly used for discussion of stabilities of frequency standards. To define it, we introduce $\{y_j\}\,(j = 1, 2\cdots, M)$ in Fig. 3.1 (B). Each y_j is obtained by averaging $m = \lfloor N/M \rfloor$ measurements of $\{\nu_i\}$, corresponding to the averaging time of $\tau = m\tau_0$. Here $\lfloor\ \rfloor$ is the floor function. The Allan variance $\sigma_{\mathrm{A}}^2(\tau)$ is defined as

$$\sigma_{\mathrm{A}}^2(\tau) = \frac{1}{M-1}\sum_{j=1}^{M-1}(y_{j+1} - y_j)^2. \tag{3.4}$$

The Allan deviation $\sigma_{\mathrm{A}}(\tau)$ is defined by $\sigma_{\mathrm{A}}(\tau) = \sqrt{\sigma_{\mathrm{A}}^2(\tau)}$. Here we choose a definition of the Allan variance which differs by the standard one [110] by a factor of 2. This is in order to match $\sigma_{\mathrm{A}}(\tau_0)$, the Allan deviation for $m = 1$ and $M = N$, to the above defined fluctuation Ξ for a large sample size N where

$$N \gg \frac{\nu_N - \nu_1}{\overline{\nu}} \Longrightarrow \overline{\delta\nu} \approx 0, \tag{3.5}$$

$$\therefore \Xi \approx \sigma_{\mathrm{A}}(\tau_0) = \sqrt{\frac{1}{N-1}\sum_{i=1}^{N-1}(\delta\nu_i)^2}. \tag{3.6}$$

with $\overline{\nu}$ being the average of $\{\nu_i\}$. In the following discussions throughout this thesis, the Allan variance/deviation of a measured quantity (e.g., voltage V) will be denoted as $\sigma_{\mathrm{A}}^2(V,\tau)$ or $\sigma_{\mathrm{A}}(V,\tau)$, when necessary.

The defined fluctuation is a relevant measure in discussion of a distribution of frequency ratios of subsequent measurements. Using the example of Fig. 3.1, we now define σ_{ratio} to be the standard deviation of ratios of subsequent measurements:

$$\sigma_{\mathrm{ratio}}^2 = \frac{1}{N-1}\sum_{i=1}^{N-1}\left(\frac{\nu_{i+1}}{\nu_i} - \overline{r}\right)^2 \tag{3.7}$$

with $\overline{r}$ defined by

$$\overline{r} = \frac{1}{N-1}\sum_{i=1}^{N-1}\left(\frac{\nu_{i+1}}{\nu_i}\right). \tag{3.8}$$

Since $\overline{r} \approx 1$ for a large sample, Eq. (3.7) becomes

$$\begin{aligned}\sigma_{\mathrm{ratio}}^2 &\approx \frac{1}{N-1}\sum_{i=1}^{N-1}\frac{(\delta\nu_i)^2}{{\nu_i}^2} \\ &\approx \frac{1}{N-1}\sum_{i=1}^{N-1}\frac{(\delta\nu_i)^2}{\overline{\nu}^2}\left(1 - \frac{2\xi_i}{\overline{\nu}} - \frac{\xi_i^2}{\overline{\nu}^2}\right)\end{aligned} \tag{3.9}$$

with ξ_i defined as

$$\xi_i = \nu_i - \overline{\nu}. \tag{3.10}$$

Since we will treat variations on the order of 10^{-2} Hz of the particle's eigenfrequencies ν_+, ν_z, ν_- in the RF range,

$$\begin{aligned}\frac{2\xi_i}{\overline{\nu}} &\lesssim \mathcal{O}(10^{-6}), \\ \frac{\xi_i^2}{\overline{\nu}^2} &\lesssim \mathcal{O}(10^{-12}).\end{aligned} \tag{3.11}$$

Therefore

$$\sigma_{\mathrm{ratio}}^2 \approx \frac{1}{N-1}\sum_{i=1}^{N-1}\frac{(\delta\nu_i)^2}{\overline{\nu}^2} \approx \frac{\Xi^2}{\overline{\nu}^2} \tag{3.12}$$

Eq. (3.12) relates the absolute cyclotron frequency fluctuation Ξ_c and the expected distribution of

the $\bar{p}$-H^- cyclotron frequency ratio in the charge-to-mass ratio comparison.

Details differ from this model in the actual data analysis of the charge-to-mass ratio comparison. For example, data obtained for the two particles is interpolated to account for a drift between a measurement of the antiproton and the measurement of the H^- ion. However, the principle discussed here remains valid.

3.1.2 Noise characterization by the Allan variance

The scaling of the Allan variance $\sigma_{\mathrm{A}}^2(\tau)$ against the averaging time τ reflects statistical properties of the noise. Allan variance $\sigma_{\mathrm{A}}^2(\tau)$ is related to the power spectrum density (PSD) $S_y(f)$ by [111]

$$\sigma_{\mathrm{A}}^2(\tau) = 4\int_0^\infty S_y(f)\frac{\sin^4(\pi f\tau)}{(\pi f\tau)^2}\mathrm{d}f. \tag{3.13}$$

The noise is characterized by its power-law spectral density. Typical noise models used in frequency metrology are $S_y(f) \sim f^\alpha$; $\alpha = -2, -1, 0, +1, +2$, as listed in Table 3.1[1]. Decomposing the PSD into these components and substituting to Eq. (3.13),

$$S_y(f) = \sum_{\alpha=-2}^{2} h_\alpha f^\alpha, \tag{3.14}$$

$$\begin{aligned}
\therefore \sigma_{\mathrm{A}}^2(\tau) &= 4\sum_{\alpha=-2}^{2}\int_0^\infty h_\alpha f^\alpha S_y(f)\frac{\sin^4(\pi f\tau)}{(\pi f\tau)^2}\mathrm{d}f \\
&= 4\sum_{\alpha=-2}^{2}\int_0^\infty \frac{h_\alpha}{(\pi\tau)^\alpha}\frac{\sin^4(\pi f\tau)}{(\pi f\tau)^{2-\alpha}}\mathrm{d}f \\
&= 4\sum_{\alpha=-2}^{2}\frac{h_\alpha}{(\pi\tau)^{\alpha+1}}\int_0^\infty \frac{\sin^4 t}{t^{2-\alpha}}\mathrm{d}t.
\end{aligned} \tag{3.15}$$

Thus the noise component $\sim f^\alpha$ in the PSD appears in the scaling of the Allan variance $\sim \tau^{-\alpha-1}$. The contributions of each noise type to the Allan variance are given in Table 3.1 in explicit forms. The integral in Eq. (3.15) converges for $\alpha = -2, -1, 0$. For $\alpha = 1, 2$, the integral is evaluated by introducing a cut-off frequency f_h, corresponding to the measurement band-width, assuming $\tau f_h \gg 1$ [112]. As a consequence, the results include a f_h dependency.

Among the noise types in Table 3.1, the white-noise FM and the random-walk FM are especially important for our experiment. Hereafter they are simply referred to as the white noise and the random walk. The white noise is observed in frequency fluctuations such as the ones originated by fluctuations of the trapping voltage. The random-walk property is observed in some noise caused by environmental variations.

[1] PM stands for phase modulation, and FM for frequency modulation

Table 3.1: Different types of noise and their contributions to the PSD $S(f)$ and the Allan variance $\sigma_A^2(\tau)$. The constant γ in the table is the Euler–Mascheroni constant $\gamma \approx 0.57721$. f_h is the band-width frequency, for which $\tau f_h \gg 1$.

Noise model	$S_y(f)$ contribution	$\sigma_{\mathrm{A}}^2(\tau)$ contribution
White noise PM	$h_2 \cdot f^2$	$h_2 \cdot 6f_h \cdot (2\pi\tau)^{-2}$
Flickr noise PM	$h_1 \cdot f^1$	$h_1 \cdot (6\ln(2\pi f_h\tau) + 6\gamma - 2\ln 2) \cdot (2\pi\tau)^{-2}$
White noise FM	$h_0 \cdot f^0$	$h_0 \cdot \tau^{-1}$
Flickr noise FM	$h_{-1} \cdot f^{-1}$	$h_{-1} \cdot 4\ln 2 \cdot \tau^0$
Random walk FM	$h_{-2} \cdot f^{-2}$	$h_{-2} \cdot 4\pi^2/3 \cdot \tau$

3.1.3 Application to simulated data

In this section, the Allan variance evaluation is applied to data generated by a simulation to show an example of how the statistical properties of noise are characterized by the Allan variance.

Frequency fluctuations were simulated by a combination of white-noise and random-walk components. The evolution of the frequencies is shown in Fig. 3.2 (A). The Allan variances were evaluated by Eq. (3.4), shown in Fig. 3.2 (B) as a function of the averaging time τ. The solid blue line is a result of a fit by the theoretical scale of a combination of the white noise and the random walk $\sigma_{\mathrm{A}}^2(\tau) = c_0 + c_{-1}\tau^{-1} + c_1\tau$. Each of the white-noise and the random-walk component is plotted separately by the dashed lines in Fig. 3.2 (B). It can be observed that the Allan variance at short averaging time τ is dominated by the contribution of $\propto \tau^{-1}$ term, while the $\propto \tau$ term is dominant at long τ. As seen in this example, the Allan deviation is a useful tool to study the statistical properties of noise.

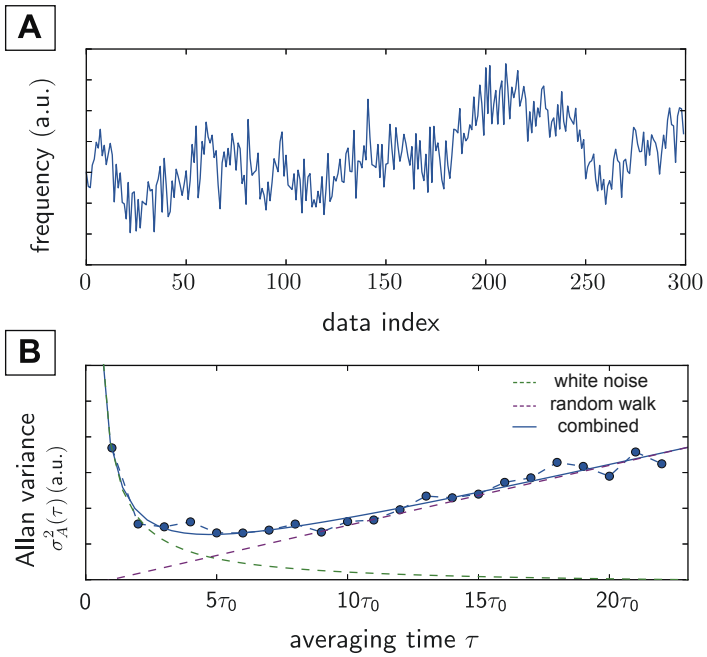

Figure 3.2: **(A)** Two datasets produced by simulations. The frequency fluctuations were generated by a combination of white-noise and random-walk components. **(B)** The Allan variance evaluated for the data shown in (A). The solid curve is the fitted curve by the model $\sigma_{\mathrm{A}}^2(\tau) = c_0 + c_{-1}\tau^{-1} + c_1\tau$. The green dashed curve indicates a contribution of the white-noise component $\propto 1/\tau$, and the purple dashed line the random-walk component $\propto \tau$.

3.2 Principle of proton-to-antiproton charge-to-mass ratio comparison

Comparison of charge-to-mass ratios is based on a simple principle of comparison of cyclotron frequencies.

As discussed in Chapter 2, a Penning trap provides a means of high-precision measurement of the cyclotron frequency of a charged particle in a magnetic field. Suppose we have two kinds of particles with charge q_1, q_2 and mass m_1, m_2. If their cyclotron frequencies are $\omega_{c,1}, \omega_{c,2}$ are measured in the same magnetic field B,

$$\begin{aligned} \frac{\omega_{c,1}}{\omega_{c,2}} &= \frac{q_1/m_1 \cancel{B}}{q_2/m_2 \cancel{B}} \\ &= \frac{q_1/m_1}{q_2/m_2}, \end{aligned} \tag{3.16}$$

thus the magnetic field is canceled out, and the ratio of the charge-to-mass ratios is obtained by the cyclotron frequency ratio. In most cases of actual measurements[2] including ours, the cyclotron frequencies of the two particles are measured at different times, and a variation of the magnetic field

[2]The exception is the two-ion technique developed by MIT ICR group [113], which simultaneous measured the cyclotron frequencies of two ions in a Penning trap, and enabled a relative precision of mass comparisons at levels of 10^{-11} or below. Application of this method to our measurement requires further technical developments and detailed understanding of systematics arising from interaction of the two particles.

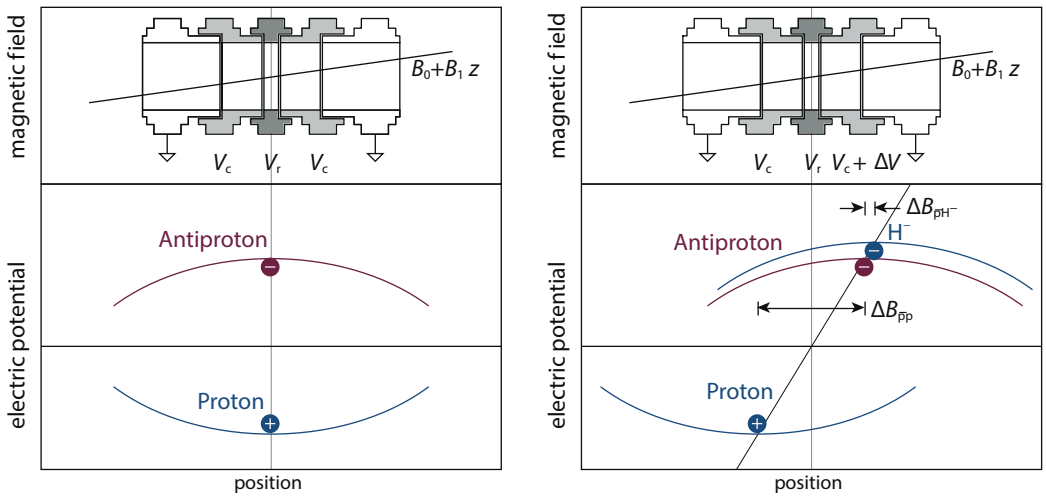

Figure 3.3: On-axis potential for cyclotron frequency comparison. **(Left)** Ideal case in the presence of no trap asymmetries. Inversion of the polarity does not shift the positions of the particles. **(Right)** A case where there is a voltage offset ΔV on one of the correction electrodes. The inversion of the polarity leads to different axial positions between a proton and an antiproton. Due to the magnetic gradient of the trap B_1, This causes a magnetic field difference $\Delta B_{\bar{p}p}$ between the two. If an H^- ion is used instead of a proton, the corresponding magnetic field difference is much smaller $\Delta B_{\bar{p}H^-} \ll \Delta B_{p\bar{p}}$, because no polarity inversion is required. The figures are adapted from Ref. [117].

between the measurements is corrected by interpolation [54, 114, 115]. The stability of the magnetic field experienced by the particles in the time scale of the repetition of the measurements contributes to the uncertainty of the measurement. This will be discussed in detail when we look at the 2014 proton-to-antiproton charge-to-mass ratio comparison (Chapter 7).

In case of the proton-antiproton comparison, the negatively charged hydrogen ion H^- is used as a proxy for the proton. The reason is to avoid a systematic effect caused by inversion of the polarity of the trapping potential. This is illustrated in Fig. 3.3. The left figure of Fig. 3.3 describes an ideal case where there is no offset potential on the electrodes. In such case, inversion of the trapping potential between a proton and an antiproton does not cause the position of the potential minimum to change. However, in reality offset potentials exist on the electrodes, and lead to an asymmetric potential as in the left figure of Fig. 3.3. In this case, the inversion of the polarity causes a large difference of the axial positions between a proton and an antiproton. Coupled with a magnetic gradient B_1 in the trap, this leads to a difference of the magnetic field experienced by a proton and an antiproton, as indicated by $\Delta B_{p\bar{p}}$ in the figure. The use of an H^- ion instead of a proton allows us to avoid the polarity inversion, thereby greatly suppressing the position difference between the two particles, and hence the magnetic fields experienced.

This idea was originally employed by the TRAP collaboration in the last of a series of its pioneering measurements in the 1990s [114], which, together with an improved sampling rate, led to an improvement of the precision by more than a factor of 10, compared to its previous run where the proton-antiproton cyclotron frequency ratio was directly measured [116].

Therefore what we measure is the $\bar{p}$-H^- cyclotron frequency ratio $R_{\bar{p}\mathrm{H}^-}$

$$R_{\bar{p}\mathrm{H}^-} \equiv \frac{\omega_{\mathrm{c},\bar{p}}}{\omega_{\mathrm{c},\mathrm{H}^-}}, \tag{3.17}$$

which should be converted to $\omega_{\bar{p}}/\omega_p$ by the relation between ω_p and ω_{H^-}. The mass of the H^- ion is expressed as

$$m_{\mathrm{H}^-} = m_p + 2m_e - E_\mathrm{b} - E_\mathrm{a}, \tag{3.18}$$

with m_p, m_e, E_b and E_a respectively being the proton mass, the electron mass, the electron binding energy and the electron affinity energy of the hydrogen atom, all known from previous works with high precision.

In addition, polarization of the H^- ion shifts its cyclotron frequency as discovered by J. K. Thompson, S. Rainville and D. E. Pritchard [118]. In the rest frame of an H^- ion rotating in the trap, the magnetic field $\boldsymbol{B} = B\hat{\boldsymbol{z}}$ of the Penning trap is experienced as an effective electric field

$$\boldsymbol{E}_m = \dot{\boldsymbol{x}} \times \boldsymbol{B} \tag{3.19}$$

which induces an electric dipole moment for a particle with polarizability α_pol as

$$\boldsymbol{d}_\mathrm{ind} = \alpha_\mathrm{pol}\boldsymbol{E}_m. \tag{3.20}$$

The potential by the interaction of $\boldsymbol{E}_m$ and $\boldsymbol{d}_\mathrm{ind}$ is given by

$$V_d = -\frac{1}{2}\alpha_\mathrm{pol}\boldsymbol{E}_m^2 = -\frac{1}{2}\alpha_\mathrm{pol}B^2(\dot{x}^2 + \dot{y}^2). \tag{3.21}$$

This potential contributes to the equations of motion Eq. (2.6) of the polarizable particle as

$$m\begin{pmatrix}\ddot{x}\\ \ddot{y}\\ \ddot{z}\end{pmatrix} + \alpha_\mathrm{pol}B^2\begin{pmatrix}\dot{x}\\ \dot{y}\\ 0\end{pmatrix} = q\dot{\boldsymbol{x}} \times \boldsymbol{B} - q\boldsymbol{\nabla}\Phi(\boldsymbol{x}), \tag{3.22}$$

leading to a shift of its cyclotron frequency

$$\frac{\Delta\omega_\mathrm{c}^{(\mathrm{pol})}}{\omega_\mathrm{c}} = -\frac{\alpha_\mathrm{pol}B^2}{m}. \tag{3.23}$$

With this effect taken into account, $\chi_{p\mathrm{H}^-}$, which we defined as the proton-H^- cyclotron-frequency ratio in the same magnetic field, is expressed as

$$\chi_{p\mathrm{H}^-} \equiv \frac{\omega_{\mathrm{c},p}}{\omega_{\mathrm{c},\mathrm{H}^-}} = 1 + 2\frac{m_e}{m_p} - \frac{E_\mathrm{b}}{m_p} - \frac{E_\mathrm{a}}{m_p} + \frac{\alpha_{\mathrm{pol},\mathrm{H}^-}B^2}{m_p}. \tag{3.24}$$

Table 3.2: Contributions and uncertainties of each term of Eq. (3.24) to the cyclotron-frequency ratio $\chi_{\bar{p}\mathrm{H}^-} = \omega_{\mathrm{c},p}/\omega_{\mathrm{c},\mathrm{H}^-}$. The polarization shift is evaluated for $B = 1.945\,\mathrm{T}$ of 2017 run-II ($B = 1.946\,\mathrm{T}$ in the 2014 measurement).

	term	contribution (10^{-12})	uncertainty (10^{-12})
	1	1 000 000 000 000.0	0
electron-proton mass ratio [119]	$2m_e/m_p$	1 089 234 043.0	0.1
binding energy [55]	$-E_\mathrm{b}/m_p$	−14 493.0	$< 10^{-3}$
electron affinity [121]	$-E_\mathrm{a}/m_p$	−803.8	$< 10^{-2}$
polarization shift [118, 122]	$\alpha_{\mathrm{pol},\mathrm{H}^-}B^2/m_p$	7.7	$< 10^{-6}$
total	$\chi_{p\mathrm{H}^-}$	1 001 089 218 753.9	0.1

Each term of Eq. (3.24) is known with precision at levels of 10^{-13} or below, as summarized in Table 3.2 with the references. This is sufficient for precision of our measurement at a level of 10^{-11}. The ratio $\chi_{p\mathrm{H}^-}$ is obtained to be

$$\chi_{p\mathrm{H}^-} = 1.001\,089\,218\,753\,9(1), \tag{3.25}$$

which converts the ratio $R_{p\mathrm{H}^-}$ obtained by the measurement to the ratio of the proton-antiproton charge-to-mass ratios:

$$\left|\frac{(q/m)_{\bar{p}}}{(q/m)_p}\right| = \frac{R_{\bar{p}\mathrm{H}^-}}{\chi_{p\mathrm{H}^-}} \tag{3.26}$$

When CPT symmetry is conserved, $R_{\bar{p}\mathrm{H}^-} = \chi_{p\mathrm{H}^-}$. The precision of $\chi_{p\mathrm{H}^-}$ is limited by knowledge of the electron-proton mass ratio. Recently, there was a new measurement of the proton's atomic mass [119], which improved the precision by a factor of about 3 than the previous measurement [120]. The term $2m_e/m_p$ in Table 3.2 is calculated with this updated proton mass and the electron mass from CODATA 2014 [11]. At the time of 2014 charge-to-mass ratio comparison [77],

$$\chi_{p\mathrm{H}^-,2014} = 1.001\,089\,218\,753\,6(1). \tag{3.27}$$

In the publication [54] we quoted a rounded value 1.001 089 218 754(1).

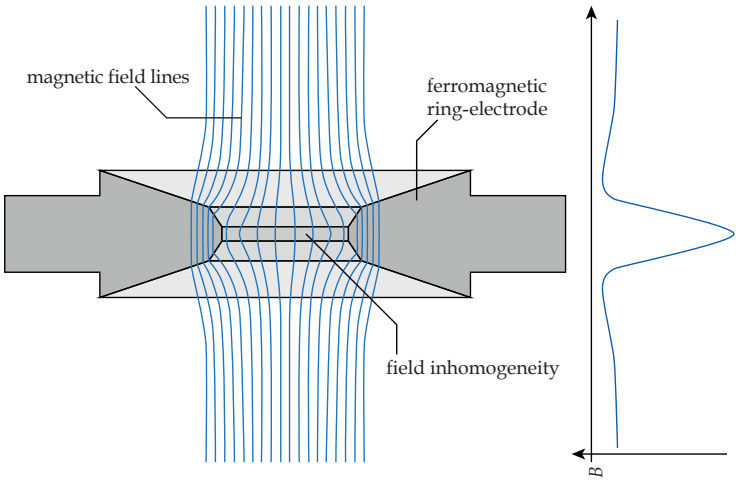

Figure 3.4: Magnetic field lines around a ferromagnetic ring electrode obtained by a simulation. The on-axis magnetic field property is shown on the right. By appropriately selecting the material and the geometry of the electrode, the trap can be designed to have a desired inhomogeneity B_2. Adapted from Ref. [92].

3.3 Principle of magnetic moment measurement

To measure the magnetic moment of a particle μ_p, the Larmor frequency ω_L

$$\omega_\mathrm{L} = \frac{\mu_p B}{\hbar} \tag{3.28}$$

has to be measured together with the cyclotron frequency. By taking the ratio of the two frequencies,

$$\begin{aligned} \frac{\omega_\mathrm{L}}{\omega_\mathrm{c}} &= \frac{\mu_p B}{\hbar} \Big/ \frac{qB}{m} \\ &= \frac{\mu_p}{(q\hbar/m)} = \frac{g_p}{2} \end{aligned} \tag{3.29}$$

is obtained, where g_p is the dimensionless g-factor which expresses the magnetic moment in unit of the nuclear magnetron $\mu_\mathrm{N} = e\hbar/(2m_p)$ in case of the proton/antiproton. Therefore the g-factor is obtained by measuring the Larmor frequency and the cyclotron frequency in the same magnetic field B. Because the spin precession of a trapped particle is not accompanied by a detectable image current, the Larmor frequency is extracted from a spin resonance obtained by measuring the transition probability as a function of an applied excitation frequency. To this end, we employ a method developed for magnetic moment measurement of the electron/positron [49, 69, 123] which makes use of an inhomogeneous magnetic field to detect spin transitions of the particle. The principle and the applications of this method to the proton/antiproton are summarized in the following sections.

3.3.1 Continuous Stern-Gerlach effect

Let us consider the particle's motion in a Penning trap with the magnetic potential due to its spin angular momentum $V_s = -\boldsymbol{\mu}_s \cdot \boldsymbol{B}$. Specifically, we take the expression of the axial frequency shift due to the second-order magnetic inhomogeneity B_2 Eq. (2.77) which now becomes

$$\ddot{z} = -\left(\omega_z^2 + \frac{2B_2(\mu_l + \mu_s)}{m}\right) z, \tag{3.30}$$

leading to rewriting Eq. (2.79) to be

$$\begin{aligned} \frac{\Delta\omega_z^{(B_2)}}{\omega_z} &= \frac{1}{m\omega_z^2}\frac{B_2}{B_0}(E_+ + |E_-| + B_0\mu_s) \\ &= \frac{\hbar\omega_+}{m\omega_z^2}\frac{B_2}{B_0}\left(\left(n_+ + \frac{1}{2}\right) + \frac{\omega_-}{\omega_+}\left(n_- + \frac{1}{2}\right) + \frac{g_p}{2}s\right), \end{aligned} \tag{3.31}$$

with $s = -1/2, +1/2$ being the spin quantum number. Therefore, with a sufficiently large B_2, a spin transition can be detected as an axial frequency shift of

$$\Delta\nu_{z,\mathrm{SF}} = g_p\frac{q\hbar B_2}{8\pi^2 m^2\nu_z}. \tag{3.32}$$

This technique was first introduced by H. G. Dehmelt [123], who named it *continuous Stern-Gerlach effect*. The magnetic inhomogeneity term B_2 is often referred to as a *magnetic bottle* in this context. Because Eq. (3.32) scales as $\propto m_p^{-2}$, its application to the proton/antiproton is much more challenging than to the electron/positron. A Penning trap for the spin-state analysis used in BASE 2015/2016 run had a very large[3] magnetic bottle $B_2 = 2.88 \times 10^5\,\mathrm{T/m^2}$ to make $\Delta\nu_{z,\mathrm{SF}}$ a detectable magnitude of $\Delta\nu_{z,\mathrm{SF}} \approx 172\,\mathrm{mHz}$ out of $\nu_z \approx 675\,\mathrm{kHz}$. Such a strong magnetic inhomogeneity in the trap is realized by utilizing a ferromagnetic material for the ring electrode. In Fig. 3.4, magnetic field lines produced around a ferromagnetic electrode placed in a homogenous magnetic field are displayed. The magnitude of B_2 can depend on the choice of the material and the geometry of the electrode [69].

As in the case of the cyclotron frequency, the electromagnetic imperfections of the trap discussed in Section 2.3.3 introduce shifts of the Larmor frequency, depending on the amplitudes of the eigenmodes. What is especially important are those caused by B_2 which are expressed as

$$\frac{\Delta\omega_{\mathrm{L}}^{(B_2)}}{\omega_{\mathrm{L}}} = \frac{1}{m\omega_z^2}\frac{B_2}{B_0}\left(-\left(\frac{\omega_z}{\omega_+}\right)^2 E_+ + E_z - 2|E_-|\right). \tag{3.33}$$

[3] As a reference, the B_2 used in the latest electron magnetic moment in Ref. [12] was $B_2 = 1.5 \times 10^3\,\mathrm{T/m^2}$ [124].

3.3.2 Methods of magnetic moment measurement

Prerequisite of the measurement

The key for application of the continuous Stern-Gerlach effect is the axial frequency stability. Obviously, high intrinsic axial frequency fluctuations mask the axial frequency shifts by spin transitions, making the detection of the transitions impossible. From Eq. (3.31), frequency shifts induced by single quantum transitions of modified-cyclotron and the magneton modes are respectively found to be 61 mHz and 39 µHz, for the 2015/2016 condition. Voltage noise on the order of $100\,\mathrm{pV}/\sqrt{\mathrm{Hz}}$ typically exists on the trap electrodes and induces these transitions. Assuming these induced transitions to be electric dipole transitions, the heating rates of these modes scale as $\partial n_{\pm}/\partial t \propto n_{\pm}$ [125, 126]. Therefore, it is required that the radii of the modified-cyclotron and magnetron modes are sufficiently reduced before the measurement.

Statistical spin-flip detection

One way to detect the spin transitions is to compare the axial frequency fluctuations between data with and without spin-flip RF drives. The frequency fluctuation $\Xi_z(\nu_{\mathrm{rf}})$ for a series of axial frequency measurements with irradiation of an RF drive at $\nu_{\mathrm{rf}} \approx \nu_{\mathrm{L}}$ before each measurement becomes

$$\Xi_z(\nu_{\mathrm{rf}}) = \sqrt{\Xi_{z,\mathrm{back}}^2 + P_{\mathrm{SF}}(\nu_{\mathrm{rf}})^2 \Delta\nu_{z,\mathrm{SF}}^2}, \tag{3.34}$$

where $\Xi_{z,\mathrm{back}}$ represents the background axial frequency fluctuation and $P_{\mathrm{SF}}(\nu_{\mathrm{rf}})$ the spin-flip probability at the drive frequency ν_{rf}. The frequency jumps induced by spin transitions increase the fluctuation. A practical experimental sequence reads as follows:[4]

1. Measure the axial frequency $\nu_{z,2k-1}$.
2. Irradiate an off-resonant drive at $\nu_{\mathrm{rf,ref}} < \nu_{\mathrm{L}}$.
3. Measure the axial frequency $\nu_{z,2k}$.
4. Irradiate a resonant drive at $\nu_{\mathrm{rf}} \approx \nu_{\mathrm{L}}$.

The purpose of inserting the off-resonant drive is to measure a reference for the frequency stability without spin transitions.

The standard deviation of the frequency differences $\{\nu_{z,2k} - \nu_{z,2k-1}\}$ is used to measure $\Xi_{z,\mathrm{back}}$, while that of the differences $\{\nu_{z,2k+1} - \nu_{z,2k}\}$ is used to measure $\Xi_z(\nu_{\mathrm{rf}})$ (see Eqs. (3.1) to (3.3)). With enough statistics, a statistically significant difference between $\Xi_z(\nu_{\mathrm{rf}})$ and $\Xi_{z,\mathrm{back}}$ can be obtained, from which the spin-flip probability at this excitation frequency $P_{\mathrm{SF}}(\nu_{\mathrm{rf}})$ is determined (see

[4] This is a simplified procedure to explain the principle of the measurement. For a measurement reported in Ref. [70], the excitation frequency around the cut of the distribution was scanned extensively. The sequence consisted of 4 axial frequency measurements each following on/off -resonant drive of $\nu_{\mathrm{rf}} \lesssim \nu_{\mathrm{L}}$ and $\nu_{\mathrm{rf}} \gtrsim \nu_{\mathrm{L}}$ [80].

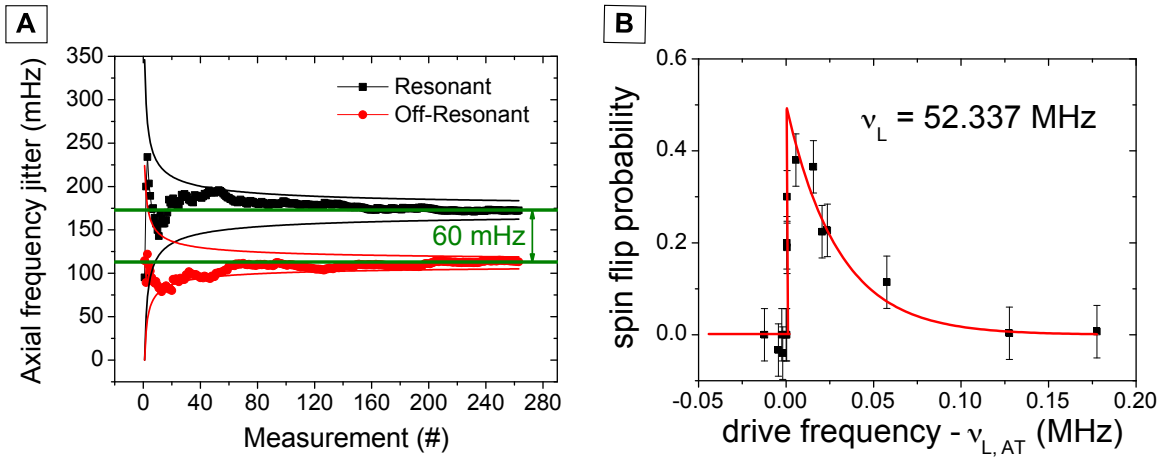

Figure 3.5: Results of spin-resonance spectroscopy with a single Penning trap. **(A)** The unit of the vertical axis is the cumulative axial frequent fluctuation. Data in the black dots (Ξ_z) is evaluated from axial frequency differences with on-resonant Larmor drives between the measurements. The data in the red dots is from the frequency differences with off-resonant drives between the measurements. The green curves indicate the uncertainty of $\Xi_z, \Xi_{z,\mathrm{back}}$. After accumulation of enough statistics, a significant difference between Ξ_z and $\Xi_{z,\mathrm{back}}$ of about 60 mHz is observed. From the difference of the spin-flip probability at the applied drive frequency is obtained by Eq. (3.34). **(B)** A Larmor resonance measured by obtained by the statistical spin-flip detection method. For each drive frequency ν_{rf}, the procedure in (A) was repeated to obtain the spin-flip probability as a function of the drive frequency $P_{\mathrm{SF}}(\nu_{\mathrm{rf}})$. The figure (A) is adapted from Ref. [80], and (B) from Ref. [70].

Fig. 3.5). By repeating the procedure above with different frequencies of ν_{rf}, the spin-flip probability as a function of the excitation frequency is obtained as in Fig. 3.5 (B). The resonance reflects the Boltzmann distribution of E_z determined by the temperature of the axial detection system, through the dependance of the Larmor frequency (Eq. (3.33)). The Larmor frequency is determined from the edge of spin-flip probability distribution which corresponds to ν_{L} without the shift due to E_z. The precision of this method is limited by the line-width caused by the coupling of the strong magnetic bottle and the Boltzmann distribution of E_z. Typically for the proton/antiproton, the precision of this method is limited to a level of 10^{-6} in a fractional precision [127, 128].

Single spin-flip detection and the double-trap technique

If the background axial frequency fluctuation is sufficiently low, individual spin transitions can be distinguished as discrete frequency jumps as demonstrated in Fig. 3.6. Typically, $E_+/k_{\mathrm{B}} \lesssim 50\,\mathrm{mK}$ is required to determine a spin state of a proton/antiproton with fidelity $> 90\%$.

Under such conditions, a novel method called *double-trap technique* [129] can be applied. The idea of this method is to use two Penning traps different magnetic field properties; an Analysis Trap (AT) dedicated to the spin-state analysis, and a Precision Trap (PT) for the cyclotron frequency measurement and spin-flip trials. The AT should have a strong magnetic bottle, while the magnetic field in the PT, where the actual spin transition takes place, is kept as homogenous as possible.

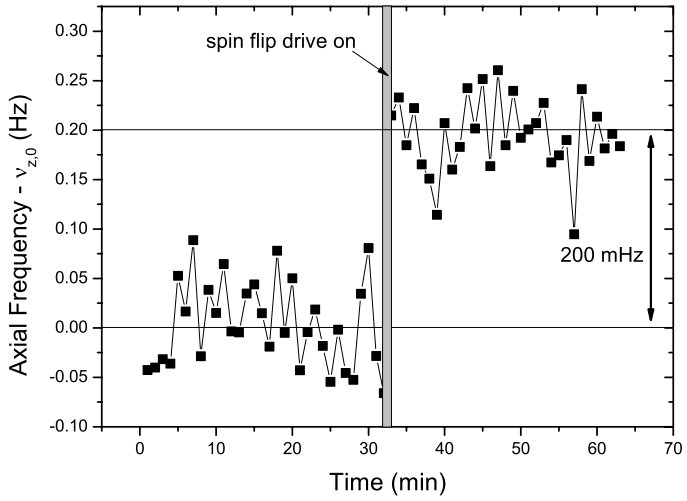

Figure 3.6: Detection of a spin transition of a single proton in a Penning trap. From the discreet upward shift of the axial frequency, it can be identified that a transition $s = +1/2 \rightarrow -1/2$ has happened. Adapted from Ref. [33].

As an example, Fig. 3.7 shows an apparatus of the latest proton magnetic moment by the Mainz group of the BASE collaboration where this method was used. The AT has a strong magnetic bottle produced by the ferromagnetic ring electrode, while the PT is placed in a homogeneous magnetic field (Fig. 3.7 (A)). The actual measurement protocol reads as follows (Fig. 3.7 (C)):

1. Prepare low radial energy states of the particle. The magnetron radius is cooled by the sideband cooling (Section 2.5). The cooling of the modified cyclotron mode is done by resistive cooling with an image-current detection system at the modified cyclotron frequency (called a cyclotron detection system) in the PT. The particle is made to interact with the PT cyclotron detection system, and the energy E_+ is subsequently estimated from the axial frequency in the AT, which reflects E_+ through the magnetic bottle B_2. A mode energy E_+ below the threshold E_{th} (typically $E_{\mathrm{th}}/k_{\mathrm{B}} = 50\,\mathrm{mK}$ [53]) for spin-state determination with sufficient fidelity is prepared.

2. Prepare an initial spin state of the particle. This is done by sequence of axial measurements accompanied by spin-flip drives at the Larmor frequency in the AT. The series is continued until an axial frequency shift identified to be from the spin transition with enough statistical significance.

3. Transport the particle to the PT, and irradiate a drive at $\nu_{\mathrm{rf}} \approx \nu_{\mathrm{L}}$.

4. Transport the particle to the AT again and examine whether the spin is flipped by the drive in the PT. The same procedure as step 2 is performed to identify the spin state.

5. Transport the particle to the PT. Measure the cyclotron frequency by the sideband coupling

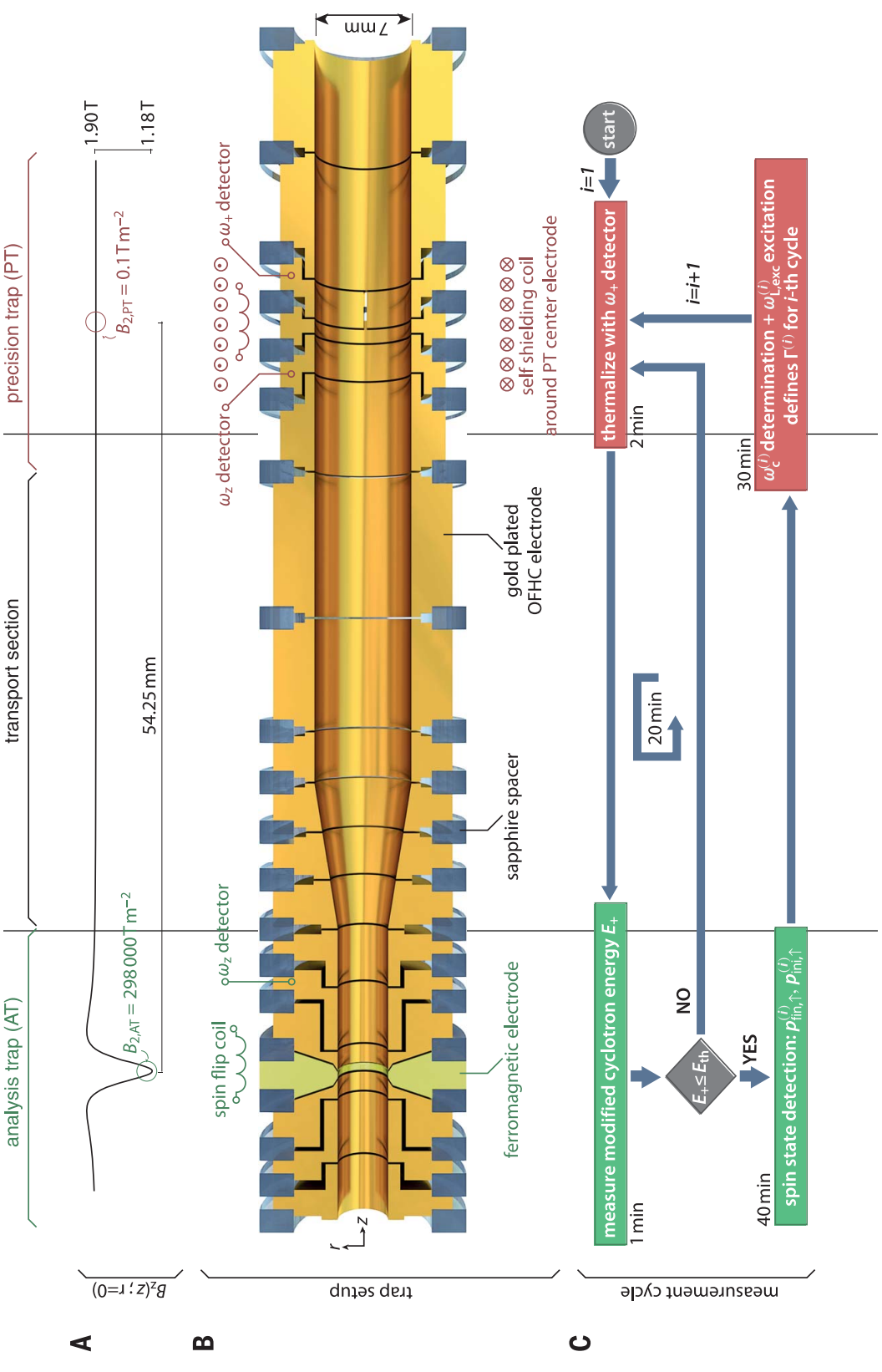

Figure 3.7: Setup for a proton magnetic moment measurement by the Mainz group of the BASE collaboration. **(A)** On-axis magnetic field. The magnetic bottle B_2 is $2.98 \times 10^5\,\mathrm{T/m^2}$ in the AT, and $0.1\,\mathrm{T/m^2}$ in the PT. **(B)** Cross-sectional view of the apparatus. Both of the PT and the AT are equipped with axial detection systems and spin-flip coils. **(C)** Measurement procedure. See the text for details. Adapted from Ref. [53].

method (Section 2.5).

The procedure above is repeated to determine a spin-flip probability at a certain $\nu_{\mathrm{rf}}/\nu_{\mathrm{c}}$. The cyclotron frequency $\nu_{\mathrm{c},i}$ measured at the end of cycle i defines $\nu_{\mathrm{rf,i+1}}$ so that $\nu_{\mathrm{rf},i+1}/\nu_{\mathrm{c},i}$ is constant. By repeating it for different $\nu_{\mathrm{rf}}/\nu_{\mathrm{c}}$, a resonance with about 3 orders of magnitude narrower width can be obtained. The example of such resonance is presented in Fig. 6.6 (c).

The BASE apparatus at CERN is equipped with a multi-Penning trap system which was designed with an aim to apply such multi-Penning trap technique to the antiproton. See Section 5.3 and Ref. [33] for details.[5]

[5]The 2017 run is dedicated to improvement of the charge-to-mass ratio comparison. Therefore the 2017 setup explained in Section 5.3 has been revised from the setup for magnetic moment measurement. Particularly, the ferromagnetic ring electrode of the AT was replaced by a copper electrode to improve the magnetic field homogeneity.

Part III

Experimental setup

4

Antiproton Decelerator

In this part, an overview of the experimental setup is given.

The BASE experiment operates in CERN's Antiproton Decelerator (AD) [130, 131] facility together with five other experiments. The AD is a unique facility in the world which supplies low energy antiprotons for precision studies. It is a part of CERN's accelerator complex, and receives a beam of protons from a 26 GeV/c Proton Synchrotron (PS). High energy protons from the PS impinge on an iridium target to produce antiprotons by a pair production process $p + p \rightarrow p + p + p + \bar{p}$. The produced antiprotons are collected by a magnetic horn, then guided to the 180 m circumference AD ring.

The layout of the AD is shown in Fig. 4.1. It is a synchrotron equipped with deceleration RF cavities and cooling systems. Six experiments: ATRAP, ASACUSA, ALPHA, AEgIS, GBAR and BASE receive the decelerated antiproton beams from the AD. The experimental zones of these experiments are seen inside the facility in Fig. 4.1.

The operation modes of the AD consist of deceleration and cooling. The deceleration is performed by RF cavities operated in a deceleration phase. Methods of the stochastic cooling [132] and the electron cooling [133] are used to reduce the transverse beam emittance.

The deceleration is performed in three steps shown in Fig. 4.2. Each step of deceleration is followed by the cooling process in order to suppress beam divergence caused by the deceleration. At the end of the deceleration cycle, the antiproton beam is ejected to the experiments at the momentum of 100 MeV/c (5.3 MeV in kinetic energy). The magnetic field of the dipole magnets in the ring is also changed after each step of deceleration according to the beam momentum. The intrinsic cycle length of the AD is about 110 s. The interval between subsequent injections varies typically between 112 and 130 s, depending on the super-cycles of the accelerator complex. At the extraction, one bunch typically contains about 3×10^7 antiprotons.

After being decelerated, the antiprotons are ejected from the AD ring, and led to the experimental

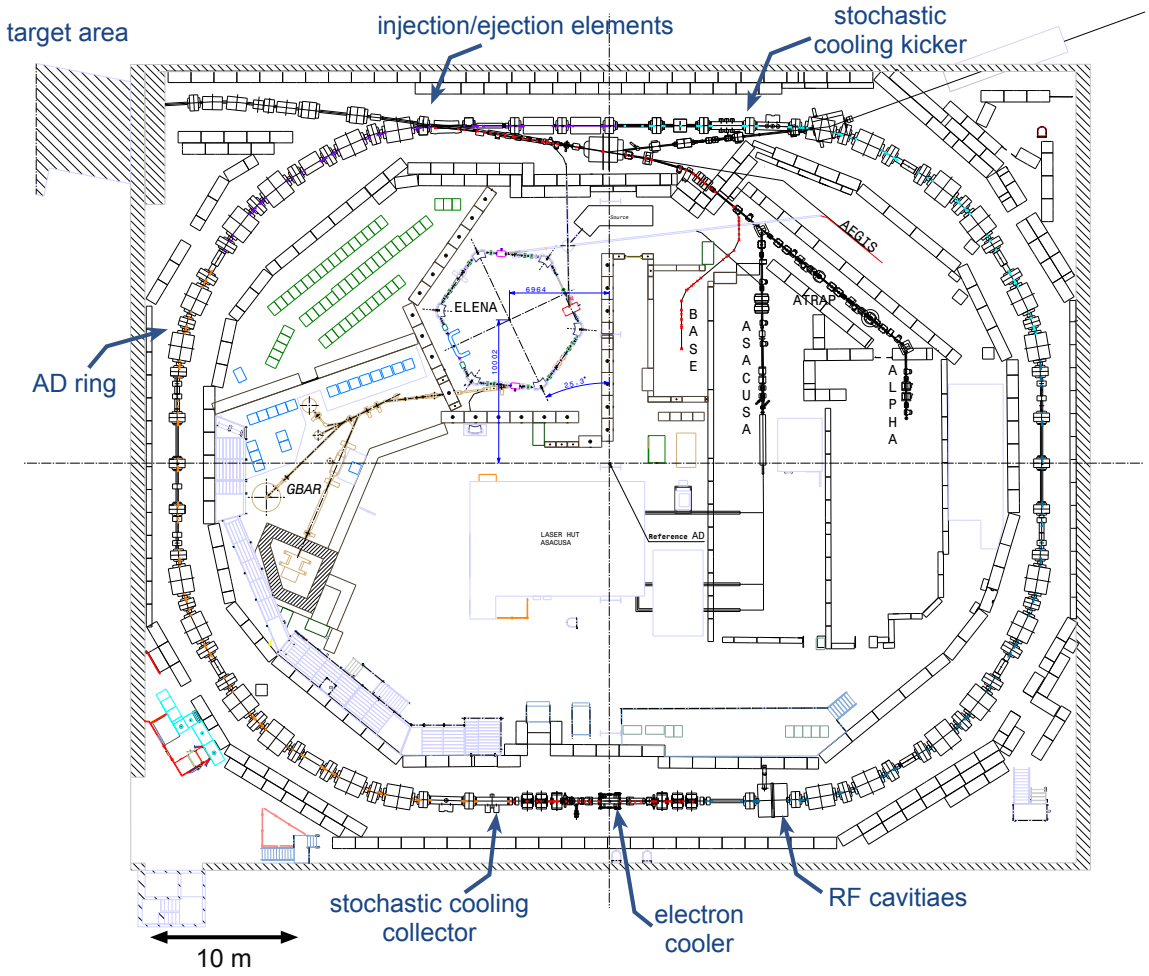

Figure 4.1: Layout of the present (2017–2018) AD facility. Antiprotons are produced in the target area on the upper left of the figure, and decelerated in the AD ring. Image credit: Olivier Choisnet (CERN). Annotated under permission by the author.

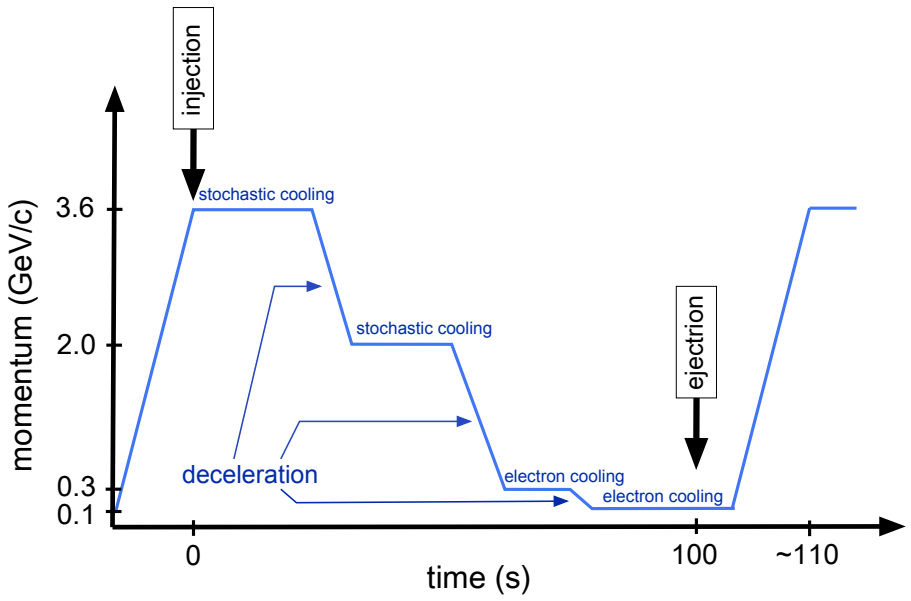

Figure 4.2: Deceleration cycle of the AD. An Antiproton beam is decelerated in three steps, each followed by a cooling process. After the deceleration, the antiprotons are ejected to one of the experiments. Time from the injection to the AD ring is indicated on the horizontal axis.

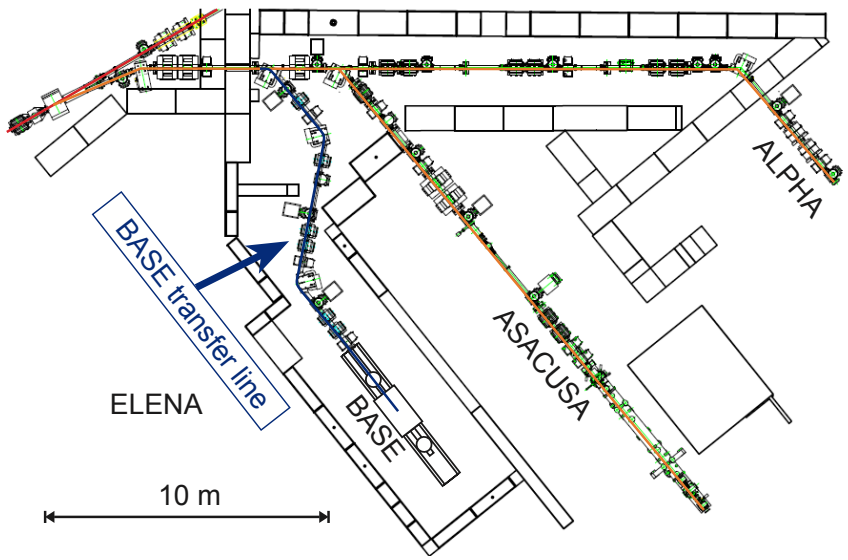

Figure 4.3: Beam transfer line to the BASE zone. The transfer line consists of three main bending magnets, three focusing quadrupole magnets, beam monitors and a set of corrector magnets.

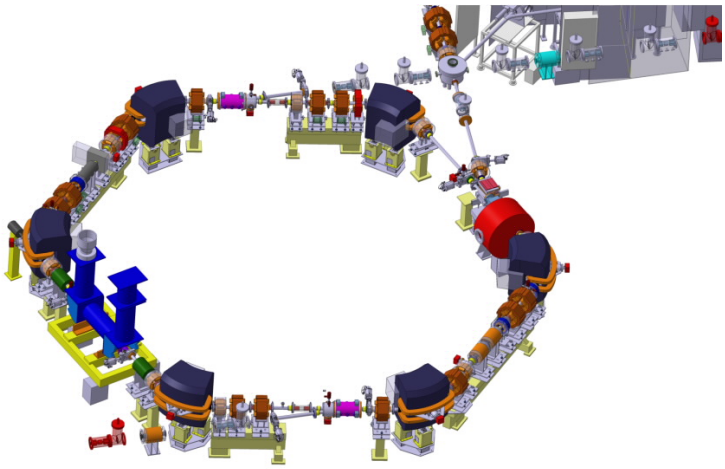

Figure 4.4: Model of the ELENA ring and its components. The ring is found at the center of Fig. 4.1. Adapted from Ref. [134].

zone of BASE through the transfer line shown in Fig. 4.3. The transfer line consists of standard beamline components such as dipole/quadrupole magnets, beam monitors for diagnostics, and dipole magnets called correctors, which deflect the beam in vertical/horizontal direction for fine tuning. By setting currents of these magnets appropriately, the beam is steered and focused into the BASE Penning trap system. Together with the beam monitors in the beamline, a cryogenic beam monitor inside the BASE magnet is used to check the position of the beam. Since 2016, a new deceleration ring called Extra Low ENergy Antiproton (ELENA) is under commission (Figs. 4.1 and 4.4). The purpose of this new ring is to decrease the energy of the beam from the AD further down to 100 keV in kinetic energy. The lower energy of the beam is expected to dramatically improve the efficiency of antiproton capturing of the most of the experiments in the AD. When it becomes operational in close future, antiprotons from the AD will be supplied to the experiments via the ELENA ring. In 2017, ELENA regularly performed test runs using H^- ions provided by its ion source. Influence of these machines to magnetic field fluctuations in the BASE experimental zone is assessed in Section 11.3.1.

5

Overview of the BASE apparatus

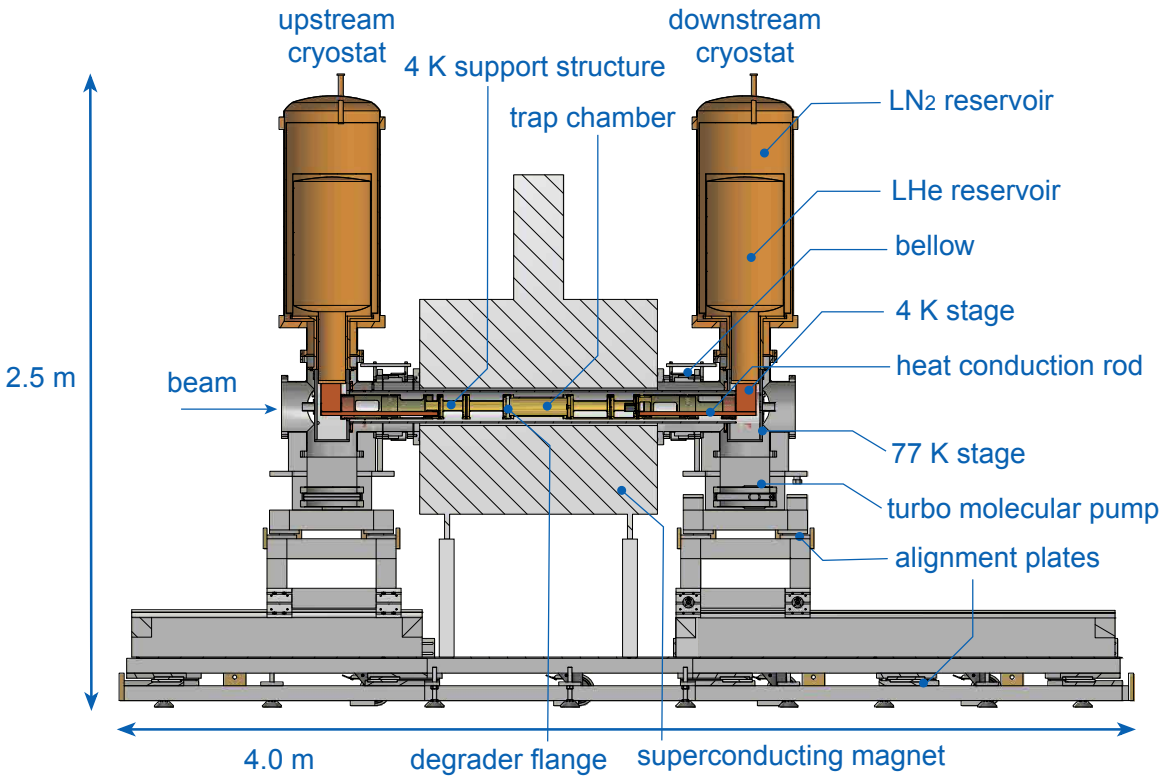

Figure 5.1: Cross-sectional view of the BASE apparatus. Adapted from Ref. [92]. Modifications were made under permission by the author.

This chapter gives an overview of the BASE apparatus. Details of each component will be described in the following sections. A sketch of the apparatus is shown in Fig. 5.1. The core components are installed in the superconducting magnet. On the upstream and the downstream sides of the magnet,

cryostats for liquid nitrogen (LN_2) and liquid helium (LHe) are installed. They provide cryogenic temperatures for the Penning traps and the superconducting electronics. The magnet has its own refrigerant vessels for LN_2 and LHe which are not shown in the figure.

The BASE Penning trap system consisting of multiple Penning traps is placed in a hermetically sealed cryogenic chamber, called the trap chamber, to provide ultra-high vacuum (UHV) for storage of antiprotons. A support structure anchors the trap chamber and associated components beneath the LHe stages of on the bottom of both cryostats and holds the apparatus in an isolation vacuum in the magnet bore. In the space downstream of the trap chamber, cryogenic electronic components are placed, which include image-current detection systems for frequency measurements, DC and RF lines, and cryogenic switches and filters.

When antiprotons are injected to the BASE magnet from the AD, they pass through a degrader window at the upstream end of the trap chamber. A fraction on the order of 10^{-4} of the decelerated antiprotons is captured in the trap by a high voltage pulse. The earlier mentioned beam monitor is placed upstream of the degrader and used to monitor the position of the beam during the beam steering.

In the following sections, each component of the system will be described in more detail. The overview of the apparatus is also found in Ref. [33]. Here, the system of 2017-run II, which is dedicated for the charge-to-mass ratio comparison is described.

- Section 5.1 summarizes characteristics of the superconducting magnet.
- An overview of the cryogenic assembly is given in Section 5.2. Roles of each component as well as the cryogenic characteristics are summarized.
- The Penning-trap system is described in Section 5.3.
- Section 5.4 gives a summary of the electronic components associated with the Penning-trap system. Among them, one crucial aspect needs to be discussed is the stability of the DC voltage source, which will be treated in Section 5.5.
- Finally, components used to catch the antiproton beams are summarized separately in Section 5.6.

5.1 BASE SUPERCONDUCTING MAGNET

A custom-made superconducting magnet by Oxford Instruments is used to provide a magnetic field for operation of Penning traps. It consists of the main coil and multiple shim coils to produce a highly homogeneous magnetic field at the central part of the apparatus.

5.1.1 ENERGIZATION OF THE MAGNET

To energize the magnet, the current of the main coil was increased up to 45.5 A to ramp the magnetic field to ≈ 1.945 T. A Hall probe[1] was placed at the approximate center of the magnet to measure the field during the ramp. The measured slope of the magnetic field against the applied current is shown in Fig. 5.2. Afterward, the magnetic field profile along the axis was measured using the Hall probe. The result is shown in Fig. 5.3. In this section, characterization of the magnet performed before 2017 run-II is summarized.

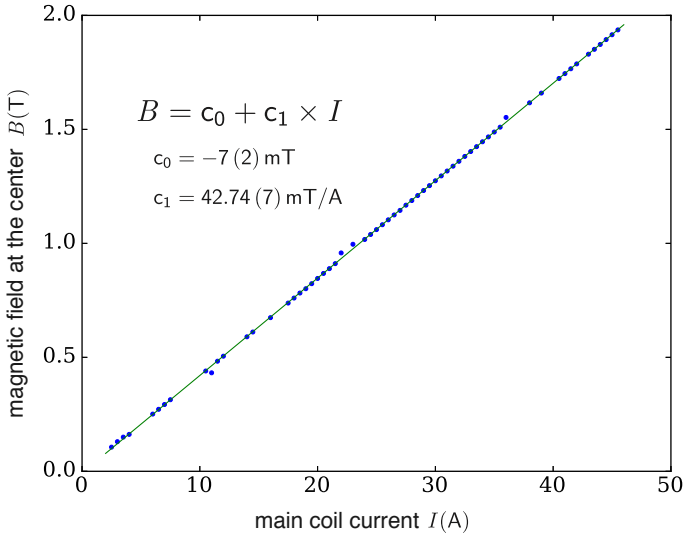

Figure 5.2: Charging slope of the magnet. The slope of the fitted line is 42.74 mT/A.

The geometry of the main coil was estimated from the axial magnetic field map. The on-axis magnetic field of a solenoid coil of a finite length is derived by the Ampère's law to be

$$B_z(z) = \frac{\mu_0 n I}{2}\left(\frac{z-(z_c-l/2)}{\sqrt{(z-(z_c-l/2)^2)+r^2}} + \frac{z-(z_c+l/2)}{\sqrt{(z-(z_c+l/2)^2)+r^2}}\right) \tag{5.1}$$

with μ_0, z_c, l, r, n and I representing the permeability of vacuum, the position of the center of the solenoid, the length, the radius, turns per unit length, and the current of the solenoid, respectively. Fitting of the measured data to this model yielded the results listed in Table 5.1. The curve obtained by the fit is shown by the green dashed line in Fig. 5.3. The center of the coil is located downstream

[1] LakeShore HMCT-3160-WN read by LakeShore475 DSP Gaussmeter.

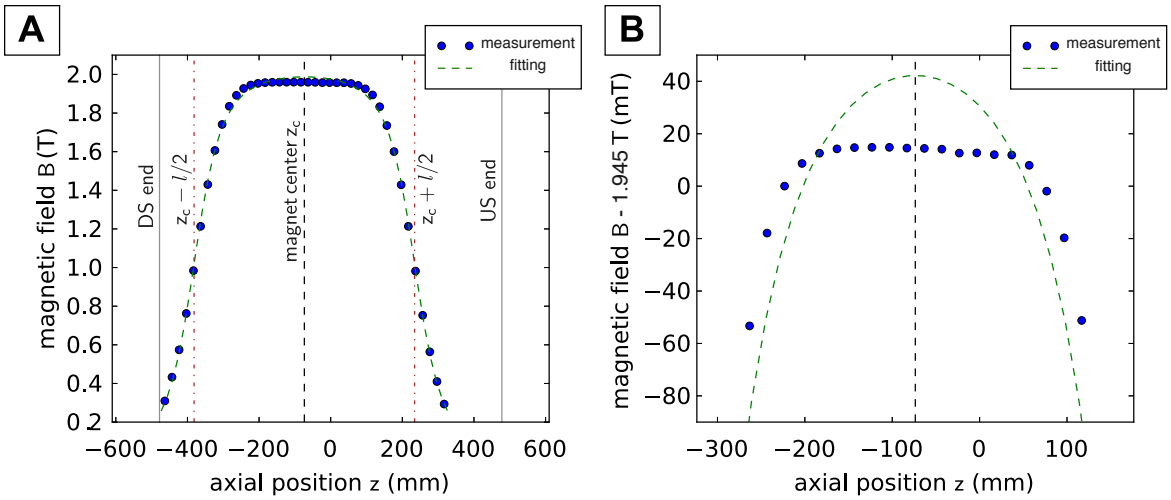

Figure 5.3: **(A)** Axial magnetic field distribution measured after the energization of the main coil of the magnet. The geometrical center of the magnet is defined as the zero of the axial position. The green dashed curve shows a fit to the model of the on-axis magnetic field distribution of a finite solenoid. A few vertical lines indicate the geometry of the magnet and the coil; the gray vertical lines at $z = \pm 478\,\mathrm{mm}$ correspond to the upstream- and the downstream end of the magnet bore; the dashed black line near the center indicate the center of the coil estimated by the fitting $z_c = -73.6\,\mathrm{mm}$; the brown dash-dot lines indicate the upstream- and the downstream ends of the main coil estimated by the fit. **(B)** Zoomed-in plot of (A) around the homogenous center.

of the geometrical center; according to the fit, $z_c = -73(1)\,\mathrm{mm}$. In Fig. 5.3 (B), the data and the fit are compared around the homogenous center. The measured magnetic field distribution deviates from the model, having a weaker magnetic field at the center and a broader homogeneous center than the model. This implies that though the coil is a solenoid, the windings near the center are more complex than simple uniform windings for production of a broad homogenous region around the center.

Table 5.1: Geometrical parameters of the main coil of the magnet obtained by the fit to the model of a finite length solenoid Eq. (5.1).

Fit parameters	Results
center z_c	$-73.6(6)\,\mathrm{mm}$
length l	$616(1)\,\mathrm{mm}$
radius r	$83(1)\,\mathrm{mm}$
turns per unit length n	$355\,111(120)\,\mathrm{m}^{-1}$

5.1.2 Shimming

After the energization, currents of the shim coils were adjusted to produce a homogeneous magnetic field at the position of the Precision Trap (PT) where the cyclotron frequency measurement takes place (see Section 5.3 for the names of the traps). Currents of two axial shim coils, respectively for a gradient of the field and a quadratic field, and two radial shim coils were adjusted sequentially.

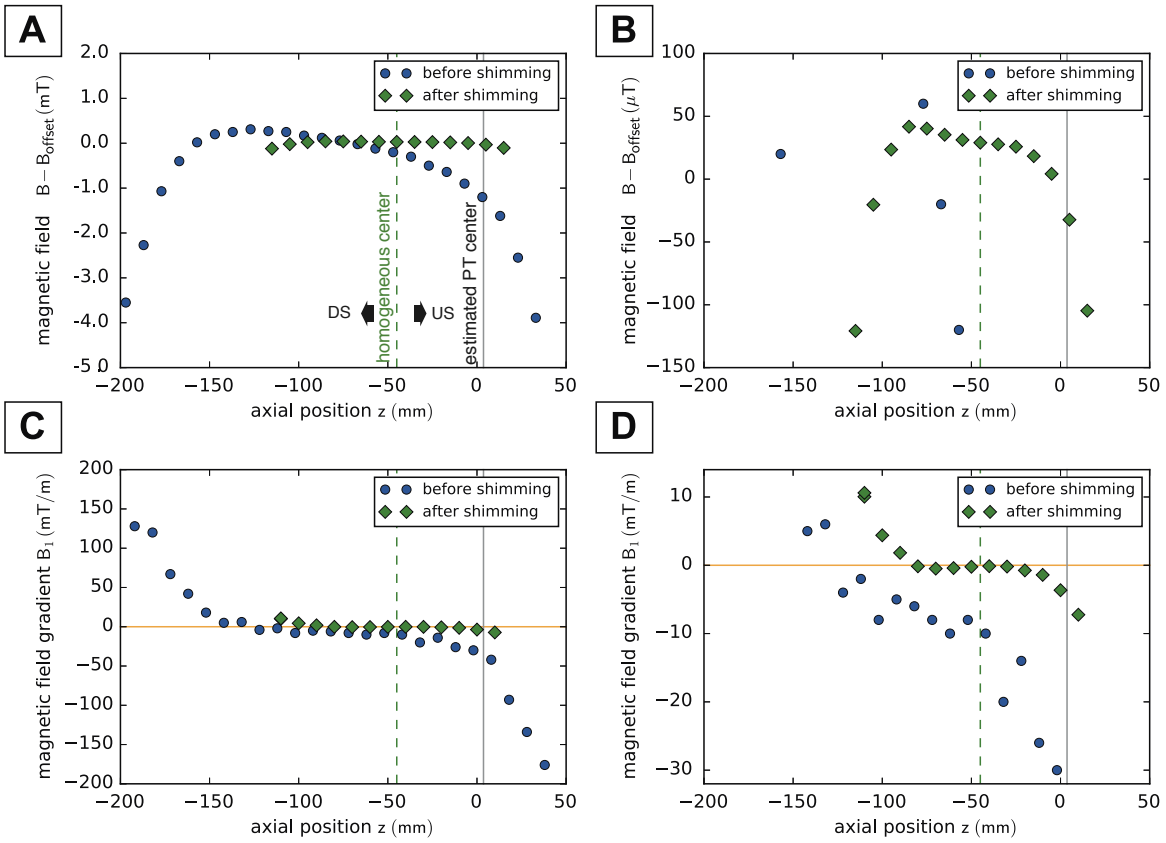

Figure 5.4: Comparison of the on-axis magnetic field distribution before and after the shimming. (A, B) show the magnetic field B and (C,D) the magnetic field gradient $B_1 = \partial B/\partial z$. Plots of (B) and (D) are zoomed-in plots of (A,C), respectively. The offsets of the magnetic fields subtracted in (A,B) are 1.9615 T for the data before shimming and 1.945 T for the data after shimming. The difference of the absolute field came from a decrease of the field between the two measurements preformed with an interval of 6 days. The homogenous center after the shimming is indicated by the green dashed line in each plot, and the estimated position of the Precision Trap center in 2017-run II by the gray solid line.

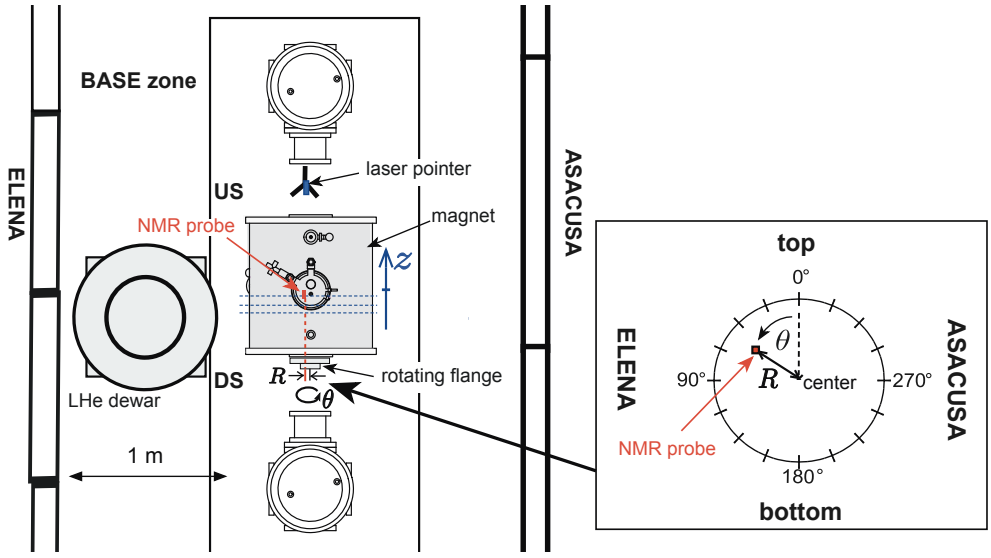

Figure 5.5: Setup of magnetic field scans. The cylindrical coordinate (R, z, θ) is defined along the axis of the magnet. The geometrical center of the magnet is defined to be $z = 0$. The angular axis is defined anticlockwise (when seen from the downstream end) with $\theta = 0°$ as the direction toward the top of the magnet. The center of bore of the magnet is defined to be $R = 0$. The NMR probe is attached at the end of the rod which is fixed to the rotating flange for angular scans in a few selected z-planes. On the upstream side of the magnet, the laser pointer is installed to measure the z position of the probe. Influence of the LHe dewar placed on the ELENA-side of the magnet was also assessed. See the text for details.

For each shim coil, the magnetic field distribution was scanned by an NMR probe[2] for different values of the current to obtain the transfer function of the coil, and then the current to be set was determined. The procedure was iterated for each shim coil. Fig. 5.4 shows the axial field maps before and after the shimming procedure. The estimated position where the center of the PT was later installed is indicated in the graph by the gray lines. The mechanical constrains didn't allow us to position the trap at the homogeneous center of the magnet. At the position of the PT, the field gradient was reduced by a factor of > 5 by shimming. The axial gradient from this measurement $B_1 = \partial B/\partial z \approx -5\,\mathrm{mT/m}$ is consistent with a later measurement by the cyclotron frequency of a single particle. Modification of geometries of the support structure will realize an even better magnetic field homogeneity $|B_1| < 1\,\mathrm{mT/m}$ in future.

After the shimming, the radial magnetic field profile around the homogeneous center was characterized by three-dimensional magnetic field scans. The setup of the measurement is shown in Fig. 5.5. The NMR probe was installed at the end of a rod which is fixed by the rotating flange installed on the downstream end of the magnet. The cylindrical coordinate (R, z, θ) is defined in the figure. A laser pointer was installed on the opposite side of the magnet to measure the position of the probe along the z axis. The same setup but with $R = 0$ was used to measure the axial map after the shimming shown earlier in Fig. 5.4.

[2]Metrolab 1062-R-10M read out by Metrolab PT 2025.

A few planes along the z axis were chosen and an angular scan $\theta = 0$–$360°$ was done on each plane with a fixed R. The results of the scans for $R = 10\,\mathrm{mm}$ is shown in Fig. 5.6. For each radial z plane, a difference from the magnetic field at $R = 0\,\mathrm{mm}$ i.e. $B(R, z, \theta) - B(0, z, \theta)$ is plotted. At $z = -95\,\mathrm{mm}$ which is about 50 mm downstream of the homogeneous center, the radial gradient of the field is $|\partial B/\partial R| < 3.8\,\mathrm{mT/m}$. Assuming the upstream/downstream asymmetry to be not large, the radial gradient at the position of the PT, which is about 50 mm upstream of the homogeneous center, to be on the same order.

All the magnetic field measurements up to this point were done with a LHe dewar (Wessington Cryogenics CH-500) placed beside the magnet at the position indicated in Fig. 5.5. The influence of the dewar to the magnetic field homogeneity was investigated by performing rough scans with and without the dewar by removing it from the zone between the two measurements. The results are shown in Fig. 5.7. It can be seen that the direction of the magnetic field has slightly changed between the two conditions, and the gradient became smaller when the dewar was removed. At $z = -15\,\mathrm{mm}$ from the dataset of $R = 5\,\mathrm{mm}$, the radial gradient $\partial B/\partial R$ is $1.46\,\mathrm{mT/m}$ (with the dewar) and $1.23\,\mathrm{mT/m}$ (without the dewar)

From these results, it seems that magnetic materials contained in the dewar influence the field distribution in the magnet, even though it is about 1 m away from the magnet bore.

Because improvement of a magnetic field gradient on the order of $10^{-4}\,\mathrm{T/m}$ is not significant for the measurement, the dewar was kept placed beside the magnet during actual measurements for practical reasons. When a more homogenous magnetic field is required in future runs, this effect should be noted.

5.1.3 Field stability of the magnet

After the energization and the shimming procedures were completed, the magnet was operated in persistent mode. The stability of the magnet soon after the energization was at $(\Delta B/B)/\Delta t = -1 \times 10^{-7}\,/\mathrm{h}$, it stabilized to $|(\Delta B/B)/\Delta t| \sim 1 \times 10^{-8}\,/\mathrm{h}$ after a few days, and reached $|(\Delta B/B)/\Delta t| < 5 \times 10^{-9}\,/\mathrm{h}$ by the time when the measurement started three months after the energization.

The magnet has no effective shielding against changes of the external magnetic field. The shielding factor S defined by $S = \Delta B_{\mathrm{ext}}/\Delta B_{\mathrm{in}}$ (see Chapter 10) was measured to be $S \approx 1$. To reduce influences of the external magnetic field fluctuations, a separate shielding system (Chapter 10) was developed and installed on the outer surface of the trap chamber.

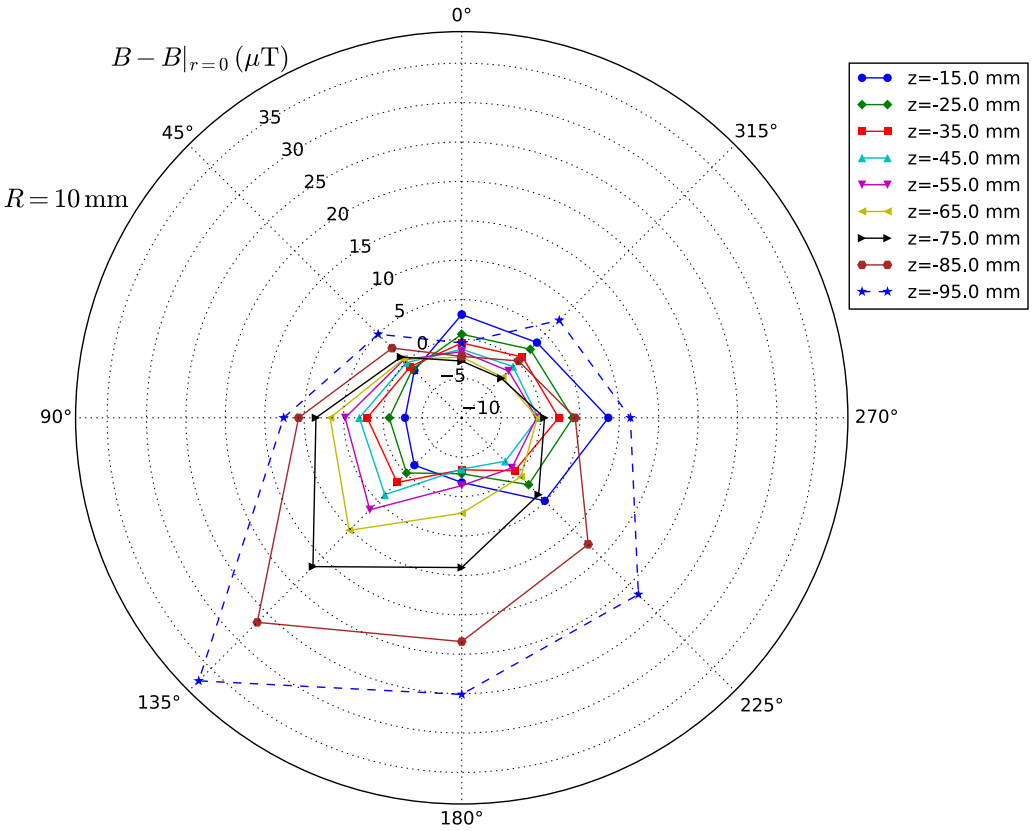

Figure 5.6: Results of three-dimensional magnetic field scans at $R = 10\,\mathrm{mm}$. $B(R, z, \theta) - B(0, z, \theta)$ is plotted for each z and θ. It can be seen that the magnetic field is pointing in the direction of $\theta \approx 135°$ as z position goes toward the downstream end from the homogeneous center.

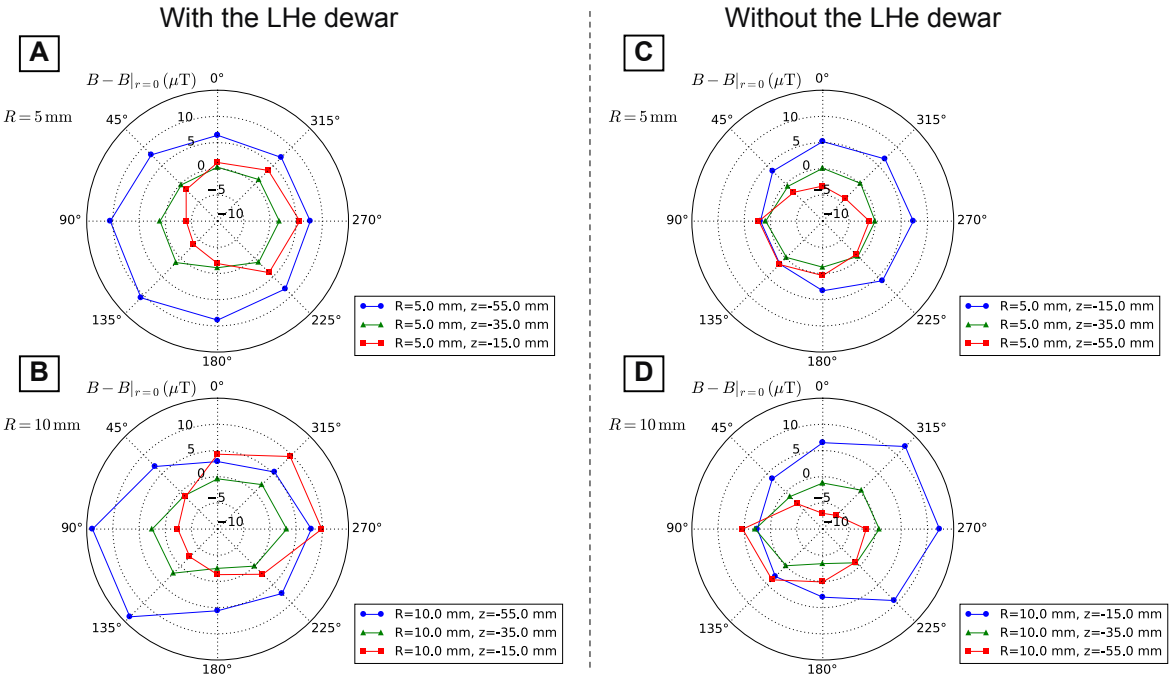

Figure 5.7: Results of three-dimensional scans with and without the LHe dewar. **(A, B)** Measured with the LHe dewar next to the magnet. **(C, D)** Measured without the LHe dewar. **(A, C)** At $R = 5\,\mathrm{mm}$. **(B, D)** At $R = 10\,\mathrm{mm}$.

5.2 Cryogenic assembly

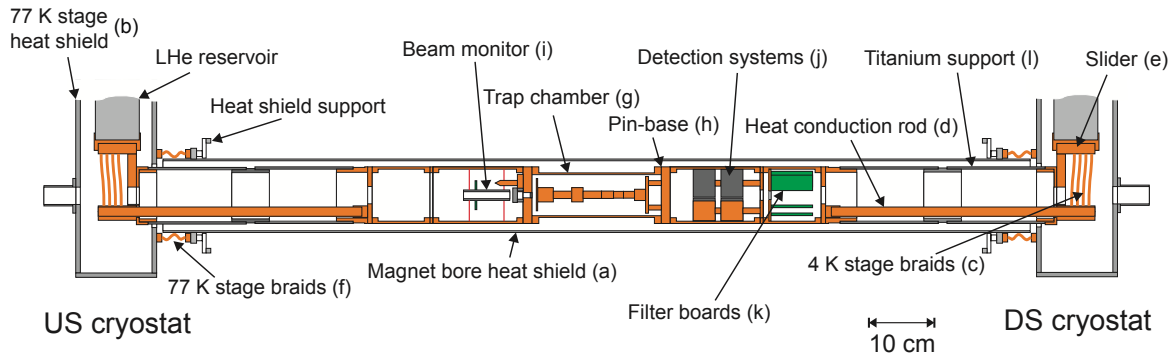

Figure 5.8: Cryogenic assembly installed in the bore of the superconducting magnet. Adapted from [33]. See the text for details.

Each of the two cryostats contains 35 L LN_2 and 35 L LHe reservoirs which provide cryogenic temperatures for operation of the experiment. The cryogenic assembly is shown in Fig. 5.8. The upstream and the downstream ends of the assembly are connected to the LHe/LN_2 reservoirs on the bottom of the cryostats. The compact structure was realized by making the mechanical support provide cryogenic thermal connections.

The assembly is divided into two stages at different temperatures: the 4 K stage connected to the LHe reservoirs of the cryostats, and the 77 K stage connected to the LN_2 reservoirs. The 77 K stage surrounds the 4 K stage to prevent direct heat radiation from an exterior at room temperature to 4 K, thereby reducing consumption of LHe by a factor of about 230. In Fig. 5.8, components of the 4 K stage at the center are covered by surfaces of the 77 K stage. Between the two stages, heat shields are installed to reduce the heat load from the 77 K stage to the 4 K stage, which are shown in Fig. 5.8:

- The heat shield in the magnet bore ((a) in Fig. 5.8) is an aluminum tube of 127 mm inner diameter and 3 mm wall thickness covering the part of the 4 K stage in the magnet bore. It is mechanically fixed in vacuum chambers at room temperature using a fiber glass disk as thermal insulation.

- The 77 K stage heat shields (b) consist of aluminum plates of 8 mm thickness assembled to form boxes which cover the connections of the 4 K stage to the bottoms of the LHe reservoirs.

In addition, the outer surfaces of each of the 4 K- and 77 K stages are entirely covered by about 20 layers of multi-layer insulation foil to further reduce the emissivity of the surfaces.

To provide good thermal connections from the LHe reservoirs to the 4 K stage, the 4 K stage braids (c) made of oxygen-free high conductivity (OFHC) copper are used in the support structure on each side. Each of them has 360 mm^2 of the total cross section. On each side, the braids are attached to the 16 mm diameter heat conduction rod (d) made of annealed OFHC copper, which conducts heat from

the 4 K stage to the LHe reservoir. The thermal link with the assembly is ensured by screwing the rods on the last sections of the copper segments of the 4 K stage. The sliders (e) with ball bearings are used in the support structure of the braids. The braids as well as the sliders compensate mechanical stress by contraction of the inlay during cool down of the apparatus. Similar copper braids (f) are also used in the 77 K stage structure for the same purpose.

The main components of the 4 K stage are the following:

- The trap chamber (g) is a cylindrical indium-sealed vacuum chamber containing a Penning trap system. It is made of high-purity copper, having dimensions of 77 mm inner diameter, 234 mm length, and 1.2 L in volume. The downstream flange called pin-base (h) has cryogenic feedthroughs of all the AC and DC lines from the trap system. The upstream flange has a 9 mm diameter degrader window at the center. The details of the degrader are described in Section 5.6.1. The degrader window is enclosed by a stainless-steel foil of 25 µm thickness which is vacuum-tight but transparent for antiprotons of kinetic energy of 5.3 MeV. The trap chamber operates under ultra-high vacuum (UHV) which enables permanent storage of antiprotons. It is achieved by the following steps: Before installation, the trap chamber is pumped to a vacuum $< 10^{-6}$ mbar. Subsequently, the pumping connection is pinched-off with a cold-weld technique, and the chamber is installed in the assembly, then the entire system is pumped and cooled down. By cryo-pumping, the vacuum inside the chamber reaches below a measurable range of conventional gauges. The vacuum in the trap chamber is estimated to be $< 10^{-17}$ mbar from storage time of antiprotons (see Section 6.5 and Ref. [76] for details).

- The beam monitor (i) mentioned in the earlier sections is installed upstream of the trap chamber. It consists of Faraday cups made from a four-fold segmented plate of 50 mm diameter with a 9 mm hole at the center. The signals on the four channels are individually recorded to identify the position of the beam. More details of this instrument are described in Ref. [135].

- The electronics segment is placed downstream of the trap chamber. Its main components are the image-current detection systems (j) and the cryogenic filter boards (k). They will be described in more detail in a later section.

The central support structure which holds these elements of the 4 K stage is made of high-purity OFHC copper. The outer segments of the support structure (l) are made of titanium because of its mechanical stiffness and low weight. The thermal link is maintained by the copper conduction rods (d).

The thermal load to the LHe reservoirs by the cryogenic inlay is estimated to be 90 mW radiative load, 15 mW conductive load due to wiring, and 20 mW load from the cryogenic amplifiers. Based on these, together with intrinsic heat load of the cryostats and heat load through windows of the 77 K stage for cabling and beam access, the overall heat consumption was estimated to be 150–200 mW,

which corresponds to about 10 days of standing time of the LHe reservoirs. In reality, due to some unidentified heat load, the apparatus consumes the refrigerant much faster. The actual standing time is about 52 h, corresponding to about 900 mW of the total heat load. The operation of the experiment is still possible, but this necessitates interventions of the experiment every two days for cryogenic maintenance.

5.3 Penning-trap system

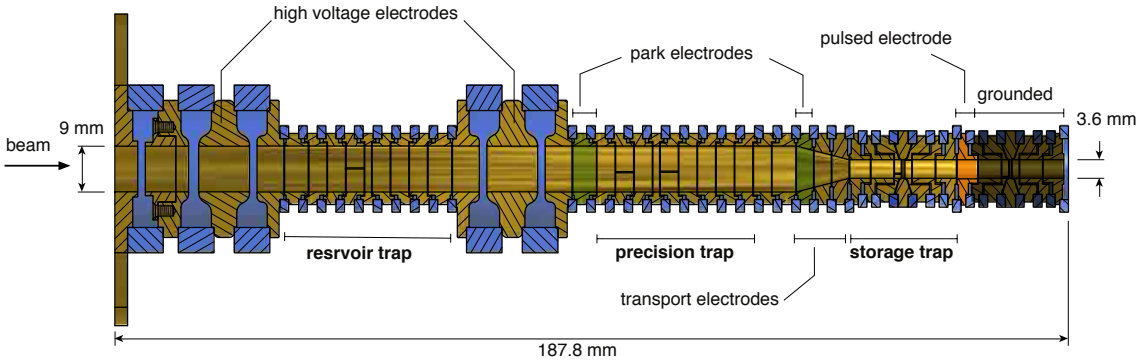

Figure 5.9: Penning trap assembly used in BASE 2017 run. Adapted from Ref. [33], modified under permission by the author.

The multi-Penning trap system is the heart of the experiment. The system used in the 2017 run is shown in Fig. 5.9. The layout of the trap stack is based on that of the 2015/2016 magnetic moment run described in Ref. [33]. Minor modifications were made for the 2017 run. The trap stack consists of three traps: the reservoir trap (RT), the precision trap (PT) and the storage trap (ST). The electrodes located downstream of the ST were grounded and not used as a trap. The role of each trap is explained below.

- Reservoir trap (RT): During beam shifts, the RT functions as a catching trap. Up to 4.5 kV of high voltages can be applied to the high voltage electrodes which are located upstream and downstream of the trap. An antiproton bunch ejected from the AD is captured by a high voltage pulse, sympathetically cooled by electrons, and stored in the RT. When the beam shifts end, the RT serves as a reservoir of particles. The ultra high vacuum in the trap chamber enables permanent storage. By potential manipulation, single particles can be extracted from the cloud of particles. In this way, the experiment can be operated independently from supplies by the AD. To protect the reservoir against power cuts, the voltage source of the RT is operated with uninterruptible power supplies. The reservoir enabled BASE to operate in 2016 without taking any beam shift during the entire antiproton run [76].

- Precision trap (PT): The PT is placed near the homogeneous center of the magnet. It is where the cyclotron frequency measurements for the charge-to-mass ratio comparison take place. The

Table 5.2: Summary of the trap parameters of the RT, PT and the ST. In the table, $a, l_{\mathrm{ec}}, l_{\mathrm{ce}}, l_{\mathrm{r}}$ stand for the inner radius, lengths of the endcap electrode, the correction electrode and the ring electrode, respectively (Section 2.3.1). C_2 is the trap parameter introduced in Section 2.1. $B_1 = \partial B/\partial z$ is the magnetic field gradient.

	a (mm)	l_{ec} (mm)	l_{ce} (mm)	l_{r} (mm)	$C_2(\mathrm{m}^{-2})$	$\lvert B_1\rvert$ (mT/m)
RT	9.0	10.87	3.53	1.31	−18508	25
PT	9.0	10.87	3.53	1.31	−18508	4.8
ST	3.6	8.668	1.336	0.386	−115357	0.2

cyclotron frequencies of two particles can be measured alternately by exchanging the positions of the particles by adiabatically transporting them along the trap stack. The cyclotron frequency measurements can be performed by using an image-current detection system implemented to the PT. Two adjacent electrodes, marked in green in Fig. 5.9, are called park electrodes, and used to park one of the particles while the other is being measured. Characterization of the PT will be discussed in more details in a following chapter.

- Storage trap (ST): The ST is used upon necessity to temporarily store a particle in the PT on the downstream side during experimental operation.

Each of the three traps is a five-pole cylindrical Penning trap in compensated and orthogonal design [91, 92] (Section 2.3.1), consisting of two end-cap electrodes, two correction electrodes and one central ring electrode. The parameters of the three traps are summarized in Table 5.2.

The radius of the RT and the PT was chosen such that it has a large enough radius compared to the beam radius while having enough detection sensitivity for the image-charge detection. The ST inherited the geometries of the analysis trap in the magnetic moment run where a strong quadratic term of the magnetic field B_2 was realized by a small radius of the trap and a ferromagnetic ring electrode. The ferromagnetic electrode was replaced to a copper electrode for 2017 run for improvement of the magnetic homogeneity in the PT. In the transport section between the PT and the ST, conical electrodes are used to bridge the traps with different radii.

The traps were constructed by stacking OFHC copper electrodes, each of them gold-plated to prevent oxidation. The thickness of the gold layer is about 8 µm, in order to prevent the gold atoms from diffusing into the copper a 7 µm barrier layer of silver is used between the copper and the gold layer. Larger segments were made by electrically connecting neighboring electrodes by wires. This way of construction facilitates manufacturing of the electrodes and makes required connection shorter. Between the electrodes, sapphire rings are used to separate the electrodes.

Electronics suited for application of voltage pulses are implemented in the DC lines of the two high-voltage electrodes and the *pulsed electrode* of the ST, indicated in orange in Fig. 5.9 (see Section 5.6.3 for more details). This enables application of pulsed high voltages for antiproton catching on the high voltage electrodes. They are also used for electron kick-out operation in the high-voltage electrodes

and the pulsed electrode. The trap stack is mounted on the pin-base as shown in Fig. 5.10. The structure made of oxygen-free electronic (OFE) copper presses the assembled electrodes and the spacers together. As seen in the lower photograph of Fig. 5.10, all the DC and the RF lines go through the feedthroughs on the pin-base, and are wired to the electronics outside the trap chamber.

Together with the trap stack, a few components are installed as seen in Fig. 5.10:

- Degrader: Part of the degrader structure is placed at the upstream end of the trap stack. The entire structure of this component is explained in Section 5.6.
- Electron gun: A field-emission electron gun is implemented at the downstream end of the trap stack. Its purpose is to produce electrons which are used for sympathetic cooling of antiprotons upon capture. It is also used to load the trap with protons for characterization of the traps. It is done by shooting electrons from the electron gun toward the upstream end, while positively biasing the degrader electrode. Electrons collide with the surface of the degrader, sputter out hydrogen atoms and subsequently ionize them to produce protons.
- Spin-flip coils: disk coils were installed near the centers of the PT and the ST. In 2015/2016 run, these coils were used to apply high-power RF drives to induce spin transitions of antiprotons for the magnetic moment measurements. In this run, they are used as auxiliary excitation lines mainly for radial excitations.
- Cyclotron detection system: Components of the detection system of the modified cyclotron mode, the cyclotron resonator and the amplifier, are installed along the trap stack. In 2015/2016 run, the effective temperature of the cyclotron detector was about 12 K, a factor of 3 higher than its specification due to electric noises produced by operation of the AD. In order to reduce interferences with the ambient electromagnetic noise in the AD hall, the cyclotron detection system was installed in the trap chamber in 2017 run. This improved the temperature of the detector to ≈ 5 K [79], lower by about a factor of 2.5 than in 2016.
- RF block: A 1 MΩ resistor is placed between two segments of a split electrode for application of quadrupole excitation and image-current detection of the modified cyclotron mode. Its functionality is detailed in Section 5.4

More details of the detection systems, the degrader, and the electron gun are explained in the following sections.

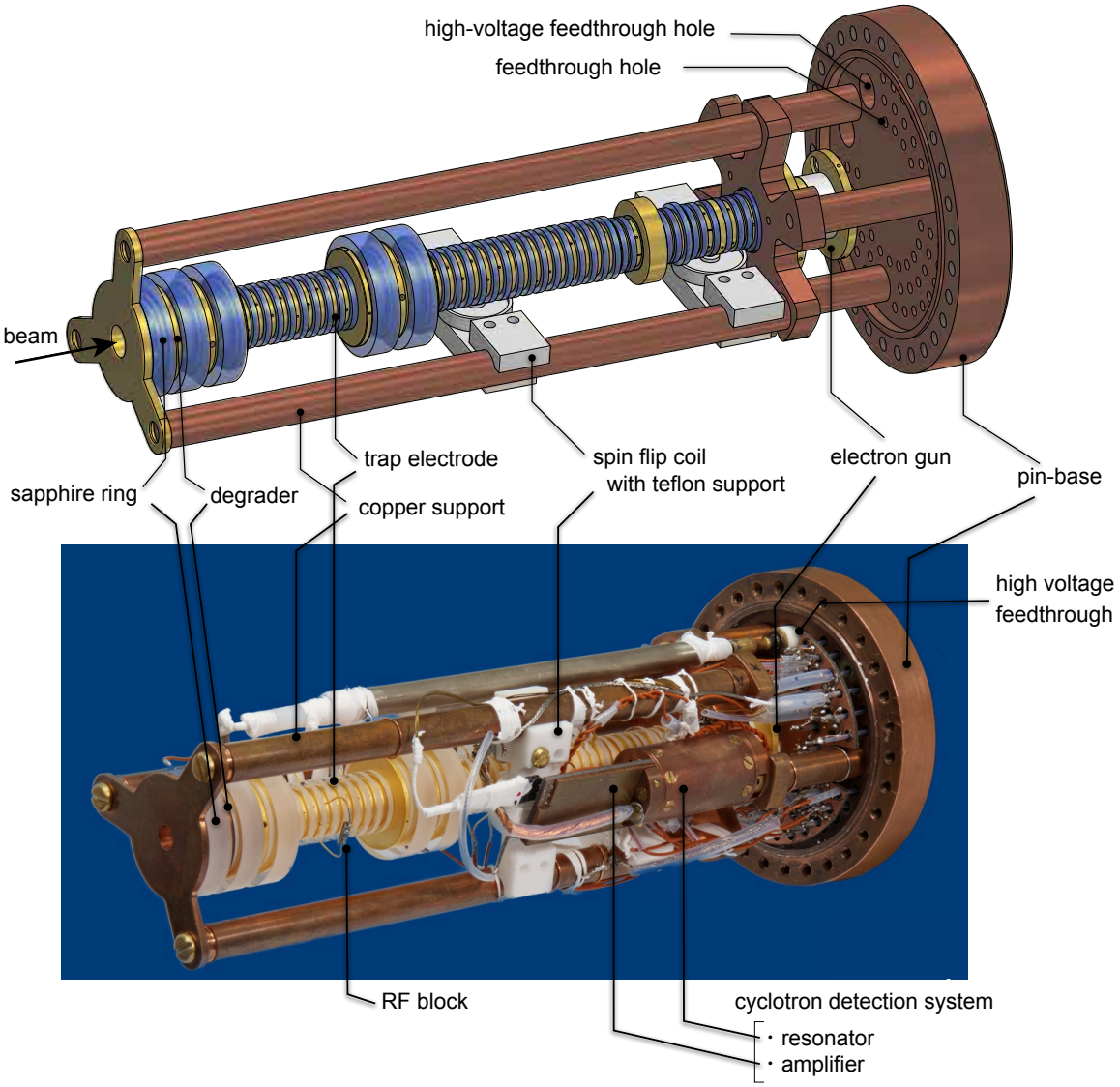

Figure 5.10: Penning-trap system assembled and mounted on the pin-base. The three-dimensional model (upper) and the photograph (lower). Key components are explained in the annotations. Minor modifications such as placement of the cyclotron detection system have been performed between the design in the 3D model and the actual assembly in the photograph.

5.4 Electronic components

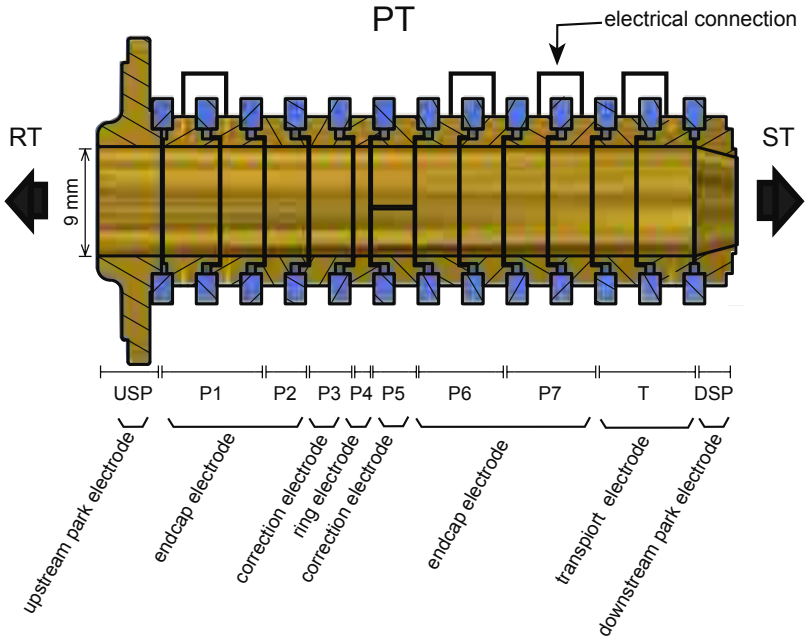

Figure 5.11: Electrode configuration of the PT. See the text for details.

In this section, an overview of the core electronic components installed with the trap system is given. Here we take the PT is as an example. The electronics of the other traps are constructed in a similar way. The configuration of the electrodes of the PT is shown in Fig. 5.11, and the connection diagram in Fig. 5.12. The electrodes are labeled as P1 to P7 from the upstream electrode to the downstream one (Fig. 5.11). Electrodes P1 and P2 function as one endcap electrode, and P6 and P7 as the second endcap electrode. They can be biased separately during particle transports. Wires connected to the electrodes go through stages at different temperatures at 4 K, 77 K and room temperature before coming out from the room temperature flange. In Fig. 5.12 (A), the different stages are marked by different colors.

The lines connected to the electrodes are categorized to DC lines for biasing of the trapping voltages and RF lines for images current detection and application of excitations.

5.4.1 DC biasing lines

The DC lines connect the electrodes to a highly stable custom-made voltage sources UM 1-14 by Stahl Electronics. See Section 5.5 for characterization of the stability of this device.

In order to effectively suppress electric noise on the electrodes, RC low-pass filters are installed at each temperature stage on each DC line. Such noise can be introduced by RF pickups and electromagnetic interferences, and if not suppressed properly, could cause unwanted heating of particles in

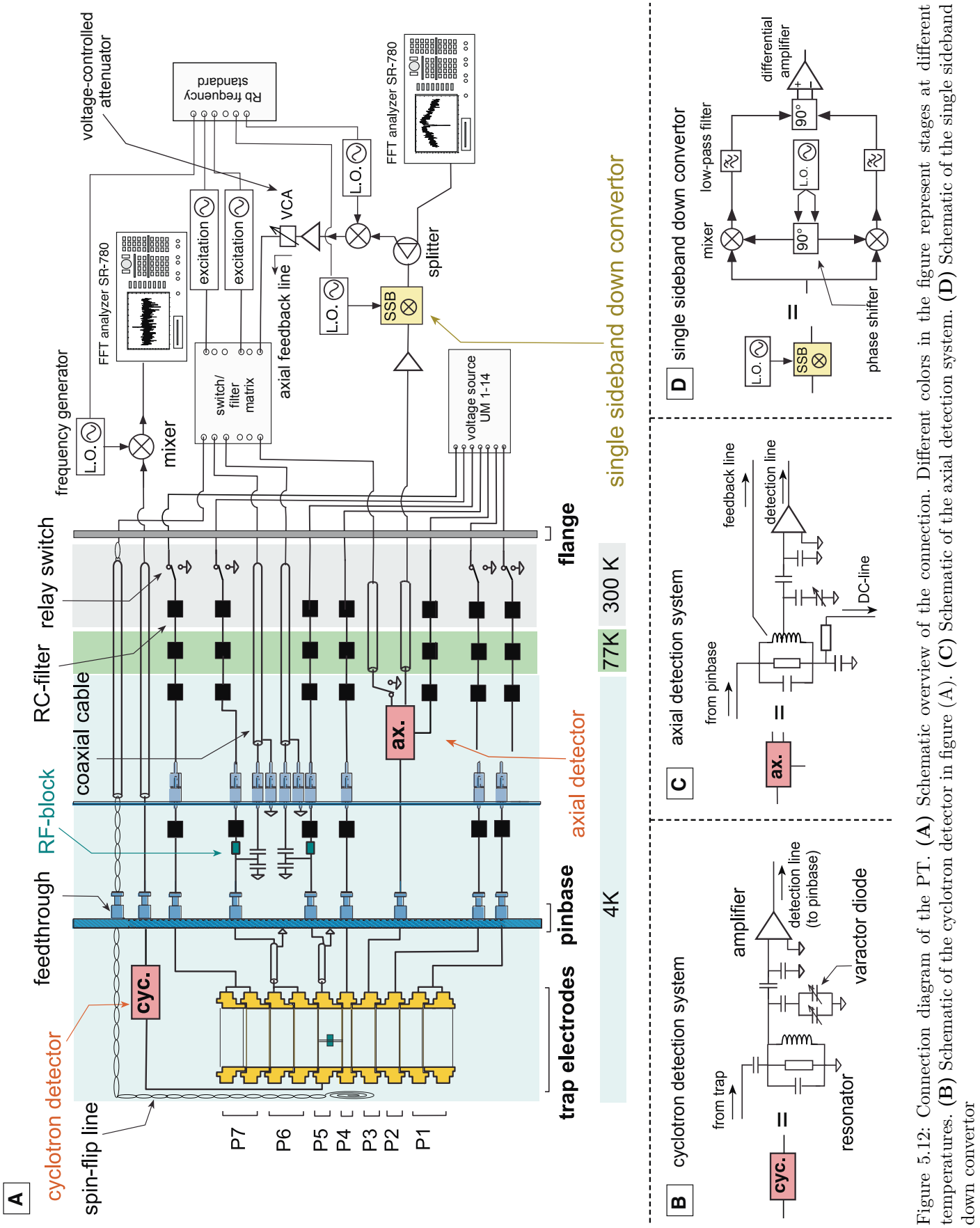

Figure 5.12: Connection diagram of the PT. **(A)** Schematic overview of the connection. Different colors in the figure represent stages at different temperatures. **(B)** Schematic of the cyclotron detector in figure (A). **(C)** Schematic of the axial detection system. **(D)** Schematic of the single sideband down convertor

the trap or frequency fluctuations. Each DC line has four filters: one at 300 K, one at 77 K, and two at 4 K. The total time constant of the filters is about 70 ms, sufficiently low to apply voltage ramps for adiabatic transports within intervals of a few 100 ms.

In the 300 K part of the DC lines of the endcap electrodes, relay switches are installed. Its purpose is to ground the transport- and endcap electrodes when precision measurements take place in the traps.

5.4.2 RF lines

The PT has two primary excitation lines: the axial excitation line connected to electrode P6 and the radial excitation line connected to P5. Electrode P5[3] is segmented into two, enabling application of quadrupole excitations by applying an AC potential to one of them. The other segment is connected to the cyclotron detector for direct detection of the modified cyclotron mode. The two segments are connected by a 20 MΩ block resistor (Fig. 5.12 (A), seen also in the photograph in Fig. 5.10). This makes the DC electric potential common between the two segments while forming an effective block once AC signals are applied. The RF line connected to electrode P6 is used for dipole excitations addressing to the axial mode. In addition to the primary excitation lines connected to the electrodes, the spin-flip line connected to the spin-flip coil is used as an auxiliary excitation line.

The axial detection line is connected to P3. The radial detection line is connected to the other segment of P5 from the excitation line. The axial detection system has a feedback line for actively control of its temperature. A cryogenic field effect transistor (FET) switch grounds the feedback line when it is not in use.

For some lines where one line is split into a DC line and an RF line (the ones from P3, P5 and P6), a capacitive voltage divider is placed at the junction to suppress potential noise from the RF line. In addition, a 1 MΩ resistor is placed between the capacitive voltage divider and the RC filter to block the RF signal to transmit through the DC biasing line (*RF-block*s in Fig. 5.12 (A). See also (C)).

Single coaxial cables with brass single lines and Copper-Nickel (CuNi) shields (GVL Cryoengineering) are employed for the excitation lines and the detection lines. They have low thermal conductivity and are suited for cryogenic environment. High-purity copper wires are used to connect the detectors to the electrodes.

5.4.3 Image-current detection systems

The image-current detection systems are the crucial electronic components of the experiment. The present apparatus is equipped with three axial detection systems for each of the RT, PT and the ST.

[3]The electrode P3 is also segmented, but for 2017 runs, the two segmented were interconnected to each other, and used as normal electrodes.

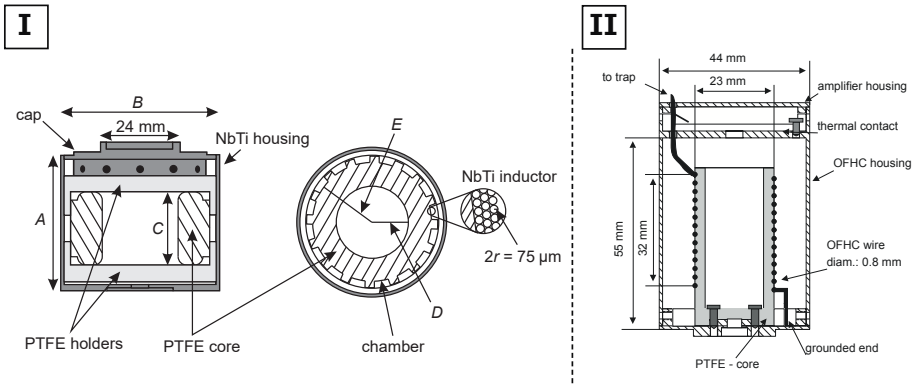

Figure 5.13: Schematics of the superconducting resonators. **(I)** Geometry of the axial resonator. From Ref. [136]. The geometrical parameters A–E are listed in Table 5.3. A three-layer toroidal coil made of a PTFE insulated NbTi wire is wound on the PTFE core. The coil is placed in a cylindrical metal housing. **(II)** Geometry of a prototype of the cyclotron resonator. From Ref. [137]. A single layer solenoid made of the NbTi wire is wound on the PTFE core. The copper cylinder houses the resonator. Detailed geometrical parameters differ from the one installed in 2017 run.

The PT is in addition equipped with a cyclotron detection system for direct detection of the modified cyclotron mode. Designs and specifications of the BASE axial detection systems are described in Ref. [136]. The design of the cyclotron detection system is based on Ref. [137], and characterized in Ref. [138]. Details of the present cyclotron detection system will be discussed in the Ph.D. thesis of James A. Harrington [79].

Schematics of the detection systems on the RF detection lines are shown in Fig. 5.12 (A, B). Each detection system consists of a superconducting resonator and a cryogenic low-noise amplifier. The superconducting resonators are made of Polytetrafluoroethylene (PTFE) insulated NbTi wires wound on PTFE cores. Toroidal coils are used for the axial detection systems and a solenoid coil for the cyclotron detection system. Examples of the geometries of the coils are shown in Fig. 5.13. The resonators were placed in metal housings to reduce dissipation of power to the exterior. The dimensions of the resonators, materials of the wires and the cores, and methods of joining the wires were chosen with care to minimize the losses of the signal in order to achieve Q-factors as much as possible.

Below the critical temperature of the NbTi (9.5 K), the resonators exhibit high Q-factors. The unloaded characteristics of the axial resonators are summarized in Table 5.4. They were obtained by tests in an offline cryogenic test setup operated with a Gifford Mac Mahon pulse tube cooler. The Q-factors of 10^4–10^5 of the axial resonators correspond to the parallel resistances R_p on the order of a GΩ. The Q-factor of the cyclotron resonator is about 14 000.

The amplifier-end of the toroidal coil of the axial resonator branches from the wire, dividing the coil into two parts of the windings (Fig. 5.12 (C)). The ratio of the windings defines the strength of coupling of the resonator to the rest of the system. It was optimized for desirable properties of the detection system (see Section 9.2 for details).

Table 5.3: Geometrical parameters of the axial resonators installed in the 2017 apparatus. See Fig. 5.13 for definition of the parameters.

	A (mm)	B (mm)	C (mm)	D (mm)	E (mm)
RT & PT	36	41	23	10	16
ST	41	48	22	12.5	19

Table 5.4: Summary of the unloaded characteristics of the axial resonators. The materials of the housings, the inductance L, the parallel capacitance C_p, the Q-factor, the resonance frequency ν_0, the turn N, the parallel resistance R_p are listed for each axial resonator. The resonator used for the ST are made of copper housing, having a smaller Q-factor than the other two.

	housing material	L (mH)	C_p (pF)	Q-factor	ν_0	N	R_p
RT	NbTi	1.71	11	196 000	1.07 MHz	800	2.3 GΩ
PT	NbTi	1.75	11	194 000	1.09 MHz	800	2.3 GΩ
ST	Cu	2.98	12	61 000	840 kHz	1200	917 MΩ

The PT axial detection system has a feedback line capacitively coupled to the resonator for control of the effective temperature of the detection system [105].

The design of the low-noise cryogenic amplifiers is based on a circuit shown in Fig. 5.14. It is a two-stage transistor amplifier made of two gallium arsenide (GaAs) FETs, consisting of a high impedance common-source input stage and a source-follower circuit for impedance matching as the output stage. The varactor diodes are used as variable capacitors, enabling tuning of resonance frequencies of the systems by variation of the bias voltage. It was installed to an axial system for the first time in 2017. The purpose is to eliminate the major systematic uncertainty of the last charge-to-ratio comparisons, as we shall discus in details in Chapter 9).

5.4.4 Room temperature RF circuit

Electronic equipment and circuit components installed outside the flanges are shown on the right half of Fig. 5.12 (A).

The DC bias lines are connected to the precision voltage source UM 1-14.

Signals through the detection lines are processed by Fast Fourier Transform (FFT) in FFT analyzers SR-780 by Stanford Research System. The primary signals are down-converted to the audio frequency range in order to match the acceptance range of the FFT analyzers. Down-conversion of the signal of the PT axial detection line is done by a single sideband (SSB) down-converter (Fig. 5.12 (D)). It was developed by Mustafa Beşirli as part of his bachelor's thesis work [139]. When an RF signal is mixed by a normal mixer, the output contains a down-converted component and an up-converted component with equal amplitude. Usually, the up-converted signal is removed by appropriate filters. The SSB down-converter transmits the power of the original signal to the down-converted signal while

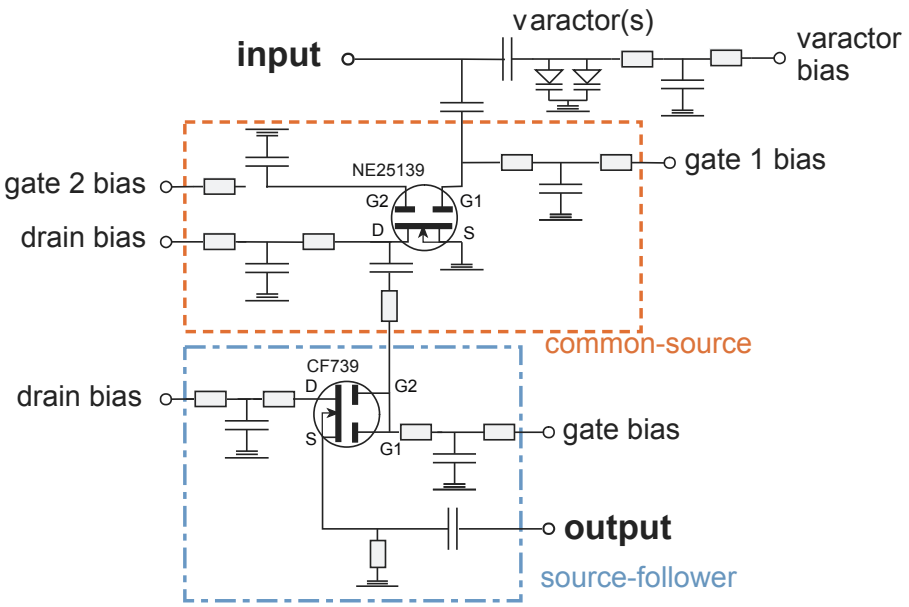

Figure 5.14: Example of a schematic of the low-noise cryogenic amplifier as part of an image-current detection system. The input stage (indicated by the orange block) is a common-source circuit. The output stage is a source-follower for a purpose of the impedance matching to the input of the FFT analyzer. The details differ between each detection system. An FET NE25139 (NEC) is used for the common-source circuit and CF739 (Siemens) for the source-follower circuit.

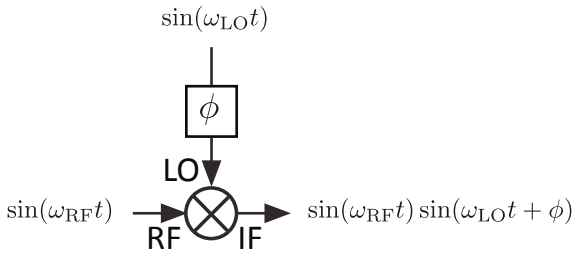

Figure 5.15: Functionality of an RF mixer. See the text for details.

canceling the up-converted output, thereby improving the signal-to-noise ratio by a factor of 2. If the *radio-frequency* (RF) and the *local oscillator* (LO) inputs are respectively denoted as $\sin(\omega_{\mathrm{RF}}t)$ and $\sin(\omega_{\mathrm{LO}}t+\phi_{\mathrm{LO}})$ with ϕ_{LO} being the phase of the LO signal (see Fig. 5.15), the principal output of the *intermediate-frequency* (IF) channel becomes

$$\sin(\omega_{RF}t)\sin(\omega_{LO}t+\phi_{LO}) = \underbrace{-\frac{1}{2}\cos((\omega_{\mathrm{RF}}+\omega_{\mathrm{LO}})t+\phi_{\mathrm{LO}})}_{\text{up-converted component}} + \underbrace{\frac{1}{2}\cos((\omega_{\mathrm{RF}}-\omega_{\mathrm{LO}})t-\phi_{\mathrm{LO}})}_{\text{down-converted component}}, \quad (5.2)$$

thus the phase of the LO is reflected oppositely between the down- and the up-converted component. Therefore, two phase shifters before and after mixing as in Fig. 5.12 (D) realize a transform which conserves the phase of the up-converted component but makes the down-converted component phase-shifted by π. By taking difference of such a signal with a mixed signal without phase shifts, unwanted

up-converted component can be canceled. The axial detection lines splits after the down-conversion. One of them goes to the FFT analyzer, and the other (the *axial feedback line* in Fig. 5.1) is up-converted and fed-back to the axial detection system for feedback control of the temperature of the detection system (Section 2.4.3). Amplifiers and attenuators are installed to adjust the strength of the feedback signal. The phase of the feedback signal is controlled by the phase of the LO for the up-conversion.

The excitation lines and the axial feedback line are connected to the frequency generators via a switch/filter matrix. This consists of filters and attenuators for each purpose (e.g. a high pass filters for cyclotron-axial sideband coupling drives, a band-pass filter for magnetron-axial sideband coupling drives) connected with an USB-controlled RF switch matrix USB-8SPDT-A18 (Mini-Circuits). Using the switch matrix makes the cabling compact and facilitates to ground the lines when they are not used.

The frequency generators are locked to a Rubidium frequency standard FS725 (Stanford Research System) through its 10 MHz outputs.

Differences of electrical ground between these equipments can produce ground loops which cause RF noise to worsen the SNR of the detection system. Grounds of the components are tightly fixed on a common ground to avoid this type of noise.

5.5 Stability of the voltage source

The stability of the trapping voltages is critical to the stability of the axial frequency. Further, when the sideband coupling method is used to measure the modified cyclotron frequency, the voltage stability also ultimately limits the precision of the cyclotron frequency measurement (see Chapter 15 for details). The highly stable voltage supplies UM 1-14 are used to provide stable trapping voltages

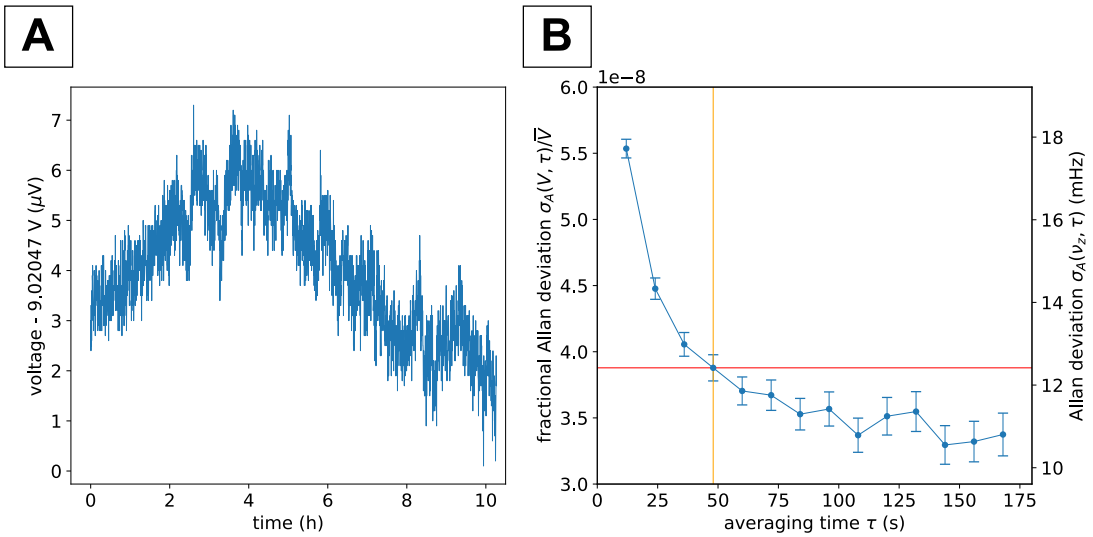

Figure 5.16: Results of a stability measurement of the high-precision voltage source UM 1-14-LN-F in the BASE zone. 9 V output was set to a high-precision test channel of the voltage source, and the voltage was continuously measured by a high precision multimeter. **(A)** The measured voltage against the time with the offset voltage 9.020 47 V is subtracted. **(B)** The Allan deviation in a unit of fractional voltage $\sigma_A(V,\tau)/\overline{V}$ as a function of the averaging time τ. The scale on the right is converted to the Allan deviation of the axial frequency $\sigma_A(\nu_z,\tau)$.

to the Penning traps. Among the series of UM 1-14, models of UM 1-14-LN are used for the RT and the ST. For the PT, a model UM 1-14-LN-F which is specifically designed for this measurement is installed. This model has a shorter time constant of voltage relaxation about 5 s, shorter by a factor of 4 than the other models.

The voltage sources were characterized in advance to installation to the apparatus. Fig. 5.16 shows the result of the stability measurement of one of the high-precision test channels of UM 1-14-LN-F performed in the BASE zone. The output voltage was continuously monitored by a high precision multimeter Fluke 8508A while a constant output voltage of 9 V was set at the test channel. Fig. 5.16 (B) shows the Allan deviation of the voltage in a unit of fractional voltage $\sigma_A(V,\tau)/\overline{V}$ (the scale on the left). The fractional stability at the averaging time of 48 s, a typical acquisition time for one axial frequency measurement, is 3.87×10^{-8}, which corresponds to 12 mHz in the axial frequency fluctuation, assuming a typical antiproton axial frequency in 2017 run-II.

5.6 Antiproton catching system

This section highlights the components used to capture antiprotons provided by the AD. These components: the degrader, the RT, and the electron gun, are shown in Fig. 5.17.

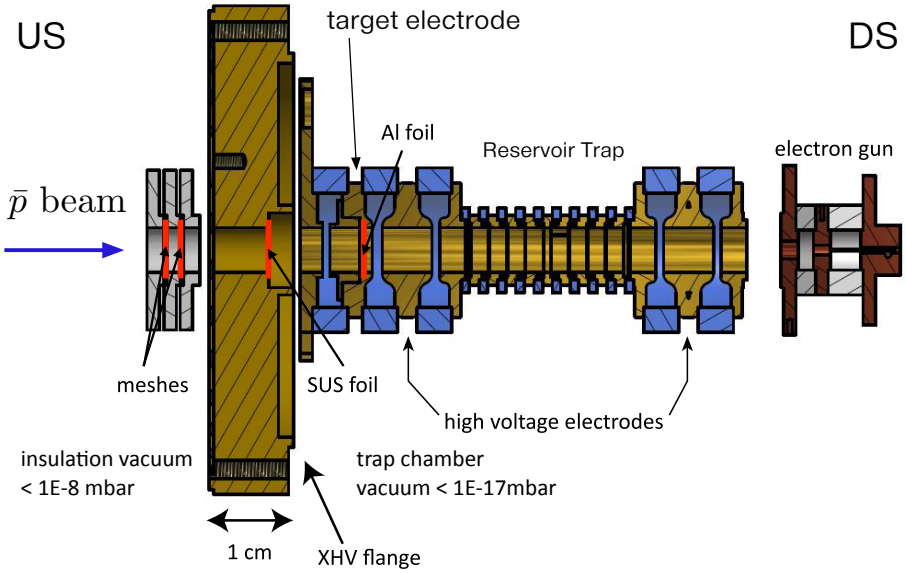

Figure 5.17: Key components for antiproton catching. The degrader is located upstream of the RT. The electron gun is at the downstream end of the trap assembly. The components between the RT and the electron gun are omitted in the figure. Adapted from Ref. [140].

5.6.1 Degrader

The degrader system consists of metal foils which decrease the energy of the incoming antiproton beam by scattering processes. Such degrader foils have been commonly used by the other experiments in the AD [141–143]. Typical catching efficiencies using such foils together with high voltage pulses are 0.1–3 %. In case of the single particle experiments of BASE, the catching efficiency is not of the utmost importance. The degrader system was rather designed to have a wide acceptance range of the incoming beam momentum as well as robustness against uncertainties of stopping power estimation. The variability is realized by the two most upstream layers of the degrader, marked as *meshes* in Fig. 5.17. Each mesh layer is a stack of three meshes, each of them having a thickness of 2.5 µm and rotated by 15° relative to each other. The grid structure of the mesh is in the interval of 15.6 µm with 44% of open area. The overlapped meshes form a pattern as shown in Fig. 5.18. Depending on the number of meshes which the beam penetrates, this structure gives a large variation in stopping power.

The second part of the degrader is a 25 µm stainless-steel foil, which also functions as a vacuum window which separates the UHV region inside the trap chamber from the insulation vacuum.

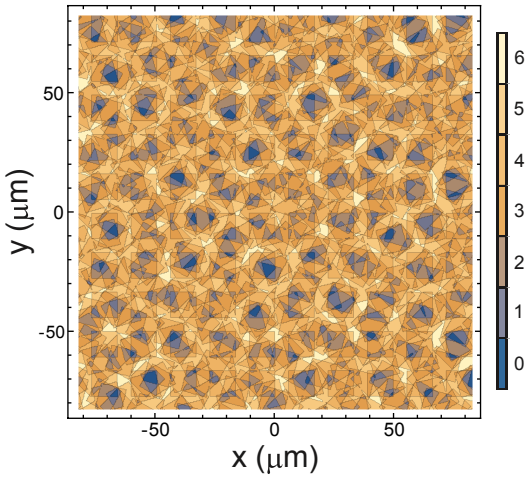

Figure 5.18: Pattern produced by overlapped six layers of copper meshes as part of the degrader system. The thickness of the layer at each position is indicated as the color density. It produces variation of thickness experienced by the beam at different positions. Adapted from Ref. [33].

The last degrader part is a 134 µm aluminum foil. The thickness of this foil was determined so that the system has enough stopping power as a whole.

The catching efficiency is estimated by simulations using SRIM, assuming that a fraction of antiprotons which are decelerated below 1 keV in the volume of the RT are captured. The estimated efficiency of this degrader structure is about 10^{-4}, which is consistent with measured data.

5.6.2 Electron gun

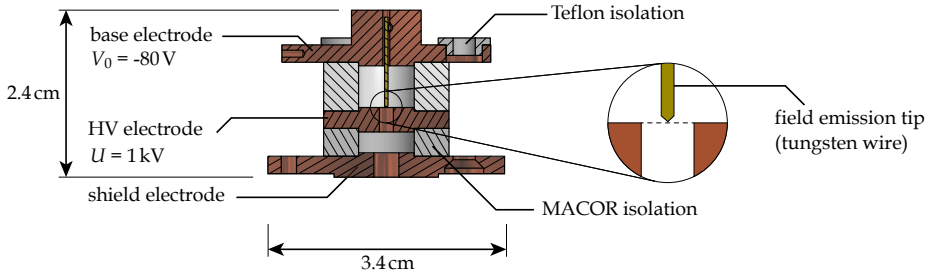

Figure 5.19: Schematic of the electron gun. Adapted from Ref. [92].

The electron gun located downstream of the traps is used to load electrons to the RT for sympathetic cooling of antiprotons and also to produce protons when the experiment is in a commissioning phase. The schematic is shown in Fig. 5.19. It makes use of field emission by the tunneling effect from a metal surface. Electrons are emitted from a custom-made field emission tip at the center, made of a 400 µm diameter tungsten wire. The tip is negatively biased through the base electrode, which defines the energy of the electrons in the metal. A high voltage is applied to the HV electrode, producing an electric field which pulls out the electrons from the metal surface by the tunneling. When the electron gun is operated, electronic currents on the aluminum foil of the degrader is read through

the electrode named *target electrode* (see Fig. 5.17). Typically, about 1.2 kV of high voltage at the acceleration electrode produces currents of ∼20 nA. On the order of 10^6 electrons are loaded in the trap before an antiproton injection.

5.6.3 High-voltage electronics

Antiprotons arriving to the RT are captured by an adequately-timed kV high-voltage pulse. When such a pulse is applied to the biasing line, the low-pass filters of the ms-total time constant limit the rise time of the pulse. Therefore, specialized electronic components are installed for these high-voltage lines.

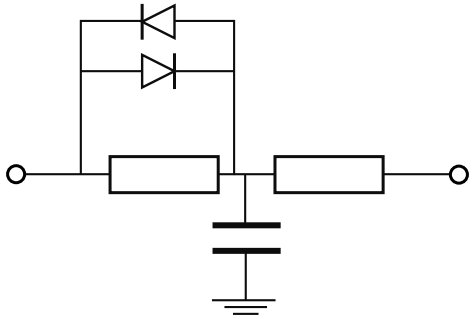

Figure 5.20: Example of the diode-bridge filter installed in the high-voltage lines.

A high voltage supply CAEN N1470 is utilized to provide high voltages up to 8 kV. To bypass a voltage pulse, diode-bridge filters are used to supply DC voltages to the high-voltage to the high-voltage electrodes and the pulsed electrode downstream to the ST.

An example of the diode-bridge filter circuit is shown in Fig. 5.20. Two oppositely directed silicon diodes are placed in parallel to the RC filter. The diode conducts a current when a voltage difference of $\gtrsim 0.7$ V is made across the component. When a constant voltage is applied, the diodes are closed and the signal passes through the low-pass filter like on the other DC lines. When a fast and large voltage pulse for catching is applied to the input, one of the diodes — depending on the polarity — opens, and the signal bypasses the filter. This type of filter allows application of voltage pulses with a rise time on the order of 10 ps.

CAEN N1470 is switched by a trigger signal synchronized to the ejection of the beam from the AD. A digital delay generator DG645 by Stanford Research System is used to add a delay time before sending a trigger to switch the high voltage. The delay time was optimized during the beam shifts so that the catching pulse is switched at the timing of arrival of the beam in the trap.

The signal from the delay generator is also used to trigger readout of a scintillator placed outside the superconducting magnet, close to the annihilation point. The scintillator is used to monitor annihilation of the antiprotons on the degrader and helped optimizing the steering parameters and delay time.

Part IV

BASE achievements 2014–2016

6

Recent results of BASE/CERN

This chapter presents recent experimental results of the BASE team at CERN, to which the author has contributed.

In the timeline of Fig. 6.1, an overview of experimental activities from 2014 to 2016 is given. The major milestones were the high-precision proton-to-antiproton charge-to-mass ratio comparison [54] and the two high-precision magnetic moment measurements of the antiproton [52, 70]. The data collection of the charge-to-mass ratio comparison took place at the end of run 2014. The 2015/2016 run was one continuous run where two magnetic moment measurements were performed. Throughout the year 2016, the experiment was operated with antiprotons stored in the RT. The storage of antiprotons also allowed us to set an improved lower limit on the directly-measured lifetime of the antiproton[76].

These measurements are summarized in the following sections.

Among them, the proton-to-antiproton charge-to-mass ratio comparison in 2014 is reviewed in detail in Chapter 7, since an improvement from this measurement is the main topic of this thesis.

6.1 High-precision comparison of proton-to-antiproton charge-to-mass ratio

This measurement was performed in the first beam-time of BASE in 2014. The final result we obtained was

$$\left|\frac{(q/m)_{\bar{p}}}{(q/m)_p}\right| - 1 = 1\,(64)(26) \times 10^{-12} \quad (68\%\,\text{C.L.}) \tag{6.1}$$

which is in agreement with CPT symmetry. This was done by alternate cyclotron frequency measurements of an antiproton and an H^- ion. The details of this measurement will be discussed in Chapter 7.

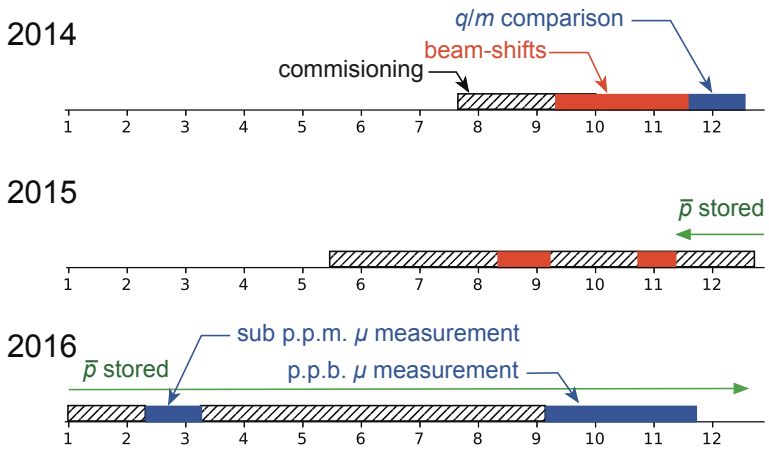

Figure 6.1: Timeline of experimental activities of the BASE team at CERN from 2014 to 2016. The unit of the horizontal axis is month. The hatched bars indicate periods where the apparatus was cooled down and commissioned/developed. The red bars indicate periods when we received antiproton beams from the AD. The blue bars indicate data-collection periods of the measurements.

6.2 Antiproton magnetic moment measurement at sub-p.p.m. precision

In 2015, the experiment was commissioned for magnetic moment measurement of the antiproton. After optimization of conditions of the system [80], a situation was realized where the axial frequency stability in the Analysis Trap was sufficiently low to observe spin transitions of an antiproton with the statistical method [71] explained in Section 3.3.2. In this condition, we performed the first antiproton magnetic moment measurement. The setup of the apparatus is shown in Fig. 6.2. The measurement was performed in the AT in a presence of a magnetic inhomogeneity $B_2 \approx 2.88 \times 10^5\,\mathrm{T/m^2}$. The trap downstream of the AT, labeled as a Co-magnetometer Trap in the figure, was used to monitor the magnetic field by continuous cyclotron frequency measurements. Detailed understanding of a broadening of the resonance line shape enabled us to determine the antiproton g-factor with fractional precisions of 5–10×10^{-6} (Fig. 6.3). From a weighted average of six measurements, the final result was obtained to be [70]

$$\frac{g_{\bar{p}}}{2} = 2.792\,846\,5\,(23) \quad (95\%\,\mathrm{C.L.}). \tag{6.2}$$

This corresponds to a relative uncertainty of 8×10^{-7} at 95% C.L.. This improved the fractional precision of the previous best measurement by the ATRAP collaboration [31] by a factor of 6. This measurement and the developments required are the main topic of Hiroki Nagahama's Ph.D. thesis [80], where its details are discussed.

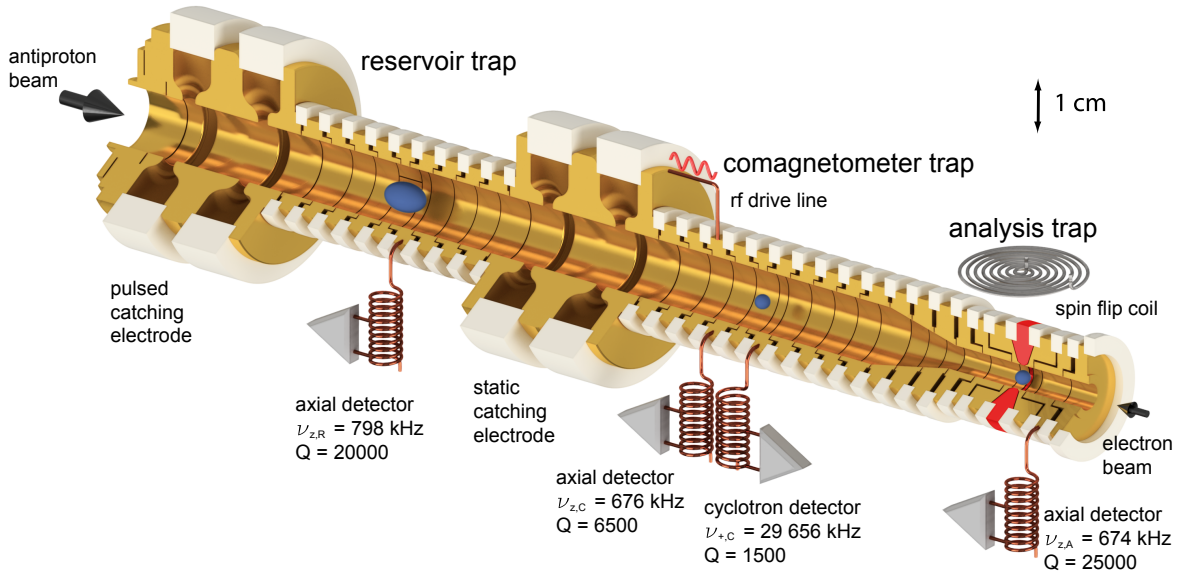

Figure 6.2: Setup used for the magnetic moment measurement at sub-parts per million relative precision. The spin-resonance experiment of a single antiproton was performed in the Analysis trap (AT). The disc coil installed beside the trap was used to apply RF drives. Another single antiproton was trapped in a downstream trap called Comagnetometer trap (CT) to monitor the magnetic field during the measurements by continual measurement of the cyclotron frequency. Adapted from Ref. [70].

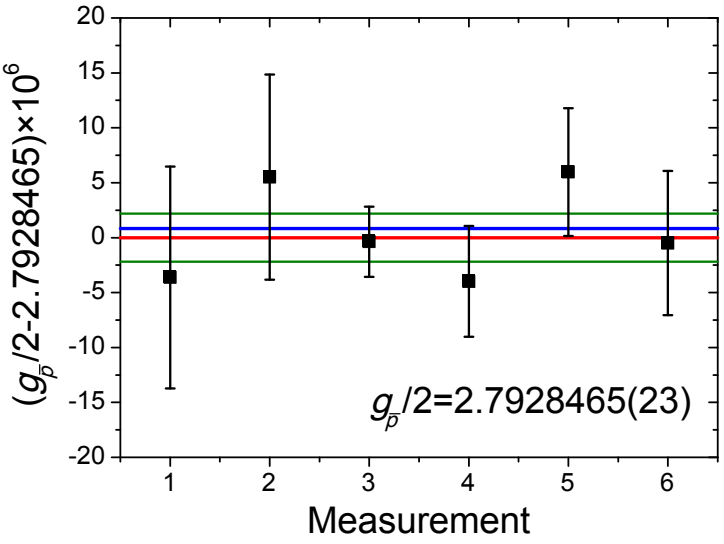

Figure 6.3: Results of the six g-factor measurements by the statistical method. The final result was obtained by their weighed average to be $g_{\bar{p}}/2 = 2.792\,846\,5(23)$. The red and green lines show the final g-factor value and its final uncertainty, respectively. The blue line represents the proton g-factor From Ref. [72], which agrees to the antiproton result within the uncertainty.

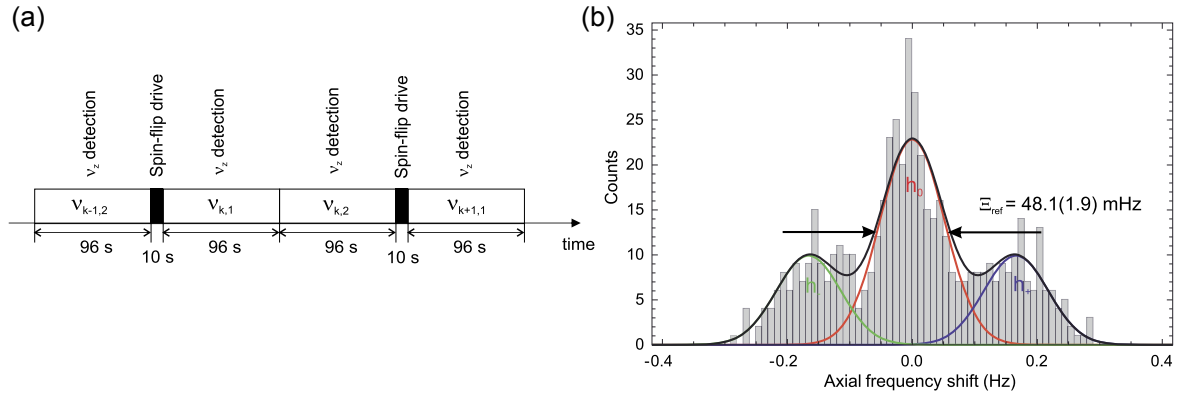

Figure 6.4: **(a)** Sequence to observe spin transitions of an antiproton in the AT. Each cycle consists of two axial frequency measurements $\nu_{k,1}$ and $\nu_{k,2}$. A spin-flip drive at the Larmor frequency of the antiproton in the AT is applied before $\nu_{k,1}$ while no drive is applied before $\nu_{k,2}$. **(b)** Distribution of the axial frequency shifts $\Delta_k = \nu_{k,1} - \nu_{k-1,2}$ obtained by 543 cycles of the sequence (a). The distribution is a superposition of three Gaussian distributions corresponding to spin-down transitions, spin-up transitions, and no transitions. The three Gaussian distributions estimated by a maximum likelihood method is shown with colored curves in green, blue and red. The black curve shows the superposition of the three.

6.3 Observation of single spin transitions of a single antiproton

The next goal after the measurement described in the last section was the application of the double-trap technique. For this purpose, the background axial frequency fluctuation in the AT had to be low enough to distinguish individual spin transitions with high fidelity. Further optimizations following the measurement in the last section allowed us to attain such a condition, which were the most stable conditions ever achieved with a single particle in a Penning trap [144]. To observe single antiproton spin transitions, the measurement sequence as shown in Fig. 6.4 (a) was carried out. Each cycle consists of two axial frequency measurements in the AT: one with a spin-flip drive before the measurement ($\nu_{k,1}$) and one without a drive ($\nu_{k,1}$). The drive frequency was set to the Larmor frequency in the AT. The axial frequency shifts $\nu_{k,2} - \nu_{k,1}$ characterize the background axial frequency fluctuation Ξ_{ref}, and the shifts $\nu_{k,1} - \nu_{k-1,2}$ are used to analyze the occurrence of spin transitions. Distribution of the frequency shift Δ_k defined by $\Delta_k = \nu_{k,1} - \nu_{k-1,2}$ was obtained by 543 cycles of measurements as Fig. 6.4 (b). The probability distribution function (PDF) of Δ_k is a superposition of three Gaussian distributions $h_0(\Delta; 0, \Xi_{\mathrm{ref}}), h_-(\Delta; -\Delta_\nu \mathrm{SF}, \Xi_{\mathrm{ref}})$ and $h_+(\Delta; +\Delta\nu_{\mathrm{SF}}, \Xi_{\mathrm{ref}})$, each describing events with no spin transition, downward $(-1/2 \to 1/2)$ spin transitions, and upward $(1/2 \to -1/2)$ spin transitions. P_{SF} corresponds to the spin-flip probability, and $\Delta\nu_{\mathrm{SF}}$ to the axial frequency shift caused by a spin transition. A Maximum-Likelihood analysis of the measured distribution yielded $\Xi_{\mathrm{ref}} = 48.1\,(1.9)\mathrm{mHz}, P_{\mathrm{SF}} = 47.3\,(2.3)\%$ and $\Delta\nu_{z,\mathrm{SF}} = 166(4)\,\mathrm{mHz}$.

In Fig. 6.5 (a), evolution of the axial frequency during a part of the measurement sequence is shown.

The gray arrows and dashed lines indicate the times of the resonant spin-flip drives between $\nu_{k-1,2}$ and $\nu_{k,1}$. The corresponding axial frequency shifts are shown in Fig. 6.5 (b). To identify individual spin transition, we define a threshold Δ_{TH}. For each frequency shift $\Delta_k = \nu_{k,1} - \nu_{k-1,2}$, we assigned an event as

- $\Delta_k > \Delta_{\mathrm{TH}}$: Transition to spin up
- $-\Delta_{\mathrm{TH}} < \Delta_k < \Delta_{\mathrm{TH}}$: No spin transition
- $\Delta_k < -\Delta_{\mathrm{TH}}$: Transition to spin down.

The probability of each assignment is evaluated by a recursive relation of $P(\uparrow_n | \{\Delta_k\}_{k=1}^{n})$ and $P(\uparrow_{n-1} | \{\Delta_k\}_{k=1}^{n-1})$ based on the PDFs $h_0(\Delta), h_-(\Delta), h_+(\Delta)$ and a chosen threshold Δ_{TH}. The probability assigned to each trial is shown in Fig. 6.4 (c). Δ_{TH} can be optimized so that the mean error rate of the assignment is minimized. For $\Delta_{\mathrm{TH,opt}} = 94\,\mathrm{mHz}$, the mean error rate was at 5.8%. A threshold higher than Δ_{TH} can be used for initialization of the spin state. The error rate of the initialization E_i is defined by conditional probabilities as

$$E_i = \frac{P(\Delta > \Delta_{\mathrm{TH}} \cap \downarrow_n) + P(\Delta < -\Delta_{\mathrm{TH}} \cap \uparrow_n)}{P(|\Delta| > \Delta_{\mathrm{TH}})}. \tag{6.3}$$

$\Delta_{\mathrm{ST},0.1\%}$ in Fig. 6.5 (c) corresponds to 190 mHz, for which the initialization fidelity is $1 - E_i > 99.9\%$.

When a sequence as in Fig. 6.4 (a) is utilized as a part of the double-trap measurement sequence (see Section 3.3.2), it is first executed with a threshold $\Delta_{\mathrm{ST},0.1\%}$ for spin-state initialization, then after irradiation of a spin-flip drive in the PT, the particle is transported back to the AT, and the observation sequence is repeated n times at a threshold Δ_f until a shift $|\Delta_k| > \Delta_f$ is observed. For a threshold optimized for such procedure, the fidelity of spin-state determination was estimated to be 92.1%.

This was the major step for application of the multi Penning trap technique to measure the antiproton magnetic moment.

6.4 Antiproton magnetic moment measurement at p.p.b. precision

The high-fidelity spin-state determination discussed in the last section was possible only when the energy of the modified cyclotron mode satisfied $E_+/k_{\mathrm{B}} < 200\,\mathrm{mK}$. However, the effective temperature of the cyclotron detection system at the time was $T_+ = 12.8(8)\,\mathrm{K}$ [52]. The high temperature was caused by electromagnetic interference with electric noise in the AD facility. Preparing a sub-thermal state of E_+ of an antiproton by resistive cooling by this detection system was extremely time consuming and took on average about 10 h per cooling attempt. Especially, cyclotron frequency measurement by

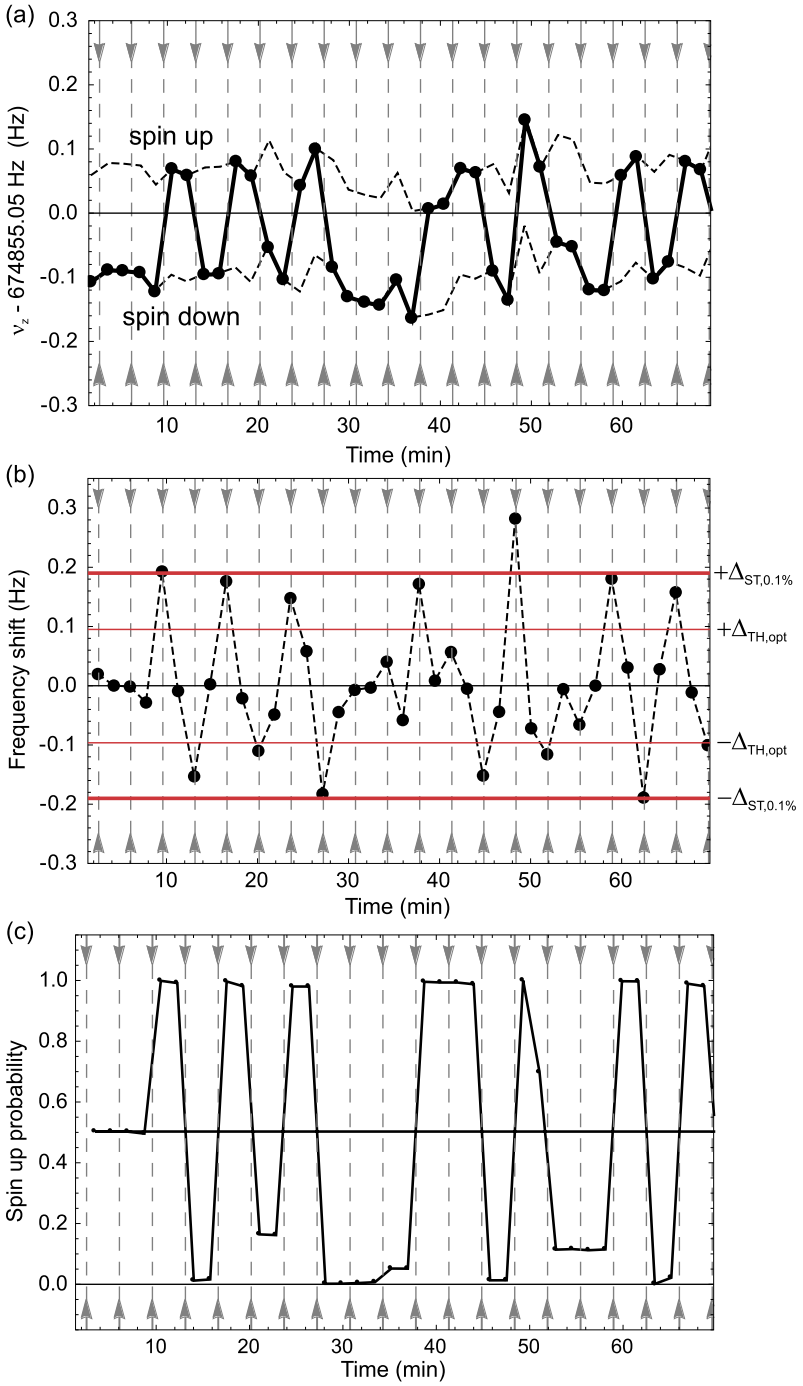

Figure 6.5: Observation of single spin-transitions with antiprotons. **(a)** Measured axial frequencies are indicated by the points connected with the solid lines. The dashed-line allow the comparison of the measured frequency to the one which the particle would have in the opposite spin state. The gray arrows and dashed lines indicate the times of resonant spin-flip drives at the Larmor frequency in the AT.**(b)** Evolution of axial frequency shifts are shown with $\Delta_{\mathrm{TH,opt}}$ and $\Delta_{\mathrm{ST,0.1\%}}$, the optimum threshold and the threshold for 99.1% fidelity, respectively. (c) The propagation of the probability to be in spin state up using conditional probabilities (solid line) is shown. Adapted from Ref. [144].

the sideband method, which is needed as part of the double-trap measurement sequence, inevitably heats the modified-cyclotron mode to $E_+ \approx \nu_+/\nu_z \cdot T_z \approx 350\,\mathrm{K}/k_\mathrm{B}$ (Section 2.5).

To overcome this difficulty, we invented a new multi-trap scheme using two particles. The setup is shown in Fig. 6.6 (a). The downstream antiproton (shown in the AT in the figure) was named the Larmor particle, and the upstream antiproton (in the PT in the figure) the Cyclotron particle. Measuring the cyclotron- and the Larmor frequencies by the two different particles greatly reduced preparation time of the measurement. Before the measurement started, an energy state of $E_{+,\mathrm{L}}$ (hereafter, the subscripts "L" and "C" are used to refer to the Larmor- and the Cyclotron particles, respectively) as low as $E_{+,\mathrm{L}}/k_\mathrm{B} < 50\,\mathrm{mK}$ was prepared by the resistive cooling. Afterward, the following measurement sequence was performed (see also Fig. 6.6):

1. Spin-state initialization: the Larmor particle was transported to the AT, there the spin-initialization sequence as described in the last section was executed. When the spin state was identified by an axial frequency shift $|\Delta_k| > \Delta_{\mathrm{ST},0.1\%} = 190\,\mathrm{mHz}$, the initial spin state of the Larmor particle of the cycle was recorded and the initialization sequence ended.

2. Cyclotron frequency measurements: the Cyclotron particle was transported to the PT. Its cyclotron frequency $\nu_{\mathrm{c},i}$ (here i denotes the cycle number) was measured three times by the sideband coupling method.

3. Irradiation of the Larmor drive: The Cyclotron particle was transported to the park electrode located upstream of the PT (see Fig. 6.6 (a)), then the Larmor particle was transported to the PT. An RF drive at frequency $\nu_{\mathrm{rf},i}$ was irradiated on the Larmor particle for 8 s.

4. Cyclotron frequency measurements: The Larmor particle was transported back to the AT. The Cyclotron particle was transported back to the PT, and the cyclotron frequency was measured by additional three measurements. The cyclotron frequency in the PT at step 3 was estimated from the results of in total six cyclotron frequency measurements per cycle in the data analysis.

5. Identification of the final spin state: Finally the final spin state of the Larmor particle was identified by the spin-state observation sequence with a threshold Δ_f.

The cycle was repeated to obtain the spin-flip probability for a constant $\Gamma = \nu_{\mathrm{rf},i}/\nu_{\mathrm{c},i}$. One cycle took typically 890 s, including time for the transports of the particles. It was crucial for the measurement that the modified-cyclotron energy of the Larmor particle $E_{+,\mathrm{L}}$ was kept low. The heating rate of the modified-cyclotron mode of the Larmor particle remained below 22 mK per cycle over the entire measurement campaign, which enabled execution of about 75 measurement cycles before $E_{+,\mathrm{L}}/k_\mathrm{B}$ exceeded 200 mK and required re-cooling. The spin-state identification fidelity ranged between 80% and 90%, depending on $E_{+,\mathrm{L}}$.

The resonance obtained after repeating the cycle above for different Γ is shown in Fig. 6.6 (c). The resonance $P_\mathrm{SF}(\Gamma, g, \Omega_\mathrm{R})$, with Ω_R being the Rabi frequency, is a convolution of a Rabi resonance

and a g-factor line shape determined by $\gamma_z/\Delta\omega$, where γ_z is the damping factor of the PT axial detection system and $\Delta\omega$ a line-width defined by a magnitude of a residual magnetic bottle B_2 in the PT [145]. From a two-dimensional maximum likelihood estimate using the line shape function $P_{\mathrm{SF}}(\Gamma, g, \Omega_{\mathrm{R}})$ with $g_{\bar{p}}$ and Ω_{R} as free parameters, the g-factor of the antiproton was obtained to be $g_{\bar{p}}/2 = 2.792\,847\,345\,3\,(30)_{\mathrm{stat}}$ at 68% C.L. interval. The resonance has a broaden peak due to saturation of the drive, and a small asymmetry due to the magnetic bottle, which are also accounted by the fit model. The log-Likelihood function is shown in a density plot in Fig. 6.6 (d). The curve determined by the estimated set of $(g_{\bar{p}}, \Omega_{\mathrm{R}})$ is shown by the red line in Fig. 6.6 (c), the gray area of the plot indicates the error band at 68% C.L.. For further details of the data analysis, see the method section of the original paper [52].

After the systematic corrections, the results became

$$\frac{g_{\bar{p}}}{2} = 2.792\,847\,3441\,(30)(28) \quad (68\%\,\mathrm{C.L.}). \tag{6.4}$$

Among the systematic effects, the most dominant cause of the uncertainty arose from the possibility that the two particles had different mode energies $E_{+,\mathrm{L}} \neq E_{+,\mathrm{C}}$ and $E_{z,,L} \neq E_{z,\mathrm{C}}$. This was accounted by $(\delta g_{\bar{p}}/2)_{\mathrm{drive}} = 2.7 \times 10^{-9}$. With the statistical and systematic uncertainties combined, the final result was obtained to be

$$\frac{g_{\bar{p}}}{2} = 2.792\,847\,3441\,(42) \quad (68\%\,\mathrm{C.L.}). \tag{6.5}$$

This corresponds to a relative uncertainty of 1.5×10^{-9}. The respective statistical and systemic uncertainty evaluations at 95% C.L. gave a relative uncertainty of $\delta g_{\bar{p}}/g_{\bar{p}} = 2.6 \times 10^{-9}$.

This is in agreement with the most recent proton result by the Mainz group of the BASE collaboration [53]

$$\frac{g_p}{2} = 2.792\,847\,344\,62(82) \quad (68\%\,\mathrm{C.L.}), \tag{6.6}$$

thus is consistent with CPT symmetry. These two recent measurements constitute an improvement by a factor of 350 compared to previous BASE measurements [70, 72], and by a factor of > 3000 compared to the results by the ATRAP collaboration [31, 127].

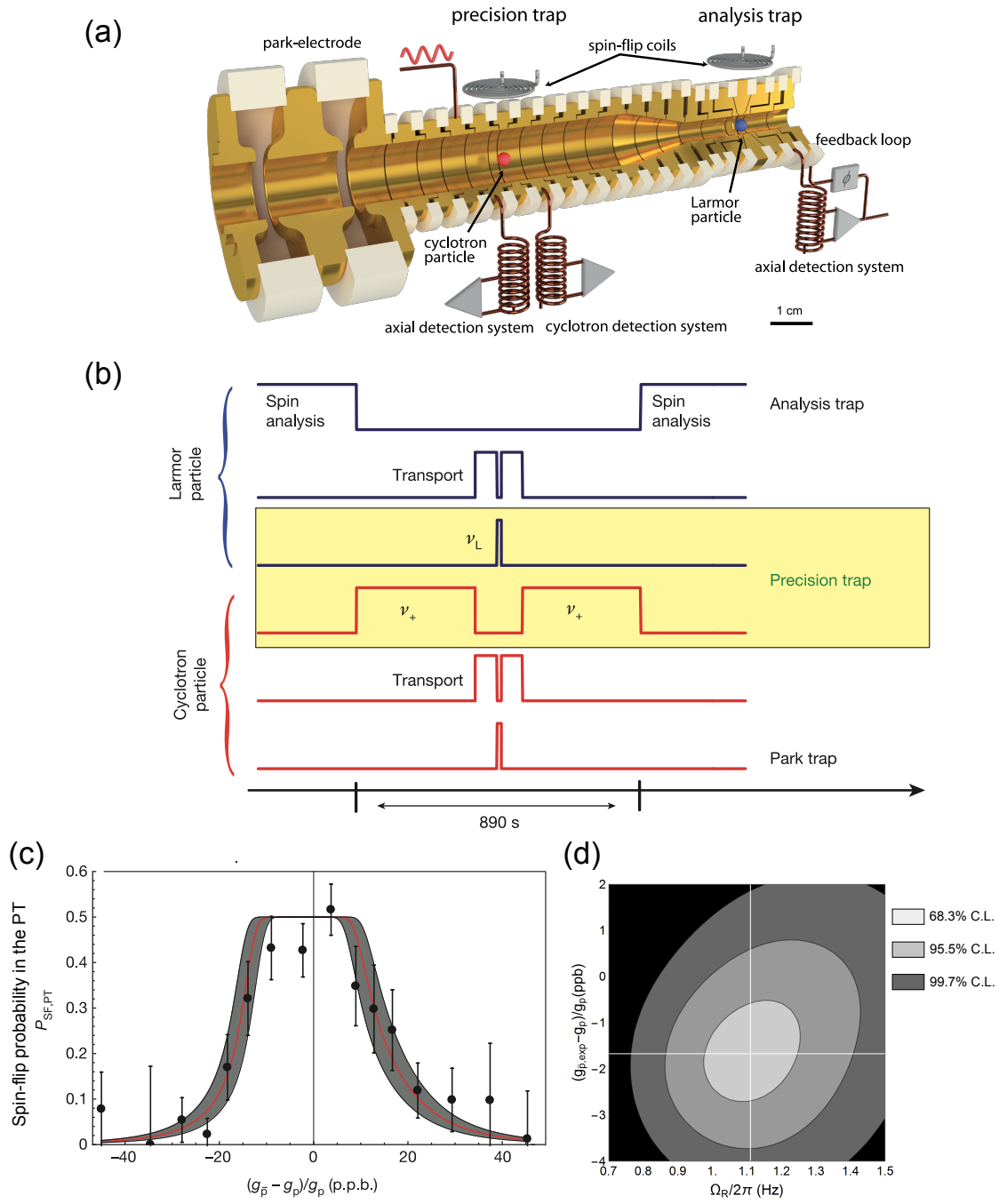

Figure 6.6: **(a)** Setup used for the magnetic moment measurement using two antiprotons. **(b)** Experimental procedure. See the text for the details. **(c)** Spin-flip probability of the Larmor particle in the PT $P_{\mathrm{SF,PT}}$ is obtained as a function of the frequency ratio $\nu_{\mathrm{rf}}/\nu_{\mathrm{c}}$. The red line is corresponds to $g_{\bar{p}}$ and Ω_{R} estimated by the maximum likelihood and the gray area indicates the 68% C.L. error band. The evaluation was performed with 10008 data points of ν_{rf} and ν_{c} evaluated for each ν_{rf} from associated cyclotron frequency measurements. The data points plotted by dots with error bars are binned averages of the measured $P_{\mathrm{SF,PT}}$ with error bars corresponding to 1 s.d.. g_p used as the offset of the horizontal axis is $g_p/2 = 2.792\,847\,350(9)$, the latest proton g-factor [72] at the time of this measurement. **(d)** Log-likelihood as a two-dimensional function of $g_{\bar{p}}$ and Ω_{R}. The white cross marks the point with the maximum likelihood. The colored areas indicate confidence intervals at 68.3%, 95.5%, 99.7%, as indicated on the right. The figures are adapted from Ref. [52].

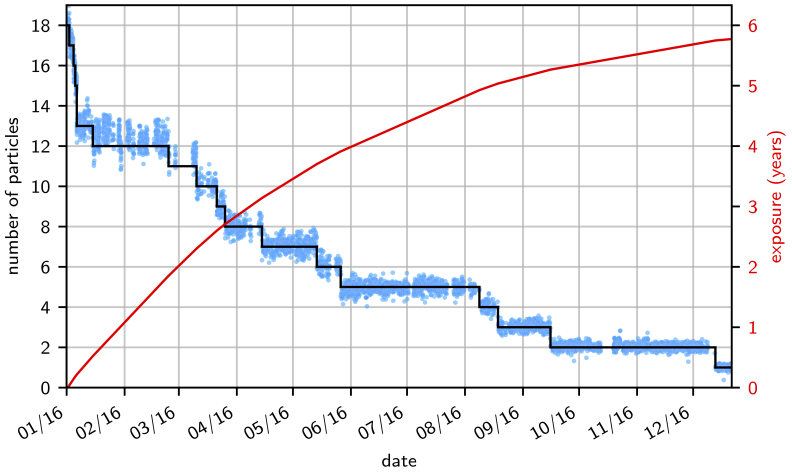

Figure 6.7: History of the number of antiprotons trapped in the RT during the year 2016 is shown by the blue dots (left axis). The equivalent single-particle exposure time calculated by the integral of the particle number is shown by the red curve (right axis). Adapted from Ref. [76].

6.5 Improvement of the directly-measured lifetime of the antiproton

The charge-to-mass ratio comparison and the magnetic moment measurements discussed in the last sections were performed with antiprotons stored in the RT, which were extracted to the measurement traps upon necessity. Such storage in the RT enabled developments and data collection during a shutdown period of the AD. In fact, the experiment in the entire year 2016 was operated with antiprotons trapped on the 21st of November 2015, resulting in the total storage time of 405 days. From the storage record of the reservoir, we set an lower limit of the directly measured lifetime of the antiproton.

In Fig. 6.7, the number of antiprotons recorded over the year 2016 is shown. The number of the particle was estimated from the dip-width of dip spectrum of the RT axial detection system. The RT content in January 2016 was 18 antiprotons. The antiprotons were consumed by the experiment until the content reached a single antiproton in December 2016. All the losses were identified either by experimental operations to extract the antiprotons to the downstream traps, or human/software failures, and we have not observed any antiproton decay or annihilation due to residual gas.

From this data, an integrate of $N(t)\mathrm{d}t$ was evaluated to calculate the equivalent single particle exposure time. This is shown in Fig. 6.7 by the red curve whose axis is on the right. The total exposure time from this data set was 5.77 a (a $\equiv 31.5576 \times 10^6$ s $= 365.25$ d). In addition, the exposure time from records of the other traps, records during 2015 run prior to the 1st of January 2016, and records from the 2014 run [146] were considered to obtain the total integrated exposure time equivalent to a single antiproton of $T_{\mathrm{exp}} = 11.66$ a.

Since this is equivalent to observe no decay of a single antiproton for 11.66 a of observation time, the lower lifetime limit τ_{lower} was evaluated as follows. We assume a possible decay to occur according to the Poisson statistics $f(n;\lambda) = \lambda^n \exp(-\lambda)/n!$ with $\lambda = T_{\text{exp}}/\tau$, τ the lifetime. As we observe $n_0 = 0$ events, this sets a lower limit of the lifetime τ_{lower} for a confidence level CL by

$$\begin{aligned} \text{CL} = 1 - \epsilon &= \sum_{n=n_0+1}^{\infty} f\left(n; \frac{T_{\text{exp}}}{\tau_{\text{lower}}}\right) \\ \implies \epsilon &= \sum_{n=0}^{n_0} f\left(n; \frac{T_{\text{exp}}}{\tau_{\text{lower}}}\right). \end{aligned} \tag{6.7}$$

By this method, the lower limit of the lifetime corresponds to $T_{\text{exp}} = 11.66\,\text{a}$ was evaluated to be $\tau_{\bar{p},\text{lower}} = 10.2\,\text{a}$ for 68% C.L. and $\tau_{\bar{p},\text{lower}} = 5.0\,\text{a}$ for 90% C.L.. This value improved the previous best limit set by the TRAP collaboration [147] by about a factor of 30[1].

The lifetime limit also gives an upper limit of the pressure in the cryo-pumped trap chamber. Considering the cross-sections of capture processes of antiprotons by residual gas:

$$\bar{p} + \text{H} \rightarrow p\bar{p} + e^- \tag{6.8}$$

$$\bar{p} + \text{He} \rightarrow \bar{p}\text{He}^+ + e^-, \tag{6.9}$$

which have been studied theoretically [148–150], the upper limit of the partial pressures were estimated to be $p_{\text{H}} < 1.2 \times 10^{-18}\,\text{mbar}$ and $p_{\text{He}} < 2.7 \times 10^{-18}\,\text{mbar}$.

[1] In 2015 we reported storage of antiprotons in the 2014 run resulting in equivalent to a single particle exposure of $T_{\text{exp},2014} = 1.56\,\text{a}$ in Ref. [146], which was included in the total exposure time $T_{\text{exp}} = 11.66\,\text{a}$ used in this analysis. Compared to this value, the result above was an improvement by a factor of 7 as quoted in the original publication [76].

7

Review of the 2014 charge-to-mass ratio comparison

This chapter reviews the proton-to-antiproton charge-to-mass comparison performed in the 2014 beam-time [54].

7.1 Measurement procedure

The setup is shown in Fig. 7.1. The antiproton beams from the AD were provided from the left hand side of the figure. The two traps were used for the experimental; the upstream measurement trap and the downstream trap used as a reservoir. The two electrodes adjacent to the measurement trap were called park electrodes. The magnetic field in the measurement trap was $B \approx 1.946\,\mathrm{T}$ and the eigenfrequencies of an antiproton were

$$\nu_{+,\bar{p}} \approx 29.656\,\mathrm{MHz}, \quad \nu_{z,\bar{p}} \approx 645.262\,\mathrm{kHz}, \quad \nu_{-,\bar{p}} \approx 7.02\,\mathrm{kHz}. \tag{7.1}$$

As discussed in Section 3.2, the advantageous way to perform proton-to-antiproton charge-to-mass ratio comparison is to compare the cyclotron frequencies of an antiproton and an H^- ion. Using the equipment installed in the system (Section 5.6), antiprotons provided by the AD were captured, cooled and cleaned from contaminant particles (see Chapter 13 for the details) to finally prepare a cloud containing only antiprotons and H^- ions. Here the H^- ions were produced by the collision of the beam on the degrader foil. From this reservoir of the particles, a single antiproton and a single H^- ion were extracted (Section 13.3) and stored in the measurement trap and one of the park electrodes as shown in Fig. 7.1.

For the prepared antiproton and the H^- ion, we performed cyclotron frequency comparisons.

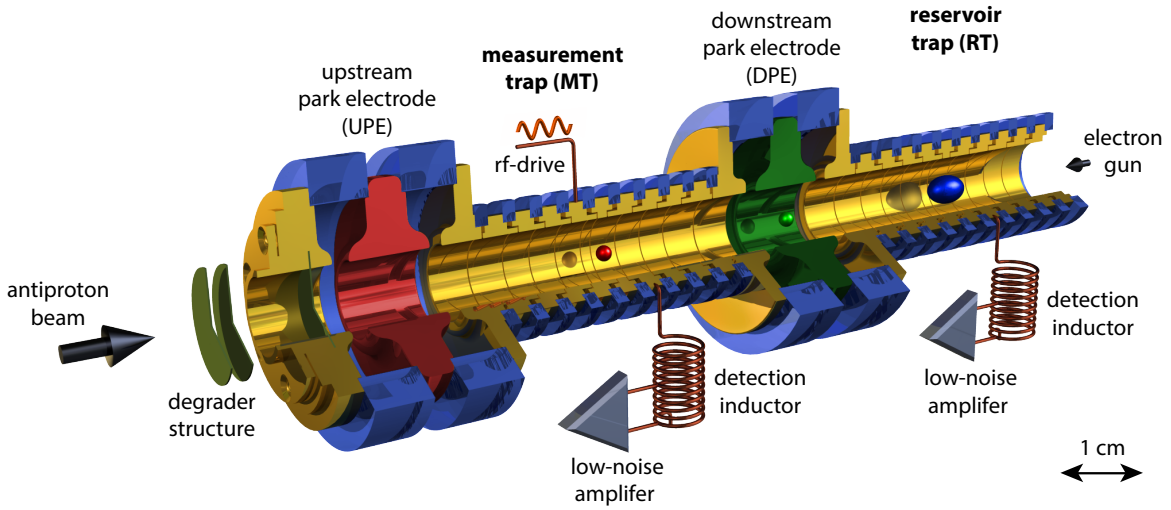

Figure 7.1: Experimental setup of the 2014 proton-to-antiproton charge-to-mass ratio comparison. Adapted from Ref. [54].

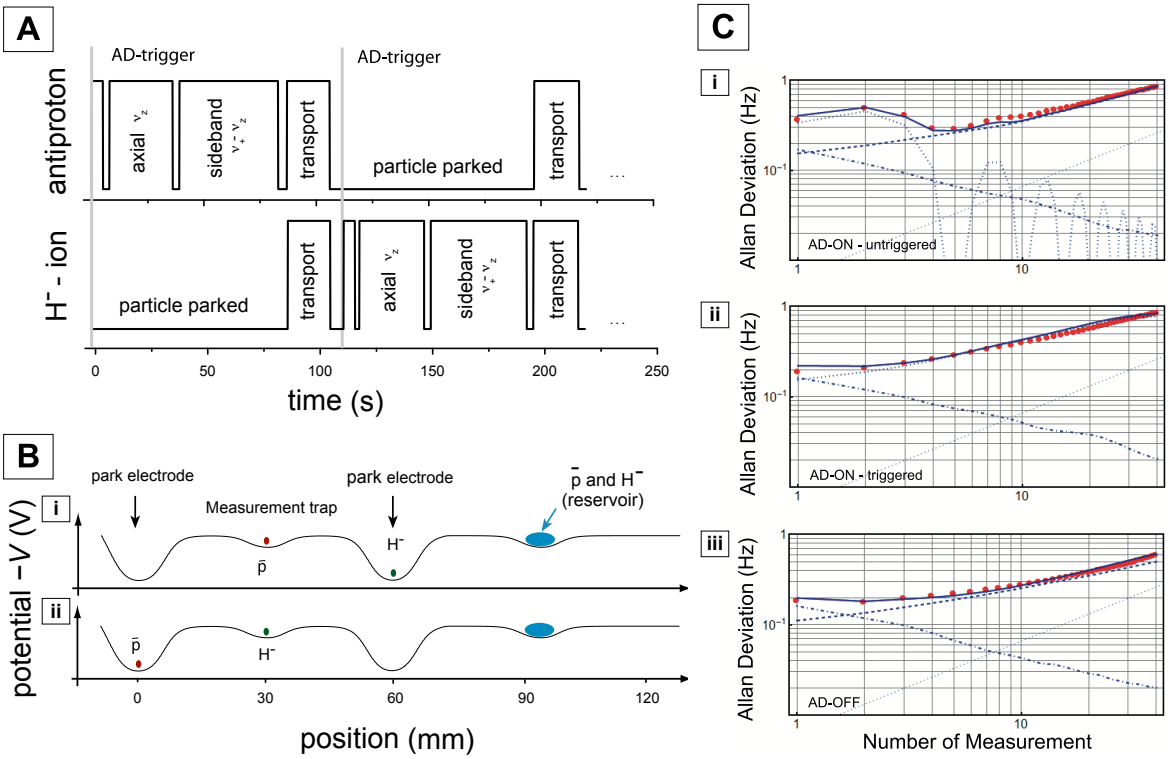

Figure 7.2: **(A)** Measurement sequence of the 2014 charge-to-mass ratio comparison. The cyclotron frequencies of an antiproton and an H^- ion were measured alternately by the sideband coupling method. Each cycle was started by a trigger signal from the AD synchronized to the beginning of the declaration cycle, and consisted of acquisition of an axial frequency spectrum, a sideband spectrum, and a rapid adiabatic transport to swap the positions of the particles. **(B)** On-axis potential configurations used for the sequence in (A). While one of the particles was being measured, the otter was stored in one of the park electrodes adjacent to the measurement trap. **(C)** Allan deviation of the cyclotron frequency of an antiproton in the measurement trap sampled under different conditions: (i) the AD was operational and the measurement cycle ran independently from the AD, (ii) the AD was operational and the measurement cycle was synchronized to the AD (iii) the AD was shut down. Figures (A,B) are adapted from Ref. [54], (C) is from Ref. [77].

The measurement sequence is shown in Fig. 7.2 (A), which alternately measured the cyclotron frequency of the two particles by the sideband coupling method, namely by acquisition of axial single-dip and sideband double-dip spectra. The magnetron frequency was obtained by an approximation Eq. (2.41)

$$\nu_{-,i} \approx \frac{\nu_{z,i}^2}{2\nu_{+,i}} \tag{7.2}$$

to obtain the cyclotron frequency by the invariance theorem Eq. (2.40)

$$\nu_{c,i}^2 = \nu_{+,i}^2 + \nu_{z,i}^2 + \nu_{-,i}^2. \tag{7.3}$$

for each cycle i. While one of them is being measured, the other was kept in one of the park electrodes. The potential configurations are displayed in Fig. 7.2 (B) for the antiproton measurements (Fig. 7.2 (B)(i)) and the H^- measurements ((B)(ii)). To switch between the two configurations, the particles were transported by sequential ramps of potentials applied on the electrodes. This shuttling method was adiabatic, that is not to heat the particles on an observable level, and fast. One set of transports was executed within 15 s. This rapid exchange realized a data sampling rate which was about 50 times higher than the previous measurement by the TRAP collaboration [114].

During a part of the data taking period, the AD was operational and effects of the magnetic field fluctuations generated by its ring to the cyclotron frequency measurement were observed. They are characterized in Fig. 7.2 (C), where the Allan deviations of the cyclotron frequencies recorded in different conditions are compared [77]. As the AD is operated, ramps of the bending magnets in the ring produce a periodic magnetic field fluctuations typically with horizontal amplitude of 100-500 nT, and in a period of 120 s (for a detailed characterization, see Section 11.3). These periodic fluctuations were experienced by the particles with a suppression of about a factor of 10 by shielding of a superconducting magnet used in 2014 beam-time. When the measurement cycle ran independently from the AD, the Allan deviation of the cyclotron frequency shows an oscillatory component caused by a beat between the AD cycle and the measurement cycle which had a period of about 21 min (Fig. 7.2 (C)(i)). To suppress the beat, we synchronized the measurement cycle to the AD operation, for his purpose, each measurement was started by a trigger signal timed at an injection of antiproton beams to the AD ring (Fig. 7.2 (A)). The oscillatory component in the cyclotron frequency Allan deviation was removed and a white noise component of $160\,\mathrm{mHz}\cdot(\mathrm{cycle})^{1/2}$ ($or 10\,\mathrm{nT}\cdot(\mathrm{cycle})^{1/2}$) and a random walk component of $220\,\mathrm{mHz}\cdot(\mathrm{cycle})^{-1/2}$ ($14\,\mathrm{nT}\cdot(\mathrm{cycle})^{-1/2}$) remained (Fig. 7.2 (C)(ii)). In a dataset sampled when the AD was shut down (Fig. 7.2 (C)(iii)), the random-walk component reduced to $160\,\mathrm{mHz}\cdot(\mathrm{cycle})^{-1/2}$ ($10\,\mathrm{nT}\cdot(\mathrm{cycle})^{-1/2}$), while the white noise component remained same. Therefore a part of the random walk component was attributed to the cycle-by-cycle magnetic field fluctuations produced by the AD operation.

7.2 Data analysis

Over a period of 35 days, we sampled 6521 sets of $\bar{p}$-H^- cyclotron frequency ratios. In Fig. 7.3 (A), the sampled cyclotron-frequency ratio $R_{\bar{p}\mathrm{H}^-}$ is shown as a function of time. The offset R_{th} is the theoreticl value (Eq. (3.24))

$$R_{\bar{p}\mathrm{H}^-\mathrm{th}} = \chi_{\bar{p}\mathrm{H}^-} = 1.001\,089\,218\,754(2). \tag{7.4}$$

To account for a magnetic field drift between the measurements, i th data point of the ratio $R_{\bar{p}\mathrm{H}^-}$ was obtained from ν_{c,H^-} and $\overline{\nu_{c,\bar{p},i,i+1}}$ defined as

$$\overline{\nu_{c,\bar{p},i,i+1}} = \nu_{c,\bar{p},i} + \frac{\nu_{c,\bar{p},i+1} - \nu_{c,\bar{p},i}}{t_{\bar{p},i+1} - t_{\bar{p},i}} \cdot (t_{\mathrm{H}^-,i} - t_{\bar{p},i}) \tag{7.5}$$

where $t_{\bar{p},i}$ and $t_{\mathrm{H}^-,i}$ express the times of the i th measurements of the antiproton and the H^- ion, respectively. The evaluation with the reciprocal data processing was also made to check the consistency.

The obtained ratios are projected to a histogram in Fig. 7.3 (B). From the obtained data, the center of the ratio distribution was estimated by a d a Maximum-Likelihood fit, assuming a Gaussian distribution and taking into account the correlations between the data points. The obtained result was

$$R_{\bar{p}\mathrm{H}^-,\mathrm{exp}} = 1.001\,089\,218\,872(64) \quad (68\%\ \mathrm{C.L.}). \tag{7.6}$$

The obtained width of the distribution was 5.5×10^{-9}. Several checks were performed on the statistical characteristics of whiteness of the data. First, the power spectrum density (PSD) of the sampled ratios $R_{\bar{p}\mathrm{H}^-}$ was evaluated. As seen in Fig. 7.3 (C) the PSD was constant against frequency. Secondly the Allan deviation of the ratio $\sigma_{\mathrm{A}}(R_{\bar{p}\mathrm{H}^-}, \tau)$ was evaluated. The result is shown in Fig. 7.3 (D) in a double-log scale. The red line shows a linear fit which had a slope α of $\alpha = -0.501(2)$. The scaling

$$\sigma_{\mathrm{A}}(R_{\bar{p}\mathrm{H}^-}, \tau) \propto \tau^{\alpha} \approx \tau^{-1/2} \tag{7.7}$$

confirms the white-noise character of the data.

To further verify the entire procedure above, we also evaluated the cyclotron frequency ratios for $\bar{p}$-to-$\bar{p}$ and H^--to-H^- by data measured in subsequent cycles in the same way as above. This comparison of the identical particles yielded a result

$$R_{\mathrm{id,exp}} - 1 = -3(79) \times 10^{-12} \quad (68\%\ \mathrm{C.L.}), \tag{7.8}$$

which is consistent with 1. After the systematic corrections in total $\Delta R_{\bar{p}\mathrm{H}^-,\mathrm{sys}} = -117(26) \times 10^{-12}$

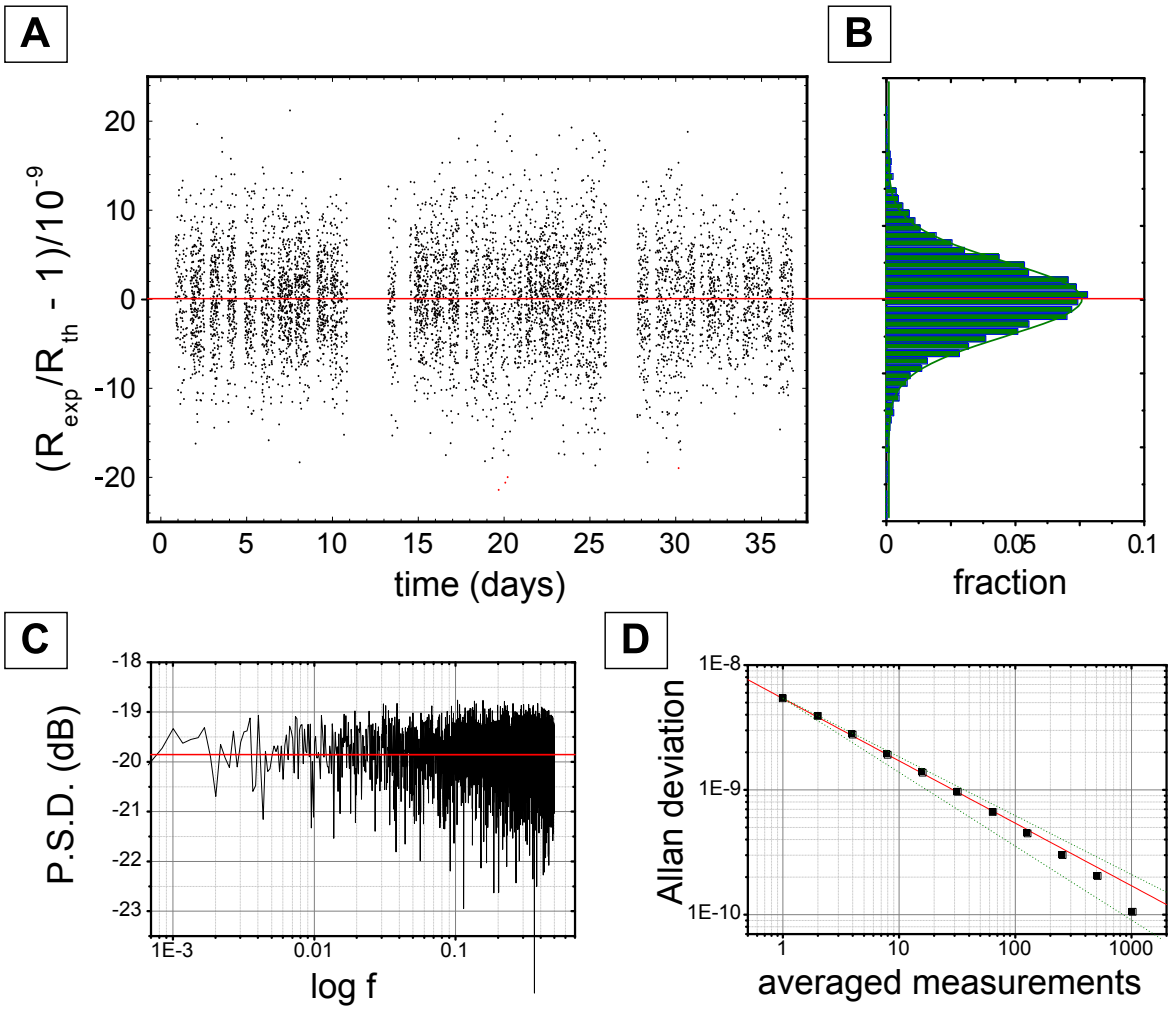

Figure 7.3: **(A)** Measured $\bar{p}$-H^- cyclotron frequency ratios $R_{\bar{p}H^-}$ as a function of time. 6521 individual ratio measurements were sampled over 35 days. **(B)** The data projected to a histogram. **(C)** Power spectrum density of the ratios as a function of the frequency. **(D)** Allan deviation of the measured ratios, plotted in a double-log scale. The red line shows a result of a linear fit with a slope $-0.501(2)$, which confirms a white-like nature of the ratio data. The figures are adapted from [54].

Table 7.1: Systematic shifts larger than 10^{-12} and the ones below are separated by the horizontal lines. See the text for details.

Effect	Correction of $R_{\bar{p}\mathrm{H}^-}$ (10^{-12})	Uncertainty $\delta R_{\bar{p}\mathrm{H}^-}$ (10^{-12})
(i) Trap asymmetry	-114	26
(ii) Detuned TR of H^- ion	-3	1
(iii) Tilt of the apparatus	-0.027	0.0070
(iv) Voltage drift	0.015	0.0030
(v) Magnetic gradient shift	-0.002	0.0002
(vi) Magnetic bottle shift	0.009	0.0120
(vii) Image charge shift	0.047	0.0040
(viii) Image current shift	$< \lvert 0.001 \rvert$	$< \lvert 0.001 \rvert$
(ix) Relativistic shift	-0.024	0.0020
(x) Rubidium frequency standard	0	3
Total systematic shift/uncertainty	-116.9	26.2

(Table 7.1) which will be discussed separately in the next section, the final result was obtained to be

$$R_{\bar{p}\mathrm{H}^-,\mathrm{fin}} = 1.001\,089\,218\,755\,(64)(26), \tag{7.9}$$

which translates to

$$\left|\frac{(q/m)_{\bar{p}}}{(q/m)_p}\right| - 1 = 1\,(64)(26) \times 10^{-12} \quad (68\%\ \mathrm{C.L.}), \tag{7.10}$$

being consistent with CPT symmetry. The combination of the statistical and systematic uncertainties are 6.9×10^{-11} in relative uncertainty at 68% C.L..

7.3 Systematic shifts and uncertainties

Detailed of the systematic corrections are discussed below. The trap parameters used to evaluate the systematic shifts are summarized in Table 7.2.

The leading systematic correction as well as the major systematic uncertainty (Table 7.1 (i)) were caused by the adjustment of the trapping potential $\Delta V_{\mathrm{H}^-\bar{p}} \approx 5\,\mathrm{mV}$ (Table 7.2 (v)) necessary to tune the axial frequencies of $\bar{p}$ and H^- in resonance with the axial detector at $\nu_{0,\mathrm{eff}} \approx 645.262\,\mathrm{kHz}$. Due to asymmetries of the trap (recall Fig. 3.3), the voltage tuning caused a shift of the axial position between the two particles by about 30 nm (Table 7.2 (vi)). This was estimated by voltage- and geometrical offsets of the measurement trap obtained by careful trap characterization (see the supplementary information of Ref. [54]). Together with a magnetic gradient $B_1 = -7.58(42)\,\mathrm{mT/m}$ (Table 7.2 (viii)), this geometric displacement induced a systematic shift of $-117(26) \times 10^{-12}$ to the ratio $R_{\bar{p}\mathrm{H}^-}$.

The second largest shift was also caused by this voltage tuning (Table 7.1 (ii)). The tuning ratio

Table 7.2: Trap parameters used for the systematic correction in then 2014 measurement.

(i) Trap radius a	$a = 4.5\,\mathrm{mm}$
(ii) Trap C_2	$C_2 = 18\,404\,\mathrm{m}^{-2}$
(iii) $\bar{p}$ ring voltage	$V_{\mathrm{R},\bar{p}} = 4.662\,035\,\mathrm{V}$
(iv) H^- ring voltage	$V_{\mathrm{R},\mathrm{H}^-} = 4.667\,038\,\mathrm{V}$
(v) H^--$\bar{p}$ voltage difference	$\Delta V_{\mathrm{H}^-\bar{p}} = 5.003\,\mathrm{mV}$
(vi) H^--$\bar{p}$ axial position difference	$\Delta z = 29(6)\,\mathrm{nm}$
(vii) Magnetic field	$B_0 = 1.946\,\mathrm{T}$
(viii) Magnetic gradient	$B_1 = -7.58(42)\,\mathrm{mT/m}$
(ix) Magnetic bottle	$B_2 = 6.8\,(9.1)\,\mathrm{mT/m}^2$
(x) TR detuning for H^-	$\Delta\mathrm{TR}_{\mathrm{H}^-} = 2.2 \times 10^{-5}$
(xi) Residual C_4/C_2^2 for H^-	$C_4/C_2^2 = -8 \times 10^{-5}$
(xii) Axial temperature	$T_z = 5.2\,(1.1)\,\mathrm{K}$
(xiii) Modified-cyclotron temperature	$T_+ = 243(49)\,\mathrm{K}$

(TR) of the measurement trap use din the measurement was optimized for the antiproton, which was slightly detuned for the H^- ion. This resulted in a small residual C_4 in case of H^- measurement (Table 7.2 (x, xi)), leading to the shift of $R_{\bar{p}\mathrm{H}^-}$ by $-3(1) \times 10^{-12}$.

The other systematic shifts are on levels below 10^{-12} (Table 7.1 (iii–x)). The entry of the tilt of the apparatus (iii) accounted for the error of the approximation formula Eq. (7.2) due to the tilt of the apparatus. The angle between the electric potential axis and the magnetic field axis θ affects this formula by [90]

$$\nu_- = \frac{\nu_z^2}{2\nu_+} \cdot \frac{9}{4} \sin^2\theta. \tag{7.11}$$

By comparing the frequency obtained by the formula of Eq. (7.2) against the magnetron frequency directly measured by the sideband method, we estimated $\theta = 0.4(1)°$, and corrected the ratio $R_{\bar{p}\mathrm{H}^-}$ by $-2.7(7) \times 10^{-14}$.

The effect of Table 7.1 (iv) accounted for voltage drift during the measurement. The rest of the effects (x–ix) are as explained in Sections 2.3.3 and 2.3.4, estimated based on the parameters in Table 7.2.

8

Discussion of physical significances and prospects for improvement

In this chapter, physical significances of the recent BASE results summarized in Chapters 6 and 7 are discussed. In the later part of the chater, we shall discuss prospects for improvement of these measures. Specifically, in Section 8.3, a strategy of 2017 run for improvement of the charge-to-mass ratio comparison is discussed.

8.1 Physical significances of the recent results

8.1.1 Improved CPT tests in the baryonic sector

The results of the charge-to-mass ratio and magnetic-moment comparisons obtained in the years 2014–2016 are summarized as

$$\left|\frac{(q/m)_{\bar{p}}}{(q/m)_p}\right| - 1 = 1\,(69) \times 10^{-12} \quad (68\%\ \text{C.L.}) \tag{8.1}$$

$$\left(\frac{g_p}{2} - \frac{g_{\bar{p}}}{2}\right) = 5(74) \times 10^{-10} \quad (95\%\ \text{C.L.}). \tag{8.2}$$

$$\tau_{\bar{p}} > 5.0\,\text{a} \quad (90\%\ \text{C.L.}) \tag{8.3}$$

Their sensitivities as CPT tests can be evaluated by converting them to unit of absolute energy. For the charge-to-mass ratio, what defines the sensitivities is the cyclotron transition energy between the proton and the antiproton. By recalling

$$\left|\frac{(q/m)_{\bar{p}}}{(q/m)_p}\right| = \frac{\omega_{\mathrm{c},\bar{p}}}{\omega_{\mathrm{c},p}}, \tag{8.4}$$

the constraint of CPT violation in this system $\delta\mathcal{E}_{\omega_c}$ is derived to be

$$\begin{aligned}\delta\mathcal{E}_{\omega_c} &= |\hbar\omega_{c,\bar{p}} - \hbar\omega_{c,p}| \\ &= \left|\hbar\left(\frac{\omega_{c,\bar{p}}}{\omega_{c,p}} - 1\right)\cdot\omega_{c,p}\right| < 8\times10^{-27}\,\mathrm{GeV} \quad (68\%\ \mathrm{C.L.}).\end{aligned} \tag{8.5}$$

This result corresponds to an improvement by a factor of 4 from the previous best limit set by the TRAP collaboration [114].

The sensitivity of the CPT test by the magnetic moment comparison of Eq. (8.2) can be discussed in a framework of the Standard Model Extension (SME) developed by V. A. Kostelecký and D. Colladay [151, 152]. It is an effective field theory conceived in search of Lorentz violation which could exist in theories such as string theory [153, 154]. It has been proven that in a unitary and local field theory, violation of CPT symmetry must be accompanied by Lorentz violation [155]. Therefore the Lorentz-violating model of the SME provides a way to quantify sensitivities of experimental CPT tests. The SME Lagrangian is constructed by adding possible Lorentz-violating operators to the Standard Model Lagrangian, each of them associated with a coefficient which defines its magnitude. These SME coefficients have been constrained by experimental tests of CPT- and Lorentz symmetry [156].

In Ref. [157], SME coefficients associated with Penning trap spectroscopies of charged particles are discussed. What defines the sensitivity in this framework is the anomaly frequency ω_a defined by $\omega_a \equiv \omega_L - \omega_c$. If a difference of anomaly frequency originated from CPT violation is denoted as $\delta\omega_a^p$ and $\delta\omega_a^{\bar{p}}$ for the proton and the antiproton, respectively, they are related to SME coefficients $\tilde{b}_p, \tilde{b}_p^*, \tilde{b}_{F,p}, \tilde{b}_{F,p}^*$, which represent couplings to a Lorentz-violating spinor field, as [157]

$$\begin{aligned}\delta\omega_a^p &= 2(\tilde{b}_p^z - \tilde{b}_{F,p}^{zz}B) \\ \delta\omega_a^{\bar{p}} &= 2(-\tilde{b}_p^{*z'} + \tilde{b}_{F,p}^{*z'z'}B^*).\end{aligned} \tag{8.6}$$

Here the superscripts z and z' represent the components of the coefficients in the non-inertial laboratory frames of the experiments of the proton and the antiproton, respectively. B and B^* represent the magnetic field strengths of the respective measurements. Using them, the difference of the proton-antiproton g-factors $g/2 = \omega_L/\omega_c$ can be expressed as

$$\frac{g_p}{2} - \frac{g_{\bar{p}}}{2} = \frac{2}{\omega_c^p\omega_c^{\bar{p}}}\left(\Sigma\omega_c^p\Delta\omega_a^p - \Delta\omega_c^p\Sigma\omega_a^p\right) \tag{8.7}$$

with $\Delta\omega_c^p, \Delta\omega_a^p, \Sigma\omega_c^p, \Sigma\omega_a^p$ defined as below:

$$\begin{aligned}\Delta\omega_c^p &\equiv \frac{1}{2}(\omega_c^p - \omega_c^{\bar{p}}), \quad \Delta\omega_a^p \equiv \frac{1}{2}(\delta\omega_a^p - \delta\omega_a^{\bar{p}}), \\ \Sigma\omega_c^p &\equiv \frac{1}{2}\left(\omega_c^p + \omega_c^{\bar{p}}\right), \quad \Sigma\omega_a^p \equiv \frac{1}{2}\left(\delta\omega_a^p + \delta\omega_a^{\bar{p}}\right).\end{aligned} \tag{8.8}$$

Table 8.1: List of constraints of the SME coefficients by the magnetic moment comparison between the proton and the antiproton. All values in 95% C.L.. The values in the table are adapted from Refs. [80, 117].

SME coefficients	Constraints 2014 [157]	Constraints 2017 [52, 53].
$\lvert\tilde{b}_p^Z\rvert$	$< 2 \times 10^{-21}\,\mathrm{GeV}$	$< 6.9 \times 10^{-25}\,\mathrm{GeV}$
$\lvert\tilde{b}_{F,p}^{XX} + \tilde{b}_{F,p}^{YY}\rvert$	$< 1 \times 10^{-5}\,\mathrm{GeV}^{-1}$	$< 3.9 \times 10^{-9}\,\mathrm{GeV}^{-1}$
$\lvert\tilde{b}_{F,p}^{ZZ}\rvert$	$< 1 \times 10^{-5}\,\mathrm{GeV}^{-1}$	$< 3.3 \times 10^{-9}\,\mathrm{GeV}^{-1}$
$\lvert\tilde{b}_p^{*Z}\rvert$	$< 6 \times 10^{-21}\,\mathrm{GeV}$	$< 1.3 \times 10^{-24}\,\mathrm{GeV}$
$\lvert\tilde{b}_{F,p}^{*XX} + \tilde{b}_p^{*YY}\rvert$	$< 2 \times 10^{-5}\,\mathrm{GeV}^{-1}$	$< 2.8 \times 10^{-9}\,\mathrm{GeV}^{-1}$
$\lvert\tilde{b}_{F,p}^{*ZZ}\rvert$	$< 8 \times 10^{-6}\,\mathrm{GeV}^{-1}$	$< 1.0 \times 10^{-8}\,\mathrm{GeV}^{-1}$

For derivation of the constraints on the SME coefficients, the different directions/locations and the different magnetic field strengths of the experiments, as represented by z, z' and B, B^* in Eq. (8.6), have to be taken into account[1]. We applied a prescription given in Ref. [157] to derive the constraints as listed in Table 8.1 [117]. The superscripts X, Y, Z of the coefficients in the table represent the sun-centered coordinate system employed in the SME. The new results improved each of these constraints by three orders of magnitudes than in 2014. Some of the coefficients are constrained at the level of $10^{-24}\,\mathrm{GeV}$. They are comparable to the constraints on the corresponding SME coefficients set by electron/positron or muon/anti-muon magnetic moment comparisons [51, 158].

These sensitivities on the orders of $10^{-27}\,\mathrm{GeV}$ set by the charge-to-mass ratio comparison, and $10^{-24}\,\mathrm{GeV}$ by the magnetic moment comparison constitute the most stringent tests of CPT symmetry in the baryonic sector.

The proton lifetime has been a subject of investigation for a long time in search of a baryon number violation which is predicted by the Grand Unified Theories (GUTs) [159–161]. Stringent limits up to $\tau_p > 2.1 \times 10^{29}\,\mathrm{a}$ (90% C.L.) [162] have been derived by direct measurements. For specific channels, limits on the order of $10^{34}\,\mathrm{a}$ have been obtained [163]. If any decay is observed for antiprotons, it indicates CPT violation accompanied by a violation of a baryon number.

The directly measured limit of the antiproton lifetime of Eq. (8.3) has improved the previous limit obtained by a similar method by a factor of about 30 [147]. The antiproton lifetime has also been constrained by other methods. In Ref. [164], the antiproton lifetime limit is derived from energy spectra of antiproton-to-proton ratio of the cosmic ray flux to be $\tau_{\bar{p}} > 8 \times 10^5\,\mathrm{a}$ (90% C.L.). This estimation is based on a model of production and propagation of antiprotons in the interstellar medium. Another limit is derived in Ref. [165], where a detector placed in an antiproton accumulator ring was used to seek for possible decays of antiprotons in forms of $\bar{p} \to e^- X$ or $\bar{p} \to \mu^- X$. No statistically significant decay signal was observed for any of these modes, setting the lower limits on the particle lifetime at

[1] The small difference of magnetic field between $B_{\mathrm{Mainz}} = 1.90\,\mathrm{T}$ and $B_{\mathrm{CERN}} = 1.945\,\mathrm{T}$ in this case does not make a significant difference in derivation of the limits.

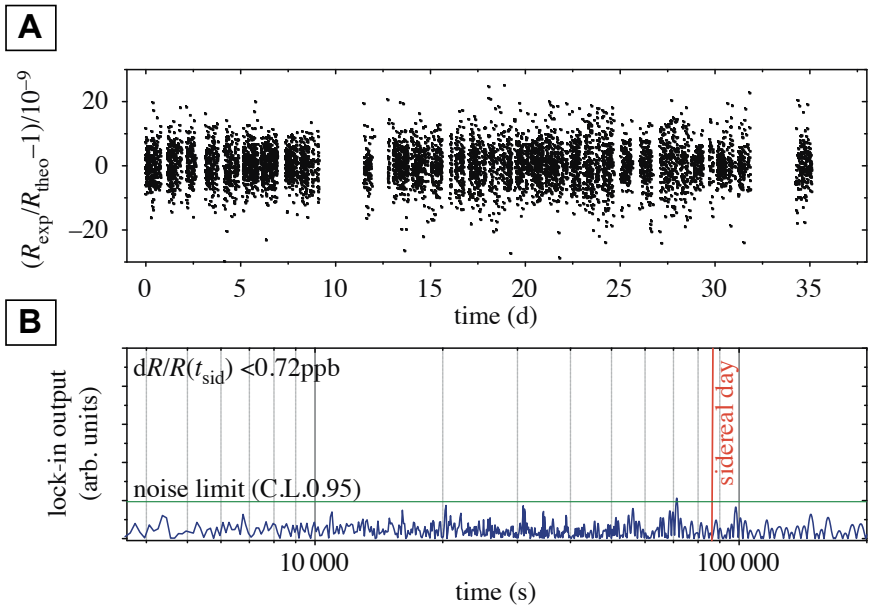

Figure 8.1: **(A)** Sampled ratio $R_{\bar{p}\mathrm{H}^-}$ as a function of time, same data as shown in Fig. 7.3. **(B)** Periodogram of data in (A). The period corresponds to the sidereal day is marked by the red vertical line. The background noise level at 95% C.L. obtained by simulations is indicated by the green horizontal line. The figures are adapted from Ref. [168].

the levels of 10^3–10^5 a, depending on the decay modes. Although our limit is less stringent than these methods, this direct method gives a model-independent inclusive limit which also constrains decay channels invisible to detectors. Examples of such decays are ones predicted by supersymmetric GUTs [166] such as $\bar{p} \to \nu_e K^-$ or $\bar{p} \to \nu_\mu K^-$.

In addition to the comparison of the final results of Eqs. (8.2) to (8.4) discussed above, the high sampling rate of the charge-to-mass ratio comparison allowed us to perform a search of sidereal variation on the $\bar{p}$-H^- cyclotron frequency ratio. If observed, this could imply an existence of a Lorentz-violating background field coupled to the antiproton or the H^- ion. A PSD periodogram [167] was obtained from the sampled ratio $R_{\bar{p}\mathrm{H}^-}$ as seen in Fig. 8.1 (B). The signal amplitude at the sidereal day $t_{\mathrm{sid}} = 86\,164.1\,\mathrm{s}$ was compared with simulated background amplitudes to set an upper limit of a sidereal variation of $R_{\bar{p}\mathrm{H}^-}$ in a unit of relative amplitude to be $< 7.2 \times 10^{-10}$ at 95% C.L..

8.1.2 Constraint on gravitational anomaly of the antiproton

The result of the charge-to-mass ratio comparison can be interpreted as a test of the weak equivalence principle on antimatter, if we assume CPT symmetry to hold.

This can be done by using an effect known as a gravitational redshift. This is a phenomenon that two clocks in different gravitational potentials oscillate at different frequencies according to the

gravitational time dilation. This has been precisely tested with ordinary matter [169–171] and has also been applied to the global positioning system (GPS) [172]. It can be shown that testing the identity of this scaling between two clocks is equivalent to testing the weak equivalence principle on these two bodies [173].

Now if we assume CPT symmetry and that the masses of the proton and the antiproton are identical, an antiproton and a proton in the magnetic field should have the same cyclotron frequency in the absence of a gravitational field. The actual measurement compares them in the gravitational field on the surface of the Earth. If the weak equivalent principle holds for the antiproton in the same as ordinary matter, the two should experience the same gravitational redshift. If a difference in the frequencies is observed, it implies an gravitational anomaly of the antiproton.

To derive the constraint, we followed the discussion by R. J. Hughes and M. H. Holzscheiter [173]. Here a form of gravitational anomaly is assumed which modifies the gravitational potential on ordinary matter U to $\alpha_g U$ for the antiproton. The gravitational redshift of a cyclotron-frequency clock is derived by considering the gravitational effects on the mass as well as on the magnetic field. It is

$$\omega_{\mathrm{c},p} \to \omega_{\mathrm{c},p}\left(1+\frac{U}{c^2}\right) \tag{8.9}$$

for a proton and

$$\omega_{\mathrm{c},\bar{p}} \to \omega_{\mathrm{c},\bar{p}}\left(1+\frac{(3\alpha_g-2)U}{c^2}\right). \tag{8.10}$$

for an antiproton. This would appear as a relative difference of the cyclotron frequencies of the two as

$$\frac{\omega_{\mathrm{c},\bar{p}}-\omega_{\mathrm{c},p}}{\omega_{\mathrm{c},p}} = \frac{3(\alpha_g-1)U}{c^2}. \tag{8.11}$$

To determine the potential magnitude of the absolute gravitational potential U on the location of the experiment, we followed the previous works and chose U to be the potential of the local super cluster $|U/c^2| \sim 10^{-5}$ [173–175] and obtained

$$|\alpha_g - 1| < 8.7 \times 10^{-7}. \tag{8.12}$$

from the result of Eq. (8.4). This method provides a stringent limit complementary to direct gravity tests on antimatter. It should be noted that this indirect limit involves assumptions on the model. As noted in the beginning, CPT symmetry is assumed. In addition, it is also assumed that a possible anomalous gravity of the antiproton follows the tensor gravity field as ordinary matter. This assumes the anomaly to be a long-scale interaction. An anomaly with a length scale shorter than the size of our Galaxy is not constrained in this framework.

8.2 Prospects for improvement

Further improvement is foreseen for each of the measurements discussed in the last section.

As for the magnetic moment measurement, the high effective temperature of the cyclotron detection system due to electromagnetic interference with noise in the AD hall had been the major issue in 2015/2016 magnetic moment measurements. After optimization of the system, the temperature was lowered to $T_+ \approx 12\,\mathrm{K}$, and the high-precision magnetic moment measurement was enabled by a newly invented multi-trap measurement scheme using two particles.

However this in turn introduced new systematic effects. The dominant error arose from the use of two particles, which contributed to a systematic uncertainty of about 0.96 p.p.b..

This issue of the cyclotron detection system has been resolved in 2017 run by installing it inside the trap chamber (see Section 5.3), which is a major part of the Ph.D. thesis of James A. Harrington [79]. This will allow an improvement of the precision of the antiproton magnetic moment to a comparable level to the recent proton measurement by the Mainz group. As a major upgrade of the experimental techniques, sympathetic cooling of protons with laser-cooled beryllium ions is currently being implemented to the Mainz experiment [73]. In the near future, the methods are planned to be transferred to CERN to be applied to antiprotons. If successfully implemented, this is expected to deterministically prepare protons and antiprotons with a mode temperature of the modified cyclotron mode of 30 mK, which will increase the data-taking rate of the high-precision magnetic moment measurements dramatically.

The last limit of the directly-measured antiproton lifetime was limited by the number of antiprotons initially stored in the RT. As will be discussed in Chapter 13, in 2017 run, the catching efficiency of antiprotons was improved by a factor of 3 than in 2015/2016 run, which will allow a much faster data accumulation rate for the lifetime measurement. In future, a dedicated experiment is planned, which will store antiprotons of order 10000 and will improve the limit to 10^3–10^4 a [76]. Trapping of such large numbers of antiprotons has been successfully demonstrated by other AD experiments [143, 176].

8.3 Strategy of the 2017 run for an improved charge-to-mass ratio comparison

The 2017 run was dedicated to improvement of the proton-to-antiproton charge-to-mass ratio comparison. Based on the measurement in 2014 discussed in Chapter 7, a two-fold strategy for improvement was conceived.

The first was to eliminate the major systematic uncertainty of the last measurement. As discussed in Section 7.3, the tuning of the ring voltage V_R between the antiproton and the H^- ion caused

the major systematic correction and the largest systematic uncertainty in the 2014 measurement. To eliminate this effect, a new axial detection system with a tunable resonance frequency was developed [81] (Chapter 9). The voltage tuning in the 2014 measurement was necessary to keep the axial frequency of each of the antiproton and the H^- ion in resonance with the detection system. With a detection system with a tunable resonance frequency, the adjustment of the ring voltage will no longer be necessary.

Secondly, we aimed to improve the cyclotron frequency stability in the apparatus. This allows sampling of high-quality data and will enable a reduction of statistical uncertainty in the final determination of the antiproton-to-H^- cyclotron frequency ratio. As discussed in Section 7.1, in the 2014 charge-to-mass ratio comparison, influences of external magnetic field fluctuations were observed in the cyclotron frequency fluctuations. Therefore, an advanced magnetic shielding system has been developed to reduce influences of the external field fluctuations (Chapter 10). Another development made for this purpose is a monitoring system which continuously records the conditions of the apparatus by various sensors (Chapter 11). This allows identification of environment-originated cyclotron frequency fluctuations, and make relevant development possible.

To discuss the required stability in a unit of the absolute cyclotron frequency fluctuation, discussion in Section 3.1.1 can be used. From Eq. (3.12), the absolute cyclotron frequency fluctuation Ξ_c is related to the width of the distribution of the frequency ratio σ_R by

$$\sigma_R \approx \frac{\Xi_{c,\bar{p}}}{\overline{\nu}_{c,\bar{p}}} \tag{8.13}$$

where σ_R denotes the distribution of the ratio $R_{\bar{p}H^-}$. The right hand side is the relative cyclotron frequency fluctuation of the antiproton. The data of $R_{\bar{p}H^-}$ sampled in the 2014 measurement had a Gaussian-like distribution with a width of $\sigma_{R,\,2014} = 5.4 \times 10^{-9}$ (Fig. 7.3 (B)). This corresponds to $\Xi_{c,\bar{p}} = 163\,\mathrm{mHz}$. A significant improvement from this condition has been the goal of improvement in the 2017 commissioning.

The uncertainty of the determination of the center of the distribution of the ratio $\delta R_{\bar{p}H^-}$ can be expressed with the width of the distribution σ_R and the sample size N as

$$\delta R_{\bar{p}H^-,\mathrm{est}} = \frac{\sigma_R}{\sqrt{N}} \approx \frac{1}{\sqrt{N}} \frac{\Xi_{c,\bar{p}}}{\overline{\nu}_{c,\bar{p}}}, \tag{8.14}$$

in case the data points are uncorrelated. In fact, there is a correlation between the data points due to the interpolation of data (see Eq. (7.5)), which should be taken into account in the final data analysis as done in case of the 2014 measurement. However Eq. (8.14) can still be used as a practical measure to estimate precision which can be achieved for a given condition of the experiment. Its validity can be checked by substituting $\sigma_{R,\,2014} = 5.4 \times 10^{-9}, N_{2014} = 6521$, from which we obtain $\delta R_{\bar{p}H^-,\mathrm{est},2014} = 6.7 \times 10^{-11}$, approximately being consistent with the statistical uncertainty of the

2014 measurement obtained by the Maximum-Likelihood estimation accounting for the correlation.

Once a significantly improved stability is reached, acquisition of data with enough statistics can be well counted from the ability of the reservoir trap demonstrated in the 2015/2016 run.

In Part V, each of the above-discussed upgrades are described.

Part V

Upgrades for an improved charge-to-mass ratio comparison

9

Tunable axial detection system

As discussed in Chapter 7, both the major systematic correction and the major systematic uncertainty of the 2014 charge-to-mass ratio comparison came from the difference of positions between the measured antiproton and H^- ion caused by the adjustment of the ring voltage V_R between the two particles.

In order to improve this aspect of the measurement, a new axial detection system with a tunable resonance frequency was developed as an upgrade specialized to this measurement. The concept is to keep the ring voltage constant between the two particles and instead tune the resonance frequency of the detector. The position correction will no longer be necessary, and the primary source of the systematic uncertainty will be eliminated.

The system has been built by collaborative efforts of the BASE team at CERN: know-how to build high-quality superconducting resonators and low-noise electronics for axial detection systems have been developed over the years [101, 177]. The detection systems currently installed to the apparatus at CERN are based mainly on works by Hiroki Nagahama [80], which have been published as Ref. [136]. Implementation of the tunable functionality was the subject of Toya Tanaka's master's thesis work [81].

The main scope of this thesis is the characterization of the system after installation to the experiment (Section 9.3). In order to provide the necessary information, the specifications of the system are summarized in Section 9.2. Details of the design and the construction should be referred to Refs [80, 81, 136].

At the end of 2017 run-I, we had an opportunity to characterize the detection system in a cryogenic environment but without a strong magnetic field. This is shortly summarized in Section 9.4.

9.1 Requirements of the tunable detection system

The required tunable range of the system is discussed based on the axial frequency of the two particles at the same ring voltage V_{R};

$$\begin{aligned}\frac{\nu_{z,\bar{p}}}{\nu_{z,\mathrm{H}^-}} &= \left(\frac{1}{2\pi}\sqrt{\frac{2qC_2V_{\mathrm{R}}}{m_{\bar{p}}}}\right)\Bigg/\left(\frac{1}{2\pi}\sqrt{\frac{2qC_2V_{\mathrm{R}}}{m_{\mathrm{H}^-}}}\right) \\ &= \sqrt{\frac{m_{\mathrm{H}^-}}{m_{\bar{p}}}} \approx 1.00054.\end{aligned} \tag{9.1}$$

For a typical axial frequency $\nu_{z,\bar{p}} = 640\,\mathrm{kHz}$, this frequency difference $\nu_{z,\bar{p}} - \nu_{z,\mathrm{H}^-}$ is about 350 Hz. The tunable range of the detector ought to cover this range.

Another requirement is on the effective temperature of the system. If the effective temperature differs largely between the tuning conditions, it could lead to a systematic shift of the cyclotron frequency ratio.

Among the temperature dependent frequency shifts (see Section 2.3.3), the dominant contribution is the shift of the modified cyclotron frequency due to the coupling of the magnetic bottle term B_2 and the axial mode energy E_z. From Eq. (2.80),

$$\frac{\Delta\omega_c}{\omega_c} \approx \frac{\Delta\omega_+}{\omega_+} \approx \frac{1}{m\omega_z^2}\frac{B_2}{B_0}\langle E_z\rangle. \tag{9.2}$$

For the PT in 2017 run-II, B_2 was measured to be $B_2 \approx -0.267\,\mathrm{T/m^2}$ (see Section 14.2.2). Substituting this to Eq. (9.2),

$$\frac{\Delta\omega_c}{\omega_c} \approx -7\times10^{-11}[\mathrm{K}^{-1}]\cdot T_z. \tag{9.3}$$

Since the comparison on the order of 10^{-11} is aimed, it is required to the detection system that the difference of the effective temperature between $\bar{p}$- and H^- operation ΔT_z to be $\lesssim 10\%$ in order that the tuning does not produce any significant frequency shifts.

9.2 Specifications of the tunable detection system

This section gives a summary of specifications of the tunable axial detection system installed in 2017 run-II, which is based on what was characterized in Toya Tanaka's master's thesis [81] with exchanges of some components.

Fig. 9.1 gives an overview of the system. In parallel to a resonator and an amplifier, the basic ingredients of the image-current detection system [136], a varactor diode is implemented for the tuning functionality. It is represented by its parallel capacitor C_{v} and effective parallel resistance R_{v}. The amplifier is expressed in the schematic as a parallel circuit of an ideal amplifier and its parallel input resistance R_{a} and the parallel input capacitance C_{a}. The coupling capacitors $C_{\mathrm{c,v}}$ and $C_{\mathrm{c,a}}$ are placed

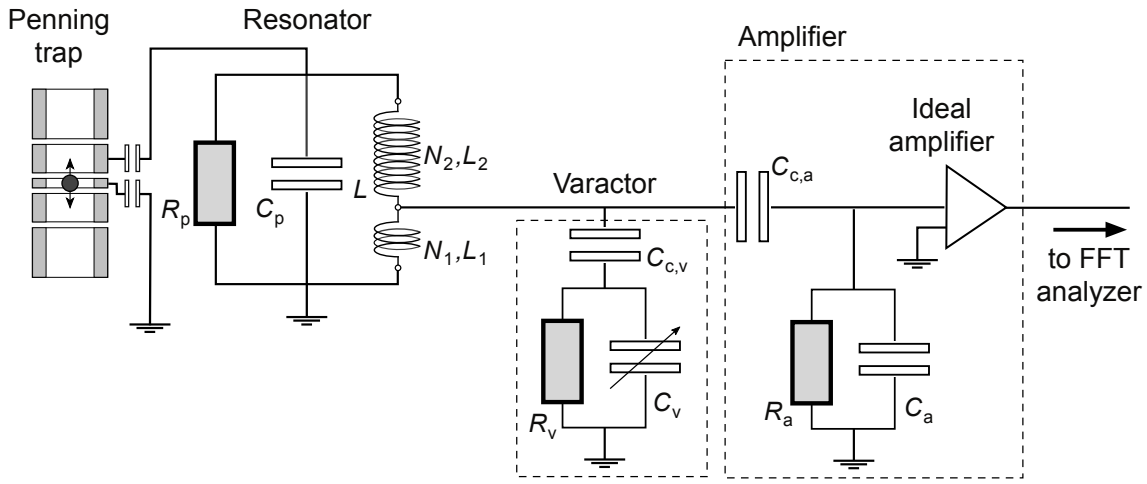

Figure 9.1: Equivalent circuit of the tunable axial detection system, consisting of the resonator, the varactor circuit, and the cryogenic amplifier. The varactor and the amplifier are coupled to the system via the coupling capacitors $C_{\mathrm{c,v}}$ and $C_{\mathrm{c,a}}$. The amplifier is expressed by its effective parallel capacitance, effective parallel resistance, and an ideal amplifier. Adapted from [81], edited under permission by the author.

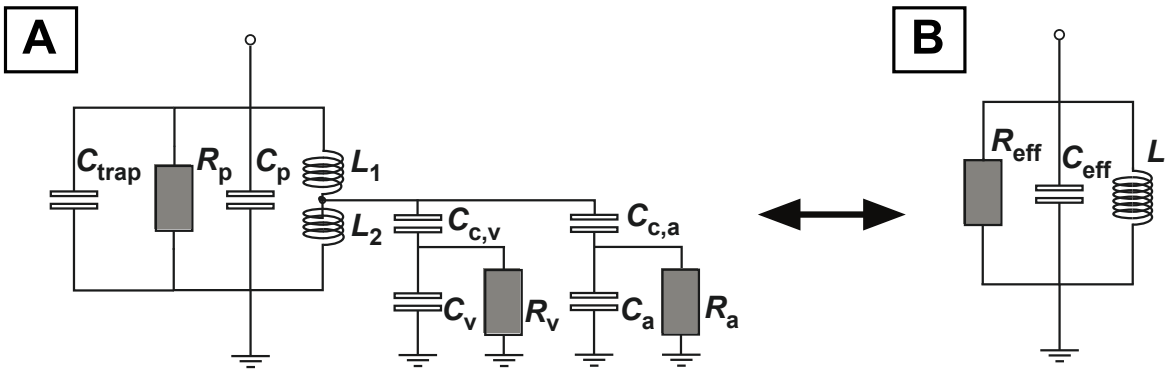

Figure 9.2: Definition of the effective parallel resistance R_{eff} and capacitance C_{eff} of the total system.

between these components and the rest of the system. Together with, the ratio of the inductances L_1 and L_2 of the two parts of the coil, they define the coupling of these components to the output.

The couplings between the components are characterized by the coupling constants $\kappa_{\mathrm{l}}, \kappa_{\mathrm{c,a}}, \kappa_{\mathrm{c,v}}$ defined by

$$\kappa_{\mathrm{l}} \equiv \frac{L_2}{L_1 + L_2}, \tag{9.4}$$

$$\kappa_{\mathrm{c,a}} \equiv \frac{C_{\mathrm{c,a}}}{C_{\mathrm{c,a}} + C_{\mathrm{a}}}, \tag{9.5}$$

$$\kappa_{\mathrm{c,v}} \equiv \frac{C_{\mathrm{c,v}}}{C_{\mathrm{c,v}} + C_{\mathrm{v}}}, \tag{9.6}$$

The effective parallel resistance R_{eff} and the effective parallel capacitance C_{eff} are defined by the

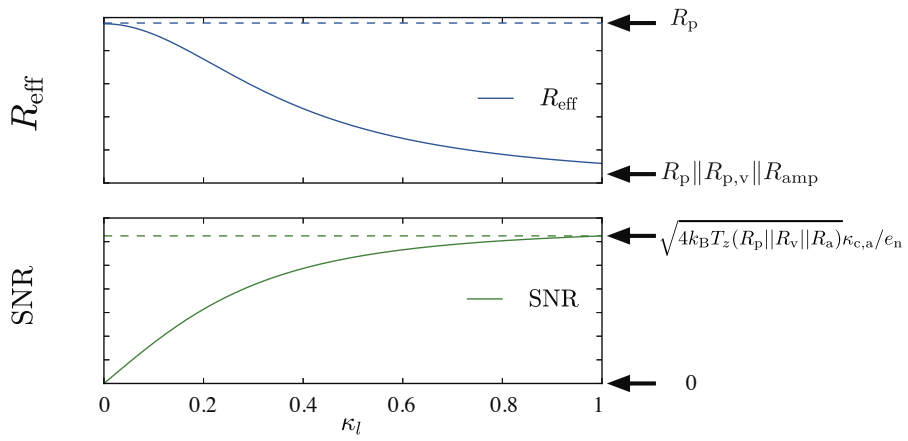

Figure 9.3: Scalings of the effective parallel resistance of the system R_{eff} and the dip SNR against the coupling constant κ_{l}. Realistic values of $\kappa_{\mathrm{c,v}}$ and $\kappa_{\mathrm{c,a}}$ are assumed. $R_{\mathrm{p}}||R_{\mathrm{v}}||R_{\mathrm{a}} \equiv (1/R_{\mathrm{p}} + 1/R_{\mathrm{v}} + 1/R_{\mathrm{a}})^{-1}$

equivalence of the circuit in Fig. 9.2 (A) and (B). Their expressions can be derived as below [80]:

$$R_{\mathrm{eff}} = \left(\frac{1}{R_{\mathrm{p}}} + \kappa_{\mathrm{l}}^2 \kappa_{\mathrm{c,v}}^2 \frac{1}{R_{\mathrm{v}}} + \kappa_{\mathrm{l}}^2 \kappa_{\mathrm{c,a}}^2 \frac{1}{R_{\mathrm{a}}} \right)^{-1} \tag{9.7}$$

$$C_{\mathrm{eff}} = C_{\mathrm{trap}} + C_{\mathrm{p}} + \kappa_{\mathrm{l}}^2 \left(\kappa_{\mathrm{c,v}} C_{\mathrm{v}} + \kappa_{\mathrm{c,a}} C_{\mathrm{a}} \right) \tag{9.8}$$

The resonance frequency ν_0 of the combined system becomes

$$\nu_{0,\mathrm{eff}} = \frac{1}{2\pi\sqrt{LC_{\mathrm{eff}}}}. \tag{9.9}$$

The tuning of $\nu_{0,\mathrm{eff}}$ is realized by variation of C_{eff} through C_{v}. The coupling constant $\kappa_{\mathrm{c,v}}$ defines how the tuning range of the capacitance of the varactor C_{v} is reflected to the tuning range of the entire system. In practice, a relation below from Eq. (2.106) is used to measure R_{eff} from the Q-factor of the resonance:

$$R_{\mathrm{eff}} = 2\pi\nu_{0,\mathrm{eff}} LQ. \tag{9.10}$$

Recalling the relations of R_{eff} to the detection of the particle, the dip-width of the particle and the SNR of the dip signal are expressed as

$$\Delta\nu_z = \frac{1}{2\pi} \frac{q^2 R_{\mathrm{eff}}}{m D_z^2}, \tag{9.11}$$

$$\mathrm{SNR} = \frac{\sqrt{4k_B T_z R_{\mathrm{eff}}} \cdot \kappa}{e_n}, \quad (\kappa \equiv \kappa_{\mathrm{l}} \kappa_{\mathrm{c,a}}) \tag{9.12}$$

with T_z being the effective temperature of the axial detection system and e_{n} the equivalent input noise of the amplifier.

The effective parallel resistance R_{eff} and the dip SNR scale with the coupling constant as shown

in Fig. 9.3. The scalings against κ_l are displayed in the figure. The scalings against $\kappa_{c,a}$ and $\kappa_{c,v}$ follow the same trends as κ_{l}, although the slopes of the curves differ. Here, it can be seen that for a large κ, the signal increases in contrast to the constant background noise and enlarges the SNR. At the same time, a stronger coupling to smaller resistors $R_{\mathrm{p,a}}$ and $R_{\mathrm{p,v}}$ causes Q to decrease, resulting in a smaller R_{eff}.

In order that the dip signal is not smeared out by fluctuations of the axial frequency, which is principally determined by the stability of the voltage source to be $\approx 25\,\mathrm{mHz}$ at a typical averaging time, the system has to have an enough R_{eff} which corresponds to $\Delta\nu_z \gtrsim 1\,\mathrm{Hz}$. Based on these considerations, $\kappa_l \approx 0.2$ is employed, which corresponds to $\Delta\nu_z \approx 3\,\mathrm{Hz}$ and SNR of 20–30 dB.

The electronic feedback (see Section 9.3) can be used to fine-tune R_{eff} to achieve an optimum $\Delta\nu_z$ (see Section 15.2.1 for more details).

More details of each component are described in the following sections.

9.2.1 Axial resonator

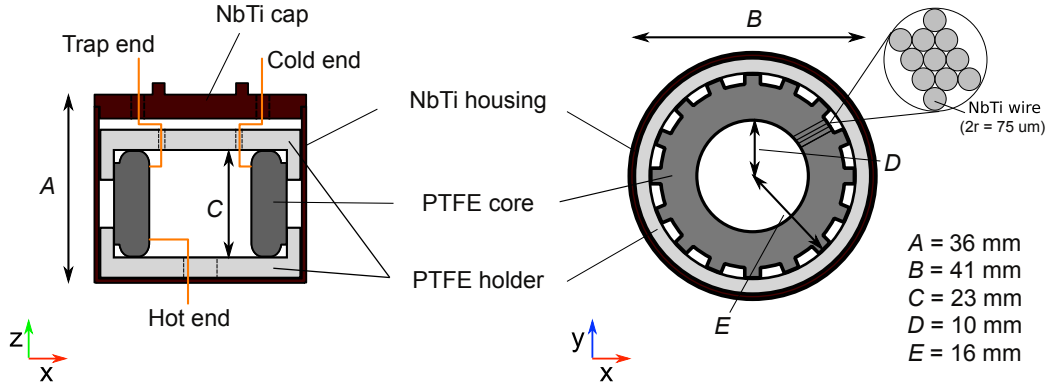

Figure 9.4: Schematic of the axial resonator used in the tunable axial detection system. Adapted from Ref. [81], modified under permission by the author. PTFE insulated NbTi wire is wound on the PTFE core. The three ends of the coil are shown on the left figure. The toroid is installed in the PTFE holder and mounted in the NbTi housing. Values of the geometrical parameters A–E are specified on the right.

As explained in Section 5.4.3, the axial resonator is a high-quality superconducting toroidal coil. It is made of three layers of PTFE insulated NbTi wire of 75 µm diameter, wound on a toroidal PTFE core. (Fig. 9.4) The three ends: the *hot, cold* and the *tap* end in Fig. 9.4 are respectively connected to the feedthrough (toward the trap electrode), the RF ground of the apparatus, and to the high-impedance input of the amplifier. The tap end is branched from the wire, separating the total turn N into N_1 and N_2 at a defined ratio. (see Fig. 9.1). The total turn N defines the inductance L of the resonator. The formula below was found to reproduce measured inductances with accuracy of 10%:

$$L = \frac{\mu_0 C(D-E)}{\pi(D+E)} N^2. \tag{9.13}$$

Table 9.1: Unloaded properties of the resonator used in the tunable axial detection system by a measurement in a cryogenic test setup. The properties of the resonator were extracted from spectra measured by a network analyzer.

Inductance L	1.75 mH
Turn N	800
Parallel capacitance C_p	11 pF
Q-factor	194 000
Resonance frequency ν_res	1.09 MHz
Parallel resistance R_p	2.3 GΩ

Here μ_0 is the permeability of vacuum, D and E are the geometrical parameters of the toroid indicated in Fig. 9.4. $N = 800$ for this resonator. It has a measured inductance of $L = 1.75\,\mathrm{mH}$.

Special cares were taken to produce low-loss soldering joints between the NbTi wires and high-purity copper wires at the ends of the windings [177].

After being wound on the core, the wires were tightly wrapped with PTFE tapes, and placed in a PTFE holder to ensure good thermal connections. The assembly is mounted in a well-polished NbTi housing which confines the signal and helps to achieve a high Q-factor. When the resonator is installed in the apparatus, the housing is attached to the 4 K stage by copper braids to compensate bad thermal conductivity of NbTi.

By these designs and methods, production of a high-quality resonator on the order of $Q \sim 10^5$ is made possible The properties of the unloaded resonator measured in a cryocooler test setup are listed in Table 9.1.

9.2.2 Varactor

The varactor is the key component for tuning of the resonance frequency which functions as a variable capacitor. A GaAs hyperabrupt junction varactor MA46H072 by MACOM which is also used in a cyclotron detection system [137, 178] is employed. The capacitance of the varactor can be controlled by a biasing voltage supplied between the ends of the diode in inverse polarity. The circuit for the biasing is shown in Fig. 9.5. As the biasing voltage changes, a change of the electron density around the pads of the varactor varies the depletion length, hence the capacitance of the component. For variations of the bias voltage in a range of −1–10 V, the capacitance of the varactor changed from approximately 1–9 pF [81].

The coupling capacitor $C_\mathrm{c,v}$ defines the coupling of the varactor with the rest of the system and also the tuning range of the system. $C_\mathrm{c,v} = 2.2\,\mathrm{pF}$ was found to provide a sufficient tuning range [81]. Looking at Eq. (9.7), it is seen that a large R_v is desirable so that the reduction of R_eff due to the coupling with this component is small. In addition to a large resistance of the varactor itself,

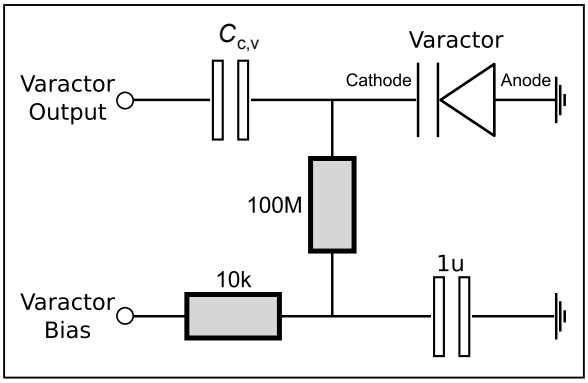

Figure 9.5: Circuit for varactor biasing. The end *Varactor Output* is connected between the resonator and the amplifier in Fig. 9.1. The end *Varactor Bias* is connected to the voltage source for biasing in the reversed polarity. As the varactor anode is grounded, the varactor behaves as a tunable capacitance by variation of the biased voltage. The 100 MΩ resistor is connected to the varactor bias to prevent reduction of the effective parallel resistance. Adapted from [81], edited under permission by the author.

a 100 MΩ resistor is placed in the biasing line to prevent reduction of R_{eff}. The effective parallel resistance R_{v} of the varactor circuit with the coupling factor is $R_{\mathrm{v}} \cdot \kappa_{\mathrm{c,v}}^{-2} \approx 216\,\mathrm{M\Omega}$.

9.2.3 Cryogenic amplifier

From Eqs. (9.7) and (9.12), it can be seen that a high input resistance R_{a} and a low equivalent input noise e_{n} are required for the amplifier together with appropriate gain.

The circuit diagram of the amplifier is shown in Fig. 9.6. The amplifier consists of two stages: a common-source amplifier as the input stage and a souse-follower circuit as the output stage. The common-source circuit was employed to achieve high R_{eff}. Since the common-source circuit has a large output impedance, the source-follower circuit is used for the output stage to match the 50 Ω impedance of the standardized laboratory RF components behind the first amplifier stage.

Considering the equivalent input noise e_{n}, the primary source of noise is the FET of the common-source input stage. We employ GaAs MESFETs, whose direct band-gap allows its operation under cryogenic environments. By denoting the respective noise on the FETs on the input stage and the output stage as $e_{\mathrm{n},1}$ and $e_{\mathrm{n},2}$, the equivalent input noise e_{n} of the amplifier can be expressed as below by accounting for the gain of the first stage G_1,

$$e_{\mathrm{n}} = \sqrt{e_{\mathrm{n},1}^2 + \frac{e_{\mathrm{n},2}^2}{G_1^2}} \tag{9.14}$$

Therefore, it is especially important to use a low-noise FET on the input stage.

Noise spectrum of a FET is characterized by contributions of Johnson-Nyquist thermal noise, 1/f noise due to the drain current, and so-called generation-recombination (GR) noise [179]. The thermal noise is much reduced at the cryogenic temperature where the amplifier is operated. Hence

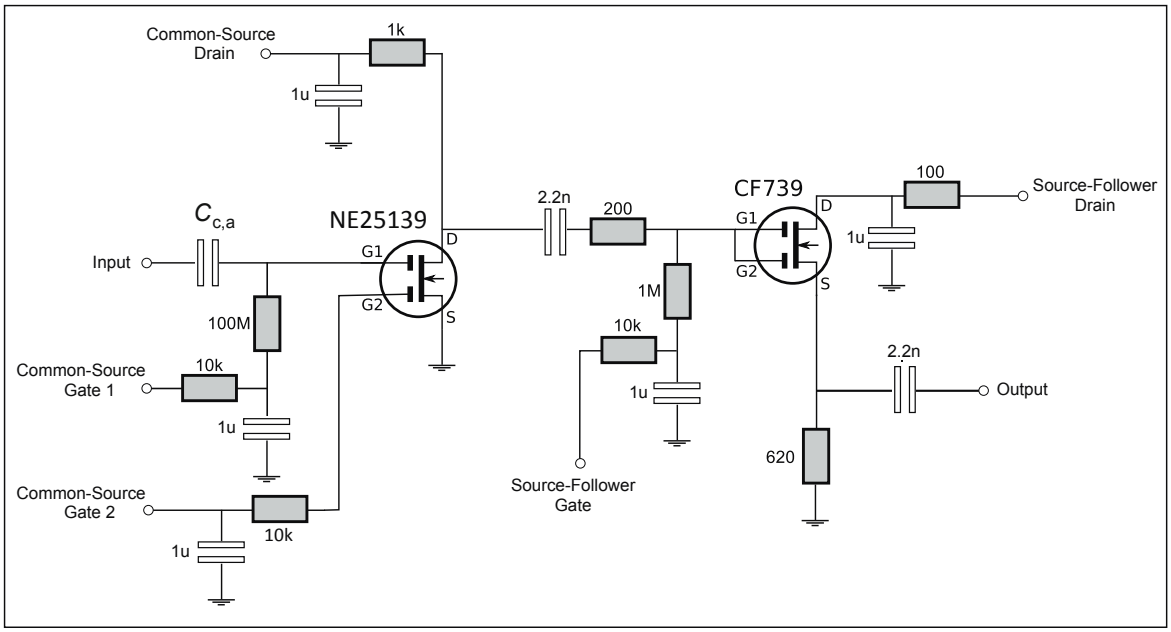

Figure 9.6: Circuit diagram of the cryogenic amplifier of the tunable axial detection system. The input stage is a common-source circuit using NE25139. The output stage is a source-follower circuit with CF739. Adapted from [81]. Modifications were made under permission by the author to reflect the present system.

Table 9.2: Characteristics of the cryogenic amplifier used in the tunable detection system.

Input resistance R_a	$7.5\,\mathrm{M\Omega}$
Input capacitance C_a	$\approx 2\,\mathrm{pF}$
Coupling capacitance $C_{c,\mathrm{a}}$	$10\,\mathrm{pF}$
Equivalent input noise e_n	$0.7\,\mathrm{nV}/\sqrt{\mathrm{Hz}}$
Gain G	$14\,\mathrm{dB}$
Heat consumption	$\approx 5\,\mathrm{mW}$

the dominant part is from the 1/f noise and the GR noise. Dual-gate FETs are used because of their smaller 1/f noise compared to the single-gate ones, owing to longer effective gate-drain distances [80]. The GR noise is produced around the terminals due to fluctuations in the number of free carriers in the sample associated with random transitions of charge carriers between different energy bands of the FET, which differs from FET to FET depending on, e.g., an effective lifetime of the carriers.

In addition to a high input resistance and a low input noise, there are some requirements for the FETs such as low heat consumption and a low input capacitance C_a.

After comparisons based on the above considerations, two types of dual-gate MES-FETs were selected: NE25139 (NEC) for the input stage and CF739 (Siemens) for the output stage [80].

The properties of the amplifier used in the axial detection system in 2017 run-II are summarized in Table 9.2.

9.3 Performance of the system installed in the experiment

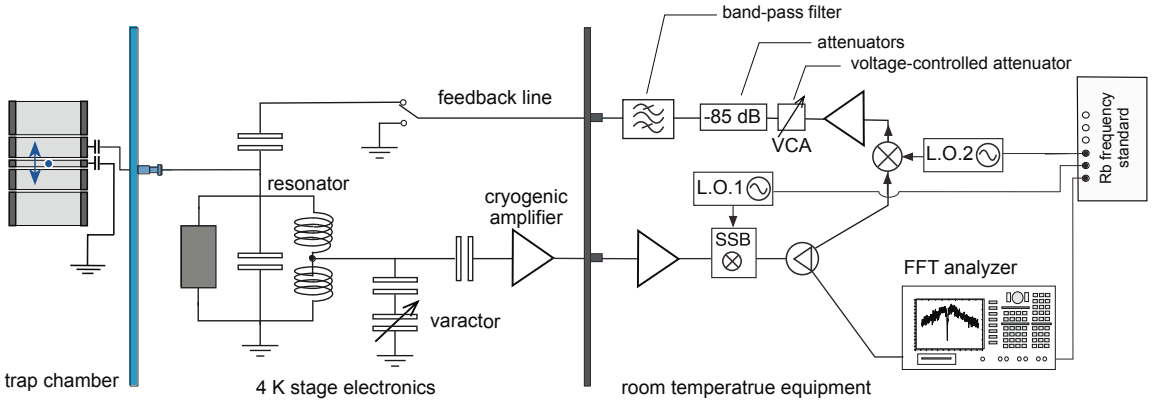

Figure 9.7: Schematic of the tunable detection system installed in the apparatus. The half of the signal is split to a feedback line at a power splitter. The frequency generators are used as local oscillators of mixing: *L.O. 1* for the down-conversion, *L.O. 2* for the up-conversion for the feedback line. They have the same frequency of 588 kHz. The phase of the feedback is controlled by the relative phase between the L.O. 1 and L.O. 2. The attenuators define the feedback gain. The attenuation of the voltage-controlled attenuator (*VCA*) is controlled by a bias voltage applied to a FET used in this component. Details of the cryogenic components, such as described in Fig. 9.1 are omitted in this figure.

The performance of the tunable detection system installed in the apparatus is summarized in this section. A schematic of the system is given in Fig. 9.7. The resonator, the varactor, and the cryogenic amplifier are installed on the 4 K stage of the electronic segments (Sections 5.2 and 5.4). In the room temperature section, the signal is down-converted by the SSB down converter (Section 5.4.4) to match the input range of the FFT analyzer, which is up to 102.4 kHz. After the down-conversion, the signal is split by a beam splitter. One half of the signal is sent to the FFT analyzer. The other is up-converted to the original frequency by another mixer (connected to *L.O. 2* in Fig. 9.7), and fed back to the resonator. The phase of the feedback is controlled by the phase between the two local oscillators which are locked to the same Rb frequency standard. The feedback gain is controlled by an amplifier and a chain of the attenuators. The attenuation of the custom-made voltage-controlled attenuator (*VCA* in the figure) can be controlled by varying its bias voltage. When the feedback line is not in use, the line is grounded by SPDT GaAs-FET switch (SW239) in the 4 K stage to prevent electromagnetic interference with ambient noise.

The properties of the detection system without application of the feedback are summarized in Table 9.3. The system exhibited one of the best performances among the axial detection systems which have been used in the BASE apparatus. The dip-width of a single antiproton $\Delta\nu_{z,\bar{p}}$ and the SNR are respectively 4.3 Hz and 29 dB, which are both sufficient for the measurement and give room

Table 9.3: Properties of the detection system without feedback.

Q-factor	≈ 22600
Effective parallel resistance R_{eff}	$\approx 159\,\mathrm{M\Omega}$
Single antiproton dip-width $\Delta\nu_{z,\bar{p}}$	$4.3(2)\,\mathrm{Hz}$
Single antiproton dip SNR	$29(2)\,\mathrm{dB}$
Effective temperature $T_{z,0}$	$10.1(1)\,\mathrm{K}$

for fine-tuning by using the electronic feedback.

9.3.1 Temperature control by the electronic feedback

Control of the effective temperature of the detection system is demonstrated in Fig. 9.8. Spectra of the detection system with a dip signal of single antiproton acquired under different conditions of the feedback are shown together. The attributes of the spectra extracted by fits are listed in Table 9.4. As the gain and phase of the feedback are tuned, they vary the Q-factor of the resonance and the dip-width $\Delta\nu_z$, as discussed in Section 2.4.3. The effective temperatures in relative to the temperature without feedback $T_{z,0}$ were evaluated using the relation below from Eq. (2.126)

$$\frac{\Delta\nu_{z,\mathrm{eff}}}{\Delta\nu_{z,0}} = \frac{T_{\mathrm{eff}}}{T_{z,0}}. \tag{9.15}$$

The feedback is used for trap characterization (Section 14.2.2) and for optimization of a measurement condition (Section 15.2.1).

9.3.2 Characterization of the tuning functionality

The tuning functionality of the detection system was characterized by evaluating spectra at different bias voltages set to the varactor. The results are shown in Figs. 9.9 and 9.10. The measurement was performed for the system without the feedback and with a negative feedback at $T_{z,\mathrm{eff}}/T_{z,0} = 0.555$.

The system has a sufficient tuning range to cover the axial frequency difference between the antiproton and the H^- ion. As shown in Fig. 9.10 (A), the resonance frequency can be tuned in a range $> 500\,\mathrm{Hz}$ by variation of the varactor bias voltage from 0 to 9 V (the maximum of the voltage applicable to the bias is 20 V). The reproducibility of the resonance frequency evaluated by the difference between the maximum and the minimum of the resonance frequency among 8 measurements was $< 2.5\,\mathrm{Hz}$ for feedback off, and $< 3.2\,\mathrm{Hz}$ for feedback on in the entire range of the varactor bias 0–9 V.

The system was thus demonstrated to have a tuning range sufficient and high reproducibility of the frequency.

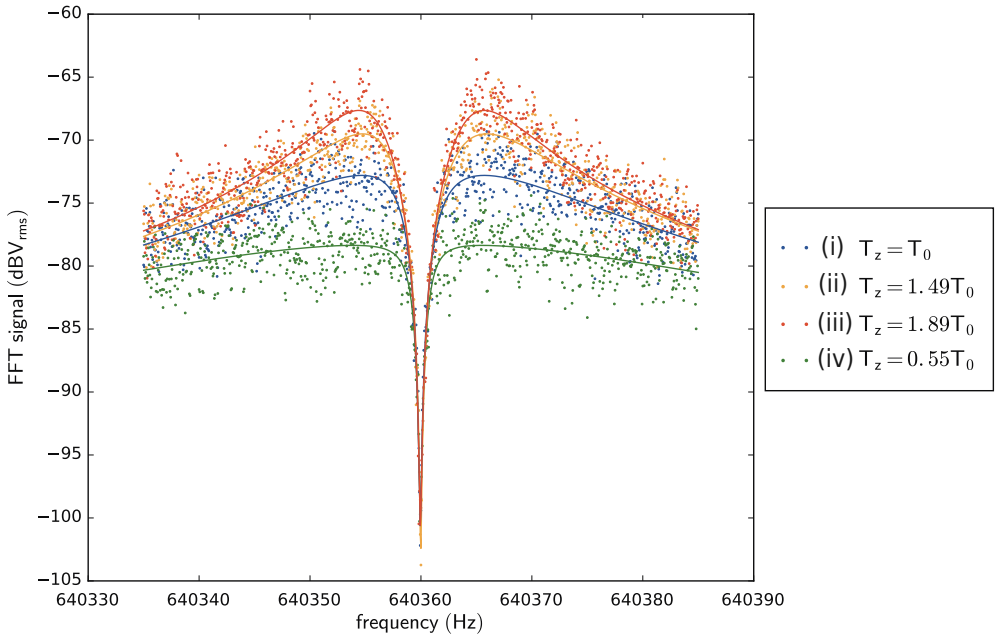

Figure 9.8: Spectra of the signal of the axial detection system with different feedback parameters. For each spectrum, the feedback settings and the parameters evaluated extracted by fits are listed in Table 9.4. The effective temperature of the detector was tuned in a range 0.6–1.9 in relative to the original temperature.

Table 9.4: Characteristics of the detection system corresponding to spectra in Fig. 9.8. The feedback setting of each condition is given in the first column. The gain was tuned by the bias voltage of the voltage-controlled attenuator (VCA). A smaller voltage of VCA corresponds to a smaller attenuation hence larger feedback gain. The phase of the feedback was set by the phase of the up-converting local oscillator (LO) (*L.O.2* in Fig. 9.7). The second to the fifth columns list the parameters of the system evaluated from fit of the dip signals. The effective temperature $T_{z,\mathrm{eff}}$ was evaluated from the single particle dip-width $\Delta\nu_{z,\bar{p}}$.

Feedback setting	SNR [dB]	Q-factor	Dip-width $\nu_{z,\bar{p}}$	Temperature $T_{z,\mathrm{eff}}$
(i) Feedback off	27.8	21300	4.0	$T_{z,0}$
(ii) Positive, VCA = 0.670 V	33.0	30800	6.0	$1.49 \cdot T_{z,0}$
(iii) Positive, VCA = 0.425 V	33.0	30800	7.6	$1.89 \cdot T_{z,0}$
(iv) Negative, VCA = −0.20 V	21.5	16600	2.2	$0.55 \cdot T_{z,0}$

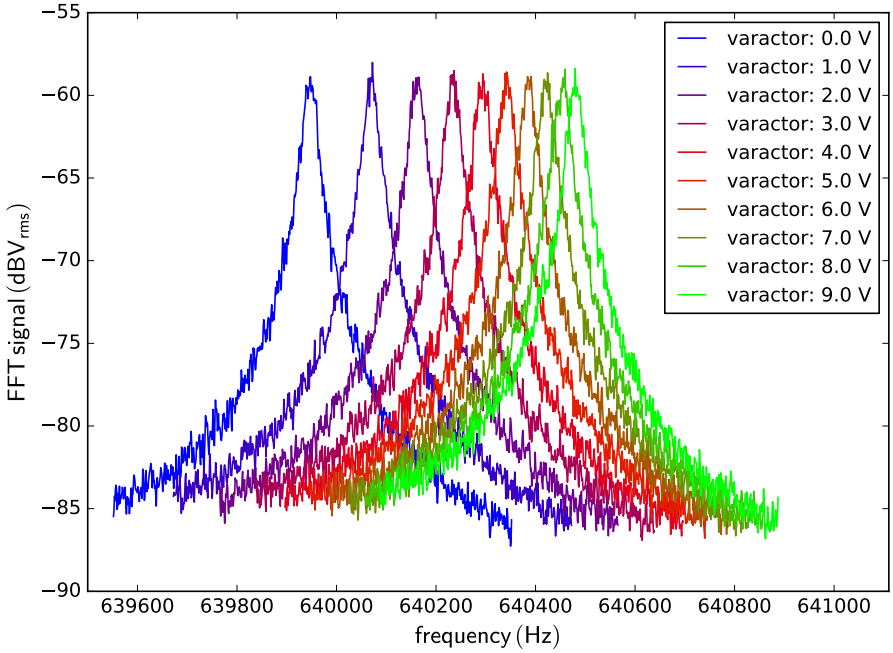

Figure 9.9: Spectra of the axial detection system with different bias voltages applied to the varactor. The dataset without feedback is presented here.

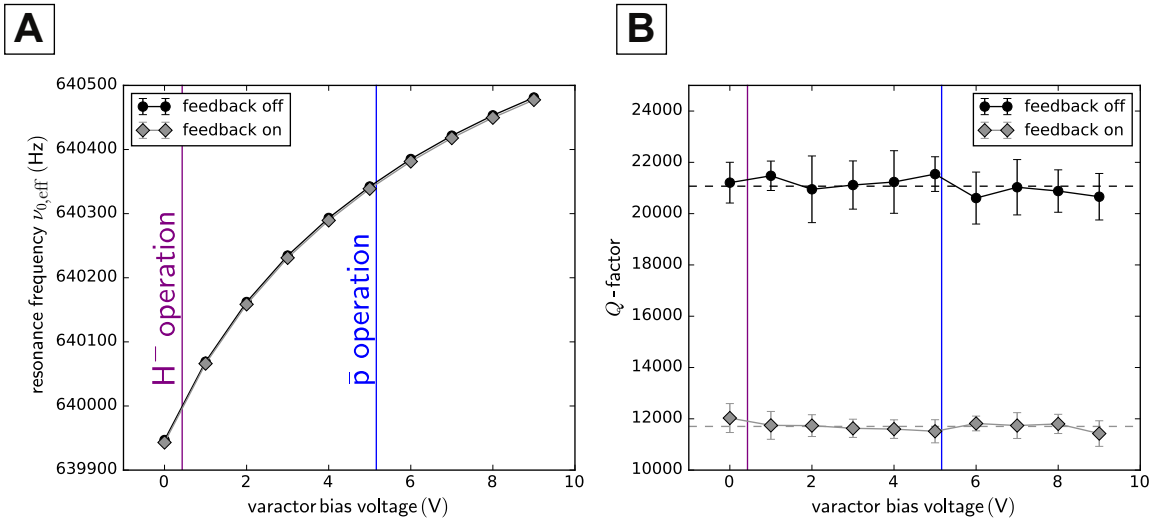

Figure 9.10: Characterization of the tuning functionality of the axial detector. The resonance frequency $\nu_{0,\mathrm{eff}}$ (A) and the Q-factor (B) were extracted from spectra such as shown in Fig. 9.9 recorded at different bias voltages of the varactor in a range of 0–9 V. The uncertainties were evaluated from standard deviations that were obtained by a repetition of 8 sets of measurements. The error bars of the plot (A) are hidden by the plot markers. The bias voltages chosen for measurements of the antiproton (blue) and the H^- ion (purple) are indicated by the vertical lines in the plots. The dashed lines of the plot (B) indicate the mean Q-factor of all the measurements for each of feedback on and off.

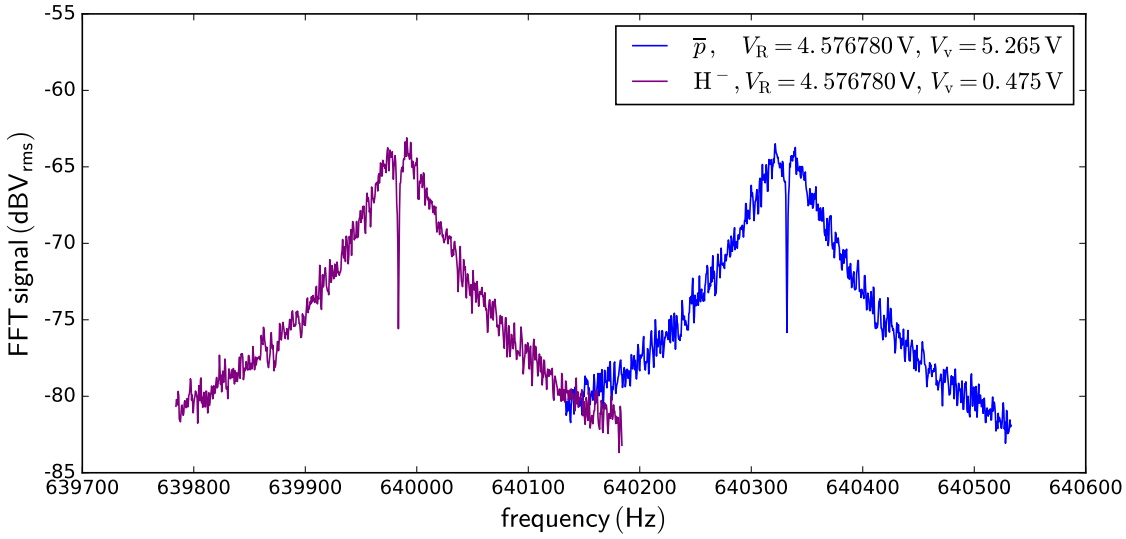

Figure 9.11: Demonstration of use of the tunable axial detection system. Axial dip signals of a single H^- and a single antiproton recorded in two subsequent measurements are plotted together. Between the two measurements, the particles were exchanged by transport operations. The varactor bias voltage was tuned between the two spectra from 0.475 V (H^-) to 5.265 V ($\bar{p}$), while the ring voltage V_R stayed constant at $V_R = 4.576\,780\,V$

The varactor biases at around 0.43 V and 5.2 V are respectively chosen for measurements of an H^- and an antiproton in actual measurement sequences. Examples of spectra recorded in alternate measurements are shown in Fig. 9.11, where spectra of axial dip signals of an H^- ion and an antiproton are recorded subsequently, with the varactor bias tuned and the particles exchanged between the measurements.

9.3.3 Temperature difference between the $\bar{p}$- and H^- operational conditions

In order to investigate a possible temperature difference between the $\bar{p}$- and H^- operational conditions, signal on the detection system in these two conditions were compared in detail.

The data used here was acquired by alternate measurements of the axial frequencies between an antiproton and an H^- ion with a native feedback corresponding to $\Delta\nu_{z,\bar{p}} \approx 2\,Hz$. For each axial dip spectrum, a fit to the model based on Eq. (2.111) was performed. An example of the spectrum acquired with a span of the FFT analyzer at 50 Hz is shown in Fig. 9.12. Indicated as P_{peak} in the figure corresponds to the signal height of the peak of the resonance of the detection system, can is obtained as one of the fit parameters. P_{peak} can be expressed as below in unit of power:

$$P_{peak} = 4k_B T R_{eff} f_b \cdot \kappa^2 G \tag{9.16}$$

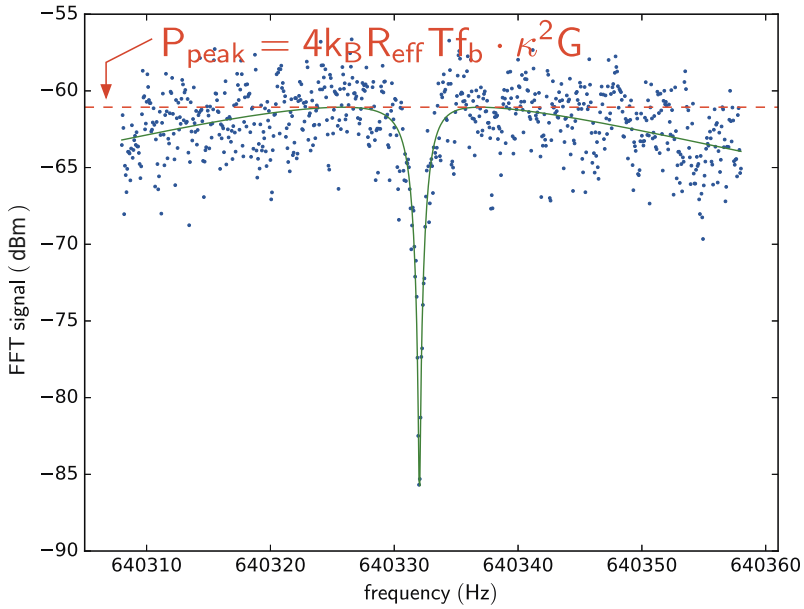

Figure 9.12: Example of a n FFT spectrum where a single dip by an antiproton in the resonance of the axial detection system recorded with a frequency span of 50 Hz. The signal level P_{peak} which corresponds to the peak of the resonance is indicated in the figure.

where κ is the coupling constant of the detection system as defined in Eq. (9.12), and G represents the gain of the amplifiers. The ratio of the temperatures during the $\bar{p}$- and H^- operational conditions can be expressed as

$$\frac{T_{\bar{p}}}{T_{\mathrm{H}^-}} = \frac{P_{\mathrm{peak},\bar{p}}}{R_{\mathrm{eff},\bar{p}}} \cdot \frac{R_{\mathrm{eff},\mathrm{H}^-}}{P_{\mathrm{peak},\mathrm{H}^-}}. \tag{9.17}$$

For the evaluation, FFT spectra simultaneously recorded with 50 Hz span and 400 Hz span were used. The spectra at 400 Hz were used to extract the Q of the resonance of the detection system at each condition, thereby determining $R_{\mathrm{eff},\bar{p}}$ and $R_{\mathrm{eff},\mathrm{H}^-}$ by $R_{\mathrm{eff}} = 2\pi\nu_{0,\mathrm{eff}}LQ$. $P_{\mathrm{peak},\bar{p}}$ and $P_{\mathrm{peak},\mathrm{H}^-}$ were extracted from 50 Hz-span spectra by fits as exemplified in Fig. 9.12. Part of the data is shown in Fig. 9.13. In Fig. 9.13 (A), P_{peak} is shown in unit of dBm for both of the antiproton data and H^- ion data. It can be observed that $\bar{p}$ data has higher level. In Fig. 9.13 (B), the difference due to $R_{\mathrm{eff},\bar{p}} and R_{\mathrm{eff},\mathrm{H}^-}$ is corrected by subtracting $10\log_{10}(R_{\mathrm{eff}})$. R_{eff} from P_{peak} in unit of dBm. For data of each index i, the temperature ratio in dB was obtained by

$$10\log_{10}\left(\frac{T_{\bar{p},i}}{T_{\mathrm{H}^-,i}}\right) = 10\log_{10}\left(\frac{P_{\mathrm{peak},\bar{p},i}}{R_{\mathrm{eff},\bar{p},i}}\right) - 10\log_{10}\left(\frac{P_{\mathrm{peak},\mathrm{H}^-,i}}{R_{\mathrm{eff},\mathrm{H}^-,i}}\right) \tag{9.18}$$

The distribution of $\log_{10}(T_{\bar{p}}/T_{\mathrm{H}^-})$ thus obtained from 2263 sets of data is shown in Fig. 9.13 (C). The obtained distribution has a width of 0.17 dB in the standard deviation. The center of the distribution was estimated to be $-0.023(4)$ dB. This corresponds to $T_{\bar{p}}/T_{\mathrm{H}^-} = 0.994\,(1)$. Therefore a possible bias of the temperatures between the two operational conditions is estimated to be about 0.6%.

In conclusion, the tunable system installed in the 2017 run demonstrated a sufficient tuning

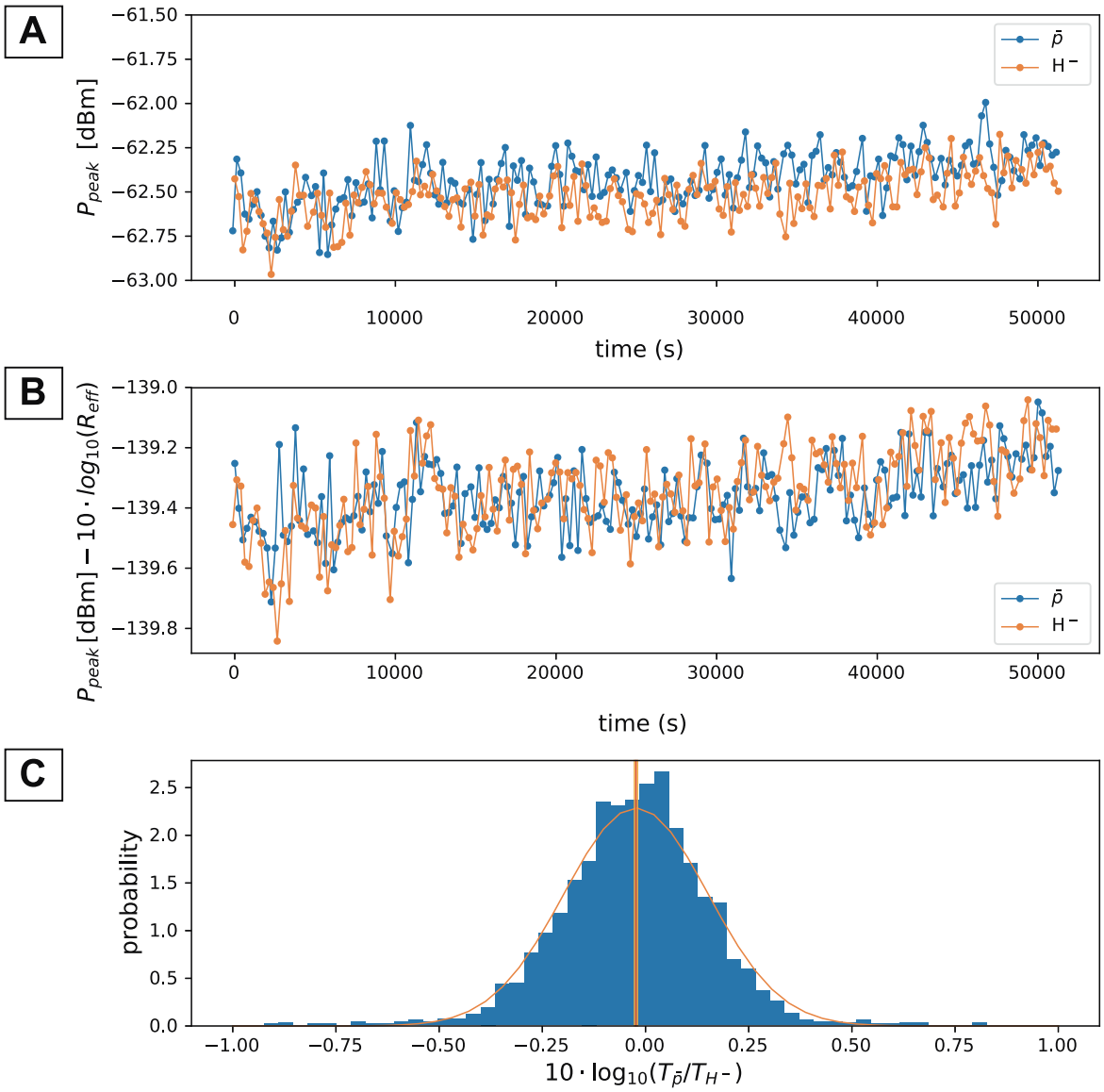

Figure 9.13: Comparison of the signal level P_{peak} between the $\bar{p}$- and H^- operational conditions. **(A)** The signal level P_{peak} in unit of dBm as s function of time. It can be observed that the signal level of the antiproton signal is slightly higher. **(B)** To correct the difference of the signal level due to the difference of R_{eff}, $10\log_{10}(R_{\text{eff}})$ is subtracted from P_{peak} [dBm]. R_{eff} was evaluated from the Q-factor of the resonance obtained by spectra recorded in 400 Hz span. **(C)** Distribution of the temperature ratio $T_{\bar{p}}/T_{H^-}$ in decibel. The center and the width of the distribution were evaluated by the mean and the standard deviation, to obtain the estimations $-0.023(4)$ dB and $0.174(4)$ dB, respectively. The center is indicated by the red vertical line, with its uncertainty range by the orange lines.

functionality for application to the improved comparison of proton-to-antiproton charge-to-mass ratio. The bias of the temperature between the operational conditions of an antiproton and an H^- ion was estimated to be below 1%, which constrains the associated systematic shifts to be $< 10^{-12}$ in relative to the cyclotron frequency. In Section 14.3, shifts of the $\bar{p}$-H^- cyclotron frequency ratio $R_{\bar{p}H^-}$ due to this temperature difference will be assessed based on the trap imperfection parameters characterized by measurements.

9.4 Influence of the magnetic field on the detection system

An accidental quench of the superconducting magnet occurred between 2017 run-I and run-II. Although unintended, this offered an opportunity to characterize the detection system installed in the cryogenic apparatus in the absence of the magnetic field.

In Fig. 9.14, data measured by the monitoring system are shown.Fig. 9.14 (A) shows the angle θ_h, the horizontal angle of the apparatus measured by accelerometers placed on the downstream- and upstream cryostat supports (see Section 11.1). In Fig. 9.14 (B), the ambient magnetic field measured by a Hall probe is shown. The moment of the quench is identified by the instantaneous change of the magnetic field, and the following mechanical movements appeared in the accelerometer data. The ambient magnetic field before quench was about 261 µT, it dropped to −14 µT after the quench.

Since a few minutes after the quench, FFT spectra of the PT axial detection system was being recorded. Evolution of the attributes of the detection system evaluated by the fitting of these spectra is shown in Fig. 9.14 (C, D). As seen in the plots, both the Q-factor and the SNR of the resonance increased significantly in a few minutes after the quench.

The properties of the PT axial detection system are compared before and after the quench in Table 9.5. Note here that components of PT detection system were replaced between run-I and run-II. Therefore the system characterized in this section was made of a different set of a resonator and an amplifier from the one which have been described until the last section. A characterization measurement of the detection system was performed 86 days before the quench, where spectra were recorded for two varactor bias voltages corresponding to $\nu_{0,\mathrm{eff}} = 515\,250\,\mathrm{Hz}$ and $515\,532\,\mathrm{Hz}$. The results are given in Table 9.5, and the corresponding spectra are shown in Fig. 9.15 as *reference 1* and *reference 2*, respectively.

The SNR was about 18 dB right before the quench, having slightly improved since the characterization measurement. The dip SNR evaluated from spectra at 50 Hz span recorded during the night before the quench is included in Table 9.5 as a reference.

The comparison reveals an increase of the Q-factor by a factor of 4, and an increase of the SNR by +10 dB in the absence of the magnetic field. Applying Eqs. (9.12) and (9.12), this corresponds to

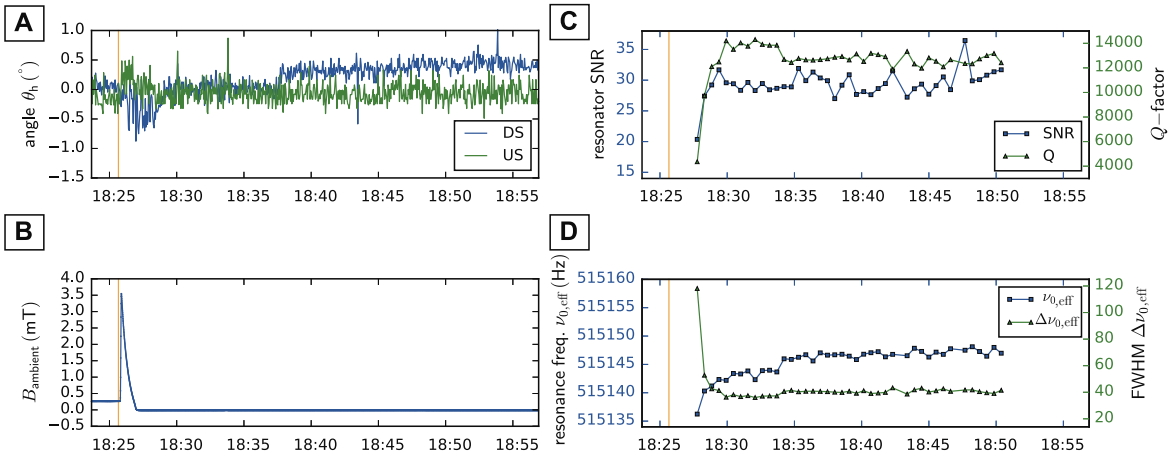

Figure 9.14: Data recorded around the time of the quench of the magnet. The orange lines indicate the moment of the quench estimated from the time of the magnetic field jump. **(A)** The angle θ_h, the horizontal angle of the apparatus measured by accelerometers attached on the cryostat supports (see Section 11.1). The offset of the angle of each series is subtracted. **(B)** Ambient magnetic field measured by the Hall probe. **(C,D)** Evolution of the attributes of the detection system. The spectra were recorded in 32 s averaging time, the time of the end of each averaging is shown as the horizontal value. **(C)** The SNR (the left axis) and the Q-factor (right axis) of the resonance. **(D)** The resonance frequency $\nu_{0,eff}$ (the left axis) and the FHWM of the resonance $\Delta\nu_{0,eff}$ (the right axis).

Table 9.5: Comparison of the properties of the PT axial detection system in run-I before and after the quench. The attributes from a reference measurement at two varactor bias voltages and the attributes after the quench are compared. The entry with * was evaluated from dip spectra recorded in 50 Hz span, while the spectra used in the three other columns were recorded in 1600 Hz span.

	Reference 1	Reference 2	Dip spectra	After quench
Resonance frequency $\nu_{0,eff}$	515 250(1) Hz	515 532(1) Hz	—	515 146.9(5) Hz
FWHM $\Delta\nu_{0,eff}$	165(4) Hz	182(5) Hz	—	41(1) Hz
SNR	15.6(3) dB	15.4(4) dB	18(3) dB*	29(1) dB
Q-factor	3130(86)	2839(82)	—	12 680(439)

an increase of R_{eff} by a factor of 4, and a reduction of e_n by a factor of 1.75. In other words, the presence of the magnetic field had suppressed the original characteristics of the system this much. This phenomenon was likewise observed for the other detection systems installed in the apparatus.

This seems to be attributed to an influence of the magnetic field to the FETs used in the amplifiers such as variation of the electron mobility by the Hall effect. For example, Ref. [180] discusses the Hall effect and the GMR effect on the mobility of a FET, and Ref. [181] assesses the influences of transverse magnetic fields to properties of the I-V curve of a GaAs MESFET and its dependency on the gate voltage.

These observations may give useful input to future works. One thing to be investigated is the dependence of performances of the amplifiers on the orientation of the of the drain-to-source channel of the their FETs with respect to the magnetic field.

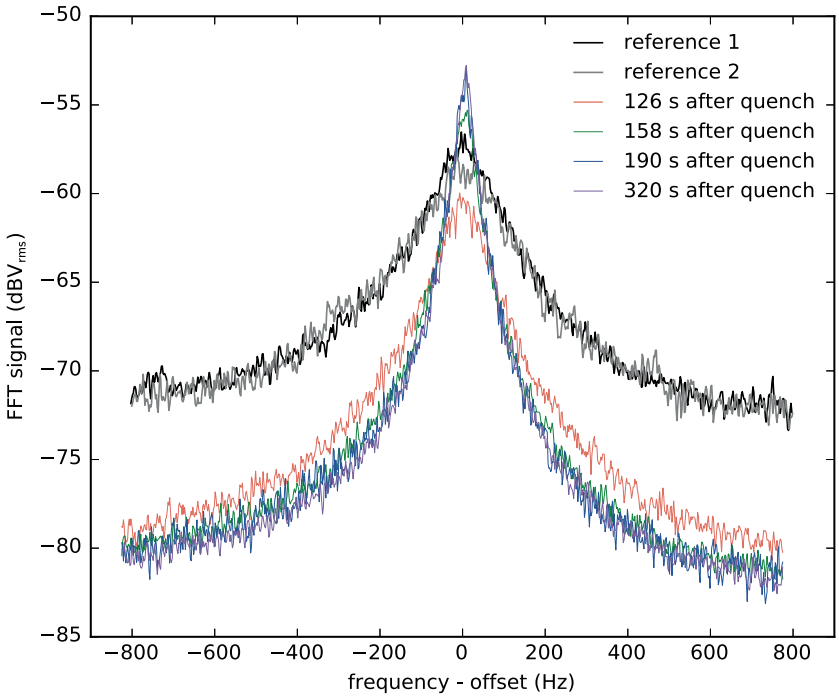

Figure 9.15: Evolution of the resonance of after the quench, corresponding to first three data points of Fig. 9.14 (C, D). Spectra from reference measurements are shown in back and gray colors. The offset frequency is 515 136 Hz for data after the quench, 515 247 Hz for *reference 1*, and 515 529 Hz for *reference 2*. The averaging time of the FFT is 32 s for the spectra after the quench, 120 s for the reference spectra. The time (at the end of averaging) since the quench is shown in the legend. The difference of the floor levels between the reference spectra and the spectra after the quench are due to differences in the setup.

10

Magnetic shielding by the self-shielding solenoids

Shielding of magnetic field fluctuations is an essential ingredient of the experiment, especially because the apparatus is located in an accelerator facility. The 2014 charge-to-mass ratio comparison was performed in an environment of the shielding factor of about 10, provided by an intrinsic shielding of a superconducting magnetic used at the time [75].

To improve the magnetic field stability, a new magnetic shielding system has been designed and installed as a part of this thesis work. The principle of the system is based on the idea of a self-shielding superconducting solenoid which was first proposed and constructed by G. Gabrielse and J. Tan in 1988 [182, 183]. It played an important role in the charge-to-mass ratio comparisons by the TRAP collaboration at the low-energy antiproton ring (LEAR) facility [114, 116, 147].

In 2015, such a self-shielding solenoid was designed and constructed for the BASE magnetic moment measurement run in 2015/2016. At the time, the performance was not as good as expected due to insufficient knowledge of the mutual inductances between the shielding coil and the coils of the superconducting magnet. To address this issue, a new shielding system consisting of three individual self-shielding solenoids has been implemented for the 2017 run.

In this chapter, the principles, designs and the performances of the self-shielding systems are summarized. The chatter is structured as follows.

In Sections 10.1 and 10.2 first discuss principle and the theoretical treatments of self-shielding systems. Firstly the case of a single solenoid Section 10.1.1, and then a coupled system of two solenoids. Analytical solutions and simulations by finite element methods (FEM) are used as tools. One issue to be treated in case FEM simulations are used is discussed in Section 10.1.2.

In Sections 10.4 and 10.5, actual shielding systems installed in the experiment are discussed. Section 10.4 summarizes the construction procedures. The results of experimental characterizations

of the system are presented in Section 10.5.

10.1 Single self-shielding solenoid

10.1.1 Principle of the single self-shielding solenoid

In the following, the principle of a self-shielding solenoid discussed in the original paper [182] is summarized.

We treat a closed, persistent single layer superconducting solenoid coil as illustrated in Fig. 10.1. It models a geometry of a solenoid made by densely winding wire of the diameter d (including the insulation) on a core of the radius R. The cylindrical coordinate system as defined in the figure.

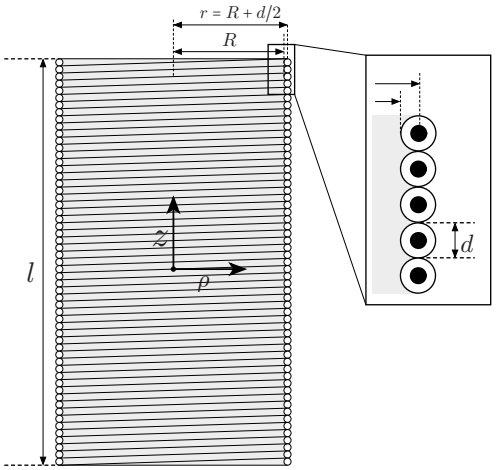

Figure 10.1: Geometry of a densely wound, single layer solenoid.

When the external magnetic field B_{ex} changes, an induced current I_c flows in the coil to produce the magnetic field B_c. Their relation is found by considering a closed circuit with zero-resistance as:

$$\int_{A_c} (B_{\mathrm{ex}} + B_{\mathrm{c}})\,\mathrm{d}A = 0.. \tag{10.1}$$

$\int_{A_c} \mathrm{d}A$ expresses a surface integral over the integrated surface A_c of the cross sections of the coil. Though the right hand side of Eq. (10.1) is not 0 in case there is a persistent field before the change B_{ex} occurs, we can redefine the original integrated flux as 0 without using losing generality.

The shielding factor at the center of the coil S is defined as

$$S = \frac{B_{\mathrm{ex}}(0,0)}{B_{\mathrm{ex}}(0,0) + B_{\mathrm{c}}(0,0)} \tag{10.2}$$

Using the flux conservation Eq. (10.1), this can be rewritten as

$$\begin{aligned} S^{-1} &= 1 + \frac{B_{\mathrm{c}}(0,0)}{B_{\mathrm{ex}}(0,0)} \\ &= 1 - \frac{B_{\mathrm{c}}(0,0)}{\int_{A_c} B_{\mathrm{c}}(\rho,z)\mathrm{d}A} \cdot \frac{\int_{A_c} B_{\mathrm{ex}}(\rho,z)\mathrm{d}A}{B_{\mathrm{ex}}(0,0)} \\ &= 1 - \frac{\overline{b}_e}{\overline{b}_c}, \end{aligned} \tag{10.3}$$

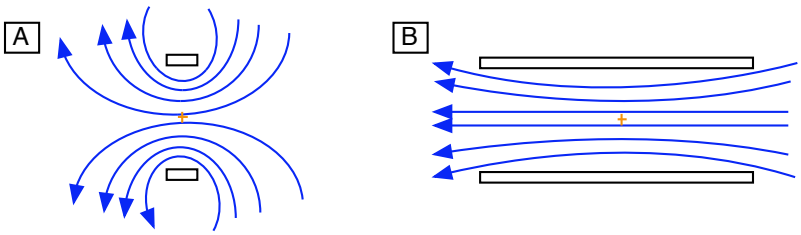

$B_c(0,0) < \overline{B_c}$ $\quad$ $B_c(0,0) > \overline{B_c}$

$\bar{b}_c > 1$ $\quad$ $\bar{b}_c < 1$

Figure 10.2: Magnetic field lines in two cases of the geometry of a solenoid coil. (A) For a short solenoid, the magnetic field near the windings is stronger than the field near the center, therefore $\bar{b}_c > 1, S > 0$ (B) For a long solenoid, the field in the bore is weaker than the field at the center because of the fringing field at its ends. Therefore $\bar{b}_c < 1, S < 0$.

with $\bar{b}_e, \bar{b}_c$ defined as

$$\begin{aligned} \bar{b}_e &= \frac{\int_{A_c} B_{\mathrm{ex}}(\rho, z)\mathrm{d}A}{B_{\mathrm{ex}}(0,0)\int_{A_c}\mathrm{d}A}, \\ \bar{b}_c &= \frac{\int_{A_c} B_{\mathrm{c}}(\rho, z)\mathrm{d}A}{B_{\mathrm{c}}(0,0)\int_{A_c}\mathrm{d}A}. \end{aligned} \tag{10.4}$$

Now, if we limit the discussion to a spatially uniform external field B_{ex}, leading to $\bar{b}_e = 1$, Eq. (10.4) becomes

$$S^{-1} = 1 - \frac{1}{\bar{b}_c}. \tag{10.5}$$

Thus it can be observed that the perfect shielding $S^{-1} = 0$ is realized at $\bar{b}_c = 1$ when the magnetic field at the center is equal to the averaged field over the coil volume. As illustrated in Fig. 10.2, when the coil is short and the spatial profile of the magnetic field can be approximated by a superposition of circular coils (Fig. 10.2 (A)), the magnetic field near the windings is larger than the field near the center; therefore $\bar{b}_c > 1, S > 0$. On the other hand, in case of Fig. 10.2 (B) where the coil is long and becomes close to an ideal solenoid, the field at the center can be approximated by that of an infinitely long solenoid, while there are stray fields which escape at the edges of the coil, resulting the field at the center to be stronger than the averaged field; therefore $\bar{b}_c < 1, S < 0$. Between these two cases, there is an optimized length of the coil which realizes a perfect shielding $S^{-1} = 0$.

Eq. (10.4) can be further simplified. Dependencies on the currents of the flux and the magnetic field at the center can be denoted by introducing g_c, L_{cc}:

$$g_c I_c \equiv B_{\mathrm{c}}(0,0) \tag{10.6}$$

$$L_{cc} I_c \equiv \int_{A_c} B_{\mathrm{c}}(\rho, z)\,\mathrm{d}A, \tag{10.7}$$

where L_{cc} represents the self inductance of the coil. Using them, Eq. (10.3) is rewritten to be

$$S^{-1} = 1 - \frac{g_c A_c}{L_{cc}}, \tag{10.8}$$

$$A_c \equiv \int_{A_c} \mathrm{d}A. \tag{10.9}$$

For a dense solenoid of N windings, A_c is

$$A_c = \int_{A_c} \mathrm{d}A = N\pi r^2. \tag{10.10}$$

The analytical solutions of g_c and L_{cc} for the geometry of Fig. 10.1 are found to be [184]

$$g_c = \frac{\mu_0 \epsilon}{d\sqrt{1+\epsilon^2}}, \tag{10.11}$$

$$L_{cc} = \frac{8\mu_0 \epsilon r^3}{d^2} \int_0^\infty \left(\frac{\sin u}{u}\right)^2 I_1\left(\frac{u}{\epsilon}\right) K_1\left(\frac{u}{\epsilon}\right) \mathrm{d}u. \tag{10.12}$$

μ_0 is the permeability of vacuum and ϵ is defined by

$$\epsilon \equiv \frac{l}{2r}, \tag{10.13}$$

$I_1(x)$ and $K_1(x)$ are the modified Bessel functions of the first and the second kinds. The solution Eq. (10.11) of g_c is obtained by the Ampère's law

$$\boldsymbol{A}(\boldsymbol{r}) = \frac{\mu_0}{4\pi} \int \frac{\boldsymbol{j}(\boldsymbol{s})}{|\boldsymbol{r}-\boldsymbol{s}|} \mathrm{d}^3 s \tag{10.14}$$

and Eq. (10.12) of L_{cc} by its relation with the magnetic energy

$$W = \frac{1}{2} L I^2 = \frac{\mu_0}{8\pi} \int\int \frac{\boldsymbol{j}(\boldsymbol{r}) \cdot \boldsymbol{j}(\boldsymbol{s})}{|\boldsymbol{r}-\boldsymbol{s}|} \mathrm{d}^3 r \mathrm{d}^3 s, \tag{10.15}$$

with the radial integration range chosen to be $[0, r]$, thus ignoring the thickness of the wire. Using Eq. (10.11) and Eq. (10.12), the analytical expression of S^{-1} is obtained to be

$$S^{-1} = 1 - \frac{\epsilon}{\sqrt{1+\epsilon^2}} \cdot \left(\frac{4}{\pi} \int_0^\infty \mathrm{d}u \left(\frac{\sin u}{u}\right)^2 I_1\left(\frac{u}{\epsilon}\right) K_1\left(\frac{u}{\epsilon}\right) \right)^{-1}. \tag{10.16}$$

The scaling of S^{-1} is shown in Fig. 10.3. The length-to-radius ratio l/r which realizes a perfect shielding $S^{-1} = 0$ is about $l/r \approx 1.75$. Since Eq. (10.16) is expressed as a function of ϵ, this scaling is robust against each of the geometrical parameters as long as the radius is large enough compared to the diameter of the wire, that is to say $d/R \ll 1$ [184].

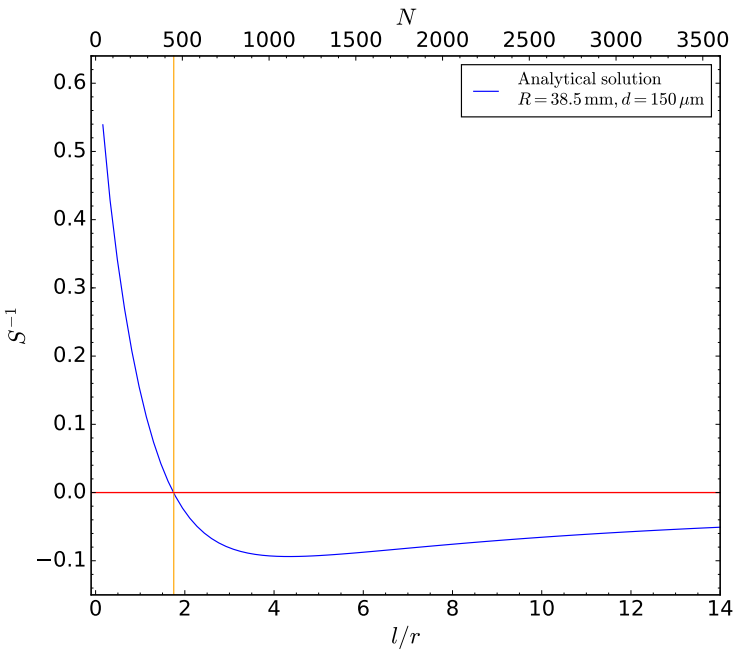

Figure 10.3: Scaling of the inverse shielding factor S^{-1} obtained by the analytical solutions Eqs. (10.11) and (10.12) for the geometry of Fig. 10.1. S^{-1} is evaluated for different turn (length) of the coil with the fixed radius defined by $R = 38.5\,\mathrm{mm}, d = 150\,\mu\mathrm{m}$. At $l/r = 1.752$, the curve of S^{-1} crosses zero.

10.1.2 Comparison of the finite element methods and the analytical solutions

A simulation based on the finite element method (FEM) is a useful tool for evaluation of magnetic fields and inductances. This has been employed by previous studies which adapted the self-shielding coils to Penning trap experiments [185, 186] to obtain the scaling of the shielding factor discussed in the last section. However, the values of l/r for the perfect shielding reported by these works are smaller than what is obtained from the analytical solution (1.72 for both of Refs. [185, 186]).

Before applying the FEM simulation to our study, a limitation of the finite element method was assessed by systematic comparisons against the analytical solutions.

A finite element analysis software COMSOL Multiphysics 5.2[1] was used for finite element magnetic field simulations.

Simulation details

The two-dimensional axis-symmetric geometry of the single layer solenoid of Fig. 10.1 with $R = 38.5\,\mathrm{mm}, d = 150\,\mu\mathrm{m}$ was modeled on COMSOL as shown in Fig. 10.4. The node in the figure indicated as 'multi-turn coil' is specified as the cross-section of the winding of the coil using the module *multi-*

[1] A previous version of the same software was used in Ref. [185].

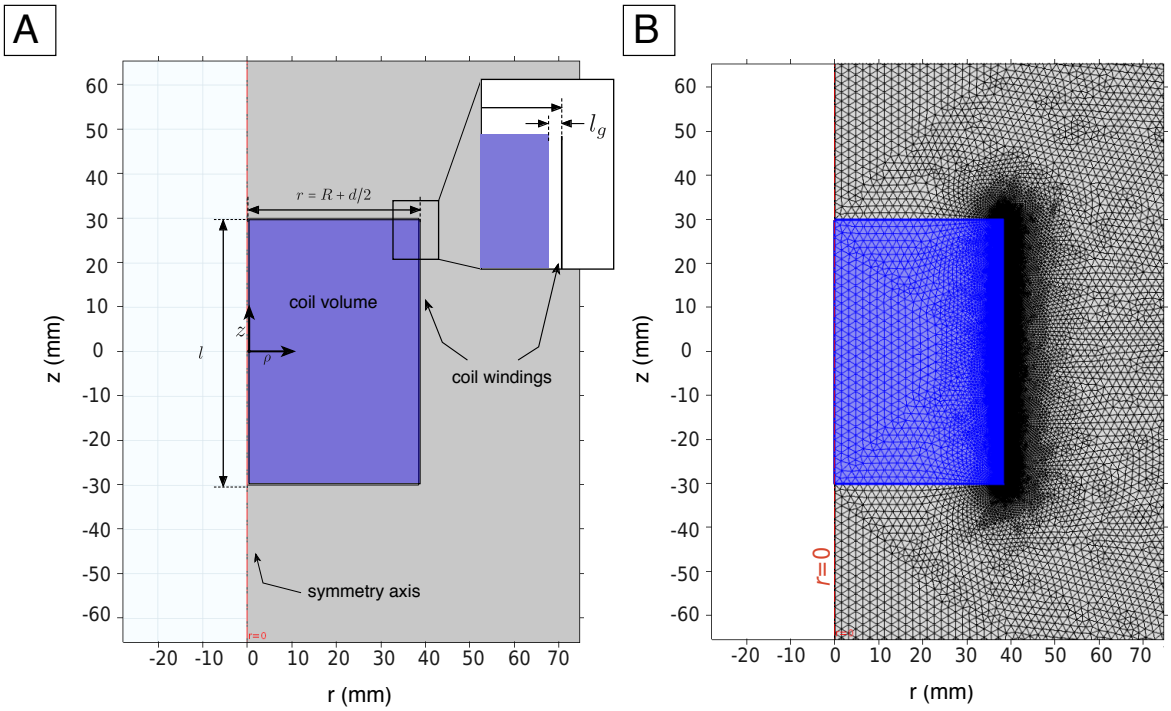

Figure 10.4: Geometry modeled on COMSOL. **(A)** On the axis-symmetric model, the node indicated as 'coil windings' in the figure is specified as the cross-section of the coil windings. The domain 'coil volume' is defined as a domain where the volume integral of the magnetic field flux is evaluated. The gap of l_g is inserted between the coil volume and the coil to avoid an overflow of the calculation. **(B)** Free triangular meshes built by the software for the geometry of $N = 400$. The meshes were rebuilt for each set of the geometrical parameters.

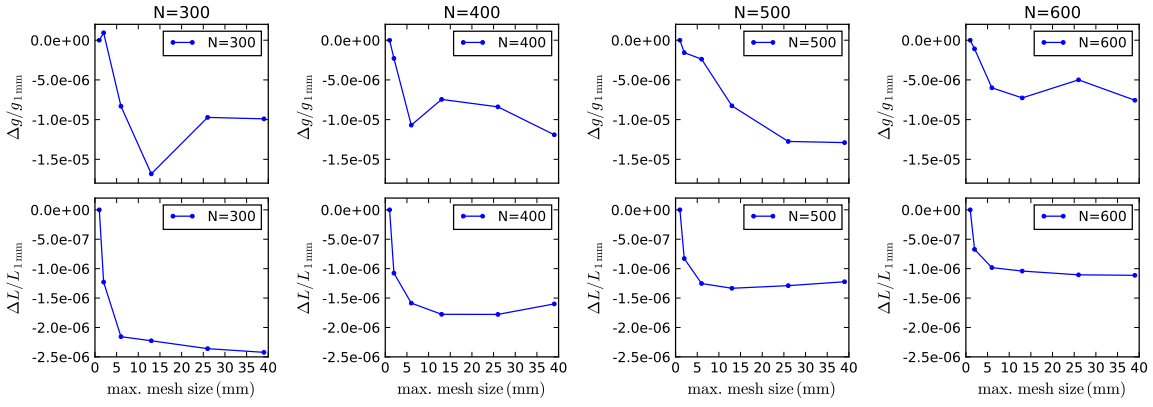

Figure 10.5: Scatters of g_c and L_c in dependence of different inputs of mesh processing are estimated. The maximum mesh element size is swept while the other input parameters are fixed. Relative difference from the result with smallest maximum mesh size used (1 mm) are plotted. This was repeated for different N. The relative differences between different mesh sizes are on the order of 10^{-5} for g_c and 10^{-6} for L_{cc}.

turn coil on COMSOL with the corresponding parameters assigned (turn N, the current I_c, the cross-sectional area of the wire, etc.). This module models a coil by a homogenized current circulates in a radial direction of an input region.

The g_c is simply evaluated by $B_{c,z}(0,0)/I_c$. The self-inductance L_{cc} is evaluated from a volume integral of the magnetic field flux in the volume of the coil $\int_{V_i} B_c(\rho, z)dV$. Since the winding is dense, it is obtained by

$$L_{cc} = \frac{1}{I_c}\int_{A_c} B_c(\rho, z)\,\mathrm{d}A = \frac{1}{I_c}\frac{N}{l}\int_{V_c} B_{c,z}(\rho, z)\,\mathrm{d}V. \tag{10.17}$$

The volume integral $\int_{V_c} dV$ is to be evaluated in the entire volume inside the coil. However, a finite gap between the coil segment and the end of the volume must be inserted in order to prevent the calculation to overflow. The gap is indicated in Fig. 10.4 with the distance l_g. In the following section, the systematics from this gap will be studied in details. The simulation was done for l_g (62.5 , 93.8 , 125 , 156 μm) to evaluate the systematics. The smallest among them 62.5 mm corresponds to the inner radius of the superconducting wire used to construct the shielding coil in 2017. The turn N was swept in a range of 200 to 800, corresponding to l/r from 0.78 to 3.11

Before the systematic comparison between different geometries, uncertainties of g_c, L_{cc} from the mesh size were assessed by comparing results of different mesh sizes for fixed geometries. The free triangular meshes built by the software are shown in Fig. 10.4 (B). The process to build mesh is automatic, but can be controlled by user-defined parameters. One of them, the maximum mesh element size, was swept between 1 mm and 39 mm. The obtained results of g_c and L_{cc} from different mesh parameters were compared to estimate the uncertainties by meshing. The results are shown in Fig. 10.5, where the relative differences of g_c and L_{cc} from the results obtained by the smallest maximum mesh element size 1 mm are plotted against the element size. From these, the uncertainties from meshing are estimated to be on the order of

$$\frac{\Delta g_c}{g_c} \sim 10^{-5}, \quad \frac{\Delta L_{cc}}{L_{cc}} \sim 10^{-6}. \tag{10.18}$$

They are a few orders of magnitude smaller than what is of concern in the discussion in the following sections. The maximum mesh element size of 2 mm was used in COMSOL simulations in the rest of the chapter.

Results of the finite element simulation and comparison against the analytical solutions

The results of the FEM simulations and the comparison against the analytical solutions are shown in Figs. 10.6 and 10.7. Fig. 10.6 shows the difference of the simulation's g_c and L_{cc} from that of the analytical solutions for each turn N as functions of the gap l_g set in the simulation. Fig. 10.7 shows the scaling of g_c, L_{cc} and S^{-1} against the length of the coil.

In Fig. 10.6, we see that the simulation constantly underestimates g_c by 4×10^{-3} to 5×10^{-3} in the fractional difference, while the difference is robust against the gap l_g within a range of 10^{-5} in the fractional difference (note a difference of units of the axes between $g_c - g_{c,\mathrm{anal.}}$ in Fig. 10.6 and g_c in Fig. 10.7). As for L_{cc}, it is observed that the simulation systematically underestimates the inductance and that the deviation from the analytical solution clearly scales with l_g. This means that the volume which is missed by insertion of the gap significantly influences the evaluated flux. Though the size of the gap is small ($l_g < 160\,\mu$m compared to $R = 38.5\,$mm), it results in errors of L_{cc} on % order, as it fails to evaluate the flux of the region close to the windings where the magnetic field is strong. For each series of turn N, L_{cc} at $l_g = 0\,\mu$m was evaluated by extrapolating the linear scaling of $L_{cc}(l_g)$ to $l_g = 0$. The series $l_g = 0\,\mu$m of S^{-1} ((Fig. 10.7 (C))) was derived from thus evaluated $L_{cc}|_{l_g=0\,\mu\mathrm{m}}$, together with $g_c|_{l_g=62.5\,\mu\mathrm{m}}$.

In Fig. 10.7 (A–C), the scalings of g_c, L_{cc} and S^{-1} against l/r are plotted to compare the FEM and the analytical solutions. In Fig. 10.7 (D–F), the scaling of the differences in the results between the two methods. The observations can be summarized as below:

- The FEM constantly underestimates g_c, and it does not depend on l/r within relative differences on the order of 0.1 %.
- The FEM underestimates L_{cc} more significantly than g_c. A characteristic l dependent scaling is observed: longer the length l is, the FEM results deviate more from the analytical solutions. This is clear from how the inductance is evaluated. The flux missed in evaluation accumulates as the dimension grows.
- Because the FEM underestimates L_{cc} significantly, it lowers the curve of S^{-1}, therefore shifting the cross point of the curve S^{-1} with 0 to a lower l/r.
- The correction by the extrapolation performed for the series $l_g = 0$ significantly improves the agreement between the simulation and the analytical solution. The scaling of S^{-1} in Fig. 10.7 (C, F), relative differences with the corrected simulation results from the analytical solution are estimated to be below $< |0.2\%|$.

In Table 10.1, how these deviations of the FEM from the analytical solution appear in parameters which are important in the scaling of the shielding factor. Denoting l/r which gives $S^{-1} = 0$ as $(l/r)_0$, the shift of the cross point is estimated by

$$(l/r)_{0,\mathrm{FEM}} - (l/r)_{0,\mathrm{anal.}} = -\left(\frac{\mathrm{d}S^{-1}(l/r)}{\mathrm{d}(l/r)}\bigg|_{S^{-1}=0} \right)^{-1} \left(S^{-1}_{\mathrm{FEM}} - S^{-1}_{\mathrm{anal.}}\right)\big|_{S^{-1}\approx 0}\,. \tag{10.19}$$

From the differential coefficient of S^{-1} obtained by the analytical expression Eq. (10.3) and the difference $(S^{-1}_{\mathrm{FEM}} - S^{-1}_{\mathrm{anal.}})\big|_{S^{-1}\approx 0}$ estimated from data of $N = 400$ (because $S^{-1}_{\mathrm{FEM}} - S^{-1}_{\mathrm{anal.}}$ plateaus between $N = 400$ and 500. See Fig. 10.7 (F)), the difference of the optimum length-to-radius ratio

Table 10.1: Results of the FEM simulation in comparison to the analytical solutions. Listed for different l_g, the gap defined in Fig. 10.4. The differences of the shielding factor S^{-1} and the optimum length-to-radius ratio $(l/r)_0$, are on the second and the third columns. The last column is the $S_{\text{anal.}}$ at $l/r = (l/r)_{0,\text{FEM}}$, signifying how much S will be if the optimum length according to the FEM is adapted, assuming the analytical solution to be correct. The difference of S^{-1} on the second column is obtained for a fixed geometry of $N = 400$, corresponding to $l/r \approx 1.56$. As can be observed in Fig. 10.7 (F) the difference $S^{-1}_{\text{FEM}} - S^{-1}_{\text{anal.}}$ at $S^{-1} = 0$ is about the same as that of $N = 400$.

l_g (μm)	$S^{-1}_{\text{FEM}} - S^{-1}_{\text{anal.}}\big\vert_{N=400}$	$(l/r)_{0,\text{FEM}} - (l/r)_{0,\text{anal.}}$	$S_{\text{anal.}}\vert_{l/r=(l/r)_{0,\text{FEM}}}$
0	-3.37×10^{-4}	-0.0027	2934
62.5	-4.29×10^{-3}	-0.0340	228
93.75	-6.00×10^{-3}	-0.0476	162
125.0	-7.90×10^{-3}	-0.0627	122
156.25	-9.81×10^{-3}	-0.0770	97.2

$(l/r)_{0,\text{FEM}} - (l/r)_{0,\text{anal.}}$, and $S_{\text{anal.}}(l/r = (l/r)_{0,\text{FEM}})$, that is, the S which one gets by designing the system based on the FEM result, are obtained, and compared in Table 10.1.

The difference $(l/r)_{0,\text{FEM}} - (l/r)_{0,\text{anal.}} = -0.0340$ for $l_g = 62.5\,\mu$m, corresponding to $(l/r)_{0,\text{FEM}} = 1.718$ is comparable to the deviations of the previous studies [185, 186] from the analytical solution. If the effect of the gap studied here is responsible for them, it is likely that these deviations were caused by underestimations of L_{cc} by the integral volume defined smaller than the entire volume by about a thickness of the wire diameter.

From Table 10.1, it can be also observed how sensitive these deviations are to the resulting shielding factors. Even the underestimations of S^{-1} on the order of 10^{-3} leads to large differences in the shielding factor S, in case $S^{-1} \sim 0$ (Table 10.1).

In conclusion, the FEM simulation underestimates the inductance L_{cc} because of a part of the volume not included in the evaluation of the magnetic field flux. This consequently gives a smaller value of the optimum length-to-radius ratio $(l/r)_0$ than the analytical solution by percent order. By dealing with the underestimation using the scaling of the inductance against the evaluated volume, this deviation is suppressed to the order of $\Delta(l/r)_0 \sim 10^{-3}$. This study is nothing more than to verify the consistency between the FEM simulation and the analytical solution. However, with the problem properly treated, the FEM simulation can now be applied to broader cases (such as the discussion in Section 10.1.3) where the analytical solutions of the magnetic field and inductance are not available. Also, the treatment to suppress the error of the FEM simulation used above can be applied to more general cases of FEM simulations.

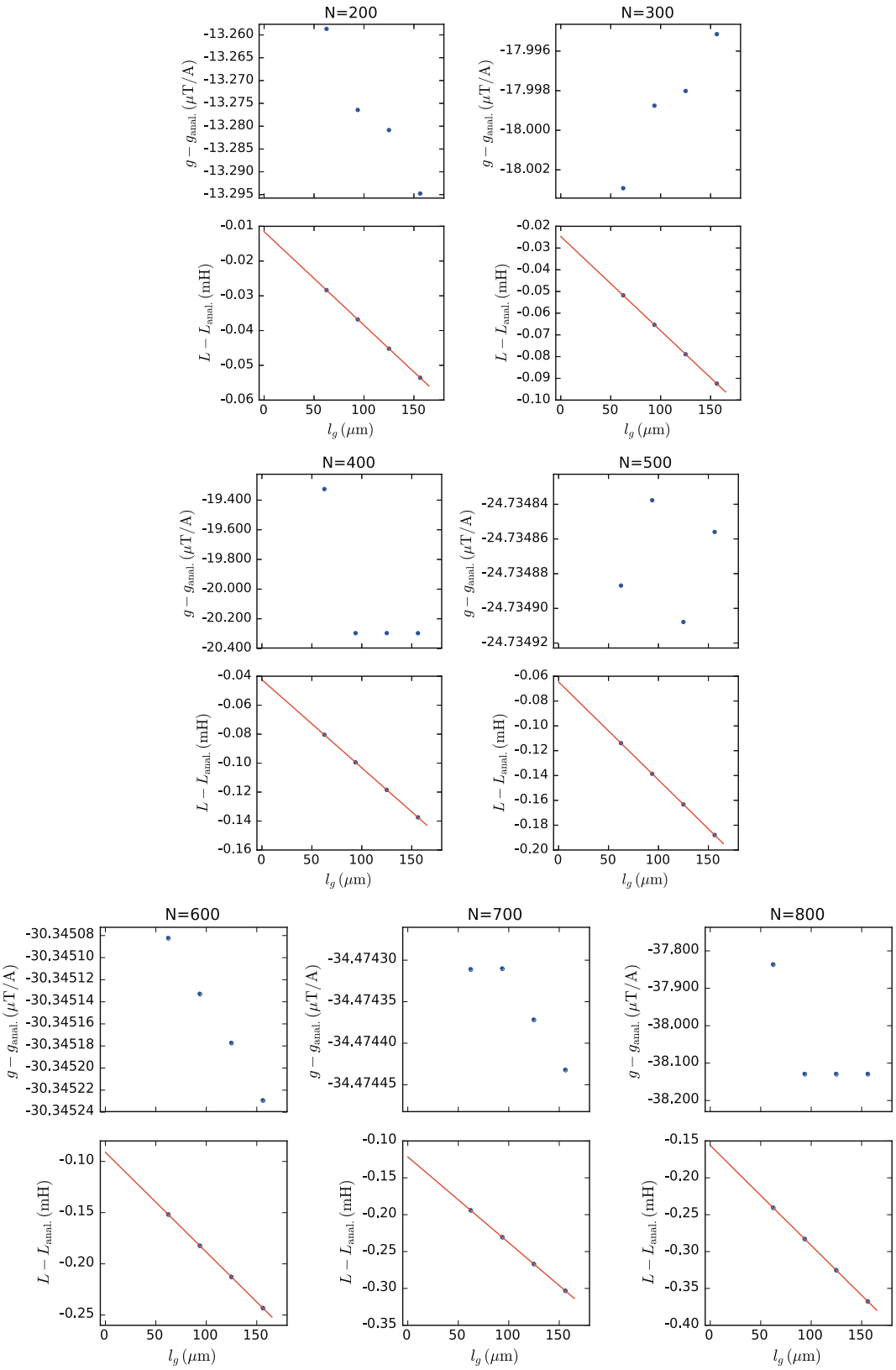

Figure 10.6: Comparison of g_c and L_{cc} between the finite element simulation and the analytical solutions. For each turn N, the difference of estimated g_c and L_{cc} from the analytical solutions are plotted against the gap l_g set on the simulation. For the absolute values of g_c and L_{cc}, see Fig. 10.7. For each N, the scaling of $L - L_{\mathrm{anal.}}$ against l_g is fitted by a straight line to estimate L_{cc} at $l_g = 0\,\mu$m.

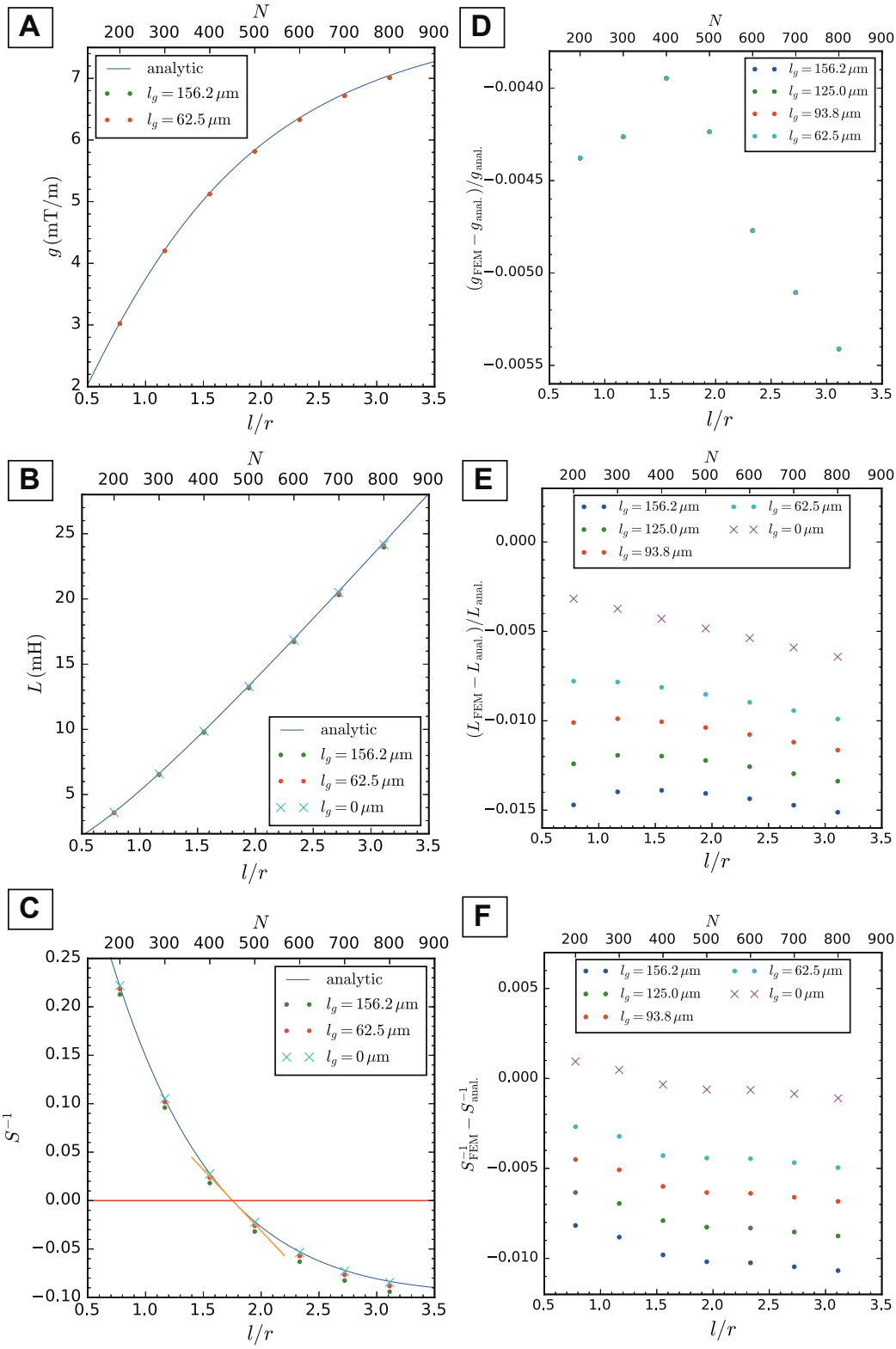

Figure 10.7: **(A–C)** g_c, L_{cc} and S^{-1} obtained by the FEM simulations are plotted as functions of the length-to-radius ratio l/r with their analytical solutions. **(D–F)** Difference between the simulations and the analytical solutions are plotted. For (D,E) in unit of relative differences, and for (F) difference $S^{-1}_{\mathrm{FEM}} - S^{-1}_{\mathrm{anal.}}$. Plotted with markers 'x' in (B, E) are L_{cc} for $l_g = 0\,\mu$m obtained by the extrapolation of data in Fig. 10.6. The series 'x' in (C, F) are obtained from the $L_{cc}|_{l_g=0\,\mu\mathrm{m}}$ and $g_c|_{l_g=62.5\,\mu\mathrm{m}}$. In (C), $S^{-1} = 0$ is marked by the red horizontal line. The tangent line of the analytical S^{-1} at $S^{-1} = 0$.

10.1.3 Position dependence of the shielding factor

The shielding factor at an off-centered position can be obtained by simply replacing g_c in Eq. (10.9) to $g_c(\rho, z)$ defined as

$$g_c(\rho, z) \equiv \frac{B_c(\rho, z)}{I_c}. \tag{10.20}$$

By replacing g_c of Eq. (10.9) to $g_c(\rho, z)$, $S^{-1}(\rho, z)$ is obtained as

$$S^{-1}(\rho, z) = 1 - \frac{g_c(\rho, z) A_c}{L_{cc}}. \tag{10.21}$$

Plots in Fig. 10.8 show z- and ρ-scaling of $S^{-1}(z, \rho)$.

$g_c(\rho, z)$ was evaluated by the magnetic field map obtained by the FEM simulation discussed in the last section. To evaluate L_{cc}, the ones for $l_g = 0\,\mu$m was obtained by the extrapolation of the FEM simulation results of $l_g > 0$, as discussed in the last section.

In Fig. 10.8 (B) and (D) the scalings of S are shown as functions of the position. The deviation from the shielding factor at the center starts to be significant from the offsets of $\sim 5\,$mm. This can be taken as a required level of precision for positioning of the center of the shielding coils in respect of the center of the Penning trap.

10.2 Coupled self-shielding solenoids

10.2.1 Principles of the coupled self-shielding solenoids

In a realistic case when a self-shielding coil is installed in the experiment, coupling with existing superconducting coils have to be taken into account. Hence the model treated in the last sections has to be expanded to include the mutual inductances between multiple coils. As will appear later, the couplings change the scaling of the shielding factor drastically.

Suppose a system consists of two superconducting solenoid coils where an external magnetic field penetrates both of them and induce currents. By redefining terms B_c, I_c etc. in Section 10.1.1 with indices $i = 1, 2$, representing the two solenoids, the flux conservation Eq. (10.1) is rewritten as

$$\begin{cases} \int_{A_1} (B_1 + B_2)\, dA + \int_{A_1} B_{\mathrm{ex}}\, \mathrm{d}A = 0 \\ \int_{A_2} (B_1 + B_2)\, dA + \int_{A_2} B_{\mathrm{ex}}\, \mathrm{d}A = 0. \end{cases} \tag{10.22}$$

By defining the mutual inductances as

$$L_{ij} \equiv \int_{A_i} B_j(\rho, z)\, \mathrm{d}A, \tag{10.23}$$

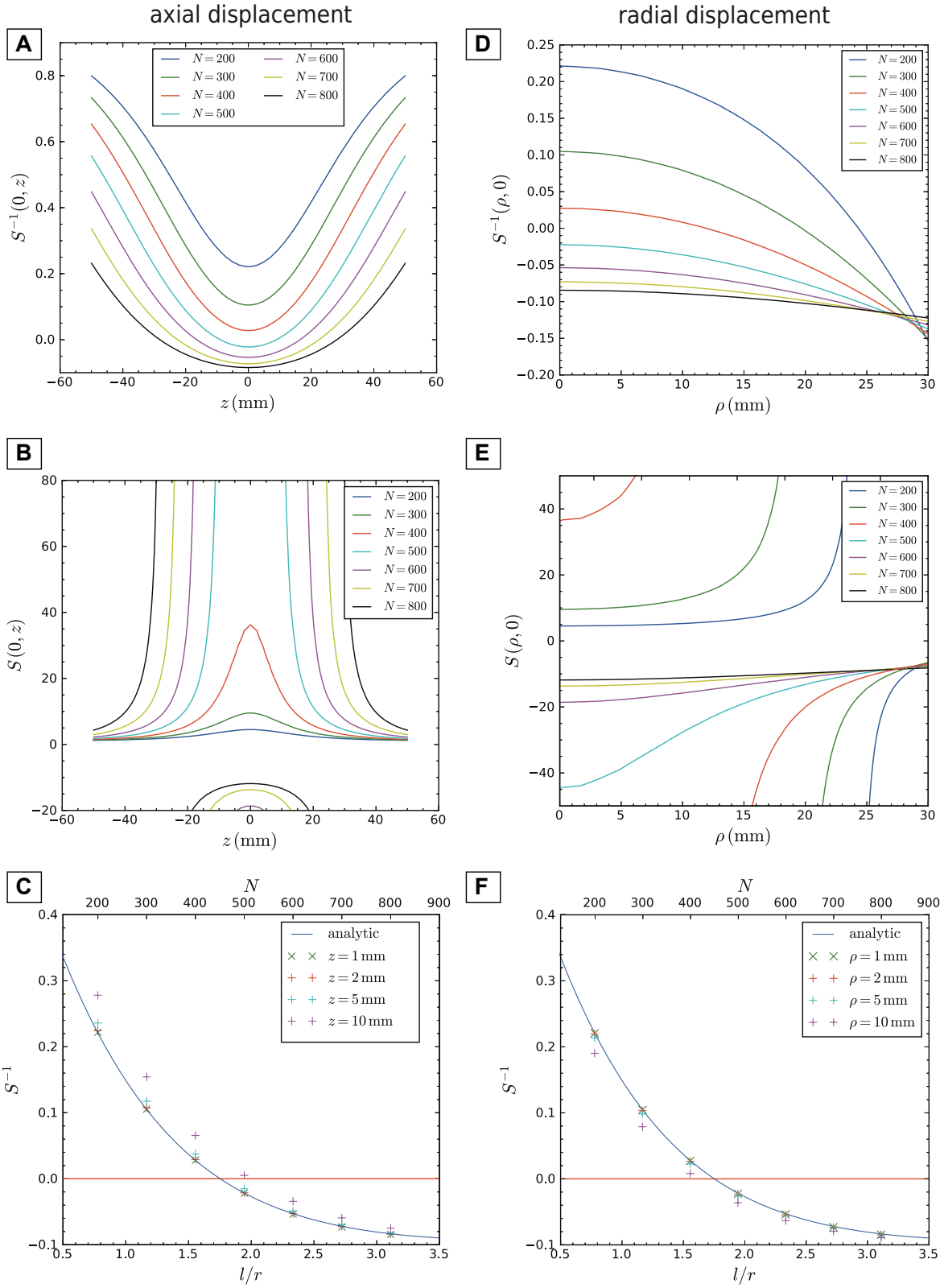

Figure 10.8: Dependences of the shielding factor on the positions. (A–C) for the dependence on z, and (D–F) for that on ρ. **(A, D)** $S^{-1}(0, z)$ ($S^{-1}(\rho, 0)$) as a function of the position, series of different turns N are indicated in the plot legend. **(B, E)** Same as (A, D), but shown in unit of $S(0, z)$ ($S(\rho, 0)$ instead of S^{-1}. **(C)** Scaling of $S^{-1}(0, z)$ against the length-radius-ratio l/r, shown for different series of z. **(F)** Scaling of $S^{-1}(\rho, 0)$ against the length-radius-ratio l/r, shown for different series of ρ.

with notations

$$\mathbf{I} \equiv \begin{pmatrix} I_1 \\ I_2 \end{pmatrix}, \ \mathbf{L} \equiv \begin{pmatrix} L_{11} & L_{12} \\ L_{21} & L_{22} \end{pmatrix}, \ \mathbf{g} \equiv \begin{pmatrix} g_1 \\ g_2 \end{pmatrix} = \begin{pmatrix} B_1(0,0)/I_1 \\ B_2(0,0)/I_2 \end{pmatrix}, \ \mathbf{A} \equiv \begin{pmatrix} A_1 \\ A_2 \end{pmatrix}, \tag{10.24}$$

Eq. (10.22) becomes

$$\begin{pmatrix} L_{11} & L_{12} \\ L_{21} & L_{22} \end{pmatrix} \begin{pmatrix} I_1 \\ I_2 \end{pmatrix} = -B_{\text{ex}} \begin{pmatrix} A_1 \\ A_2 \end{pmatrix} \tag{10.25}$$

$$\therefore \mathbf{I} = -B_{\text{ex}} \mathbf{L}^{-1} \mathbf{A}. \tag{10.26}$$

The correspondences of Eqs. (10.3) and (10.9) are

$$\begin{aligned} S^{-1} &= 1 + \frac{B_1(0,0)}{B_{\text{ex}}} + \frac{B_2(0,0)}{B_{\text{ex}}} \\ &= 1 + \frac{g_1 I_1}{B_{\text{ex}}} + \frac{g_2 I_2}{B_{\text{ex}}} \\ &= 1 + \frac{1}{B_{\text{ex}}} \mathbf{g}^T \mathbf{I}, \end{aligned} \tag{10.27}$$

$$\therefore S^{-1} = 1 - \mathbf{g}^T \mathbf{L}^{-1} \mathbf{A}. \tag{10.28}$$

Eq. (10.28) can be generalized to coupling of more than two shielding coils.

10.2.2 Scaling of the shielding factor of coupled shielding systems

Here we consider the scaling of the inverse shielding factor S^{-1} of a system of two coupled solenoids. In case of a system of two coils, Eq. (10.28) becomes

$$S^{-1} = 1 - \frac{1}{1-\gamma^2} \Big(\underbrace{\frac{g_1 A_1}{L_{11}} + \frac{g_2 A_2}{L_{22}}}_{\text{(a)}} - \underbrace{\gamma^2 \frac{g_1 A_2 + g_2 A_1}{M}}_{\text{(b)}} \Big) \tag{10.29}$$

where the mutual inductance M and the coupling factor γ are defined by

$$M \equiv L_{12} = L_{21}, \tag{10.30}$$

$$\gamma \equiv \sqrt{\frac{M^2}{L_{11} L_{22}}}. \tag{10.31}$$

The scaling of S^{-1} is characterized by γ. From Eq. (10.29), when $\gamma \ll 1$, the terms (a) become dominant:

$$S^{-1} \sim 1 - \left(\frac{g_1 A_1}{L_{11}} + \frac{g_2 A_2}{L_{22}} \right), \tag{10.32}$$

which means that the self inductances of the two coils contribute independently to the shielding factor.

In the other limit of $\gamma \gg 1$, the terms (b) become dominant:

$$S^{-1} \sim 1 + \left(\frac{g_1 A_2 + g_2 A_1}{M} \right). \tag{10.33}$$

Hereafter, a case is considered where a self-shielding solenoid of the radius of 38.575 mm is placed in a larger solenoid of radius 116 mm. They model a system where a solenoid is wound on the trap chamber (Fig. 10.12). The densely wound geometry of coils such as treated in previous sections (Fig. 10.1) are used for both of the inner and the outer coil. The parameters of the outer solenoid are fixed, and the scaling of S^{-1} by the length of the inner solenoid is studied. Table 10.2 lists the parameters used for the inner solenoid, labeled with i.

Three sets of parameters in Table 10.3 are utilized to model the outer solenoid, respectively representing strong coupling ($\gamma > 1$), weak coupling ($\gamma < 1$), and intermediate coupling ($\gamma \sim 1$). The geometry of the main solenoid of the BASE superconducting magnet (Section 5.1.1) falls into the region of the intermediate coupling with the inner coil wound on the trap chamber. In Fig. 10.9, the modeled geometries are shown in comparison with the geometry of the magnet.

When the outer solenoid is much longer than the inner solenoid, the mutual inductance M increases linearly with the turn of the inner solenoid N_i:

$$M = M^{(1)} N_i. \tag{10.34}$$

If the field produced by the outer solenoid is approximated by that of an infinitely long solenoid $\mu_0 N_o I_o / l_o$,

$$M = \frac{\mu_0 N_o}{l_o} \pi r_i^2 N_i \tag{10.35}$$

where the terms labeled by o indicate the parameters of the outer solenoid. $M^{(1)}$ can differ from that of Eq. (10.35) by the limited length of the coil (it becomes bigger in the regime of Fig. 10.2 (B.)). It can also change by the position of the inner coil in respect of the outer coil, and be adjusted by using multiple layers of winding for the inner coil. In this study, the order of M is estimated by $\mu_0 N_o \pi r_i^2 / l_o$, and a few sets of $M^{(1)}$ on the estimated order were used to model M by Eq. (10.34). The range of the values used for $M^{(1)}$ are shown in Table 10.3. g_i, g_c and L_{ii}, L_{oo} are evaluated by the analytical solutions Eqs. (10.11) and (10.12). Using these results, the scaling of the inverse shielding factor S^{-1} by the length of the inner solenoid l_i is obtained by Eq. (10.29).

The results are shown in Fig. 10.10. The coupling factor γ and the inverse shielding factor S^{-1} are shown as functions of l_i/r_i. It can be seen that the coupling with the larger coil changes the scaling drastically from that of an independent single coil studied in A few things can be observed:

- In the strong coupling regime (Fig. 10.10 (A, B)), for the series with $0.1\,\mathrm{mH} < M^{(1)} < 1.3\,\mathrm{mH}$,

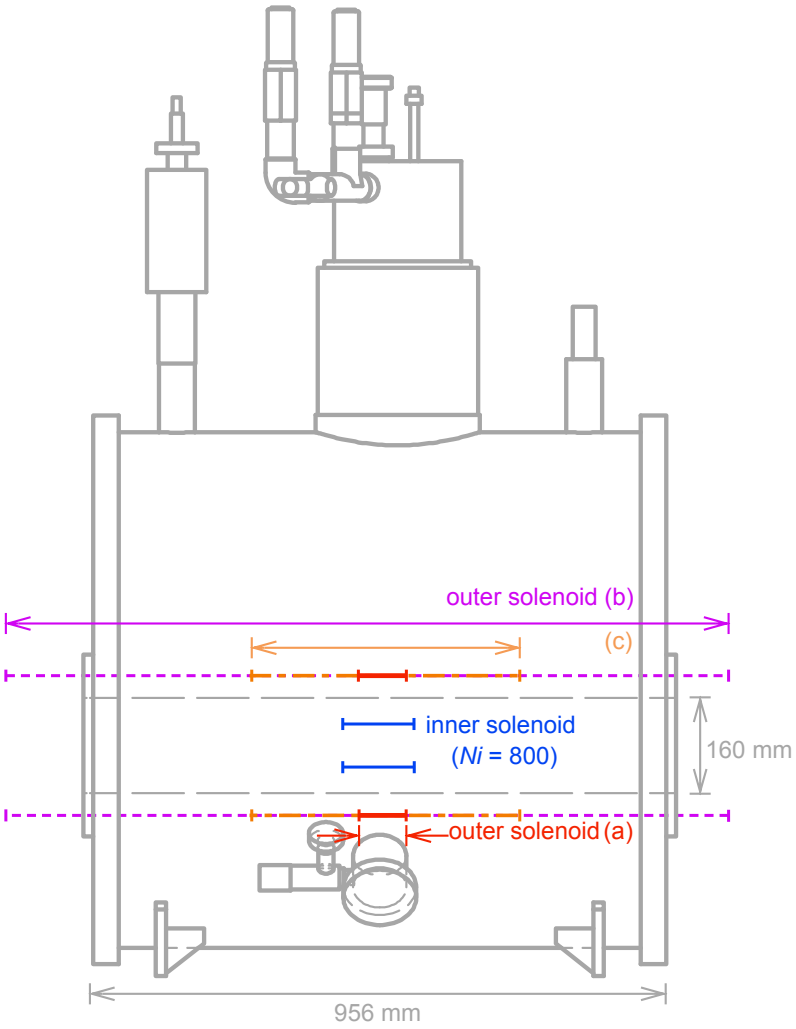

Figure 10.9: Geometries of the inner and the outer solenoids used for the study of the coupled shielding solenoids are shown together with the geometry of the BASE superconducting magnet. The inner solenoid is shown for $N_i = 800$. The three cases: (a) strong coupling (b) weak coupling (c) intermediate coupling are shown for the outer solenoid.

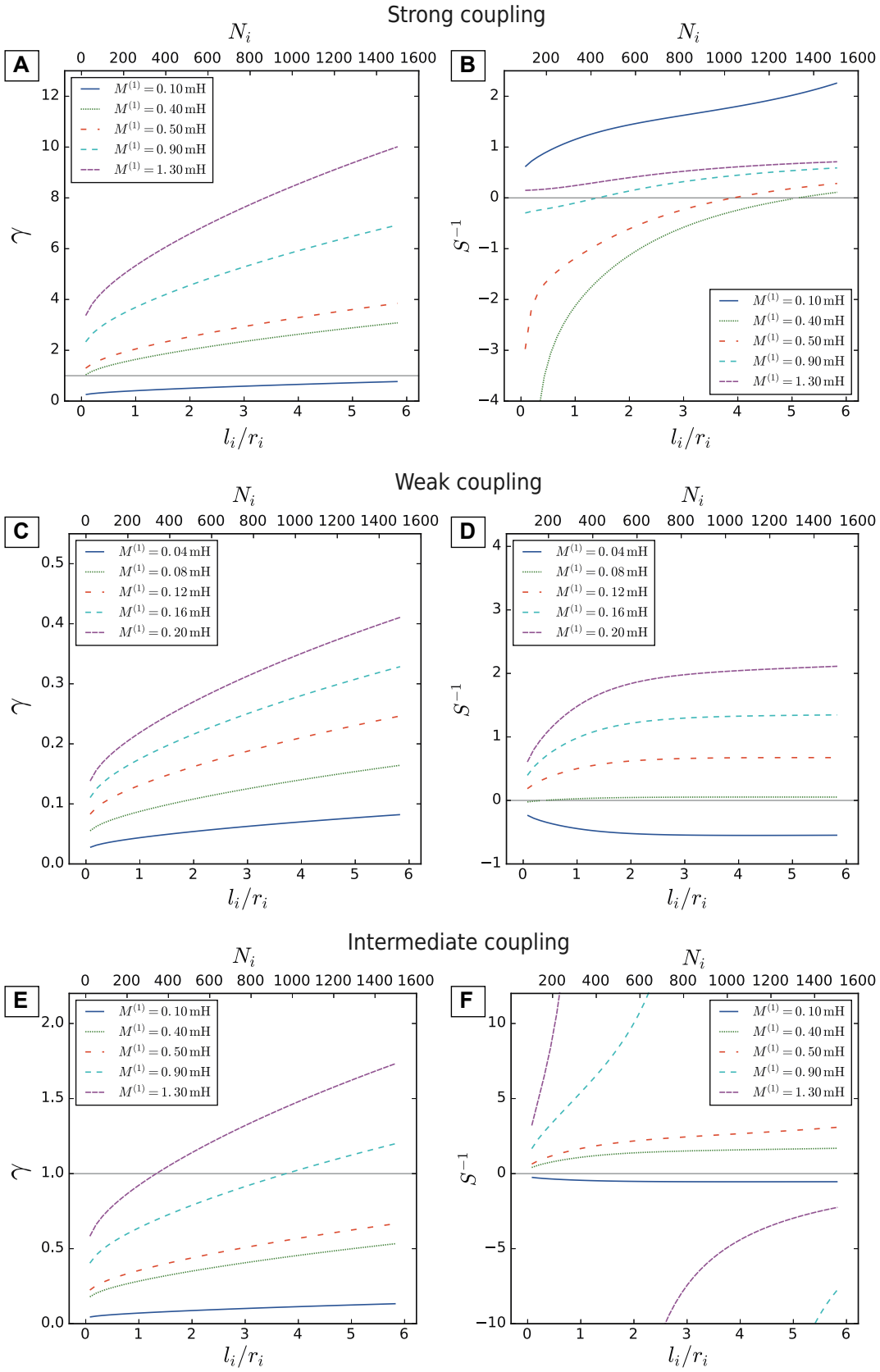

Figure 10.10: Scaling of the coupling factor γ and the inverse shielding factor S^{-1} against the length-to-ratio l_i of the inner solenoid. Shown for each regime of (A,B) strong coupling, (C,D) weak coupling, and (E,F) intermediate coupling.

Table 10.2: Parameters of the inner solenoid. N_i was swept over the range to study the scaling of the γ and S^{-1} against the length of the inner coil.

N_i	20–1500
l_i	$N_i \cdot d_1$
r_i	38.575 μm
d_i	150 μm

Table 10.3: Three sets of parameters used to model the outer coil.

	(a) strong coupling	(b) weak coupling	(c) intermediate coupling
N_o	1600	16000	16000
l_o	80 mm	1200 mm	445 mm
r_o	116 mm	116 mm	116 mm
d_o	50 μm	75 μm	27.8 μm
L_{oo}	0.743 H	10.5 H	24.8 H
$\pi\mu_0 N_o r_i^2/l_o$	1.17×10^{-4} H	7.83×10^{-5} H	2.11×10^{-4} H
$M^{(1)}$	0.10–1.3 mH	0.04–0.20 mH	0.1–1.3 mH

S^{-1} crosses zero. The cross point becomes closer to $l_i/r_i = 0$ for larger $M^{(1)}$.

- In the weak coupling regime (Fig. 10.10 (C, D)), S^{-1} does not cross zero except for the series with $M^{(1)} = 0.08$ mH which has the cross points at around $l_i/r_i = 0.4$. The sign of the scaling depends on the balance between the terms (a) and (b) in Eq. (10.29).

- In the intermediate coupling regime (Fig. 10.10 (E, F)), the scaling behaves similarly to the weak coupling for series which satisfy $\gamma < 1$ for the entire range of l_i/r_i. For the series which cross $\gamma = 1$, the curves of S^{-1} have singularities at $\gamma = 1$.

Only in the strong coupling regime, S^{-1} crosses zero for a wide range of $M^{(1)}$. Otherwise, the solution of a perfect shielding exits only for a limited range of $M^{(1)}$. Therefore, if one designs a system of coupled two shielding solenoids from scratch, it is recommended to work in the strong coupling regime, as was done by G. Gabrielse and J. Tan in their original work [182, 183].

In case of the BASE superconducting magnet, although it is known from the estimated geometry of the magnet that coupling between the main solenoid of the magnet and the shielding coil wound on the trap chamber is in the intermediate range, specific parameters are unknown due to limited knowledge about the magnet. Further, coupling with the shim coils adds more complication. Therefore it is difficult to design a coil which realizes perfect shielding while considering the coupling with other coils.

10.3 Design of multi-solenoid self shielding system

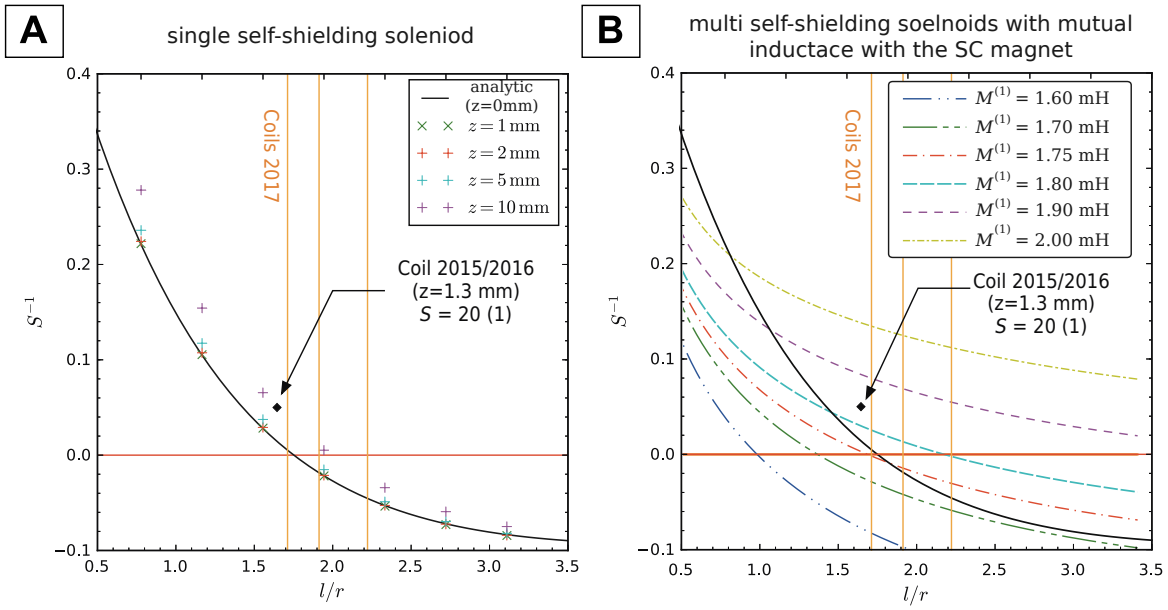

Figure 10.11: Measured inverse shielding factor $S^{-1}_{2015/2016} = 0.050(3)$ of the single self-shielding solenoid installed in the 2015/2016 run is plotted with the black diamond. This coil was off-centered from the center of the PT by about 1.3 mm. **(A)** Scaling of the inverse shielding factor of an isolated single solenoid. In order to account for off-centering, the scalings of S^{-1} at off-centered positions studied in Section 10.1.3 are shown together. The inverse shielding factor of the 2015/2016 coil deviates from the analytical scaling as much as off-centering of 10 mm, which indicates the modification of the scaling due to the mutual inductance with the superconducting magnet. **(B)** Scaling of the inverse shielding factor of a coupled solenoids. The black curve is the scaling of the isolated single solenoid. The dashed/dotted curves are obtained by a system of two coupled solenoids. The geometry of the outer coil is chosen to be that of the main solenoid of the Oxford magnet estimated in Table 5.1. A linear form of the mutual inductance of $M = M^{(0)} + M^{(1)}N_i$ is assumed for the mutual inductance M. The scalings here are obtained by $M^{(0)} = 120$ mH and $M^{(1)} = 1.6$–2.00 mH, shown in the legend. It can be seen that the scaling is sensitive to small differences of the parameters. It seemed likely that the optimum length exists at l/r > 1.645 (2015/2016), but our knowledge was not enough to determine the optimum length *ab initio*. The three vertical orange lines indicate the l/r chosen for the three-layer system constructed for then 2017 run.

In the 2015/2016 run, a single self-shielding solenoid was installed. The coil was designed to have $l/r = 1.752$, the ideal for the isolated single self-shielding solenoid without consideration of the mutual inductance (Section 10.1.1). Due to practical problems during the construction, the geometry of the actually constructed coil had $l/r = 1.645$, and was off-centered by 1.3 mm. The shielding factor of this coil was measured to be $S = 20(1)$, or $S^{-1}_{2015/2016} = 0.050(3)$ (for the measurement procedure, see Section 10.5). This result was compared with the shielding factor at off-centered positions of a single self-shielding solenoid discussed in Section 10.1.3. In Fig. 10.11 (A), the scalings of the inverse shielding factor S^{-1} (both at $z = 0$ and off-centered z positions) of an isolated self-shielding solenoid, same as Fig. 10.8 (C), are shown with the measured inverse shielding factor of the 2015/2016 coil. As

can be observed in the plot, the measured inverse shielding factor deviates from the analytical scaling of a single shielding coil, even considering the off-centered position. The deviation of the measured inverse shielding factor from the theoretical scaling corresponds to the off-centering of about 10 mm, instead of the actual 1.3 mm. Thus we see the modification of the scaling from an isolated single self-shielding solenoid due to the mutual inductance with the superconducting magnet. Assuming that the coupling is in the intermediate regime as discussed in the last section, and from a relatively small deviation of the 2015/2016 coil from the isolated single-solenoid scaling, we expected the ideal l/r for this system to be $l/r > 1.645$.

As discussed in the last section, the ideal length of the coil in the presence of the mutual inductance is difficult to be determined *ab initio* by the calculation because of limited knowledge of the coils included in the magnet. In Fig. 10.11 (B), examples of the scaling of the inverse shielding factor of a coupled self-shielding solenoids with different sets of assumed parameters of the mutual inductance scaling are shown. It can be seen that the saplings is sensitive to small difference of the parameter $M^{(1)}$, being the proportional factor mutual inductance and the turns of the inner solenoid. For more details of the parameters assumed here, see the figure caption.

Repeating the construction and characterization of the coils with different lengths is also not realistic, because each of the tests requires assembling and commissioning of the entire apparatus where the shielding coil and the Penning-trap system is installed.

In order to address this issue, we invented a system consisting of three layers of self-shielding solenoids for the 2017 run. The system consists of three solenoids with different lengths, separately wound on the trap chamber. Each of the three coils is equipped with a film resistor which functions as a heater to quench each solenoid. This gives a selectivity of the length of the coil, and enables us to characterize the scaling of the inverse shielding factor in the presence of the mutual inductance with the magnet.

The lengths of the coils are chosen as $l/r = 1.71, 1.91, 2.22$, covering a range around $l/r = 1.752$, the ideal for an isolated single solenoid. The l/r of the three solenoids of the 2017 system are indicated by the orange vertical lines in Fig. 10.11.

In the next section, the construction procedure of the shielding system used in 2017 is summarized. The shielding system installed in the 2015/2016 run was constructed similarly, and is mentioned to along the explanation.

10.4 Construction of the self-shielding systems

The construction procedure of the multi-layer self-shielding solenoid reads as below:

1. Winding of the coils on the trap chamber

2. Placement of the quench resistors

Table 10.4: Parameters of the constructed self-shielding system. Comment*: The coil installed in 2015/2016 was slightly off-centered. The center of the coil was located upstream (toward the RT) by 1.3 mm from the PT center where the shielding factor was measured.

	2015/2016*	2017		
		68 mm-coil	75 mm-coil	86 mm-coil
Length l	63.5 mm	68 mm	75 mm	86 mm
Radius r	38.6 mm	39.7 mm	39.2 mm	38.7 mm
l/r	1.645	1.712	1.913	2.222
Wire inner diameter	125 μm	125 μm	75 μm	75 μm
Wire outer diameter d	150 μm	150 μm	90 μm	90 μm

3. Production of persistent superconducting joints

Each step is described in details in the following parts of this section.

10.4.1 Construction procedure 1: winding

First, superconducting wires were wound on the trap chamber. Fig. 10.12 describes the structure of the coils. Densely wound, single-layer solenoids with three different lengths: 68, 75 and 86 mm were constructed. Their centers were positioned to match the point where the center of the PT was to be installed. Formvar insulated Niobium Titanium (NbTi) wires from GVL Cryoengineering were utilized. Due to availabilities of the wires, a wire with a different diameter from the other two was adapted for the 68-mm coil. In order to provide electrical insulation between the coils, a layer of Kapton sheets of ≈ 0.1 mm thickness was wrapped before each coil. See the photograph Fig. 10.13 taken during the construction. After being wound, the windings were fixed by several layers of PTFE tapes with an integrated thickness of ≈ 0.5 mm. When the system is cooled down, heat conducts through the trap chamber to the cryostats via the 4 K stage of the apparatus. Therefore, it is essential that the outer coils are pressed tightly with the inner coil so that the entire system thermalizes below the critical temperature of NbTi. The geometrical parameters measured after the construction are listed in Table 10.4. In 2015, a single shielding solenoid was designed by the optimum length of a single solenoid (see Section 10.1.1). However, due to a practical issue, the coil had shorter length-to-radius ratio than the design and was off-centered by 1.3 mm. The 2017 system had three coils were constructed as designed.

Correspondence with the parameters of the model which has been employed for the simulation (Fig. 10.1) is also shown as l, r and d in the table.

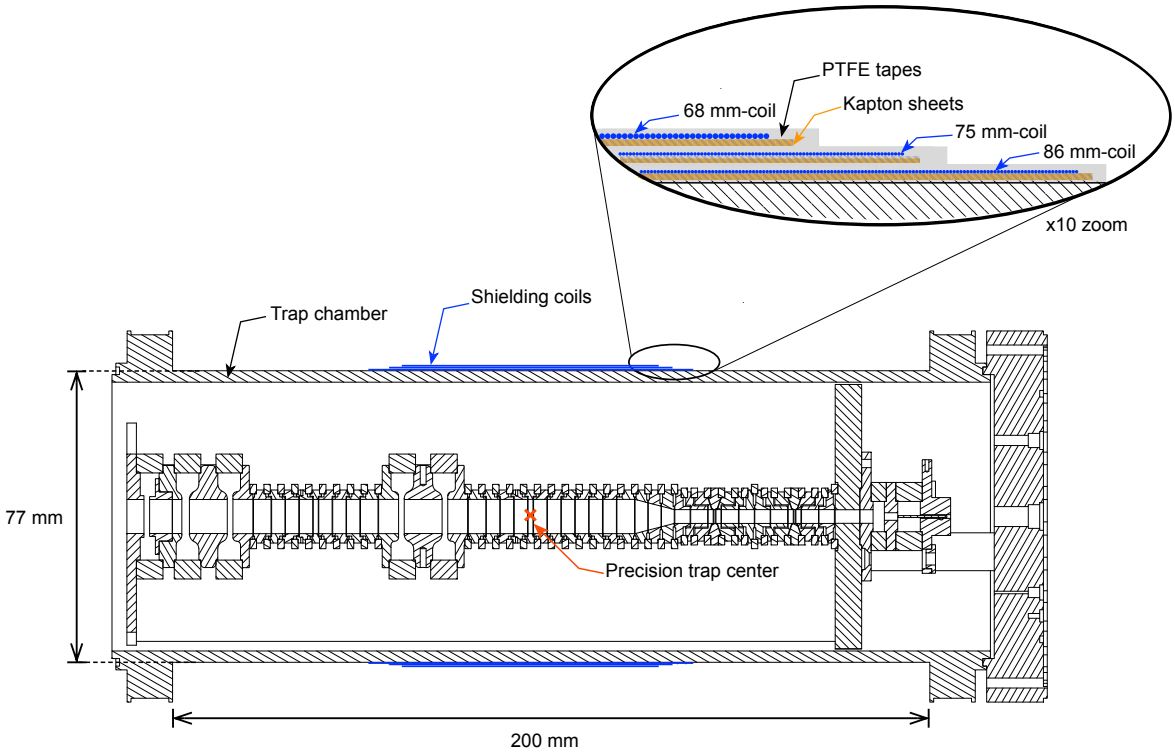

Figure 10.12: Cross-sectional view of the multi-solenoid self-shielding system. The blue lines indicate the positions of the three coils. The trap assembly which will be later installed in the chamber is shown together. The centers of the coils are positioned so that they match to the center of the trap. In the zoomed-in view, the structure which covers the windings is depicted. The windings of the coils are represented by the blue circles.

Figure 10.13: Photograph taken during the construction of the 2017 self-shielding system. The coil is being wound on a layer of Kapton sheets wrapped on the trap chamber.

10.4.2 Construction procedure 2: placement of the quench resistors

After the coils were wound on the trap chamber, the quench resistors were installed for each of the three coils. For each coil, one of the two ends of the NbTi wire was wound by a few turns on a film resistor to make a thermal connection between the wire and the resistor. Resistors of 10 kΩ were typically used. When it is operational after installation, the coil can be quenched by heating the resistor by application of a current. Fig. 10.14 (A) illustrates how the resistor is installed. The capacitor on the PCB board in the figure was added in the bias line as a low-pass filter. The quench resistors were covered by pieces of Kapton sheets to thermally isolate the resistor so that operation of a resistor associated to one of the coils would not heat the other coils (Fig. 10.14 (B)).

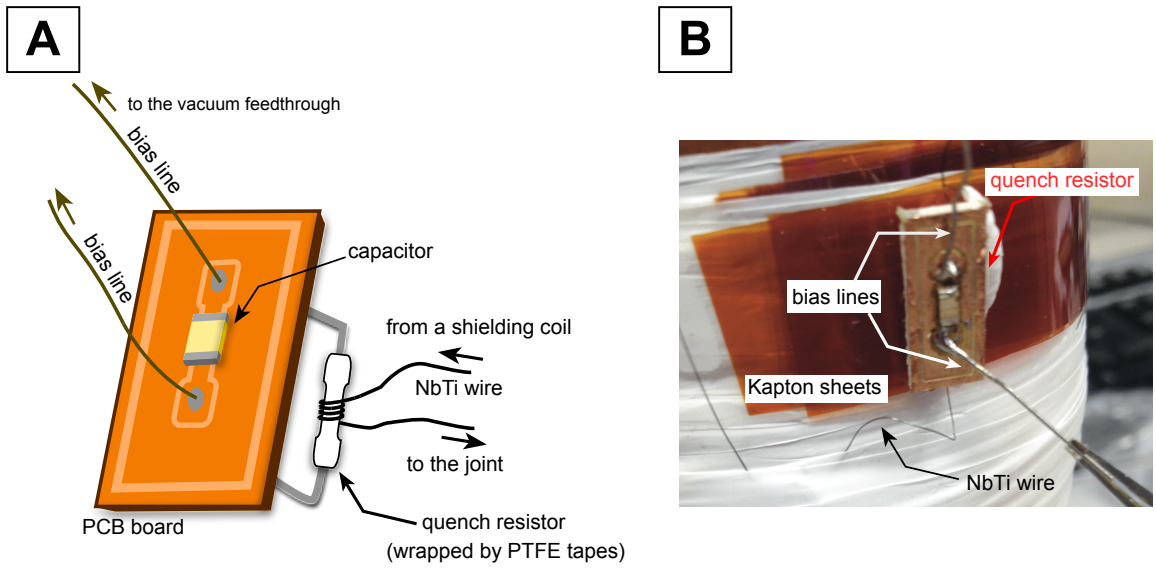

Figure 10.14: Installation of a quench resistor. (A) One of the ends of the NbTi wire of a shielding coil is wound on the file resistor for a few turns. Before winding, the resistor was wrapped by PTFE tapes to make a grip with the wire. Afterward, PTFE tapes will be covered over the resistor to fix the windings (not shown in the figure). The bias line of the resistor goes toward a feedthrough of a flange, via a PCB board where a capacitor was placed as an RF block. (B) Kapton sheets were placed beneath the quench resistor and the PCB board to thermally isolate them from the rest of the system.

10.4.3 Construction procedure 3: production of welded superconducting joints

After placing the quench resistors, the two ends of the wire of each coil had to be connected to form a closed superconducting loop. This is the most crucial part of the construction. It is not a simple task, as one has to join two ends of thin NbTi wires, which are inflexible and fragile. Another difficulty is

that the joints can only be tested non-destructively by the functioning of the coils after the system is cooled down and the wires become superconducting.

Two methods of welding which were employed in the 2017 run are described below.

Welding method 1: resistance spot welding

The resistance spot welding was used for the system installed in 2017 run-I. Photographs in Fig. 10.15 were taken in each step of the welding procedure. The welded joint of the coil used in 2015/2016 was also done in a similar method.

First, thin, V-shaped sheets of NbTi were made by laminating small pieces of NbTi (Fig. 10.15 (A, B)). Insulation layers were stripped from the NbTi wires, then the ends of the wire to be joined were twisted and inserted into the V-shaped NbTi sheet. Then spot welding was performed to join the components over the V-shape NbTi sheets. (Fig. 10.15 (C,D)). Two welded spots were made for each joint. At the moment when the spot was made, a strong current flowed through the tip electrodes of the spot welder, heating the pieces and melting a part of the NbTi alloy surrounding the wires to form a connection.

Examination of the superconducting joints after run-I

During run-I, it was suspected that either of the 75 mm- or 86 mm-coil was not functioning. After the end of run-I, the two joints were removed from the wires for examination. The examination was carried out by Mickaël Sebastien Meyer from CERN EN-MME group [187]. To examine the cross sections by a microscope, the joints were cold mounted in resin, and longitudinal cross sections along the V-shaped sheets were produced by polishing the surface by silicon carbide (SiC) papers. The obtained microscope images are shown in Fig. 10.17. It can be clearly seen that the joint of the 75 mm coil fell off from the V-shaped sheet, likely during the cool down. On the contrary, the wires of the 86 mm coil look well attached to the V-shaped sheet. In conclusion, the resistive spot welding was successful for two out of the three joints.

Welding method 2: cold pressing and arc welding

A new method of welding was used to re-join the joints of the 75 mm- and 86 mm-coils. This method is a combination of cold pressing and arc welding, and was developed by Thomas Arne Hensel as part of his internship in BASE [188].

The ends of the NbTi wire to be joined were folded together with a 0.2 mm diameter bare NbTi wire, twisted to produce a dense helix with a length of about 1 cm. The helix was then pressed by a stainless steel bench vise to produce a single piece of NbTi as seen in Fig. 10.18 (A). This cold-pressed joint was welded by an arc welder PUK U5 operated with Argon gas. Fig. 10.18 (B) shows the piece

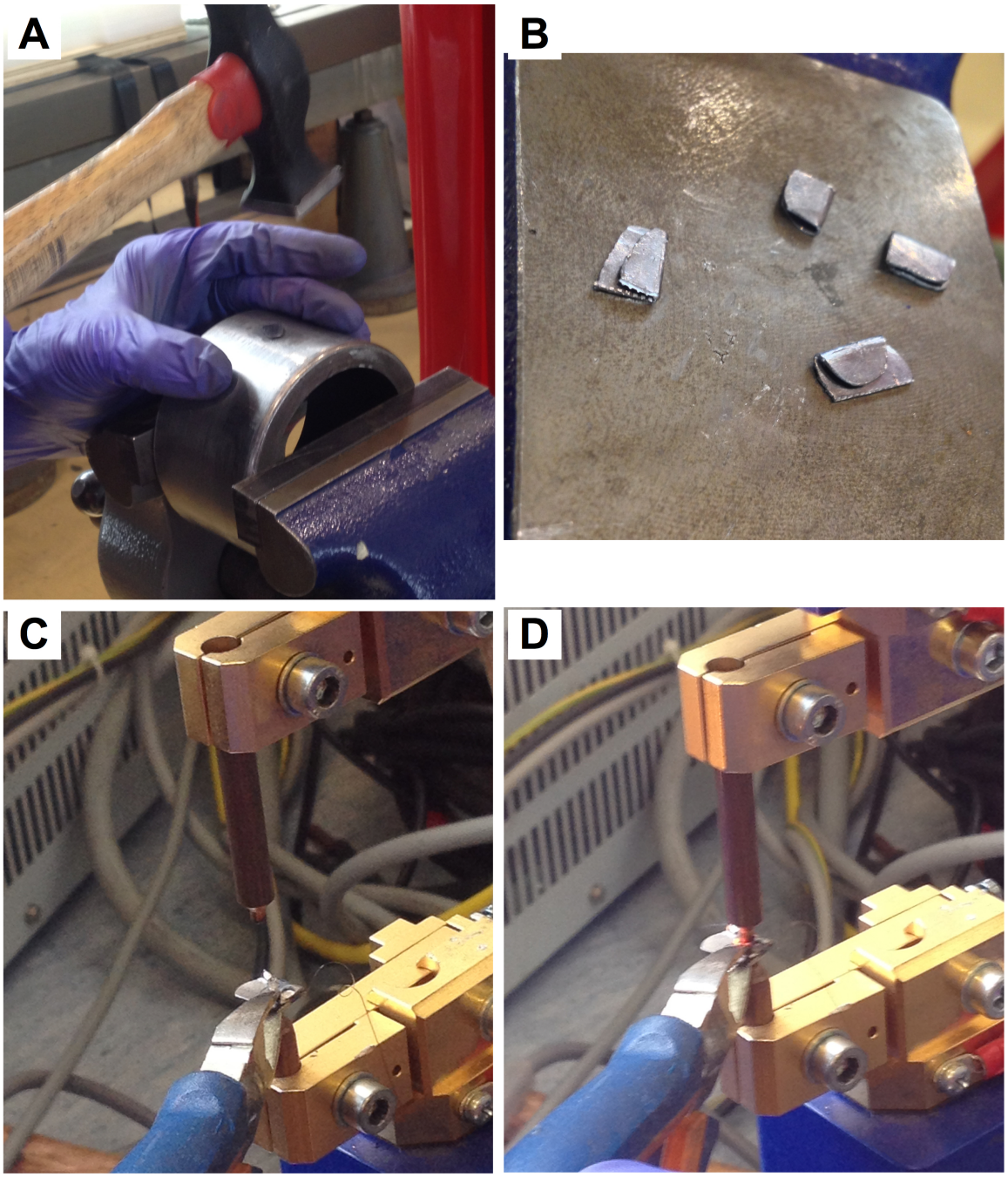

Figure 10.15: Procedure of the resistance spot welding of the NbTi wires of the self-shielding coils. (A, B) Preparation of V-shaped thin NbTi sheets. (C, D) Spot welding of the V-shaped piece and inserted NbTi wires. (C) A twisted pair of the wires are inserted in the V-shaped sheet, placed on the spot welder.

Figure 10.16: Photograph of one of the resistance welded joints. Image credit: Stefan Sellner.

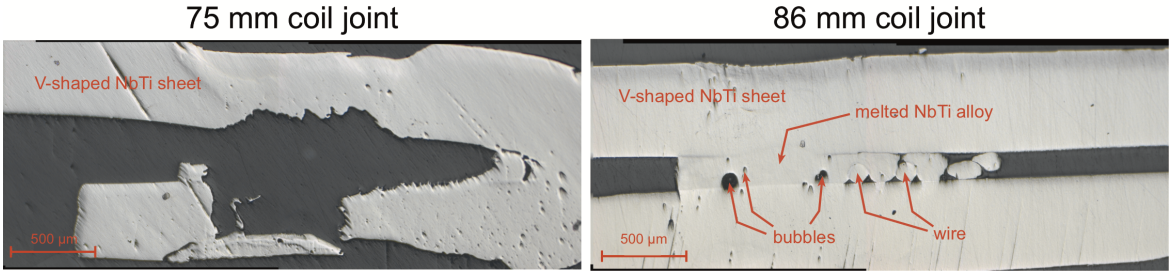

Figure 10.17: Microscope images of the joints of the 75 mm (left) and the 86 mm (right) coils. The connection between the V-shaped sheet and the wire can be seen for the 86 mm (right) coil joint, while in case of the 75 mm coil, the joint seemed to have fallen from the assembly. Image credit: Mickaël S. Meyer (CERN).

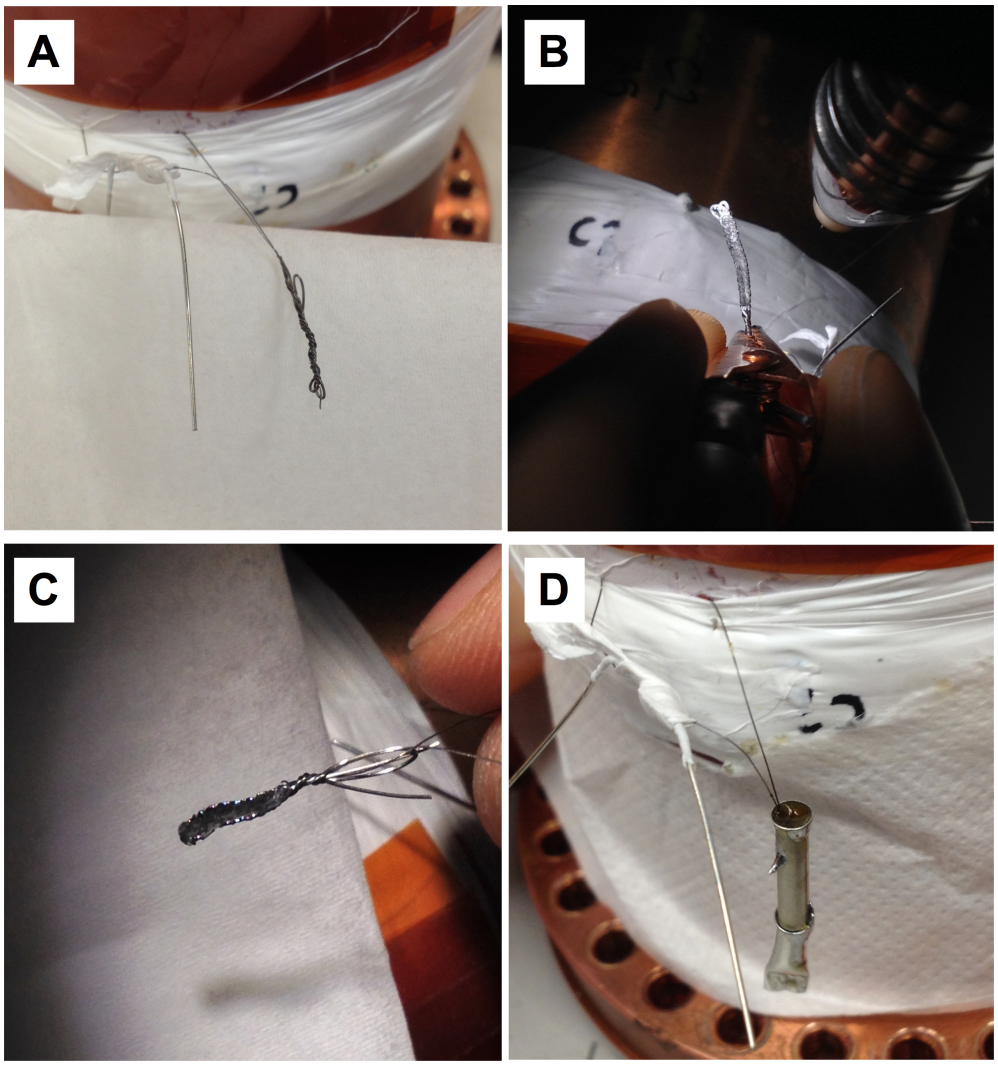

Figure 10.18: Procedure of the new welding method. **(A)** Helix made by winding the NbTi wires. **(B)** The cold-pressed NbTi piece before the arc-welding. **(C)** The joint after the arc-welding. **(D)** The joint is fixed with solder in a ferrule. Photo credit: Thomas Arne Hensel.

right before it is welded. The joint after the arc welding is shown in (C) Afterward, the whole joint was covered with regular solder in a ferrule to add mechanical stability and robustness (Fig. 10.18 (D)).

Although this method was successful in an offline test[2], and the produced joint looked well connected as one piece (Fig. 10.18 (C)), it appeared that the two joints made by this method for 2017 run-II were both unsuccessful (Section 10.5). Further development is required to make this method reliable.

[2]The offline test was done by winding a dummy shielding coil on a copper holder smaller than the diameter of the actual shielding coil with a GMR sensor installed inside the holder. The joint was welded by the cold-pressed + arc-welding method, and a quench resistor was installed. The system was cooled in a pulsed-tube cryocooler. After the cool down, the joint was tested by observing a shift of magnetic field strengths in the holder by quenching the test shielding coil.

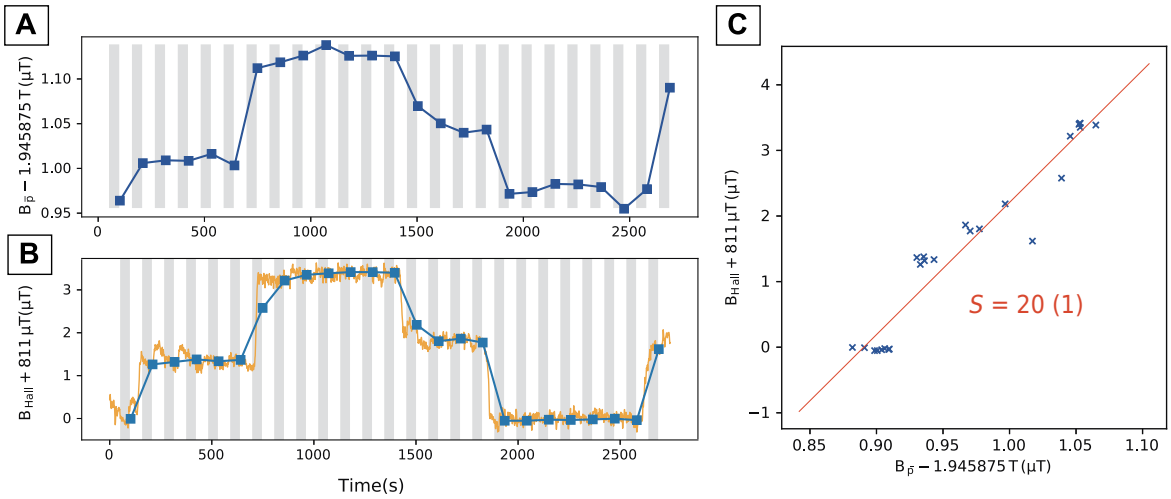

Figure 10.19: Measurement of the shielding factor performed in 2016. **(A)** Internal magnetic field extracted from the cyclotron frequency of a single antiproton in the PT. **(B)** External magnetic field measured by a Hall probe placed near the magnet. The overhead crane was operated to produce steps of magnetic field variations at time $\approx 100, 700, 1500, 1800, 2600$ s. The gray bands of (A) and (B) indicate time windows of a duration 48 s for the acquisition of double-dip spectra to measure the cyclotron frequency. The data points blue squares in (B) are obtained by averaging the magnetic field over the gray time windows. **(C)** Extraction of the shielding factor. The external magnetic field, averaged over the respective time window, is plotted against the internal magnetic field. The red line indicates the result of a linear fit, whose slope is 20(1)

10.5 Performances of the installed shielding systems

In this section, the performances of the different self-shielding systems installed in the experiment in 2015/2016 run, 2017 run-I and run-II are summarized.

10.5.1 Measurement procedure

The shielding factor of the system was measured by comparing the magnetic field measured from the cyclotron frequency of the particle against the external field variation which was measured by external magnetic field sensors (see Chapter 11). As an example, data of the measurement performed to characterize the 2015/2016 system is shown in Fig. 10.19. The cyclotron frequency of a single antiproton in the PT was measured by the sideband coupling method over the period shown in the graph. The measured cyclotron frequency is converted into magnetic field units in Fig. 10.19 (A). The ambient magnetic field monitored by a Hall probe attached on the support of the apparatus is plotted in Fig. 10.19 (B). The gray bands in Fig. 10.19 (A, B) indicate time windows of acquisition of double-dip spectra for ν_+ measurement. The data points plotted in squares in Fig. 10.19 (B) are the ambient magnetic field averaged over each of these time windows. An overhead crane in the AD hall (see Section 11.3.2) was used to produce the step-like magnetic field variations as seen in the plots. The steel body of the crane is magnetized after years of its operation in the facility. When

Table 10.5: Summary of results of the shielding factor measurements.

	2015/2016 RUN	2017 RUN-I	2017 RUN-II
Coil configuration	63.5 mm	68 mm + 86 mm	68 mm
Shielding factor S	20(1)	−36(4)	90(5)
Inverse shielding factor S^{-1}	0.050(3)	−0.027(3)	0.011(1)

it approaches the BASE zone, the magnetic field by the crane varies the field in the zone by a few µT. When operated slowly, it can be used to produce a controlled, spatially uniform magnetic field variations.

In Fig. 10.19 (C), the internal magnetic field and the external magnetic field sampled in Fig. 10.19 (A, B) are plotted in a scattered plot. From the slope of a linear fit of the data, corresponding to $\Delta B_{\mathrm{ext}}/\Delta B_{\mathrm{in}}$, the shielding factor was obtained to be $S_{2015/2016} = 20\,(1)$.

10.5.2 Results of the measurements

For each run, the measurement as described in the previous section was performed. The results are summarized in Table 10.5.

In 2017 run-I, only two coils: 68 mm- and 86 mm coils were operational. It also appeared that they were not able to be quenched independently due to insufficient thermal isolation between the quench resistors. The shielding factor under this integrated configuration was about −36. Repairs of the joints were attempted before 2017 run-II as mentioned in Section 10.4.3, but the new method used for the welding was not successful. As a consequence, only the 68 mm coil was functional in run-II. The measured shielding factor was about 90. It should be noted that the shielding performance of the system depends on the spatial character of the external magnetic field variation, and it shields uniform variations better. What is listed in Table 10.5 are the shielding factors for spatially uniform field variations estimated by the test measurement discussed in the last section.

The inverse shielding factor of the 68 mm-coil, $S^{-1}_{2017-\mathrm{II}} = 0.011(1)$, obtained in 2017 run-II is added to Fig. 10.11 in Fig. 10.20. The result of 2017 run-I, where the mutual inductance between the shielding coils was also effective, is beyond the model discussed in Section 10.2. From these two data points obtained in the 2015/2016 run and 2017 run-II, it can be observed that the coupling to the superconducting magnet shifts the scaling of the inverse shielding factor from the original one of the isolated single shielding solenoid to a steeper curve around $S^{-1} = 0$. The optimum l/r in this case is expected to be found slightly above $l/r = 1.712$. Acquisition of the data in the other l/r and further characterization of the mutual inductance will be a subject of future works.

The shielding factor realized in 2017 run-II is better by a factor of 4 than in the 2015/2016 run, and by a factor of 9 compared to 2014 [75]. This has significantly improved the magnetic field stability in the system compared to the condition of the last charge-to-mass ratio comparison.

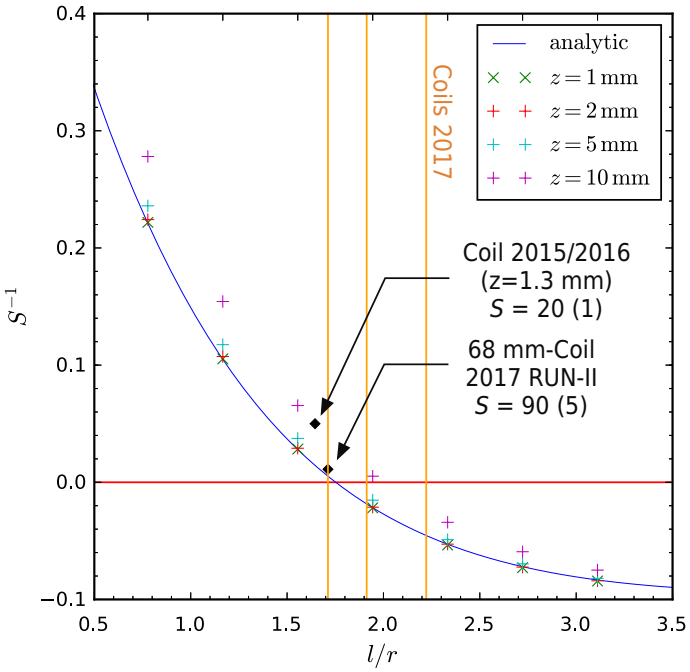

Figure 10.20: Inverse shielding factor $S^{-1}_{\text{2017-II}} = 0.011(1)$ of the 68 mm-coil measured in 2017 run-II is added to Fig. 10.11 (A). The measured inverse shielding factor of the 2015/2016 system and the analytical scaling of the isolated single self-shielding solenoid are shown together. A rough scaling of the inverse shielding factor in this system could be deduced from the two measured data points.

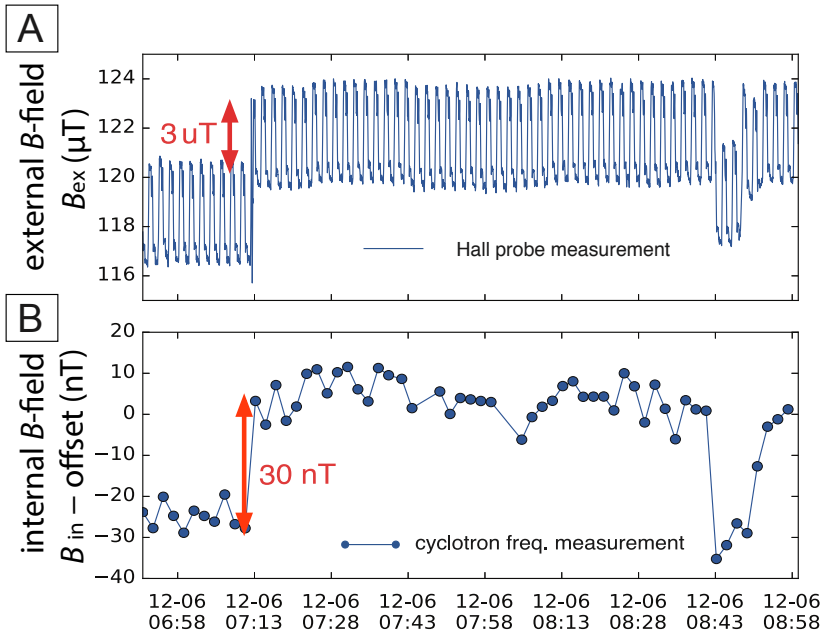

Figure 10.21: Performance of the shielding system in 2017 run-II. **(A)** External magnetic field measured by the Hall probe. **(B)** Internal magnetic field obtained from the cyclotron frequency of a single trapped particle in the PT. The offset of 1.944 98 T is subtracted. It can be observed that the external magnetic field variations are reduced by about a factor of 100 in the internal field.

In Fig. 10.21, the shielding performance of the system in 2017 run-II is demonstrated in the

comparison of the magnetic field in the PT measured by a single trapped particle and the external magnetic field measured by the Hall probe. It can be observed that the external field variation of about 3 µT is suppressed to about 30 nT in the PT.

11

Monitoring system of environmental conditions

For improvement of the frequency stability, an important aspect is to monitor the conditions of the apparatus continuously. This enables us to identify environmental conditions which cause instabilities in the frequency measurements and to improve them. In addition, such information helps to filter out outlier data on the stage of data analysis.

A system described in this chapter was developed for this purpose. It consists of sensors of various kinds, controlled and managed in a consistent way for easy referencing. The system has been developed and maintained over the last few years and was also used during 2015/2016 magnetic moment measurement run, although many additions and upgrades were made during 2017 run. The data collected by the system was effectively used to identify sources of frequency fluctuations and optimize the conditions of the system throughout 2017 run. These activities, together with the comparison of the sensor data and the frequency stabilities will be discussed in detail in Chapter 16.

This chapter summarizes information of the sensors composing the system. In Section 11.3, we shall discuss a detailed characterization of the magnetic field fluctuations caused by operation of the AD using the data obtained by the monitoring system.

11.1 Overview of the monitoring system

Major categories of information logged by the monitoring system are magnetic fields, temperatures, pressures, angles, and a gas flow rate. In what follows, the sensors are explained according to these categories. Their locations are indicated in Figs. 11.1 and 11.2. A summary of the information is found in Table 11.1.

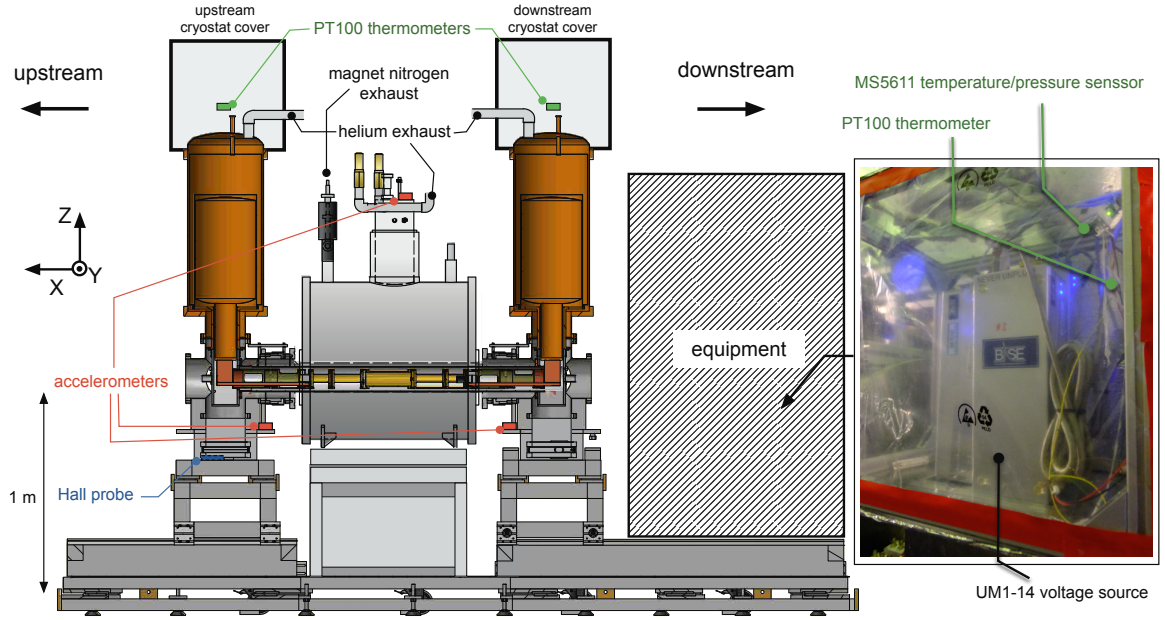

Figure 11.1: Overview of the monitoring system. Positions of the sensors are indicated.

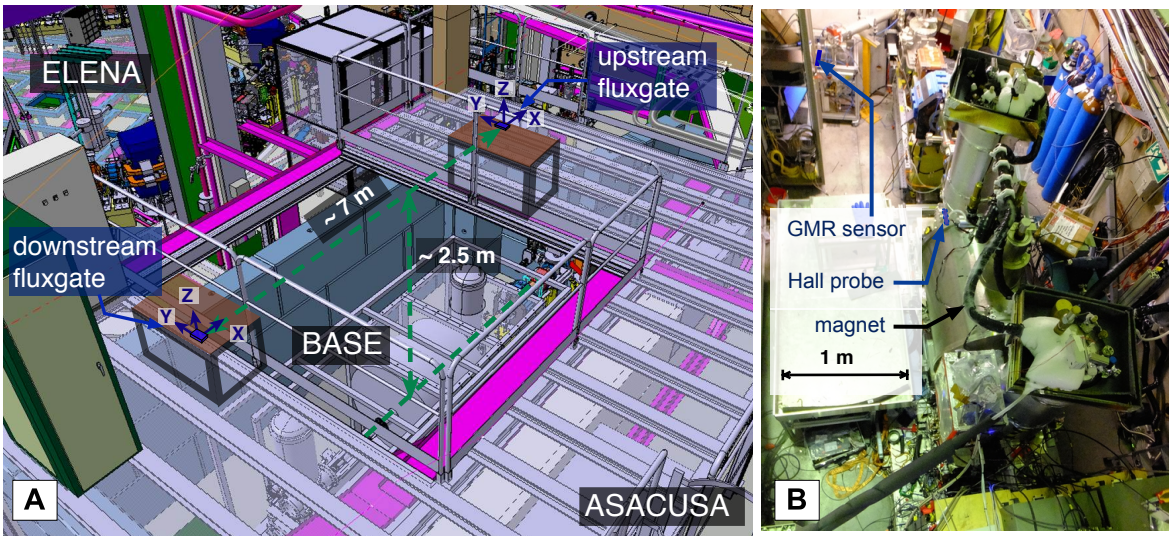

Figure 11.2: Positions of the magnetic field sensors. **(A)** Two triaxial fluxgate sensors FLC3-70 are installed on tables on the upper stage which is located above the level of the apparatus by 3 m. The vertical distance between the fluxgate sensors and the center of the magnet is about 2.5 m. The three axes X, Y, Z of the sensors are defined in the figure. The axis X is in parallel to the magnet's axis. **(B)** A GMR sensor is attached on a rack located about 4 m upstream of the magnet. A Hall probe is attached to the support structure of the upstream cryostat as is also shown in Fig. 11.1. The GMR sensor and the Hall probe are aligned in parallel to the axis of the magnet.

Magnetic fields

Magnetic fields are one of the most important information to be monitored. The following three types of magnetic field sensors are installed to log the magnetic field variations from different aspects. Their locations are indicated in Figs. 11.1 and 11.2:

- A Hall probe HMNA-2518-VR-HF (Lake Shore), read out by DSP 475 Gaussmeter (Lake Shore)
- A Giant magnetoresistance (GMR) sensor AA002-02 (NVE), read out by a digital multimember Keithley 2000
- Two triaxial fluxgate sensors FLC3-70 (Stefan Mayer Instruments), read out by a digital multimeters USB-4065 (National Instruments).

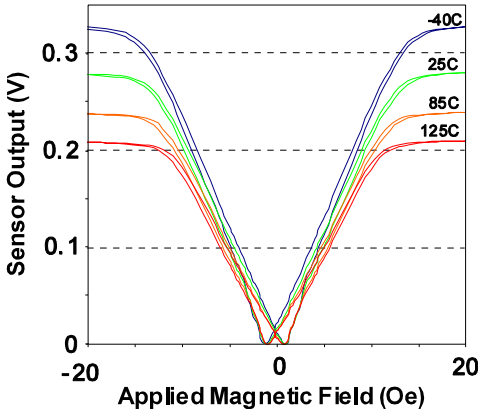

Figure 11.3: Calibration curves of a GMR sensor AA002-02 with a 5 V supply. Adapted from Ref. [189]. The unit of a magnetic field H on the horizontal axis is Oersted (Oe): $1\,\mathrm{Oe} = 1\,\mathrm{G} = 1 \times 10^{-4}\,\mathrm{T}$ in vacuum. The sensor output is bidirectional and saturates at $|B| \gtrsim 1.1\,\mathrm{mT}$. In a range $0.2\,\mathrm{mT} \lesssim |B| \lesssim 1\,\mathrm{mT}$, the scaling is linear with a slope $\Delta B/\Delta V \approx 2.5\,\mu\mathrm{T/mV}$. It can also be seen that the response of the sensor has a temperature dependence.

The Hall probe and the GMR sensor are aligned approximately in parallel to the axis of the magnet. The directions of the fluxgates are indicated in the left figure of Fig. 11.2. The axis X is in parallel to the magnet. The GMR sensor and the fluxgates need supply voltages for their operations. For both, 5 V is chosen as operational voltages, and supplied by a source meter Keithley 2401 for the GMR sensor and by Keithley 2100 for the fluxgates.

The different magnetic field sensors are used complementarily. The GMR sensor and the fluxgate have high sensitivities (2.5 uT/mV (the GMR sensor), 35 uT/V (the fluxgates)), but in return have small saturation magnetic fields (1.1 mT (GMR), 200 µT (fluxgates)). In order to avoid the saturation, the GMR sensor is placed on a rack upstream of the magnet by about 4 m (Fig. 11.2 (B)). The two fluxgates are placed on tables on an upper stage of the BASE zone, having about 3 m of vertical distance from the center of the magnet (Fig. 11.2 (A)). The horizontal distance between the two fluxgates is about 7 m, and the magnet is located approximately in the middle of the two.

Among the three types, only the Hall probe is orientation sensitive, while the others have bidirectional outputs. This feature of the Hall probe is particularly important in characterizing magnetic field changes caused by operation of an overhead crane which has nonuniform spatial properties. Comparing the readouts of the multiple sensors also helps for the characterization. The Hall is attached on the support structure of the upstream cryostat. The distance from the center of the magnet is about 80 cm (Fig. 11.1).

Because of their operational principles[1], the GMR sensor and the Hall probe have temperature dependencies of their outputs, while the principle of fluxgates does not make theirs readouts temperature dependent. Therefore the fluxgates are most suited for a detailed characterization of the background magnetic field fluctuations (Section 11.3).

The Hall probe needs calibration of the offset by the use of its zero-field holder. With this done, it returns a well-calibrated output. The calibration curve from the datasheet [189] as shown in Fig. 11.3 are used when necessary. As for the fluxgates, a linear scaling of the output voltage to the magnetic field given in its datasheet is assumed [192].

Temperatures/atmospheric pressure

The three kinds of temperature sensors below are installed:

- Temperature readout of the Hall probe (see the section of magnetic fields)
- A piezo-resistive barometric sensor MS5611-01BA03 (TE connectivity)
- Platinum resistance thermometers PT-100 read out by REDLAB TEMP CF (Meilhaus).

Due to a limited number of channels, the resistances of PT-100 thermometers are measured by two-wire measurement. The resistance offsets due to the wires were calibrated by measuring them in the same environment with the pre-calibrated MS5611-01BA03.

In addition to the temperature sensors above, thermometers (CERNOX and PT-100) are installed on the 4 K- and the 77 K stages of the apparatus which are read out by Lake Shore Model 218. They are crucial during the cool-down of the apparatus. However, recording these thermometers was found to interfere the measurement as it generates electronic noise close to the cyclotron frequency of the antiproton in the apparatus. Therefore the cryogenic thermometry lines are usually grounded.

The Hall probe measures the ambient temperature near the magnet. The barometric sensor MS5611-01BA03 is installed in a box which hosts the high-precision voltage supplies UM1-14 (Sections 5.4 and 5.5), and measures temperature and atmospheric pressure in the box (Fig. 11.1). One of the PT-100 thermometers is installed in the same box as the barometric sensor. Two are installed inside covers of the cryostats which were installed in earlier part of 2017 run (Section 16.3). The covers are made of acrylic plates with an aluminum structure, covered by thermal foam to isolate the surfaces of the cryostats from the exterior. Typical temperatures inside the covers are 13–18 °C. The pressure in these covers is interesting information, but a suited sensor which operates in under a humid and low-temperature environment was not found.

The primary cause of temperature variations is an air conditioning system of the AD-hall, which makes the zone temperature to vary with roughly in a period of 24 h. As an example, the temperature

[1] The principle of the Hall probe is the Hall effect [190], that of the GMR sensor is the GMR effect [191], which are both dependent on resistance measurements of the samples.

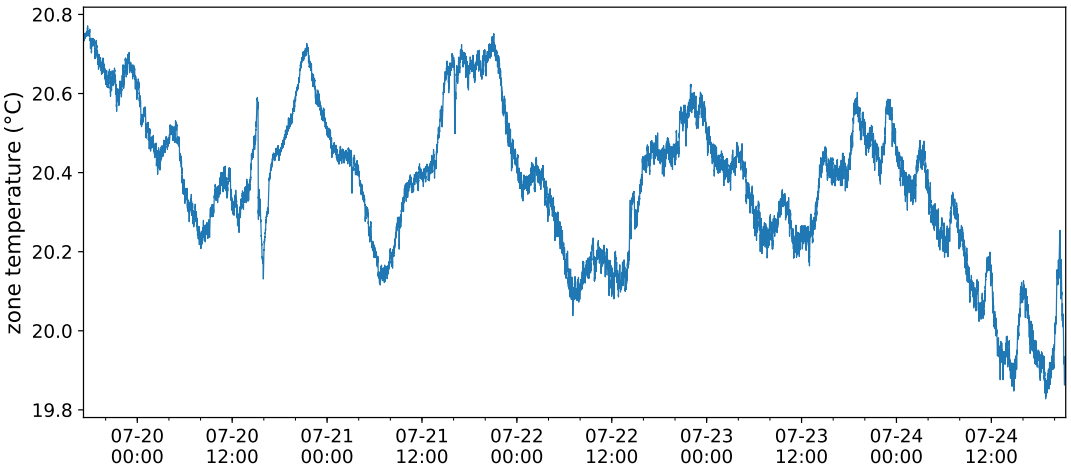

Figure 11.4: Temperature in the BASE zone measured in four consecutive days in July 2017. A periodic variation caused by the AD air conditioning system can be observed. Measured by the Hall probe.

in the BASE zone measured by the Hall probe in July 2017 is shown in Fig. 11.4. A typical day/night differences of temperature in the zone is 0.4–0.6 °C throughout the year. In December 2017, the entire BASE zone was covered by a nylon sheet to suppress such temperature fluctuations (Section 16.5). The installation of the zone cover suppressed the day/night difference of the temperature to about 0.1 °C. Subsequently to the installation of the cover, one more PT-100 thermometer was installed to monitor the ambient temperature outside the zone.

Helium pressures

Pressures of the helium vessel of the magnet were found to be important for the effective magnetic field stability. During 2017 run, a pressure stabilization system was installed (see Section 16.4). The pressures at the exhaust of the helium vessel (1000–1100 mbar) and that of a buffer volume of the stabilization system (14–60 mbar) are monitored by a pressure sensor 120AA-01000DCJ (MKS Instruments), read out and powered by PR 4000B-F (MKS Instruments). Details of the pressure variations and their effects on the frequency stability will be discussed in Section 16.4.

Mass flow

Mass flow sensor EM1 (Sensirion) is installed at the nitrogen exhaust of the magnet. This information is mostly used to diagnose the condition of the magnet. Typically, a constant mass flow of about 3.2 l_n/minis measured at the nitrogen exhaust in normal conditions when the magnet is stabilized after filling of the cryogen. A flow rate significantly smaller than this value often indicates that the LN_2 vessel of the magnet is close to empty.

Angles

Three of triaxial accelerometers MMA8451 (Adafruit) are attached on the apparatus at the positions indicated in Fig. 11.1: one on the top of the magnet, and two on the upstream- and downstream cryostat supports. The photographs in Fig. 11.5 show the one installed on the upstream support. As seen in the upper photograph, each sensor is read-out and controlled by a micro-controller board Ardunino Micro (Adafruit) which sends the acquired data to a computer.

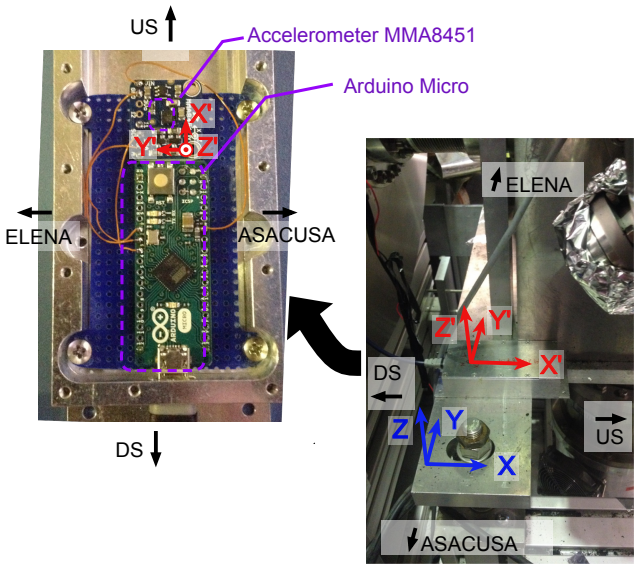

Figure 11.5: Accelerometer MMA8451 installed on the support structure of the upstream cryostat. The photograph on the left shows the content of the project box where the sensor and the micro-controller Arduino Micro used for control and readout are installed. The local coordinate system of the sensor (X', Y', Z') is defined in the same orientation as the fixed coordinate system (X, Y, Z) (common as Figs. 11.1 and 11.2).

From components of the gravitational acceleration measured by the sensor, the tilts of the sensor can be evaluated. The principle of the acceleration measurement is called a capacitive sensing technique, based on detection of the force between two-plate capacitors by voltage measurement, making the sensors sensitive to electrical noise. In order to filter out high-frequency noise, an average of 10 recent measurements acquired in an interval of 300 ms is calculated by the Arduino Micro and taken as the output.

For each sensor, an local coordinate system (X', Y', Z') is defined as shown in Figs. 11.5 and 11.6 (A,B). From the three components of the gravitational acceleration $g_{X'}, g_{Y'}$ and $g_{Z'}$ measured by the sensor, the angles θ_h and θ_v defined in Fig. 11.6 (B), which respectively correspond to horizontal- and vertical tilts, are determined by the following relations:

$$\begin{aligned} \theta_\mathrm{h} &= \tan^{-1}\left(-\frac{g_{Y'}}{g_{X'}}\right) \\ \theta_\mathrm{v} &= \cos^{-1}\left(\frac{g_{Z'}}{\sqrt{g_{X'}^2 + g_{Y'}^2 + g_{Z'}^2}}\right). \end{aligned} \tag{11.1}$$

Fig. 11.6 (C) shows results of a two-day measurement of the angles $\theta_\mathrm{h}, \theta_\mathrm{v}$ measured by the sensor on the magnet. As mentioned earlier, LHe and LN_2 have to be dispensed to the apparatus every two days. The filling actions typically cause jumps of angles by $|\Delta\theta_\mathrm{h}| = 4$–$10°$, $|\Delta\theta_\mathrm{v}| = 0.1$–$0.3°$. Cyclotron frequency measurement is normal performed from a few hours after a filling, where typically angle

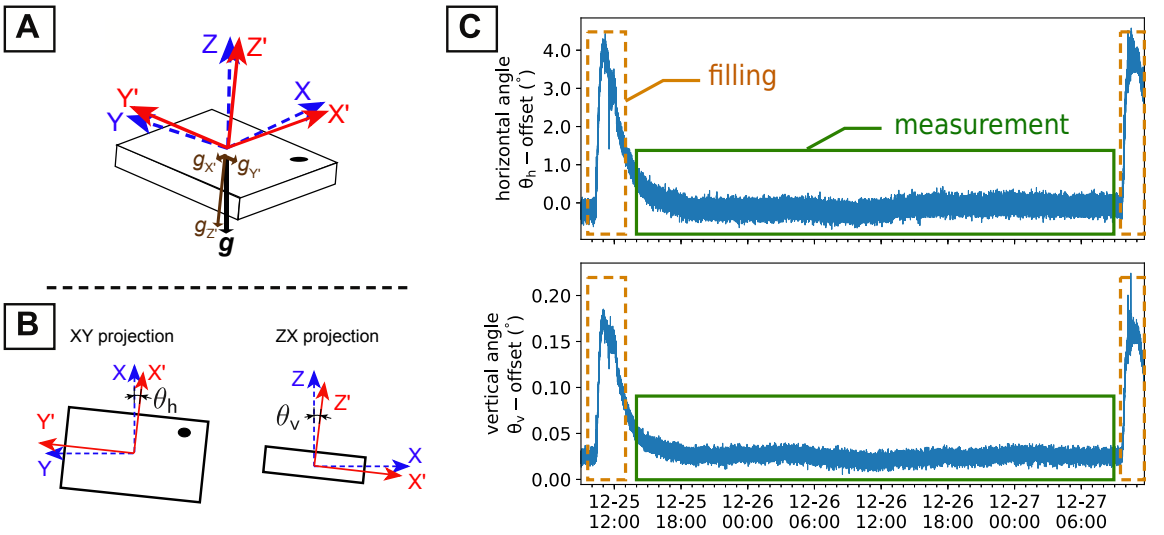

Figure 11.6: **(A)** Definition of the local coordinate system and the principle of the angle measurement. The local coordinate system (X', Y', Z') is indicated by the red arrows. The sensor measures the X'-, Y'- and Z' components of the gravitational acceleration. **(B)** Definition of the angles θ_h and θ_v. They can be evaluated by Eq. (11.1) and $g_{X'}, g_{Y'}, g_{Z'}$ measured by the sensor. **(C)** Measurement of the angles θ_h and θ_v of the sensor placed on top of the magnet. Times when filling of cryogen took place are indicated by dashed orange rectangles. A time window where a cyclotron frequency measurement took placed is marked by green rectangles.

variations are $|\Delta\theta_h| = 1$–$4°$, $|\Delta\theta_v| = 0.01$–$0.07°$ within 40 h. The drifts of the angles reflect variation of the balance of the apparatus according to consumption of the cryogen. The above values are for the sensor on the magnet, and for the ones on the cryostat support have variations smaller by about a factor of 4.

Other sensors

In addition to the sensors discussed above, the monitoring system also includes vacuum gauges which measure the pressure of the insulation vacuum between the trap chamber and the outer vacuum chamber, and CERNOX and PT-100 thermometers (read out by Lake Shore 218) installed on the 4 K- and 77 K stages of the apparatus. They were important at a cool-down of the apparatus. However they were found to generate undesired electric noise for the experiment, therefore are normally turned off during the development and measurement phases of the experiment.

11.2 Data acquisition and management

Fig. 11.7 shows the flow of data in the system. The data acquisition programs on the computers are made in `LabVIEW` (National Instruments). The communications between the devices/sensors are made in the RS-232 serial or IEEE-488 (GPIB) communication. As for the barometric sensor MS5611-01BA03 and the accelerometers MMA8451, the sensors are controlled and read out by Arduino Micro

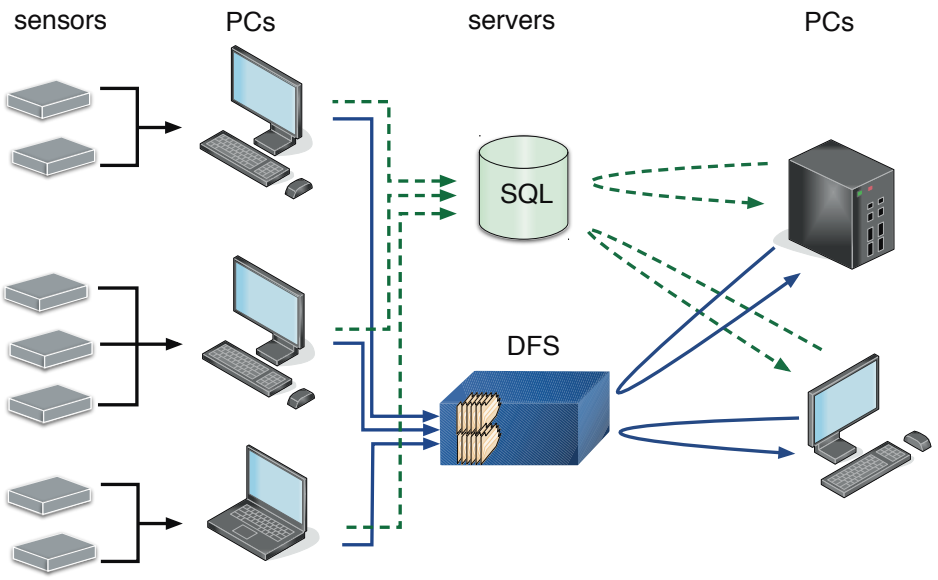

Figure 11.7: Flow of data acquired by the monitoring system. The data from the sensors are first saved locally on the computers. The system automatically copies the data to the CERN DFS and optionally to the Oracle SQL server. The stored data can be accessed by client computers.

micro-controllers in the I^2C communication, and then the data recorded in the Arduino Micro is sent to the computers in RS-232.

Data recorded on computers are automatically copied in the form of text files in a structured way on CERN Distributed File System (DFS). As an optional feature, data is also copied on an Oracle database hosted on CERN servers. The use of the SQL database enables implementation of useful functionalities such as automatic emails which daily send a summary of data logged by the system.

The `LabVIEW` Oracle Open Database Connectivity (ODBC) toolkit and a `python` interface `cx_Oracle` are used to access the SQL database.

Table 11.1: Summary of the sensors which compose the monitoring system. The data categories, names, locations, resolutions, and a typical sampling interval used in 2017 run are listed.

Sensor type	**Data category**	**Name (manufacturer)**	**Location**	**Resolution**	**Interval**
Hall probe	Magnetic field Temperature	HMNA-2518-VR-HF (Lake Shore) Lakeshore 475 DSP Gaussmeter	US cryostat support (Fig. 11.1)	0.7 µT 0.1 °C	0.2 s
GMR sensor	Magnetic field	AA002-02 (NVE) Keithley 2000	Upstream rack (Fig. 11.2, right)	0.25 µT	0.2 s
Fluxgates	Magnetic field	FLC 3-70 (Stefan Mayer Instruments) USB-4065 (National Instruments)	On the upper level (Fig. 11.2, left)	0.35 nT	0.5 s
Barometric sensor	Temperature Atmospheric pressure	MS5611-01BA03 (TE connectivity)	Inside UM box (Fig. 11.1)	0.01 °C 0.01 mbar	2 s
Thermometers	Temperature	PT-100 REDLAB TEMP CF (Meilhaus)	Inside cryostat covers, inside UM box (Fig. 11.1), ambience	0.14 mΩ 4×10^{-4} °C	2 s
Pressure sensor	Helium pressure	120AA-01000DCJ (MKS Instruments) PR 4000B-F (MKS Instruments)	Magnet helium exhaust (Fig. 11.2) Buffer volume pressure (Fig. 16.8)	0.1 mbar	1 s
Accelerometers	Angles	MMA8451 (Adafruit)	US/DS supports, magnet (Fig. 11.2)	$2.4 \times 10^{-4} g$	0.25 s
Mass flow meter	Nitrogen flow	EM1 (Sensirion)	Magnet nitrogen exhaust (Fig. 11.1)	$8\,\mathrm{ml_n/min}$	1 s

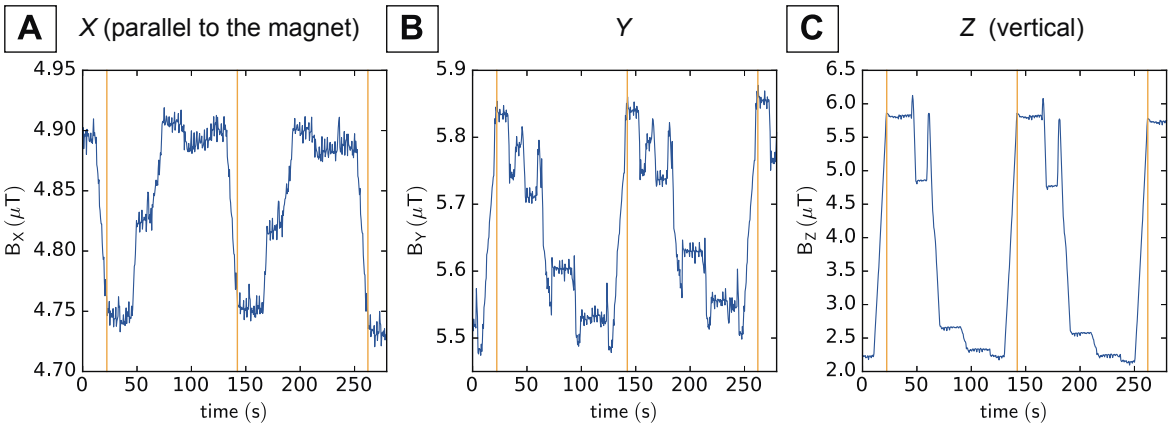

Figure 11.8: Magnetic field produced by the AD operation measured by the downstream fluxgate (Fig. 11.2). The vertical orange lines indicate the timing of the injection of antiproton beams to the AD ring.

11.3 Magnetic field fluctuations in the AD

As the experiment is situated in an accelerator facility, there are various sources of magnetic field variations. What matters the most to the measurement is periodic magnetic field variations produced by operation of the AD, which have about the same time scale with cyclotron frequency measurements. In addition to the AD, the new ELANA ring also became operational in 2017. A detailed characterization of the magnetic field fluctuations by operation of the AD/ELENA is presented in Section 11.3.1. In Section 11.3.2, the other causes of magnetic field fluctuations are summarized.

11.3.1 Magnetic field fluctuations by the AD/ELENA

Typical magnetic field variations produced by the AD measured by the downstream fluxgate are plotted in Fig. 11.8. Fig. 11.8 (A),(B) and (C) respectively correspond to the X, Y and Z axes defined in Fig. 11.2. The orange vertical lines indicate the timing of trigger signals synchronized to injections of antiproton beams in the AD ring. Steps of magnetic field variations corresponding to that of the deceleration cycle (Fig. 4.2) are observed in each channel. Because the sensor has bidirectional outputs, the AD magnetic field appears inversely in the X component, which is parallel to the axis of the magnet and measures its stray field. The Y component is therefore more appropriate to evaluate the horizontal component of the pure magnetic fluctuations by the AD.

The amplitude of the AD magnetic field variation is about 100–500 nT in the horizontal directions (X, Y) and about 3.5 μT in the vertical direction (Z).

Actual measurements are synchronized to the AD cycle to avoid beats between the measurement cycle and the AD cycle. Therefore what is of interest is the statistical properties of the magnetic field for a time window selected in each cycle. For a detailed analysis of the periodic magnetic field fluctuations, measures $\Xi_{\overline{B}}$ and $\overline{\sigma}_B$ are defined as the following. These measures are defined as functions

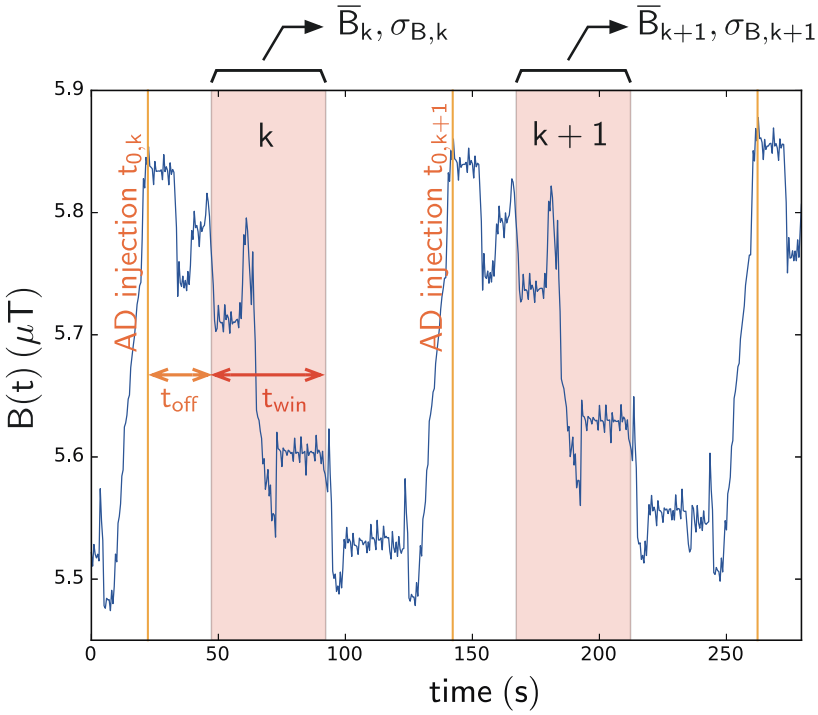

Figure 11.9: Definition of the variables used for the evaluation. The time $t_{0,k}$ corresponds to injection of antiprotons in the AD ring at the beginning of each cycle. The time window for analysis is defined in respect of $t_{0,k}$ by the offset $t_{\rm off}$ and the window length $t_{\rm win}$. $\overline{B}_k$ and $\sigma_{B,k}$ are defined by Eq. (11.2), calculated with data included in the selected time window.

a time window for analysis in the cycle as exemplified in Fig. 11.9.

Let $\{B(t_i)\}$ be sampled magnetic field at points of time t_i, and $\{t_{0,k}\}\,(k = 1, 2, \cdots, N)$ to be an array of time at the antiproton injection in the beginning of each cycle, with N being the number of AD cycles included in the analyzed dataset. The time window for analysis, indicated by red bands in Fig. 11.9, is defined for cycle k by the offset $t_{\rm off}$ in respect of t_k and the window length $t_{\rm win}$. For sampled magnetic field data included in the time window k, we define $\overline{B}_k$ and $\sigma_{B,k}$ as

$$\begin{aligned} \overline{B}_k &= \overline{\{B(t_i)\,|\,t_{0,k} + t_{\rm off} < t_i < t_{0,k} + t_{\rm off} + t_{\rm win}\}}, \\ \sigma_{B,k} &= {\rm STD}\left(\{B(t_i)\,|\,t_{0,k} + t_{\rm off} < t_i < t_{0,k} + t_{\rm off} + t_{\rm win}\}\right). \end{aligned} \tag{11.2}$$

Here $\overline{\{\cdots\}}$ and ${\rm STD}(\{\cdots\})$ stand for operations to an array $\{\cdots\}$, respectively averaging and calculation of the standard deviation. For an array of $\{\overline{B}_k\}$ and $\{\sigma_{B,k}\}$, we define $\Xi_{\overline{B}}$ and $\overline{\sigma}_B$ by

$$\Xi_{\overline{B}} = \sqrt{\frac{1}{N-1}\sum_{k=1}^{N-1}(\delta\overline{B}_k - \overline{\delta\overline{B}})^2} \tag{11.3}$$

$$\text{with} \quad \delta\overline{B}_k = \overline{B}_{k+1} - \overline{B}_k \quad (k = 1, 2, \cdots, N-1), \quad \overline{\delta\overline{B}} = \frac{1}{N-1}\sum_{k=1}^{N-1}\delta\overline{B}_k$$

$$\overline{\sigma}_B = \sum_{k=1}^{N} \frac{\sigma_{B,k}}{N}. \tag{11.4}$$

Thus $\Xi_{\overline{B}}$ is an estimate of cycle-to-cycle fluctuations of the mean magnetic field in the selected time window, and $\overline{\sigma}_B$ estimates the magnetic field fluctuations within the time window. The primary interest for the charge-to-mass ratio comparison is $\Xi_{\overline{B}}$ which may affect the cycle-to-cycle cyclotron frequency stability. A high $\overline{\sigma}_B$ is not much of a problem as long as the spectra have enough dip SNR. However its was also analyzed for a possible future implication.

Two datasets were selected for the evaluation, as summarized in Table 11.2. Dataset 1 was sampled in August 2017 when the ELENA ring was operational, while Dataset 2 was sampled in December 2017 when the ELENA ring was stopped. The other conditions are close between the two datasets. Both datasets were sampled in early morning where there was less human activities. The difference of the sampling interval Δt_i by 20% do not cause any significant change in the resulting values.

The raw Y component of the magnetic field of each dataset is displayed in Fig. 11.10. It can be observed that there is no significant jumps or drifts. In the figure insets, the zoomed-in plot of one cycle is shown. In the zoomed-in plot of the Dataset 1 (Fig. 11.10 (A)), the magnetic field fluctuations caused by the ELENA with an amplitude of about 200 nT are observed as superposition onto the variations by the AD.

For each component of B_X, B_Y, B_Z of each of Dataset 1 and 2, $\Xi_{\overline{B}}$ and $\overline{\sigma}_{\overline{B}}$ are evaluated as two-dimensional functions of t_{off} and t_{win}, for ranges $t_{\text{off}} \in [5\,\text{s}, 70\,\text{s}]$ and $t_{\text{win}} \in [10\,\text{s}, 60\,\text{s}]$. The results are shown in Figs. 11.11 and 11.12.

Table 11.2: Summary of the characteristics of the analyzed datasets. In the table, Δt_i stands for the sampling interval of the fluxgate, with its error obtained by the standard deviation of all the raw data in the dataset. N stands for the number of the AD cycles included in the dataset, as used in Eqs. (11.3) and (11.4).

Dataset	Period	ELENA	Experiment on shift	Δt_i	N
Dataset 1	Tue. August 8 04:00–06:00	operational	AEgIS	0.591(6) s	60
Dataset 2	Wed. December 6 04:00–06:00	stopped	AEgIS	0.500(3) s	60

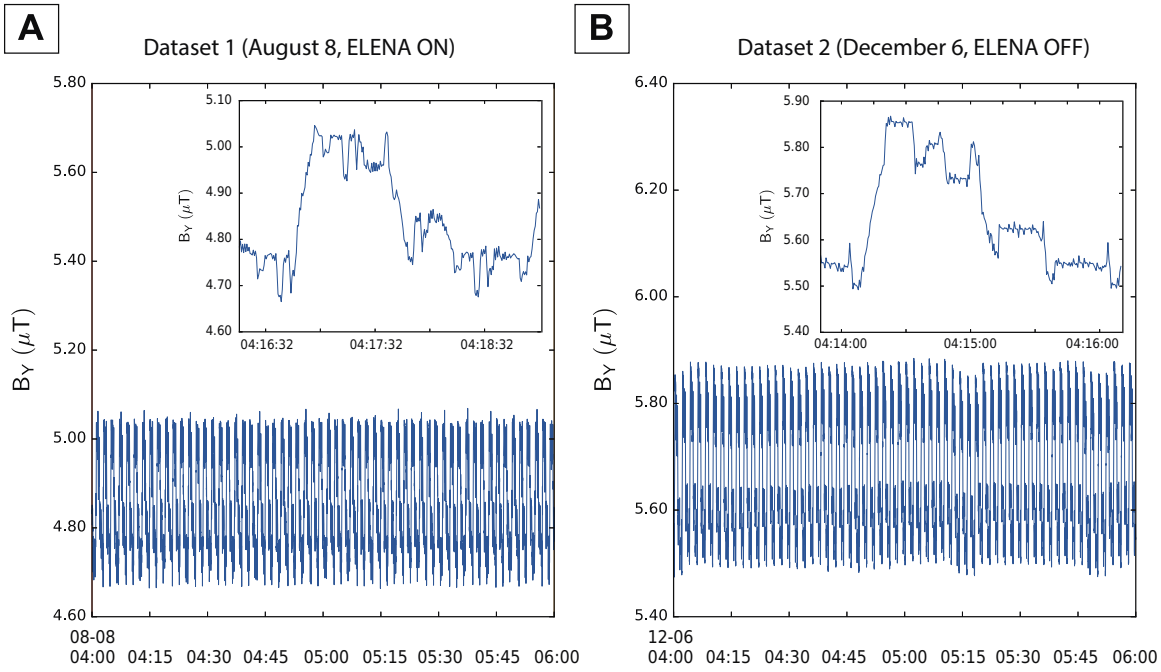

Figure 11.10: Y-components of the magnetic field of Dataset 1 (A) and 2 (B) used for the evaluation. In the inset, zoomed-in plot on one cycle is shown for each dataset. In the zoomed-in plot of (A), magnetic field ramps by the ELENA ring are observed together with the variations by the AD.

What can be observed in the results are summarized below:

1. The region which has the highest $\Xi_{\overline{B}}$ is where the selected time window is overlapped to a large magnetic ramp from the kicker magnet before the antiproton injection. This is enclosed by red dashed lines in each of Figs. 11.11 and 11.12(A–C). The fact that this comes near $(t_{\mathrm{off}}, t_{\mathrm{win}}) = (70\,\mathrm{s}, 60\,\mathrm{s})$ in case of Dataset 1 implies that the cycle length of the AD in this dataset was slightly shorter than Dataset 2. The exact timing of this region differs between the axes, reflecting the differences of their magnetic field properties (see Fig. 11.8).

2. Looking at $\Xi_{\overline{B}_Y}$ of Dataset 2, a region with small $\Xi_{\overline{B}_Y}$ is found at $t_{\mathrm{win}} + t_{\mathrm{off}} > 60$ (enclosed by the green dotted-dash line in Fig. 11.12 (B)). The time $t_{0,k} + 60\,\mathrm{s}$ corresponds to the middle of the cycle. The first half of the cycle contains more frequent magnetic ramps. It seems that

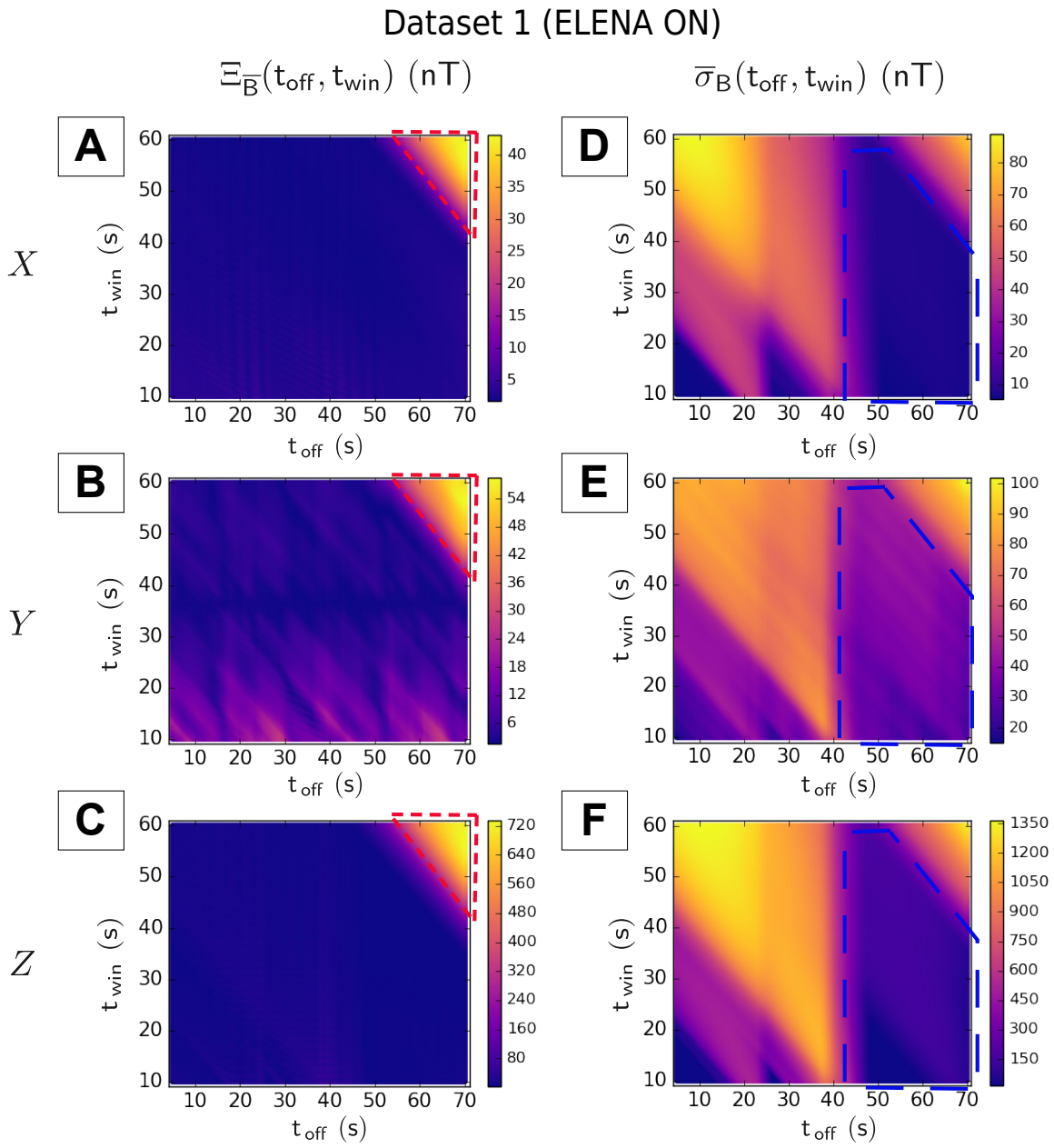

Figure 11.11: Results of the evaluation of magnetic field fluctuations for Dataset 1 recorded in August 2017 when the ELENA ring was operational. (A) $\Xi_{\overline{B}_X}$, (B) $\Xi_{\overline{B}_Y}$, (C) $\Xi_{\overline{B}_Z}$, (D) $\overline{\sigma}_{B_X}$, (E) $\overline{\sigma}_{B_Y}$, (F) $\overline{\sigma}_{B_Z}$. The unit of the color density map is in nT. See the text for further discussion.

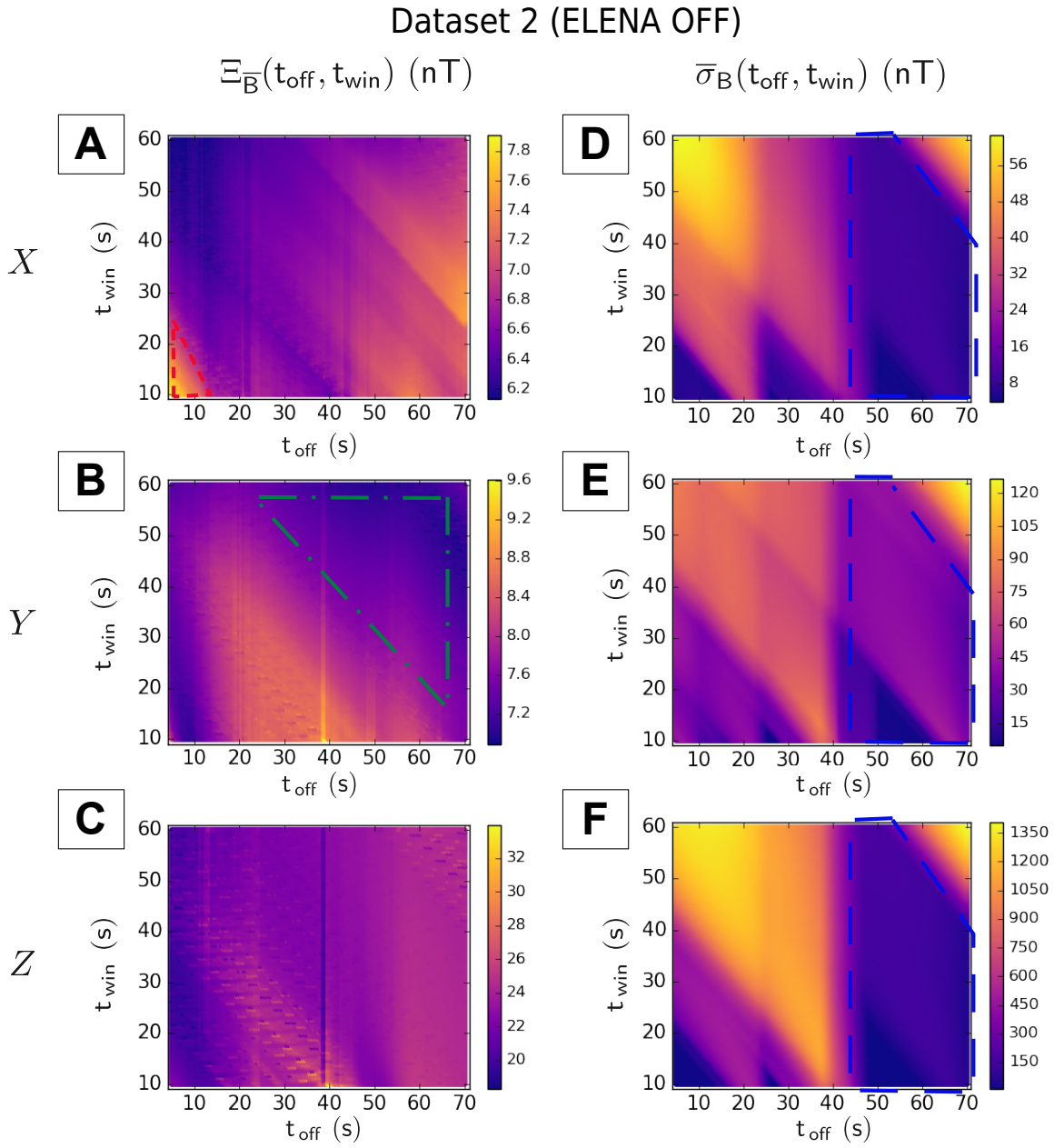

Figure 11.12: Results of the evaluation of magnetic field fluctuations for Dataset 2 recorded in December 2017. The ELENA was not under operation. (A) $\Xi_{\overline{B}_X}$, (B) $\Xi_{\overline{B}_Y}$, (C) $\Xi_{\overline{B}_Z}$, (D) $\overline{\sigma}_{B_X}$, (E) $\overline{\sigma}_{B_Y}$, (F) $\overline{\sigma}_{B_Z}$. The unit of the color density map is in nT. See the text for further discussion.

Table 11.3: Comparison of $\Xi_{\overline{B}}(t_{\mathrm{off}}, t_{\mathrm{win}})$ between Dataset 1 and 2 for different window settings.

$\Xi_{\overline{B}}(t_{\mathrm{off}}, t_{\mathrm{win}})$	Dataset 1 (ELENA ON)	Dataset 2 (ELENA OFF)
$\Xi_{\overline{B},X}(30\,\mathrm{s}, 30\,\mathrm{s})$	2.6 nT	6.6 nT
$\Xi_{\overline{B},Y}(30\,\mathrm{s}, 30\,\mathrm{s})$	3.7 nT	8.4 nT
$\Xi_{\overline{B},Z}(30\,\mathrm{s}, 30\,\mathrm{s})$	13.4 nT	22.9 nT
$\Xi_{\overline{B},X}(50\,\mathrm{s}, 50\,\mathrm{s})$	2.3 nT	6.8 nT
$\Xi_{\overline{B},Y}(50\,\mathrm{s}, 50\,\mathrm{s})$	4.0 nT	7.2 nT
$\Xi_{\overline{B},Z}(50\,\mathrm{s}, 50\,\mathrm{s})$	3.1 nT	23.6 nT
$\Xi_{\overline{B},X}(64\,\mathrm{s}, 48\,\mathrm{s})$	7.6 nT	6.9 nT
$\Xi_{\overline{B},Y}(64\,\mathrm{s}, 48\,\mathrm{s})$	12.2 nT	7.1 nT
$\Xi_{\overline{B},Z}(64\,\mathrm{s}, 48\,\mathrm{s})$	169 nT	24.3 nT

for the earlier half of the cycle, either the cycle-to-cycle fluctuations of the magnetic field are stronger, or the timing between the deceleration steps fluctuates more strongly than the latter half of the cycle.

3. The influence of the ELENA operation is observed most clearly in $\Xi_{\overline{B},Y}$ Fig. 11.11 (B) in a region $t_{\mathrm{win}} < 40\,\mathrm{s}$. The oscillatory structure indicates that the operation of the ELENA was synchronized to the AD and made four times of magnetic ramps in one AD cycle, each continuing for about 30 s. The appearance is less significant in the $\Xi_{\overline{B},X}$, however a similar oscillatory stricture can be observed in a region $20\,\mathrm{s} \leq t_{\mathrm{off}} \leq 50\,\mathrm{s}$. For this mode of the ELENA operation, its effect can be suppressed by choosing $t_{\mathrm{win}} \geq 35\,\mathrm{s}$. In Table 11.3, absolute values of $\Xi_{\overline{B}}$ are compared between Dataset 1 and 2 for sleeted sets of $(t_{\mathrm{off}}, t_{\mathrm{win}})$. If compared for $(t_{\mathrm{off}}, t_{\mathrm{win}}) = (30\,\mathrm{s}, 30\,\mathrm{s}), (50\,\mathrm{s}, 50\,\mathrm{s})$, it can be found that the fluctuations $\Xi_{\overline{B}}$ are smaller for Dataset 1 (ELENA on) than Dataset 2 (ELENA off). From this, it seems that the operation of the AD ring was more stable apropos of the magnetic fields that the ring produced, at the time when Dataset 1 was sampled. It can be said that effects of the ELENA is not significant as long as the region where $t_{\mathrm{win}} < 30\,\mathrm{s}$ is avoided. This has an important implication for future when the ELENA will constantly be operational.

4. As for $\overline{\sigma}_B$, a region of low $\overline{\sigma}_B$ is found in $t_{\mathrm{off}} > 45\,\mathrm{s}$ (enclosed by blue dashed lines in each of Fig. 11.11 (D–F) and Fig. 11.12 (D–F)). This corresponds to the end of the first two magnetic ramps in the AD cycle.

If only the magnetic field fluctuations are considered, it is best to adjust the averaging time window of the double-dip spectra acquisition during the sideband measurement sequence to match to the area

discussed in the above point 2. $t_{\rm off} = 64\,{\rm s}$, $t_{\rm win} = 48$–$58\,{\rm s}$ correspond to typical settings of the double-dip spectra acquisition of the measurement. The results of $\Xi_{\overline{B}}(64\,{\rm s}, 48\,{\rm s})$ are listed in Table 11.3. The values for $(t_{\rm off}, t_{\rm win}) = (30\,{\rm s}, 30\,{\rm s}), (50\,{\rm s}, 50\,{\rm s})$ are also listed for references. More precise tuning, which could improve the magnetic field fluctuation by a few nT is not significant under conditions in 2017 run-II where the shielding factor of the magnetic shielding system was about 90 (Section 10.5.2). As will be discussed in Chapter 15, contributions of the axial frequency fluctuations also needs to be accounted. They are more significant than the magnetic field contribution, and was taken into account in determining the final setting of the averaging window lengths.

Comparison with 2014 cyclotron frequency fluctuations

The magnitudes of the magnetic field fluctuations discussed above can be compared to the characterization of the cyclotron frequency stability by Allan deviations performed to data of the 2014 charge-to-mass ratio comparison. As discussed in Section 7.1, the Allan deviation of the cyclotron frequency was compared between datasets with different configurations in terms of the syntonization to the AD operations. For data recorded when the measurement cycle was synchronized to the AD operation, the white noise component was about $160\,{\rm mHz}\cdot({\rm cycle})^{-1/2}$ and the random walk component was $220\,{\rm mHz}\cdot({\rm cycle})^{1/2}$. The random walk component was reduced to $160\,{\rm mHz}\cdot({\rm cycle})^{1/2}$ for data recorded during a AD shutdown, while reduction in the white noise component was not significant. Therefore, the difference in the random walk components between the datasets of AD on and off

$$\sqrt{220^2 - 160^2} \approx 150\,{\rm mHz}\cdot({\rm cycle})^{1/2} \quad (\text{or } 10\,{\rm nT}\cdot({\rm cycle})^{1/2}) \tag{11.5}$$

can be considered as a contribution of the shot-to-shot magnetic field fluctuations, corresponding to what is evaluated by $\Xi_{\overline{B}}$ to the cyclotron frequency stability. The fluctuations evaluated in Table 11.3 are consistent to Eq. (11.5), considering the magnetic field shielding by a factor of 10 provided by the superconducting magnet used in the 2014 measurement.

11.3.2 Other magnetic field fluctuations

Sources of magnetic field disturbances besides the AD/ELENA are summarized in the list below:

- Magnetic field variations due to ramp up/down of magnets of other experiments (typically 0.5–1 μT)
- Magnetic field variations due to switching of the beam destination (typically 50–500 nT)
- Operations of an overhead crane (typically 2–5 μT).

In Fig. 11.13 (A), examples of magnetic field variations caused by the beamline switchings and the crane operations are found. The magnetic field changes by the beamline switches typically occur in

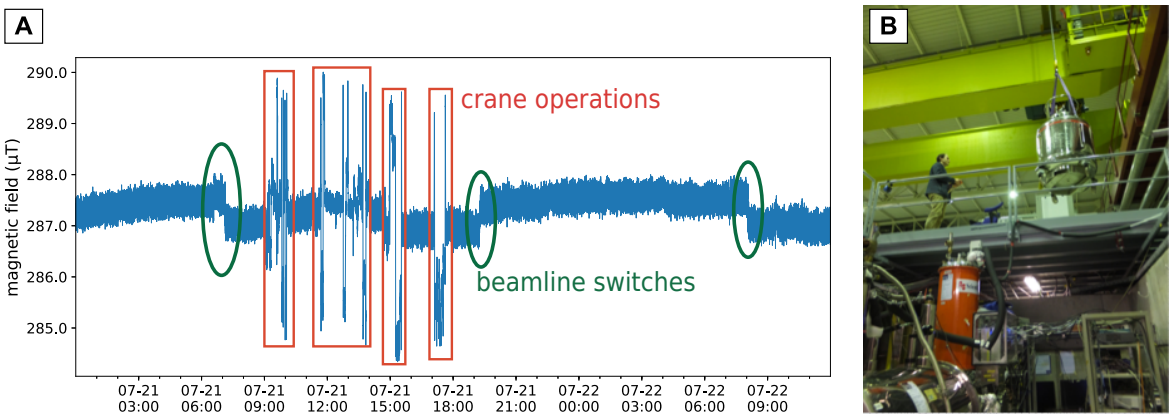

Figure 11.13: **(A)** Magnetic field measured by the Hall probe. The field variations caused by the beamline switchings and crane operations are marked by the green ovals and red rectangles, respectively. **(B)** Photograph of the overhead crane.

time scales of a few minutes. The overhead crane is another source of magnetic field fluctuations, whose photograph is shown in Fig. 11.13 (B). It is used for transport of material such as dewars of the cryogen. When the crane passes over the BASE zone, the magnetized steel body of the crane varies the magnetic field in the zone. This magnetic field disturbance also happens typically on time scales of minutes. In Section 10.5.1, the crane was used to deliberately produce magnetic field variations to measure the shielding factors of the magnetic shielding system.

These momentary variations do not impose a limitation on the measurement. As they can be clearly identified in the results of the cyclotron frequency measurements as well as in the monitored external magnetic fields. Therefore the affected data points can be excluded as outliers in the data analysis.

The slow variations such as the ones caused by the magnet ramps of the other experiments do not cause a problem, either. What is important is stability of the frequency ratio obtained in subsequent measurements. Frequency drifts which have longer time scales than dat sampling are canceled by the interpolation discussed in Section 7.2.

Part VI

Experimental results in 2017

12

Overview of BASE 2017 run

In the next chapters, experimental works in the 2017 run are summarized. The goal was to perform an improvement of the proton-to-antiproton charge-to-mad ratio comparison. To this end, the upgrades described in Part V were implemented to the system. The apparatus was commissioned and had been developed to finally reach a condition where a significant improvement from the 2014 result was possible.

Major events and experimental activities during the run are summarized in the timeline in Fig. 12.1. The run was divided in two parts by disassembling and reinstallation in September/October. They are called run-I and run-II.

Before the beginning of the run, several upgrades were performed to the apparatus for an improved charge-to-mass ratio comparison. The two major upgrades were installation of the tunable axial detection of the PT (Chapter 9) and the advanced magnetic shielding system (Chapter 10). The apparatus was cooled down on the 17th of May. Subsequently, it was commissioned first with protons and then with antiprotons from the antiproton beam-time starting in June.

The cyclotron frequency fluctuation at the beginning of run-I was about a factor of 2 worse than the condition of the 2014 measurement. Efforts were made since then to identify the sources of fluctuations and to optimize the environmental conditions. Over the course, the cyclotron frequency stability improved to finally reach about 72 mHz in early September, which is a factor of > 2 better than in 2014.

The first part of the run (run-I) ended by an accidental quench of the superconducting magnet on the 13th of September. This was unintended, but gave us an opportunity to characterize the detection system in an environment without s strong magnetic field (Section 9.4). We decommissioned the system, recharged (Section 5.1.1) and shimmed (Section 5.1.2) the magnet, upgraded some components, and reinstalled the apparatus in the middle of October (run-II). The three major upgrades performed between run-I and run-II were :

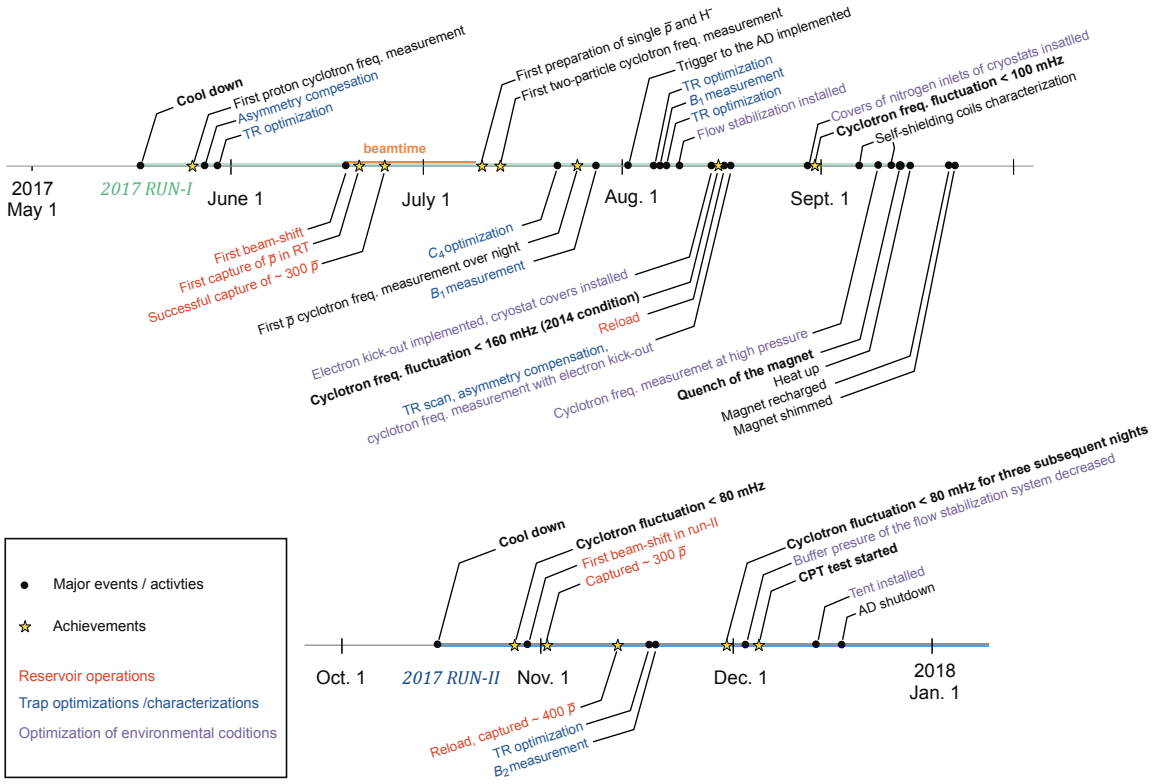

Figure 12.1: Major events and activities during the 2017 run. Works particularly related to the following chapters are highlighted in different colors.

- Exchange of the degrader foil: the in-trap aluminum degrader foil used since 2014 was found to have become radioactive by collisions of energetic antiproton beams,[1] and replaced to a new one. The radioactive degrader frequently caused a problem of electron contamination during run-I (Section 16.6). In run-II, when radioactivity due to short-lived nuclei has settled a few weeks after the beam-time, a typical rate of observing contamination became only one event in two weeks.

- Modifications on the PT axial detection system: the Q-factor of the PT axial detection system in run-I was significantly lower than what was previously measured in a cryogenic test setup. The feedthrough on the pin-base used for the detection line had a deficit, and have caused the reduction of the Q-factor by RF power losses. A different feedthrough was used in run-II. In addition, the resonator and the amplifier were replaced to a set with better performances. As a result, the Q-factor of the PT detection system was improved from ≈ 3100 (run-I) to ≈ 22600 (run-II).

- Examination and modification on the self-shielding solenoids (Sections 10.4.3 and 10.4.3): The joints of the 75 mm- and 86 mm coils of the self-shielding system were remade. Although the repair was unsuccessful, the new coil configuration improved the shielding factor from $-36(4)$

[1] The radioactivity of the foil measured by CERN radiation protection department was 2 Bq.

(run-I) to 90(5) (run-II).

Stability comparable to the end of run-I was soon reached as a result of an improved performance of the system and optimized environmental conditions. After further developments, data taking of the charge-to-mass ratio comparison started on the 5th of December (*CPT test started* in Fig. 12.1).

In the following chapters, experimental results obtained during BASE 2017 run are presented. Works particularly related to the contents of these chapters are highlighted in color in Fig. 12.1 .

In Chapter 13, methods which have been used and developed to prepare a single antiproton and an H^- ion are described. They include methods to catch antiproton beams, to clean the cloud from contaminant particles, and to extract a single particle from the reservoir. Although these are used mostly during the beam-times, the extraction of a single particle from the reservoir (Section 13.3) was regularly performed to prepare a single particle during the development phase.

In Chapter 14, methods used to characterize and optimize the parameters of the PT are summarized. Parameters of the trap such as the magnetic gradient or the asymmetry of the potential are characterized / optimized by using a single particle as a probe.

In Chapter 16, works performed to improve the cyclotron frequency stability are summarized. Before seeing the actual developments and the improvement, the cyclotron frequency stability with the sideband coupling method and the principal stability limit is discussed in Chapter 15.

13

Preparation of a single antiproton/H^- ion

In this chapter, experimental methods to prepare single particles necessary for measurements are discussed, from catching of beams (Section 13.1) until the procedure to extract single particles from a particle cloud (Section 13.3). These methods were established during the beam time in 2014, and have been published as Ref. [146]. A few points particular to 2017 run are discussed in Section 13.3.2.

The operations described in this chapter are performed in the RT, except the electron kick-out (Section 13.2.3) which is also performed in the PT upon necessity.

13.1 Catching

Fig. 13.1 shows the setup around the RT, which functions as a catching trap. For more details of the associated components such as the electron gun, see Section 5.6.

To capture 5.3 MeV antiproton beams from the AD, we employ experimental methods established by preceding antiproton experiments [193–197]. The antiprotons injected to the apparatus are first slowed down by the degrader structure at the entrance, then are captured by a closure of the potential wall by the high-voltage electrode, and gradually lose their energy by both sympathetic- and resistive cooling.

The series of procedures is described in Fig. 13.2.

- Prior to injection of the beam, electrons are loaded to the trap for sympathetic cooling. Potential walls are formed by application of -1 kV on two high-voltage electrodes adjacent to the RT. An electron beam of 50–100 nA is injected by the electron gun located at the downstream end of the trap system (see Fig. 5.10). The downstream potential wall is opened for a few seconds to load typically 7×10^6 electrons [135]. After being captured in the trap, the electrons quickly lose their energy via the cyclotron radiation. The time constant of the cooling $\tau_{e,\mathrm{cool}}$ is given

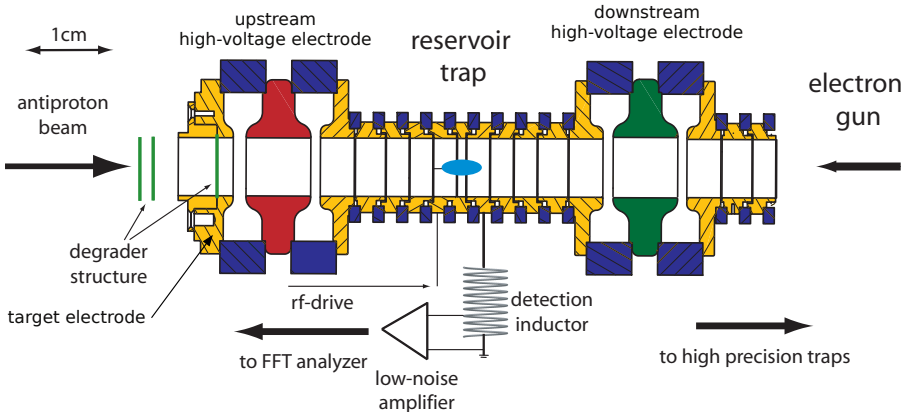

Figure 13.1: Schematic of the RT and the associated components. The antiproton beams are injected from the left (upstream) of the figure through the degrader structure. Electrons for sympathetic cooling are provided by the electron gun located downstream (right in the figure). The axial detection system of the RT is also depicted in the figure. Adapted from Ref. [146], modified under permission.

by [198]

$$\tau_{e,\mathrm{cool}} = \left(\frac{1}{6\pi\epsilon_0} \frac{e^4 B^2}{m_e^3 c^3} \right)^{-1} \approx 0.68\,\mathrm{s}. \tag{13.1}$$

- Next, antiprotons are injected to the trap by setting appropriate currents on the beam line magnets. The upstream potential wall of $-1\,\mathrm{kV}$ is opened for typically $100\,\mu\mathrm{s}$ before the arrival of the beam to the trap, and closed at adequate timing to capture the beam. This is done by using the delay generator which adds an appropriate offset to a trigger signal from the AD, and activates the high-voltage switch (see Section 5.6.3). The beam, typically containing $\sim 3 \times 10^7$ antiprotons at arrival, has a broadened energy distribution by passing through the degrader. Among them, a fraction which has kinetic energy of $\lesssim 1\,\mathrm{keV}$ is captured in the trap. The captured fraction at this stage was estimated to be on the order of $10^3 \bar{p}$ by ejecting the trapped content by another voltage pulse and observing the annihilation signals by the scintillator.

- The captured antiprotons are sympathetically cooled by interactions with radiatively cooled electrons to the order of 100 meV [194]. After they are cooled enough to be confined in the trap center, they are further cooled via resistive cooling by the RT detection system [196]. The time constant of the sympathetic cooling depends on the electron density and temperature of the antiproton- and electron clouds [196], but on the order of 10 s or below. The high-voltage potential walls are ramped down after waiting time sufficient for the cooling.

Before execution of the procedure above, parameters such as the currents of the magnets on the beamline, the offset and the duration of the catching pulse must be optimized. Extensive parameter searches were performed in 2017 run-I, which led to an improvement in the number of finally trapped antiprotons (see Section 13.2.5). Their details are found in Natalie Schön's master's thesis [135].

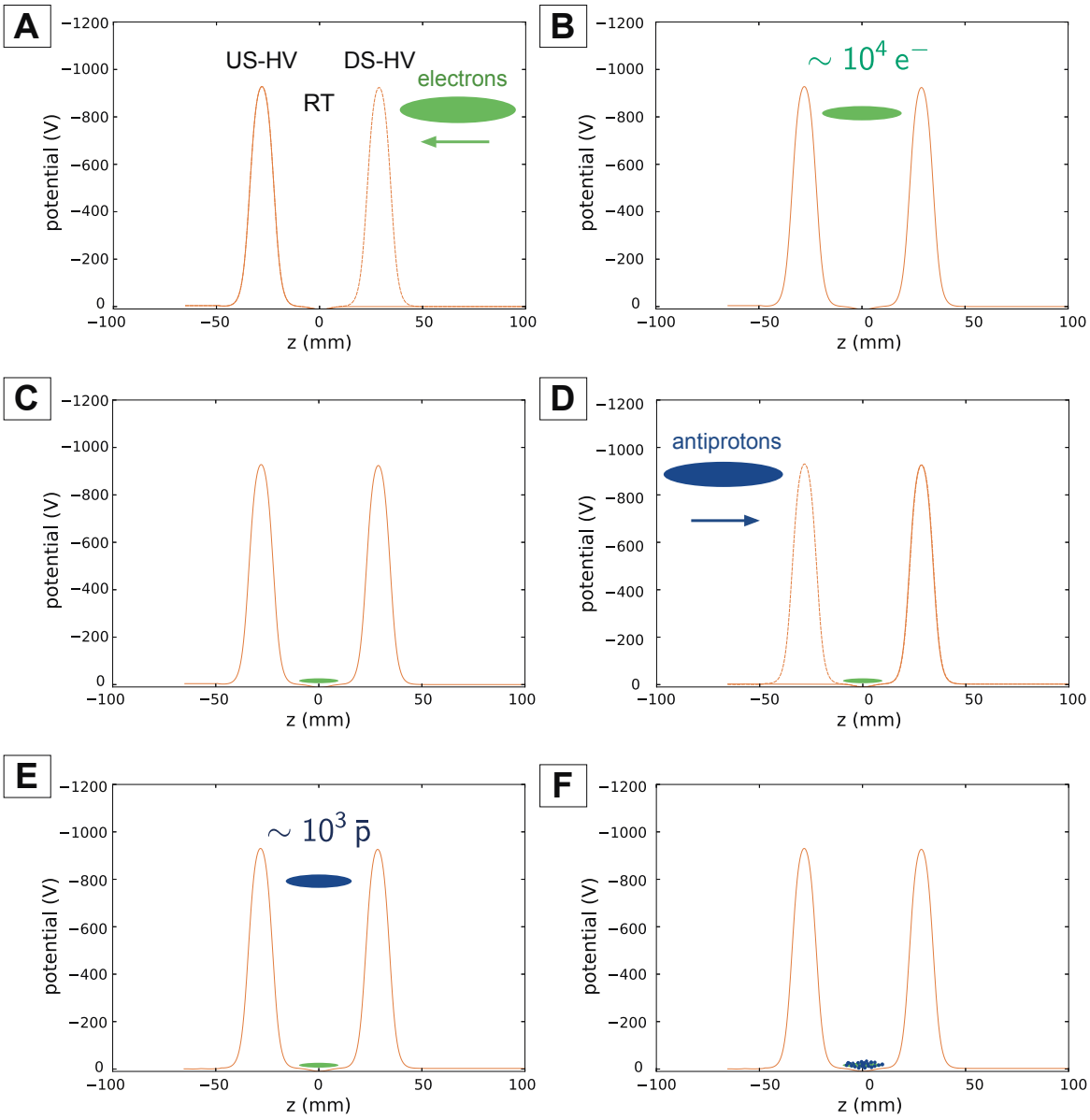

Figure 13.2: On-axis electric potentials during the catching operation. **(A,B)** Electron loading. An electron beam is injected from the electron gun located on the downstream end of the trap stack. The potential wall by the downstream high-voltage electrode is ramped down for a short time to introduce the electrons in the RT. Typically 10^4 electrons are captured. **(C)** The electrons captured in the last step is cooled by radiative cooling. **(D, E)** Antiproton loading. A fraction of antiprotons injected through the degrader structure is captured by an adequately timed voltage pulse on the upstream high-voltage electrode. Typically, 10^3 antiprotons are trapped at this stage from original 10^7 in the beam. **(F)** The captured antiprotons are sympathetically cooled by the electrons pre-loaded to the trap, then resistively cooled by interactions with the RT axial detection system.

Table 13.1: Typical parameters of the RT in 2017 run-I and run-II. The resonance frequency $\nu_{0,\mathrm{eff}}$ and the with $\Delta\nu_{0,\mathrm{eff}}$ and the Q-factor of the detection system, the ring voltage $V_{\mathrm{R},\bar{p}}$ to adjust antiprotons to the resonance frequency, and the dip-width of a single antiproton $\Delta\nu_{z,\bar{p}}$ are listed for each.

	$\nu_{0,\mathrm{eff}}$ (Hz)	$\Delta\nu_{0,\mathrm{eff}}$ (Hz)	Q_{eff}	$V_{\mathrm{R},\bar{p}}$ (V)	$\Delta\nu_{z,\bar{p}}$ (Hz)
2017 run-I	784987	40.8	19240	6.896	3.29
2017 run-II	793892	37.3	21280	7.101	3.67

Table 13.2: Eigenfrequencies of different species of negatively charged particles calculated for trap $B = 1.945\,\mathrm{T}$ and $V_{\mathrm{R}} = 7.104\,\mathrm{V}/0.7\,\mathrm{V}$. The ion masses are based on Ref. [199].

	$V_{\mathrm{R}} = 7.104\,\mathrm{V}$			$V_{\mathrm{R}} = 0.7\,\mathrm{V}$		
particle	ν_+ (MHz)	ν_z (kHz)	ν_- (kHz)	ν_+ (MHz)	ν_z (kHz)	ν_- (kHz)
e^-	54 445	34 228	10.759	54 445	10 744	1.0601
$\bar{p}$	29.641	798.77	10.763	29.651	250.74	1.0602
H^-	29.609	798.34	10.763	29.616	250.60	1.0602
C^-	2.4782	231.42	10.806	2.4879	72.645	1.0606
O^-	1.8565	200.45	10.821	1.8663	62.922	1.0607

13.2 Removal of contaminant particles

After the catching procedure, the RT contains negative-charged particles besides antiprotons; electrons and ions such as H^-, C^-, O^-. These negative ions are produced by the collisions of the incoming antiprotons on the degrader via dissociation of atoms and molecules on the degrader surface. Among them, H^- ions are necessary for the measurement, while the others obstruct measurements. These contaminant particles disturb the frequency of the antiprotons and prevent them from being observed as a stable dip signal. The next step of preparation is to remove these contaminant particles. In what follows, different methods employed for the trap cleaning are summarized. For discussion of trap operations below, typical RT parameters in 2017 run-I/II are listed in Table 13.1.[1]

13.2.1 Cleaning by RF excitations

The simplest cleaning method is selective excitation of eigenmodes of the contaminant particles in the trap. On the left half of Table 13.2, eigenfrequencies of different species of particles calculated for the operational conditions of the RT in 2017-run II are listed.

The ions heavier than H^- ions are distinguished by antiprotons and H^- ions by their axial frequencies. They are excited by a broad-band noise signal [200] with a range from 20 kHz to 500 kHz through the axial excitation line (Section 5.4.2). When it is necessary to remove antiprotons or H^- ions[2], the modified cyclotron mode is excited by a quadruple drive through the radial excitation line.

[1] During proton commissioning, the same cleaning methods as described in Sections 13.2.1 and 13.2.2 are used to remove positively charged contaminant ions. $H_2{}^+$ ions are removed in the same way as H^- ions in the antiproton case by exciting their modified cyclotron mode (Section 13.2.1).

[2] A typical situation to remove antiprotons is extraction of an H^- ion. See Section 13.3.

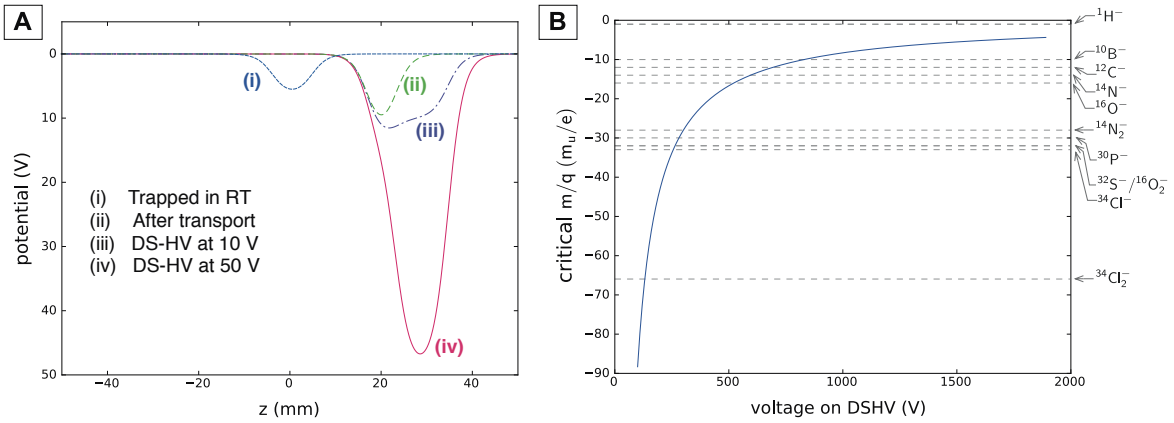

Figure 13.3: **(A)** Procedure of removal of the contaminant ions by the trap instability condition. The trap content is first located at the center of the RT (i). It is transported to the electrode adjacent to the downstream high-voltage electrode (ii). The voltage on the high-voltage electrode is increased in steps up to 1800 V; the potentials for 10 V (iii) and 50 V (iv) are plotted. In the process of ramping the high voltage, the trap content drops into the deep well formed by the high voltage, from which the contaminant ions escape. **(B)** The critical mass-to-charge ratio for stable trapping (Eq. (13.2)) is calculated by the curvature of the potential for the cleaning. The critical m/q is plotted against the voltage applied on the downstream high-voltage electrode. The unit is m_u/e (m_u: the atomic mass unit, e: the elementary charge).

After the excitation, trapping potential is made shallower, typically to 0.3 V[3], to evaporate excited particles.

For removal of electrons, a dipole drive at 10 MHz is kept on while the trapping potential is slowly decreased to 0.3 V and then ramped back to normal $V_R \approx 7$ V. This drive frequency corresponds to the axial frequency of electrons at $V_R \approx 0.7$ V. Electrons which have high radii have higher axial frequencies than this. Lowering the potential during the excitation makes these high-radii electrons in resonant with the drive.

During the operations of voltage ramps and excitations, a positive potential is applied to the most upstream target electrode (see Fig. 13.1) in order to attract negative particles escaping from the RT.

13.2.2 Cleaning by trap instability condition

This method makes use of the condition of the stable trapping potential mentioned in Section 2.1.1. From Eq. (2.10),

$$\frac{m}{|q|} < \frac{B^2}{4|C_2 V_0|} = \frac{B^2}{2}\left|\left(\frac{\partial^2 \Phi}{\partial z^2}\right)^{-1}_{z=z_0}\right| \tag{13.2}$$

is a criterion for stable trapping of particles of mass m and charge q. Here z_0 represents the axial position of the potential minimum. This can be used to remove ions heavier than antiprotons/H^- ions by providing a deep trapping potential. For particles which have higher mass-to-charge ratios $m/|q|$ than the right hand side of Eq. (13.2), radial confinement by the magnetic field does not balance to

[3] At $V_R < 0.256$ V(run-I)/0.385 V(run-II) a loss of antiprotons from a cloud thermalized to the detection system started to be observed.

the strong axial potential, and the particles escape in the radial direction.

The procedure is shown in Fig. 13.3 (A). To apply this method, the cloud is transported to the electrode next to the downstream high-voltage electrode (Fig. 13.3, (A) (ii)), then the trapping potential is deepened by slowly increasing the voltage on the high-voltage electrode (Fig. 13.3 (A) (iii, iv)) to 1800 V. The ions which do not satisfy the stability condition escape from the trap in the radial direction. After waiting for about 60 s at 1800 V, the potential is ramped down, then the cloud is transported back to the trap by the reversed procedure.

In Fig. 13.3, (B) the scaling of the critical mass-to-charge ratio m/q of Eq. (13.2) in this deep potential is shown against the voltage applied on the downstream high-voltage electrode. On the right of the graph, m/q are indicated for ion species which are likely to exist in the trap. Applying 1800 V on the high-voltage electrode makes the potential unstable for all the ions heavier than H^-. This method was found to be very efficient in removing the contaminant ions.

13.2.3 Electron kick-out

Electrons on large magnetron orbits are not removed by the axial excitation discussed in Section 13.2.1. To remove such electrons efficiently, the electron kick-out technique [195] is employed. The basic idea is to open the potential for a short duration by applying a fast voltage pulse. Because of the mass differences, it is possible to choose the opening duration which lets electrons escape, but keeps antiprotons/H^- ions trapped in the potential. The kick-out was configured for the following three positions of the trap stack:

- Kick-out at the upstream high-voltage electrode, in the upstream direction
- Kick-out at the downstream high-voltage electrode
- Kick-out at the pulsed electrode located downstream of the ST, in the downstream direction.

These electrodes are equipped with the diode-bridge filters (see Section 5.6.3) for application of pulse signals. The kick-outs at the downstream high-voltage electrode and the ST pulsed electrode are used to clean the PT content. In Fig. 13.4, potentials for the kick-outs at the upstream high-voltage electrode (A) and at the ST pulsed electrode (B) are displayed together with the cross sectional views of the corresponding parts of the trap stack. The procedure reads as follows for the kick-out at the upstream high-voltage (Fig. 13.4 (A)):

1. A cloud is transported from the RT center, and parked in the electrode upstream of the upstream high-voltage electrode by the potential (i).
2. The potential (ii) is applied and the cloud is trapped in the well formed between the end of the RT and the upstream high-voltage electrode.

Table 13.3: Properties of the potential formed before the electron kick-out. It corresponds to potential (ii) in Fig. 13.4 (A, B).

	$\frac{\partial^2\Phi}{\partial z^2}\Big\vert_{z=z_0}$ (V/m^2)	$\nu_{z,\bar{p}}$ (MHz)	ν_{z,e^-} (GHz)	$1/\nu_{z,\bar{p}}$ (ns)	$1/\nu_{z,e^-}$ (ns)
US-HV	-2.554×10^5	1.113	47.707	898.2	21.0
DS-HV	-2.533×10^5	1.109	47.503	902.1	21.1
ST pulsed	-1.719×10^5	0.913	39.132	1095	25.6

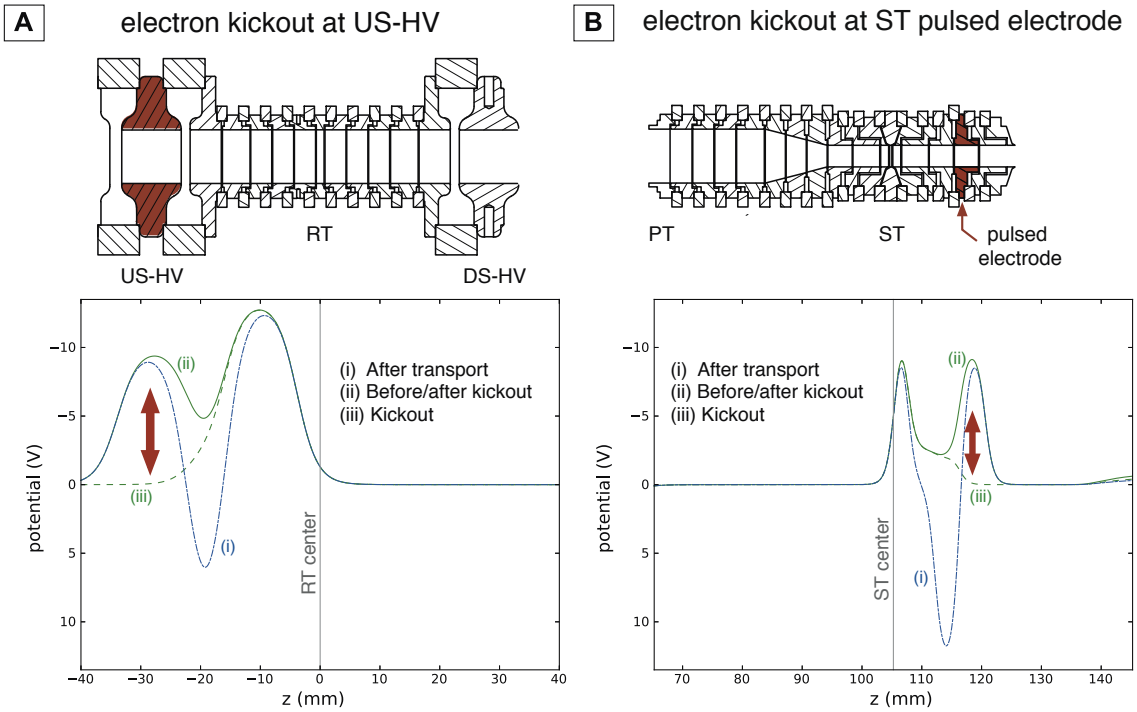

Figure 13.4: On-axis electric potentials used for electron kick-out operations at the upstream high-voltage electrode (A) and the pulsed electrode located downstream of the ST (B). The center of the RT is defined as $z = 0$ of the horizontal axis. The cross-sectional view of part of the trap stack is shown above in the same scale as the horizontal axis. The electrode where a pulsed voltage is applied is marked in brown for each of (A) and (B). For each of (A) and (B), (i) potential after transport to the position of the kick-out, (ii) the potential before and after the kick-out, (iii) the potential during the kick-out. A pulsed voltage opens the potential from (ii) to (iii) for a duration on the order of 100 ns.

3. The voltage on the upstream high-voltage electrode is grounded for a short time, typically 100–180 ns, to form the kick-out potential (iii) to make electrons escape. Afterward the wall is closed and the potential (ii) is again formed.

4. The potential (i) is formed again, and the cloud is transported back to the RT center.

A function generator[4] is used to provide a low-noise voltage pulse with a well-defined length at step 3. The potential (ii) applied before and after the kick-out should be defined such that the length of the

[4] Agilent AG33250 or Keysight 33612A.

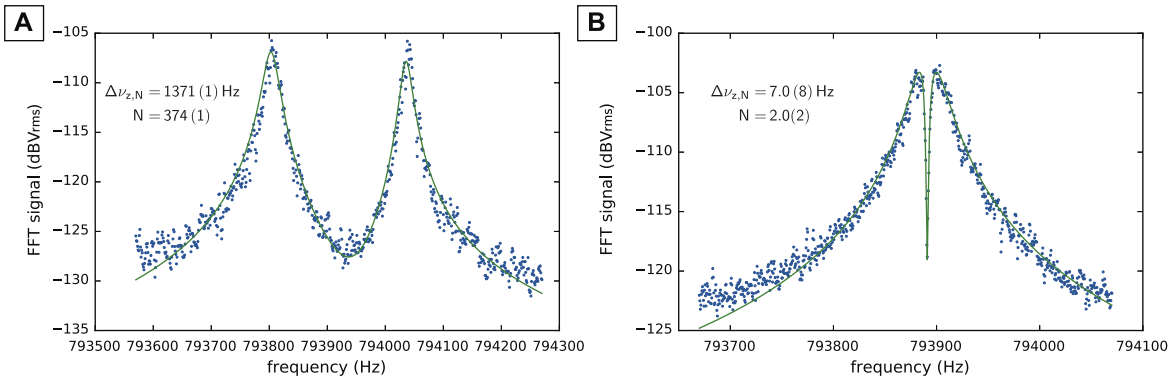

Figure 13.5: Dip signal observed during 2017 run-II corresponding to about 370 antiprotons (A). The signal from two antiprotons is shown in Fig. 13.5 (B) for reference. Note that the large size of the cloud in Fig. 13.5 (A) corresponds to a case $\Delta\nu_z > \Delta\nu_0$ of Eq. (2.115).

voltage pulse is longer for electrons but sufficiently shorter for antiprotons/H^- ions. The oscillation periods $1/\nu_z$ can be estimated by the curvature of the potential at the potential minimum $z = z_0$. These characteristics of the pre-kick-out potential used for kick-out at each of the three positions are listed in Table 13.3. For the employed potentials, the length of the voltage pulse is an order of magnitude shorter than $1/\nu_{z,\bar{p}}$, and an order of magnitude longer than $1/\nu_{z,e^-}$.

13.2.4 Sideband cooling

Between the cleaning procedures, sideband cooling (Section 2.5) is performed frequently to cool the magnetron- and the modified-cyclotron modes of antiprotons and H^- ions to keep them on small radii. Magnetron cooling is also performed after transports which may heat the cloud.

13.2.5 Observation of the dip signal

After removing contaminant particles by the procedures above, a dip of the cloud of antiprotons can be observed. Fig. 13.5 (A) shows a dip signal of the antiproton cloud recored during run-II. A fit to the theoretical line shape yields a dip-width of $\Delta\nu_{z,N} = 1371(1)$ Hz. By the relation $\Delta\nu_{z,N} = N\Delta\nu_z$ (Eq. (2.118)) and the single-particle dip-width of 3.67 Hz (run-II), this corresponds to the number of antiprotons in this cloud of 374(1).

In 2017 run, successful catching and cleaning procedures typically prepare > 300 antiprotons in this stage. This is an improvement by about a factor of 5 compared to previous years, owing to the optimized catching parameters [135].

13.3 Extraction of a single particle

The last step of preparation is extraction of a single particle from a cloud.

13.3.1 Principle of separation of a particle cloud

During 2014 beam-time, we developed methods to store and manipulate particles in the reservoir [146]. They enabled operation of the experiment even during shutdown periods of the AD, and have been key techniques for the recent achievements of BASE (Chapter 6).

Separation of a particle cloud is done by a sequence of voltage ramps. The on-axis potential of each step is displayed in Fig. 13.6. First, the cloud is trapped by a potential well formed by the ring electrode and the two correction electrodes (Fig. 13.6 (a)). A negative voltage of $-13.5\,\mathrm{V}$ is applied on the ring electrode to separate a cloud into two fractions (b). Each of the fractions can be analyzed while the other is being parked in one of the high-voltage electrodes (c/d). Including transport of the particles between each step, the entire procedure takes about 120 s. By a reversed sequence, two clouds can be merged into one. The separated fraction can be controlled by deliberately applying an asymmetric potential at stage (a) by setting an appropriate voltage on one of the correction electrodes. By considering the distribution of the axial coordinates of the particles in a cloud in thermal equilibrium with a detection system (see Section B.1), the number of extracted particles is expected to follow

$$N_{\mathrm{down}} = C \cdot \int_{z_0}^{\infty} |z| \exp\left(-\frac{2\pi^2 m(\nu_z z)^2}{k_{\mathrm{B}} T_z}\right) \mathrm{d}z, \tag{13.3}$$

with N_{down} being the number of particles extracted to the downstream fraction, C the normalization factor (Eqs. (B.4) and (B.9)).

A characterization measurement was performed in 2014 with the same setup as Fig. 13.1. The results are given in Fig. 13.7. The data was obtained by repeating the separation and the merging procedures for a cloud of about 100 antiprotons. The number of particles of each fraction was counted by measuring the dip-width (Fig. 13.7 (b)). In Fig. 13.7 (a), the extracted fraction of each cloud (upstream fraction: red circles, downstream fraction: black squares) is plotted against the center-of-mass position z_0 before separation. The upstream/downstream fraction calculated by Eq. (13.3) is plotted in Fig. 13.7 (a) for $T_z = 1$–$10\,\mathrm{K}$. The measured scaling of the extracted fractions is consistent with $T_z = 5.3(11)\,\mathrm{K}$, obtained by an independent measurement.

Plotted by the green stars are the sum of both fractions normalized to the number of particles of the cloud before each separation procedure. It can be seen that the total number of particles was constant over the entire measurement sequence, and the operations were lossless within the uncertainties.

This method allows extraction of a selective number of particles, down to a single one. In case of Fig. 13.7 (a), $z_0 = \pm 100\,\mu\mathrm{m}$ correspond to single particle extractions. This is a statistical process,

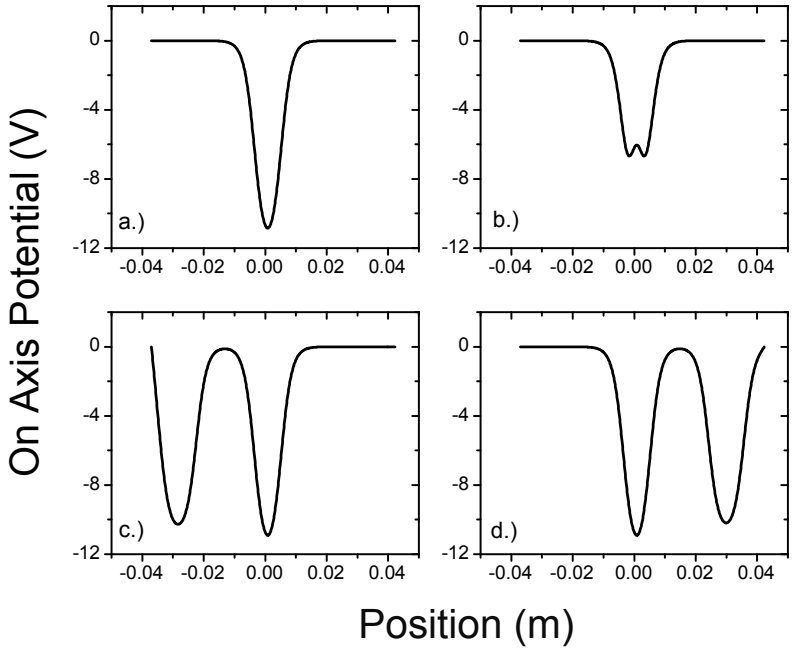

Figure 13.6: On-axis potentials used for particle extractions. **(a)** Potential before separation. **(b)** Potential after separation ramp. **(c)** Potential after shuttling the upstream fraction to the high-voltage electrode. The content of the downstream fraction can be counted by the dip-width measurement. **(d)** Potential after shuttling the downstream fraction to the RT and the upstream fraction to the upstream high-voltage electrode Adapted from [146].

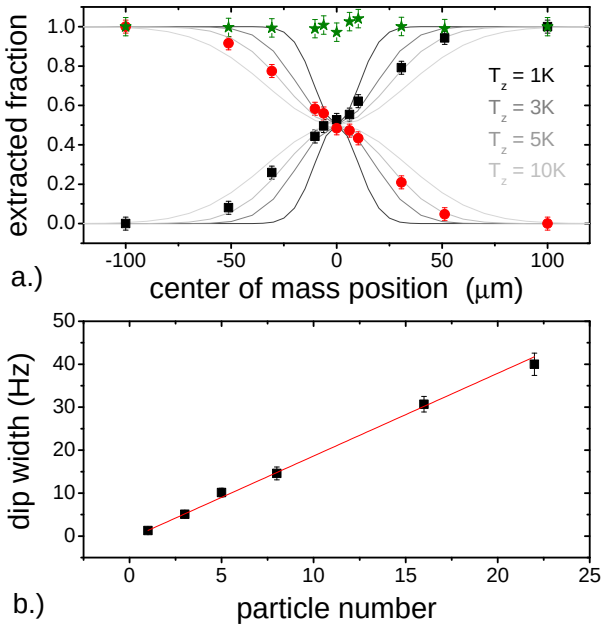

Figure 13.7: **(a)** Extracted fractions as functions of the center-of-mass position defined by the minimum of the electric potential before the separation. The red circles represent the fraction of particles extracted to upstream fraction, the black squares represent the downstream fraction. The green stars show the sum of both fractions normalized to the number of particles of the cloud before each separation procedure. **(b)** Dip-width as a function of the number of particles. The dip-width of a single antiproton was 1.9 Hz at the time of this measurement. Numbers of antiprotons from 22(1) down to one were observed in this measurement. Adapted from [146].

hence in practice multiple trials at are required to obtain a desired number of particles.

13.3.2 Extraction operation in 2017 run

The principle described in the last section is applied to extract single particles from the reservoir in 2017 run. However, there are minor differences in the situation compared to the previous years. The first is that extraction is needed to be performed to a cloud of a larger number of particles. We employed a two-step extraction procedure to efficiently extract a single parcel from a large cloud. Another point is that unlike 2015/2016 run for magnetic moment measurement of the antiproton, the reservoir in 2017 contains two species of particles, namely antiprotons and H^- ions. Some signs in the spectrum were found which helped distinguishing between antiprotons and H^- ions. Theses methods and observations are discussed in this section.

Two-step extraction

As mentioned in Section 13.2.5, a cloud of more than 300 particles are obtained after successful cleaning procedures in 2017 run. Direct extraction of a single particle from such a large cloud was found to be difficult. This is understandable, as the number of the original cloud increases, the adjustment of the asymmetry of the initial stage of extraction becomes more sensitive (see a detailed discussion in Section B.2).

Therefore, extraction in 2017 run is done in two steps. The procedure is described in Fig. 13.8. First, a small fraction, typically of 30–100 particles. is extracted to the upstream side (Fig. 13.8 (A)), then the downstream fraction is parked in the upstream high-voltage electrode, and the upstream fraction in the RT. At the second extraction from the RT (Fig. 13.8 (B)), extraction of a single particle is attempted. The separation and the merging operations are repeated until a single particle is extracted to the downstream high-voltage electrode. After a successful extraction, the extracted single particle is transported to the PT, and the left fractions are merged into one to be stored in the RT. In this scheme, the contents of the fractions in the first step and the upstream fraction of the second step can be counted by individual dip measurements. The content of the downstream fraction of the second step is either measured in the PT after transport, or deduced from the information of the upstream fraction.

In Fig. 13.9, the scaling of the extracted fraction is plotted for data accumulated by two-step extraction procedures. Three datasets below are plotted together:

1. Two-step extractions in run-II applied to an antiproton cloud initially containing about 360 antiprotons (plotted by dots)

2. Two-step extractions in run-II applied to a proton cloud initially containing about 88 particles.

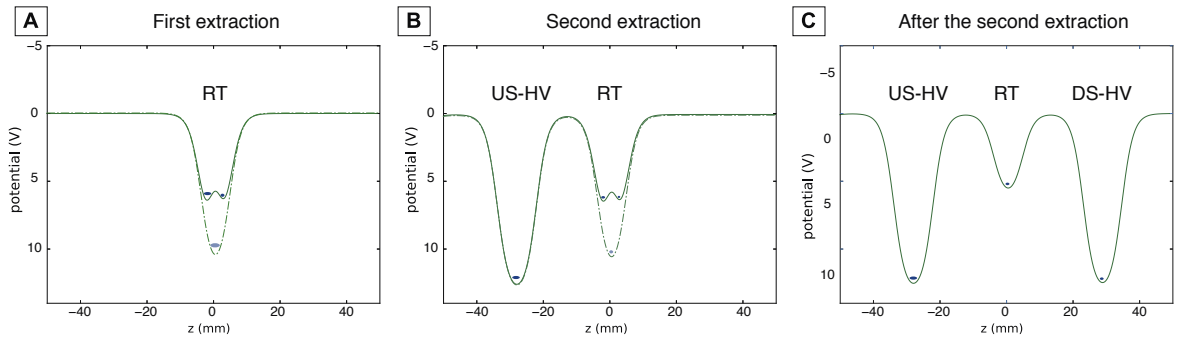

Figure 13.8: On-axis potentials used in the two-step extraction procedure employed in 2017 run.

This was before the beam-time (plotted by '+')[5]

3. Characterization measurement in run-I where separation and merging were repeated for the same cloud containing about 115 antiprotons (plotted by 'x').

Data points of the first and the second datasets are plotted in different colors according to the number of particles before separation. The downstream fraction extracted at each trial is plotted in Fig. 13.9 (A), the number of particles of a cloud before each extraction is plotted in (B). The common horizontal value of Fig. 13.9 (A) and (B) is the voltage on the downstream correction electrode before separation which adjusts the asymmetry of the potential. The voltage corresponds to the even separation is subtracted as the offset. The solid lines are the scaling of the extracted fraction calculated from Eq. (13.3) for $T_z = 5\,\mathrm{K}$.

It can be seen that results of the characterization measurement in run-I as well as antiproton data in run-II $N_{\mathrm{before}} > 200$ scale consistently with $T_z = 5\,\mathrm{K}$. However, data points of smaller initial numbers of particles, especially those for which $N_{\mathrm{before}} \leq 30$, seem to follow a steeper scaling against the voltage. The same tendency is also observed for the proton data. This is merely a statical effect and does not mean that these small clouds had a lower temperature. If the initial number of the particles is small, large fluctuations broaden the scaling thus data points which deviate from the original scaling are more likely to be observed (see a detailed discussion in Section B.2). In addition, in the second step of extraction, we typically aimed a separation near half-by-half, making sampling of these points concentrated around the parameter of the even separation. This makes the results look as if they followed a scaling at a lower temperature.

Identifying antiprotons and H^- ions

H^- ions contained in a cloud prepared after the cleaning procedures are of smaller number than antiprotons. The signs of H^- ions are not evidently observed as long as the antiprotons are dominant. One reproduced observation below seems to be attributed to an effect of the mixed cloud. In many cases, a dip signal of an antiproton cloud does not stay stable for long time, but disappears typically

[5]The data of the proton measurement is plotted with inversion of the polarity e.g., $V_{\text{DS-CE}} = -13.42\,\mathrm{V} \rightarrow 13.42\,\mathrm{V}$.

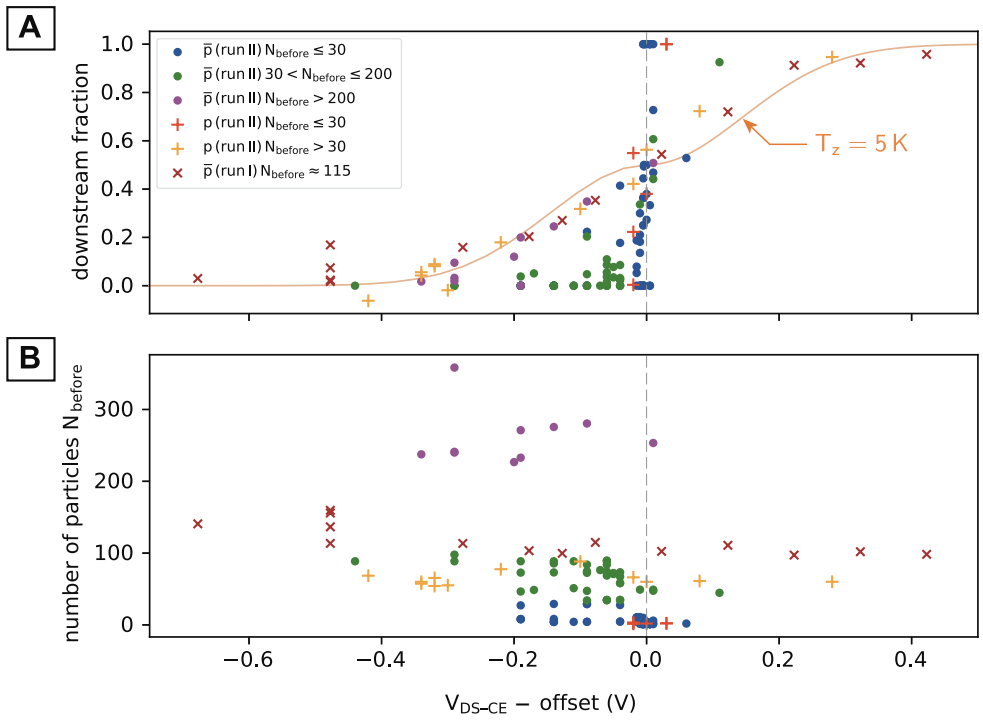

Figure 13.9: **(A)** Extracted fraction as a function of the voltage applied on the downstream correction electrode of the RT (offset: 13.29 V for dataset 1, 13.42 V for dataset 2, 13.28 V for dataset 3.) **(B)** The number of particles before each separation operation.

within 10–20 min, with the dip frequency drifting downward. It has been verified that it is not from contaminants other than H^- ions, and the dip is always recovered by the sideband magnetron cooling of antiprotons without showing a sign of heating.

When comparable numbers of antiprotons and H^- ions are contained in an extracted fraction, the effect of the H^- ions are observed more clearly. A spectrum of Fig. 13.10 (A) is a signal of one antiproton and one H^- ion acquired in run-I. Afterward this fraction was separated to one antiproton (Fig. 13.10 (B)) and one H^- ion (Fig. 13.10 (C)). In Table 13.4, the characteristics of these dips obtained by fitting are listed. As seen in the plots and the table, the dip of the mixture of the antiproton and the H^- had a dip SNR significantly lower than the normal conditions. The ring voltages for the mixture and the H^- needed to be adjusted higher than the antiproton to make the axial frequency in resonant to the detection system. To compare the differences as equivalent frequency shifts, the axial frequency scaled to the ring voltage of the antiproton are listed at the last column of Table 13.4. The frequency difference of 454 Hz between the single antiproton and the single H^- ions is consistent with their mass difference. The frequency difference in case of the mixture of about 135 Hz is attributed to an interaction between the two particles. Such systems have been studied by previous mass spectrometry works [201, 202]. What seems likely in this case is an averaged effect of the outer particle which can be experienced as a screening of the electric potential by the inner particle [202]. The significantly smaller dip SNR of the mixture can be understood as a result

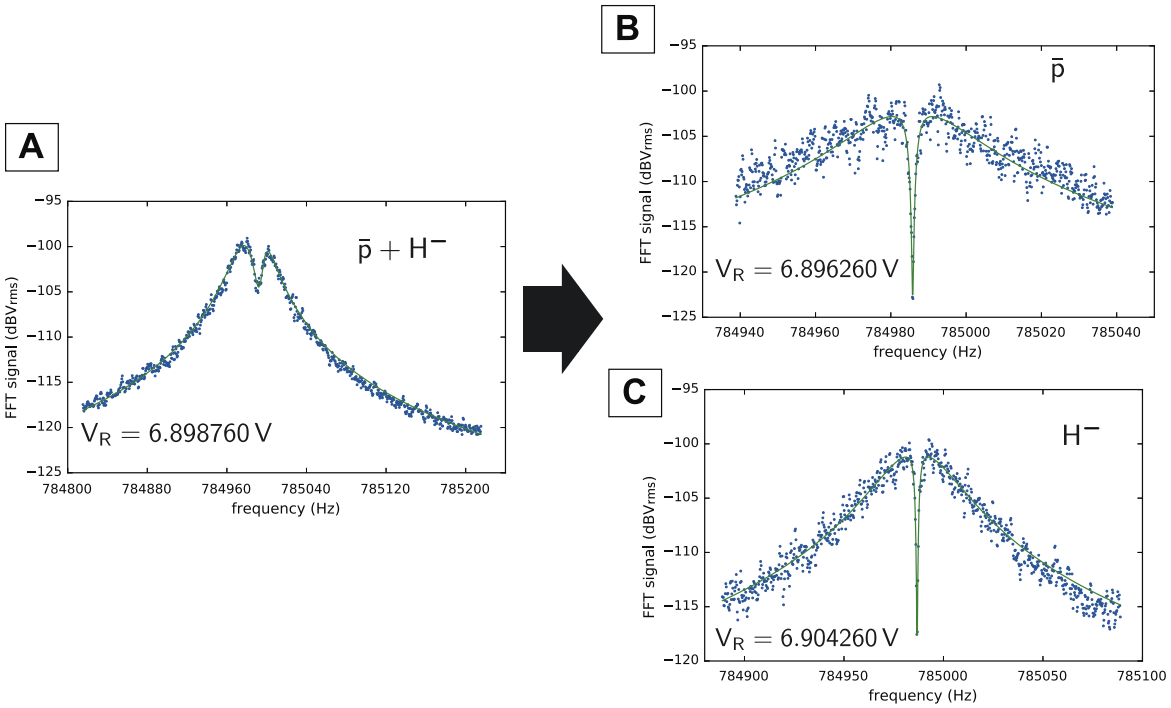

Figure 13.10: Signs of a mixture of the two kinds of particles observed in a dip signal. The dip signal found in (A) has a significantly low SNR and a dip frequency shifted downward by about 130 Hz than a normal antiproton dip. The ring voltage was set higher than usual to keep the signal in resonance with the RT axial detection system. By the separation operation, this trap content was separated into one antiproton (B) and one H^- ion. The frequency of the antiproton returned to the normal condition. The high SNRs in (B, C) indicate that what is observed in (A) are not due to contamination. The spectra (A–C) were acquired with different FFT spans. The vertical axis of the graphs are scaled to a unit of dBV_{rms} at bandwidth 0.5 Hz.

Table 13.4: Properties of the dip signals in Fig. 13.10 extracted by fits of the spectra. The ring voltage V_R, the axial frequency ν_z, the dip-wdith $\Delta\nu_z$, the dip SNR, and the axial frequency scaled to the ring voltage of the antiproton are listed for each spectrum.

	V_R (V)	ν_z (Hz)	$\Delta\nu_z$ (Hz)	dip SNR (dB)	ν_z at $V_R = 6.89626$ V(Hz)
$\bar{p}$ and H^-	6.898760	784992.76	10.56	2.86	784850.51
$\bar{p}$	6.89626	784985.81	3.29	20.2	784985.81
H^-	6.904260	784986.74	2.93	17.8	784531.83

of particle-particle interactions which occur in a shorter time scale than the axial oscillation, causing the secular axial frequency to be unstable.

The above-discussed effects of the interaction between antiprotons and H^- ions were observed reproducibly for mixtures of the two particles, namely the smaller dip SNR and downward axial frequency shifts of typically 100–200 Hz compared to that of antiprotons clouds.

These signs have helped identifying the content of the extracted fraction in the second extraction without transporting it to the PT, thereby making the operation efficient. In Table 13.5, a practical

Table 13.5: Practical recipe for distinguishing trap content from features of the dip signal of an extracted fraction. When one of the characteristics on the left of the table are observed, the trap content is likely to be the species on the right. The frequency shift $\delta\nu_z$ is defined as the frequency shift before and after the extraction; $\delta\nu_z = \nu_{z,\text{fraction}} - \nu_{z,\text{cloud}}$.

Properties of the dip of an extracted fraction		Likely trap content
Dip SNR	Frequency shift $\delta\nu_z$	
$\text{SNR}\vert_{\text{dip}} > 15\,\text{dB}$	$0 \lesssim \delta\nu_z \lesssim 50\,\text{Hz}$	$\bar{p}$
$\text{SNR}\vert_{\text{dip}} > 15\,\text{dB}$	$\delta\nu_z \approx -450\,\text{Hz}$	H^-
$\text{SNR}\vert_{\text{dip}} < 10\,\text{dB}$	$-200\,\text{Hz} \lesssim \delta\nu_z \lesssim -100\,\text{Hz}$	$\bar{p}$ and H^-

recipe of distinguishing the content of the trap during extraction procedure from observations in the dip signals is given based on these experiences.

14

Optimization and characterization of the Precision Trap

In this chapter, methods are discussed which are used to optimize and characterize the trap imperfections of a Penning trap. They use single particle as the probe to measure the trap imprecation parameters. This step is essential in preparing the trap for high-precision measurements. Their principles are explained and the results of their application to the Precision Trap in the 2017 run are discussed. The trap parameters were later characterized with higher precision for a systematic evaluation of the final data analysis. These final results will be presented in Ref. [79].

14.1 Optimization of electrical trap parameters

14.1.1 Compensation of electric anharmonicity

The tuning ratio (TR) is an important parameter for operation of a compensated Penning trap to tune the trapping potential to a harmonic one. Recalling Eq. (2.57), a TR determines the C_j through

$$C_j = E_j + D_j \cdot \mathrm{TR}. \tag{14.1}$$

The purpose of the optimization procedures below are to optimize the TR such that $C_4 = 0$ in order to minimize frequency shifts due to C_4. Two methods which used for the optimization are discussed.

Optimization by dip signal-to-noise ratio

A residual C_4 is reflected to the signal-to-noise (SNR) of a dip signal. We shall discuss a spectrum of the axial detection system near the peak of the resonance $\nu_{0,\mathrm{eff}}$. The signal of the dip appears in the

power dissipation spectrum of the detection system is expressed as Eqs. (2.112) and (2.113)

$$P_{\mathrm{th}}(\nu) = B_{\mathrm{cir}} \cdot 4k_{\mathrm{B}}T_z \cdot \frac{R_{\mathrm{eff}}}{1 + \dfrac{\Delta\nu_z^2}{4(\nu - \nu_z)^2}} \cdot f_{\mathrm{b}}. \tag{14.2}$$

with B_{cir} representing constants determined by the circuit properties, such as the amplifier gain. T_z represents the temperature of the detection system. If C_4 is present, a shift of the axial frequency depending on the axial mode energy E_z is induced. Denoting the shifted frequency as $\tilde{\nu}_z$, from Eq. (2.70),

$$\tilde{\nu}_z(E_z) = \nu_z \left(1 + \frac{3}{4}\frac{C_4}{C_2^2}\frac{E_z}{qV_{\mathrm{R}}}\right). \tag{14.3}$$

We define a detuning of TR from the optimum value as $\Delta\mathrm{TR}$, therefore $C_4 = D_4\Delta\mathrm{TR}$. In the thermal equilibrium with the detection system, E_z distributes according to a Boltzmann distribution $\Pi_{\mathrm{B}}(E_z|T_z)$ defined by the axial temperature T_z :

$$\Pi_{\mathrm{B}}(E_z|T_z) = \frac{1}{k_{\mathrm{B}}T_z} \exp\left(-\frac{E_z}{k_{\mathrm{B}}T_z}\right). \tag{14.4}$$

As a consequence, what we measure by a spectrum acquired over a long averaging time becomes a line shape where the E_z depended shift Eq. (14.3) is convolved in Eq. (14.2):

$$P_{\mathrm{th}}(\nu, \Delta\mathrm{TR}, T_z) = B_{\mathrm{cir}} \cdot 4k_{\mathrm{B}}T_z \cdot \int_0^\infty \mathrm{d}E_z\, \Pi_{\mathrm{B}}(E_z|T_z) \cdot \frac{R_{\mathrm{eff}}}{1 + \dfrac{\Delta\nu_z^2}{4(\nu - \tilde{\nu}_z(E_z))^2}} \cdot f_{\mathrm{b}}. \tag{14.5}$$

Considering the SNR, in case of $C_4 = 0$, where the minimum of the signal is $P_{\mathrm{th}}(\nu_z) = 0$, the power SNR is Eq. (2.117)[1]

$$\mathrm{SNR}^2 = \frac{4k_{\mathrm{B}}T_zR_{\mathrm{eff}}\kappa^2 + e_{\mathrm{n}}^2}{e_{\mathrm{n}}^2} \approx \frac{4k_{\mathrm{B}}T_zR_{\mathrm{eff}}\kappa^2}{e_{\mathrm{n}}^2}. \tag{14.6}$$

where κ is a constant defines the coupling to the output of the circuit, and e_{n} the input noise of the amplifier. Now the dip SNR in case of a detuned TR,

$$\mathrm{SNR}^2(\Delta\mathrm{TR}, T_z) = (4k_{\mathrm{B}}T_zR_{\mathrm{eff}}\kappa^2 + e_{\mathrm{n}}^2) \cdot \left(4k_{\mathrm{B}}T_zR_{\mathrm{eff}}\kappa^2 \int_0^\infty \mathrm{d}E_z \frac{\Pi_{\mathrm{B}}(E_z|T_z)}{1 + \dfrac{4}{9}\left(\dfrac{\Delta\nu_z}{\nu_z}\dfrac{C_2^2qV_{\mathrm{R}}}{D_4\Delta\mathrm{TR}E_z}\right)^2} + e_{\mathrm{n}}^2\right)^{-1} \tag{14.7}$$

$\Delta\mathrm{TR} = 0$ gives the maximum SNR. Therefore, by comparing the dip SNR with different TRs, the optimum TR is determined as the one which gives the maximum dip SNR.

The results of an actual measurements are shown in Fig. 14.1. For each of a selected set of TRs, an

[1]Since we define SNR for the ratio of voltages in Eq. (2.116), here the SNR of power is denoted as SNR^2.

axial dip spectra of a single antiproton was acquired with an FFT span of 25 Hz. In Fig. 14.1 (A,B), spectra for two different TRs are compared as examples. In Fig. 14.1 (C), the dip SNR is shown as a function of the TR. Each of the data points is obtained by an average of 12 measurements, and the error bars are assigned by the standard deviations.

By performing linear fits to each of the slopes, the optimum TR was determined as the TR which gives the maximum of the SNR to be $\mathrm{TR}_{\mathrm{opt}} = 0.88730\,(1)$ in case of this measurement. This method allows optimization of the TR at a level of $\delta\mathrm{TR} \sim 10^{-5}$, corresponding to $|C_4/C_2^2| \sim 10^{-4}$. In addition to the optimum TR, this measurement also gives information about the temperature of the axial detection system T_z through Eq. (14.7). By comparing results of detailed scans around the optimum TR against simulations, the temperature of the detection system in 2017 run-II was estimated to be $T_z = 10.1(9)\,\mathrm{K}$ for the system without the feedback [79]. In Fig. 14.1 (C), a theoretical curve from Eq. (14.7) at 10.11 K is shown in comparison to the measured data.

Optimization by excitation of the magnetron mode

More precise TR optimization can be performed by use of controlled excitations of the magnetron mode. In this measurement we excite the magnetron mode to the radii corresponding to $|E_-|/k_\mathrm{B} \sim 100\,\mathrm{K}$. Among the frequency shifts due to the electrical trap imperfections C_4, C_6 Eq. (2.70), terms coupled to the magnetron mode are

$$\begin{aligned}\left(\frac{\Delta\nu_z}{\nu_z}\right)^{(E_-)} &= \frac{1}{qV_\mathrm{R}}\left[\frac{C_4}{C_2^2}\cdot(-3|E_-|) + \frac{C_6}{C_2^3}\left(\frac{45}{4}|E_-|^2 + \frac{45}{2}\left(\frac{\nu_z}{\nu_+}\right)^2 E_+|E_-| - \frac{45}{4}E_z|E_-|\right)\right] \\ &\approx \frac{1}{qV_\mathrm{R}}\left[-3\frac{C_4}{C_2^2}|E_-| + \frac{45}{4}\frac{C_6}{C_2^3}|E_-|^2\right] \quad \left(\because E_z/k_\mathrm{B} \sim 10\,\mathrm{K},\ \left(\frac{\nu_z}{\nu_+}\right)^2 \cdot E_+/k_\mathrm{B} \sim 0.1\,\mathrm{K}\right) \\ &= -\frac{3}{2}\frac{C_4}{C_2}\rho_-^2 + \frac{45}{16}\frac{C_6}{C_2}\rho_-^4.\end{aligned} \tag{14.8}$$

Thus the relative frequency shift is expected to scale as a polynomial function of the magnetron radius ρ_-. If C_4 and C_6 varies by adjusting the TR, it will appear as a difference in this polynomial scaling. The excitation of the magnetron mode was performed by use of the burst mode of a signal generator Agilent 33522A. Signals of the sinusoidal function at frequency ν_- of a defined number of cycles were generated. The amplitude of the signal was set low ($-45\,\mathrm{dBm}$ at the output of the device), and the amount of the excitation was controlled by the number of bursts. By introducing the proportional factor α between the magnetron radius and the number of bursts N, Eq. (14.8) is rewritten as

$$\left(\frac{\Delta\nu_z}{\nu_z}\right)^{(E_-)} = -\frac{3}{2}\frac{C_4}{C_2}(\alpha N)^2 + \frac{45}{16}\frac{C_6}{C_2}(\alpha N)^4. \tag{14.9}$$

The result of a measurement is shown in Fig. 14.2. What is presented here was recorded in 2017 run-I with a single antiproton. The measurement was also repeated during run-II.

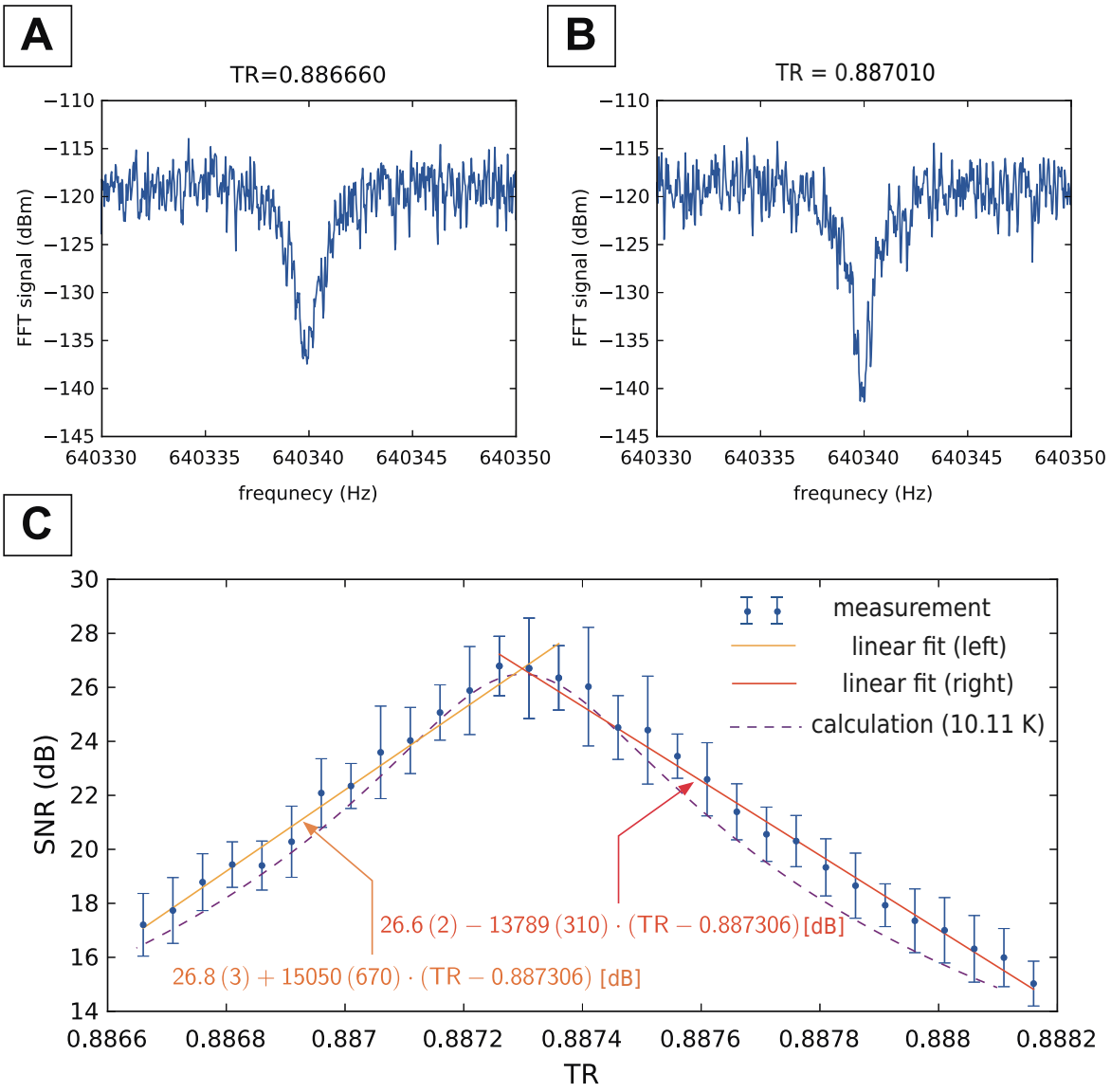

Figure 14.1: Tuning Ratio optimization by the scaling of the dip SNR. **(A, B)** Examples of spectra are given for TR = 0.886660 (A) and TR = 0.887010 (B). **(C)** Scaling of the SNR against the TR, the each data point is an average of 12 measurements, its error bar assigned by the standard deviation of the 12 sets. The linear fit was performed for the left half (the orange line) and the right half (the red line) of data, respectively. The optimum TR was determined from the intersection point of the two fit lines. The theoretical scaling at $T_z = 10.11\,\mathrm{K}$ is given by the purple dashed curve.

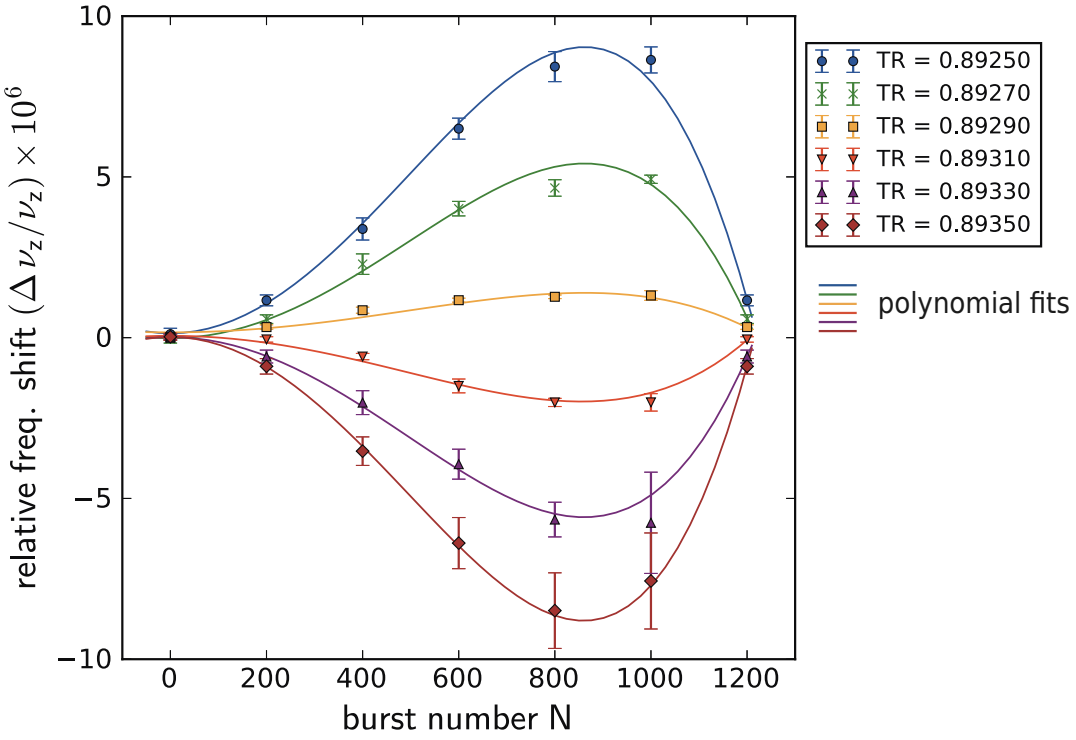

Figure 14.2: Measurements of the axial frequency shift as a function of the number of burst signals applied to excite the magnetron mode. The different series correspond to different TRs. The error bars are assigned from the standard deviations of the results of 7 repetitions. For each series, a polynomial fit to the model Eq. (14.10) was performed.

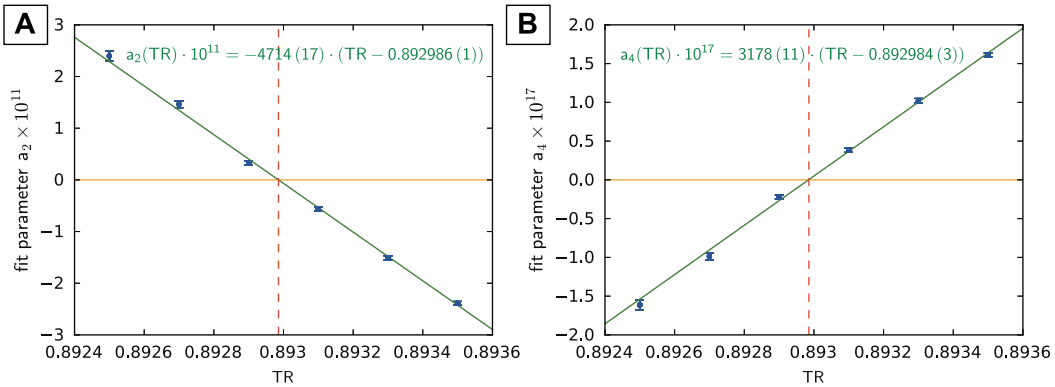

Figure 14.3: Scalings of the fit parameters a_2 (A) and a_4 (B) against the TR. The error bars of each data point is assigned from uncertainty of a polynomial fit performed for each series of TR. The linear scaling is obtained for both and a_2 and a_4. A linear fit of the scaling a_2 gives the optimum TR at which $C_4 = 0$. The residual C_6 for the optimum TR can be evaluated from the scaling of a_6. The orange horizontal lines indicate $a_2 = 0$ for (A) and $a_4 = 0$ for (B). The red dashed vertical lines indicate $\mathrm{TR} = \mathrm{TR}_{\mathrm{opt}} = 0.892986$ corresponding to $a_2 = 0$.

The results obtained with different TRs are specified in the figure legend. For each TR, the relative frequency shifts are fitted to a polynomial function

$$\frac{\Delta\nu_z}{\nu_z}(N) = a_0 + a_2 \cdot N^2 + a_4 \cdot N^4, \tag{14.10}$$

which is related to Eq. (14.10) by

$$a_2 = -\frac{3}{2}\frac{C_4}{C_2}\alpha^2, \quad a_4 = \frac{45}{16}\frac{C_6}{C_2}\alpha^4. \tag{14.11}$$

The scaling of these coefficients against the TR are of interest. This is found in Fig. 14.3. The scalings of a_2 and a_4 against the TR are shown in Fig. 14.3 (A) and (B), respectively. by performing a linear fit to each, the scalings were obtained to be

$$\begin{aligned} a_2(\mathrm{TR}) \cdot 10^{11} &= -4714\,(17) \cdot (\mathrm{TR} - 0.892986\,(1)) \\ a_4(\mathrm{TR}) \cdot 10^{17} &= \ \ 3178\,(11) \cdot (\mathrm{TR} - 0.892984\,(3)). \end{aligned} \tag{14.12}$$

The optimum TR which realized $a_2 = 0 \iff C_4 = 0$ was determined in this case[2] to be $\mathrm{TR}_{\mathrm{opt}} = 0.892986\,(1)$. The slope of $a_2(\mathrm{TR})$ is related to the proportionality factor α by

$$\begin{aligned} \frac{\mathrm{d}a_2(\mathrm{TR})}{\mathrm{dTR}} &= -\frac{3}{2}\frac{D_4}{C_2} \cdot \alpha^2 \\ \therefore \alpha^2 &= -\frac{2}{3}\frac{C_2}{D_4} \cdot \frac{\mathrm{d}a_2(\mathrm{TR})}{\mathrm{dTR}}. \end{aligned} \tag{14.13}$$

C_2 can be measured from the relation of the axial frequency and the ring voltage V_{R}. D_4 can be calculated form Eq. (2.56). It is a trap parameter robust against possible offset potentials within a level of 1%. Thus α is obtained to be

$$\alpha = 0.679(2)\,\mu\mathrm{m/cycle} \tag{14.14}$$

This method allows the optimization of TR with precision of $\delta\mathrm{TR} \sim 10^{-6}$, or $|C_4/C_2^2| \sim 10^{-6}$. The residual C_6 in case $\mathrm{TR} = \mathrm{TR}_{\mathrm{opt}}$ is evaluated to be $a_4 \approx 3 \times 10^{-20} \iff C_6/C_2^3 \approx 2 \times 10^{-4}$.

14.2 Characterization of magnetic trap imperfections

The magnetic trap imperfections cannot be controlled as in the case of the electrical trap imperfection parameters. However, they can be measured and the obtained results enable us to estimate frequency shifts caused by these imperfections. The specific subjects of the section are methods to extract the magnetic gradient term B_1 and the magnetic bottle term B_2.

[2]This result is from 2017 run-I. Differences of conditions make it different from the optimum TR discussed in the last section.

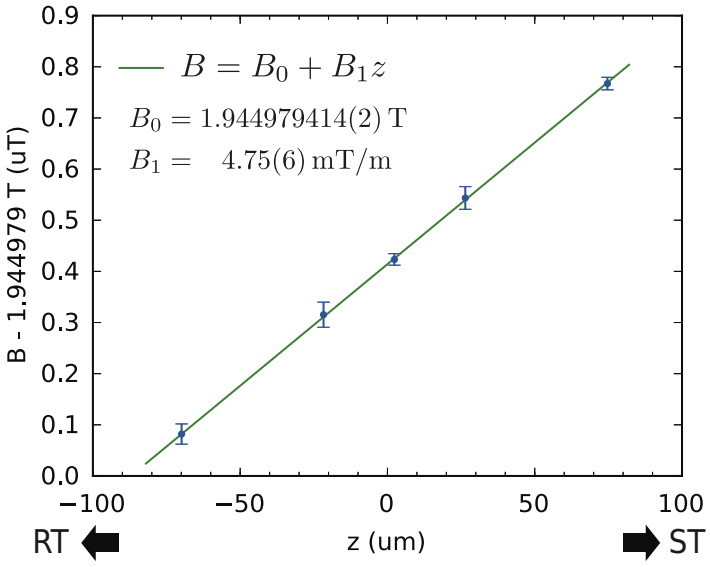

Figure 14.4: Measurement of the magnetic gradient B_1. Each data point was obtained by an average of 7 sets of measurements, and its error bar by the standard deviation. By a fit to a linear function, the gradient B_1 was determined to be $B_1 = 4.75(6)\,\mathrm{mT/m}$. The orientation of the z is from upstream (toward the RT) to downstream (toward the ST), as indicated in the figure.

14.2.1 Measurement of the magnetic gradient

The magnetic gradient term B_1 can be measured by shifting the axial position of the particle by deliberately applying an offset voltage on one of the correction electrodes, and measuring the cyclotron frequency as a function of the axial position. For each set of applied voltages, the potential minimum z_0 is evaluated by

$$z_0 = -\frac{C_1(\{V_i\})}{2C_2(\{V_i\})} \tag{14.15}$$

with $\{V_i\}$ representing a set of voltages applied to the electrodes. $C_1(\{V_i\})$ and $C_2(\{V_i\})$ can be calculated from Eq. (2.54) to estimate z_0 for each setting. The result of such a measurement is shown in Fig. 14.4. By a linear fit of data, the gradient B_1 was obtained to be $B_1 = 4.75(6)\,\mathrm{mT/m}$. The measured B_1 was consistent with the magnetic field maps of the magnet obtained prior to installation of the apparatus (see Fig. 5.4). The B_1 measurement was regularly repeated over the run, and consistent results were obtained.

14.2.2 Measurement of the magnetic bottle

The magnetic bottle B_2 is one of the crucial trap parameters to be characterized, as it often gives the leading contribution to the systematic uncertainty among those from the other trap imperfection terms (see Section 7.3). To measure the magnetic bottle term B_2, we use the axial frequency shift

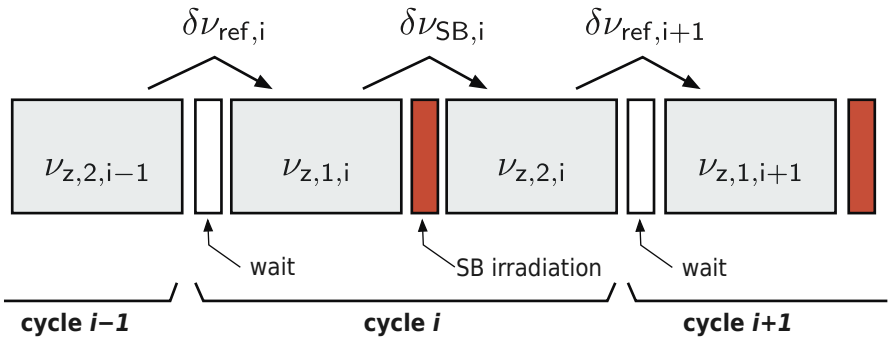

Figure 14.5: Procedure of the B_2 measurement. Each cycle consists of two axial frequency measurements $\nu_{1,i}, \nu_{i,2}$ with an irradiation of the sideband drive between the two. During the sideband drive, the feedback is activated to control the temperature. Typically, 48 s of averaging time was used for axial frequency measurements, and the duration of the sideband drive 4 s was used. The actual sequence cycles between different settings of the feedback defining different temperatures during the sideband. For example: $T_{z,\mathrm{eff},1}$ $(i = 1, \cdots 5, 16, \cdots 20, \cdots)$, $T_{z,\mathrm{eff},2}(i = 6, \cdots 10, 21 \cdots 25, \cdots)$, $T_{z,\mathrm{eff},3}(i = 11 \cdots 15, 26 \cdots 30, \cdots)$.

due to the coupling of the B_2 term and the modified cyclotron mode (Eq. (2.80)):

$$\Delta\nu_z^{(B_2,E_+)} = \frac{1}{4\pi^2 m\nu_z}\frac{B_2}{B_0}E_+. \tag{14.16}$$

When the modified cyclotron mode is coupled to the axial mode by the sideband coupling method (Section 2.5), the distribution of the modified-cyclotron energy E_+ follows a Boltzmann distribution defined by a temperature $\nu_+/\nu_z \cdot T_z$. The value of the B_2 can be extracted from the axial frequency distribution when this coupling is applied.

The measurement sequence is shown in Fig. 14.5. Each cycle consists of two axial frequency measurements $\nu_{1,i}, \nu_{i,2}$ with irradiation of sideband coupling drive at $\nu_{\mathrm{SB}} \approx \nu_+ - \nu_z$ inserted between the two. Positive feedback is activated during the sideband drive to increase the effect of B_2 by a higher modified-cyclotron temperature during the coupling. The distribution of frequency differences $\{\delta\nu_{\mathrm{ref},i}\} = \{\nu_{1,i} - \nu_{2,i-1}\}$ is from the intrinsic axial frequency fluctuations, and the differences $\{\delta\nu_{\mathrm{SB},i}\} = \{\nu_{2,i} - \nu_{1,i}\}$ reflect the effect of the E_+ dependent shifts.

The expected distribution of these frequency differences are discussed by convolutions of the original frequency distributions. We denote the probability density functions (PDFs) of the Gaussian distribution and the exponential distribution as $\Pi_{\mathrm{G}}(x|\mu,\sigma)$ and $\Pi_{\mathrm{E}}(x|\beta)$, i.e.,

$$\Pi_{\mathrm{G}}(x|\mu,\sigma) = \frac{1}{\sqrt{2\pi}\sigma}\exp\left(-\frac{(x-\mu)^2}{2\sigma^2}\right) \tag{14.17}$$

$$\Pi_{\mathrm{E}}(x|\beta) = \beta\exp\left(-\beta x\right). \tag{14.18}$$

If the drifts are ignored, the intrinsic axial frequency distributes according to a Gaussian distribution, let its mean and width to be $\mu = \mu_0$ and be $\sigma = \sigma_0$. The distribution of the frequency shifts $\Delta\nu_z$

Eq. (14.16) follow an exponential distribution reflecting the Boltzmann distribution of E_+, whose mean is

$$\begin{aligned}\langle \Delta\nu_z^{(B_2,E_+)} \rangle &= \frac{1}{4\pi^2 m\nu_z}\frac{B_2}{B_0}\frac{\nu_+}{\nu_z}\cdot k_{\mathrm{B}}T_{z,\mathrm{eff}} \\ &\approx 7.8\times 10^{-3}\,[\mathrm{Hz}\cdot(\mathrm{T/m^2}\cdot\mathrm{K})^{-1}]\cdot B_2 T_{z,\mathrm{eff}}.\end{aligned} \tag{14.19}$$

$T_{z,\mathrm{eff}}$ represents the temperature during the sideband coupling defined by the feedback parameters. Thus $\Delta\nu_z$ follows an exponential distribution defined by β_0

$$\beta_0 \equiv \frac{1}{\langle \Delta\nu_z^{(B_2,E_+)} \rangle}. \tag{14.20}$$

The probability distribution of a variable z defined as a difference of variables $z = x - y$, with x, y both following the Gaussian distribution $x, y \in \Pi_{\mathrm{G}}(x|0,\sigma_0)$, is obtained by a convolution of two Gaussian distributions to be

$$\begin{aligned}\Pi_1(z) &= \int \mathrm{d}y\, \Pi_{\mathrm{G}}(z-y|0,\sigma_0)\Pi_{\mathrm{G}}(y|0,\sigma_0) \\ &= \Pi_{\mathrm{G}}(z|0,\sigma_{\mathrm{d}}) \quad (\sigma_{\mathrm{d}} \equiv \sqrt{2}\sigma_0).\end{aligned} \tag{14.21}$$

For a difference $\Delta = x_1 + x_2 - x_3 - x_4$, with $x_1, x_3 \in \Pi_{\mathrm{G}}(0,\sigma)$ and $x_2, x_4 \in \Pi_{\mathrm{E}}(x|\beta_0)$,

$$\begin{aligned}\Pi_2(\Delta) &= \int \mathrm{d}y \int \mathrm{d}z\, \Pi_{\mathrm{G}}(\Delta - y|0,\sigma_{\mathrm{d}})\Pi_{\mathrm{E}}(y+z|\beta_0)\Pi_{\mathrm{E}}(z|\beta_0) \\ &= \frac{\beta_0}{4}\exp\left(-\beta_0\Delta + \frac{\sigma_{\mathrm{d}}^2\beta_0^2}{2}\right)\left(\mathrm{erfc}\left(-\frac{\Delta}{\sqrt{2}\sigma_{\mathrm{d}}} + \frac{\beta_0\sigma_{\mathrm{d}}}{\sqrt{2}}\right) + e^{2\beta_0\Delta}\mathrm{erfc}\left(\frac{\Delta}{\sqrt{2}\sigma_{\mathrm{d}}} + \frac{\beta_0\sigma_{\mathrm{d}}}{\sqrt{2}}\right)\right).\end{aligned} \tag{14.22}$$

Eq. (14.21) is what should be followed by $\{\delta\nu_{\mathrm{ref},i}\}$, and $\{\delta\nu_{\mathrm{SB},i}\}$ is expected to follow Eq. (14.22).

The results of an actual measurement performed in 2017 run-II are shown in in Fig. 14.6. Fig. 14.6 (A) is the distribution of $\{\delta\nu_{\mathrm{ref},i}\}$. (B) and (C) are the distributions of $\{\delta\nu_{\mathrm{SB},i}\}$ at two different feedback conditions, corresponding to $T_{z,\mathrm{eff}}/T_{z,0} = 2.62$ (B) and 4.85 (C). The orange lines show Maximum Liklihood fits of the distributions to the PDFs Eq. (14.21) for (A), and Eq. (14.22) for (B, C).

The parameters obtained from the fits are summarized in Table 14.1. From the results of the two feedback settings, $|B_2 \cdot T_z| = 2.4\,(2)\,\mathrm{T/m^2}\cdot\mathrm{K}$ is obtained. Combined with the temperature of the axial desertion system $T_z = 10.1(9)\,\mathrm{K}$, $|B_2| = 0.25(4)\,\mathrm{T/m^2}$ was estimated.

The B_2 was also measured by directly exciting the modified cyclotron mode and observing the axial frequency difference [79]. The modified-cyclotron energy E_+ can be calibrated by the E_+ dependent frequency shifts due to B_2 and the relativistic shifts (see Section 2.3.4). This method measured the term more precisely and also determined its sign. The result was $B_2 = -0.267(24)\,\mathrm{T/m^2}$ [79].

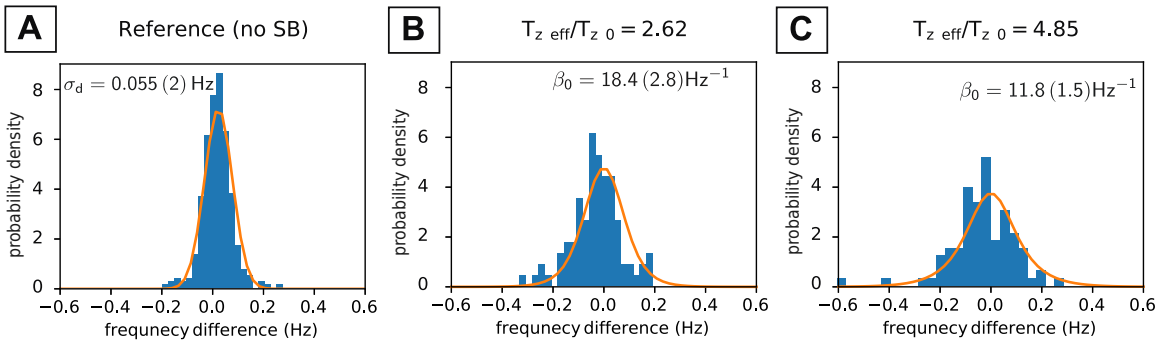

Figure 14.6: Distributions of the axial frequency differences. **(A)** Distribution of the reference frequency differences $\{\delta\nu_{\mathrm{ref},i}\}$ (see Fig. 14.5). **(B, C)** Distribution of the frequency differences $\{\delta\nu_{\mathrm{SB},i}\} = \{\nu_{2,i} - \nu_{1,i}\}$. The orange lines indicate results of Maximum Likelihood fits using the model Eq. (14.21) for (A) and Eq. (14.22) for (B,C). The parameter σ_d determined by the fit of (A) was used as a fixed parameter for fitting of (B) and (C). The offsets of the distributions due to frequency drifts were subtracted when the fits were performed.

Table 14.1: Summary of the parameters obtained by the Maximum Likelihood fits. β_0 is determined by the fit for each feedback setting Fig. 14.6 (B,C), which is converted to $\langle\Delta\nu_z^{(B_2,E_+)}\rangle$ by Eq. (14.20), and then to $B_2 \cdot T_z$ by Eq. (14.19).

$T_{z,\mathrm{eff}}/T_{z,0}$	$\beta_0\,(\mathrm{Hz}^{-1})$	$\lvert\langle\Delta\nu_z^{(B_2,E_+)}\rangle\rvert\,(\mathrm{Hz})$	$\lvert B_2 \cdot T_z\rvert\,(\mathrm{T/m^2 \cdot K})$
2.62 (1)	18.4 (2.8)	0.054 (8)	2.6 (4)
4.85 (1)	11.8 (1.5)	0.085 (11)	2.2 (3)

14.3 Influence on the charge-to-mass ratio comparison

In this section, based on the optimization and characterization above, the influence of the trap imperfections to the charge-to-mass ratio comparison is assessed.

Non-zero trap imprecations cause frequency shifts depending on the energies of the eigenmodes. The dominant terms of the cyclotron frequency shifts due to couplings to C_4, C_6, B_1, B_2 are found to be (Eqs. (2.70), (2.76) and (2.80))

$$\frac{\Delta\nu_c}{\nu_c}^{(C_4)} \approx -\frac{3}{2}\frac{1}{qV_R}\frac{C_4}{C_2^2}\left(\frac{\nu_+}{\nu_z}\right)^2 E_z \tag{14.23}$$

$$\frac{\Delta\nu_c}{\nu_c}^{(C_6)} \approx -\frac{45}{16}\frac{1}{qV_R}\frac{C_6}{C_2^3}\left(\frac{\nu_+}{\nu_z}\right)^2 E_z \tag{14.24}$$

$$\frac{\Delta\nu_c}{\nu_c}^{(B_1)} \approx -\frac{1}{4\pi^2 m\nu_z^2}\left(\frac{B_1}{B_0}\right)^2 E_+ \tag{14.25}$$

$$\frac{\Delta\nu_c}{\nu_c}^{(B_2)} \approx -\frac{1}{4\pi^2 m\nu_z^2}\frac{B_2}{B_0}E_z \tag{14.26}$$

As will be discussed in Section 15.2.1, feedback cooling of the axial detection system, corresponding to

Table 14.2: Summary of the relative shift of the cyclotron frequencies of the antiproton and the H^- ion and the relative shift of the ratio $R_{\bar{p}H^-}$ assuming the values based on the characterization results discussed in the last sections and $T_{z,\bar{p}} = 5.05\,\mathrm{K}, T_{z,H^-} = 5.08\,\mathrm{K}$.

Term	Magnitude	$\left(\frac{\Delta\nu_c}{\nu_c}\right)_{\bar{p}}$	$\left(\frac{\Delta\nu_c}{\nu_c}\right)_{H^-}$	$\frac{\Delta R_{\bar{p}H^-}}{R_{\bar{p}H^-}}$
C_4	$< \lvert 4 \times 10^{-6} \cdot C_2^2 \rvert$	$< \lvert 2.651 \times 10^{-13} \rvert$	$< \lvert 2.665 \times 10^{-13} \rvert$	$< \lvert 1.48 \times 10^{-15} \rvert$
C_6	$< \lvert 4 \times 10^{-4} \cdot C_2^3 \rvert$	$< \lvert 4.97 \times 10^{-11} \rvert$	$< \lvert 5.00 \times 10^{-11} \rvert$	$< \lvert 2.78 \times 10^{-13} \rvert$
B_1	$4.75(6)\,\mathrm{mT/m}$	$-7.110(1) \times 10^{-13}$	$-7.155(1) \times 10^{-13}$	$4.45(16) \times 10^{-15}$
B_2	$-0.267(24)\,\mathrm{T/m^2}$	$3.535(69) \times 10^{-11}$	$3.556(69) \times 10^{-11}$	$-2(10) \times 10^{-13}$

$\Delta\nu_z \approx 2\,\mathrm{Hz} \iff T_{z,\mathrm{eff}}/T_z \approx 0.5$ is employed for the final measurement configuration. In Section 9.3, a possible difference between the effective axial temperatures of an antiproton and an H^- ion was estimated to be $T_{z,\bar{p}}/T_{z,H^-} = 0.994(1)$.

Based on above, the cyclotron frequency shifts due to the trap imperfections Eqs. (14.23) to (14.26) were estimated for the magnitudes of the trap imperfection terms characterized by the measurements in the previous sections, and for $T_{z,\bar{p}} = 5.05\,\mathrm{K}, T_{z,H^-} = 5.08\,\mathrm{K}$. The results are listed in Table 14.2. Here it can be seen that the shifts of the ratio $R_{\bar{p}H^-}$ due to the trap imperfections are on the level of 10^{-11} at most, and the associated uncertainties are on the order of 10^{-12} or less. Therefore the trap imperfections do not pose any limitation to a measurement at the level of 10^{-11}.

15

Cyclotron frequency measurement by the sideband coupling method

Before we discuss the details of the achieved cyclotron frequency stability in the following chapter, the necessary considerations and experimental studies to select parameters of cyclotron frequency measurements in the PT are summarized in this chapter.

15.1 Measurement sequence

As introduced in Section 2.2, the cyclotron frequency ν_c of a particle in a Penning trap is determined from its three eigenfrequencies ν_+, ν_z and ν_- via the invariance theorem [90]

$$\nu_c = \sqrt{\nu_+^2 + \nu_z^2 + \nu_-^2}. \tag{15.1}$$

This leads to a relation between the uncertainties of these frequencies

$$\delta\nu_c^2 = \left(\frac{\nu_+}{\nu_c}\right)^2 \delta\nu_+^2 + \left(\frac{\nu_z}{\nu_c}\right)^2 \delta\nu_z^2 + \left(\frac{\nu_-}{\nu_c}\right)^2 \delta\nu_-^2. \tag{15.2}$$

As mentioned in Section 2.1.1, there is a hierarchy between the eigenfrequencies: $\nu_+ \gg \nu_z \gg \nu_-$. For typical parameters of the PT in 2017 run-II,

$$\nu_+ \approx 29.656\,\mathrm{MHz}, \quad \nu_z \approx 640\,\mathrm{kHz}, \quad \nu_- \approx 6.9\,\mathrm{kHz} \tag{15.3}$$

$$\therefore \frac{\nu_+}{\nu_c} \approx 1, \quad \frac{\nu_z}{\nu_c} \approx \frac{1}{50}, \quad \frac{\nu_-}{\nu_c} \approx \frac{1}{4000}. \tag{15.4}$$

Therefore, what contributes most to the precision of ν_c is ν_+. while the precision required for ν_- is much relaxed. For example. if ν_c is to be measured with a relative precision of 10^{-9}, what is required

for ν_- is 10^{-2}.

The sideband coupling method [106] is employed to measure ν_+. As discussed in Section 2.5, an RF-drive at $\nu_{\rm rf} \approx \nu_+ - \nu_z$ is irradiated to couple the modified cyclotron mode to the axial mode. The axial frequencies $\nu_{\rm l}, \nu_{\rm r}$ of the coupled mode are measured from a double-dip spectrum, from which the modified cyclotron frequency ν_+ is determined by

$$\nu_+ = \nu_{\rm l} + \nu_{\rm r} - \nu_z + \nu_{\rm rf}. \tag{15.5}$$

This method is implemented in the experiment by the measurement sequence shown in Fig. 15.1 which is used to characterize the frequency stability by subsequent measurements of the same particle. Each cycle is started by a trigger signal at an injection of the beam to the AD ring. The purpose of this synchronization is to avoid possible systematic effects from super-cycles of the AD and the measurement sequence. This defines the length of one cycle to be the same as the repetition period of the AD of about 120 s. Following the trigger, a single-dip and a double-dip spectra are subsequently recorded. To keep the sideband drive locked while ν_+ and ν_z change, the drive frequency of the i th measurement $\nu_{{\rm rf},i}$ is determined from ν_+ and ν_z measured in the last cycle;

$$\nu_{{\rm rf},i} = \nu_{+,i-1} - \nu_{z,i-1}. \tag{15.6}$$

The magnetron frequency ν_- is not explicitly measured in the sequence, but was determined by an approximate relation Eq. (2.41)

$$\nu_- \approx \frac{\nu_z^2}{2\nu_+} \tag{15.7}$$

with sufficient precision.

In a later part of 2017 run, the two-particle sequence such as shown in Fig. 15.2 was implemented in the experiment. This is what was used for the proton-to-antiproton charge-to-mass ratio comparisons. Two particles were prepared in separate potential wells, and their cyclotron frequencies were measured alternately by measuring one of them in the PT while storing the other in the park electrode adjacent to the PT (See Fig. 5.11). Before each measurement, the particles were exchanged by an adiabatic transport by means of sequential potential ramps, which took about 10 s for each. When an antiproton and an H^- ion are measured, the varactor voltage is adjusted to tune the resonance frequency of the axial detection system in resonance to the axial frequency of the particles (see Chapter 9).

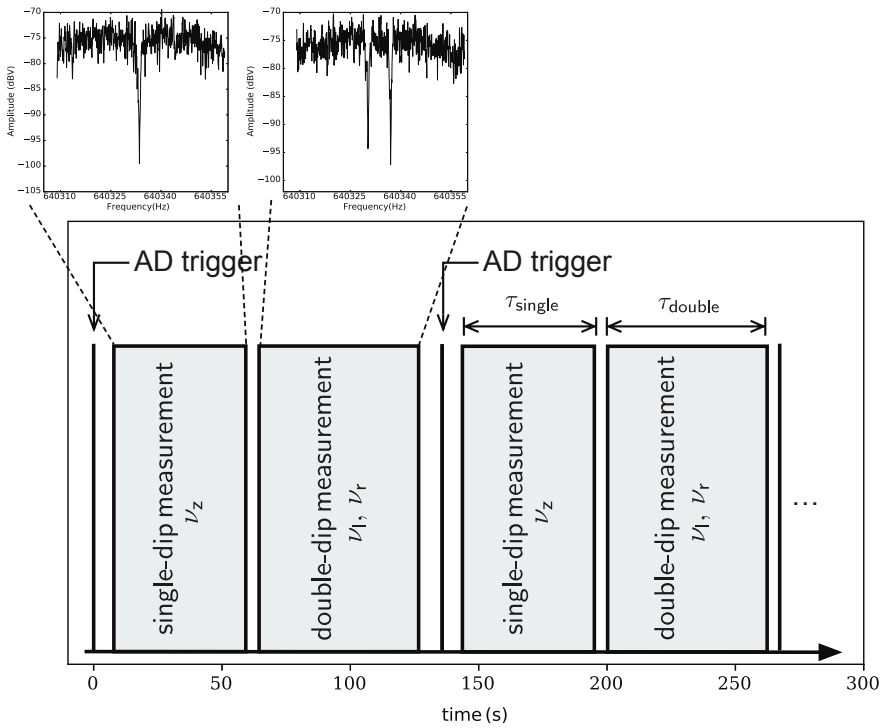

Figure 15.1: Sequence of the cyclotron frequency measurements of the particle by the sideband coupling method. Each cycle is started by a trigger synchronized to an injection of antiprotons into the AD ring. (see Fig. 4.2). One cycle consists of acquisitions of a single-dip spectrum and a double-dip spectrum. Their averaging times are noted as τ_{single} and τ_{double}, respectively.

15.2 Stability limit of the cyclotron frequency and selection of the averaging parameters

In the next chapter, development works to improve the cyclotron frequency stability will be summarized. Before discussing the actual cyclotron frequency stability, here we shall derive the principal limit of the cyclotron frequency stability when the sideband coupling method is used.

Looking at Eq. (15.5), it can be observed that the precision of ν_+ is dominated by that of ν_z, ν_{l} and ν_{r}, since the drive frequency ν_{rf} is precise to a relative precision of 10^{-11}, defined by the specifications of the frequency generator and the frequency standard. Thus, the axial frequency stability defines the principal limit of the cyclotron frequency fluctuation reachable by the sideband coupling method. Therefore, a detailed understanding of the axial frequency fluctuation is necessary to discuss the limit of the cyclotron frequency fluctuation. Furthermore, as the total averaging time can be used for the measurement is constrained by the AD cycle, the understanding of the statistical properties of the axial frequency fluctuation allows us to choose the single-dip averaging time τ_{single} and the double-dip averaging time τ_{double} so that the fluctuation of the cyclotron frequency fluctuation is minimized.

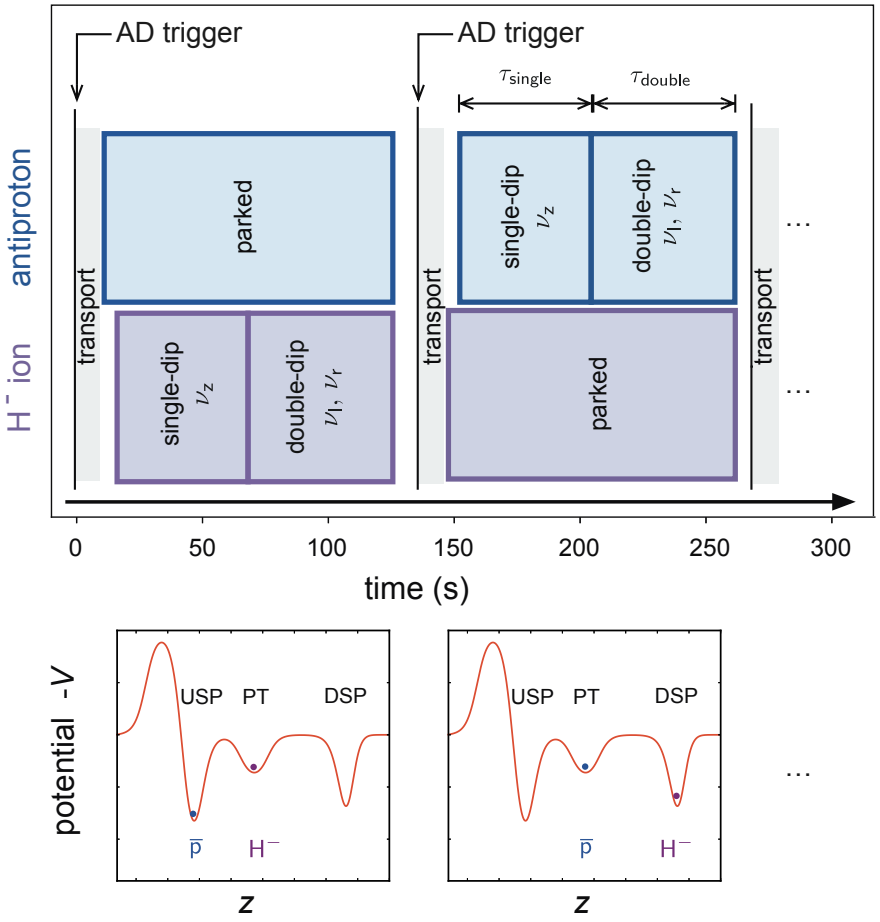

Figure 15.2: Two-particle sequence using the sideband coupling method. Tow particles, in this example, an antiproton (downstream) and an H^- ion (upstream) were prepared and stored in separate potential wells. The sideband coupling sequence is alternately applied to each particle by transporting them at the beginning of each cycle. As in Fig. 15.1, each cycle is synchronized to the AD by the trigger. Below the sequence, the potential and particle configuration during each cycle are displayed. In the potential plots, USP=upstream park electrode, DSP=downstream park electrode. See the electrode definition on Fig. 5.11.

15.2.1 Characterization of the axial frequency fluctuation

The statistical properties of the axial frequency fluctuation can be studied by analyzing its Allan variance.

In Fig. 15.3, the Allan variance $\sigma_{\mathrm{A}}^2(\nu_z, \tau)$ is evaluated for a series of axial frequency measurements in the sideband coupling sequence. The scaling of the fractional Allan variance $\sigma_{\mathrm{A}}^2(\nu_z, \tau)/\overline{\nu}_z^2$ matches to a model

$$\frac{\sigma_{\mathrm{A}}^2(\nu_z, \tau)}{\overline{\nu}_z^2} = \hat{c}_0 + \frac{\hat{c}_{-1}}{\tau} + \hat{c}_1 \tau. \tag{15.8}$$

Recalling the discussion in Section 3.1, the term c_{-1} represents a white-noise contribution and c_1 a random-walk contribution. A least-squares fitting of the Allan variance curve in Fig. 15.3 to this model yields

$$\hat{c}_0 = -4(2) \times 10^{-16}, \quad \hat{c}_{-1} = 2.1(1) \times 10^{-13}\,\mathrm{s}, \quad \hat{c}_1 = 1.4(2) \times 10^{-18}\,\mathrm{s}^{-1}. \tag{15.9}$$

These coefficients correspond to $0.293(7)\,\mathrm{Hz} \cdot \sqrt{\mathrm{s}}$ of white noise, and $7.6(5) \times 10^{-4}\,\mathrm{Hz}/\sqrt{\mathrm{s}}$ of random walk in unit of absolute frequency, assuming the antiproton's axial frequency of $\nu_{z,\bar{p}} \approx 640\,250\,\mathrm{Hz}$[1].

What appears here as a random walk is caused by slow drifts of the frequency induced by variation of environmental conditions, typically temperature drifts. In Fig. 15.4 (A), an evolution of the axial frequency is shown, from which the Allan variance of Fig. 15.3 was obtained. Shown in Fig. 15.4 (B) is the temperature in the box where the high-precision voltage source UM1-14 is placed. Comparing the two plots. an anti-correlated relation of long-term drifts between the axial frequency and the temperature is observed, which can be also seen in the scatter plot (C), where the axial frequency is plotted against the temperature. This is due to a thermoelectric effect widely known as the Seebeck effect [203]; for a sample made of two different materials, a temperature difference between two parts of a junction generates an electric potential. This produces slow drifts in the axial frequency, which appear as a random-walk like contribution in the Allan variance.

In a range $\tau < 100\,\mathrm{s}$ which we are interested in, the contribution of this random-walk like contribution is much smaller than that of the white noise, hence can be neglected. In case of this example, from Eq. (15.9),

$$\frac{\hat{c}_1 \cdot \tau}{\hat{c}_{-1} \cdot \tau^{-1}} \sim 10^{-2}. \tag{15.10}$$

Hereafter, we will focus on the white-noise components of the axial frequency fluctuation.

Accounting only the relevant components, the axial frequency Allan variance $\sigma_{\mathrm{A}}^2(\nu_z, \tau)$ can be decomposed to contributions from different sources as

$$\sigma_{\mathrm{A}}^2(\nu_z, \tau) = \sigma_{\mathrm{A,V}}^2(\nu_z, \tau) + \sigma_{\mathrm{A,fit}}^2(\nu_z, \tau) + \sigma_{\mathrm{A},E_+}^2(\nu_z, \tau) \tag{15.11}$$

[1]The axial frequency difference of $\nu_{z,\bar{p}} - \nu_{z,\mathrm{H}^-} \approx 260\,\mathrm{Hz}$ between the antiproton and the H^- ion does not make a significant difference in this conversion. So for the conversions to unit of the axial frequency in the rest of the chapter.

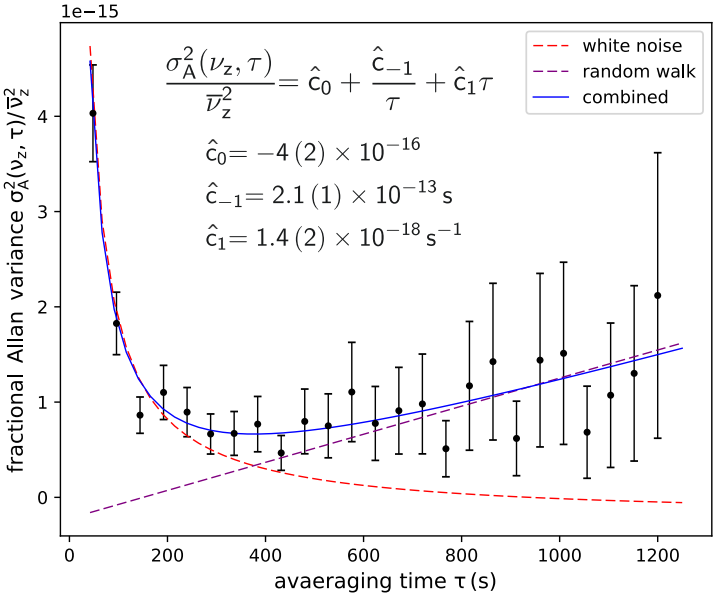

Figure 15.3: Allan variance of the axial frequencies obtained during a sideband coupling measurement sequence. The scaling of the fractional Allan variance $\sigma_A^2(\nu_z,\tau)/\overline{\nu}_z^2$ against the averaging time τ is fitted to the scaling of a combination of a white-noise and a random-walk components.

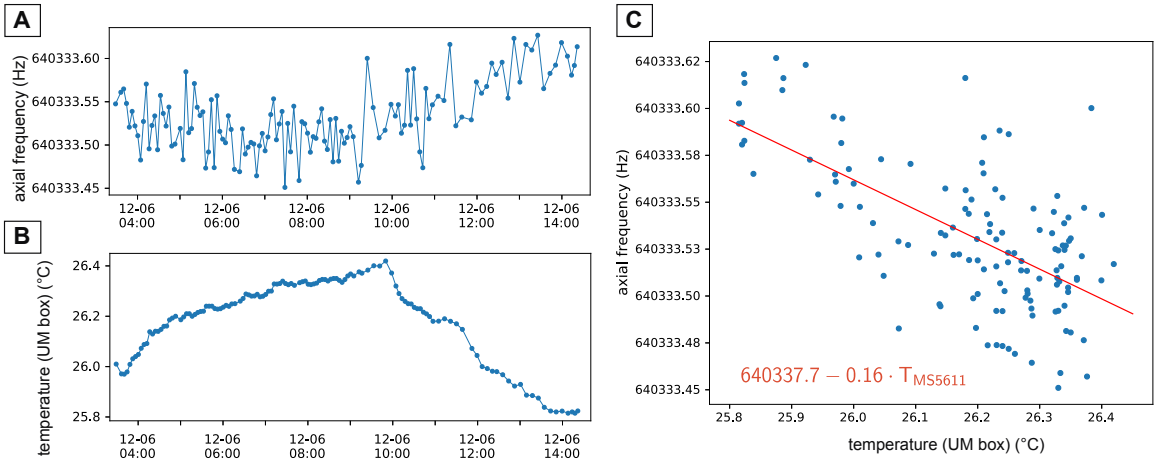

Figure 15.4: Temperature-correlated drifts of the axial frequency are observed. **(A)** Evolution of the axial frequency. The Allan variance in Fig. 15.3 was obtained from this dataset. **(B)** Evolution of temperature in a box where UM 1-14, the high-precision voltage source to provide trapping voltage, is placed. The temperature is measured by the sensor MS5611 (see Section 11.1). Each data point in the plot was obtained by averaging the temperature in the averaging time-window of each axial frequency. **(C)** Scattered plot between the axial frequency and the temperature. A negative correlation between the two is observed.

where $\sigma^2_{\mathrm{A,V}}(\nu_z,\tau)$, $\sigma^2_{\mathrm{A,fit}}(\nu_z,\tau)$ and $\sigma^2_{\mathrm{A},E_+}(\nu_z,\tau)$ respectively represent contributions from different sources:

- $\sigma^2_{\mathrm{A,V}}(\nu_z,\tau)$: a contribution by the fluctuation of the ring voltage V_{R}.
- $\sigma^2_{\mathrm{A,fit}}(\nu_z,\tau)$: a contribution by the uncertainty of fitting of dip signals.
- $\sigma^2_{\mathrm{A},E_+}(\nu_z,\tau)$: a contribution by the energy fluctuation of the modified cyclotron mode E_+, shifting the axial frequency through couplings via trap imperfections. This contribution is present when the modified cyclotron mode is coupled to the axial mode in the sideband coupling sequence.

Each of them will be discussed in more detail in the following. The goal is to characterize them as functions of the averaging time τ.

The most part of the characterization is discussed in a unit of a relative Allan variance, whose coefficients denoted as $\hat{c}_{-1}$ etc.. To convert them to a unit of the axial frequency,

$$\sigma_{\mathrm{A}}(\nu_z,\tau) = \nu_z\sqrt{\frac{\sigma^2_{\mathrm{A}}(\nu_z,\tau)}{\nu_z^2}} \tag{15.12}$$

should be used. A typical axial frequency in 2017 run-II is $\nu_z \approx 640\,\mathrm{kHz}$. As seen in Eq. (15.9), the target of the discussion is on the order of

$$\frac{\sigma^2_{\mathrm{A}}(\nu_z\tau)}{\nu_z^2} \sim 10^{-15}, \quad \frac{\sigma_{\mathrm{A}}(\nu_z\tau)}{\nu_z} \sim 10^{-8}, \quad \sigma_{\mathrm{A}}(\nu_z,\tau) \sim 10^{-2}\,\mathrm{Hz}. \tag{15.13}$$

Contribution of the voltage fluctuation $\sigma^2_{\mathrm{A,V}}(\nu_z,\tau)$

The voltage noise of the high-precision voltage source UM 1-14 is well characterized as the white noise, and causes the major part of the white noise of the axial frequency. The fractional Allan variance of the voltage is fitted to the white-noise scaling in Fig. 15.5. The data shown here was obtained by the characterization measurement mentioned in Section 5.5. By the least-squares fit to the white-noise scaling of the Allan variance,

$$\begin{gathered}\frac{\sigma^2_{\mathrm{A}}(V,\tau)}{\overline{V}^2} = c_{0,\mathrm{V}} + \frac{c_{-1,\mathrm{V}}}{\tau} \\ c_{0,\mathrm{V}} = 9.7(2)\times 10^{-16}, \quad c_{-1,\mathrm{V}} = 2.50(5)\times 10^{-14}\,\mathrm{s}\end{gathered} \tag{15.14}$$

was obtained.

Since $\nu_z \propto \sqrt{V_{\mathrm{R}}}$, the Allan deviations of the voltage and of the axial frequency are related by

$$\frac{\sigma_{\mathrm{A,V}}(\nu_z,\tau)}{\overline{\nu}_z} = \frac{1}{2}\frac{\sigma_{\mathrm{A}}(V,\tau)}{\overline{V}}, \tag{15.15}$$

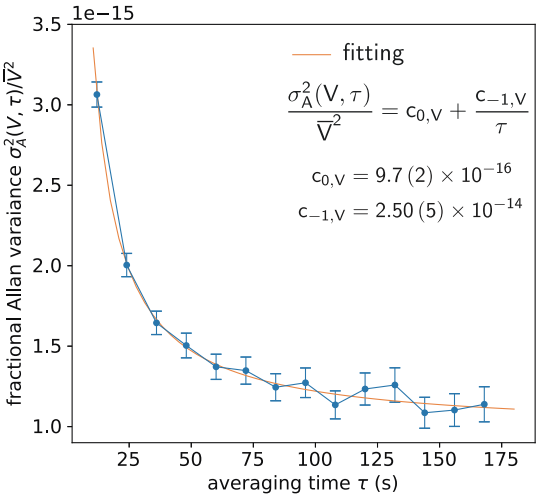

Figure 15.5: Characterization of the Allan variance of the trapping voltage. The Allan variance was evaluated for a series of voltages obtained by measurements of a high-precision test channel of UM 1-14-LN-F utilized for the PT (see Fig. 5.16). The fractional Allan variance $\sigma_{\mathrm{A}}^2(V,\tau)/\overline{V}^2$ is fitted to the white noise scaling $c_{0,\mathrm{V}} + c_{-1,\mathrm{V}} \cdot \tau^{-1}$.

therefore

$$\frac{\sigma_{\mathrm{A,V}}^2(\nu_z,\tau)}{\overline{\nu}_z^2} = \hat{c}_{0,\mathrm{V}} + \frac{\hat{c}_{-1,\mathrm{V}}}{\tau} \qquad (15.16)$$
$$\hat{c}_{0,\mathrm{V}} = 2.43(4) \times 10^{-16}, \quad \hat{c}_{-1,\mathrm{V}} = 6.3(1) \times 10^{-15}\,\mathrm{s},$$

corresponding to $5.08(4) \times 10^{-2}\,\mathrm{Hz} \cdot \sqrt{\mathrm{s}}$ of white noise in unit of absolute frequency.

Contribution of the fitting uncertainty $\sigma_{\mathrm{A,fit}}^2(\nu_z,\tau)$

If the Allan variance is evaluated for a series of measured axial frequencies, one finds that the white noise is a greater than $\sigma_{A,\mathrm{V}}^2(\nu_z,\tau)$ discussed in the last section. Such an example is shown in Fig. 15.6. In Fig. 15.6 (A), the voltage-contributed $\sigma_{\mathrm{A,V}}^2(\nu_z,\tau)$ evaluated by Eq. (15.16) is subtracted from the measured Allan variance $\sigma_{\mathrm{A}}^2(\nu_z,\tau)$. The residual $\sigma_{\mathrm{A}}^2(\nu_z,\tau) - \sigma_{\mathrm{A,V}}^2(\nu_z,\tau)$ can be fitted with the white-noise scaling. This is named $\sigma_{\mathrm{A,fit}}^2(\nu_z,\tau)$ and shown together with $\sigma_{\mathrm{A,V}}^2(\nu_z,\tau)$ in Fig. 15.6 (B).

This additional white-noise is mainly attributed to an uncertainty of fitting of the dip signals. To obtain the axial frequency from an FFT spectrum, the signal in the dBm scale is fitted to the theoretical line shape (Eq. (2.111)) by the Levenberg-Marquardt algorithm.

The uncertainty of this fitting produces an effective white-noise contribution to the Allan variance of the axial frequency. To characterize the magnitude of the fitting uncertainty, the Allan variance of the axial frequency was recorded for different line-shape parameters.

The uncertainty of the fitting σ_{fit} is expected to scale against the parameters of the dip line shape

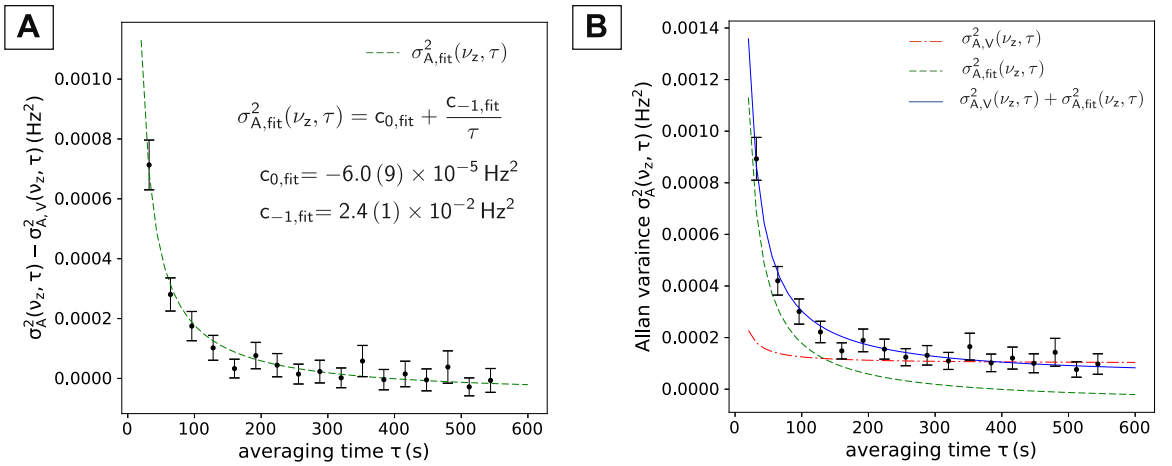

Figure 15.6: **(A)** The residual $\sigma^2_{\mathrm{A}}(\nu_z,\tau) - \sigma^2_{\mathrm{A,V}}(\nu_z,\tau)$, obtained by the Allan variance of the axial frequency $\sigma^2_{\mathrm{A}}(\nu_z,\tau)$ and the contribution of the voltage fluctuation $\sigma^2_{\mathrm{A,V}}(\nu_z,\tau)$. It is fitted by the white-noise scaling to extract the coefficients $c_{0,\mathrm{fit}}, c_{-1,\mathrm{fit}}$. **(B)** Allan variance of measured axial frequency $\sigma^2_{\mathrm{A}}(\nu_z,\tau)$ is shown with daw points with error bars. The red dotted-dashed curve indicates the contribution of the voltage fluctuation to the axial frequency Allan variance $\sigma^2_{\mathrm{A,V}}(\nu_z,\tau)$, the green dashed curve indicates the contribution attributed to the fit $\sigma^2_{\mathrm{A,fit}}(\nu_z,\tau)$, as evaluated in (A). The blue line is the combination of the two, which matches to the measurement well.

as [204]

$$\sigma_{\mathrm{fit}} \propto \sqrt{\frac{1}{\tau_{\mathrm{avg}}} \frac{\Delta\nu_z}{\sqrt{\mathrm{SNR}|_{\mathrm{dip}}}}} \tag{15.17}$$

with $\Delta\nu_z, \tau_{\mathrm{avg}}, \mathrm{SNR}|_{\mathrm{dip}}$ being the dip-width, the averaging time, and the dip SNR, respectively.

The experimental characterization was made by varying the line shape by application of the feedback of the axial detection system. When the effective temperature $T_{z,\mathrm{eff}}$ is varied by the feedback from its original $T_{z,0}$, this scales the line shape according to

$$\Delta\nu_z \propto T_{z,\mathrm{eff}}, \quad \mathrm{SNR}|_{\mathrm{res}} \propto \sqrt{T_{z,\mathrm{eff}}}. \tag{15.18}$$

Results of such measurements are summarized in Fig. 15.7. Four conditions of negative feedback (A–D) were chosen, corresponding to $\Delta_z = 1.7$–$4.2\,\mathrm{Hz}$, SNR= 21–30 dB. In Fig. 15.7, SNR is noted in linear unit, because this should be used in applying Eq. (15.18). In a sequence of measurements without sideband drive, 70–200 axial dip spectra were recorded for each feedback setting, fitted by the theoretical line shape. One of the spectra is shown for each setting in Fig. 15.7 (A1–D1) with the fitted curve. The Allan variance $\sigma^2_{\mathrm{A}}(\nu_z,\tau)$ was then evaluated for each sequence of measurements (Fig. 15.7 (A2–D2)). Assuming

$$\sigma^2_{\mathrm{A}}(\nu_z,\tau) = \sigma^2_{\mathrm{A,V}}(\nu_z,\tau) + \sigma^2_{\mathrm{A,fit}}(\nu_z,\tau) \tag{15.19}$$

and $\sigma^2_{\mathrm{A,V}}(\nu_z,\tau)$ to be Eq. (15.16) as discussed above, the contribution $\sigma^2_{\mathrm{A,fit}}(\nu_z,\tau)$ was obtained by

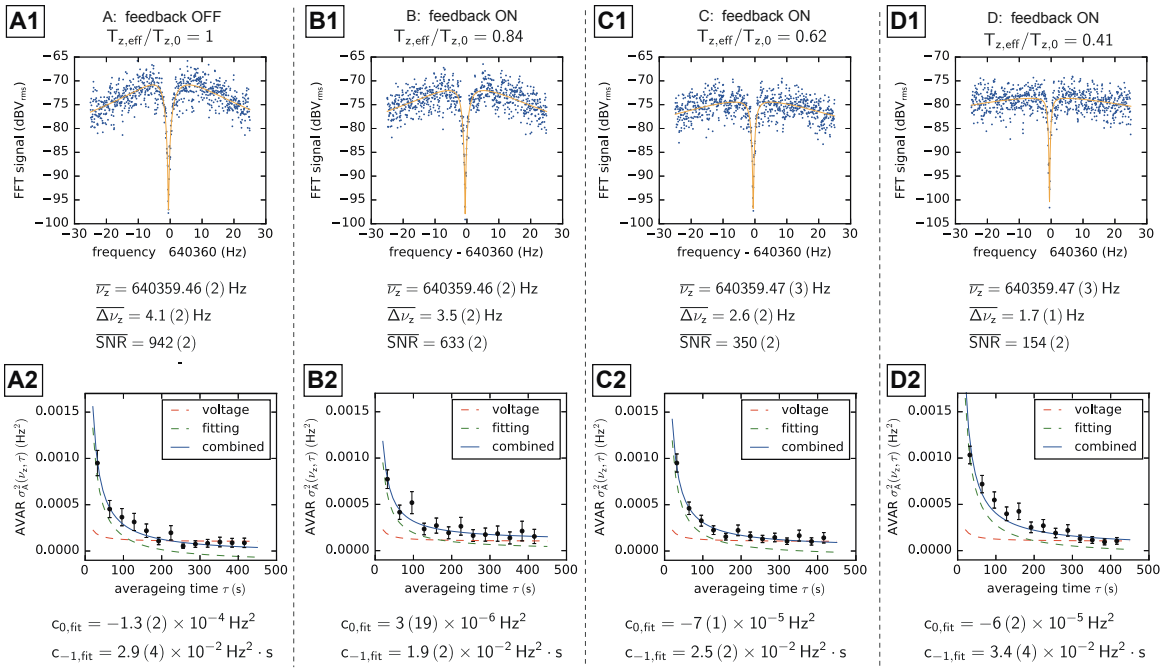

Figure 15.7: Characterization of the axial frequency fluctuation from the fitting uncertainties. The scaling of the Allan variance was characterized for sets A, B, C and D, which correspond to different strengths of the negative feedback of the detection system. **(A1, B1, C1, D1)** One of the FFT spectra of each feedback setting is shown with the fitted curve. The averaged values of the line-shape parameters over each dataset are listed below the spectrum. **(A2, B2, C2, D2)** The Allan variance $\sigma_A^2(\nu_z,\tau)$ was obtained for each series. The contribution of the voltage fluctuation was subtracted (see Eq. (15.19)), and the residual attributed to the fitting uncertainty is fitted with the white noise scaling Eq. (15.20). The voltage contribution is shown by the red dashed line, the obtained fit contribution by the green dashed line, and a combination of the two $\sigma_{A,V}^2 + \sigma_{A,fit}^2$ by the blue line.

fitting $\sigma_A^2(\nu_z,\tau) - \sigma_{A,V}^2(\nu_z,\tau)$ to the white-noise scaling

$$\sigma_{A,fit}^2(\nu_z,\tau) = c_{0,fit} + \frac{c_{-1,fit}}{\tau}. \tag{15.20}$$

The obtained $c_{0,fit}$ and $c_{-1,fit}$ are shown below each Allan variance plot in Fig. 15.8 (A2–D2).

These results were used to study the scaling of the frequency fluctuation against the line-shape parameters. To compare different datasets recorded in different conditions, $\sigma_{A,fit}^2(\nu_z,\tau)$ for a fixed $\tau = 48\,s$ were evaluated by the scaling obtained by the fit. In Fig. 15.8 (A–C), $\sigma_{A,fit}(\nu_z, 48\,s)$ thus obtained are plotted against the line-shape parameters (the dip-width in case of (A), the dip SNR for (B)). In Fig. 15.8 (C), The three datasets included in the plot were recorded on different dates and had different details in the settings e.g. the amplifier gain. Among the three, *dataset 1* is from the data presented in Fig. 15.7.

When the line-shape is changed by negative electric feedback, a low effective temperature $T_{z,eff}$ decreases both of the dip-width $\Delta\nu_z$ and the dip SNR (see Eqs. (2.122) and (2.126)). As observed in Eq. (15.17), a smaller dip-width decreases σ_{fit}, while a smaller SNR contributes to enlarge σ_{fit}.

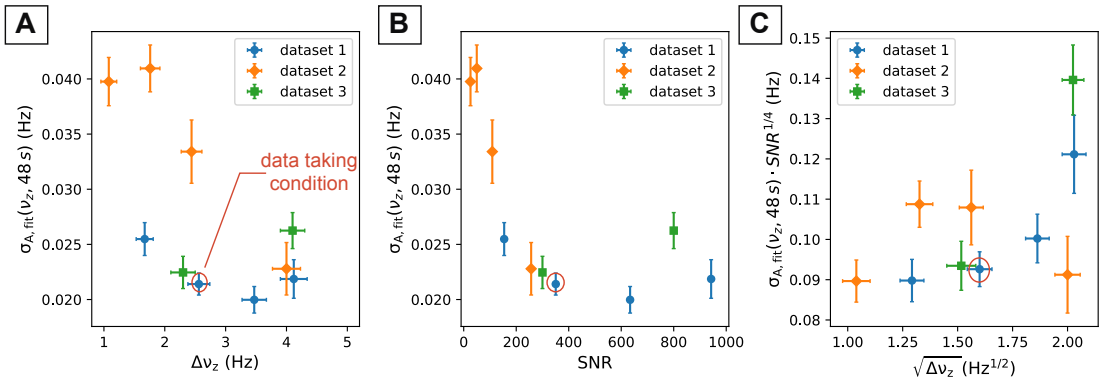

Figure 15.8: Scalings of $\sigma_{\mathrm{A,fit}}(\nu_z, \tau)$, the fitting contribution to the axial frequency Allan deviation, against the line-shape parameters. Each data point of $\sigma_{\mathrm{A,fit}}(\nu_z, 48\,\mathrm{s})$ was obtained by the fitted scaling of $\sigma^2_{\mathrm{A,fit}}(\nu_z, \tau)$ (see Fig. 15.7 (A2–D2)). Datasets recorded on different dates are sorted in the legend. Among them, the *dataset 1* is evaluated from the results shown in Fig. 15.7 (A2–D2). All the datasets were recorded with a single H^- ion. The condition finally chosen for the data taking of the charge-to-mass ratio comparison is marked by red circles. **(A)** The scaling against the dip-width $\Delta\nu_z$. $\sigma_{\mathrm{A,fit}}(\nu_z, 48\,\mathrm{s})$ reaches a minimum at around $\Delta\nu_z \approx 3\,\mathrm{Hz}$. The difference of the fluctuation between the datasets are attributed to different SNRs. **(B)** The scaling against the dip SNR. The data follow a common monotonically decreasing trend against SNR. **(C)** $\sigma_{\mathrm{A,fit}}(\nu_z, 48\,\mathrm{s}) \cdot \mathrm{SNR}^{1/4}$ is plotted against $\sqrt{\Delta\nu_z}$. The data points follow the same, an approximately linear trend, which confirms the expected scaling of Eq. (15.17).

The two competing effects result in a minimum of σ_{fit} for feedback settings around $\Delta\nu_z \approx 3\,\mathrm{Hz}$ as observed in Fig. 15.8 (A) for $\sigma_{\mathrm{A,fit}}(\nu_z, 48\,\mathrm{s})$. For actual data taking of the charge-to-mass comparison, a feedback setting corresponding $\Delta\nu_z \approx 2.5\,\mathrm{Hz}, \mathrm{SNR}|_{\mathrm{dip}} \approx 350$ (or 25 dB) was employed. The data point recorded under this condition is circled in red in each of Fig. 15.8(A–C).

Besides the scaling Eq. (15.17) discussed above, several data points of *dataset 2* in Fig. 15.8 (A) are out of trend of the other two datasets. This is due to differences in the dip SNR between the measurement conditions, as found in Fig. 15.8 (B). Different SNRs between datasets resulted mainly from difference differences in the electrical imperfection C_4 for not optimized TRs (see Section 14.1.1).

In Fig. 15.8 (C), $\sigma_{\mathrm{A,fit}}(\nu_z, 48\,\mathrm{s}) \cdot \mathrm{SNR}|^{1/4}_{\mathrm{dip}}$ is plotted against $\sqrt{\Delta\nu_z}$. As a whole, the data points follow roughly the same linear trend, which confirms the scaling Eq. (15.17).

For the feedback setting chosen as the final setting,

$$\frac{\sigma^2_{\mathrm{A,fit}}(\nu_z, \tau)}{\overline{\nu}_z^2} = \hat{c}_{0,\mathrm{fit}} + \frac{\hat{c}_{-1,\mathrm{fit}}}{\tau}$$
$$\hat{c}_{0,\mathrm{fit}} = -2.1(5) \times 10^{-16}, \quad \hat{c}_{-1,\mathrm{fit}} = 6.9(7) \times 10^{-14}\,\mathrm{s} \tag{15.21}$$

was obtained as part of the procedure above. This is translated to $0.168(9)\,\mathrm{Hz} \cdot \sqrt{\mathrm{s}}$ in unit of absolute frequency.

Contribution of the energy fluctuation of the modified cyclotron mode $\sigma^2_{\mathrm{A},E_+}(\nu_z,\tau)$

The axial frequency fluctuation in the sideband coupling sequence has yet another component. When the axial mode is coupled to the modified cyclotron mode during the sideband drive, the temperature of the modified cyclotron mode T_+ reaches

$$T_+ = \frac{\nu_+}{\nu_z} T_z \approx 50 \cdot 5\,\mathrm{K} \tag{15.22}$$

from the thermal equilibrium relation by the sideband (see Eq. (2.157)). Coupled to imperfections of the trap, the energy of the modified cyclotron mode E_+, distributed according to the Boltzmann distribution defined by T_+, causes Boltzmann distributing axial frequency fluctuations $\Delta\nu_z^{(B_2,E_+)} \propto B_2 {E_+}^2$ [2] (Eq. (14.16)), whose mean is on the order of $\langle\Delta\nu_z^{(B_2,E_+)}\rangle \sim 10\,\mathrm{mHz}$ (Eq. (14.19)).

This adds fluctuations of the axial frequency due to fluctuations of E_+ from measurement to measurement. This additional fluctuation was characterized by comparing the Allan variance between axial frequencies measured in a sideband sequence and a sequence without sideband drives (as in the case until the last section). From the axial Allan variance obtained by a sideband measurement sequence (Fig. 15.1), $\sigma^2_{\mathrm{A,V}}/\overline{\nu}_z^2(\nu_z,\tau)$ (Eq. (15.16)) and $\sigma^2_{\mathrm{A,fit}}/\overline{\nu}_z^2(\nu_z,\tau)$ (Eq. (15.21)) are subtracted and the residual is shown in Fig. 15.9 (A). The remaining component which is attributed the effect of E_+ fluctuations is fitted to the white-noise scaling to obtain

$$\begin{gathered}\frac{\sigma^2_{\mathrm{A},E_+}(\nu_z,\tau)}{\overline{\nu}_z^2} = \hat{c}_{0,E_+} + \frac{\hat{c}_{-1,E_+}}{\tau} \\ \hat{c}_{0,E_+} = -2(6)\times 10^{-17}, \quad \hat{c}_{-1,E_+} = 4(1)\times 10^{-14}\,\mathrm{s},\end{gathered} \tag{15.23}$$

corresponding to $0.13(2)\,\mathrm{Hz}\cdot\sqrt{\mathrm{s}}$ in unit of absolute frequency. This contribution is shown in Fig. 15.9 (B) with the other contributions. The measured Allan variance fits well to the combination of the three white-noise components.

Derivation of the cyclotron frequency stability limit

Summarizing what have been discussed until the last section, the Allan variance of the axial frequency $\sigma^2_{\mathrm{A}}(\nu_z,\tau)$ has been characterized by the three white noise components, attributed to the voltage fluctuation, the uncertainty of the dip fitting, and the fluctuations of the modified cyclotron energy E_+:

$$\sigma^2_{\mathrm{A}}(\nu_z,\tau) = \sigma^2_{\mathrm{A,V}}(\nu_z,\tau) + \sigma^2_{\mathrm{A,fit}}(\nu_z,\tau) + \sigma^2_{\mathrm{A},E_+}(\nu_z,\tau) \tag{15.24}$$

[2] Although there are also contributions from the other trap imperfection terms, the one from B_2 is the most dominant. See Table 14.2.

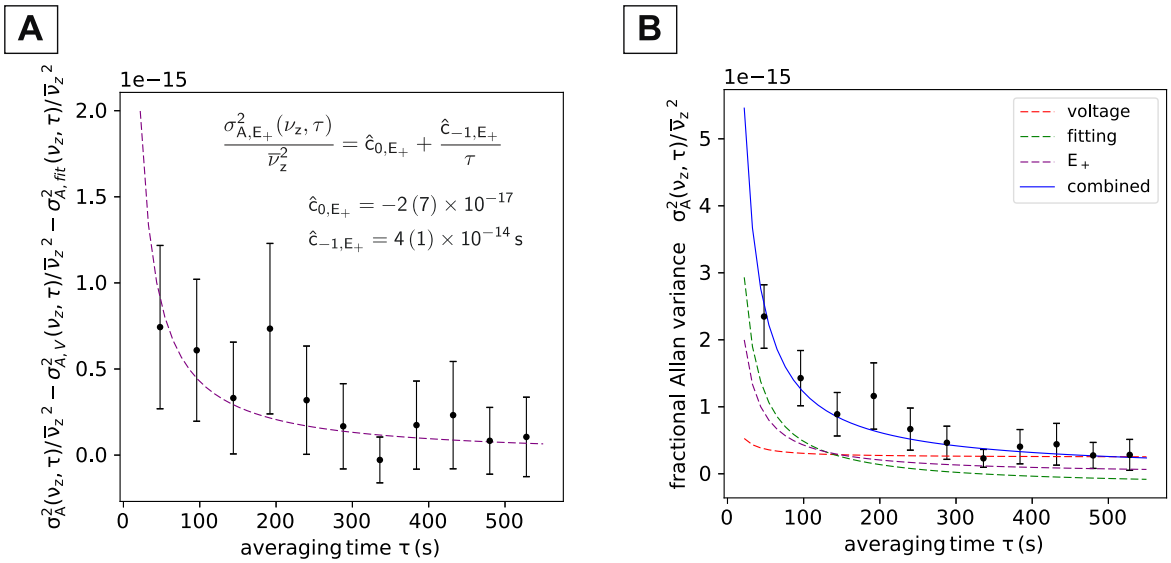

Figure 15.9: Extraction of the contribution from fluctuations of the modified cyclotron energy E_+ to the Allan variance of the axial frequency. The Allan variance was obtained by a series of axial frequency measurements in a single-particle sideband sequence (Fig. 15.1). **(A)** From the measured axial frequency Allan variance, the contributions of the voltage fluctuation and the fitting uncertainty are subtracted. The remaining part is fitted to the white-noise scaling to extract the component attributed to E_+ fluctuations. **(B)** The each contribution discussed thus far are shown with the measured Allan variance. The combination of the three fits well to the measured data.

Table 15.1: Summary of the coefficients $\hat{c}_0, \hat{c}_{-1}$ in Eq. (15.25). The index k represents the source of the fluctuation. The last column is the white-noise component $\hat{c}_{-1}$ converted into the unit of absolute axial frequency.

k	$\hat{c}_{0,k}$	$\hat{c}_{-1,k}$	white noise (absolute frequency)
V	$2.43(4) \times 10^{-16}$	$6.3(1) \times 10^{-15}\,\mathrm{s}$	$0.0508(4)\,\mathrm{Hz} \cdot \sqrt{\mathrm{s}}$
fit	$-2.1(5) \times 10^{-16}$	$6.9(7) \times 10^{-14}\,\mathrm{s}$	$0.168(9)\,\mathrm{Hz} \cdot \sqrt{\mathrm{s}}$
E_+	$-2(6) \times 10^{-17}$	$4(1) \times 10^{-14}\,\mathrm{s}$	$0.13(2)\,\mathrm{Hz} \cdot \sqrt{\mathrm{s}}$

$$\begin{aligned}
\frac{\sigma^2_{A,\mathrm{V}}(\nu_z,\tau)}{\overline{\nu}_z^2} &= \hat{c}_{0,\mathrm{V}} + \frac{\hat{c}_{-1,\mathrm{V}}}{\tau} \\
\frac{\sigma^2_{\mathrm{A,fit}}(\nu_z,\tau)}{\overline{\nu}_z^2} &= \hat{c}_{0,\mathrm{fit}} + \frac{\hat{c}_{-1,\mathrm{fit}}}{\tau} \\
\frac{\sigma^2_{\mathrm{A},E_+}(\nu_z,\tau)}{\overline{\nu}_z^2} &= \hat{c}_{0,E_+} + \frac{\hat{c}_{-1,E_+}}{\tau}
\end{aligned} \tag{15.25}$$

with the coefficients $\hat{c}_0, \hat{c}_{-1}$ listed in Table 15.1.

Based on this model and the sideband relation Eq. (15.5), the limit of the cyclotron frequency stability can be derived. Now we denote the cyclotron frequency fluctuation by the sideband coupling sequence as $\Xi_{\mathrm{c}}(\tau_{\mathrm{s}}, \tau_{\mathrm{d}})$, with $\tau_{\mathrm{s}}, \tau_{\mathrm{d}}$ to be averaging times assigned to single-dip and double-dip measurements, respectively. The total averaging time $\tau_{\mathrm{s}} + \tau_{\mathrm{d}}$ ought to be within the cycle length of the

measurement mentioned earlier. This is related to the Allan variances of the frequencies $\nu_z, \nu_\mathrm{l}, \nu_\mathrm{r}$ as

$$\begin{aligned}\Xi_\mathrm{c}^2(\tau_\mathrm{s},\tau_\mathrm{d}) &= \sigma_\mathrm{A}^2(\nu_\mathrm{l},\tau_\mathrm{d}) + \sigma_\mathrm{A}^2(\nu_\mathrm{r},\tau_\mathrm{d}) + \sigma_\mathrm{A}^2(\nu_z,\tau_\mathrm{s}) + \cancel{\sigma_\mathrm{A}^2(\nu_\mathrm{rf},\tau_\mathrm{d})} \\ &= (2\,\sigma_{\mathrm{A,V}}(\nu_\mathrm{l},\tau_\mathrm{d}))^2 + \sigma_{\mathrm{A,fit}}^2(\nu_\mathrm{l},\tau_\mathrm{d}) + \sigma_{\mathrm{A,fit}}^2(\nu_\mathrm{r},\tau_\mathrm{d}) + (2\,\sigma_{\mathrm{A},E_+}(\nu_\mathrm{l},\tau_\mathrm{d}))^2 \\ &\quad + \sigma_{\mathrm{A,V}}^2(\nu_z,\tau_\mathrm{s}) + \sigma_{\mathrm{A,fit}}^2(\nu_z,\tau_\mathrm{s}) + \sigma_{\mathrm{A},E_+}^2(\nu_z,\tau_\mathrm{s})\end{aligned} \tag{15.26}$$

here it is assumed that the uncertainties on the drive frequency ν_rf (typically on the order of mHz or below) are negligible. In addition, correlations between the contributions of the voltage fluctuations and the E_+ fluctuations to ν_l and ν_r are assumed to be correlated. Since the frequency differences between ν_z and $\nu_\mathrm{l}, \nu_\mathrm{r}$, typically about $\pm 5\,\mathrm{Hz}$, relative differences on the order of 10^{-6}, is negligible compared to the uncertainties of the coefficients $\hat{c}_0, \hat{c}_{-1}$,

$$\begin{aligned}\sigma_{\mathrm{A,V}}^2(\nu_l,\tau) &\approx \sigma_{\mathrm{A,V}}^2(\nu_z,\tau) \\ \sigma_{\mathrm{A},E_+}^2(\nu_l,\tau) &\approx \sigma_{\mathrm{A},E_+}^2(\nu_z,\tau).\end{aligned} \tag{15.27}$$

As for $\sigma_{\mathrm{A,fit}}^2(\nu_\mathrm{l},\tau), \sigma_{\mathrm{A,fit}}^2(\nu_\mathrm{r},\tau)$, they can be deduced from the scaling Eq. (15.17). From the properties of a double-dip spectrum (Eq. (2.166)),

$$\begin{aligned}\Delta\nu_\mathrm{l} \approx \Delta\nu_\mathrm{r} &\approx \frac{\Delta\nu_z}{2} \\ \mathrm{SNR}|_{\mathrm{dip,l}} \approx \mathrm{SNR}|_{\mathrm{dip,r}} &\approx \frac{\mathrm{SNR}|_{\mathrm{dip},z}}{2}.\end{aligned} \tag{15.28}$$

Applying Eq. (15.17),

$$\sigma_{\mathrm{A,fit}}^2(\nu_l,\tau) \approx \sigma_{\mathrm{A,fit}}^2(\nu_r,\tau) \approx \frac{\sigma_{\mathrm{A,fit}}^2(\nu_z,\tau)}{\sqrt{2}}. \tag{15.29}$$

Eqs. (15.26), (15.27) and (15.29) are summarized as

$$\begin{aligned}\Xi_\mathrm{c}^2(\tau_\mathrm{s},\tau_\mathrm{d}) \approx\ & 4\sigma_{\mathrm{A,V}}^2(\nu_z,\tau_\mathrm{d}) + \sqrt{2}\sigma_{\mathrm{A,fit}}^2(\nu_z,\tau_\mathrm{d}) + 4\sigma_{\mathrm{A},E_+}^2(\nu_z,\tau_\mathrm{d}) \\ & + \sigma_{\mathrm{A,V}}^2(\nu_z,\tau_\mathrm{s}) + \sigma_{\mathrm{A,fit}}^2(\nu_z,\tau_\mathrm{s}) + \sigma_{\mathrm{A},E_+}^2(\nu_z,\tau_\mathrm{s}).\end{aligned} \tag{15.30}$$

The length of the repetition cycle of the AD is about 110 s. After subtracting time necessary for the particle transport and wait time to let the trapping voltage stabilize, about 104 s remains. This should be shared appropriately between a single-dip and a double-dip measurement so that the cyclotron frequency fluctuation is minimized.

In Fig. 15.10, $\Xi_\mathrm{c}(\tau_\mathrm{s},\tau_\mathrm{d})$ is evaluated as a function of the averaging times $\tau_\mathrm{s}, \tau_\mathrm{d}$ under a constrain of the total averaging time $\tau_\mathrm{s} + \tau_\mathrm{d} = 104\,\mathrm{s}$.

The minimum of the $\Xi_\mathrm{c}(\tau_\mathrm{s},\tau_\mathrm{d})$ is found to be $58(15)\,\mathrm{m\,Hz}$. This is the principal limit imposed by the sideband coupling method. This corresponds to the distribution of the $\bar{p}$-H^- cyclotron ratio $\sigma_R = 1.96 \times 10^{-9}$ from Eq. (3.12).

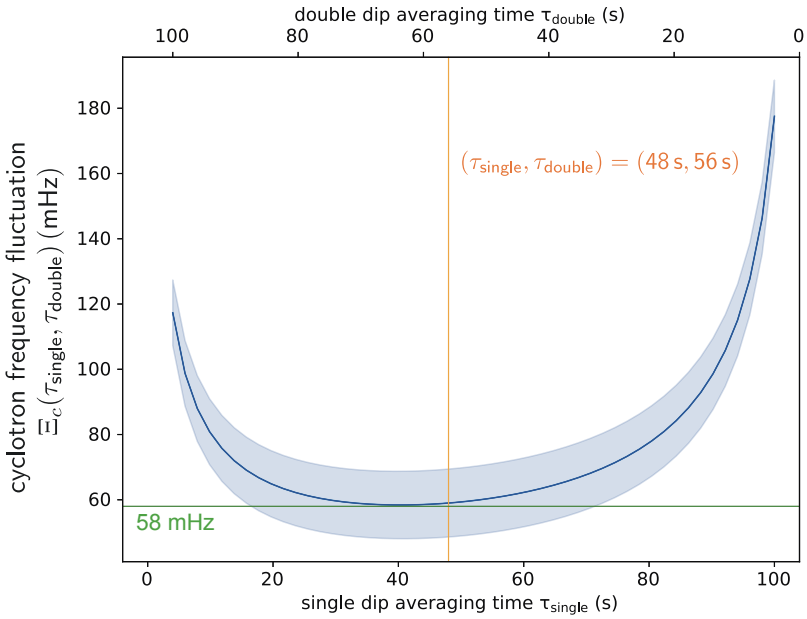

Figure 15.10: Cyclotron frequency fluctuation as a function of the averaging times $(\tau_{\mathrm{single}}, \tau_{\mathrm{double}})$ in the sideband sequence. Evaluated under a constrain $\tau_{\mathrm{single}} + \tau_{\mathrm{double}} = 104\,\mathrm{s}$. The colored band indicates the uncertainty evaluated from the uncertainties of the coefficients $\hat{c}_0, \hat{c}_{-1}$. The green horizontal line (58 mHz) indicates the principal limit of the cyclotron frequency stability by the sideband coupling method. The orange vertical line indicates a typical set of averaging times adapted for the measurement.

For the data taking of the charge-to-mass ratio comparison, $(\tau_{\mathrm{s}}, \tau_{\mathrm{d}}) = (48\,\mathrm{s}, 56\,\mathrm{s})$, close to the optimum condition, was adapted as a typical set of the averaging times while the AD was under operation. This is indicated by the vertical orange line in Fig. 15.10. After the AD was shut down, $(\tau_{\mathrm{s}}, \tau_{\mathrm{d}}) = (52\,\mathrm{s}, 56\,\mathrm{s})$ (total averaging time 108 s) was typically used.

16

Development of the cyclotron frequency stability

In this chapter, developmental works performed to improve the cyclotron frequency stability are described, and the stability of the state finally achieved is discussed.

16.1 Overview of the development of the stability

The distribution of the $\bar{p}$-H^- cyclotron frequency ratio $R_{\bar{p}H^-}$ in the 2014 measurement had a distribution of 5.5 p.p.b., which corresponds to the cyclotron frequency fluctuation of $\Xi_c = 163\,\mathrm{mHz}$ (see Section 8.3). Over the 2017 run, a significant improvement of the cyclotron frequency stability from this value had been aimed.

In Fig. 16.1, development of the cyclotron frequency fluctuation throughout the 2017 run is shown with major events and activities. Each data point was obtained from 100 consecutive cyclotron frequency measurements in each data set which had the lowest Ξ_c.

At the beginning of 2017 run-I, the cyclotron frequency fluctuation was $> 200\,\mathrm{mHz}$, still worse than the condition in 2014. Since then, continual efforts were made to search for the causes of the frequency fluctuations and optimize the environmental conditions accordingly. After various optimization campaigns, in December, a condition was achieved where the cyclotron frequency fluctuation was constantly below 100 mHz. In this condition, the data taking of the proton-to-antiproton charge-to-mass ratio comparison was started. Under the best conditions, the cyclotron frequency fluctuation of 58(6) mHz was recorded, reaching the principal limit of the sideband coupling method discussed in Chapter 15.

The major optimization works are summarized to the following points:

- Thermal insulation of cryostat surfaces

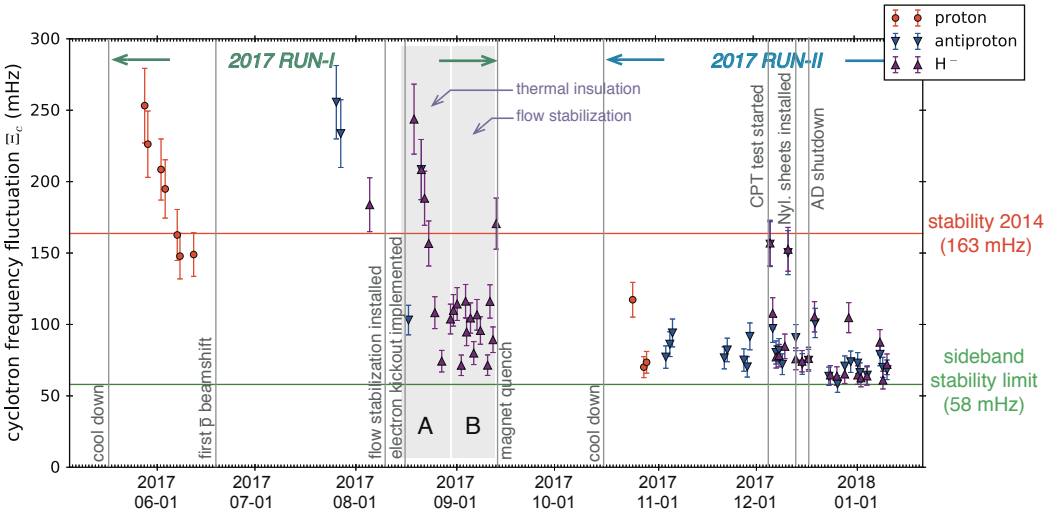

Figure 16.1: Development of the short-term cyclotron frequency stability over the 2017 run, shown together with major events and activities. From each dataset of cyclotron frequency measurements, the cyclotron frequency fluctuation Ξ_c was evaluated by choosing a sample of consecutive 100 measurements which has the smallest Ξ_c. The gray bands A and B mark the periods when works related to the thermal insulation and the flow stabilization took place. Reproduced from [78].

(related works were mostly performed in the period A in Fig. 16.1)

- Stabilization of flow and pressure
  (works mostly performed in the period B in Fig. 16.1)
- Stabilization of the temperature in the zone by covering the zone nylon sheets
- Implementation of electron kick-outs

They will be discussed in detail in the following sections. Among them, the last point of the electron kick-out was an issue treated in different ways between 2017 run-I and run-II, therefore summarized in a separate section. The rest of the items follow the chronological order of the development.

16.2 Data evaluation by the block-fluctuation

To identify frequency fluctuations correlated with environmental conditions, a measure named *block-fluctuation* was found to be practically useful. Its definition and formulation are given here for the following discussion.

In Fig. 16.2, an example of measured cyclotron frequencies $\{\nu_{c,i}\}$ $(i = 1, 2, \cdots)$ is shown. To define the block-fluctuation for this dataset, blocks of a unit of N_B measurements ($N_B = 8$ in this example) are defined. The *block-average* $\{\overline{\nu}_{c,k}\}$ and the *block-fluctuation* $\{\overline{\Xi}_{c,k}\}$ $(k = 1, 2, \cdots)$ are defined by

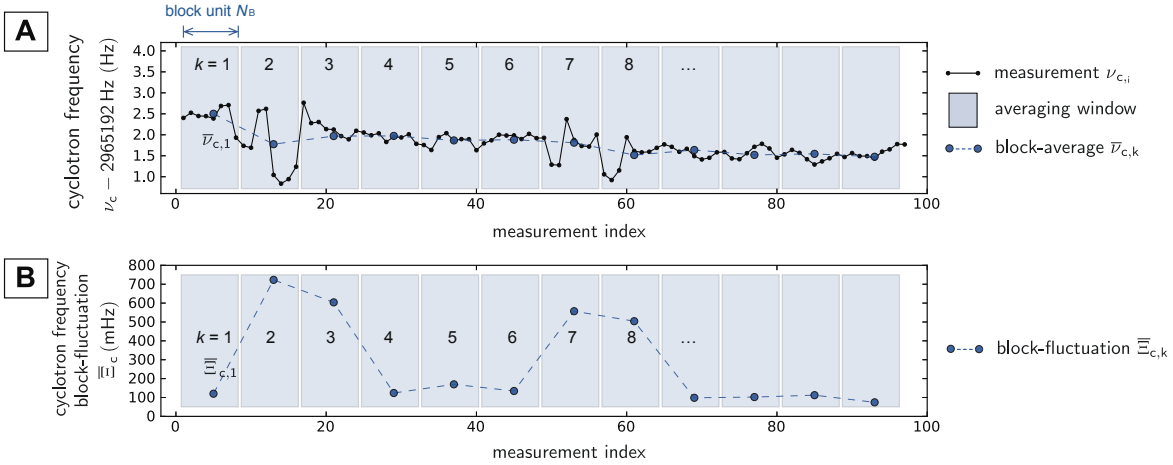

Figure 16.2: Definition of the block-average (A) and the block-fluctuation (B) for a series of measured cyclotron frequencies.

the average and the fluctuation of frequencies included in each block i.e. the k th elements defined by

$$\overline{\nu}_{c,k} = \frac{1}{N_B}\left(\sum_{i=N_B(k-1)+1}^{N_B k} \nu_{c,i}\right), \tag{16.1}$$

$$\overline{\Xi}_{c,k} = \sqrt{\frac{1}{N_B - 1}\left(\sum_{i=N_B(k-1)+1}^{N_B k-1} (\delta\nu_{c,i} - \overline{\delta\nu}_{c,k})^2\right)} \tag{16.2}$$

with

$$\delta\nu_{c,i} = \nu_{c,i+1} - \nu_{c,i}, \tag{16.3}$$

$$\overline{\delta\nu}_{c,k} = \frac{1}{N_B - 1}\left(\sum_{i=N_B(k-1)+1}^{N_B k-1} \delta\nu_{c,i}\right). \tag{16.4}$$

The variations of block-fluctuation reflect transitions of short-term frequency stability. In Fig. 16.2, the block-average (A) and the block-fluctuation (B) of the example dataset are plotted with the original frequencies. It can be seen that the block-fluctuation is significantly larger than the other blocks for $k = 2, 3, 7, 8$, reflecting more fluctuating frequencies in these blocks. This evaluation was useful especially when we were on the earlier stage of the optimization where $\Xi_c > 100\,\mathrm{mHz}$.

16.3 Thermal insulation of the cryostat surfaces

Development of the cyclotron frequency fluctuation in the last five weeks of run-I is shown in Fig. 16.3. The first major step of the stability improvement was achieved by isolating the surfaces of the cryostats from the atmosphere. The surfaces of the cryostats are connected to the central part of the apparatus through the 4- and the 77 K support structures (see Figs. 5.1 and 5.8). Expansions and shrinkages of

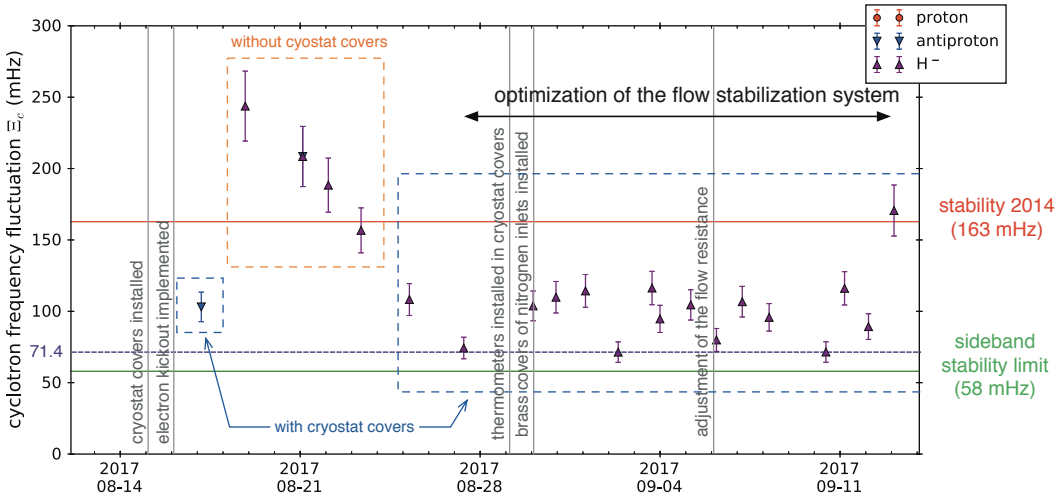

Figure 16.3: Short-term cyclotron frequency fluctuation in 2017-run I, when the thermal insulation of the cryostat surfaces and installation / optimization of the flow stabilization took place.

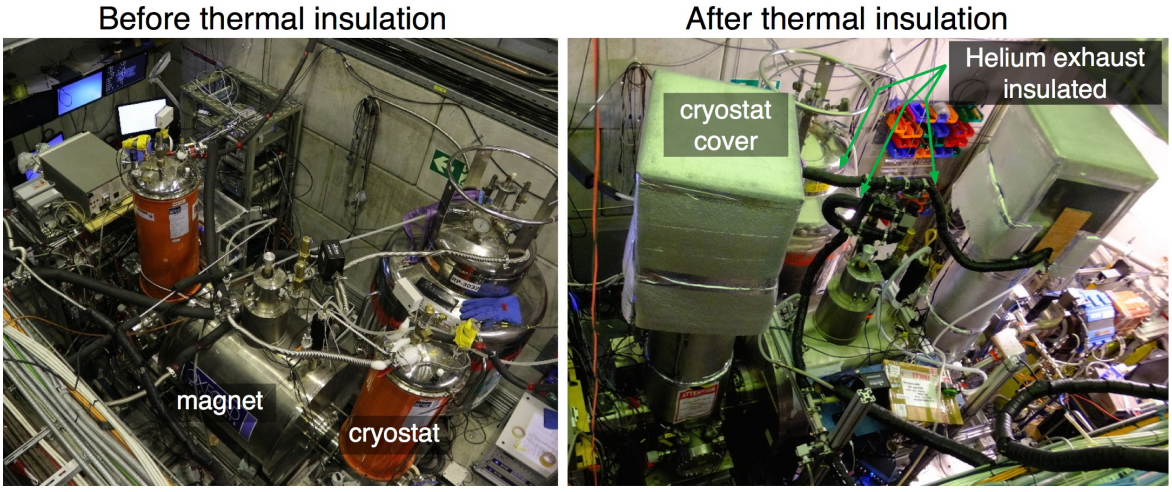

Figure 16.4: Photographs of the apparatus before (left) and after (right) the thermal insulation. The top of the cryostats were covered by the plexiglass boxes, which were found to improve the cyclotron frequency stability significantly. Later, the side surfaces of the cryostat and the bellows on the helium exhaust were covered with thermal foam, and the sleeves of the covers were tightened with glasswool sheets in order to reduce thermal fluctuations on the metal surfaces which are indirectly connected to the 4 K stage of the apparatus.

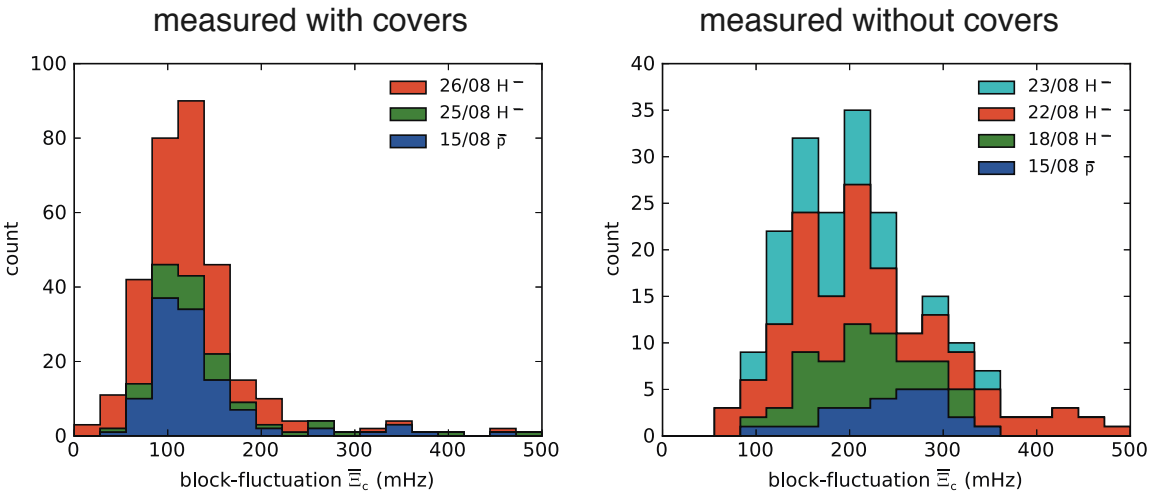

Figure 16.6: Comparison of the block-fluctuation of the cyclotron frequency between datasets measured with (left) and without (right) the covers on the cryostats. For each dataset of cyclotron frequency measurements, the block-fluctuation $\overline{\Xi}_c$ is evaluated in uint of 8 measurements. The distribution of $\overline{\Xi}_c$ is plotted in histograms. It can be observed that the datasets measured without the covers have distributions at higher block-fluctuations. The corresponding data points (3 sets with the covers, 4 sets without the covers) are found in Fig. 16.3.

the metal surfaces of the cryostats seemed to have caused frequency fluctuations through mechanical movements of the inner components of the apparatus.

First, the top of each cryostat was covered by the plexiglass box with aluminum support structures shown in the right photograph of Fig. 16.4. This reduced the cyclotron frequency fluctuation significantly as shown in Fig. 16.3, where the data points measured with and without the covers are marked by the colored dashed rectangles. In Fig. 16.6, the block-fluctuations of these datasets were compared. A significant difference is observed between the datasets in the two conditions: the datasets recorded with the covers have the most frequent values of $\overline{\Xi}_c$ around 120–150 mHz while those without the covers have them around 200–300 mHz, implying that the exposure of the top surfaces of the cryostats to the atmosphere increased the short-term frequency fluctuations.

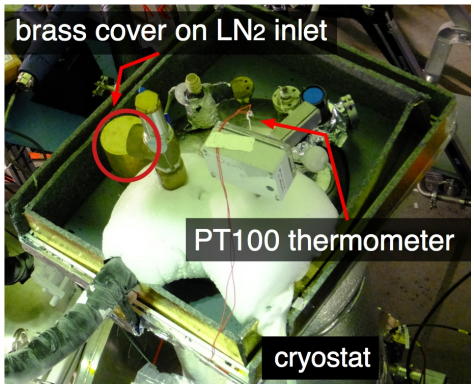

Figure 16.5: Photograph of the top of the upstream cryostat after installation of a thermometer and a brass cover on the LN_2 inlet of the cryostat.

Following the installation of the covers, PT-100 thermometers were installed inside the covers (shown in Fig. 16.5) to investigate this correlation in more detail. In Fig. 16.7, one dataset of cyclotron frequency measurements (A) is shown together with temperatures (B) and an ambient magnetic field (C). The temperatures in Fig. 16.7 were measured by two sensors installed in the upstream- and

the downstream covers of the cryostats. The Hall probe was placed outside the covers, attached on the cryostat support (see Section 11.1). In the range marked by the purple rectangles in the figure, frequency fluctuations correlated to fluctuations of the temperature in the upstream cover are observed. A similar time structure is also observed in fluctuations of the zone temperature in the same time window, but not in the temperature in the downstream cover. This implies that the upstream cryostat cover was not well closed during the measurement, and caused the atmospheric temperature fluctuations to affect the cyclotron frequency fluctuations through the temperature fluctuations in the cover.

Based on this observation, glasswool sheets were added around the sleeves of the covers to ensure the sealing. The plugs of the LHe- and LN_2 inlets of the cryostats were made sure to be closed tightly after regular filling of the cryogen to the cryostats. The brass covers shown in Fig. 16.5 were installed to improve closure of the LN_2 inlets. Furthermore, the metal surfaces of the bellow on the helium exhaust lines and side surfaces of the cryostats were covered by thermal foam to reduce possible influences of the ambient temperature fluctuations to the experiment. The photograph on the right in Fig. 16.4 was taken after these implementations. After these improvements, the correlation was no longer observed in an evident way.

16.4 Pressure/flow stabilization

The pressure in the LHe vessels of the cryostats were found to significantly affect the cyclotron frequency stability. As the 4 K part of the apparatus, including the Penning trap system, is anchored on the bottom of the cryostats, the pressure variations in the cryostats caused variations of the position of the traps. To improve this aspect of the apparatus, a pressure stabilization system was installed. The system was designed and constructed by James A. Harrington, and its details will be described in his Ph.D. thesis [79].

The BASE helium system consists of the two cryostats and the LHe vessel of the cryostats, interconnected with bellows. In the default setup, the helium exhaust of the BASE system was connected to a helium recovery system of CERN, which has frequent pressure fluctuations due to works in the upstream facilities and activities of the other experiments. The pressure stabilization system was installed to decouple the system from the recovery line as described in Fig. 16.8. The stabilization system includes a smaller buffer volume kept pumped to a low pressure, and valves between the main helium system of BASE, the recovery line and the buffer volume. The system blocks the flow from the recovery line to the main system, and instead makes a regulated one-directional flow from the main system to the buffer volume. PTFE discs with small holes were inserted between bellows in front of the buffer volume to create a resistance in the circuit of flow. The discs with one or two holes whose diameters differing from 0.5 to 0.8 mm were prepared to adjust the flow rate. The pressures of the BASE system and the buffer volume are monitored by two channels of PR 4000B-F

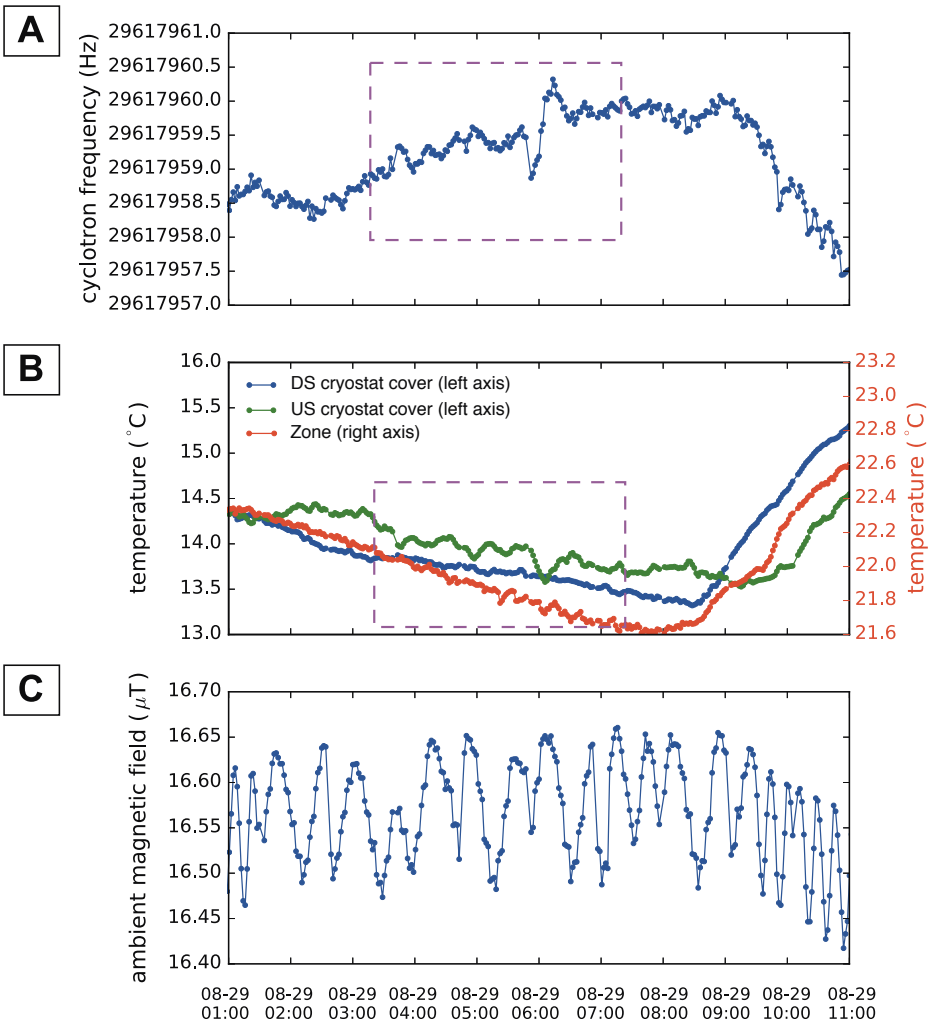

Figure 16.7: Observation of cyclotron frequency fluctuations correlated to temperature fluctuations. **(A)** Evolution of the cyclotron frequency of a single H^- ion. **(B)** Temperatures measured by thermometers in the downstream- (blue) and upstream (green) covers, and the ambient temperature (red) measured by a Hall probe. The axis of the temperatures in the covers is on the left of the graph. The axis of the ambient temperature is on the right. **(C)** The ambient magnetic field measured by the downstream fluxgate, the axis in parallel to the magnet. (see Section 11.1) The temperatures and the magnetic field are averaged over a time window of each cyclotron frequency measurement. In the time window marked by the purple rectangles in (A, B), cyclotron frequency fluctuations correlated to temperature fluctuations are observed. Similar time structures are observed between the cyclotron frequency and the temperature in the upstream cover, and the ambient temperature. The measurement sequence at the time was not synchronized to the AD cycle, which caused the magnetic field to oscillate over the measurement period by the super-cycle of the measurement sequence and the AD cycle. However, it does not have stronger amplitudes than the rest of the data within the purple time window, which supports the observation that these frequency fluctuations were induced by the temperature fluctuations.

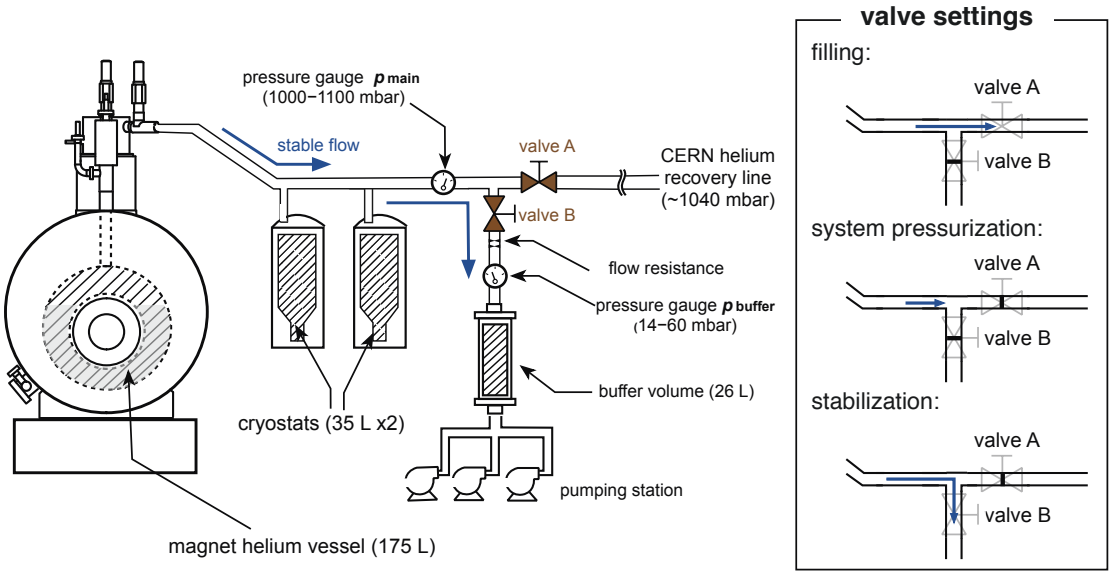

Figure 16.8: Schematic of the pressure/flow stabilization system. The BASE helium system consists of the helium vessel of the magnet, and the helium vessels of the two cryostats. The valves control the connection between the main system, the buffer volume and the CERN recovery line. The flow resistances are installed to control the flow entering the buffer volume pressure. Two pressure gauges, measuring the pressure of the main system and that of the buffer volume are installed. On the right, the valve configurations for different occasions are described. When the stabilization is activated, the valve A is classed and the valve B is opened to produce a regulated one-directional flow from the main helium system to the buffer volume.

(MKS Instruments).

After the installation of the stabilization system, variations of the cyclotron frequency correlated to the pressure variations were observed. Such examples can be found in a dataset shown in Figs. 16.9 and 16.10. In Fig. 16.9, the evolution of the cyclotron frequency of an H^- ion (A) is shown together with the pressures of the main system (B) and the buffer volume (C), and the external magnetic field (D). A correlation between the drift component of the cyclotron frequency and the drift of the system's pressure is clearly observed in (A) and (B). In (E), the scaling of the cyclotron frequency against the system pressure is fitted to a linear function $f(p_{\mathrm{main}})$. From the resulted function $f(p_{\mathrm{main}})$ and the measured p_{main}, the red curve in (A) is obtained. It can also be observed that some of spikes in the cyclotron frequency are correlated to fluctuations in the buffer volume pressure. For further investigation, in Fig. 16.10 fluctuating components of the cyclotron frequency are extracted by subtracting the pressure-correlated drift $f(p_{\mathrm{main}})$ from the cyclotron frequency. By comparing $\nu_{\mathrm{c}} - f(p_{\mathrm{main}})$ (Fig. 16.10 (A)) and the buffer volume pressure (B), it becomes clear that some parts of the frequency fluctuations have common time structures with fluctuations of the buffer volume pressure, while some others were obviously caused by jumps of the external magnetic filed. The proportionality factors between the jumps in the buffer volume pressure and the cyclotron frequency jumps are on the order of 10^{-2} Hz/mbar.

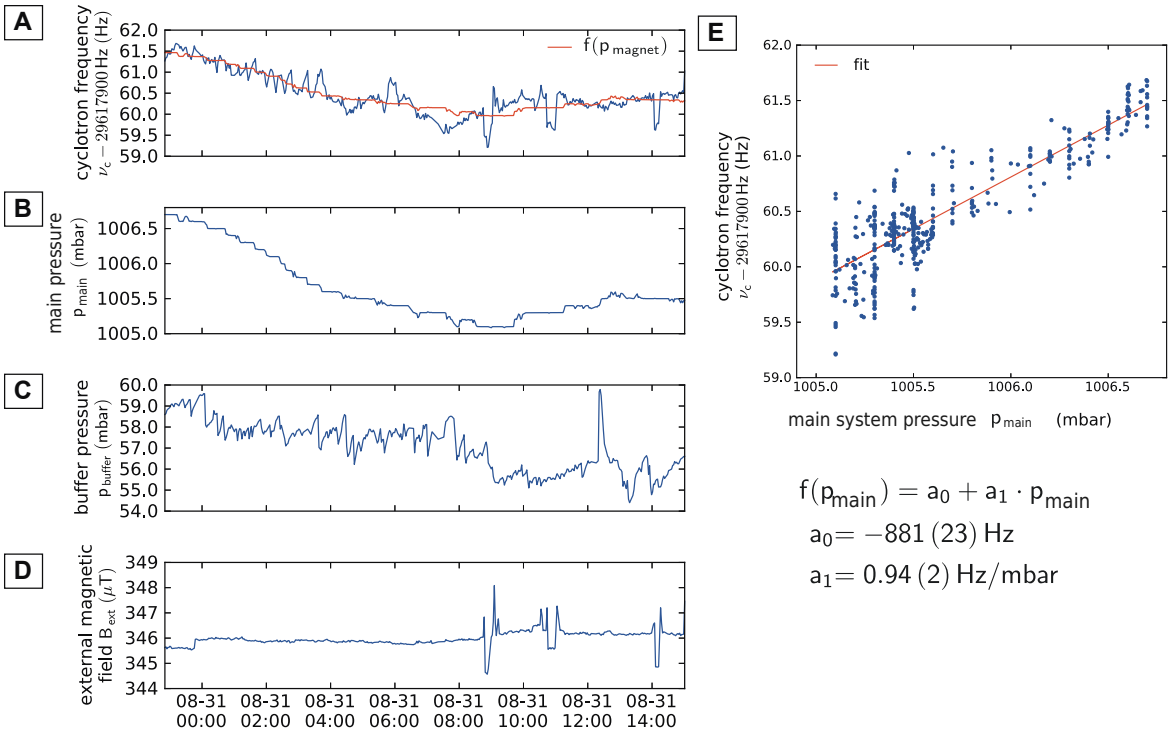

Figure 16.9: Correlation of the drifts of the cyclotron frequency to pressures of the main system. **(A)** Cyclotron frequency of an H^- ion in the PT. The red curve was obtained by fitting in (E) **(B)** Pressure of the BASE helium system p_{main}. **(C)** Pressure of a buffer volume of the stabilization system. **(D)** The ambient magnetic field measured by the Hall probe. **(E)** A linear fit of the cyclotron frequency as a function of the main system pressure. The parameters of the linear function $f(p_{\mathrm{main}}) = a_0 + a_1 \cdot p_{\mathrm{main}}$ were obtained to be $a_0 = -881(23)\,\mathrm{Hz}, a_1 = 0.94(2)\,\mathrm{Hz/mbar}$. The red curve in (A) is drawn by the $f(p_{\mathrm{main}})$ determined by the fit and p_{main} at corresponding data point.

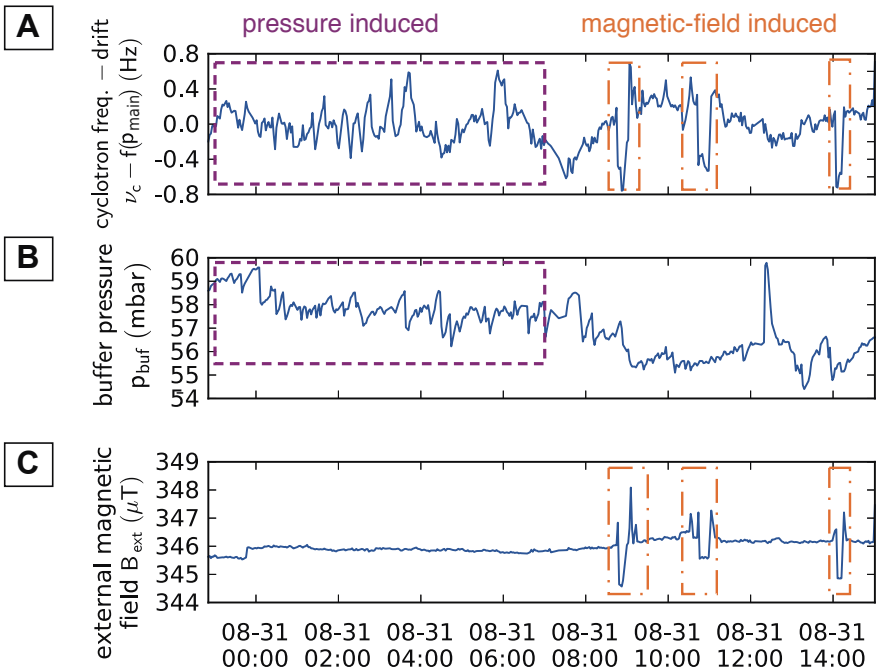

Figure 16.10: **(A)** Fluctuating components of the cyclotron frequency extracted by $\nu_c - f(p_{\mathrm{main}})$ (Fig. 16.9 (A)). **(B)** Buffer volume pressure. **(C)** Ambient magnetic field.

The correlations discussed above i.e.,

- correlation between the cyclotron frequency drifts and drifts of the BASE system pressure p_{main}
- correlation between the frequency fluctuations and the fluctuations of the buffer volume pressure p_{buffer}

were reproducibly observed. The correlation of frequency fluctuations and the fluctuations of p_{main} may also exist, but it was not detected with the resolution of the gauge which is at 0.1 mbar.

Comparing different datasets record during run-I, the proportionality factors between the pressures and the cyclotron frequency ranged as

$$\begin{aligned} \frac{\Delta\nu_{\text{c}}}{\Delta p_{\text{main}}} &= 1\text{–}2\,\text{Hz/mbar} \quad \text{(for drift)} \\ \left|\frac{\Delta\nu_{\text{c}}}{\Delta p_{\text{buffer}}}\right| &\sim 10^{-2}\text{–}10^{-1}\,\text{Hz/mbar} \quad \text{(for fluctuations).} \end{aligned} \tag{16.5}$$

From the observed correlation with the buffer volume pressure, it seems that variations of the flow from the main system to the buffer volume were causing frequency fluctuations. A likely explanation of this is that fluctuations of gas flow from the cryostats caused instabilities of the apparatus through thermal fluctuations of the inner surfaces of the cryostats which are connected to the cryogenic stages of the apparatus.

Therefore, different settings of the pressure stabilization as well as different absolute pressures were tested in search of conditions which induce least frequency fluctuations. Part of the settings are noted in Fig. 16.11 along with the history of the cyclotron frequency fluctuation. Over the course of these tests, it was found that the fluctuations of the buffer volume pressure were suppressed by operating the main system at a high pressure (> 1100 mbar), thereby creating a stable flow from the main system to the buffer volume.

The following procedure was established to prepare the system for cyclotron frequency measurements after a routine filling of the cryogen to the cryostats and the magnet (see Fig. 16.8 for configuration of the valves).

1. During filling, the system is connected to the recovery line. The valves are configured as (A,B) = (open, closed).
2. After filling, the valves are set to be (A,B) = (closed, closed) to pressurize the system by evaporating helium gas.
3. When the pressure of the main system reaches to about 20 mbar above the operational pressure, the valve A is closed and the valve B is opened i.e., (A,B) = (closed, open). The gas from the vessels starts flowing to the buffer volume. Within 3–4 h, the flow rate stabilizes.

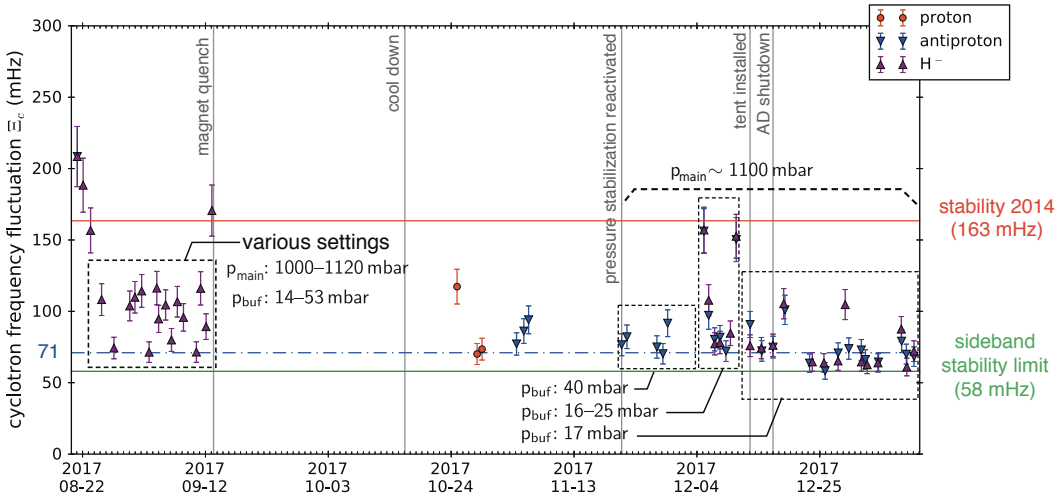

Figure 16.11: History of the short-term cyclotron frequency fluctuation shown together with part of tested parameters of the pressure stabilization system.

The operational pressures $(p_{\mathrm{main}}, p_{\mathrm{buffer}}) \approx (1100\,\mathrm{mbar}, 18\,\mathrm{mbar})$ were selected in the final setting.

The best cyclotron frequency stability achieved after the optimization of the stabilization system was $\Xi_c \approx 71\,\mathrm{mHz}$ when the AD was still under operation.

16.5 Further temperature stabilization

After the pressure/flow-induced fluctuations were reduced, influences of temperature fluctuations to the cyclotron frequency fluctuations were observed in a more sensitive scale than what was discussed in Section 16.3. As shown in Fig. 16.13, cyclotron frequency fluctuations caused by fluctuations of the ambient temperature in the zone were observed at times. The main cause of these temperature fluctuations was the air conditioning in the AD (see Section 11.1).

To suppress the influences of the air conditioning and reduce the temperature fluctuations in the zone, the zone was covered by nylon sheets as shown in Fig. 16.14. The effect of the sheet can be seen in comparison of 24-hour measurements of the temperature in the zone before and after the installation in Fig. 16.15. Significant reduction of drifts and fluctuations of the temperature can be seen in Fig. 16.15 (A,B). The Allan deviation of the temperature was reduced by a factor of 5.8 at the averaging time $\tau = 120\,\mathrm{s}$, a typical cycle length of the measurement sequence (Fig. 16.15 (C)). The small oscillations with amplitudes of 50–80 mK (Fig. 16.15 (B)) remained, which were caused by heat from the equipment in the zone and air trapped and circulated within the zone. To suppress these oscillations, the hatches as indicated in Fig. 16.14 were made on top of the sheets, and the door of the zone (downstairs, not shown in the photograph) was left open to create a path of air flow which entered from the hatches and escaped from the exit of the zone on the floor level, thereby preventing

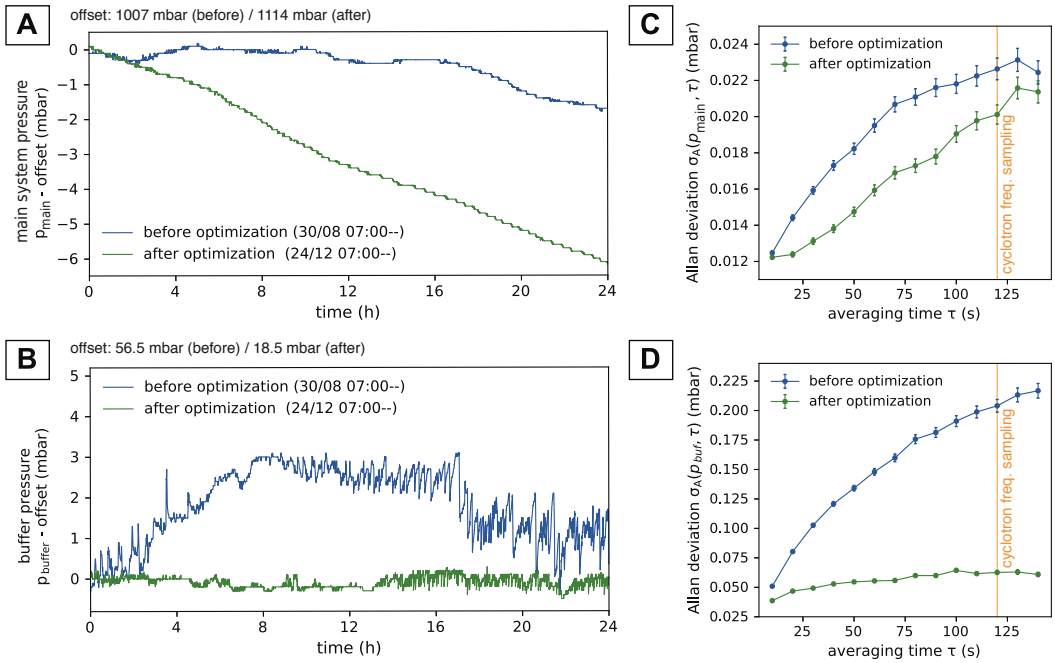

Figure 16.12: Comparison of pressures of the flow stabilization system before and after the optimization of the stabilization parameters. **(A, B)** 24 hour measurements of pressures of the main system (A) and of the buffer volume (B). The subtracted offsets are 1007 mbar (before) / 1114 mbar (after) for (A), and 56.5 mbar (before) / 18.5 mbar (after) for (B). **(C, D)** Allan deviations of the pressure in the main system (C) and the buffer volume (D).

the air from being trapped in the zone.

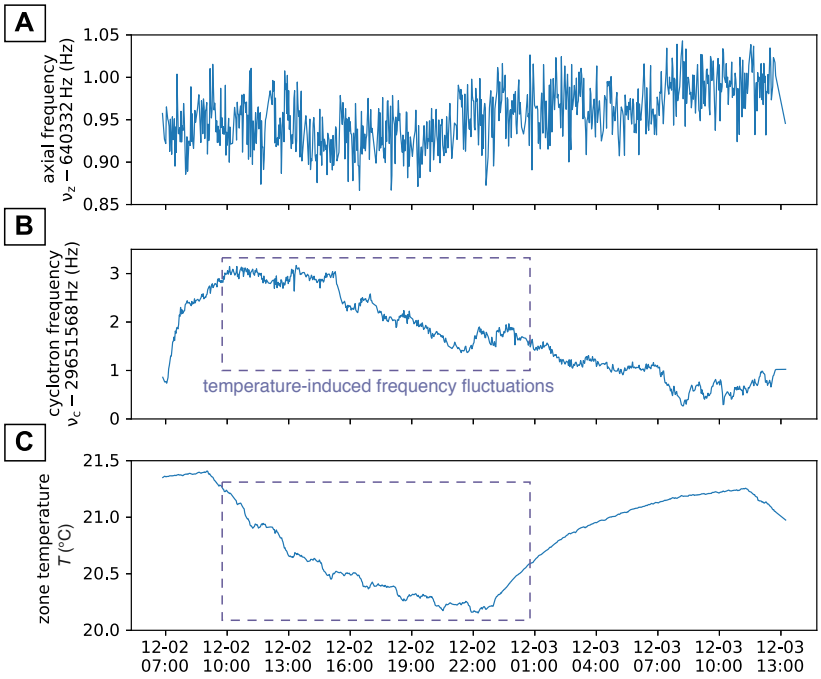

Figure 16.13: Observation of temperature-induced fluctuations of the cyclotron frequency. Common features are observed between the cyclotron frequency (B) and the ambient temperature in the zone (C) in the time window indicated by the purple rectangles. The oscillatory structures of the temperature are reflected in the cyclotron frequency with proportionality factors of1.3–3.8 Hz/K.

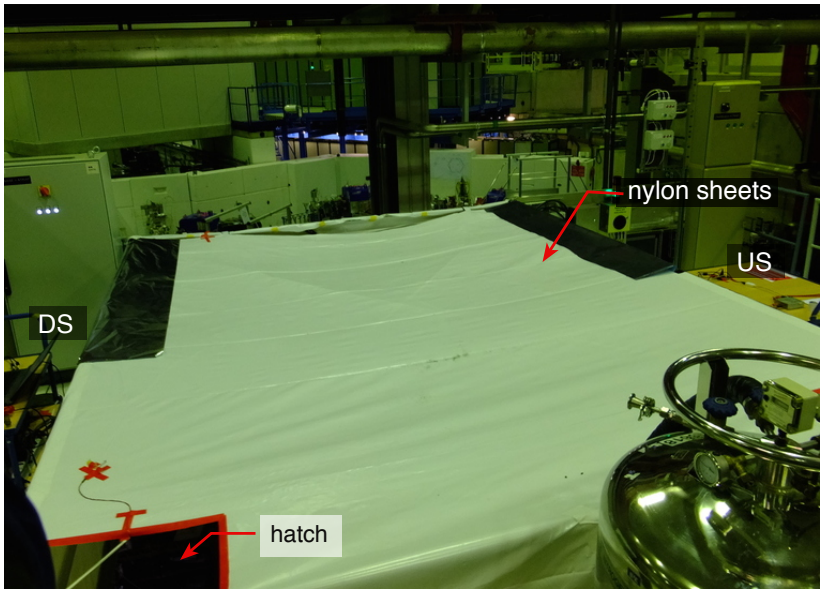

Figure 16.14: Nylon sheets covering the BASE for suppression of temperature fluctuations. The hatch on the front was made to prevent air to be trapped in the zone. A similar hatch was made on the upstream end of the cover (hidden by the dewar).

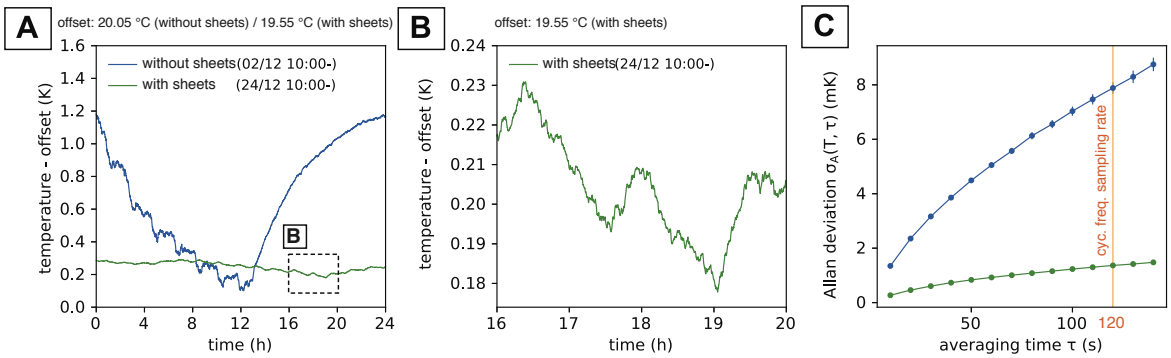

Figure 16.15: Comparison of the temperature in the zone before and after the installation of the nylon sheets. **(A)** Comparison of 24-hour measurements of the ambient temperature of the zone with and withe the tent. The temperature was significantly stabilized by the installation of the tent. The subtracted offset is 20.05 °C (or 293.2 K) for the data without the tent, and 19.55 °C (292.7 K) for the data with the tent. **(B)** Zoomed-in plot of the region marked by a dashed rectangle in (A). Oscillatory structures with amplitudes of about 5 mK are observed. **(C)** The Allan deviations of the temperature $\sigma_{\mathrm{A}}(T,\tau)$. At $\tau = 120\,\mathrm{s}$ which was a typical sampling rate of the cyclotron frequency by the sideband sequence, $\sigma_{\mathrm{A}}(T,\tau) = 7.8(1)\,\mathrm{mK}$ (without tent) / $1.4(4)\,\mathrm{mK}$ (with tent).

16.6 Detection and treatment of electron contamination

Electrons entering to the trap caused problems in the cyclotron frequency measurement. When they entered the trap, their interaction with an antiproton/H^- ion caused an increase of the cyclotron frequency fluctuation. This electron contamination was especially of a problem during run-I. To remove the electrons, the electron kick-out (Section 13.2.3) was implemented in the measurement routine about once per hour. This was necessary to make the cyclotron frequency fluctuation Ξ_{c} less than 150 mHz at an early optimization stage of run-I (see Fig. 16.1).

The exchange of the in-trap layer of the degrader between run-I and run-II significantly reduced the frequency of occurrence of the electron contamination. In run-II, the contamination was observed about 1 event in 2 week when the conditions settled after beam-shifts. Therefore the electron kick-out was not included in the sequence in run-II, but manually performed upon necessity.

Two datasets are shown in Figs. 16.16 and 16.17 as examples of the electron contamination events. These events were identified by

- an increase of the axial/cyclotron frequency fluctuation
- a decrease of the dip SNR
- a shift of the axial frequency.

In Fig. 16.16 (A), evolution of the cyclotron frequency is shown with its block-fluctuations in unit of 8 measurements. The occurrence of the contamination can be identified by a jump the cyclotron

frequencies at around 05:00. The increase of the cyclotron frequency fluctuation is clearly observed by comparing the block-fluctuation before and after the event. Dip spectra before and after the electron contamination are compared in Fig. 16.16 (B,C) where significant decreases of the dip SNR are observed in both the single-dip (B) and the double-dip (C) spectra.

In Fig. 16.17, another electron contamination event is observed. It occurred during a two-particle sequence alternately measuring an antiproton and an H^- ion. At around 04:00, electrons entered the trapping potential of the antiproton. Later at around 06:00, the electrons were automatically removed by a transport between the measurements. In this case, an increase of the frequency fluctuation or the decrease of the dip SNR are not significant, which implies that they were a small number of, possibly a single, electron(s) interacting with the antiproton in a coherent way. However the shift of the axial frequency of about 450 mHz is clearly observed. This clear indication of electron contamination in the axial frequency is important in data analysis, as it enables to identify and remove data recorded with contaminating electrons.

When electron contamination was noticed by these features during the measurement, the measurement was stopped, and an electron kick-out was executed to remove the electrons.

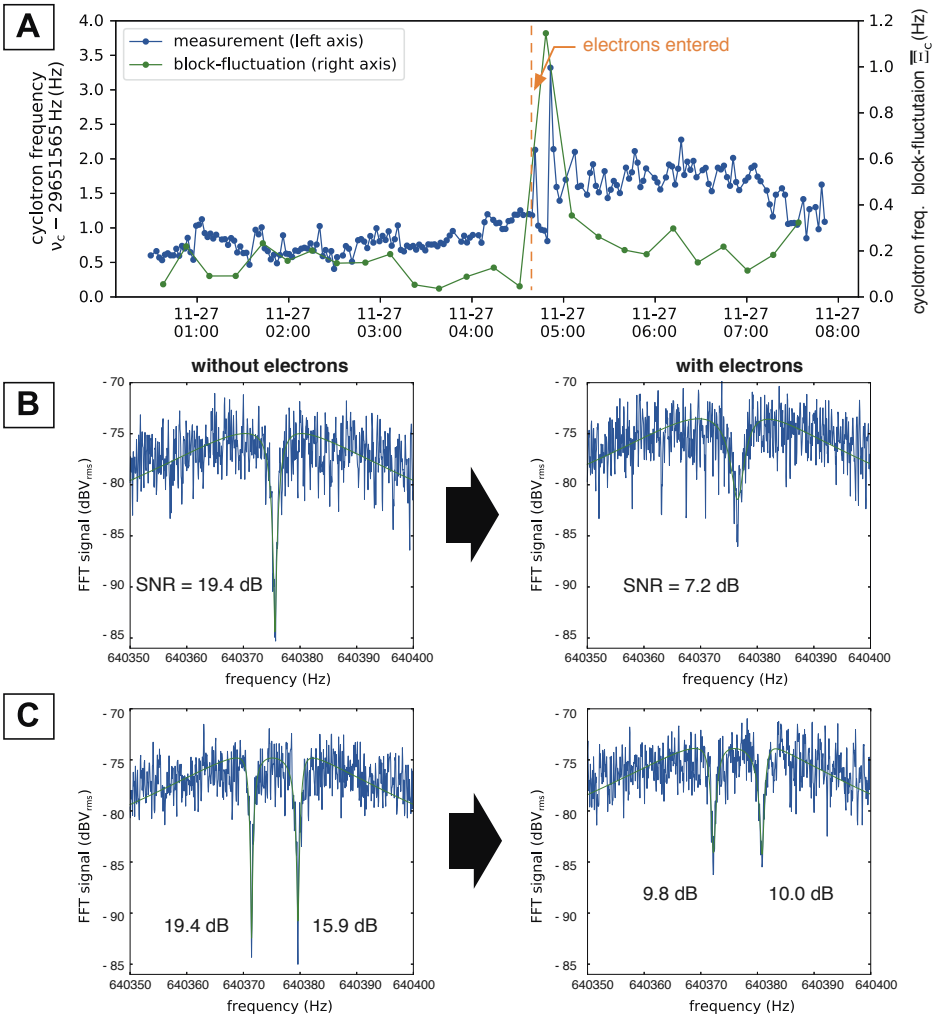

Figure 16.16: Electron contamination event occurred 16 days after loading antiprotons. Evolution of the axial frequency (A) and the cyclotron frequency (B) are shown with their block-fluctuations Ξ_z, Ξ_c in unit of 8 measurements whose axes shown on the right of the plots. At around 05:00, electrons entered in the trap to cause frequency jumps of both of the axial and the cyclotron frequencies. A step-like shift of the axial frequency as well as an increase of the cyclotron frequency fluctuation caused by the entrance of the electrons are observed.

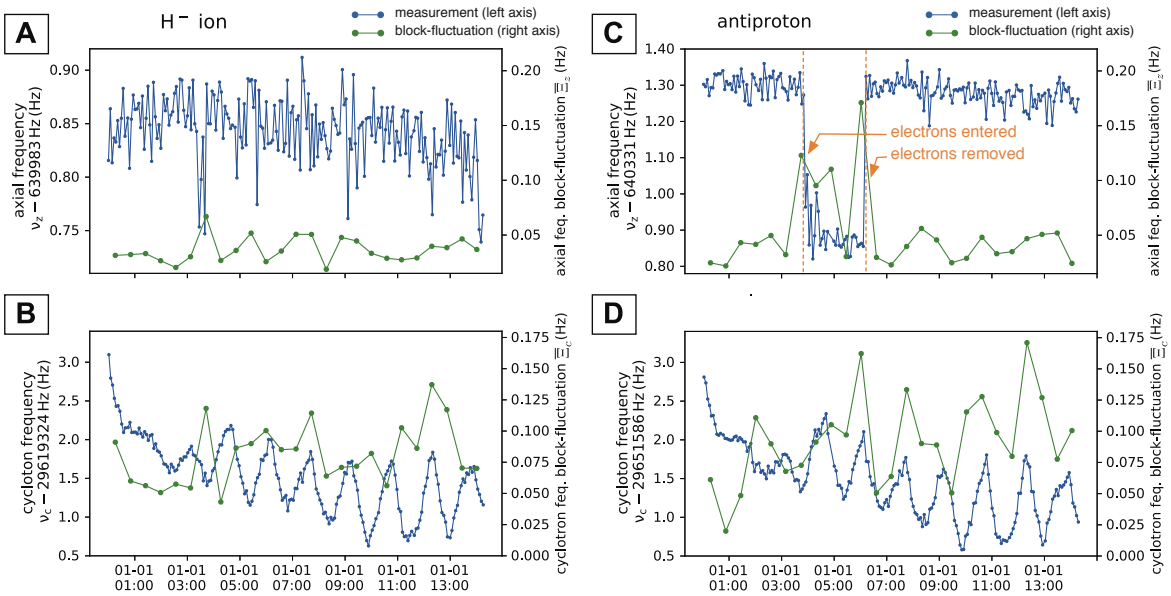

Figure 16.17: Observation of an electron contamination event during a two-particle sequence. The sequence measured the cyclotron frequency of an H^- ion and an antiproton alternately by the sideband coupling method. **(A, B)** Axial frequency (A) and cyclotron frequency (B) of the H^- ion. **(C,D)** Axial frequency (C) and cyclotron frequency (D) of the antiproton. The green dots indicate the block-fluctuation of respective frequency. The electron contamination event occurred to the antiproton, which is observed as its clear downward frequency shift.

16.7 Stability in the final condition

After the optimization processes described above, the apparatus reached a state where the cyclotron frequency fluctuations close to the principal stability limit $\Xi_c = 58\,\mathrm{mHz}$ were recorded at best conditions, as shown in Fig. 16.1. Under this condition, the data collection of the proton-to-antiproton charge-to-mass ratio comparison was started. This section takes a closer look on the finally achieved state.

In Fig. 16.18 (A–D), axial and cyclotron frequencies of an H^- ion recorded in the end of December are shown with their block-fluctuations of 16 measurements. The measurement was started about 2 h after filling LN_2 and LHe to the cryostats and continued for more than 40 h before the next filling. In the later part of the measurement, a time-window was observed when the cyclotron frequency becomes exceptionally stable. This is marked by purple rectangle in the plots. In this stable window, the cyclotron frequency block-fluctuation was $\overline{\Xi}_c < 75\,\mathrm{mHz}$. The cyclotron frequency fluctuation calculated for the data of the entire range is about 87 mHz.

Such stabilization of the cyclotron frequency after $\sim 30\,\mathrm{h}$ from filling was repeatedly observed. Apparently, the stable condition was realized when the cryostat reached to a certain level of the cryogen. One likely factor causing this phenomenon is the mechanical stability of the apparatus. In Fig. 16.18 (E–H), the angles of the apparatus measured by an accelerometer are compared with the frequencies. As explained in Section 11.1, three accelerometers are installed to monitor the angles of

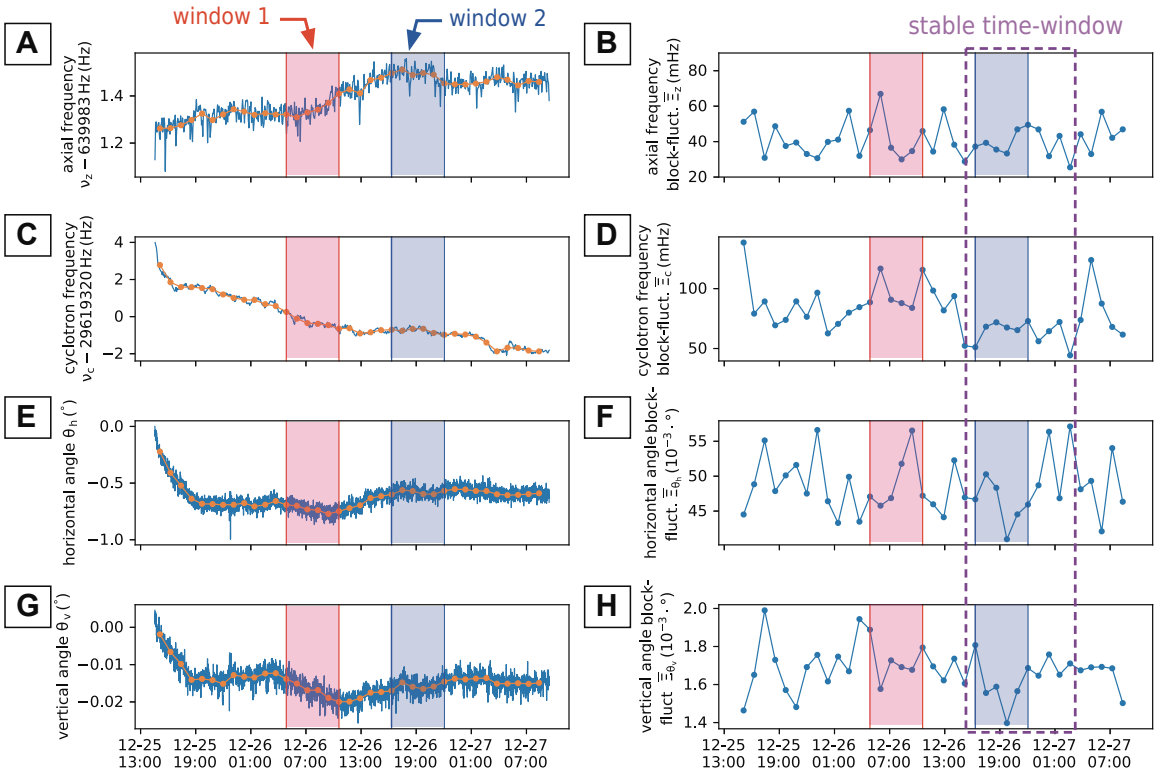

Figure 16.18: Comparison of the cyclotron/axial frequency of an H^- ion and angles of the magnet measured by the accelerometer. See Section 11.1 for the location of the sensors and the definition of the angles. **(A, B)** Cyclotron frequency (A) and its block-fluctuation (B). **(C, D)** Axial frequency (C) and its block-fluctuation (D). **(E, F)** Horizontal angle of the sensor attached on the magnet (E) and its block-fluctuation (F). The offset is subtracted from the angle. **(G, H)** Vertical angle of the sensor and its block-fluctuation. The offset subtracted. After 30 h since the beginning of the measurement, (corresponding to about 32 h from the last filling of the cryogen) there is a period marked by the purple dashed rectangle where the cyclotron frequency became stable ($\overline{\Xi}_c < 75\,\mathrm{mHz}$). It can be observed that in the same period, the angle fluctuations were also relatively low. The time window 1 and 2 marked by colored bands of red and blue, respectively, are defined for further investigation shown in Fig. 16.19.

the apparatus. Their locations are the upstream- and downstream supports of the cryostats and top of the magnet (Fig. 11.1). What is shown here is from the one on top of the magnet. Transitions of the horizontal angle θ_h and the vertical angle θ_v of the apparatus (see Eq. (11.1)) evaluated from data of this sensor are shown in Fig. 16.18 (E, G). In Fig. 16.18 (F, H), the block-fluctuations of the angles $\theta_\mathrm{h}, \theta_\mathrm{v}$ are evaluated for the same averaging windows as the frequencies. It can be observed from the comparison of the block-fluctuations of the frequencies and the angles, that the time window of the stable cyclotron frequency coincides to a time window when the fluctuations of the angles are relatively low.

For further investigation, time windows 1 and 2 marked by the red and blue bands in Fig. 16.18 (A–H) are selected. The window 2 is selected from the stable time window of the cyclotron frequency, and the window 1 from the rest of the range where relatively high block-fluctuations of cyclotron frequency were recorded. Each of them includes 80 sets of frequency measurements, and has the total length of about 5.73 h. In Fig. 16.19, the Allan deviations of the frequencies and the angles are compared between the windows 1 and 2. The Allan deviation of the angles are evaluated for each of the three sensors for the vertical and the horizontal angles. In the Allan deviations of the axial and the cyclotron frequencies in Fig. 16.19 (A,B), it can be observed that the Allan deviations of data from window 1 have larger random-walk components. Looking at that of the angels, a significantly larger random-walk component of window 1 is observed for the Allan deviation of the horizontal angle for each of the sensors. The larger random-walk components of the Allan deviation of the frequencies in window 1 seem to be attributed to the larger random-walk component of the Allan deviation of the horizontal angle.

Therefore it seems that the cyclotron frequency fluctuations which remained in the final condition were mainly induced by mechanical instabilities such as vibrations. It is implied that there is a point which is reached at the end of the mechanical relaxation of the apparatus after filling, where these mechanical instabilities are relatively small.

16.8 Comparison of cyclotron frequency stabilities

In this section, cyclotron frequency stabilities in different conditions of the system are quantitatively compared by their Allan deviations. The comparison is made between datasets recorded during the 2014 measurement: one with the AD operational (the measurement synchronized to the AD), and one during the AD shutdown[1], and a few sets in early December in 2017 around the date when the AD was shutdown: one with the AD operational, two after the AD was shut down. Between the two datasets of the AD non-operational, the installation of the nylon sheets for temperature stabilization (Section 16.5) took place.

[1] A study discussed in Section 7.1 is done in the same way as discussed in this section. Minor differences in the result came from differences between chosen detests.

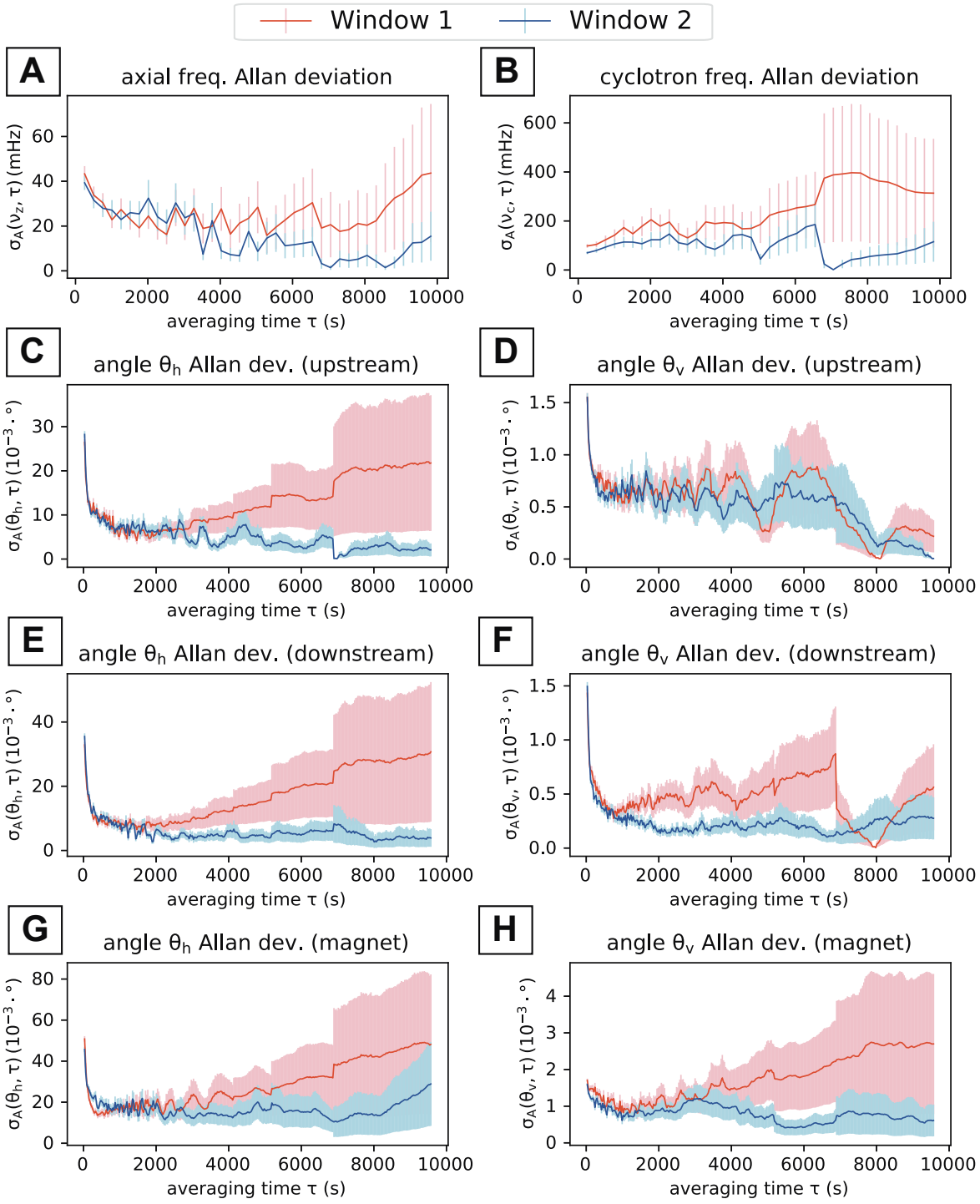

Figure 16.19: Allan deviations of the frequencies and the angles compared between time window 1 and 2 defined in Fig. 16.18. The red data is the Allan deviation of data in the window 1 and blue data is the one from window 2. The bars with lighter colors indicate the statistical uncertainties of the Allan deviations. **(A)** Allan deviation of the axial frequency. **(B)** Allan deviation of the cyclotron frequency. **(C, D)** Allan deviations of the horizontal angle θ_h (A) and the vertical angle θ_v (B) measured by the upstream accelerometer. **(E, F)** Allan deviations of the horizontal (E) and the vertical (F) angles measured by the downstream accelerometer. **(G, H)** Allan deviations of the horizontal (E) and the vertical (F) angles measured by the accelerometer placed on top of the magnet.

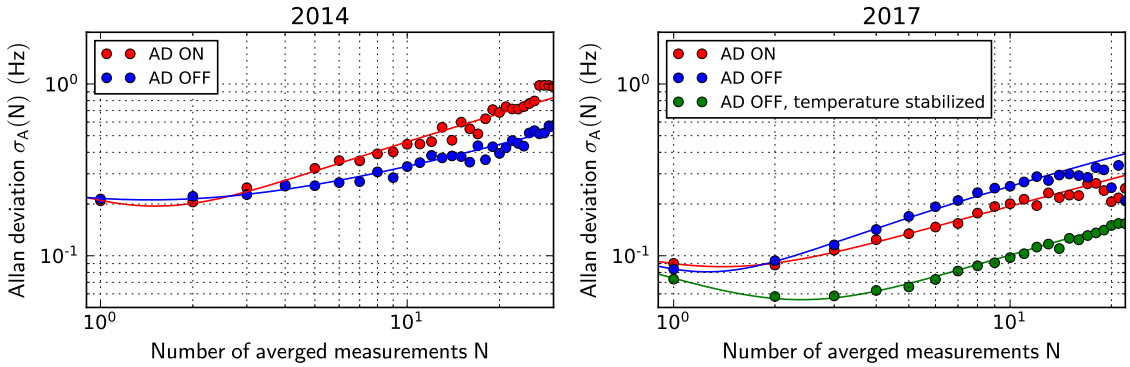

Figure 16.20: Comparison of the Allan deviation of the cyclotron frequency between datasets recorded in different conditions. The number of the averaged measurements for calculation of the Allan deviations are taken as the horizontal values. **(Left)** From detests recorded in the 2014 run. **(Right)** From the 2017 run. The curves show the results of fits to the scaling of Eq. (16.6). The results of the fits are given in Table 16.1. The sampling interval was about 170 s for the 2014 datasets and 120–130 s for the 2017 datasets.

Table 16.1: Results of fitting of the Allan deviation data in Fig. 16.20 to the model of Eq. (16.6), which assumes a white-noise and a random-walk component. The date when each dataset was recorded is shown together with the name of the dataset.

Dataset (date)	b_0 (Hz^2)	c_w (Hz)	c_r (Hz)
2014 AD ON (13/12/2014)	-0.035 (6)	0.23 (1)	0.155 (4)
2014 AD OFF (21/12/2014)	0.019 (4)	0.14 (1)	0.094 (2)
2017 AD ON (17/12/2017–18/12/2017)	-0.004 (1)	0.089 (5)	0.064 (2)
2017 AD OFF (19/12/2017–20/12/2017)	-0.012 (1)	0.109 (4)	0.087 (1)
2017 AD OFF, temperature stabilized (23/12/2017–24/12/2017)	-0.0028 (2)	0.084 (1)	0.0350 (4)

For each dataset, the $\bar{p}$ data and H^- data were combined by scaling the H^- cyclotron frequencies by the theoretical ratio $R_{\bar{p}H^-} = 1.001089218754$. For each series of data thus obtained, containing about 100–300 measurements, the Allan deviation of the cyclotron frequency was evaluated. They are shown in Fig. 16.20. The scaling of the Allan deviation of the cyclotron frequency was fitted to a scaling which considers a random-walk and a white-noise contributions:

$$\sigma_A(\nu_c, N) = \sqrt{b_0 + \left(\frac{c_w}{\sqrt{N}}\right)^2 + \left(c_r \cdot \sqrt{N}\right)^2} \tag{16.6}$$

with N being the number of averaged measurements for calculation of the Allan deviations. The coefficients c_w and c_r represent the white-noise and the random-walk components, respectively. The results obtained by the fits are listed in Table 16.1.

In 2014, a part of the random-walk component of the cyclotron frequency fluctuations was caused by the AD magnetic noise, which can be seen as a significantly larger random-walk component of the

dataset *2014 AD ON* than that of *2014 AD OFF*. this difference corresponds to that random walk of

$$\sqrt{155^2 - 94^2} \approx 120\,\mathrm{mHz} \cdot (\mathrm{cycle})^{1/2} \quad (\text{or } 8\,\mathrm{nT} \cdot (\mathrm{cycle})^{1/2}) \quad . \tag{16.7}$$

The Allan deviations of the 2017 data largely reduced from 2014 resulted from the improved magnetic field shielding which reduced the component Eq. (16.7) by a factor of 10, as well as the optimization processes discussed in Sections 16.3 and 16.4. Owing to the performance of the self-shielding system, the external magnetic field was no longer a limiting factor in the 2017 run. In fact, the dataset *2017 AD ON* has smaller random-walk and white-noise components than *2017 AD OFF*. The dominant factor at this stage was temperature fluctuations which were treated by installing the nylon sheets covering the apparatus (Section 16.5). This was effective, reducing the random-walk component of the cyclotron-frequency Allan deviation by more than a factor of 2.

17

Conclusions

The data of the new proton-to-antiproton charge-to-mass ratio comparison was collected under the condition reached after the stabilization procedures discussed in the last chapter. In Fig. 17.1, a distribution of the antiproton-H^- ion cyclotron frequency ratio $R_{\bar{p}H^-}$ sampled between the 6th of December 2017 and the 26th of January 2018 is presented in comparison to that of the 2014 measurement. Their statistical figures are summarized in Table 17.1.

The width of the ratio distribution in 2017 data is $\sigma_{R,\,2017} = 2.3 \times 10^{-9}$, having been narrowed from the 2014 distribution by a factor of 2.3. Together with the larger sample number, it led to reduce the uncertainty of determination of the center of the distribution $\delta R_{\bar{p}H^-,\mathrm{est}}$ (see Eq. (8.14)) by a factor of 2.9. The dataset evaluated in Fig. 17.1 and Table 17.1 contained about 9156 frequency ratios. The final dataset contains data with the sample size > 12000, including ones collected in February 2018. Therefore, in the final dataset, an improvement of the statistical precision by a factor > 3 than in 2014 is expected.

With respect to the systematic uncertainty, this data was collected by the new tunable axial detection system, which allowed the measurements of an antiproton and an H^- ion with the same ring voltage V_R. This eliminated the source of the largest systematic uncertainty of the 2014 measurement. As reported in Section 9.3, the tunable detection system exhibited robust reproducible performances against the tuning operation. The major systematic effects which are possibly introduced by this approach are those from a possible difference of the axial mode temperature between the antiproton and the H^- ion. The temperature difference was evaluated to be $\approx 0.6\%$ (Section 9.3.3). Coupled with the electromagnetic trap imperfections, this temperature difference causes shifts of the eigenfrequencies of the particles. In Section 14.3, uncertainties accompanying the estimations of the shifts of ratio $\Delta R_{\bar{p}H^-}$ due to these frequency shifts were evaluated to be on the order of $\delta(\Delta R_{\bar{p}H^-})/R_{\bar{p}H^-} \sim 10^{-12}$ or below. Therefore this does not limit the precision of the measurement.

In conclusion, the development performed for an improved charge-to-mass ratio comparison led

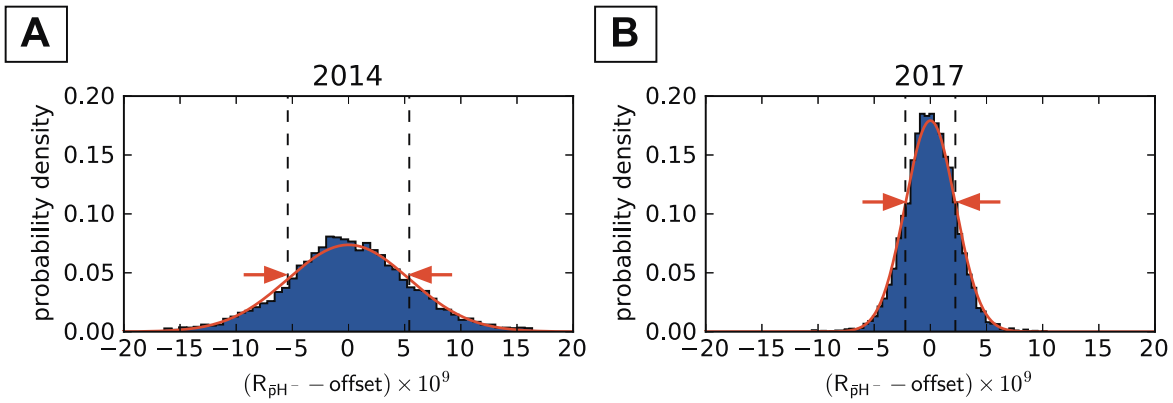

Figure 17.1: Histogram of sampled ratio data recorded in the 2017 run, compared with that of the 2014 measurement. The full width of the distribution corresponding to $2 \cdot \sigma$ is indicated by the red arrows in each graph. The statistical figures of the data are summarized in Table 17.1.

Table 17.1: Comparison of statistical figures between the 2014 data and the preliminary 2017 data shown in Fig. 17.1. The sample size N, the distribution of the ratio σ_R evaluated by the standard deviation, and the estimate of the uncertainty of the determination of the center of the distribution $\delta R_{\bar{p}\mathrm{H}^-,\mathrm{est}}$, evaluated by $\delta R_{\bar{p}\mathrm{H}^-,\mathrm{est}} = \sigma_R/\sqrt{N}$, are listed for each of the 2014 data and the 2017 data.

	2014	2017
Sample size N	6521	9156
Ratio distribution σ_R	5.4×10^{-9}	2.2×10^{-9}
Uncertainty of center determination $\delta R_{\bar{p}\mathrm{H}^-,\mathrm{est}}$	6.7×10^{-11}	2.3×10^{-11}

to the significantly improved condition of the system than in the 2014 measurement. In the best conditions, the short-term cyclotron frequency stability reached the principal limit under the sideband coupling method. Together with a drastic reduction of the systematic uncertainty achieved by the new tunable axial detection system, an improvement of the precision over the 2014 measurement by at least a factor of 3 is expected in the final data analysis.

Appendices

A

Supplementary calculations of a cylindrical Penning trap

This chapter supplements calculations of the electrical potential formed in a cylindrical Penning trap discussed in Section 2.3.1.

A.1 Potential expression in spherical and cylindrical coordinates

The C_j coefficients of the electrical potential are defined by the expression of an electric potential in a spherical coordinate system (r, θ, ϕ) which has its origin at the trap center. The solution of the Laplace equation $\nabla^2\Phi = 0$ in this coordinate system is expressed as (Eq. (2.44))

$$\Phi(r, \theta) = \sum_{j=0}^{\infty} V_3 C_j r^j P_j(\cos\theta) \tag{A.1}$$

assuming the rotational symmetry around the pole. Here V_3 represents the voltage applied to the ring electrode of the trap. On the other hand, the potential in a cylindrical Penning trap can be calculated in a straightforward way in a cylindrical coordinate system (ρ, z, θ), having the trap center as its origin and the trap axis as its zenith axis (Fig. 2.4 (A)). As discussed in Section 2.3.1, the Laplace equation in this coordinate system under azimuthal symmetry (Eq. (2.46))

$$\frac{1}{\rho}\frac{\partial}{\partial\rho}\left(\rho\frac{\partial\Phi}{\partial\rho}\right) + \frac{\partial^2\Phi}{\partial z^2} = 0 \tag{A.2}$$

finds its general solution in the following form expressed by real parameters A_n (Eq. (2.50))

$$\Phi(\rho, z) = \sum_{n=1}^{\infty} A_n I_0(k_n \rho) \sin\left(k_n z + \frac{n\pi}{2}\right) \quad \left(\text{with } k_n \equiv \frac{n\pi}{\Lambda}\right) \tag{A.3}$$

under a boundary condition $\Phi(\rho, \Lambda/2) = \Phi(\rho, -\Lambda/2) = 0$, with Λ being the length of the trap. A_n which can be obtain from a boundary condition of the cylindrical trap as will be discussed in the next section. In the following, we seek a correspondence between Eqs. (A.1) and (A.3) in order to express C_j from A_n.

By use of $(\rho, z) = (r\sin\theta, r\cos\theta)$, the expression in the spherical coordinates is transformed to that in the cylindrical coordinates. The Legendre polynomials which appear in Eq. (A.1) can be expanded by the Rodrigues' formula as [87]

$$P_n(x) = \sum_{k=0}^{\lfloor n/2 \rfloor} \frac{(-1)^k}{2^n} \binom{n}{k} \binom{2n-2k}{n} x^{n-2k} \tag{A.4}$$

with $\lfloor\ \rfloor$ being the floor function:

$$\left\lfloor \frac{n}{2} \right\rfloor = \begin{cases} n/2 & \text{for } n\text{: even} \\ (n-1)/2 & \text{for } n\text{: odd.} \end{cases} \tag{A.5}$$

Applying Eq. (A.4) to the terms of Eq. (A.1),

$$\begin{aligned} r^j P_j(\cos\theta) &= \sum_{k=0}^{\lfloor j/2 \rfloor} \frac{(-1)^k}{2^j} \binom{j}{k} \binom{2j-2k}{j} r^{2k} (r\cos\theta)^{j-2k} \\ &= \sum_{k=0}^{\lfloor j/2 \rfloor} \frac{(-1)^k}{2^j} \binom{j}{k} \binom{2j-2k}{j} (z^2+\rho^2)^k z^{j-2k}. \end{aligned} \tag{A.6}$$

$$\therefore \Phi = \sum_{j=0}^{\infty} V_3 C_j \sum_{k=0}^{\lfloor j/2 \rfloor} \frac{(-1)^k}{2^j} \binom{j}{k} \binom{2j-2k}{j} (z^2+\rho^2)^k z^{j-2k} \tag{A.7}$$

is obtained.

On the other hand, Eq. (A.3) is expanded as follows [87]:

$$I_0(x) = \sum_{m=0}^{\infty} \frac{\left(x^2/4\right)^m}{(m!)^2}, \tag{A.8}$$

$$\sin\left(k_n z + \frac{n\pi}{2}\right) = \sum_{l=0}^{\infty} \frac{(-k_n)^l}{l!} \sin\left(\frac{n-l}{2}\pi\right) z^l \tag{A.9}$$

$$\therefore \Phi = \sum_{n=0}^{\infty} \left(\sum_{m=0}^{\infty} \frac{\left((k_n\rho)^2/4\right)^m}{(m!)^2} \right) \left(\sum_{l=0}^{\infty} \frac{A_n(-k_n)^l}{l!} \sin\left(\frac{n-l}{2}\pi\right) z^l \right). \tag{A.10}$$

By comparing the terms $\rho^0 z^{\,j}$ of Eqs. (A.7) and (A.10), we find

$$V_3 C_j \sum_{k=0}^{\lfloor j/2 \rfloor} \frac{(-1)^k}{2^{\,j}} \binom{j}{k} \binom{2j-2k}{j} = \sum_{n=0}^{\infty} \frac{A_n(-k_n)^{\,j}}{j!} \sin\left(\frac{n-j}{2}\pi\right) \tag{A.11}$$

$$C_j = \sum_{n=1}^{\infty} \frac{A_n}{V_3} \frac{(-k_n)^{\,j}}{j!} \sin\left(\frac{n-j}{2}\pi\right) \quad (\because P_j(1) = 1), \tag{A.12}$$

as quoted in Eq. (2.51).

A.2 Explicit form of the electrical potential in a cylindrical Penning trap

In this section, we derive an explicit form of the electric potential formed in a five-electrode cylindrical Penning trap quoted in Eqs. (2.52) to (2.54). This is done by applying a Dirichlet boundary condition defined by the five-electrode Penning trap to Eqs. (A.2) and (A.3). From the determined A_n of Eq. (A.3), coefficients C_j can be also determined by Eq. (A.12).

We use the geometry of a five-electrode cylindrical Penning trap defined in Fig. 2.4 (A, B). The z coordinates of the five electrodes are defined as $[z_0, z_1], [z_2, z_3], \cdots, [z_8, z_9]$. The central ring electrode $[z_4, z_5]$ is centered to the origin of the coordinate systems i.e. $z_4 + z_5 = 0$. The gap between the electrodes is denoted as d and the inner radius of the trap a. The voltages applied on the electrodes are represented by $V_1, \cdots, V_5$, forming the boundary condition below at $\rho = a$ (Eq. (2.43), see also Fig. 2.4 (B)).

$$\Phi(a,z) = \begin{cases} V_1 & (z_0 \le z \le z_1) \\ V_1 + \dfrac{V_2 - V_1}{z_2 - z_1}(z - z_1) & (z_1 \le z \le z_2) \\ V_2 & (z_2 \le z \le z_3) \\ \vdots & \vdots \\ V_5 & (z_8 \le z \le z_9). \end{cases} \tag{A.13}$$

We determine A_n under the above boundary condition using the orthogonality relations

$$\begin{aligned} \frac{2}{\Lambda} \int_{-\Lambda/2}^{\Lambda/2} \sin(k_m z) \sin(k_n z)\, \mathrm{d}z &= \delta_{mn} \\ \frac{2}{\Lambda} \int_{-\Lambda/2}^{\Lambda/2} \cos(k_m z) \cos(k_n z)\, \mathrm{d}z &= \delta_{mn} \\ \frac{2}{\Lambda} \int_{-\Lambda/2}^{\Lambda/2} \sin(k_m z) \cos(k_n z)\, \mathrm{d}z &= 0. \end{aligned} \tag{A.14}$$

From Eq. (A.3),

$$\Phi(\rho,z)=\sum_{n=1}^{\infty}A_nI_0(k\rho)\left(\sin(k_nz)\cos\left(\frac{n\pi}{2}\right)+\cos(k_nz)\sin\left(\frac{n\pi}{2}\right)\right). \tag{A.15}$$

By applying Eq. (A.14) to Eq. (A.15), we obtain for n: even,

$$\begin{aligned}A_n&=\frac{(-1)^{\frac{n}{2}}}{I_0(k_na)}\frac{2}{\Lambda}\int_{-\Lambda/2}^{\Lambda/2}\Phi(a,z)\sin(k_nz)\mathrm{d}z\\&=\frac{(-1)^{\frac{n}{2}}}{I_0(k_na)}\frac{2}{\Lambda}\left[-\frac{V_5\cos(k_nz_9)-V_1\cos(k_nz_0)}{k_n}+\sum_{i=1}^{4}\frac{V_{i+1}-V_i}{k_n^2d}(\sin(k_nz_{2i})-\sin(k_nz_{2i-1}))\right]\end{aligned} \tag{A.16}$$

and for n: odd,

$$\begin{aligned}A_n&=\frac{(-1)^{\frac{n-1}{2}}}{I_0(k_na)}\frac{2}{\Lambda}\int_{-\Lambda/2}^{\Lambda/2}\Phi(a,z)\cos(k_nz)\mathrm{d}z\\&=\frac{(-1)^{\frac{n-1}{2}}}{I_0(k_na)}\frac{2}{\Lambda}\left[\frac{V_5\sin(k_nz_9)-V_1\sin(k_nz_0)}{k_n}+\sum_{i=1}^{4}\frac{V_{i+1}-V_i}{k_n^2d}(\cos(k_nz_{2i})-\cos(k_nz_{2i-1}))\right].\end{aligned} \tag{A.17}$$

Eqs. (A.16) and (A.17) can be written in one form as (Eq. (2.52))

$$\begin{aligned}A_n=\frac{2}{\Lambda I_0(k_na)}\Bigg[&\frac{1}{k_n}\left(V_5\sin\left(k_nz_9+\frac{n\pi}{2}\right)-V_1\sin\left(k_nz_0+\frac{n\pi}{2}\right)\right)\\&+\sum_{i=1}^{4}\frac{V_{i+1}-V_i}{k_n^2d}\left(\cos\left(k_nz_{2i}+\frac{n\pi}{2}\right)-\cos\left(k_nz_{2i-1}+\frac{n\pi}{2}\right)\right)\Bigg].\end{aligned} \tag{A.18}$$

Substituting this to Eq. (A.3), we obtain the explicit form of the potential $\Phi(\rho,z)$ as (Eq. (2.53))

$$\begin{aligned}\Phi(\rho,z)=\sum_{n=1}^{\infty}\Bigg[&\frac{1}{k_n}\left(V_5\sin\left(k_nz_9+\frac{n\pi}{2}\right)-V_1\sin\left(k_nz_0+\frac{n\pi}{2}\right)\right)\\&+\sum_{i=1}^{4}\frac{V_{i+1}-V_i}{k_n^2d}\left(\cos\left(k_nz_{2i}+\frac{n\pi}{2}\right)-\cos\left(k_nz_{2i-1}+\frac{n\pi}{2}\right)\right)\Bigg]\\&\cdot\frac{2}{\Lambda}\frac{I_0(k_n\rho)}{I_0(k_na)}\sin\left(k_nz+\frac{n\pi}{2}\right).\end{aligned} \tag{A.19}$$

By Eq. (A.12), the explicit form of C_j of the cylindrical trap is obtained (Eq. (2.54)) to be

$$\begin{aligned}C_j=\sum_{n=1}^{\infty}\Bigg[&V_5\sin\left(k_nz_9+\frac{n\pi}{2}\right)-V_1\sin\left(k_nz_0+\frac{n\pi}{2}\right)\\&+\sum_{i=1}^{4}\frac{V_{i+1}-V_i}{k_nd}\left(\cos\left(k_nz_{2i}+\frac{n\pi}{2}\right)-\cos\left(k_nz_{2i-1}+\frac{n\pi}{2}\right)\right)\Bigg]\\&\cdot\frac{2\cdot(-1)^j}{j!\Lambda V_3}\cdot\frac{k_n^{j-1}}{I_0(k_na)}\cdot\sin\left(\frac{n-j}{2}\pi\right).\end{aligned} \tag{A.20}$$

B

Simulation studies of particle extraction

This chapter provides results of simulations performed to supplement discussions on particle extraction in Section 13.3.

B.1 Probability functions

As explained in Section 13.3, the separation of a cloud of particles is performed by first setting the equilibrium position of the cloud by a proper asymmetry of the electric potential, and then applying a potential wall which separate the cloud into two fractions. The fraction of extracted particles can be related to the distribution of the axial coordinate z of the particles in the cloud.

Consider such separation of a particle cloud. We treat a cloud of antiprotons being thermal equilibrium with an axial detection system at temperature T_z. Let us treat the moment before application of the separation potential where the equilibrium z position of the cloud is shifted by z_0 by an asymmetric potential, as illustrated in Fig. B.1 (A). Here the z axis points toward the upstream end of the trap, and the center of the trap is defined as the origin $z = 0$. The cloud is distributed around z_0. In (B), the origin of the coordinate $z = 0$ is redefined to the equilibrium position of the cloud, the coordinate at the cut is redefined to $-z_0$, accordingly. Consider now the number of particles N_{up} contained in the upstream fraction which is indicated as the shaded area in Fig. B.1 (A). We denote the probably density function (PDF) of z of the particles distributed around $z = 0$ to be $\Pi(z)$, which is defined by thermal equilibrium with the axial detection system. The number of particles contained in the upstream fraction N_{up} is expressed with $\Pi(z)$ as

$$N_{\mathrm{up}} = N_{\mathrm{total}} \int_{-z_0}^{\infty} \Pi(z - z_0) \mathrm{d}z \tag{B.1}$$

with N_{total} being the number of the total cloud. By translation of the coordinate in (B), and assuming

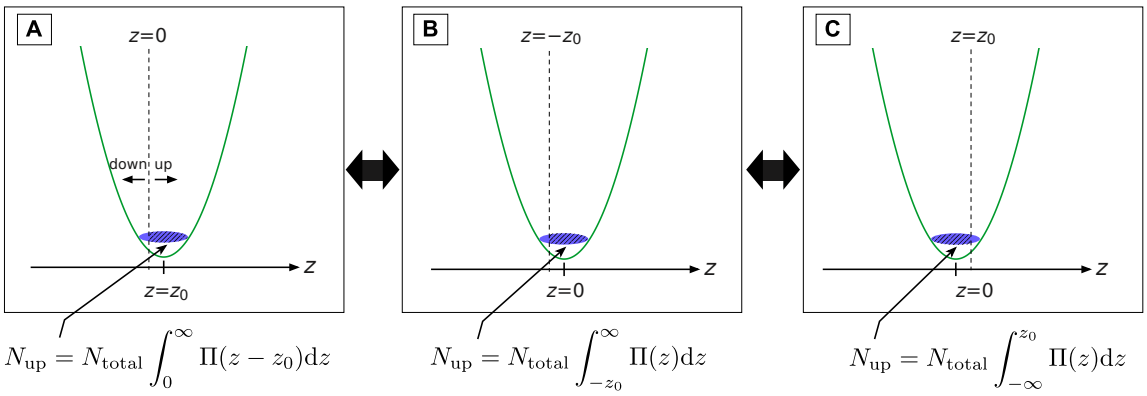

Figure B.1: Separation of a particle cloud and z distribution of the particles. A situation after the application of an asymmetric trapping potential and before the separation potential wall is illustrated. The line which separates the cloud at the ken ted of the trap is indicated by the dashed line. The position z_0 indicates the equilibrium position of the cloud. In (B), the coordinate is redefined so that the equilibrium point z_0 becomes the origin. In (C), the coordinate is mirrored in respect of $z = 0$ from the one in (B).

a symmetry of $\Pi(z)$ by $z \to -z$ (C),

$$N_{\mathrm{up}} = N_{\mathrm{total}} \int_{-\infty}^{z_0} \Pi(z)\mathrm{d}z = N_{\mathrm{total}} \Phi(z_0). \tag{B.2}$$

Here $\Phi(z)$ is the cumulative distribution function (CDF) of the z coordinate of the particles

$$\Phi(z) = \int_{-\infty}^{z} \Pi(z')\mathrm{d}z'. \tag{B.3}$$

The number of particles in the downstream cloud N_{down} is expressed as (Eq. (13.3))

$$N_{\mathrm{down}} = N_{\mathrm{total}} - N_{\mathrm{up}} = N_{\mathrm{total}} \int_{z_0}^{\infty} \Pi(z)\mathrm{d}z. \tag{B.4}$$

In the following, we derive the explicit forms of the PDF and the CDF. The PDF of the axial energy E_z is a Boltzmann distribution defined by the axial temperature T_z:

$$\Pi_{\mathrm{B}}(E_z|T_z) = \frac{1}{k_{\mathrm{B}}T_z} \exp\left(-\frac{E_z}{k_{\mathrm{B}}T_z}\right). \tag{B.5}$$

Using the relation between the axial amplitude and the energy

$$E_z = \frac{1}{2} m\omega_z^2 z^2, \tag{B.6}$$

we find that the PDF of $|z|$ is given by

$$\Pi_{|z|}(|z|\,|T_z) = \frac{2|z|}{z_{\mathrm{m}}^2} \exp\left(-\frac{|z|^2}{z_{\mathrm{m}}^2}\right) \tag{B.7}$$

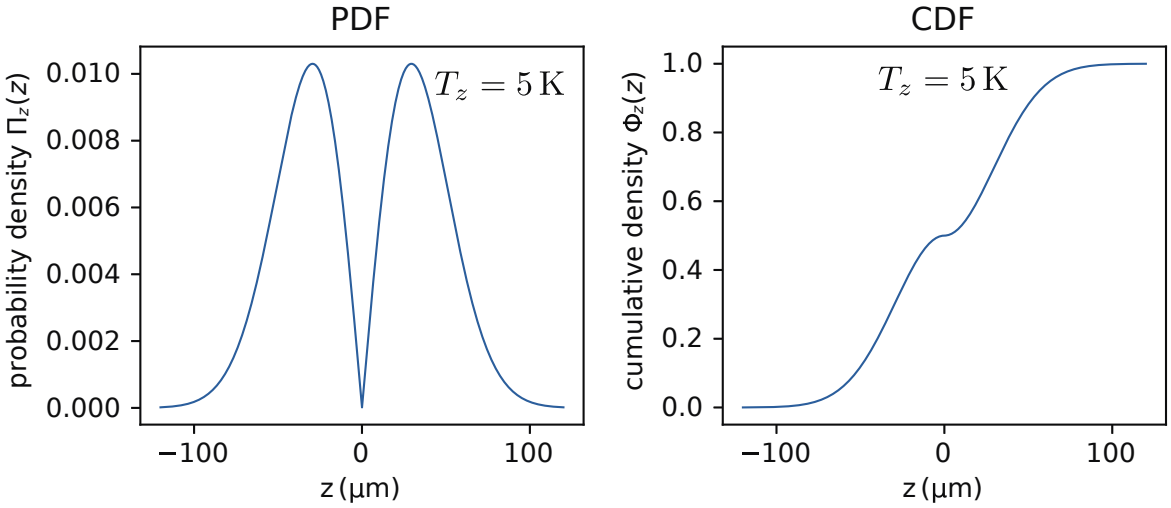

Figure B.2: Scaling of the PDF $\Phi_z(z|T_z)$ and the CDF $\Phi_z(z|T_z)$ of the z coordinate at the axial temperature $T_z = 5\,\mathrm{K}$.

where z_m^2 is the mean of z^2 expressed as

$$z_\mathrm{m}^2 = \int_0^\infty z^2 \Pi_{|z|}(|z|\,|T_z)\mathrm{d}|z| = \frac{k_\mathrm{B} T_z}{m\omega_z^2}. \tag{B.8}$$

Assuming that the coordinate z distributes in the regions $z < 0$ and $z > 0$ equally, the PDF of z is given by

$$\Pi_z(z|T_z) = \frac{|z|}{z_\mathrm{m}^2} \exp\left(-\frac{|z|^2}{z_\mathrm{m}^2}\right). \tag{B.9}$$

By explicitly integrating Eq. (B.9), the CDF of z is obtained as

$$\Phi_z(z|T_z) = \begin{cases} \dfrac{1}{2}\exp\left(-\dfrac{z^2}{z_m^2}\right) & (z \leq 0) \\ 1 - \dfrac{1}{2}\exp\left(-\dfrac{z^2}{z_m^2}\right) & (z > 0). \end{cases} \tag{B.10}$$

The scalings of PDF and the CDF for $T_z = 5\,\mathrm{K}$ are shown in Fig. B.2 (A) and (B), respectively. By comparing Fig. B.2 (B) with Fig. 13.7, it can be seen that the scalings Eqs. (B.2) and (B.4) based on this CDF reproduce the experimental observations.

B.2 Studies of influences of the initial cloud size on the separation

In the experimental operation in 2017, we experienced that extraction of a single particle from a cloud containing a large number (~ 300) of particles was more difficult than from smaller clouds. In this context, here we investigate the influence of the cloud size on the results of the extraction by

using the PDF derived in the last section.

We use the following assumptions as the basis of the simulations:

1. A cloud of $N_{\rm sample}$ antiprotons is simulated by choosing $N_{\rm sample}$ times of random variables from the PDF $\Phi_z(z|T_z)$ of Eq. (B.9) (let us call this step *sampling*).

2. The z distribution of particles in the cloud is obtained by the distribution of the sampled set of $\{z_i\}\,(i = 1, 2, \cdots, N_{\rm sample})$. We can also evaluate the number of particles which would be extracted to the upstream fraction $N_{\rm up}(z_0)$ as a function of the equilibrium position z_0 by

$$N_{\rm up}(z_0) = (\#\text{ of particles which satisfy } z_i < z_0). \tag{B.11}$$

For a fixed $N_{\rm sample}$, we repeat the sampling (step 1) and the evaluations of step 2 for an enough number $N_{\rm trials}$ of trials. In Fig. B.3, examples of distribution of thus sampled z are shown. The examples are given for $T_z = 5\,\mathrm{K}$, 50 mK and $N_{\rm sample} = 30$, 300. It is clearly observed that larger the sample size $N_{\rm sample}$, the sampled distribution resembles the PDF in Fig. B.2 more.

In Fig. B.4, the results of the simulations are shown. In each graph, the $N_{\rm up}(z_0)$ is shown for 20 trials with different colors. The red dashed curve is $P(N_{\rm up} = 1|z_0)$, the probability of extracting a single particle to the upstream fraction as a function of the equilibrium position z_0. $P(N_{\rm up} = 1|z_0)$ is obtained by

$$P(N_{\rm up} = 1|z_0) = \frac{(\#\text{ of trials when } N_{\rm up}(z_0) = 1)}{N_{\rm trials}} \tag{B.12}$$

with trials of $N_{\rm trials} = 8000$. The axis of $P(N_{\rm up} = 1|z_0)$ is shown on the right of the graph. This evaluation was done for each combination of $T_z = 5\,\mathrm{K}$, 50 mK and $N_{\rm sample} = 30$, 300 as shown in Fig. B.4 (A–D). It can be observed that for $N_{\rm sample} = 30$, the scaling scatters more than $N_{\rm sample} = 300$. If one would evaluate temperature from the scaling of the particle extraction with a cloud with a small size, much statistics is required to resolve the scaling from the temperature (see Section 13.3.2, particularly Fig. 13.9).

The characteristics of the peak of the probability function $P(N_{\rm up} = 1|z_0)$ of each condition are summarized in Table B.1. By comparing data with different $N_{\rm sample}$, it is found that the z_0 corresponding to the peak shifts outwardly for the larger $N_{\rm sample}$, and that the FWHM of the peak becomes narrower. However the maximum of the probability $P(N_{\rm up} = 1|z_0)$ at does not differ significantly between $N_{\rm sample} = 30$ and 300.

These characteristics are common in both of $T_z = 5\,\mathrm{K}$ and 50 mK. From these observations, it can be said that finer tuning of the extraction potential is required to extract a single particle from a larger size of the cloud, although the probability of getting a single particle with the optimum separation parameters do not differ significantly. It is also use for actual experiments to note the difference of the optimum z_0 which gives the maximum of $P(N_{\rm up} = 1|z_0)$ depending on the size of the initial cloud.

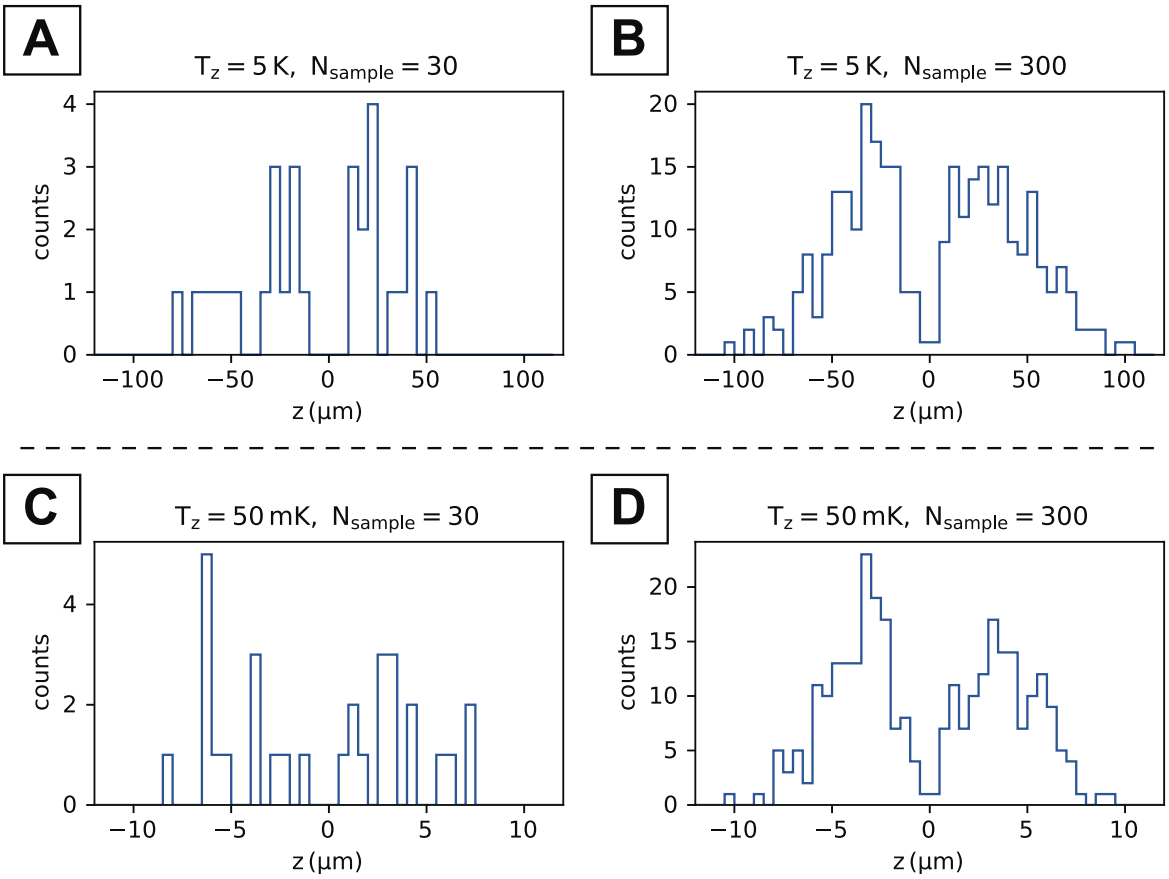

Figure B.3: Examples of z distribution of clouds simulated for different sizes and temperatures. For each of (A–D), distribution of z coordinate is simulated by sampling N_{sample} z's from the PDF Eq. (B.9) with the axial temperature T_z. **(A)** $T_z = 5\,\text{K}, N_{\text{sample}} = 30$, **(B)** $T_z = 5\,\text{K}, N_{\text{sample}} = 300$, **(C)** $T_z = 50\,\text{mK}, N_{\text{sample}} = 30$, **(D)** $T_z = 50\,\text{mK}, N_{\text{sample}} = 300$.

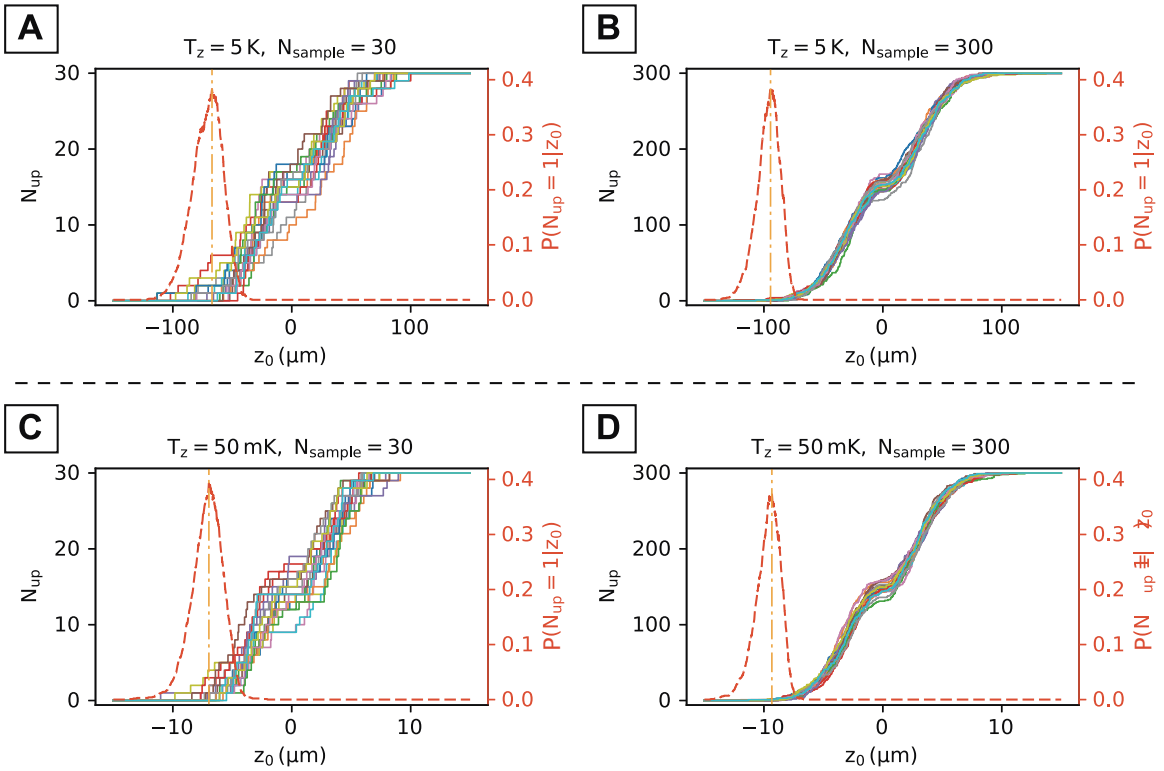

Figure B.4: Results of the simulations based on the PDF Eq. (B.9). The procedure of sampling and evaluation of $N_{\mathrm{up}}(z_0)$ explained the text was repeated for $N_{\mathrm{trials}} = 8000$. $N_{\mathrm{up}}(z_0)$ for 20 of the sampled sets are shown in different colors. The red dashed curve in each plot shows $P(N_{\mathrm{up}} = 1|z_0)$, the probability of single-particle extraction as a function of z_0. The axis of $P(N_{\mathrm{up}} = 1|z_0)$ is on the right of each graph. **(A)** $T_z = 5\,\mathrm{K}, N_{\mathrm{sample}} = 30$, **(B)** $T_z = 5\,\mathrm{K}, N_{\mathrm{sample}} = 300$, **(C)** $T_z = 50\,\mathrm{mK}, N_{\mathrm{sample}} = 30$, **(D)** $T_z = 50\,\mathrm{mK}, N_{\mathrm{sample}} = 300$.

Table B.1: Characteristics of the peak of the probability function $P(N_{\mathrm{up}} = 1|z_0)$ shown in Fig. B.4 are summarized. For each dataset obtained by the simulations, the maximum probability $P_{\mathrm{max}}(N_{\mathrm{up}} = 1)$ at the peak, z_0 which gives $P_{\mathrm{max}}(N_{\mathrm{up}} = 1)$, and the FWHM of the peak are shown.

Dataset	$P_{\mathrm{max}}(N_{\mathrm{up}} = 1)$	z_0 at $P_{\mathrm{max}}(N_{\mathrm{up}} = 1)$	peak FWHM
$T_z = 5\,\mathrm{K},\ N_{\mathrm{sample}} = 30$	0.383	$-67.0\,\mu\mathrm{m}$	$28.4\,\mu\mathrm{m}$
$T_z = 5\,\mathrm{K},\ N_{\mathrm{sample}} = 300$	0.385	$-94.4\,\mu\mathrm{m}$	$20.8\,\mu\mathrm{m}$
$T_z = 50\,\mathrm{mK},\ N_{\mathrm{sample}} = 30$	0.393	$-7.00\,\mu\mathrm{m}$	$2.78\,\mu\mathrm{m}$
$T_z = 50\,\mathrm{mK},\ N_{\mathrm{sample}} = 300$	0.376	$-9.32\,\mu\mathrm{m}$	$2.26\,\mu\mathrm{m}$

Bibliography

[1] William Huggins. "On the Spectrum of the Flame of Hydrogen". *Proc. R. Soc. London*, **30** (1879), 576–580 (cited on p. 2).

[2] Albert A. Michelson. "On the application of interference methods to spectroscopic measurements. —II". *London, Edinburgh, Dublin Philos. Mag. J. Sci.*, **34** (1892), 280–299. DOI: 10.1080/14786449208620318 (cited on p. 2).

[3] P. Zeeman. "The Effect of Magnetisation on the Nature of Light Emitted by a Substance". *Nature*, **55** (1897), 347–347. DOI: 10.1038/055347a0 (cited on p. 2).

[4] Willis E. Lamb and Robert C. Retherford. "Fine Structure of the Hydrogen Atom by a Microwave Method". *Phys. Rev.*, **72** (1947), 241–243. DOI: 10.1103/PhysRev.72.241 (cited on p. 2).

[5] J. J. Balmer. "Notiz über die Spectrallinien des Wasserstoffs". *Ann. Phys.*, **261** (1885), 80–87. DOI: 10.1002/andp.18852610506 (cited on p. 2).

[6] N. Bohr. "On the constitution of atoms and molecules". *London, Edinburgh, Dublin Philos. Mag. J. Sci.*, **26** (1913), 1–25. DOI: 10.1080/14786441308634955 (cited on p. 2).

[7] W. Pauli. "Über den Zusammenhang des Abschlusses der Elektronengruppen im Atom mit der Komplexstruktur der Spektren". *Zeitschrift für Phys.*, **31** (1925), 765–783. DOI: 10.1007/BF02980631 (cited on p. 2).

[8] P. A. M. Dirac. "Relativistic Quantum Mechanics". *Proc. R. Soc. A Math. Phys. Eng. Sci.*, **136** (1932), 453–464. DOI: 10.1098/rspa.1932.0094 (cited on p. 2).

[9] F. J. Dyson. "The Radiation Theories of Tomonaga, Schwinger, and Feynman". *Phys. Rev.*, **75** (1949), 486–502. DOI: 10.1103/PhysRev.75.486 (cited on p. 2).

[10] M. Tanabashi et al. "Review of Particle Physics". *Phys. Rev. D*, **98** (2018), 030001. DOI: 10.1103/PhysRevD.98.030001 (cited on pp. 2, 3, 5).

[11] Peter J. Mohr, David B. Newell, and Barry N. Taylor. "CODATA recommended values of the fundamental physical constants: 2014*". *Rev. Mod. Phys.*, **88** (2016), 035009. DOI: 10.1103/RevModPhys.88.035009 (cited on pp. 2, 56).

[12] D. Hanneke, S. Fogwell, and G. Gabrielse. "New Measurement of the Electron Magnetic Moment and the Fine Structure Constant". *Phys. Rev. Lett.*, **100** (2008), 120801. DOI: 10.1103/PhysRevLett.100.120801 (cited on pp. 2, 5, 58).

[13] G. Arnison et al. "Experimental observation of lepton pairs of invariant mass around 95 GeV/c^2 at the CERN SPS collider". *Phys. Lett. B*, **126** (1983), 398–410. DOI: 10.1016/0370-2693(83)90188-0 (cited on p. 2).

[14] ATLAS Collaboration. "Observation of a new particle in the search for the Standard Model Higgs boson with the ATLAS detector at the LHC". *Phys. Lett. B*, **716** (2012), 1–29. arXiv: 1207.7214 [hep-ex] (cited on p. 2).

[15] CMS Collaboration. "Observation of a new boson at a mass of 125 GeV with the CMS experiment at the LHC". *Phys. Lett. B*, **716** (2012), 30–61. DOI: 10.1016/j.physletb.2012.08.021. arXiv: 1207.7235 [hep-ex] (cited on p. 2).

[16] Y. Fukuda et al. "Evidence for Oscillation of Atmospheric Neutrinos". *Phys. Rev. Lett.*, **81** (1998), 1562–1567. DOI: 10.1103/PhysRevLett.81.1562 (cited on p. 2).

[17] P. Ramond. "Dual Theory for Free Fermions". *Phys. Rev. D*, **3** (1971), 2415–2418. DOI: 10.1103/PhysRevD.3.2415 (cited on p. 3).

[18] Steven Weinberg. "Implications of dynamical symmetry breaking". *Phys. Rev. D*, **13** (1976), 974–996. DOI: 10.1103/PhysRevD.13.974 (cited on p. 3).

[19] C. Giunti, C. W. Kim, and U. W. Lee. "Running Coupling Constants And Grand Unification Models". *Mod. Phys. Lett. A*, **06** (1991), 1745–1755. DOI: 10.1142/S0217732391001883 (cited on p. 3).

[20] CMS Collaboration. "Search for dijet resonances in proton–proton collisions at $\sqrt{s} = 13\,\text{TeV}$ and constraints on dark matter and other models". *Phys. Lett. B*, **769** (2017), 520–542. DOI: 10.1016/j.physletb.2017.02.012 (cited on p. 3).

[21] ATLAS Collaboration. "Search for new phenomena using the invariant mass distribution of same-flavour opposite-sign dilepton pairs in events with missing transverse momentum in $\sqrt{s} = 13$ TeV pp collisions with the ATLAS detector". *Eur. Phys. J. C*, **78** (2018). DOI: 10.1140/epjc/s10052-018-6081-9 (cited on p. 3).

[22] M. S. Safronova et al. "Search for new physics with atoms and molecules". *Rev. Mod. Phys.*, **90** (2018), 025008. DOI: 10.1103/RevModPhys.90.025008. arXiv: 1710.01833 (cited on p. 3).

[23] T. E. Chupp et al. "Electric dipole moments of atoms, molecules, nuclei, and particles". *Rev. Mod. Phys.*, **91** (2019), 015001. DOI: 10.1103/RevModPhys.91.015001 (cited on p. 3).

[24] P. A. M. Dirac. "The Quantum Theory of the Electron". *Proc. R. Soc. A Math. Phys. Eng. Sci.*, **117** (1928), 610–624. DOI: 10.1098/rspa.1928.0023 (cited on p. 3).

[25] Carl D. Anderson. "The Positive Electron". *Phys. Rev.*, **43** (1933), 491–494. DOI: 10.1103/PhysRev.43.491 (cited on p. 3).

[26] Owen Chamberlain et al. "Observation of Antiprotons". *Phys. Rev.*, **100** (1955), 947–950. DOI: 10.1103/PhysRev.100.947 (cited on p. 3).

[27] Bruce Cork et al. "Antineutrons Produced from Antiprotons in Charge-Exchange Collisions". *Phys. Rev.*, **104** (1956), 1193–1197. DOI: 10.1103/PhysRev.104.1193 (cited on p. 3).

[28] Yu.M. Antipov et al. "Observation of antihelium-3". *Nucl. Phys. B*, **31** (1971), 235–252. DOI: 10.1016/0550-3213(71)90228-8 (cited on p. 3).

[29] G. Baur et al. "Production of antihydrogen". *Phys. Lett. B*, **368** (1996), 251–258. DOI: 10.1016/0370-2693(96)00005-6 (cited on p. 3).

[30] M. Hori and J. Walz. "Physics at CERN's Antiproton Decelerator". *Prog. Part. Nucl. Phys.*, **72** (2013), 206–253. DOI: 10.1016/j.ppnp.2013.02.004. arXiv: arXiv:1304.3721v1 (cited on p. 3).

[31] J. DiSciacca et al. "One-Particle Measurement of the Antiproton Magnetic Moment". *Phys. Rev. Lett.*, **110** (2013), 130801. DOI: 10.1103/PhysRevLett.110.130801. arXiv: 1301.6310 (cited on pp. 4, 96, 102).

[32] Masaki Hori. "Recent progress of laser spectroscopy experiments on antiprotonic helium". *Philos. Trans. R. Soc. A Math. Phys. Eng. Sci.*, **376** (2018), 20170270. DOI: 10.1098/rsta.2017.0270 (cited on p. 4).

[33] C. Smorra et al. "BASE – The Baryon Antibaryon Symmetry Experiment". *Eur. Phys. J. Spec. Top.*, **224** (2015), 3055–3108. DOI: 10.1140/epjst/e2015-02607-4 (cited on pp. 4, 7, 8, 61, 63, 70, 77, 79, 92).

[34] M. Zieliński et al. "Studies on Antihydrogen Atoms with the ATRAP Experiment at CERN". *Acta Phys. Pol. B Proc. Suppl.*, **6** (2013), 1093. DOI: 10.5506/APhysPolBSupp.6.1093 (cited on p. 4).

[35] C. Malbrunot et al. "The ASACUSA antihydrogen and hydrogen program: results and prospects". *Philos. Trans. R. Soc. A Math. Phys. Eng. Sci.*, **376** (2018), 20170273. DOI: 10.1098/rsta.2017.0273 (cited on p. 4).

[36] S. Eriksson. "Precision measurements on trapped antihydrogen in the ALPHA experiment". *Philos. Trans. R. Soc. A Math. Phys. Eng. Sci.*, **376** (2018), 20170268. DOI: 10.1098/rsta.2017.0268. arXiv: 1803.10057 (cited on p. 4).

[37] T. D. Lee and C. N. Yang. "Question of Parity Conservation in Weak Interactions". *Phys. Rev.*, **104** (1956), 254–258. DOI: 10.1103/PhysRev.104.254 (cited on p. 4).

[38] C. S. Wu et al. "Experimental Test of Parity Conservation in Beta Decay". *Phys. Rev.*, **105** (1957), 1413–1415. DOI: 10.1103/PhysRev.105.1413 (cited on p. 4).

[39] M. Goldhaber, L. Grodzins, and A. W. Sunyar. "Helicity of Neutrinos". *Phys. Rev.*, **109** (1958), 1015–1017. DOI: 10.1103/PhysRev.109.1015 (cited on p. 4).

[40] J. H. Christenson et al. "Evidence for the 2π deacy of the K_2^0 Meson". *Phys. Rev. Lett.*, **13** (1964), 138–140. DOI: 10.1103/PhysRevLett.13.138 (cited on p. 4).

[41] E. C. G. Sudarshan and R. E. Marshak. "Chirality Invariance and the Universal Fermi Interaction". *Phys. Rev.*, **109** (1958), 1860–1862. DOI: 10.1103/PhysRev.109.1860.2 (cited on p. 4).

[42] Nicola Cabibbo. "Unitary Symmetry and Leptonic Decays". *Phys. Rev. Lett.*, **10** (1963), 531–533. DOI: 10.1103/PhysRevLett.10.531 (cited on p. 4).

[43] Makoto Kobayashi and Toshihide Maskawa. "CP-Violation in the Renormalizable Theory of Weak Interaction". *Prog. Theor. Phys.*, **49** (1973), 652–657. DOI: 10.1143/PTP.49.652 (cited on p. 4).

[44] Gerhart Lüders. "Proof of the TCP theorem". *Ann. Phys.*, **2** (1957), 1–15. DOI: 10.1016/0003-4916(57)90032-5 (cited on p. 4).

[45] W. Buchmüller, P. Di Bari, and M. Plümacher. "Cosmic microwave background, matter–antimatter asymmetry and neutrino masses". *Nucl. Phys. B*, **643** (2002), 367–390. DOI: 10.1016/S0550-3213(02)00737-X (cited on p. 4).

[46] Andrei D. Sakharov. "Violation of CP Invariance, C asymmetry, and baryon asymmetry of the universe". *Pisma Zh. Eksp. Teor. Fiz.*, **5** (1967), 32–35. DOI: 10.1070/pu1991v034n05abeh002497 (cited on p. 4).

[47] Laurent Canetti, Marco Drewes, and Mikhail Shaposhnikov. "Matter and antimatter in the universe". *New J. Phys.*, **14** (2012), 095012. DOI: 10.1088/1367-2630/14/9/095012. arXiv: 1204.4186 (cited on p. 5).

[48] O. Bertolami et al. "CPT violation and baryogenesis". *Phys. Lett. B*, **395** (1997), 178–183. DOI: 10.1016/S0370-2693(97)00062-2 (cited on p. 5).

[49] Robert S Van Dyck, Paul B Schwinberg, and Hans G Dehmelt. "New High-Precision Comparison of Electron and Positron g Factors". *Phys. Rev. Lett.*, **59** (1987), 26–29. DOI: 10.1103/PhysRevLett.59.26 (cited on pp. 5, 57).

[50] G. W. Bennett et al. "Final report of the E821 muon anomalous magnetic moment measurement at BNL". *Phys. Rev. D*, **73** (2006), 072003. DOI: 10.1103/PhysRevD.73.072003. arXiv: 0602035 [hep-ex] (cited on p. 5).

[51] G. W. Bennett et al. "Search for Lorentz and CPT Violation Effects in Muon Spin Precession". *Phys. Rev. Lett.*, **100** (2008), 091602. DOI: 10.1103/PhysRevLett.100.091602. arXiv: 0709.4670 [hep-ex] (cited on pp. 5, 115).

[52] C. Smorra et al. "A parts-per-billion measurement of the antiproton magnetic moment". *Nature*, **550** (2017), 371–374. DOI: 10.1038/nature24048 (cited on pp. 5–8, 27, 29, 95, 99, 102, 103, 115).

[53] Georg Schneider et al. "Double-trap measurement of the proton magnetic moment at 0.3 parts per billion precision". *Science*, **358** (2017), 1081–1084. DOI: 10.1126/science.aan0207 (cited on pp. 5, 6, 61, 62, 102, 115).

[54] S. Ulmer et al. "High-precision comparison of the antiproton-to-proton charge-to-mass ratio". *Nature*, **524** (2015), 196–199. DOI: 10.1038/nature14861 (cited on pp. 5–8, 29, 54, 56, 95, 106, 107, 110, 111).

[55] Christian G. Parthey et al. "Improved Measurement of the Hydrogen 1S–2S Transition Frequency". *Phys. Rev. Lett.*, **107** (2011), 203001. DOI: 10.1103/PhysRevLett.107.203001 (cited on pp. 5, 56).

[56] M. Ahmadi et al. "Characterization of the 1S–2S transition in antihydrogen". *Nature*, **557** (2018), 71–75. DOI: 10.1038/s41586-018-0017-2 (cited on p. 5).

[57] L. Essen et al. "Frequency of the Hydrogen Maser". *Nature*, **229** (1971), 110–111. DOI: 10.1038/229110a0 (cited on p. 5).

[58] M. Ahmadi et al. "Observation of the hyperfine spectrum of antihydrogen". *Nature*, **548** (2017), 66–69. DOI: 10.1038/nature23446 (cited on p. 5).

[59] E.G. Adelberger et al. "Torsion balance experiments: A low-energy frontier of particle physics". *Prog. Part. Nucl. Phys.*, **62** (2009), 102–134. DOI: 10.1016/j.ppnp.2008.08.002 (cited on p. 6).

[60] Michael Martin Nieto and T. Goldman. "The arguments against "antigravity" and the gravitational acceleration of antimatter". *Phys. Rep.*, **205** (1991), 221–281. DOI: 10.1016/0370-1573(91)90138-C (cited on p. 6).

[61] M. Villata. "CPT symmetry and antimatter gravity in general relativity". *EPL (Europhysics Lett.*, **94** (2011), 20001. DOI: 10.1209/0295-5075/94/20001 (cited on p. 6).

[62] Dragan Slavkov Hajdukovic. "Quantum vacuum and dark matter". *Astrophys. Space Sci.*, **337** (2012), 9–14. DOI: 10.1007/s10509-011-0938-9 (cited on p. 6).

[63] Aurélien Benoit-Lévy and Gabriel Chardin. "Introducing the Dirac-Milne universe". *Astron. Astrophys.*, **537** (2012), A78. DOI: 10.1051/0004-6361/201016103. arXiv: 1110.3054 (cited on p. 6).

[64] The ALPHA Collaboration and A. E. Charman. "Description and first application of a new technique to measure the gravitational mass of antihydrogen". *Nat. Commun.*, **4** (2013), 1785. DOI: 10.1038/ncomms2787 (cited on p. 6).

[65] W. A. Bertsche. "Prospects for comparison of matter and antimatter gravitation with ALPHA-g". *Philos. Trans. R. Soc. A Math. Phys. Eng. Sci.*, **376** (2018), 20170265. DOI: 10.1098/rsta.2017.0265 (cited on p. 6).

[66] R S Brusa et al. "The AEgIS experiment at CERN: measuring antihydrogen free-fall in earth's gravitational field to test WEP with antimatter". *J. Phys. Conf. Ser.*, **791** (2017), 012014. DOI: 10.1088/1742-6596/791/1/012014 (cited on p. 6).

[67] P. Pérez et al. "The GBAR antimatter gravity experiment". *Hyperfine Interact.*, **233** (2015), 21–27. DOI: 10.1007/s10751-015-1154-8 (cited on p. 6).

[68] S. Ulmer et al. *Letter of Intent to the CERN SPSC, Direct High-Precision Measurement of the g-Factor of a Single Antiproton Stored in a Cryogenic Penning Trap*. Tech. rep. Geneva: CERN, 2012, SPSC–2012–019; SPSC–I–241 (cited on p. 6).

[69] Lowell S. Brown and Gerald Gabrielse. "Geonium theory: Physics of a single electron or ion in a Penning trap". *Rev. Mod. Phys.*, **58** (1986), 233–311 (cited on pp. 6, 11, 28, 57, 58).

[70] H. Nagahama et al. "Sixfold improved single particle measurement of the magnetic moment of the antiproton". *Nat. Commun.*, **8** (2017), 14084. DOI: 10.1038/ncomms14084 (cited on pp. 6–8, 59, 60, 95–97, 102).

[71] S. Ulmer et al. "Observation of Spin Flips with a Single Trapped Proton". *Phys. Rev. Lett.*, **106** (2011), 253001. DOI: 10.1103/PhysRevLett.106.253001 (cited on pp. 6, 96).

[72] A. Mooser et al. "Direct high-precision measurement of the magnetic moment of the proton". *Nature*, **509** (2014), 596–599. DOI: 10.1038/nature13388 (cited on pp. 6, 97, 102, 103).

[73] M. Bohman et al. "Sympathetic cooling of protons and antiprotons with a common endcap Penning trap". *J. Mod. Opt.*, **65** (2018), 568–576. DOI: 10.1080/09500340.2017.1404656. arXiv: 1709.00433 (cited on pp. 6, 118).

[74] Teresa Meiners et al. "Towards Quantum Logic Inspired Cooling and Detection for Single (Anti-)Protons". *JPS Conf. Proc.*, **18** (2017), 011006. DOI: 10.7566/JPSCP.18.011006 (cited on p. 7).

[75] Takashi Higuchi. "High precision measurement of the cyclotron frequency of the single-trapped antiproton". Master's thesis. University of Tokyo, 2015 (cited on pp. 7, 140, 168).

[76] S. Sellner et al. "Improved limit on the directly measured antiproton lifetime". *New J. Phys.*, **19** (2017), 083023. DOI: 10.1088/1367-2630/aa7e73 (cited on pp. 7, 8, 78, 79, 95, 104, 105, 118).

[77] Andreas Mooser et al. "A Test of Charge-Parity-Time Invariance at the Atto-Electronvolt Scale". *JPS Conf. Proc.*, **18** (2017), 011019. DOI: 10.7566/JPSCP.18.011019 (cited on pp. 7, 56, 107, 108).

[78] Takashi Higuchi et al. "Progress towards an improved comparison of the proton-to-antiproton charge-to-mass ratios". *Hyperfine Interact.*, **239** (2018), 27. DOI: 10.1007/s10751-018-1499-x (cited on pp. 8, 235).

[79] James A. Harrington. *to be published*. 2019 (cited on pp. 8, 81, 86, 118, 208, 210, 216, 239).

[80] Hiroki Nagahama. "High-Precision Measurements of the Fundamental Properties of the Antiproton". Ph.D. thesis. University of Tokyo, 2017 (cited on pp. 9, 59, 60, 96, 115, 122, 125, 129).

[81] Toya Tanaka. "Development of tunable single particle detection system for an improved measurement of proton-to-antiproton charge-to-mass ratio". Master's thesis. University of Tokyo, 2017 (cited on pp. 9, 119, 122–124, 126–129).

[82] H. G. Dehmelt. "Radiofrequency Spectroscopy of Stored Ions I: Storage". *Adv. At. Mol. Opt. Phys.*, **3** (1968), 53–72. DOI: 10.1016/S0065-2199(08)60170-0 (cited on p. 11).

[83] H. G. Dehmelt. "Radiofrequency Spectroscopy of Stored Ions II: Spectroscopy". *Adv. At. Mol. Opt. Phys.*, **617** (1969), 109–154. DOI: 10.1016/S0065-2199(08)60156-6 (cited on p. 11).

[84] Klaus Blaum. "High-accuracy mass spectrometry with stored ions". *Phys. Rep.*, **425** (2006), 1–78. DOI: 10.1016/J.PHYSREP.2005.10.011 (cited on p. 11).

[85] Edmund G Myers. "The most precise atomic mass measurements in Penning traps". *Int. J. Mass Spectrom.*, **349-350** (2013), 107–122. DOI: 10.1016/j.ijms.2013.03.018 (cited on p. 11).

[86] S. Eliseev, T. Eronen, and Yu N. Novikov. "Penning-trap mass spectrometry for neutrino physics". *Int. J. Mass Spectrom.*, **349-350** (2013), 102–106. DOI: 10.1016/j.ijms.2013.03.010 (cited on p. 11).

[87] John David Jackson. *Classical electrodynamics*. Third Edit. New York: John Wiley & Sons, Inc., 1999 (cited on pp. 14, 21, 23, 260).

[88] Martin Kretzschmar. "Single particle motion in a Penning trap: description in the classical canonical formalism". *Phys. Scr.*, **46** (1992), 544–554. DOI: 10.1088/0031-8949/46/6/011 (cited on p. 15).

[89] J. J. Sakurai. *Modern Quantum Mechanics (Revised Edition)*. Addison Wesley, 1993 (cited on p. 17).

[90] Lowell S. Brown and Gerald Gabrielse. "Precision spectroscopy of a charged particle in an imperfect Penning trap". *Phys. Rev. A*, **25** (1982), 2423–2425. DOI: 10.1103/PhysRevA.25.2423 (cited on pp. 18, 112, 219).

[91] G. Gabrielse, L. Haarsma, and S. L. Rolston. "Open-endcap Penning traps for high precision experiments". *Int. J. Mass Spectrom. Ion Process.*, **88** (1989), 319–332. DOI: 10.1016/0168-1176(89)85027-X (cited on pp. 19, 23, 80).

[92] Georg Schneider. "Development of a Penning trap system for the high precision measurement of the antiproton's magnetic moement". Master's thesis. Johannes Gutenberg-Universität Mainz, 2014 (cited on pp. 23, 57, 69, 80, 92).

[93] L. D. Landau and E. M. Lifshitz. *Mechanics*. 3rd ed. Butterworth-Heinemann, 1982 (cited on pp. 25, 45).

[94] Jochen Ketter et al. "First-order perturbative calculation of the frequency-shifts caused by static cylindrically-symmetric electric and magnetic imperfections of a Penning trap". *Int. J. Mass Spectrom.*, **358** (2014), 1–16. DOI: 10.1016/j.ijms.2013.10.005 (cited on pp. 26, 28).

[95] Jochen Ketter et al. "Classical calculation of relativistic frequency-shifts in an ideal Penning trap". *Int. J. Mass Spectrom.*, **361** (2014), 34–40. DOI: 10.1016/j.ijms.2014.01.028 (cited on p. 28).

[96] J. V. Porto. "Series solution for the image charge fields in arbitrary cylindrically symmetric Penning traps". *Phys. Rev. A*, **64** (2001), 023403. DOI: 10.1103/PhysRevA.64.023403 (cited on p. 28).

[97] Vasant Natarajan. "Penning Trap Mass Spectroscopy at 0 .1 ppb". Ph.D. thesis. Massachusetts Institute Of Technology, 1993 (cited on p. 29).

[98] Martín Lara and J. Pablo Salas. "Dynamics of a single ion in a perturbed Penning trap: Octupolar perturbation". *Chaos An Interdiscip. J. Nonlinear Sci.*, **14** (2004), 763–773. DOI: 10.1063/1.1775331 (cited on p. 29).

[99] D. J. Wineland and H. G. Dehmelt. "Principles of the stored ion calorimeter". *J. Appl. Phys.*, **46** (1975), 919–930. DOI: 10.1063/1.321602 (cited on p. 30).

[100] W. Shockley. "Currents to Conductors Induced by a Moving Point Charge". *J. Appl. Phys.*, **9** (1938), 635–636. DOI: 10.1063/1.1710367 (cited on p. 30).

[101] Stefan Ulmer. "First Observation of of Spin Flips with a Single Proton Stored in a Cryogenic Penning Trap". Ph.D. thesis. Ruperto-Carola University of Heidelberg, 2011 (cited on pp. 31, 122).

[102] Sven Sturm. "The g-factor of the electron bound in $^{28}Si^{13+}$: The most stringent test of bound-state quantum electrodynamics". PhD thesis. Johannes Gutenberg-Universität Mainz, 2012 (cited on p. 31).

[103] J. B. Johnson. "Thermal Agitation of Electricity in Conductors". *Phys. Rev.*, **32** (1928), 97–109. DOI: 10.1103/PhysRev.32.97 (cited on p. 33).

[104] H. Nyquist. "Thermal Agitation of Electric Charge in Conductors". *Phys. Rev.*, **32** (1928), 110–113. DOI: 10.1103/PhysRev.32.110 (cited on p. 33).

[105] B. D'Urso, B. Odom, and G. Gabrielse. "Feedback Cooling of a One-Electron Oscillator". *Phys. Rev. Lett.*, **90** (2003), 043001. DOI: 10.1103/PhysRevLett.90.043001 (cited on pp. 37, 87).

[106] Eric A. Cornell et al. "Mode coupling in a Penning trap: π pulses and a classical avoided crossing". *Phys. Rev. A*, **41** (1990), 312–315. DOI: 10.1103/PhysRevA.41.312 (cited on pp. 39, 45, 220).

[107] Claude Cohen-Tannoudji, Bernard Diu, and Frank Laloe. *Quantum Mechanics*. New York: Wiley, 1977 (cited on p. 42).

[108] J. Dalibard and C. Cohen-Tannoudji. "Dressed-atom approach to atomic motion in laser light: the dipole force revisited". *J. Opt. Soc. Am. B*, **2** (1985), 1707. DOI: 10.1364/JOSAB.2.001707 (cited on p. 42).

[109] D. W. Allan. "Statistics of atomic frequency standards". *Proc. IEEE*, **54** (1966), 221–230. DOI: 10.1109/PROC.1966.4634 (cited on p. 49).

[110] W. J. Riley. *Handbook of Frequency Stability Analysis*. NIST special publication. U.S. Department of Commerce, National Institute of Standards and Technology, 2008, pp. –136 (cited on p. 50).

[111] L. S. Cutler and C. L. Searle. "Some aspects of the theory and measurement of frequency fluctuations in frequency standards". *Proc. IEEE*, **54** (1966), 136–154. DOI: 10.1109/PROC.1966.4627 (cited on p. 51).

[112] James A. Barnes et al. "Characterization of Frequency Stability". *IEEE Trans. Instrum. Meas.*, **IM-20** (1971), 105–120. DOI: 10.1109/TIM.1971.5570702 (cited on p. 51).

[113] Simon Rainville, James K. Thompson, and David E. Pritchard. "An Ion Balance for Ultra-High-Precision Atomic Mass Measurements". *Science*, **303** (2004), 334–338. DOI: 10.1126/science.1092320 (cited on p. 53).

[114] G. Gabrielse et al. "Precision Mass Spectroscopy of the Antiproton and Proton Using Simultaneously Trapped Particles". *Phys. Rev. Lett.*, **82** (1999), 3198–3201. DOI: 10.1103/PhysRevLett.82.3198 (cited on pp. 54, 108, 114, 140).

[115] E. G. Myers et al. "Atomic Masses of Tritium and Helium-3". *Phys. Rev. Lett.*, **114** (2015), 013003. DOI: 10.1103/PhysRevLett.114.013003 (cited on p. 54).

[116] G. Gabrielse et al. "Special Relativity and the Single Antiproton: Fortyfold Improved Comparison of $\bar{p}$ and p Charge-to-Mass Ratios". *Phys. Rev. Lett.*, **74** (1995), 3544–3547. DOI: 10.1103/PhysRevLett.74.3544 (cited on pp. 54, 140).

[117] Georg Schneider. "300 ppt Measurement of the Proton g-Factor". Ph.D. thesis. Johannes Gutenberg-Universität, 2017 (cited on pp. 54, 115).

[118] James K. Thompson, Simon Rainville, and David E. Pritchard. "Cyclotron frequency shifts arising from polarization forces". *Nature*, **430** (2004), 58–61. DOI: 10.1038/nature02682 (cited on pp. 55, 56).

[119] F. Heiße et al. "High-Precision Measurement of the Proton's Atomic Mass". *Phys. Rev. Lett.*, **119** (2017), 033001. DOI: 10.1103/PhysRevLett.119.033001. arXiv: 1706.06780 (cited on p. 56).

[120] Robert S. Van Dyck et al. "High precision Penning trap mass spectroscopy and a new measurement of the proton's "atomic mass"". *AIP Conf. Proc.*, **101** (1999), 101–110. DOI: 10.1063/1.57450 (cited on p. 56).

[121] K R Lykke, K K Murray, and W C Lineberger. "Threshold photodetachment of H^-". *Phys. Rev. A*, **43** (1991), 6104–6107. DOI: 10.1103/PhysRevA.43.6104 (cited on p. 56).

[122] A. K. Bhatia and R. J. Drachman. "Polarizability of helium and the negative hydrogen ion". *J. Phys. B At. Mol. Opt. Phys.*, **27** (1994), 1299–1305. DOI: 10.1088/0953-4075/27/7/005 (cited on p. 56).

[123] Hans Dehmelt. "Continuous Stern-Gerlach effect: Principle and idealized apparatus." *Proc. Natl. Acad. Sci. U. S. A.*, **83** (1986), 2291–2294. DOI: 10.1073/pnas.83.8.2291 (cited on pp. 57, 58).

[124] David Andrew Hanneke. "Cavity Control in a Single-Electron Quantum Cyclotron : An Improved Measurement of the Electron Magnetic Moment". Ph.D. thesis. Harvard University, 2007 (cited on p. 58).

[125] T. A. Savard, K. M. O'Hara, and J. E. Thomas. "Laser-noise-induced heating in far-off resonance optical traps". *Phys. Rev. A*, **56** (1997), R1095–R1098. DOI: 10.1103/PhysRevA.56.R1095 (cited on p. 59).

[126] A. Mooser et al. "Demonstration of the double Penning Trap technique with a single proton". *Phys. Lett. B*, **723** (2013), 78–81. DOI: 10.1016/j.physletb.2013.05.012. arXiv: 1305.1362 (cited on p. 59).

[127] J. DiSciacca and G. Gabrielse. "Direct Measurement of the Proton Magnetic Moment". *Phys. Rev. Lett.*, **108** (2012), 153001. DOI: 10.1103/PhysRevLett.108.153001. arXiv: 1201.3038 (cited on pp. 60, 102).

[128] C. C. Rodegheri et al. "An experiment for the direct determination of the g-factor of a single proton in a Penning trap". *New J. Phys.*, **14** (2012), 063011. DOI: 10.1088/1367-2630/14/6/063011 (cited on p. 60).

[129] H. Häffner et al. "Double Penning trap technique for precise g factor determinations in highly charged ions". *Eur. Phys. J. D*, **22** (2003), 163–182. DOI: 10.1140/epjd/e2003-00012-2 (cited on p. 60).

[130] S. Baird et al. "The Antiproton Decelerator: AD". *Nucl. Instruments Methods Phys. Res. Sect. A Accel. Spectrometers, Detect. Assoc. Equip.*, **391** (1997), 210–215. DOI: 10.1016/S0168-9002(97)00359-8 (cited on p. 65).

[131] S. Maury. "The Antiproton Decelerator: AD". *Hyperfine Interact.*, **109** (1997), 43–52. DOI: 10.1023/A:1012632812327 (cited on p. 65).

[132] S. van der Meer. "Stochastic cooling and the accumulation of antiprotons". *Rev. Mod. Phys.*, **57** (1985), 689–697. DOI: 10.1103/RevModPhys.57.689 (cited on p. 65).

[133] G. I. Budker and A. N. Skrinskiĭ. "Electron cooling and new possibilities in elementary particle physics". *Sov. Phys. Uspekhi*, **21** (1978), 277–296. DOI: 10.1070/PU1978v021n04ABEH005537 (cited on p. 65).

[134] Walter Oelert. "The ELENA Project at CERN". *Acta Phys. Pol. B*, **48** (2017), 1895. DOI: 10.5506/APhysPolB.48.1895 (cited on p. 68).

[135] Natalie Schön. "Optimizing catching efficiencies of antiprotons in a Penning trap and Developments towards resonant coupling of single protons and laser cooled beryllium ions". Master's thesis. Johannes-Gutenberg-Universität Mainz, 2018 (cited on pp. 78, 193, 194, 200).

[136] H. Nagahama et al. "Highly sensitive superconducting circuits at 700 kHz with tunable quality factors for image-current detection of single trapped antiprotons". *Rev. Sci. Instrum.*, **87** (2016), 113305. DOI: 10.1063/1.4967493 (cited on pp. 86, 122, 123).

[137] S. Ulmer et al. "A cryogenic detection system at 28.9 MHz for the non-destructive observation of a single proton at low particle energy". *Nucl. Instruments Methods Phys. Res. Sect. A Accel. Spectrometers, Detect. Assoc. Equip.*, **705** (2012), 55–60. DOI: 10.1016/J.NIMA.2012.12.071 (cited on pp. 86, 127).

[138] C. Smorra et al. "Towards a high-precision measurement of the antiproton magnetic moment". *Hyperfine Interact.*, **228** (2014), 31–36. DOI: 10.1007/s10751-014-1018-7 (cited on p. 86).

[139] Mustafa Beşirli. "Development of Single Sideband Down Converters for Precise Measurements of the Axial Frequency of a Single Trapped Antiproton". Bachelor's thesis. Sabanci University, 2016 (cited on p. 87).

[140] S. Ulmer et al. "The magnetic moments of the proton and the antiproton". *J. Phys. Conf. Ser.*, **488** (2014), 012033. DOI: 10.1088/1742-6596/488/1/012033 (cited on p. 91).

[141] Cody H. Storry. "ATRAP antihydrogen experiments and update". *Hyperfine Interact.*, **172** (2006), 91–96. DOI: 10.1007/s10751-007-9528-1 (cited on p. 91).

[142] D. Krasnický et al. "AEgIS experiment commissioning at CERN". *AIP Conf. Proc.*, **1521** (2013), 144–153. DOI: 10.1063/1.4796070 (cited on p. 91).

[143] C. Amole et al. "The ALPHA antihydrogen trapping apparatus". *Nucl. Instruments Methods Phys. Res. Sect. A Accel. Spectrometers, Detect. Assoc. Equip.*, **735** (2014), 319–340. DOI: 10.1016/j.nima.2013.09.043 (cited on pp. 91, 118).

[144] C. Smorra et al. "Observation of individual spin quantum transitions of a single antiproton". *Phys. Lett. B*, **769** (2017), 1–6. DOI: 10.1016/j.physletb.2017.03.024 (cited on pp. 98, 100).

[145] Lowell S. Brown. "Geonium Lineshape". *Ann. Phys.*, **159** (1985), 62–98 (cited on p. 102).

[146] C. Smorra et al. "A reservoir trap for antiprotons". *Int. J. Mass Spectrom.*, **389** (2015), 10–13. DOI: 10.1016/j.ijms.2015.08.007. arXiv: 1507.04147 (cited on pp. 104, 105, 193, 194, 201, 202).

[147] G. Gabrielse et al. "Thousandfold improvement in the measured antiproton mass". *Phys. Rev. Lett.*, **65** (1990), 1317–1320. DOI: 10.1103/PhysRevLett.65.1317 (cited on pp. 105, 115, 140).

[148] L. Bracci, G. Fiorentini, and O. Pitzurra. "Protonium formation in flight". *Phys. Lett. B*, **85** (1979), 280–284. DOI: 10.1016/0370-2693(79)90597-5 (cited on p. 105).

[149] James S. Cohen. "Capture of antiprotons by some radioactive atoms and ions". *Phys. Rev. A - At. Mol. Opt. Phys.*, **69** (2004), 9. DOI: 10.1103/PhysRevA.69.022501 (cited on p. 105).

[150] Kazuhiro Sakimoto. "Full quantum-mechanical study of protonium formation in slow collisions of antiprotons with hydrogen atoms". *Phys. Rev. A - At. Mol. Opt. Phys.*, **65** (2002), 12. DOI: 10.1103/PhysRevA.65.012706 (cited on p. 105).

[151] Don Colladay and V. Alan Kostelecký. "*CPT* violation and the standard model". *Phys. Rev. D*, **55** (1997), 6760–6774. DOI: 10.1103/PhysRevD.55.6760. arXiv: 9703464 [hep-ph] (cited on p. 114).

[152] D. Colladay and V. Alan Kostelecký. "Lorentz-violating extension of the standard model". *Phys. Rev. D*, **58** (1998). DOI: 10.1103/physrevd.58.116002 (cited on p. 114).

[153] V. Alan Kostelecký and Stuart Samuel. "Spontaneous breaking of Lorentz symmetry in string theory". *Phys. Rev. D*, **39** (1989), 683–685. DOI: 10.1103/physrevd.39.683 (cited on p. 114).

[154] V. Alan Kostelecký. "Gravity, Lorentz violation, and the standard model". *Phys. Rev. D*, **69** (2004), 105009. DOI: 10.1103/PhysRevD.69.105009 (cited on p. 114).

[155] O. W. Greenberg. "CPT Violation Implies Violation of Lorentz Invariance". *Phys. Rev. Lett.*, **89** (2002), 231602. DOI: 10.1103/PhysRevLett.89.231602 (cited on p. 114).

[156] Alan Kostelecky and Neil Russell. "Data Tables for Lorentz and CPT Violation". *Rev. Mod. Phys.*, **83** (2008), 11–31. DOI: 10.1103/RevModPhys.83.11. arXiv: 0801.0287 (cited on p. 114).

[157] Yunhua Ding and V. Alan Kostelecký. "Lorentz-violating spinor electrodynamics and Penning traps". *Phys. Rev. D*, **94** (2016), 056008. DOI: 10.1103/PhysRevD.94.056008. arXiv: 1608.07868 (cited on pp. 114, 115).

[158] R. K. Mittleman et al. "Bound on CPT and Lorentz Symmetry with a Trapped Electron". *Phys. Rev. Lett.*, **83** (1999), 2116–2119. DOI: 10.1103/PhysRevLett.83.2116 (cited on p. 115).

[159] Jogesh C. Pati and Abdus Salam. "Unified Lepton-Hadron Symmetry and a Gauge Theory of the Basic Interactions". *Phys. Rev. D*, **8** (1973), 1240–1251. DOI: 10.1103/PhysRevD.8.1240 (cited on p. 115).

[160] Jogesh C. Pati and Abdus Salam. "Is Baryon Number Conserved?" *Phys. Rev. Lett.*, **31** (1973), 661–664. DOI: 10.1103/PhysRevLett.31.661 (cited on p. 115).

[161] Howard Georgi and S. L. Glashow. "Unity of All Elementary-Particle Forces". *Phys. Rev. Lett.*, **32** (1974), 438–441. DOI: 10.1103/PhysRevLett.32.438 (cited on p. 115).

[162] S. N. Ahmed et al. "Constraints on Nucleon Decay via Invisible Modes from the Sudbury Neutrino Observatory". *Phys. Rev. Lett.*, **92** (2004), 102004. DOI: 10.1103/PhysRevLett.92.102004. arXiv: arXiv:1309.1338v1 (cited on p. 115).

[163] K. Abe et al. "Search for proton decay via $p \to e^+\pi_0$ and $p \to \mu^+\pi_0$". *Phys. Rev. D*, **95** (2017), 012004. DOI: 10.1103/PhysRevD.95.012004 (cited on p. 115).

[164] Stephen H. Geer and Dallas C. Kennedy. "A New Limit on the Antiproton Lifetime". *Astrophys. J.*, **532** (2000), 648–652 (cited on p. 115).

[165] S. Geer et al. "New Limit on CPT Violation". *Phys. Rev. Lett.*, **84** (2000), 590–593. DOI: 10.1103/PhysRevLett.84.590 (cited on p. 115).

[166] K. Kobayashi et al. "Search for nucleon decay via modes favored by supersymmetric grand unification models in Super-Kamiokande-I". *Phys. Rev. D*, **72** (2005), 052007. DOI: 10.1103/PhysRevD.72.052007 (cited on p. 116).

[167] D.J. Thomson. "Spectrum estimation and harmonic analysis". *Proc. IEEE*, **70** (1982), 1055–1096. DOI: 10.1109/PROC.1982.12433 (cited on p. 116).

[168] S. Ulmer et al. "Challenging the standard model by high-precision comparisons of the fundamental properties of protons and antiprotons". *Philos. Trans. R. Soc. A Math. Phys. Eng. Sci.*, **376** (2018). DOI: 10.1098/rsta.2017.0275 (cited on p. 116).

[169] R. F. C. Vessot et al. "Test of Relativistic Gravitation with a Space-Borne Hydrogen Maser". *Phys. Rev. Lett.*, **45** (1980), 2081–2084. DOI: 10.1103/PhysRevLett.45.2081 (cited on p. 117).

[170] Holger Müller, Achim Peters, and Steven Chu. "A precision measurement of the gravitational redshift by the interference of matter waves". *Nature*, **463** (2010), 926–929. DOI: 10.1038/nature08776. arXiv: arXiv:0901.2377v3 (cited on p. 117).

[171] Tetsushi Takano et al. "Geopotential measurements with synchronously linked optical lattice clocks". *Nat. Photonics*, **10** (2016), 662–666. DOI: 10.1038/nphoton.2016.159 (cited on p. 117).

[172] Neil Ashby. "Relativity in the Global Positioning System". *Living Rev. Relativ.*, **6** (2003), 1. DOI: 10.12942/lrr-2003-1 (cited on p. 117).

[173] Richard J. Hughes and Michael H. Holzscheiter. "Constraints on the gravitational properties of antiprotons and positrons from cyclotron-frequency measurements". *Phys. Rev. Lett.*, **66** (1991), 854–857. DOI: 10.1103/PhysRevLett.66.854 (cited on p. 117).

[174] Myron L. Good. "${K_2}^0$ and the Equivalence Principle". *Phys. Rev.*, **121** (1961), 311–313. DOI: 10.1103/PhysRev.121.311 (cited on p. 117).

[175] I.R. Kenyon. "A recalculation on the gravitational mass difference between the K^0 and $\overline{K}^0$ mesons". *Phys. Lett. B*, **237** (1990), 274–277. DOI: 10.1016/0370-2693(90)91443-F (cited on p. 117).

[176] G. Gabrielse et al. "Stacking of cold antiprotons". *Phys. Lett. B*, **548** (2002), 140–145. DOI: 10.1016/S0370-2693(02)02850-2 (cited on p. 118).

[177] S. Ulmer et al. "The quality factor of a superconducting rf resonator in a magnetic field". *Rev. Sci. Instrum.*, **80** (2009), 123302. DOI: 10.1063/1.3271537 (cited on pp. 122, 127).

[178] Crícia de Carvalho Rodegheri. "Neuartige kryogene Penning-Falle für den Nachweis von Spin-Übergängen eines Protons und Bestimmung seines g-Faktors". Ph.D. thesis. Johannes Gutenberg-Universität Mainz, 2013 (cited on p. 127).

[179] V. Mitin, L. Reggiani, and L. Varani. "Generation-Recombination Noise in Semiconductors". *Noise and Fluctuations Control in Electronic Devices*. Ed. by Alexander A. Balandin. American Scientific Publisher, 2002 (cited on p. 128).

[180] Andreas G. Andreou. "In-Situ Characterization of Carrier Mobility in Field Effect Transistors". *Review of Progress in Quantitative Nondestructive Evaluation*. Boston, MA: Springer US, 1989, pp. 1247–1254. DOI: 10.1007/978-1-4613-0817-1_156 (cited on p. 138).

[181] B.O. Onodipe and M.G. Guvench. "Transverse magnetic field effects on GaAs MESFETs: analytical model and experiments". *Proceedings., Eighth Biennial University/Government/Industry Microelectronics Symposium*. IEEE, 1989, 215–218. DOI: 10.1109/UGIM.1989.37338 (cited on p. 138).

[182] G. Gabrielse and J. Tan. "Self-shielding superconducting solenoid systems". *J. Appl. Phys.*, **63** (1988), 5143–5148. DOI: 10.1063/1.340416 (cited on pp. 140, 141, 157).

[183] G. Gabrielse et al. "A Superconducting Solenoid Systen Which Cancels Fluctuations in the Ambient Magnetic Field". *J. Magn. Reson.*, **91** (1991), 564–572 (cited on pp. 140, 157).

[184] Kurt Fischer. *private communication*. 2017 (cited on p. 143).

[185] Anke A. Wagner. "The g-factor of the valence electron bound in lithiumlike silicon $^{28}Si^{11+}$". Ph.D. thesis. Ruperto-Carola University of Heidelberg, 2013 (cited on pp. 144, 148).

[186] Peter Koß. "Eine passive Magnetfeldstabilisierung zur Erhöhung der Präzision der g-Faktor-Messung an einem einzelnen in einer Penning-Falle gespeicherten Proton". Master's thesis. Johannes Gutenberg-Universität Mainz, 2014 (cited on pp. 144, 148).

[187] Mickaël Sebastien Meyer. *Metallurgy Report: Welded connection of Superconducting coil*. Tech. rep. CERN, 2017, EDMS 1811635 (cited on p. 163).

[188] Thomas Arne Hensel. *DAAD-Internship report at BASE, CERN*. Tech. rep. 2017 (cited on p. 163).

[189] NVE corporation. *AA/AB-Series Analog Magnetic Sensors*. URL: https://www.nve.com/Downloads/analog_catalog.pdf (visited on 10/09/2018) (cited on pp. 173, 174).

[190] Edward Ramsden. *Hall-Effect Sensors*. 2nd ed. Elsevier, 2006. DOI: 10.1016/B978-0-7506-7934-3.X5000-5 (cited on p. 174).

[191] Candid Reig, Susana Cardoso, and Subhas Chandra Mukhopadhyay. *Giant Magnetoresistance (GMR) Sensors*. Vol. 6. Smart Sensors, Measurement and Instrumentation. Berlin, Heidelberg: Springer Berlin Heidelberg, 2013. DOI: 10.1007/978-3-642-37172-1 (cited on p. 174).

[192] Stefan Mayer Instruments. *Magnetic Field Sensor FLC3-70*. URL: http://www.tecit.com.tw/DM/DatasheetFLC3-70.pdf (visited on 10/15/2018) (cited on p. 174).

[193] G. Gabrielse et al. "First Capture of Antiprotons in a Penning Trap: A Kiloelectronvolt Source". *Phys. Rev. Lett.*, **57** (1986), 2504–2507. DOI: 10.1103/PhysRevLett.57.2504 (cited on p. 193).

[194] G. Gabrielse et al. “Barkas effect with use of antiprotons and protons”. *Phys. Rev. A*, **40** (1989), 481–484. DOI: 10.1103/PhysRevA.40.481 (cited on pp. 193, 194).

[195] G. Gabrielse et al. “Cooling and Slowing of Trapped Antiprotons below 100 meV”. *Phys. Rev. Lett.*, **63** (1989), 1360–1363. DOI: 10.1103/PhysRevLett.63.1360 (cited on pp. 193, 198).

[196] S. L. Rolston and G. Gabrielse. “Cooling antiprotons in an ion trap”. *Hyperfine Interact.*, **44** (1989), 233–245. DOI: 10.1007/BF02398673 (cited on pp. 193, 194).

[197] M. H. Holzscheiter. “Slowing down and trapping of MeV antiprotons”. *Phys. Scr.*, **46** (1992), 272–277. DOI: 10.1088/0031-8949/46/3/011 (cited on p. 193).

[198] B. R. Beck, J. Fajans, and J. H. Malmberg. “Temperature and anisotropic-temperature relaxation measurements in cold, pure-electron plasmas”. *Phys. Plasmas*, **3** (1996), 1250–1258. DOI: 10.1063/1.871749 (cited on p. 194).

[199] Meng Wang et al. “The AME2016 atomic mass evaluation (II). Tables, graphs and references”. *Chinese Phys. C*, **41** (2017), 030003. DOI: 10.1088/1674-1137/41/3/030003 (cited on p. 196).

[200] Shenheng Guan and Alan G. Marshall. “Stored waveform inverse Fourier transform (SWIFT) ion excitation in trapped-ion mass spectometry: Theory and applications”. *Int. J. Mass Spectrom. Ion Process.*, **157-158** (1996), 5–37. DOI: 10.1016/S0168-1176(96)04461-8 (cited on p. 196).

[201] Eric A. Cornell et al. “Two ions in a Penning trap: Implications for precision mass spectroscopy”. *Phys. Rev. A*, **45** (1992), 3049–3059. DOI: 10.1103/PhysRevA.45.3049 (cited on p. 205).

[202] Martin Jürgen Höcker. “Precision Mass Measurements at THe-Trap and the FSU trap”. Ph.D. thesis. Ruperto-Carola-University of Heidelberg, 2016 (cited on p. 205).

[203] H. Julian Goldsmid. “The Thermoelectric and Related Effects”. *Introduction to Thermoelectricity*. Springer-Verlag Berlin Heidelberg, 2016, pp. 1–7. DOI: 10.1007/978-3-662-49256-7_1 (cited on p. 223).

[204] Kurt Alan Franke. *unpublished* (cited on p. 227).

Acknowledgements

Here I would like to express my appreciation to those who supported me, from the beginning of my works in BASE until the completion of this thesis.

Firstly, I would like to deeply thank Prof. Yasuyuki Matsuda, who has given me the opportunity to work on this project. Over the last years, he has given me advice and encouragements at times in need. Especially, writing of the thesis has been only possible with his strong support through valuable discussions and encouraging words.

I would like to express my wholehearted thankfulness to Dr. Stefan Ulmer, the spokesperson of the BASE collaboration, who has supervised me through the entire period of my time at CERN. I thank him for giving me a role to play in the collaboration, and particularly for allowing me to be involved in the 2017 run.

I am deeply indebted to each of the core members of the BASE team at CERN. Among them, I would first like to thank Mr. James A. Harrington, who has made incomparable efforts and sacrifice for the experiment in 2017. It would not have been done without him. I thank him also for days and nights we spent in the zone, and for having patiently born my inadequacies in collaborative works. Dr. Christian Smorra and Dr. Stefan Sellner have been great examples of experienced physicists. Dr. Smorra has taught me a lot about data analysis, and often consulted me with my questions and problems. He also helped me for the thesis with his careful proofreading. Dr. Sellner has instructed me `python`, server management, and many other aspects of research. His positive and friendly personality made these discussions always enjoyable. Dr. Hiroki Nagahama has been my good adviser since the time I decided to join BASE. I thank his kind guidance and warm fellowship. I thank Mr. Matthias J. Borchert, whom I shared time since I joined BASE in 2014. During the 2017 run, he gladly helped me with some measurements, most of which have become an important part of the thesis. I thank Mr. Jonathan Morgner, for memorable times I spent with him and his practical help in installing accelerometers. I would also like to thank newer members of the team who joined after my leave. Among them, Dr. Jack A. Devlin and Dr. Elise Wursten have helped me when I needed to access data and devices at CERN when I was in Japan.

I gratefully acknowledge Mr. Toya Tanaka, who has made an important work on the tunable detection system, which is now fully operational in the experiment. He helped me also by looking up his notes when I needed more detailed information from his thesis. I thank Mr. Mustafa Beşirli for his ingenious works on electronics for the experiment and having been my good office mate. I thank Mr. Kurt A. Franke, on whose works most of our data analysis is based. I would like to thank him also for having introduced me to work on sensor communications and with `LabVIEW`. Dr. Simon Van

Gorp helped me adapt to the group when I started at BASE by introducing to me the lab works, and have always been an encouraging mate. He has also introduced me to `simbuca`[1] simulation.

I thank all the summer students and internship students on BASE in these years, with whom I shared joys and hardnesses of experiments. Among them, I would like to particularly thank Thomas Arne Hensel for his important contribution on welding of superconducting joints, and showing me his faithful attitude.

Among the Mainz group of BASE, Ms. Natalie Schön visited CERN during the 2017 run to make great contributions to beam-time operations. She also provided me with some data which was necessary to write the chapter of the reservoir trap. I sincerely acknowledge Dr. Georg L. Schneider, who has been a fellow Ph.D. student of BASE. He has helped me through helpful advice and comments on problems on data analysis which I faced, and by providing me beautiful figures. Dr. Andreas H. Mooser had taken great care of me at my earlier time in BASE. He also kindly offered help in proofreading a part of this thesis. My thanks extend to the rest of the BASE collaboration, who make this project possible.

I truly enjoyed working in a community surrounding the AD, and am glad to have been its part. Dr. Stefan Heider introduced to me the delivery system of liquid nitrogen when I was not familiar to it. Dr. Pierre Dupré consulted me on many occasions on simulations and helped me to learn `C++`. Mr. Olivier Choisnet generously provided me with some very useful images of the AD, even recreating an image upon my particular requests. Mr. Pierre Freyermuth helped me by letting me compare the temperature data with his log. Mr. Bertrand Lefort helped me finding these contacts. Dr. Christian Carli and Mr. Sergio Pasinelli helped me by providing information about the ELENA operation. I thank all the other friends from other experiments with whom I had a good fellowship and stimulating discussions.

I am also grateful for experts and engineers who have given me immense help on different occasions with their skills and in their professionalism. Many thanks to the CERN cryolab team and Dr. Henric Wilkens, for always reserving helium delivery to BASE and arranging special supplies for the end of years so that we can survive shutdowns. Ms. Laetitia Dufay-Chanat and Mr. Sébastien Prunet gave us generous help in repairing liquid nitrogen dewars. I would like to say my personal thanks to Mr. Jean-Claude Carrere.

Mr. Julian Perret and Mr. Laurent Prever-Loiri from CERN workshop helped us by making resistance welding for self-shielding coils. I thank their reliable works and having arranged the urgent jobs to be in time for the cool down of the experiment. Mr. Mickaël S. Meyer has given me important information on the superconducting joints by acquiring their microscopy images.

I thank Mr. Azelarab El Hajri. and Mr. Benjamin Schaller from PanGas AG for their always reliable liquid nitrogen delivery. I cordially thank Mme. Joelle Donche for her immense help in communicating with the suppliers and having rescued us from a few nitrogen crises.

[1] https://sourceforge.net/projects/simbuca/

Mr. Julian Maciejewski has been a very helpful advisor about the SQL and the Data Control System, and has also been my good friend.

I thank Dr. Sven Friedel for his assistance in COMSOL simulations, who has always given me the exact advice that I need and rapidly answered my questions.

Prof. Kurt Fischer (National Institute of Technology, Tokuyama College) has greatly helped me with calculations related to the self-shielding solenoids. I appreciate professionalism and insight in his theoretical works. The collaboration with him has truly inspired me.

I sincerely thank Mr. Masatomi Iizawa from Rikkyo University for his advice and help on some calculations of Chapter 2.

I thank members of Matsuda group of the University of Tokyo, former and present. I love an open and relaxed atmosphere of the group, and remember enjoyable discussions on many occasions. I thank Prof. Emeritus. Yasunori Yamazaki for his warm encouragements and giving me insightful comments on my analysis problems. Prof. Hiroyuki A. Torii has given me helpful advice on theoretical details and on scientific writing. He has also given me useful tips for life at CERN and in France. It was Dr. Naofumi Kuroda who first introduced me to the antiproton experiments and its history when I was a master's student. On numerous occasions during my writing, he has helped me by pointing me to the right references. I admire his lifelong dedication to antiproton/antihydrogen physics. I thank the students and the graduates of the group, with each of whom I shared nice time and good fellowship: Dr. Kazuo Tanaka, Ms. Miki Ohtsuka, Mr. Satoshi Takaki, Mr. Takehiro Mizutani, Mr. Shoichiro Ishikawa, Mr. Yoshitaka Higashi, Mr. Takuya Matsudate, Dr. Hiroki Nagahama, Dr. Minori Tajima, Mr. Daisuke Yagi, Mr. Tatsuhito Kobayashi, Mr. Yasuhiro Ueno, Mr. Toya Tanaka, Mr. Shun Seo, Mr. Markus Fleck, and Mr. Ryoma Nishi. Particularly, I thank Mr. Ueno for often being a discussion partner, Mr. Markus Fleck for a lot of help with TEX, and Mr. Seo for helping me printing out and binding this thesis on submission.

I would like to thank Ms. Ulla Tihinen for her help in all the administrative works at CERN, especially on visa application. I am also thankful for the administrative assurances of Ms. Chikako Kuramochi, Ms. Hitomi Wada and Ms. Megumi Morita from RIKEN, who also taught me tremendously how to deal with administrative works needed in research. I also thank Dr. Yasuyuki Kanai, who gave me helpful advice in future directions and encouraging words over the writing period.

Some friends offered help to improve English of the text. I would like to thank Ms. Christine T. Nguyen, Ms. Rhea Moutafis and Dr. Carlan Wendler and Mr. Ash Curkpatrick in this regard, especially to Ms. Nguyen for patiently bearing my persistent questions.

I gratefully acknowledge financial support by RIKEN Junior Research Associate program (from April 2015 to March 2018) and by RIKEN Ulmer Fundamental Symmetries Laboratory (from April 2018 to December 2018).

I want to thank everyone who has encouraged me, advised me, and prayed for me, over the course of this path. Although I cannot list you all here, I remember each of you with gratitude, thank you.

I am thankful for continuous love and support from my family. I totally owe my parents in education which I was granted in my childhood. After growing up, they gladly allowed me to pursuit my study. My sister and my brother have helped me in many practical ways. Particularly, my brother Hiroshi Higuchi has helped me by verifying some calculations. I would also like to thank my extended family, especially my grandmother who seriously cared for me and whether I could finish the study.

Finally, I thank my Lord, who is my hope and my sustenance.

By the word of the Lord the heavens were made,
and by the breath of his mouth all their host.
He gathers the waters of the sea as a heap;
He puts the deeps in storehouses.
Let all the earth fear the LORD;
let all the inhabitants of the world stand in awe of Him!
For He speaks, and it came to be;
He commanded, and it stood firm.

Psalm 33:6–7, the Holy Bible[2]

Soli Deo Gloria.

February 13, 2019
Takashi Higuchi

[2]The Holy Bible, English Standard Version ©2001 Crossway